

THERAPEUTIC APPLICATIONS OF MONTE CARLO CALCULATIONS IN NUCLEAR MEDICINE

Series in Medical Physics and Biomedical Engineering

Series Editors:

C G Orton, Karmanos Cancer Institute and Wayne State University, Detroit, USA

J A E Spaan, University of Amsterdam, The Netherlands

J G Webster, University of Wisconsin-Madison, USA

Other books in the series

Minimally Invasive Medical Technology

J G Webster (ed)

Intensity-Modulated Radiation Therapy

S Webb

Physics for Diagnostic Radiology

P Dendy and B Heaton

Achieving Quality in Brachytherapy

B R Thomadsen

Medical Physics and Biomedical Engineering

B H Brown, R H Smallwood, D C Barber, P V Lawford and D R Hose

Monte Carlo Calculations in Nuclear Medicine: Applications in Diagnostic Imaging

M Ljungberg, S-E Strand and M A King (eds)

Introductory Medical Statistics, third edition

R F Mould

Ultrasound in Medicine

F A Duck, A C Barber and H C Starritt (eds)

Design of Pulse Oximeters

J G Webster (ed)

The Physics of Medical Imaging

S Webb

Forthcoming titles in the series

The Physical Measurement of Bone

C Langton and C Njeh (eds)

The Physics of MRI

W T Sobol

The Physics of High Dose Rate Brachytherapy

D Baltas, H Kreiger and N Zamboglou

Series in Medical Physics and Biomedical Engineering

THERAPEUTIC APPLICATIONS OF MONTE CARLO CALCULATIONS IN NUCLEAR MEDICINE

Edited by

Habib Zaidi, PhD

*Division of Nuclear Medicine,
Geneva University Hospital,
Switzerland*

George Sgouros, PhD

*Memorial Sloan-Kettering Cancer Center,
New York,
USA*

IOP

**Institute of Physics Publishing
Bristol and Philadelphia**

© IOP Publishing Ltd 2003

All rights reserved. No part of this publication may be reproduced, stored in a retrieval system or transmitted in any form or by any means, electronic, mechanical, photocopying, recording or otherwise, without the prior permission of the publisher. Multiple copying is permitted in accordance with the terms of licences issued by the Copyright Licensing Agency under the terms of its agreement with Universities UK (UUK).

British Library Cataloguing-in-Publication Data

A catalogue record for this book is available from the British Library.

ISBN 0 7503 816 8

Library of Congress Cataloguing-in-Publication Data are available

Series Editors:

C G Orton, Karmanos Cancer Institute and Wayne State University, Detroit, USA

J A E Spaan, University of Amsterdam, The Netherlands

J G Webster, University of Wisconsin-Madison, USA

Commissioning Editor: John Navas

Production Editor: Simon Laurenson

Production Control: Sarah Plenty

Cover Design: Victoria Le Billon

Marketing: Nicola Newey and Verity Cooke

Published by Institute of Physics Publishing, wholly owned by The Institute of Physics, London

Institute of Physics Publishing, Dirac House, Temple Back, Bristol BS1 6BE, UK

US Office: Institute of Physics Publishing, The Public Ledger Building, Suite 929, 150 South Independence Mall West, Philadelphia, PA 19106, USA

Typeset by Academic + Technical Typesetting, Bristol

Printed in the UK by MPG Books Ltd, Bodmin, Cornwall

The Series in Medical Physics and Biomedical Engineering is the official book series of the International Federation for Medical and Biological Engineering (IFMBE) and the International Organization for Medical Physics (IOMP)

IFMBE

The IFMBE was established in 1959 to provide medical and biological engineering with an international presence. The Federation has a long history of encouraging and promoting international cooperation and collaboration in the use of technology for improving the health and life quality of man.

The IFMBE is an organization that is mostly an affiliation of national societies. Transnational organizations can also obtain membership. At present there are 42 national members and one transnational member with a total membership in excess of 15000. An observer category is provided to give personal status to groups or organizations considering formal affiliation.

Objectives

- To reflect the interests of the affiliated organizations.
- To generate and disseminate information of interest to the medical and biological engineering community and international organizations.
- To provide an international forum for the exchange of ideas and concepts.
- To encourage and foster research and application of medical and biological engineering knowledge and techniques in support of life quality and cost-effective health care.
- To stimulate international cooperation and collaboration on medical and biological engineering matters.
- To encourage educational programmes which develop scientific and technical expertise in medical and biological engineering.

Activities

The IFMBE has published the journal *Medical and Biological Engineering and Computing* for over 35 years. A new journal *Cellular Engineering* was established in 1996 in order to stimulate this emerging field in biomedical engineering. In *IFMBE News* members are kept informed of the developments in the Federation. *Clinical Engineering Update* is a publication of our division of Clinical Engineering. The Federation also has a division for Technology Assessment in Health Care.

Every three years the IFMBE holds a World Congress on Medical Physics and Biomedical Engineering, organized in cooperation with the IOMP and the IUPESM. In addition, annual, milestone and regional conferences are organized in different regions of the world, such as Asia Pacific, Baltic, Mediterranean, African and South American regions.

The administrative council of the IFMBE meets once or twice a year and is the steering body for the IFMBE. The council is subject to the rulings of the General Assembly which meets every three years.

For further information on the activities of the IFMBE, please contact Jos A E Spaan, Professor of Medical Physics, Academic Medical Centre, University of Amsterdam, PO Box 22660, Meibergdreef 9, 1105 AZ, Amsterdam, The Netherlands. Tel: 31 (0) 20 566 5200. Fax: 31 (0) 20 691 7233. E-mail: IFMBE@amc.uva.nl. WWW: <http://www.ifmbe.org/>.

IOMP

The IOMP was founded in 1963. The membership includes 64 national societies, two international organizations and 12 000 individuals. Membership of IOMP consists of individual members of the Adhering National Organizations. Two other forms of membership are available, namely Affiliated Regional Organization and Corporate members. The IOMP is administered by a Council, which consists of delegates from each of the Adhering National Organizations; regular meetings of Council are held every three years at the International Conference on Medical Physics (ICMP). The Officers of the Council are the President, the Vice-President and the Secretary-General. IOMP committees include: developing countries, education and training; nominating; and publications.

Objectives

- To organize international cooperation of medical physics in all its aspects, especially in developing countries.
- To encourage and advise on the formation of national organizations of medical physics in those countries which lack such organizations.

Activities

Official publications of the IOMP are *Physiological Measurement*, *Physics in Medicine and Biology* and the *Series in Medical Physics and Biomedical Engineering*, all published by the Institute of Physics Publishing. The IOMP publishes a bulletin *Medical Physics World* twice a year.

Two council meetings and one General Assembly are held every three years at the ICMP. The most recent ICMPs were held in Kyoto, Japan (1991), Rio de Janeiro, Brazil (1994), Nice, France (1997) and Chicago, USA (2000). These conferences are normally held in collaboration with the IFMBE to form the World Congress on Medical Physics and Biomedical Engineering. The IOMP also sponsors occasional international conferences, workshops and courses.

For further information contact: Hans Svensson, PhD, DSc, Professor, Radiation Physics Department, University Hospital, 90185 Umeå, Sweden. Tel: (46) 90 785 3891. Fax: (46) 90 785 1588. E-mail: Hans.Svensson@radfys.umu.se. WWW: <http://www.iomp.org>.

Contents

LIST OF CONTRIBUTORS	xv
PREFACE	xviii
1 THE MONTE CARLO METHOD: THEORY AND COMPUTATIONAL ISSUES	1
1.1. Introduction	1
1.1.1. Early approaches to Monte Carlo simulations	1
1.1.2. Conceptual role of Monte Carlo simulations	2
1.2. Random number generation	3
1.2.1. Linear congruential generators	5
1.2.2. Lagged-Fibonacci generators	6
1.3. Photon transport	6
1.3.1. Photon cross section data	7
1.3.2. Simulating interaction of photons with matter	12
1.4. Electron transport	13
1.4.1. Stopping power data	15
1.5. Analogue sampling	16
1.5.1. Direct method	17
1.5.2. Rejection method	17
1.5.3. Mixed methods	17
1.6. Non-analogue sampling ‘variance reduction’	18
1.6.1. Photon-specific methods	18
1.6.2. Electron-specific methods	20
1.6.3. General methods	21
1.7. Summary	22
Acknowledgements	23
References	23
2 MONTE CARLO TECHNIQUES IN NUCLEAR MEDICINE DOSIMETRY	28
2.1. Introduction	28

2.2.	Monte Carlo techniques in medical radiation physics	29
2.3.	Applications of Monte Carlo techniques in nuclear medicine imaging	31
2.3.1.	Diagnostic nuclear medicine imaging	31
2.3.2.	Therapeutic nuclear medicine imaging	36
2.4.	Monte Carlo techniques in nuclear medicine dosimetry	38
2.4.1.	Calculation of absorbed fractions	38
2.4.2.	Derivation of dose-point kernels	39
2.4.3.	Pharmacokinetic modelling	41
2.5.	Monte Carlo techniques in radiation protection	42
2.5.1.	Shielding calculations	43
2.5.2.	Characterization of detectors and radiation monitoring instruments	43
2.5.3.	Radiation dose calculations to staff	44
2.5.4.	Revisiting release criteria for patients administered therapeutic doses	44
2.6.	Future applications of Monte Carlo	45
2.6.1.	Patient-specific dosimetry and treatment planning	45
2.6.2.	On-line PET monitoring of radiotherapy beams	46
	References	48
3	MEDICAL IMAGING TECHNIQUES FOR RADIATION DOSIMETRY	55
3.1.	Introduction	55
3.2.	Determination of the total mass. Determination of spatial distribution of attenuation coefficient, and of mass	56
3.3.	Segmentation of patient data into VoI	57
3.4.	Determination of the distribution of radioactivity in both space and time	58
3.4.1.	Quantitative whole-body imaging	59
3.4.2.	Quantitative imaging with conjugate views	60
3.4.3.	Quantitative imaging with SPECT	62
3.4.4.	Effect of reconstruction algorithm on SPECT imaging	66
3.4.5.	Effect of attenuation, scatter and blurring correction on SPECT imaging	68
3.4.6.	Time series of images	71
3.4.7.	Methods used to register multimodality images	72
3.4.8.	Quantitative imaging with PET	74
3.4.9.	Effect of attenuation and scatter correction on PET imaging	76
3.4.10.	Reconstruction algorithms for fully-three-dimensional PET	76
3.5.	Auxiliary contribution from PET	77

3.6.	Treatment planning	78
	Acknowledgements	79
	References	79
4	COMPUTATIONAL METHODS IN INTERNAL RADIATION DOSIMETRY	84
4.1.	Introduction	84
4.2.	Radiation quantities and units	85
4.2.1.	Stochastic versus deterministic quantities	85
4.2.2.	Definitions of dosimetric quantities	85
4.3.	The MIRD schema	89
4.4.	Patient- and position-specific dosimetry	95
4.4.1.	Patient-specific dosimetry: case study—radioiodine therapy of metastatic thyroid cancer	95
4.4.2.	Adaptation of the MIRD schema to patient-specific dosimetry	98
4.4.3.	Position-specific dosimetry: calculation of non-uniform dose distributions	100
4.5.	Summary	101
	References	102
5	MATHEMATICAL MODELS OF THE HUMAN ANATOMY	108
5.1.	Introduction	108
5.1.1.	Early approaches to dose assessment	108
5.1.2.	Need for mathematical models in dose assessment	109
5.1.3.	Conceptual role of mathematical phantoms	109
5.2.	Historical developments	110
5.2.1.	Simple models of Brownell, Ellett and Reddy	110
5.2.2.	Early models developed by Snyder	110
5.2.3.	The Snyder–Fisher phantom	111
5.2.4.	The MIRD-5 Phantom	112
5.2.5.	Photon and electron transport	113
5.2.6.	Similitude and paediatric phantoms	114
5.2.7.	Development of MIRDOSE codes	115
5.3.	The current stylized models	115
5.3.1.	The ORNL phantom series	115
5.3.2.	The MIRD stylized models	116
5.3.3.	Stylized models of the lower abdomen	118
5.3.4.	Other stylized models of the human anatomy	120
5.3.5.	Use of stylized models in therapeutic nuclear medicine	120
5.4.	Tomographic models	121
5.4.1.	Methods of construction	122
5.4.2.	Review of representative models	123

5.4.3.	Comparisons with stylized mathematical models	124
5.5.	Summary	126
	References	126
6	MONTE CARLO CODES FOR USE IN THERAPEUTIC NUCLEAR MEDICINE	133
6.1.	Introduction	133
6.2.	Historical developments	134
6.2.1.	The 'Reference Man' phantoms and the ALGAMP code	136
6.2.2.	Development of MIRDOSE codes	138
6.3.	Public domain Monte Carlo codes	139
6.3.1.	The EGS code	139
6.3.2.	The MCNP code	139
6.3.3.	The ETRAN code	140
6.3.4.	ITS	141
6.3.5.	The GEANT code	141
6.3.6.	Other Monte Carlo codes	141
6.4.	Limitations of current nuclear medicine dose calculations	142
6.4.1.	Introduction	142
6.5.	Improvements in models for nuclear medicine therapy	144
6.5.1.	Current approaches to patient-specific dose calculations	144
6.5.2.	Innovation in software development tools	149
6.5.3.	Parallel computing aspects	150
6.5.4.	Towards clinical applications of 'on-the-fly' Monte Carlo-based dosimetry calculations	152
6.6.	Summary	153
	Acknowledgements	153
	References	153
7	DOSE POINT-KERNELS FOR RADIONUCLIDE DOSIMETRY	158
7.1.	Introduction	158
7.2.	Methods used to generate dose point-kernels	160
7.3.	Review of dose point-kernels available for radionuclide dosimetry	162
7.3.1.	Photons	162
7.3.2.	Electrons	163
7.3.3.	Combined approaches	165
7.3.4.	Impact of the medium	166
7.4.	A general approach for use of dose point-kernels in calculations	168
7.4.1.	Absorbed fractions on a cellular scale	169

7.4.2.	Absorbed fractions on a millimetre scale	169
7.4.3.	Absorbed fractions on an organ scale	170
7.5.	Conclusions	170
	References	171
8	RADIOBIOLOGY ASPECTS AND RADIONUCLIDE SELECTION CRITERIA IN CANCER THERAPY	175
8.1.	Introduction	175
8.2.	Radiobiological effects	175
8.2.1.	Molecular lesions	175
8.2.2.	Cellular responses	176
8.2.3.	Tissue responses	179
8.2.4.	Radiation quality	181
8.3.	Targeting principles in radionuclide therapy	182
8.3.1.	Choice of radionuclide	182
8.3.2.	Half-life	185
8.3.3.	Choice of vector or ligand	186
8.3.4.	Properties of targets	187
8.4.	Experimental therapeutics	187
8.4.1.	β particle emitters	187
8.4.2.	α particle emitters	189
8.4.3.	Auger electron emitters	191
	References	194
9	MICRODOSIMETRY OF TARGETED RADIONUCLIDES	202
9.1.	Introduction	202
9.2.	Alpha emitters	204
9.2.1	Monte Carlo simulation of energy deposition by α particle emitters	205
9.2.2.	Applications of microdosimetry to α particle emitters	209
9.3.	Auger electron emitters	213
9.3.1.	Monte Carlo simulation of Auger decays and their energy deposition	215
9.3.2.	Targeted therapy with Auger electron emitters	218
9.4.	Future directions	219
	References	221
10	THE MABDOSE PROGRAM FOR INTERNAL RADIONUCLIDE DOSIMETRY	228
10.1.	Introduction—the need for better dosimetry	228
10.2.	Dosimetry software design considerations	229
10.2.1.	Dosimetry considerations	230
10.2.2.	Dosimetry approaches	232

10.3.	Historic development of MABDOSE	233
10.3.1.	Version 1	233
10.3.2.	Version 2	234
10.3.3.	Version 3	235
10.3.4.	Version 4	235
10.4.	MABDOSE: from start to finish	236
10.4.1.	Overview	236
10.4.2.	The target lattice	236
10.4.3.	Declaring source volumes	237
10.4.4.	Time-activity data and the generation of cumulated activities	239
10.4.5.	Selection of a radionuclide	240
10.4.6.	Simulation of radioactive decay	241
10.4.7.	Simulation—cross section lookup tables	241
10.4.8.	Simulation—radiation transport	242
10.4.9.	Dose display	243
10.5.	Future developments	244
10.5.1.	Automated or semi-automated image segmentation	244
10.5.2.	Generalization of the atomic composition of target voxels	245
10.5.3.	Incorporation of electron simulation	245
10.5.4.	Incorporation of nonlinear models	245
10.6.	Summary	246
	References	246
11	THE THREE-DIMENSIONAL INTERNAL DOSIMETRY SOFTWARE PACKAGE, 3D-ID	249
11.1.	Introduction	249
11.2.	Background to 3D-ID development	250
11.3.	Programming aspects/development philosophy	250
11.4.	Monte Carlo-based implementation	251
11.5.	Point-kernel based implementation	252
11.6.	Individual modules	252
11.7.	Considerations in clinical implementations	257
11.8.	Future potential uses	258
	Acknowledgements	258
	References	258
12	EVALUATION AND VALIDATION OF DOSE CALCULATION PROCEDURES IN PATIENT-SPECIFIC RADIONUCLIDE THERAPY	262
12.1.	Introduction	262
12.2.	Dose–volume information versus mean–average organ/tumour dose	262

12.3.	Monte Carlo simulation of imaging systems	263
12.3.1.	Monte Carlo programs for radionuclide imaging	264
12.3.2.	Software phantoms	265
12.4.	Evaluation of image quality degradation by Monte Carlo methods	266
12.4.1.	Evaluation of planar ^{131}I imaging	267
12.4.2.	Evaluation of SPECT ^{131}I imaging	269
12.4.3.	Other radionuclides	272
12.5.	Evaluation of absorbed dose calculation procedures by Monte Carlo methods	273
12.6.	Evaluations based on direct measurements	275
12.6.1.	Thermoluminescence dosimeters	275
12.6.2.	Biological dosimeters	276
12.6.3.	Other dosimetry methods	278
12.6.4.	Phantoms for experimental measurements	279
12.6.5.	<i>In vivo</i> verifications—experimental animals	279
12.6.6.	<i>In vivo</i> verifications—humans	280
12.6.7.	Stack phantom for realistic RNT dosimetry verifications	280
	Acknowledgements	281
	References	281
13	MONTE CARLO METHODS AND MATHEMATICAL MODELS FOR THE DOSIMETRY OF SKELETON AND BONE MARROW	286
13.1.	Introduction	286
13.1.1.	Anatomy of the skeletal system	286
13.1.2.	Dosimetry of the skeletal system	288
13.2.	Trabecular bone models	290
13.2.1.	Research at the university of Leeds	290
13.2.2.	Model of trabecular bone in MIRD Pamphlet 11	290
13.2.3.	Skeletal dosimetry in ICRP Publication 30	291
13.2.4.	Spherical model of trabecular bone	291
13.2.5.	The Eckerman trabecular bone model	292
13.2.6.	The Bouchet <i>et al.</i> trabecular bone model	293
13.2.7.	Differences between the three-dimensional model of Bouchet <i>et al.</i> and the one-dimensional model of Eckerman	293
13.2.8.	Model of a trabecular bone lesion	295
13.2.9.	High-resolution imaging for trabecular bone dosimetry	295
13.3.	Cortical bone models	296
13.3.1.	Research at the University of Leeds	296
13.3.2.	The ICRP-30 cortical bone model	297

13.3.3.	The Eckerman cortical bone model	297
13.3.4.	The Bouchet <i>et al.</i> cortical bone model	298
13.3.5.	The research of Akabani	298
13.4.	Improving the models: patient-specific dosimetry	299
13.4.1.	The clinical experience—ability to predict toxicity with current dosimetric models	299
13.4.2.	Correcting the models using patient-specific data	301
13.4.3.	<i>In-vivo</i> high-resolution imaging	303
13.5.	Summary	304
	References	305
14	MONTE CARLO MODELLING OF DOSE DISTRIBUTIONS IN INTRAVASCULAR RADIATION THERAPY	310
14.1.	Introduction	310
14.2.	Candidate radionuclides and technologies	312
14.3.	Radiation dosimetry studies	313
14.3.1.	Vessel wall dose—calculations	313
14.3.2.	Vessel wall dose—measurements	317
14.3.3.	Dose to body organs in case of a balloon rupture	317
14.4.	Radiation effects—artery walls	321
	References	322
15	THE MONTE CARLO METHOD AS A DESIGN TOOL IN BORON NEUTRON CAPTURE SYNOVECTOMY	324
15.1.	Introduction	324
15.1.1.	Rheumatoid arthritis and current methods of treatment	325
15.2.	Boron neutron capture synovectomy	326
15.3.	Neutron beam design calculations for BNCS	328
15.3.1.	Optimal beam energy	329
15.3.2.	Optimal beam design	329
15.4.	Experimental characterization of the BNCS beam	334
15.5.	Experimental investigation of BNCS in an animal model	338
15.6.	Whole-body dosimetry for BNCS	340
15.7.	Summary and conclusions	343
	References	344
16	SUMMARY	348
	BIOSKETCHES	350
	INDEX	361

List of contributors

Habib Zaidi, PhD

Division of Nuclear Medicine, Geneva University Hospital, CH-1211 Geneva, Switzerland

George Sgouros, PhD

Memorial Sloan-Kettering Cancer Center, Department of Medical Physics, 1275 York Avenue, New York 10021, USA

Pedro Andreo, PhD, DSc, Professor

Department of Medical Radiation Physics, University of Stockholm–Karolinska Institute, PO Box 260, SE-17176 Stockholm, Sweden

Manuel Bardies, PhD

Institut National de la Santé et de la Recherche Médicale (INSERM), Unité 463, 9 quai Moncousu, Nantes 44035, France

Wesley Bolch, PhD

Department of Nuclear and Radiological Engineering, University of Florida, Gainesville, FL 32611-8300, USA

Lionel Bouchet, PhD

University of Florida Brain Institute, Department of Neurological Surgery, 100 S Newell Dr., Gainesville, FL 32610-0265, USA

A Bertrand Brill, PhD

Department of Radiology and Radiological Sciences, Vanderbilt University, 1161 21st Avenue South, Nashville, TN 37232-2675, USA

Yuni Dewaraja, PhD

Radiology Department, The University of Michigan Medical Center, Ann Arbor, MI 48109-0552, USA

Dennis Duggan, PhD

Department of Radiation Oncology, B902 The Vanderbilt Clinic, Vanderbilt University Medical Center, Nashville, TN 37232-5671, USA

Keith Eckerman, PhD

Life Sciences Division, Oak Ridge National Laboratory, 1060 Commerce Park, MS 6480, TN 37831, USA

David Gierga, PhD

Department of Nuclear Engineering, Massachusetts Institute of Technology, Room NW14-2207, 150 Albany Street, Cambridge, MA 02139-4307, USA

John Humm, PhD

Memorial Sloan-Kettering Cancer Center, Department of Medical Physics, 1275 York Avenue, New York 10021, USA

Timothy K Johnson, PhD

Anschutz Cancer Pavilion, Department of Radiation Oncology, Box 6510, Mail Stop F706, Aurora, CO 80010-0510, USA

Amin I Kassis, PhD

Department of Radiology, Harvard Medical School, Boston, MA 02115-5729, USA

Katherine S Kolbert, MS

Memorial Sloan-Kettering Cancer Center, Department of Medical Physics, 1275 York Avenue, New York 10021, USA

Kenneth F Koral, PhD

Internal Medicine Department, The University of Michigan Medical Center, Ann 3480 Kresge III, 204 Zina Pitcher Place, Ann Arbor, MI 48109-0552, USA

Cheuk S Kwok, PhD

Hong Kong Polytechnic University, Department of Optometry and Radiography, Hung Hom, Kowloon, Hong Kong

Michael Ljungberg, PhD

Lund University, Department of Radiation Physics, S-22185 Lund, Sweden

John W. Poston Sr, PhD, Professor

Department of Nuclear Engineering, Texas A&M University, 3133 TAMU, College Station, TX 77843-3133, USA

John Roeske, PhD

Department of Radiation and Cellular Oncology, University of Chicago, Chicago, IL 60637, USA

Ruth Shefer, PhD

Newton Scientific, Inc., 245 Bent St, Winchester, MA 01890, USA

Michael Stabin, PhD

Department of Radiology and Radiological Sciences, Vanderbilt University,
1161 21st Avenue South, Nashville, TN 37232-2675, USA

Sven-Erik Strand, PhD, Professor

Lund University, Department of Radiation Physics, S-22185 Lund, Sweden

Jacquelyn Yanch, PhD

Department of Nuclear Engineering, Massachusetts Institute of Technology,
Room NW14-2207, 150 Albany Street, Cambridge, MA 02139-4307, USA

Pat Zanzonico, PhD

Memorial Sloan-Kettering Cancer Center, Nuclear Medicine Service, 1275
York Avenue, New York 10021, USA

Preface

This book provides a review of the Monte Carlo method as it is applied in the field of therapeutic nuclear medicine. Driven in part by the remarkable increase in computing power and its ready and inexpensive availability, this is a relatively new yet rapidly expanding field. Likewise, although the use of radionuclides for therapy has origins dating back almost to the discovery of natural radioactivity itself, radionuclide therapy and, in particular, targeted radionuclide therapy has only recently emerged as a promising approach for therapy of cancer and, to a lesser extent, other diseases. An effort has, therefore, been made to place the reviews provided in this book in a broader context. The effort to do this is reflected by the inclusion of chapters that do not directly address Monte Carlo techniques, but rather provide an overview of issues that are closely related to therapeutic nuclear medicine and to the potential role of Monte Carlo in this field. A brief overview of each chapter is provided below.

Chapters 1, 2 and 6 review the fundamental theory of Monte Carlo, techniques that have been used in nuclear medicine dosimetry and Monte Carlo codes currently available for carrying out absorbed dose calculations. Unlike external radiotherapy or brachytherapy, the kinetics and biodistribution of internally administered radionuclides must be measured. Imaging is, therefore, an integral part of nuclear medicine dosimetry. As such, imaging considerations are incorporated in almost every chapter of the book. The contributions of Monte Carlo in nuclear medicine imaging are specifically reviewed in chapter 3. The anatomical input required for Monte Carlo-based dose calculations may be provided either as idealized geometric representations of anatomy or as discrete, voxel-based representations that reflect the actual shape and composition of a human. Again, these considerations are present throughout the book, but chapters 5 and 13 focus on this specifically for the whole body and for the bone marrow, respectively, the latter being a particularly important and challenging portion of the anatomy. The role of Monte Carlo in providing a means for validating the overall scheme of imaging-based, patient-specific absorbed dose calculations is reviewed in chapter 12. Chapters 9, 14 and 15 examine specific

implementations of the Monte Carlo approach in the special cases of microdosimetry, intravascular therapy and boron neutron capture synovectomy. Microdosimetry is becoming increasingly important as high linear energy transfer (LET) (see chapter 8) emissions are being considered for therapeutic use. In alpha-emitter therapy, for example, a small number of decays can substantially influence cell survival; the Monte Carlo method is therefore indispensable in simulating such a stochastic process and thereby understanding experimental cell survival studies and potentially translating such results into the clinic. Intravascular radiation therapy using radionuclides is a relatively new area of radionuclide therapy. The potential efficacy of this approach is heavily dependent upon the spatial distribution of absorbed dose relative to the anatomical distribution of the cells involved in restenosis. The absorbed dose distribution is, in turn, dependent upon the radionuclide emissions, the configuration of emitters and the heterogeneous environment that is traversed in going from the source region to the target regions. These aspects are best addressed by Monte Carlo calculations. Boron neutron capture therapy incorporates aspects of both external radiotherapy (the neutron beam) and systemic radionuclide therapy (the biodistribution and kinetics of boron-enriched compounds). In chapter 15, Monte Carlo is used to investigate the design of a neutron beam configuration that is optimized for synovectomy.

Conventional, non-Monte Carlo-based approaches to radionuclide dosimetry are described in chapters 4 and 7. Chapter 4, in particular, provides a review of the dose schema, developed by the Medical Internal Radionuclide Dose (MIRD) Committee, that is most widely implemented for radionuclide dosimetry. Chapter 7 describes the point-kernel methodology which has been used extensively in patient-specific absorbed dose calculations and which may be thought of as a precursor to a full Monte Carlo implementation of imaging-based patient-specific dosimetry. Chapters 10 and 11 briefly review two software packages that have been developed for carrying out radionuclide dosimetry in therapeutic nuclear medicine. The first, MABDOSE, facilitates implementation of the MIRD schema while also allowing for on-line Monte Carlo calculations that make it possible to incorporate idealized tumour geometries within the MIRD formalism. The second, 3D-ID, describes an imaging-based approach to patient-specific dosimetry.

Chapter 8 provides a comprehensive review of the radiobiology relevant to therapeutic nuclear medicine. This chapter is essential in understanding the biological aspects critical to the design of successful radionuclide therapy for cancer. It serves as a reminder that regardless of how precisely the distribution of ionizing energy density (i.e., absorbed dose) is estimated, this information will predict biologic response only if the pertinent biologic considerations are also incorporated.

Finally, we would like to thank all of the contributors for their invaluable hard work and for keeping to a very tight schedule. The topic

of this book is rapidly evolving and the editors felt it important to minimize the time required to get this book into press. That this problem was so very well overcome speaks of the commitment and dedication of the contributors. We found compilation of this book to be a rewarding and educational experience and hope that the reader is left with the same experience.

Chapter 1

The Monte Carlo method: theory and computational issues

Habib Zaidi

1.1. INTRODUCTION

Usually, physicists and mathematicians like to give funny names to things that are otherwise boring. There is a gaming aspect to Monte Carlo calculations. Every simulation is based upon events that happen randomly, and so the outcome of a calculation is not always absolutely predictable. This element of chance reminds one of gambling and so the originators of the Monte Carlo technique, Ulam and von Neumann, both respectable scientists, called the technique *Monte Carlo* to emphasize its gaming aspect [1, 2].

This introductory chapter briefly reviews the historical developments and conceptual role of the Monte Carlo method, then summarizes its derivation and methodological basis. Emphasis is given to applications where photon and/or electron transport in matter are simulated. Some computational aspects of the Monte Carlo method, mainly related to random number generation, sampling and variance reduction, are discussed. A general presentation of potential applications of Monte Carlo techniques in different areas of nuclear medicine is given in chapter 2. Widely used Monte Carlo codes in connection with computing facilities, vectorized and parallel implementations are described in chapter 6 of this book.

1.1.1. Early approaches to Monte Carlo simulations

The Monte Carlo method describes a very broad area of science, in which many processes, physical systems and phenomena are simulated by statistical methods employing random numbers. The history of using random or chance events to ascertain truths hidden from common perception may date back to the documented practice of the ancient Israelites of a

dice-throwing method (the Urim and Thummim) to divine the will of God in a given situation [3]. Dr de Buffon showed that by randomly tossing needles on to a table on which parallel lines were drawn, one could determine experimentally the value of π [4] (it is said that this experiment started by de Buffon throwing French stick loaves over his shoulder on to a tiled floor and counting the number of times the loaves fell across the lines between tiles on the floor). In 1899, Lord Rayleigh showed how the use of a one-dimensional random walk could provide an approximate solution to a parabolic differential equation [5]. In 1931 Kolmogorov showed the relationship between Markov stochastic processes and certain integro-differential equations [6].

Ulam in his autobiography [7] writes that shortly after his return to Los Alamos, probably in 1946–1947, he gave two seminars that ‘had good or lucky ideas and led to successful further development’. One was on what became known as the Monte Carlo method. He describes an earlier discussion of the basic idea with von Neumann as they drove from Los Alamos to Lamy. This part of the book is vague on chronology—the seminar may have been as late as 1948. The abbreviated bibliography lists one paper by Ulam on Monte Carlo [8]. About 1948 Fermi, Metropolis and Ulam obtained Monte Carlo estimates for the eigenvalues of the Schrödinger equation [1] (the reference does not include Fermi, but he was involved in the derivation). Ulam and von Neumann coined the name ‘Monte Carlo’ in about 1944 in the Manhattan Project during World War II, taken from the name of the well-known city in Monaco famous for its games of chance. Both of them led the modern Monte Carlo age and were pioneers in the development of Monte Carlo techniques and their realizations on digital computers.

The earliest application of the Monte Carlo method to radiation transport problems appears to be a study by Spencer [9] of the effects of polarization on multiple (successive) Compton scatterings, a problem further examined later on using the Boltzmann equation and diffusion theory [10]. This is further emphasized in the pioneering work of Kahn [11] for predicting neutron fluxes associated with nuclear reactors designed and brought on line in the 1940s. Mayer used one of the first automatic computers, the ENIAC, as early as 1949 for neutron transport Monte Carlo calculations as reported at a 1949 symposium on the Monte Carlo method [12].

1.1.2. Conceptual role of Monte Carlo simulations

The general idea of Monte Carlo analysis is to create a model which is as similar as possible to the real system of interest, and to create interactions within that system based on known probabilities of occurrence, with random sampling of the probability density functions (pdfs). As the number of individual events (called ‘histories’) is increased, the quality of

the reported average behaviour of the system improves, meaning that the statistical uncertainty decreases. Almost any complex system in principle can be modelled; perhaps we wish to model the number of cars passing a particular intersection during certain times of the day, to optimize traffic management, or the number of people that will make transactions in a bank, to evaluate the advantages of different queuing systems. If we know from experience the distribution of events that occur in our system, we can generate a pdf and sample it randomly to simulate the real system. Detailed descriptions of the general principles of the Monte Carlo method are given in a number of publications [13, 14] and will not be repeated here. The major components of a Monte Carlo method are briefly described below. These components comprise the foundation of most Monte Carlo applications. The following sections will explore them in more detail. An understanding of these major components will provide a sound foundation for the developer to construct his own Monte Carlo method. The primary components of a Monte Carlo simulation method include the following:

- (i) Probability density functions (pdfs): the physical system must be described by a set of pdfs.
- (ii) Random number generator: a source of random numbers uniformly distributed on the unit interval must be available.
- (iii) Sampling rule: a prescription for sampling from the specified pdfs.
- (iv) Scoring: the outcomes must be accumulated into overall tallies or scores for the quantities of interest.
- (v) Error estimation: an estimate of the statistical error (variance) as a function of the number of trials and other quantities must be determined.
- (vi) Variance reduction techniques: methods for reducing the variance in the estimated solution to reduce the computational time for Monte Carlo simulation.
- (vii) Parallelization and vectorization algorithms to allow Monte Carlo methods to be implemented efficiently on advanced computer architectures.

1.2. RANDOM NUMBER GENERATION

Computational studies requiring the generation of random numbers are becoming increasingly common. All random number generators (RNGs) are based upon specific mathematical algorithms, which are repeatable. As such, the numbers are just pseudo-random. Here, for simplicity, we shall term them just ‘random’ numbers. Formally, random is defined as exhibiting ‘true’ randomness, such as the time between ‘tics’ from a Geiger counter exposed to a radioactive element. Pseudo-random is defined as having the appearance of randomness, but nevertheless exhibiting a specific, repeatable

pattern. Quasi-random is defined as filling the solution space sequentially (in fact, these sequences are not at all random; they are just comprehensive at a preset level of granularity). Monte Carlo methods make extensive use of random numbers to control the decision-making process when a physical event has a number of possible results. The RNG is always one of the most crucial subroutines in any Monte Carlo-based simulation code. A large number of generators are readily available [15], and many of these are suitable for implementation on any computer system since today there is no significant distinction in floating-point processing capabilities between a modern desktop and a mainframe computer. A typical simulation uses from 10^7 to 10^{12} random numbers, and subtle correlations between these numbers could lead to significant errors [16]. The largest uncertainties are typically due more to approximations arising in the formulation of the model than those caused by lack of randomness in the RNG. Mathematically speaking, the sequence of random numbers used to effect a Monte Carlo model should possess the following properties [17]:

- (i) Uncorrelated sequences: the sequences of random numbers should be serially uncorrelated. Most especially, n -tuples of random numbers should be independent of one another.
- (ii) Long period: ideally, the generator should not repeat; practically, the repetition should occur only after the generation of a very large set of random numbers.
- (iii) Uniformity: the sequence of random numbers should be uniform, and unbiased. That is, suppose we define n -tuples $u_i^n = (u_{i+1}, \dots, u_{i+n})$ and divide the n -dimensional unit hypercube into many equal sub-volumes. A sequence is uniform if, in the limit of an infinite sequence, all the sub-volumes have an equal number of occurrences of random n -tuples.
- (iv) Reproducibility: when debugging programs, it is necessary to repeat the calculations to find out how the errors occurred. The feature of reproducibility is also helpful while porting the program to a different machine.
- (v) Speed: it is of course desirable to generate the random numbers quickly.
- (vi) Parallelization: the generator used on vector machines should be vectorizable, with low overhead. On massively parallel architectures, the processors should not have to communicate among themselves, except perhaps during initialization.

Although powerful RNGs have been suggested including shift register, inverse congruential, combinatorial and ‘intelligent’ methods such as those implemented in the MCNP code [18], the most commonly used generator is the linear congruential RNG (LCRNG) [19]. Recently, Monte Carlo researchers have become aware of the advantages of lagged-Fibonacci series (LFRNG). With extremely long periods, they are generally faster than LCRNG and have excellent statistical properties [20]. Those generators are briefly described below.

1.2.1. Linear congruential generators

The LCRNG has the form [19]

$$u_{n+1} = a(u_n + c) \bmod(m), \quad (1.1)$$

where m is the modulus, a the multiplier, and c the additive constant or addend. The size of the modulus constrains the period, and is usually chosen to be either prime or a power of 2 [21]. An important subset of LCRNG is obtained by setting $c = 0$ in equation (1.1), which defines the multiplicative linear congruential RNG (MLCRNG). This generator (with m a power of 2 and $c = 0$) is the *de facto* standard included with FORTRAN and C compilers [22]. One of the biggest disadvantages to using a power of 2 modulus is that the least significant bits of the integers produced by these LCRNGs have extremely short periods. For example, $u_n \bmod(2^j)$ will have a period of 2^j [21]. In particular, this means the least-significant bit of the LCRNG will alternate between 0 and 1. Some cautions to the programmer are in order: (i) the bits of u_n should not be partitioned to make several random numbers since the higher-order bits are much more random than the lower-order bits; (ii) the power of 2 modulus in batches of powers of 2 should be avoided; (iii) RNGs with large modulus are preferable to ones with small modulus. Not only is the period longer, but also the correlations are lower. In particular, one should not use 32 bit modulus for applications requiring a high resolution in the random numbers. In spite of this known defect of power of 2 LCRNGs, 48 bit multipliers (and higher) have passed many very stringent randomness tests.

The initial seed should be set to a constant initial value, such as a large prime number (it should be odd, as this will satisfy period conditions for any modulus). Otherwise, the initial seed should be set to a ‘random’ odd value. Anderson [23] recommends setting the initial seed to the following integer:

$$u_0 = i \text{ yr} + 100 \times (i \text{ month} - 1 + 12 \times (i \text{ day} - 1 + 31 \\ \times (i \text{ hour} + 24 \times (i \text{ min} + 60 \times i \text{ sec}))))), \quad (1.2)$$

where the variables on the right-hand side are the integer values of the date and time. Note that the year is 2 digits long, i.e., the domain of $i \text{ yr}$ is [0–99]. However, it may be preferable to introduce the maximum variation in the seed into the least significant bits by using the second of this century, rather than the most significant bits. The following equation is preferable:

$$u_0 = i \text{ sec} + 60 \times (i \text{ min} + 60 \times (i \text{ hour} + 24 \times (i \text{ day} - 1 + 31 \\ \times (i \text{ month} - 1 + 12 \times i \text{ yr}))))). \quad (1.3)$$

Generally parametrizing the iteration process, either through the multiplier or the additive constant, best parallelizes LCRNGs. Based on the modulus, different parametrizations have been tried [23].

1.2.2. Lagged-Fibonacci generators

The lagged-Fibonacci series RNG (LFRNG) have the following general form [15]

$$u_n = u_{n-l} \otimes u_{n-k}(m), \quad l > k, \quad (1.4)$$

where \otimes may be one of the binary arithmetic operators $+$, $-$ or $*$; l and k are the lags, and m is a power of 2 ($m = 2^p$). In recent years the additive lagged-Fibonacci RNG (ALFRNG) has become a popular generator for serial as well as scalable parallel machines [24] because it is easy to implement, it is cheap to compute and it does well on standard statistical tests, especially when the lag k is sufficiently high (such as $k = 1279$). The maximal period of the ALFRNG is $(2^k - 1)2^{p-1}$ and has $2^{(k-1)(p-1)}$ different full-period cycles [25]. Another advantage of the ALFRNG is that one can implement these generators directly in floating-point to avoid the conversion from integer to floating-point that accompanies the use of other generators. However, some care should be taken in the implementation to avoid floating-point round-off errors.

Instead the ALFRNG can be parametrized through its initial values because of the tremendous number of different cycles. Assigning each stream a different cycle produces different streams. An elegant seeding algorithm that accomplishes this is described by Mascagni *et al.* [24]. An interesting cousin of the ALFRNG is the multiplicative lagged-Fibonacci RNG (MLFRNG). While this generator has a maximal period of $(2^k - 1)2^{p-3}$, which is a quarter the length of the corresponding ALFRNG, it has empirical properties considered to be superior to ALFRNGs [15]. Of interest for parallel computing is that a parametrization analogous to that of the ALFRNG exists for the MLFRNG. This latter algorithm was used for generating uniformly distributed random numbers on a parallel computer based on the MIMD principle [26]. The sequence of 24 bit random numbers has a period of about 2^{144} and has passed stringent statistical tests for randomness and independence [20].

1.3. PHOTON TRANSPORT

For radiation transport problems, the computational model includes geometry and material specifications. Every computer code contains a database of experimentally obtained quantities, known as cross sections, that determine the probability of a particle interacting with the medium through which it is transported. Every cross section is peculiar to the type and energy of the incident particle and to the kind of interaction it undergoes. These partial cross sections are summed to form the total cross section; the ratio of the partial cross section to the total cross section gives the probability of this particular interaction occurring. Cross section data for the interaction

types of interest must be supplied for each material present. The model also consists of algorithms used to compute the result of interactions (changes in particle energy, direction, etc.) based on the physical principles that describe the interaction of radiation with matter and the cross section data provided. Therefore, it is extremely important to use an accurate transport model, as the Monte Carlo result is only as valid as the data supplied.

1.3.1. Photon cross section data

When a photon (having an energy below 1 MeV for isotopes of interest in nuclear medicine) passes through matter, any of the three interaction processes (photoelectric, incoherent scattering, coherent scattering) may occur. The probability of a photon of a given energy E undergoing absorption or scattering when traversing a layer of material Z can be expressed quantitatively in terms of a linear attenuation coefficient μ (cm^{-1}) which is dependent on the material's density, ρ (g cm^{-3}):

$$\mu = \mu_{\text{photo}} + \mu_{\text{incoh}} + \mu_{\text{coh}}. \quad (1.5)$$

Many approximations are made in Monte Carlo simulation packages to either simplify the computational model or improve the speed of operation. For example, when simulating positron emission tomography systems, it is common to neglect coherent scattering in Monte Carlo simulation of photon transport because of its low contribution to the total cross section at 511 keV. In the following examples, the relative importance of the various processes involved in the energy range of interest (below 1 MeV) are considered for some compounds and mixtures used in nuclear medicine to justify some of the approximations made in Monte Carlo codes. Figure 1.1 illustrates the relative strengths of the photon interactions versus energy for water (H_2O) and bismuth germanate (BGO), respectively. For water, a moderately low- Z material, we note two distinct regions of single interaction dominance: photoelectric below and incoherent above 20 keV. The almost order of magnitude depression of the coherent contribution is some justification for the approximations discussed. The coherent contribution to the total cross section is less than 1% for energies above 250 keV. However, this contribution is in the order of 7% for high- Z materials like BGO. Therefore, efforts should be made to treat the coherent scattering process adequately for detector materials.

Accurate Monte Carlo simulations rely on detailed understanding and modelling of radiation transport and on the availability of reliable, physically consistent databases or cross section libraries used for photon/electron transport calculations [27]. As discussed and historically reviewed in some detail by Hubbell [28], there exist many compilations of photon cross section data. The discrepancies and envelope of uncertainty of available interaction data have been examined from time to time, including the effects of molecular and ionic chemical binding, particularly in the vicinity of absorption edges.

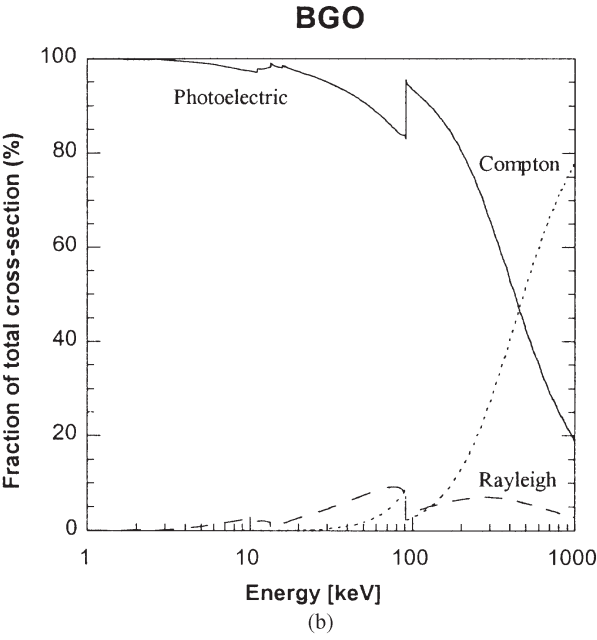
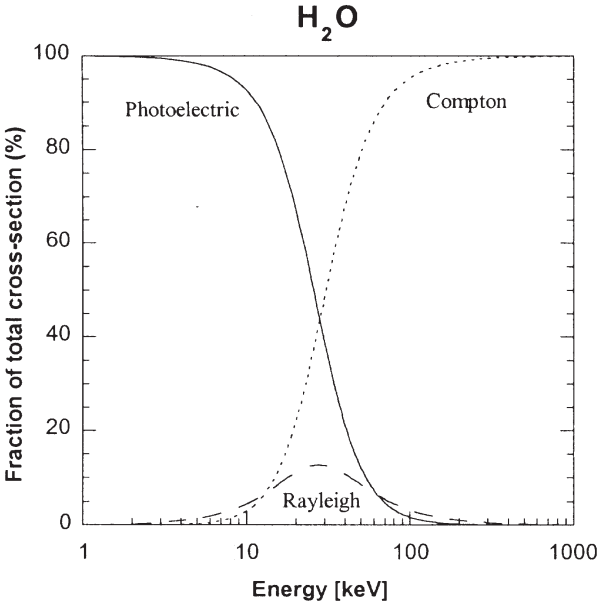


Figure 1.1. Components of photon cross-sections for H₂O and BGO of interest in PET imaging illustrating the relative contribution of each process.

Calculations of photon interaction data are generally in terms of atomic cross sections, in units of cm^2/atom , customarily in units of barns/atom (or b/atom) where $1 \text{ barn} = 10^{-24} \text{ cm}^2$.

The Storm and Israel [29] photon cross section data have been used extensively in medical physics. This is a 1970 compilation of data for elements 1–100 and energies 1 keV to 100 MeV, and contains mass attenuation coefficients, mass energy transfer coefficients, and mass energy absorption coefficients, presented in units of barns/atom. The medical physics community makes extensive use of these coefficients in different applications including Monte Carlo modelling. The various Monte Carlo codes developed to simulate nuclear medicine imaging systems use different photon cross section libraries. In the MCNP Monte Carlo code [30], the photon interaction tables for $Z = 84, 85, 87, 88, 89, 91$ and 93 are based on the compilation of Storm and Israel from 1 keV to 15 MeV. For all other elements $Z = 1$ – 94 the photon interaction tables are based on data from Evaluated Nuclear Data Files (ENDF) [31] from 1 keV to 100 MeV. Data above 15 MeV for the Storm and Israel data and above 100 MeV for the ENDF data come from adaptation of the Livermore Evaluated Photon Data Library (EPDL89) [32] and go up to 100 GeV. The original EGS4 system [33] also uses compilation by Storm and Israel for the photoelectric and pair production cross sections. Recently, cross section data for this code, based on the PHOTX library [34], was created by Sakamoto [35]. ITS [36] includes cross sections for bound electrons, the effect of which is ignored in the default EGS4 package. For the photon energy range over 1 keV to 50 MeV, of most interest to medical physicists, particular attention is called to a recently assembled electronic database, including values of energy absorption coefficients, developed by Boone and Chavez [37]. In addition to attenuation coefficients, other useful data such as the density, atomic weight, K , L_1 , L_2 , L_3 , M and N edges, and numerous characteristic emission energies are output from the program, depending on a single input variable.

In a recent investigation, photon cross section libraries (XCOM [38], PHOTX [34]) and parametrizations implemented in simulation packages (GEANT [39], PETSIM [40]) were compared with the recent library provided by the Lawrence Livermore National Laboratory (EPDL97) [41] for energies from 1 keV to 1 MeV for a few human tissues and detector materials of interest in nuclear imaging [42]. The cross section data for mixtures and compounds were obtained from the equation

$$\mu = \rho \sum_i w_i (\mu/\rho)_i, \quad (1.6)$$

where ρ is the density of the material, w_i the fraction by weight of the i th atomic constituent as specified in ICRU report 44 [43], and $(\mu/\rho)_i$ the mass attenuation coefficients. Different photon cross section libraries show quite large variations as compared to the most recent EPDL97 data files (figure 1.2). The EPDL97

H₂O

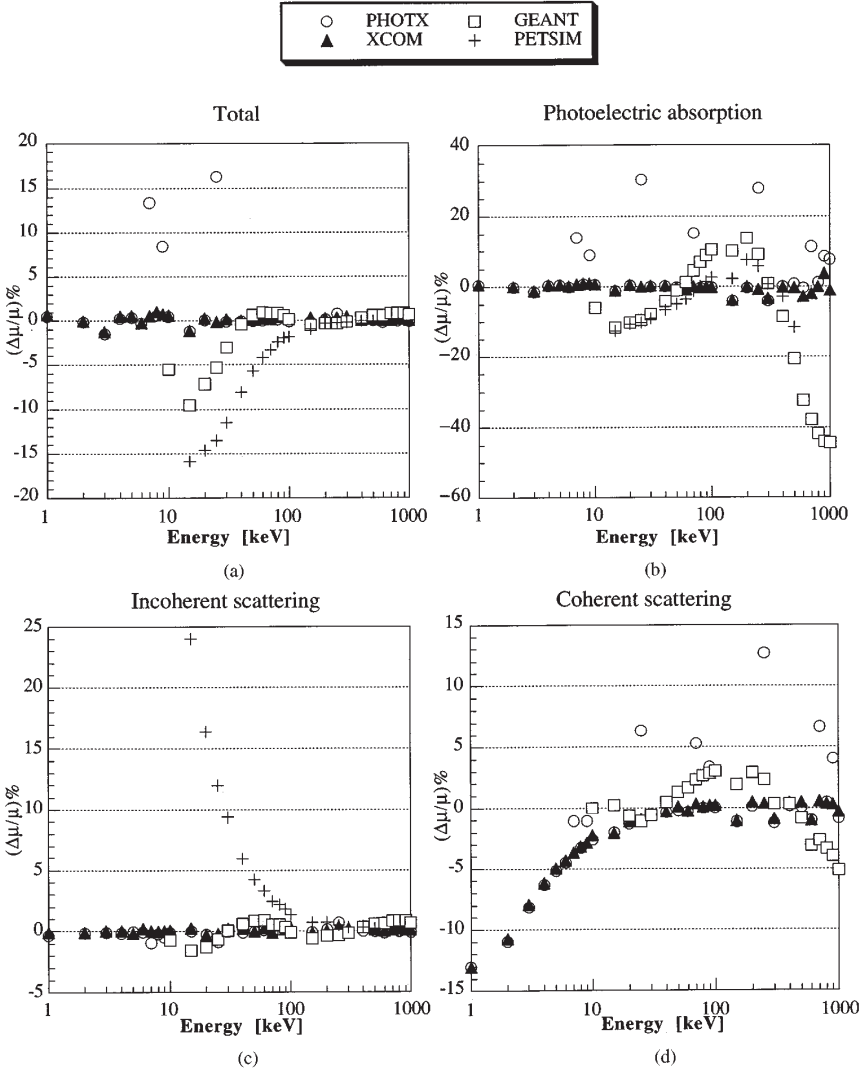


Figure 1.2. Comparisons (percentage differences) between the different libraries and the EPDL97 database for water (H₂O). The coefficients shown are: (a) total, (b) photoelectric, (c) incoherent and (d) coherent. The comparisons were calculated at energies given to the keV resolution between 1 and 1000 keV for both XCOM and PHOTX, between 10 and 1000 keV for GEANT, and between 15 and 511 keV for PETSIM. Reprinted from [42] © 2000 IEEE, with permission.

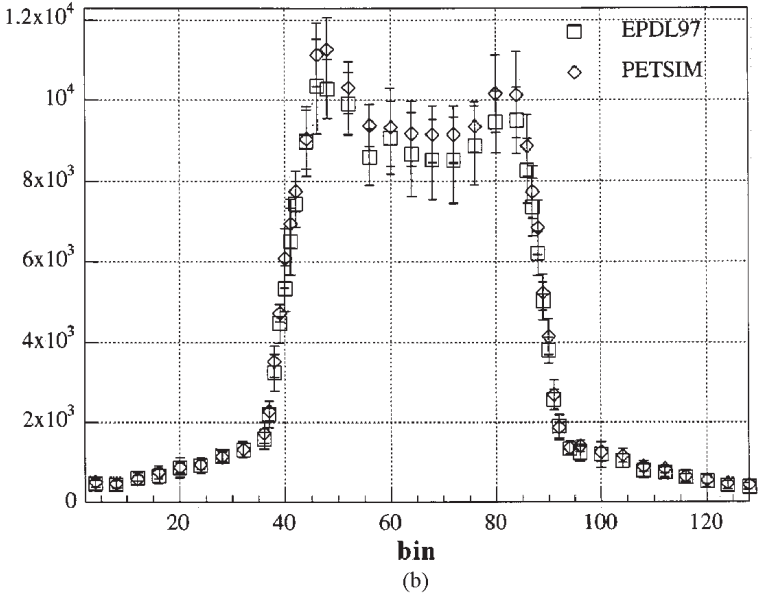
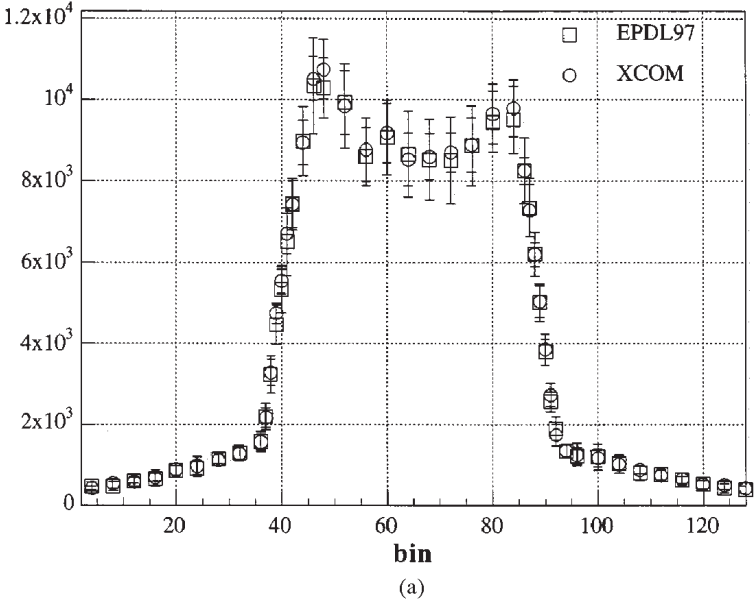


Figure 1.3. (a) Integral profile through a two-dimensional projection (single angular view) of a simulated Hoffman three-dimensional brain phantom generated using EPDL97 and XCOM photon cross section libraries. (b) Same as (a) for EPDL97 and PETSIM. Error bars are shown on the plots. Reprinted from [42] © 2000 IEEE, with permission.

library is the most up-to-date, complete and consistent library available and is already a standard in the nuclear reactor industry. It is recommended that Monte Carlo developers only use the most recent version of this library. Its use as a standard in the simulation of medical imaging systems will help to eliminate potential differences between the results obtained with different codes.

Further evaluation of the effect of the photon cross section library on actual simulation of PET data was performed by generating data sets for the three-dimensional Hoffman brain phantom contained in a cylindrical homogeneous water phantom (20 cm diameter, 17.5 cm height) with apparent relative concentrations of 4, 1 and 0 for grey matter, white matter and the ventricles, respectively, simulating the activity distributions found in normal human brain for cerebral blood flow and metabolism studies currently employed in PET [44]. Comparisons between the profiles through a simulated two-dimensional projection of the three-dimensional brain phantom estimated using different libraries are illustrated in figure 1.3. The statistical analysis of the data sets revealed the existence of a statistically significant difference between the resulting projections generated using different libraries ($p < 0.025$) [42].

1.3.2. Simulating interaction of photons with matter

For radiation transport problems, the computational model includes geometry and material specifications. Object modelling is fundamental to perform photon transport efficiently using the Monte Carlo method. It consists of a description of the geometry and material characteristics for the object. The material characteristics of interest are density and energy-dependent cross sections. Different steps are followed when tracing the photon in both the phantom/patient and the detector volume and depending on the application sought relevant parameters are stored. The relative ratios of the cross sections for photoelectric effect, incoherent and coherent scattering to the total cross section are used to choose randomly which process occurs at each interaction vertex.

In the case of photoelectric absorption, the total photon energy is transferred to an atomic electron and the random walk is terminated. In an incoherent photon interaction, a fraction of the photon energy is transferred to the atomic electron. The direction of the scattered photon is changed to conserve the total momentum of the interaction. The Klein–Nishina expression for the differential cross section per electron for an incoherent interaction is used to sample the energy and polar angle of the incoherently scattered photon taking into account the incoherent scattering factor [45]. The coherent scattering only results in a change in the direction of the scattered photon since the momentum change is transferred to the whole atom. The random number composition and rejection technique [46] is used to sample the momentum of the scattered photon and the scattering angle according to the form-factor distributions. Coherent scatter distributions are sharply forward peaked and vary considerably with atomic number and energy [47]. The pathlength of

the interacting photon is randomly generated according to the exponential attenuation based on the interaction length. The total cross section at the energy of the interacting photon determines the interaction length of the exponential distribution. Calculation of the distances between interactions in a medium are performed by sampling from the exponential attenuation distribution (see equation 1.12). Different techniques have been proposed to improve the computation speed when sampling from the probability distributions. They are described in more detail in sections 1.5 and 1.6.

For example when simulating data acquisition for a PET scanner operating in three-dimensional mode, the tomograph is simulated as a number of detection rings, each ring consisting of a number of scintillator crystals [48]. Grouping crystals in matrices simulates the detection block, typical of current generation PET scanners. Photon history is tracked within a crystal, across crystals within a block and across blocks. Crystals are considered as adjacent in the transaxial plane and in the axial direction. Two external shields are simulated as tungsten rings located at the two axial edges of the tomograph, partly shielding radiation coming from outside the scanner field of view. In the detector blocks, at each interaction vertex, the local energy deposition is recorded. Tracking is stopped either by photoelectric absorption, escape of the photon from the block volume, or by Compton scattering leaving less than 5 keV to the recoil photon. The energies of all interaction vertices are summed to yield the total absorbed energy in the scintillation detector. This total energy is assumed to be converted to scintillation light using Gaussian random smearing to account for the combined energy resolution, $\Delta E/E$, of the scintillator and its photomultipliers. $\Delta E/E$ is assumed to be proportional to $1/\sqrt{E}$. The position blurring step then calculates the mean detection coordinates (X, Y, Z) of each incident photon. This is done by computing the centroid of all interaction vertices, each weighted by the ratio of its individual energy to the total energy. The mean X and Y coordinates of each photon are smeared to account for spatial resolution degradation due to positron range effect, annihilation photon acollinearity and position miscoding in the detector block.

1.4. ELECTRON TRANSPORT

The Monte Carlo simulation of electron transport, as opposed to the local absorption of electrons in their site of production, should be included in all calculations where the complete electromagnetic cascade is to be considered. The interest in medical radiation physics focuses on situations where electron ranges are comparable with the dimensions or the spatial resolution of the problem to be solved, or the contribution of bremsstrahlung plays a significant role in the amount of energy locally deposited or transported away. Because of the low energies involved in nuclear medicine, secondary

electrons are generally assumed to deposit all their energy at the point of interaction and their bremsstrahlung production is negligible. Thus, electron transport has not received particular attention in nuclear imaging applications of the Monte Carlo method. However, a number of investigators in the field have considered the simulation of electron transport, mainly for dosimetry calculations [49–53], and for this reason a brief description of electron transport techniques is given in this section.

Strictly, all the different electron interaction types should be considered in detail in a Monte Carlo simulation, much in the same way as it is done with photon interactions. This is a technique called *microscopic* simulation [54], which is used at low electron energies, for example in electron microscopy. The complexity of the procedures used in microscopic techniques varies considerably, although a common approach is to neglect bremsstrahlung interactions due to the low energies involved. The most common simple models used are based on the simulation of all the single-scattering events, calculating the electron step-length between consecutive collisions with the elastic mean-free-path. Energy losses are determined from the Bethe theory of stopping power [55] and energy-loss straggling is accounted for approximately. These models have been improved by taking inelastic collisions into account.

When the electron energy increases above a few tens of keV, the large number of interactions that occur during electron slowing-down makes it unrealistic to simulate all the single physical interactions. Instead, multiple collisions are taken into account in what resembles a series of ‘snapshots’ of an electron *history* taken at certain time or energy intervals; single interactions of different kinds are considered between two consecutive snapshots. This grouping scheme constitutes the *macroscopic* [54] or condensed-history techniques [56]. In a seminal work, Berger [56] established the basis of these techniques for charged-particle transport, where algorithms are based on multiple scattering theory (Moliere, Goudsmit–Saunderson) and stopping power calculations to describe the grouped angular deflections and energy losses, respectively. He divided algorithms into two broad classes, class I and class II, which are distinguished mainly by the way in which energy losses are grouped and, more specifically, by how the individual interactions leading to a large energy transfer, namely the production of energetic knock-on electrons and bremsstrahlung photons, are described.

The Monte Carlo system ITS3 [57] with its physics based on the original ETRAN code by Berger and Seltzer [58], and EGS4 [33] are, respectively, the most widely used examples of class I and class II algorithms in medical physics. Unbiased comparisons of the two systems for a variety of situations and energies have been made by Andreo [59]. In recent years, the most advanced electron transport algorithms, with physics that has overcome that of older Monte Carlo systems, combine macroscopic and microscopic

techniques, where the latter are used in situations that require sophisticated boundary-crossing algorithms [60, 61].

1.4.1. Stopping power data

As is well known, the stopping power of an electron in a material gives the average rate at which the electron loses energy, be it transferred to the medium, or to secondary electrons and/or bremsstrahlung photons that transport the energy away from the interaction site; its integral provides the average distance an electron can travel in the material, that is, the electron range. Although a deterministic quantity, stopping powers are the foundation stones of the Monte Carlo simulation of electron transport. They are also key quantities in dosimetry, as they allow the determination of the energy absorbed in a medium based on the knowledge of the energy absorbed in a different medium, the detector (cavity theory). Stopping powers are calculated according to Bethe theory [55], applicable to electrons and heavy charged particles. ICRU Report 37 [62] provides details on how the key quantity *mean ionization potential*, I , has been derived for elements and compounds, and on the evaluation of the density-effect correction; it also describes the limitations of Bethe theory at energies below 1–10 keV approximately. A similar ICRU Report 49 has been published for protons and alpha particles [63]. A set of computer programs, ESTAR, PSTAR and ASTAR [64], calculate stopping-powers and ranges for electrons, protons and alpha particles, respectively, in different elements and compounds from a pre-computed set of data, which form the basis of the two mentioned ICRU reports. These data are not only necessary for transport calculations but have become standard reference data for the radiological sciences.

In the case of dosimetry, the interest rests on the calculation of stopping-power ratios, medium to detector, where the use of the Monte Carlo method to derive electron spectra, combined with analytical cavity theories, has enabled the determination of stopping-power ratios that include all generations of electrons and photons produced during the simulation of the transport of incident electrons or photons. There is extensive literature on the use of the Monte Carlo method for producing such data, mainly for radiotherapy dosimetry [65–70], and for the set of values in current use, the agreement between the various calculations is at the impressive 0.1% level, even when different Monte Carlo codes have been used. It is worth emphasizing that, in the evolution of the use of the Monte Carlo method in radiotherapy dosimetry, the most important changes (of the order of several per cent), as well as a dramatic improvement in our knowledge and interpretation of physical phenomena, occurred during the 1980s as a result of the extended use of Monte Carlo calculations by Berger and Seltzer. The 1990s have mainly been characterized by a refinement of the

data, at the level of 1% or so, associated with the computer revolution that has improved so dramatically many other aspects of medical radiation physics.

1.5. ANALOGUE SAMPLING

Analogue Monte Carlo attempts to simulate the full statistic development of the electromagnetic cascade. If we assume that a large number of particle histories, N , are included in a batch, the individual batch estimates can be considered as drawn from a normal distribution. For a given calculation, the estimated uncertainty is proportional to the inverse of the square root of the number of histories simulated. The efficiency ε of a Monte Carlo calculation can therefore be defined as [71]

$$\varepsilon = \frac{1}{\sigma^2 T}, \quad (1.7)$$

where T is the calculation time required to obtain a variance estimate σ^2 . For large N , ε should be constant as long as the calculation technique remains the same.

As discussed earlier, the imaging system and/or source distribution can be described in terms of probability density functions (pdfs). These pdfs, supplemented by additional computations, describe the evolution of the overall system, whether in space, energy, time, or even some higher-dimensional phase space. The goal of the Monte Carlo method is to simulate the imaging system by random sampling from these pdfs and by performing the necessary supplementary computations needed to describe the system evolution. In essence, the physics and mathematics are replaced by random sampling of possible states from pdfs that describe the system. Thus, it is frequently necessary to sample some physical event, the probability of which is described by a known pdf. Examples include the distance to the next interaction and the energy of a scattered photon. Let x be the physical quantity to be selected and $f(x)$ the pdf. Among the properties of the pdf is that it is integrable and non-negative. Assume that the domain of $f(x)$ is the interval $[x_{\min}, x_{\max}]$ and that it is normalized to unit area. The cumulative distribution function $F(x)$ of the frequency function $f(x)$ gives the probability that the random variable τ is less than or equal to x . It is defined as

$$F(x) \equiv \text{probability}(\tau \leq x) = \int_{x_{\min}}^x f(\tau) d\tau. \quad (1.8)$$

A stochastic variable can be sampled by the use of uniformly distributed random numbers R in the range $[0-1]$ using one of the techniques described below.

1.5.1. Direct method

This method can be used if the inverse of the cumulative distribution function $F^{-1}(x)$ is easily obtainable. Since $F(x)$ is uniformly distributed in $[0-1]$, the sampled value of x could be obtained by substituting $F(x)$ in equation (1.8) by a uniform random number \mathbf{R} , that is $x = F^{-1}(\mathbf{R})$. A practical example of using this technique is the calculation of the distance to the next interaction vertex. The inversion is not always possible, but in many important cases the inverse is readily obtained.

1.5.2. Rejection method

Another method of performing this when it is too complicated to obtain the inverse of the distribution function is to use the rejection technique [46], which follows the following steps:

- (i) Define a normalized function $f'(x) = f(x)/f_{\max}(x)$, where $f_{\max}(x)$ is the maximum value of $f(x)$.
- (ii) Sample two uniformly distributed random numbers \mathbf{R}_1 and \mathbf{R}_2 .
- (iii) Calculate x using the equation $x = x_{\min} + \mathbf{R}_1(x_{\max} - x_{\min})$.
- (iv) If \mathbf{R}_2 is less than or equal to $f'(x)$ then x is accepted as a sampled value, otherwise a new value of x is sampled.

Over a large number of samples, this technique will yield a set of values of x within the required distribution. It does, however, require two random numbers per trial and many trials may be required depending on the area under of the curve of $f(x)$. A typical example of using this technique is the sampling of the photon energy and scattering angle resulting from incoherent scattering.

1.5.3. Mixed methods

When the previous two methods are impractical, the mixed method, which combines the two, may be used [71]. Assume that the pdf can be factored as follows:

$$f(x) = h(x) \cdot g(x) \quad (1.9)$$

where $h(x)$ is an invertible function and $g(x)$ is relatively flat but contains most of the mathematical complexity. The method consists in the following steps:

- (i) Normalize $h(x)$ producing $h'(x)$ such that $\int_{x_{\min}}^{x_{\max}} h'(x) dx = 1$.
- (ii) Normalize $g(x)$ producing $g'(x)$ such that $g'(x) \leq 1$ for x in $[x_{\min}, x_{\max}]$.
- (iii) Use the direct method to select an x using $h'(x)$ as the pdf.
- (iv) Use x and apply the rejection method using $g'(x)$, i.e., choose a random number \mathbf{R} ; if $g'(x) \leq \mathbf{R}$, accept x , otherwise go back to step (iii).

1.6. NON-ANALOGUE SAMPLING ‘VARIANCE REDUCTION’

A direct Monte Carlo simulation using true probability functions may require an unacceptably long time to produce statistically relevant results. Emission of photons is isotropic, so directional parameters may be sampled uniformly within their individual ranges. Nuclear imaging systems have a low geometrical efficiency because of the small solid angle defined by the collimator and/or the small axial aperture. Therefore, the calculation would be very ineffective in terms of required computing time [72]. It is thus desirable to bias the sampling (non-analogue sampling) by introducing different types of importance sampling and other variance reduction techniques to improve the computational efficiency of the Monte Carlo method [73]. The results obtained by non-analogue simulation are, however, biased by the variance reduction technique and a correction for this is required. A particle history weight, W , is introduced, which describes the probability of the particle following the current path. This weight is calculated for each particle history, and used in the calculation of the results. If an event occurs, the weight W is added to the counter rather than incrementing the counter by one unit. Bielajew and Rogers [71] divided variance reduction techniques into three categories: those that concern photon transport only, those that concern electron transport only, and other more general methods. The most useful techniques are described below. It is worth noting that concerning the Poisson nature of the activity distributions in nuclear imaging, these variance reduction approximations may result in statistically relevant deviations from an otherwise unbiased simulation result since Monte Carlo simulated projection data are (as a result of variance reduction) not count but probability data.

1.6.1. Photon-specific methods

Interaction forcing. In an analogue Monte Carlo simulation, photons are tracked through the object until they either escape the object, are absorbed, or their energy drops below a selected threshold. The probability function for a photon interaction is given by

$$p(x) = \mu e^{-\mu x}. \quad (1.10)$$

The probability that a photon will travel a distance d or less is given by

$$p(d) = \int_0^d \mu e^{-\mu x} dx = 1 - e^{-\mu d}. \quad (1.11)$$

To sample the pathlength, a uniform random number R is substituted for $p(d)$ and the problem is solved for d :

$$d = -\frac{\log(1 - R)}{\mu}. \quad (1.12)$$

Since the maximum distance, d_{\max} , the photon travels before interaction is infinite and the number of mean free paths across the geometry in any practical situation is finite, there is a large probability that photons leave the geometry of interest without interacting. To increase the statistical accuracy in the imparted energy calculation, we force the photons to interact by assigning d_{\max} a finite distance, e.g., the thickness of the detector being simulated. A true distributed photon pathlength d within d_{\max} can be sampled from the equation

$$d = -\frac{1}{\mu} \ln(1 - R[1 - e^{-\mu d_{\max}}]). \quad (1.13)$$

The photon’s weight must be multiplied by the interaction probability

$$W_{n+1} = W_n[1 - e^{-\mu d_{\max}}]. \quad (1.14)$$

In emission computed tomography, the photon is allowed to interact through coherent or incoherent interactions only within the phantom since photo-absorption does not contribute to energy imparted in the crystal. The weight is then multiplied by the probability of the photon being scattered:

$$W_{n+1} = W_n \left[\frac{\mu_{\text{incoh}} + \mu_{\text{coh}}}{\mu} \right], \quad (1.15)$$

where μ_{incoh} and μ_{coh} are the cross section data for incoherent and coherent scattering, respectively, and μ is the total linear attenuation coefficient.

Stratification. Stratification refers to the process of determining the frequencies with which the various regions of state space are used to start a particle [74]. The solid angle of acceptance of the detector array, Ω_{\max} , is small due to collimation and to the size of the detector array itself. This results in significant computational inefficiencies with analogue Monte Carlo simulation, because only a few per cent of the photons generated and tracked will actually be detected. The goal of stratification is to simulate only photons that are emitted in directions within the solid angle which can be calculated from the maximum acceptance angle, θ_{\max} , which in turn can be estimated from the dimensions of the phantom and the detection system. The solid angle does not change in magnitude when simulating source locations off-centre. The photon escaping from the phantom is either primary or scattered. If the photon happens to be a primary photon, its direction within the solid angle could be sampled from

$$\cos(\theta) = 1 - R[1 - \cos \theta_{\max}]. \quad (1.16)$$

In this case, the weight is multiplied by the probability of escape without interaction in the solid angle Ω_{\max}

$$W_{n+1} = W_n \frac{[1 - \cos \theta_{\max}]}{2}. \quad (1.17)$$

Exponential transform, Russian roulette and particle splitting. The exponential transform is a variance reduction technique used to bias the sampling procedure to give more interactions in the regions of interest and thus improve the efficiency of the calculation for those regions. To implement this method, the distance to the next interaction in number of mean free paths, d_λ , should be sampled from [71]

$$d_\lambda = -\frac{\ln(\mathbf{R})}{(1 - C \cos \theta)}, \quad (1.18)$$

where C is a parameter that adjusts the magnitude of the scaling and θ the angle of the photon with respect to the direction of interest. The new weighting factor is given by

$$W_{n+1} = W_n \frac{\exp(-d_\lambda C \cos \theta)}{(1 - C \cos \theta)}. \quad (1.19)$$

Note that the new weighting factor is dependent on d_λ . If $0 < C < 1$, the particle pathlength is stretched in the forward direction, which is used for shielding problems. For $-1 < C < 0$, the average distance to the next interaction is shortened in the forward direction, which is used for surface problems. For $C = 0$, we recover the unbiased sampling. The optimal choice of this parameter is dependent on the problem to be solved. The general guideline is to avoid to use large weighting factors because they may increase the variance.

Russian roulette and splitting are often used together with the exponential transform, although they are still effective when used independently. In Russian roulette, a random number is selected and compared with a threshold, λ . If the random number turns out to be smaller than λ , the particle is allowed to survive but the weight should be updated accordingly: $W_{n+1} = W_n/\lambda$. In particle splitting, a particle coming from a region of interest can be divided into N particles, each having a new weighting: $W_{n+1} = W_n/N$.

1.6.2. Electron-specific methods

Electron range rejection. A fundamental difference between the transport of photons and electrons in a condensed-history simulation code is that photons travel relatively long distances before interacting while electron tracks are interrupted not only by geometrical boundaries but also by multiple scattering ‘steps’. A large amount of simulation time is spent on checking boundaries and selecting deflection angles and so on. Electron range rejection means that electrons with their residual range smaller than the distance to the nearest boundary or to the region of interest in the simulation will be terminated to save computing time. Different methods have been suggested

for electron range rejection. The reduced interrogation of geometry (RIG) method calculates the distance to the nearest boundary and compares it with the maximum multiple-scattering step length. If the electron cannot reach any of the boundaries during this step, the boundary checking routine will not be called and this will save computing time. Another method called ‘disregard within a zone’ is usually used with RIG to further speed up the simulation. It consists of disregarding electrons whose energies are so low that they cannot reach the nearest boundary. Those methods are, however, inefficient for simulations involving curved surfaces where the time required to calculate the distance to the closest boundary may be considerable [71]. An alternative way is to use a range-related ‘region rejection’ technique. In this method, different energy cut-offs are chosen for the regions surrounding the region where energy deposition is to be scored, each energy cut-off being chosen according to the distance to the nearest boundary of the region of interest.

Parameter-reduced electron step. This algorithm allows using small electron steps in the vicinity of interfaces and boundaries and large steps elsewhere [75]. Its components are: a path-length correction algorithm which is based on the multiple scattering theory of Moliere and which takes into account the differences between the straight path length and the total curved path length for each electron step; a lateral correlation algorithm which takes into account lateral transport; and a boundary crossing algorithm which ensures that electrons are transported accurately in the vicinity of interfaces. The algorithm has been implemented in the EGS4 Monte Carlo system and proved that substantial savings in computing time may be realized when using this method. The most recent version of the code system called EGSnrc [61] incorporates more accurate electron physics and transport algorithms which include an improved electron-step algorithm, a correct implementation of the fictitious cross section method for sampling distances between discrete interactions, a more accurate evaluation of energy loss, as well as an exact boundary crossing algorithm.

1.6.3. General methods

Correlated sampling. The correlated sampling technique can be used in transport of both photons and electrons. It is especially effective for calculating ratios or differences of two quantities which are nearly equal. The basic idea is that the simulations of the geometries of interest are kept as closely correlated as possible so that most of the statistical fluctuations will cancel in the ratios and differences. The real difference between the two geometries will be better reflected in the ratios and the differences obtained. The calculational uncertainties in the ratios and the differences obtained with correlated

sampling are in general smaller than those obtained from uncorrelated simulations.

There are several ways of doing correlated sampling in radiation transport. In coupled photon–electron transport, a simple method has been used in which random number seeds of the particle histories, for which a primary particle or any of the secondaries has deposited energy in the region of interest for one geometry, is stored and used for the simulations of the alternative geometry [71]. A correlated sampling method for the transport of electrons and photons has been developed in which a main particle history is split up whenever a particle meets the boundary of the region where the medium differs between two or more cases [76]. This particle is then followed separately for each case until it and all its descendants terminate. Holmes *et al.* [77] described a correlated sampling technique which forces histories to have the same energy, position, direction and random number seed as incident on both a heterogeneous and homogeneous water phantom. This ensures that a history that has, by chance, travelled through only water in the heterogeneous phantom will have the same path as it would have through the homogeneous phantom, resulting in a reduced variance when a ratio of heterogeneous dose to homogeneous dose is formed.

Use of geometry symmetry. The use of some of the inherent symmetry of the geometry may realize considerable increase in efficiency. If both the source and target configurations contain cylindrical planar or spherical–conical simulation geometries, the use of symmetries is more obvious. Other uses of symmetry are less obvious but the saving in computing time is worth the extra care and coding.

1.7. SUMMARY

Today’s applications of Monte Carlo techniques include diagnostic imaging and radiation therapy, traffic flow, Dow-Jones forecasting, and oil well exploration, as well as more traditional physics applications like stellar evolution, reactor design, and quantum chromo-dynamics. Monte Carlo methods are widely used in modelling of materials and chemicals, from grain growth modelling in metallic alloys, to behaviour of nanostructures and polymers, and protein structure predictions.

The application of Monte Carlo modelling in medical physics is an everlasting enthusiastic topic and an area of considerable research interest. Monte Carlo modelling has contributed to a better understanding of the physics of photon and electron transport by clinical physicists. The large number of applications of the Monte Carlo method attests to its usefulness as a research tool in different areas of nuclear medicine.

Recent developments in diagnostic and therapeutic nuclear medicine combined with advanced computing facilities and physics support have created new opportunities for Monte Carlo simulation in this exciting field. Important developments and applications are summarized in the following chapters of the book.

ACKNOWLEDGMENTS

The author would like to thank Professor Pedro Andreo and Dr Mike Stabin for fruitful discussions. Their comments and suggestions on this chapter are gratefully acknowledged.

REFERENCES

- [1] Metropolis N and Ulam S 1949 The Monte Carlo method *J. Am. Stat. Assoc.* **44** 335–41
- [2] McCracken D D 1955 The Monte Carlo method *Sci. Am.* **192** 90–6
- [3] Van Dam C 2000 *The Urim and Thummim: A Means of Revelation in Ancient Israel* ed I Eisenbrauns (Winona Lake, IN)
- [4] de Buffon G 1777 Essai d'arithmétique morale *Supplément à l'Histoire Naturelle* vol 4
- [5] Rayleigh J W S 1899 On the theory of resonance *Collected Scientific Papers* **1** 33–75
- [6] Kolmogorov A N 1933, 1956 *Foundations of the Theory of Probability* (2nd English edition) transl ed N Morrison (New York: Chelsea)
- [7] Ulam S M 1976 *Adventures of a Mathematician* (New York: Scribners)
- [8] Ulam S M 1951, 1949 On the Monte Carlo Method *Symposium on Large-Scale Digital Calculating Machines* (Cambridge, MA: Harvard University Press)
- [9] L V Spencer 1948 'Polarization of multiply scattered gamma rays' (unpublished) (National Bureau of Standards Interim Report on Contract with US Office of Naval Research)
- [10] Spencer L V and Wolff C 1953 Penetration and diffusion of hard X-rays: Polarization effects *Phys. Rev.* **90** 510–14
- [11] Kahn H 1949 'Stochastic (Monte Carlo) attenuation analysis' *Report p-88* (RAND)
- [12] Mayer M 1951 Report on a Monte Carlo calculation performed with the ENIAC *Monte Carlo Method* eds A S Householder, G E Forsythe and H H Germond US National Bureau of Standards Applied Math Series No 12, pp 19–20
- [13] Raeside D E 1976 Monte Carlo principles and applications *Phys. Med. Biol.* **21** 181–97
- [14] Turner J E, Wright H A and Hamm R N 1985 A Monte Carlo primer for health physicists *Health Phys.* **48** 717–33
- [15] Marsaglia G and Zaman A 1994 Some portable very-long-period random number generators *Comput. Phys.* **8** 117–21

- [16] Ferrenberg A M, Landau D P and Wong Y J 1992 Monte Carlo simulations: hidden errors from 'good' random number generators *Phys. Rev. Lett.* **69** 3382–4
- [17] Vattulainen I, Kankaala K, Saarinen J and Ala-Nissila T 1995 A comparative study of some pseudorandom number generators *Comp. Phys. Comm.* **86** 209–26
- [18] Booth T E 1998 The intelligent random number technique in MCNP *Nucl. Sci. Eng.* **100** 248–54
- [19] Lehmer D H 1949 Mathematical methods in large-scale computing units *2nd Symposium on Large-Scale Digital Calculating Machinery*, Cambridge (Cambridge, MA: Harvard University Press) pp 141–6
- [20] Marsaglia G and Zaman A 1993 Monkey tests for random number generators *Comp. Math. Appl.* **23** 1–10
- [21] Knuth D E 1981 *The Art of Computer Programming, Seminumerical Algorithms* 2nd edition (Reading, MA: Addison-Wesley) vol 2
- [22] Press W H 1992 *Numerical Recipes in C, The Art of Scientific Computing* (Cambridge: Cambridge University Press)
- [23] Anderson S L 1990 Random number generators on vector supercomputers and other advanced architectures *SIAM Rev.* **32** 221–51
- [24] Mascagni M, Cuccaro S A, Pryor D V and M L Robinson 1995 A fast, high-quality, and reproducible lagged-Fibonacci pseudorandom number generator *J. Comput. Phys.* **15** 211–19
- [25] Brent R P 1994 On the periods of generalized Fibonacci recurrences *Math. Comput.* **63** 389–401
- [26] Zaidi H, Labbé C and Morel C 1998 Implementation of an environment for Monte Carlo simulation of fully 3D positron tomography on a high-performance parallel platform *Parallel Comput.* **24** 1523–36
- [27] Zaidi H 1999 Relevance of accurate Monte Carlo modeling in nuclear medical imaging *Med. Phys.* **26** 574–608
- [28] Hubbell J H 1999 Review of photon interaction cross section data in the medical and biological context *Phys. Med. Biol.* **44** R1–22
- [29] Storm E and Israel H I 1970 Photon cross sections from 1 keV to 100 MeV for elements $Z = 1$ to $Z = 100$ *Nucl. Data Tables* **A7** 565–681
- [30] Briesmeister J F 1997 (Los Alamos, NM: Los Alamos National Laboratory)
- [31] Hubbell J H *et al.* 1975 Atomic form factors, incoherent scattering functions, and photon scattering cross sections *J. Phys. Chem. Ref. Data* **4** 471–538
- [32] Cullen D E *et al.* 1989 'Tables and graphs of photon interaction cross sections from 10 eV to 100 GeV derived from the LLNL Evaluated Photon Data Library (EPDL)' *UCRL-50400* (Lawrence Livermore National Laboratory, CA)
- [33] Nelson W R, Hirayama H and Rogers D W O 1985 (Stanford, CA: Stanford Linear Accelerator Center)
- [34] Trubey D K, Berger M J and Hubbell J H 1989 Photon cross sections for ENDF/B-IV. *American Nuclear Society Topical Meeting, Advances in Nuclear Engineering Computation and Radiation Shielding*, Santa Fe, NM
- [35] Sakamoto Y 1993 Photon cross section data PHOTX for PEGS4 code. *EGS4 users' meeting, Japan (KEK Proceedings)* pp 77–82
- [36] Halbleib J A, Kensek R P, Valdez G D, Seltzer S M and Berger M J 1992 ITS: The Integrated TIGER Series of electron/photon transport codes—version 30 *IEEE Trans. Nucl. Sci.* **39** 1025–30

- [37] Boone J M and Chavez A E 1996 Comparison of x-ray cross sections for diagnostic and therapeutic medical physics *Med. Phys.* **23** 1997–2005
- [38] Berger M J and Hubbell J H 1987 ‘XCOM: Photon cross sections on a personal computer’ *NBSIR 87-3597* (US National Bureau of Standards)
- [39] Brun R, Bruyant F, Maire M, McPherson A C and Zanarini P 1994 ‘GEANT detector description and simulation tool’ *DD/EE/84-1* (CERN)
- [40] Picard Y, Thompson C J and Marrett S 1993 Improving the precision and accuracy of Monte Carlo simulation in positron emission tomography *IEEE Trans. Nucl. Sci.* **39** 1111–16
- [41] Cullen D E, Hubbell J H and Kissel L 1997 ‘EPDL97: the Evaluated Photon Data Library’ *UCRL-50400* (Lawrence Livermore National Laboratory, CA)
- [42] Zaidi H 2000 Comparative evaluation of photon cross section libraries for materials of interest in PET Monte Carlo simulations *IEEE Trans. Nucl. Sci.* **47** 2722–35
- [43] ICRU 1989 *Tissue Substitutes in Radiation Dosimetry and Measurement* vol 44 (International Commission on Radiological Units and Measurements)
- [44] Hoffman E J, Cutler P D, Digby W M and Mazziotta J C 1990 3-D phantom to simulate cerebral blood flow and metabolic images for PET *IEEE Trans. Nucl. Sci.* **37** 616–20
- [45] Klein O and Nishina Y 1929 Über die Streuung von Strahlung durch freie Elektronen nach der neuen relativistischen Quantendynamik von Dirac *Z. Phys.* **52** 853–68
- [46] Kahn H 1956 *Use of Different Monte Carlo Sampling Techniques in Monte Carlo Methods* ed H A Meyer (New York: Wiley)
- [47] Kaplan M S, Harrison R L and Vannoy S D 1998 Coherent scatter implementation for SimSET *IEEE Trans. Nucl. Sci.* **45** 3064–8
- [48] Zaidi H, Scheurer A H and Morel C 1999 An object-oriented Monte Carlo simulator for 3D cylindrical positron tomographs *Comput. Methods Programs Biomed.* **58** 133–45
- [49] Stabin M and Konijnenberg M W 2000 Re-evaluation of absorbed fractions for photons and electrons in spheres of various sizes *J. Nucl. Med.* **41** 149–60
- [50] Bouchet L G and Bolch W E 1999 A three-dimensional transport model for determining absorbed fractions of energy for electrons within cortical bone *J. Nucl. Med.* **40** 2115–24
- [51] Bouchet L G, Jokisch D W and Bolch W E 1999 A three-dimensional transport model for determining absorbed fractions of energy for electrons within trabecular bone *J. Nucl. Med.* **40** 1947–66
- [52] Furhang E E, Chui C S, Kolbert K S, Larson S M and Sgouros G 1997 Implementation of a Monte Carlo dosimetry method for patient-specific internal emitter therapy *Med. Phys.* **24** 1163–72
- [53] Yoriyaz H, Stabin M and dos Santos A 2001 Monte Carlo MCNP-4B-based absorbed dose distribution estimates for patient-specific dosimetry *J. Nucl. Med.* **42** 662–9
- [54] Andreo A 1991 Monte Carlo techniques in medical radiation physics *Phys. Med. Biol.* **36** 861–920
- [55] Bethe H A 1930 Zur Theorie des Durchgangs schneller Korpuskularstrahlen durch Materie *Ann. Phys., Lpz.* **5** 325
- [56] Berger M J 1963 Monte Carlo calculation of the penetration of diffusion of fast charged particles *Methods in Computational Physics* ed B Alder, S Feinbach and M Rotenberg (New York: Academic) pp 135–215

- [57] J A Halbleib *et al.* 1992 'ITS version 3.0: The integrated TIGER Series of coupled electron/photon Monte Carlo transport codes' *Report SAND91-1634* (Sandia National Laboratories)
- [58] Berger M J and Seltzer S M 1968 'Electron and photon transport programs: I. Introduction and notes on program DATAPAC 4; II. Notes on program ETRAN-15' *Reports NBS 9836 and 9837. Report ORNL-RSIC CCC-107* (Oak Ridge: Oak Ridge National Laboratory; National Bureau of Standards)
- [59] Andreo P 1995 *A Comparison Between the ITS3 and EGS4 Monte Carlo Codes in Radiation Physics*, Advanced Monte Carlo Computer Programs for Radiation Transport (Saclay: Publications Service OECD)
- [60] Salvat F, Fernandez-Varea J M, Sempau J and Mazurier J 1999 Practical aspects of Monte Carlo simulation of charged particle transport: mixed algorithms and variance reduction techniques *Radiat. Environ. Biophys.* **38** 15–22
- [61] Kawrakow I 2000 Accurate condensed history Monte Carlo simulation of electron transport. I. EGSnrc, the new EGS4 version *Med. Phys.* **27** 485–98
- [62] ICRU 1984 'Stopping powers for electrons and positrons' *Report 37* (International Commission on Radiological Units and Measurements)
- [63] ICRU 1993 'Stopping powers and ranges for protons and alpha particles' *Report 49* (International Commission on Radiological Units and Measurements)
- [64] Berger M J 1993 'ESTAR, PSTAR, and ASTAR: computer programs for calculating stopping-power and range tables for electrons, protons, and helium ions' *NIST Report NISTIR 4999* (National Institute of Standards and Technology)
- [65] Berger M J, Seltzer S M, Domen S R and Lamperti P J 1975 Stopping-power ratios for electron dosimetry with ionization chambers. *Biomedical Dosimetry* (Vienna: IAEA) pp 589–609
- [66] Nahum A E 1978 Water/air mass stopping power ratios for megavoltage photon and electron beams *Phys. Med. Biol.* **23** 24–38
- [67] Andreo P and Brahme A 1986 Stopping power data for high-energy photon beams *Phys. Med. Biol.* **31** 839–58
- [68] Ding G X, Rogers D W and Mackie T R 1995 Calculation of stopping-power ratios using realistic clinical electron beams *Med. Phys.* **22** 489–501
- [69] Malamut C, Rogers D W and Bielajew A F 1991 Calculation of water/air stopping-power ratios using EGS4 with explicit treatment of electron–positron differences *Med. Phys.* **18** 1222–8
- [70] ICRU 1984 'Radiation dosimetry: electron beams with energies between 1 and 50 MeV' *Report 35* (International Commission on Radiological Units and Measurements)
- [71] Bielajew A F and Rogers D W O 1989 Variance-reduction techniques *Monte Carlo Transport of Electrons and Photons* ed T Jenkins, A Rindi, A Nahum and D W O Rogers (New York: Plenum) pp 407–19
- [72] Haynor D R, Harrison R L and Lewellen T K 1990 Improving the efficiency of emission tomography using variance reduction techniques *IEEE Trans. Nucl. Sci.* **37** 749–53
- [73] Zubal I G and Harrell C R 1992 Voxel-based Monte Carlo calculations of nuclear medicine images and applied variance reduction techniques *Image Vision Computing* **10** 342–8
- [74] Haynor D R, Harrison R L and Lewellen T K 1991 The use of importance sampling techniques to improve the efficiency of photon tracking in emission tomography simulations *Med. Phys.* **18** 990–1001

- [75] Bielajew A F and Rogers D W O 1987 PRESTA: The parameter reduced electron-step transport algorithm for electron Monte Carlo transport *Nucl. Instrum. Methods Phys. Res.* **B18** 165–81
- [76] Ma C M and Nahum A E 1993 Calculation of absorbed dose ratios using correlated Monte Carlo sampling *Med. Phys.* **20** 1189–99
- [77] Holmes M A *et al.* 1993 The application of correlated sampling to the computation of electron beam dose distributions in heterogeneous phantoms using the Monte Carlo method *Phys. Med. Biol.* **38** 675–88

Chapter 2

Monte Carlo techniques in nuclear medicine dosimetry

Habib Zaidi and Pedro Andreo

2.1. INTRODUCTION

The use of the Monte Carlo method to simulate radiation transport has become the most accurate means of predicting absorbed dose distributions and other quantities of interest in the radiation treatment of cancer patients using either external or radionuclide radiotherapy. The same trend has occurred for the estimation of the absorbed dose in diagnostic procedures using radionuclides. There is broad consensus in accepting that the earliest Monte Carlo calculations in medical radiation physics have been made in the area of nuclear medicine, where the technique has been used for dosimetry modelling and computations. Formalism and data based on Monte Carlo calculations, developed by the Medical Internal Radiation Dose (MIRD) Committee of the Society of Nuclear Medicine, have been published in a series of supplements to the *Journal of Nuclear Medicine*, the first one being released in 1968 [1]. Some of these pamphlets made extensive use of Monte Carlo calculations to derive specific absorbed fractions for electron and photon sources uniformly distributed in organs of mathematical phantoms. Interest in Monte Carlo-based dose calculations with α and β emitters has been revived with the application of radiolabelled monoclonal antibodies to radioimmunotherapy (RIT). As a consequence of this generalized use, many questions are being raised, primarily about the need and potential of Monte Carlo techniques, but also about how accurate it really is, and what it would take to apply it clinically and make it available widely to the nuclear medicine community at large.

In this chapter, we try to answer many of these questions, sometimes without explicitly stating them. Many other questions will be answered when Monte Carlo techniques are implemented and used for more routine calculations and for in-depth investigations. A survey is presented of the

different applications of the Monte Carlo method in medical physics in general, and diagnostic and therapeutic nuclear medicine in particular, with special emphasis on internal dose calculations in radionuclide therapy. Interested readers are encouraged to consult the detailed and comprehensive reviews [2, 3] and books [4, 5] published on the subject. The main purpose of this chapter is to present a framework for applying Monte Carlo simulations for a wide range of problems in nuclear medicine dosimetry. Emphasis is given to applications where photon and/or electron transport in matter are simulated. Some computational aspects of the Monte Carlo method, mainly related to the generation of random numbers, sampling and variance reduction techniques are presented in chapter 1.

2.2. MONTE CARLO TECHNIQUES IN MEDICAL RADIATION PHYSICS

Monte Carlo techniques have become one of the most popular tools in different areas of medical physics following the development and subsequent implementation of powerful computing systems for clinical use. In particular, they have been extensively applied to simulate processes involving random behaviour and to quantify physical parameters that are difficult or even impossible to calculate analytically or to determine by experimental measurements.

Following the review by Andreo [2], the applications of the Monte Carlo method in medical radiation physics cover almost all topics including radiation protection, nuclear medicine, diagnostic radiology and radiotherapy, with an increasing enthusiastic interest in exotic and exciting new applications such as intravascular radiation therapy and boron neutron capture therapy and synovectomy. The use of Monte Carlo techniques in the last two areas falls outside the scope of this survey whereas applications in radiation protection and nuclear medicine imaging and dosimetry are covered in the following sections. The present authors are not aware of a comprehensive review on applications of the Monte Carlo method in diagnostic radiology and would recommend a recent paper by Boone *et al.* [6] for an up-to-date validation study providing a general overview of the field. Interested readers in radiotherapy physics are encouraged to check the reviews by Ma and Jiang [7] for electron beams, and by Ahnesjö and Aspradakis [8] for photon beams. With the rapid development of computer technology, Monte Carlo-based treatment planning for radiation therapy is becoming practical.

An area which has received considerable attention during the past few years is intravascular brachytherapy (see chapter 14). The irradiation of the coronary arteries is being studied by a number of researchers worldwide, with the hope of reducing the rate of restenosis. Currently, there is

considerable discussion about the best radionuclides and radiation delivery systems that will be effective. Stabin *et al.* [9] used both the MCNP-4B and EGS4 Monte Carlo systems to simulate radiation sources, and results have been crosschecked between the two systems using ^{186}Re and ^{188}Re balloon sources as well as an ^{192}Ir wire source. Three-dimensional dose distributions have also been calculated for a ^{32}P impregnated stent and a ^{198}Au stent using EGS4 [10].

The promise of a new experimental cancer therapy with some indication of its potential efficacy has led many scientists from around the world to work on an approach called neutron capture therapy (NCT), where the use of boron (BNCT) has dominated this type of application. The idea behind BNCT is straightforward. A tumour-seeking compound containing boron-10 (^{10}B), a non-radioactive isotope, is introduced into the brain and given time to accumulate in the tumour. The patient is then exposed to a beam of neutrons, usually in a nuclear reactor facility, which are 'captured' or absorbed by the ^{10}B . Capturing neutrons causes the boron nuclei to break apart, resulting in the emission of α radiation and lithium nuclei. Both α particles and lithium are high in energy but short in range, which means they potentially can destroy the malignant cells in which ^{10}B is imbedded without hurting the adjacent healthy cells. Advanced methods of BNCT use an epithermal neutron beam in conjunction with tumour-targeting boron compounds for irradiation of glioblastomas and metastatic melanomas. Recently, a systematic Monte Carlo investigation of the dosimetric properties of near-threshold neutron beams has been performed indicating that accelerator proton energies between 1.93 and 1.99 MeV, using 5 cm of H_2O moderator followed by thin ^6Li and Pb shields, can provide therapeutically useful beams with treatment times less than one hour and accelerator currents less than 5 mA [11]. A comprehensive review of the state of the art in NCT has been published recently by the IAEA [12].

On the other hand, boron neutron capture synovectomy (BNCS) is a potential application of the $^{10}\text{B}(\text{n},\alpha)^7\text{Li}$ nuclear reaction for the treatment of rheumatoid arthritis [13]. In BNCS, a stable ^{10}B labelled compound is injected directly into the joint, and the joint is irradiated with an epithermal neutron beam. BNCS is currently being investigated at the laboratory for accelerator beam applications at the MIT in collaboration with Newton Scientific, Inc. and Brigham and Women's Hospital (see chapter 15). A dedicated BNCS beamline, consisting of an accelerator target and cooling system mounted in a neutron moderator and reflector assembly, has been constructed, installed, and is now operational on a high-current tandem electrostatic accelerator. Monte Carlo simulations have indicated that treatment times range from 4 to 25 min-mA (e.g. 4 minutes for a 1 mA beam current) depending on the size of the joint and the neutron source reaction used in the irradiation. The feasibility of using ^{157}Gd as an alternative to boron as a neutron capture agent for NCS, termed gadolinium neutron

capture synovectomy (GNCS), has also been conducted using Monte Carlo simulations where ^{10}B and ^{157}Gd have been compared as isotopes for accelerator-based NCS [14].

2.3. APPLICATIONS OF MONTE CARLO TECHNIQUES IN NUCLEAR MEDICINE IMAGING

Recent nuclear medical imaging innovations such as single-photon emission computed tomography (SPECT), positron emission tomography (PET), and multiple emission tomography (MET) as well as combined functional and structural imaging (see chapter 3) are ideal for Monte Carlo modelling techniques because of the stochastic nature of radiation emission, transport and detection processes. Factors which have contributed to the wider use of Monte Carlo techniques include improved models of radiation transport processes, the practicality of its application following the development of acceleration schemes and the improved speed of computers. This section summarizes potential areas of application of Monte Carlo techniques in nuclear imaging. An overview of existing simulation programs is presented in [3] together with examples of useful features of such sophisticated tools in connection with common computing facilities and more powerful multiple-processor parallel processing systems.

Recent developments in nuclear medicine instrumentation and multiple-processor parallel processing systems have created new opportunities for Monte Carlo simulation in nuclear medicine imaging. One of the aims of the medical physicist involved in nuclear medical imaging research is to optimize the design of imaging systems and to improve the quality and quantitative accuracy of reconstructed images. Several factors affect the image quality and the accuracy of the data obtained from a nuclear medicine scan. These include the physical properties of the detectors, collimator and gantry design, attenuation and scatter compensation, and reconstruction algorithms [15]. Integrating improvements in these topics with current tracers, and sensitive and specific tracers under development, will provide major advantages to the general nuclear medicine clinician and research investigator (figure 2.1). Mathematical modelling is necessary for the assessment of various parameters in nuclear medical imaging systems since no analytical solution is possible when the radiation transport equation, describing the interaction of photons with non-uniformly attenuating body structures and complex detector geometries, is solved.

2.3.1. *Diagnostic nuclear medicine imaging*

There has been an enormous increase and interest in the use of Monte Carlo techniques in all aspects of nuclear imaging, including planar imaging [16],

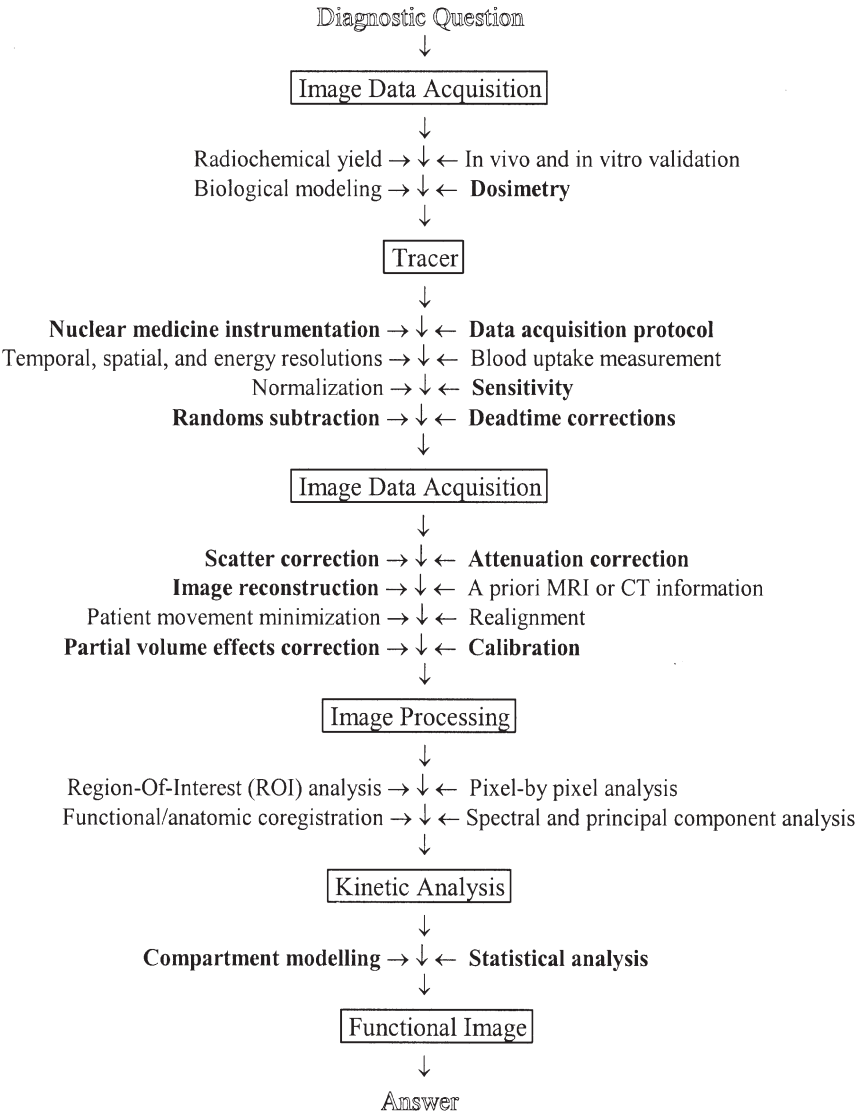


Figure 2.1. Scientific and technical strategy for recording accurate functional images. In bold, the parts where Monte Carlo simulation plays an important role. Reprinted with permission from AAPM [3].

SPECT [17, 18], PET [19, 20] and MET [21]. However, due to computer limitations, the method has not yet fully lived up to its potential. With the advent of high-speed supercomputers, the field has received increased attention, particularly with parallel algorithms, which have much higher execution rates.

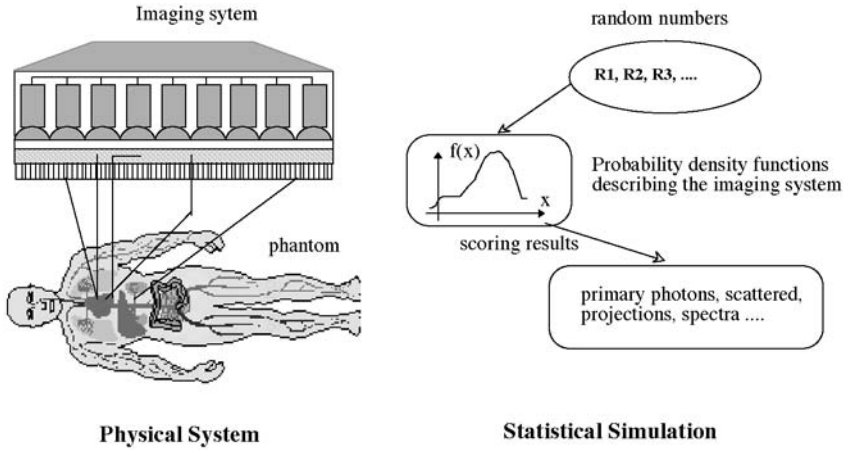


Figure 2.2. Principles of Monte Carlo simulation of a nuclear medical imaging system. Adapted and reproduced with permission from AAPM [3].

Figure 2.2 illustrates the idea of Monte Carlo or statistical simulation as applied to an imaging system. Assuming that the behaviour of the imaging system can be described by probability density functions (pdfs), then the Monte Carlo simulation can proceed by sampling from these pdfs, which necessitates a fast and effective way to generate random numbers uniformly distributed. Photon emissions are generated within the phantom and are transported by sampling from pdfs through the scattering medium and detection system until they are absorbed or escape the volume of interest without hitting the crystal. The outcomes of these random samplings, or trials, must be accumulated or tallied in an appropriate manner to produce the desired result, but the essential characteristic of Monte Carlo is the use of random sampling techniques to arrive at a solution of the physical problem.

The Monte Carlo method is a widely used research tool in different areas of nuclear imaging such as detector modelling and systems design, image correction and reconstruction techniques, internal dosimetry and pharmacokinetic modelling [3]. The method has proven to be very useful for solving complex problems that cannot be modelled by computer codes using deterministic methods or when experimental measurements may be impractical. Monte Carlo simulation of detector responses and determination of their efficiencies is one of the areas which has received considerable attention. Many detector modelling applications have been developed in the PET field including the pioneering work of Derenzo [22] who simulated arrays of detectors of different materials and sizes to study the effect of the inter-crystal septa and later on to optimize the optical coupling between BGO crystals and PMTs [23] by taking into account the reflection and scattering along the detection system. The search for an appropriate detector for this

imaging modality has been conducted in a comparative study of several crystals including BGO, CsF and NaI(Tl) [24], BaF₂ used in time-of-flight PET [25], and liquid xenon [26].

The design of SPECT and PET systems using the Monte Carlo method has received considerable attention and a large number of applications were the result of such investigations. During the past two decades, simulation of scintillation camera imaging using both deterministic and Monte Carlo methods has been developed to assess qualitatively and quantitatively the image formation process and interpretation [27] and to assist in the development of collimators [28]. Several researchers have used Monte Carlo simulation methods to study potential designs of dedicated small animal positron tomographs [29, 30]. An important conclusion drawn from these studies is that, unlike human imaging where both sensitivity and spatial resolution limitations significantly affect the quantitative imaging performance of a tomograph, the imaging performance of dedicated animal tomographs is almost solely based upon its spatial resolution limitations.

Simulation of transmission scanning allowed study of the effect of down-scatter from the emission (^{99m}Tc) into the transmission (¹⁵³Gd) energy window in SPECT [32] and investigation of detected scattered photons in single-photon transmission measurements using ¹³⁷Cs single-photon sources for PET [33]. A comparative evaluation of pre- and post-processing attenuation correction methods in lung SPECT has been also conducted using Monte Carlo simulations of a digital thorax phantom containing a homogeneous activity distribution in the lung [34].

Another promising application of Monte Carlo calculations is quantification and correction for photon attenuation and scattering in nuclear medicine imaging, since the user has the ability to separate the detected photons into their components, e.g., primary events, scatter events, contribution of down-scatter events. Monte Carlo modelling thus allows a detailed investigation of the spatial and energy distribution of Compton scatter, which would be difficult to perform using present experimental techniques, even with very good energy resolution detectors [35]. A Monte Carlo study of the acceptance of scattered events in a depth-encoding large-aperture camera made of position-encoding blocks modified to resolve the depth of interaction through a variation in the photopeak pulse-height has been performed by Moison *et al.* [31]. Figure 2.3 shows a comparison between measured and simulated single-energy spectra of the ECAT-953B PET scanner as well as measured and simulated scatter fractions as a function of the lower energy threshold. An energy resolution of 23% FWHM has been assumed since this is a typical value for BGO block detectors. Monte Carlo simulations have also been extensively used to evaluate and compare scatter correction schemes in both SPECT [36] and PET [37].

Monte Carlo simulations have been shown to be very useful for validation and comparative evaluation of image reconstruction techniques.

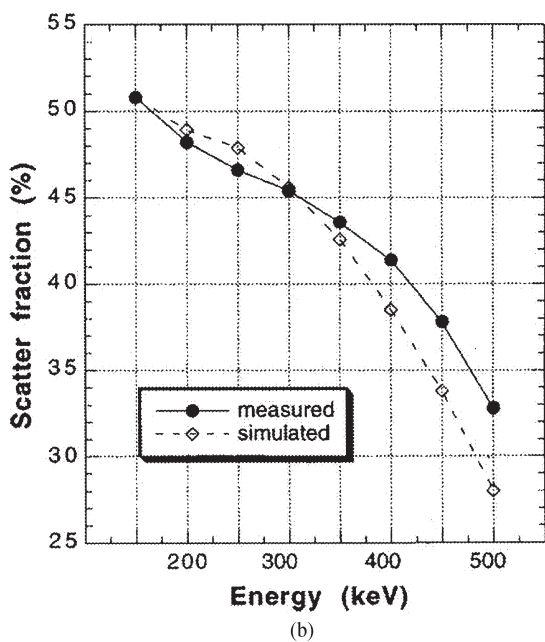
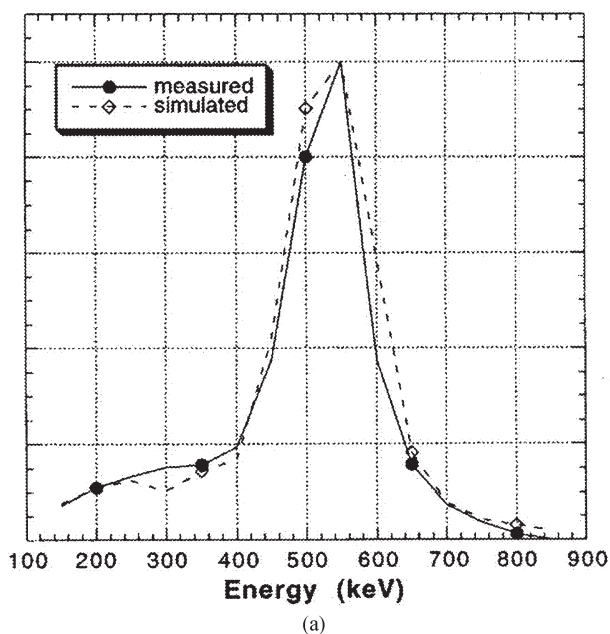


Figure 2.3. (a) Comparison between measured and simulated single-energy spectra and (b) measured and simulated scatter fractions for the ECAT 953B PET scanner. Reprinted from [31] © 1996 IEEE, with permission.

Smith *et al.* [38] used Monte Carlo modelling to study photon detection kernels, which characterize the probabilities that photons emitted by radioisotopes in different parts of the source region will be detected at particular projection pixels of the projection images for the case of parallel-hole collimators. The authors also proposed a reconstruction method using the three-dimensional kernels in which projection measurements in three adjacent planes are used simultaneously to estimate the source activity of the centre plane. The search for unified reconstruction algorithms led to the development of inverse Monte Carlo (IMC) reconstruction techniques. The principal merits of IMC are that, like direct Monte Carlo, the method can be applied to complex and multivariable problems, and variance reduction procedures can be applied [39]. Floyd *et al.* [40] used IMC to perform tomographic reconstruction for SPECT with simultaneous compensation for attenuation, scatter, and distance-dependent collimator resolution.

The Monte Carlo code *Eidolon* [20], for example, has been developed using modern software development tools. This simulator is an efficient tool that can be used to generate data sets in a controllable manner in order to assess different reconstruction algorithms and scatter correction methods [37]. As the 'best' algorithm can only be selected with respect to a certain task, different 'basic' performance measures can be used. Image degrading effects are illustrated using simulated projections of the digitized three-dimensional Hoffman brain phantom [41]. A slice of this phantom is shown in figure 2.4(A). The ratio between the activity in white, grey matter and ventricles has been chosen as 1:4:0, respectively. The projections of this phantom at different levels of fidelity are generated. The strengths of the image degrading factors are characteristic of an [^{18}F]-FDG-brain study. Figure 2.4(F–I) shows the effects of different aspects of image degradation on filtered backprojection reconstructions. The loss of resolution caused by detector blurring (FWHM = 4 mm) on projection data and FBP reconstructions is shown in figures 2.4(C) and 2.4(G), respectively, while in D and H, effects of detector blurring, attenuation and scatter are included in the simulation and no corrections performed on the simulated data sets. Finally, in E and I, effects of detector blurring, attenuation and scatter are included and appropriate corrections for attenuation and scatter applied.

2.3.2. Therapeutic nuclear medicine imaging

For internal radiation dose estimates, the biodistribution of a trace ^{131}I -labelled monoclonal antibody is generally used to predict the biodistribution of a high-dose administration for therapy. Imaging therapeutic doses would further confirm the hypothesis that the biodistribution is similar; however, current generation scintillation cameras are unable to handle accurately the corresponding high counting rate. Monte Carlo calculations have been used in the development of a method for imaging therapeutic doses of ^{131}I

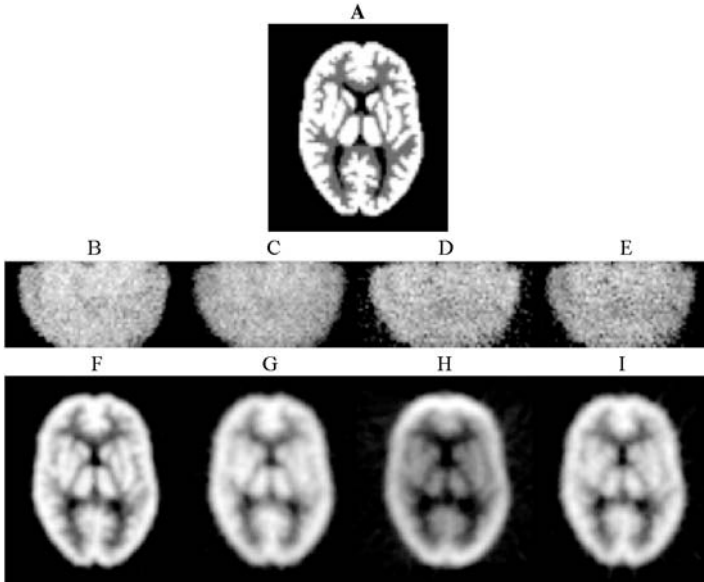


Figure 2.4. *A. Transaxial slice of the digital three-dimensional Hoffman brain phantom. Monte Carlo simulation of the three-dimensional Hoffman brain phantom in different imaging situations showing two-dimensional projections (middle row) and their filtered backprojection reconstructions (bottom row). In case B and F, a two-dimensional projection and reconstructed image neglecting attenuation, scatter and detector blurring. In C and G, effects of detector blurring are included, while in D and H, effects of detector blurring, attenuation and scatter are included in the simulation and no corrections performed on the simulated data sets. Finally, in E and I, effects of detector blurring, attenuation and scatter are included and appropriate corrections for attenuation and scatter are applied.*

by using thick Pb sheets placed on the front surface of a high-energy parallel-hole collimator [42]. The accuracy of ^{131}I tumour quantification after RIT has been further investigated with an ultra-high-energy (UHE) collimator designed for imaging 511 keV photons [43]. It has been shown that the difference in tumour size, relative to the size of a calibration sphere, has the biggest effect on accuracy, and recovery coefficients are needed to improve quantification of small tumours.

There has been renewed interest in pinhole collimation for high-resolution imaging of small organs and structures (e.g., the thyroid) and for regionally administered monoclonal antibody imaging since it provides an improved spatial resolution and an increase in sensitivity as the distance between the source and the pinhole aperture decreases [44]. Huili *et al.* [45] simulated point response functions for pinhole apertures with various aperture span angle, hole size and materials. The point responses have been

parametrized using radially circular symmetric two-dimensional exponential functions, which can be incorporated into image reconstruction algorithms that compensate for the penetration effect. The effect of pinhole aperture design parameters on angle-dependent sensitivity for high-resolution pinhole imaging has been also investigated using Monte Carlo modelling [46]. Simulated ^{131}I SPECT studies for uniform cylinders showed that activity concentrations have been underestimated towards the outside of the cylinders when a $\sin^3\theta$ rather than the correct $\sin^x\theta$ sensitivity correction has been applied in image reconstruction, where x is a parameter describing the sensitivity and θ is the angle of the incident ray with the surface of the detector crystal.

Different strategies are being developed to improve image quality and quantitative accuracy in tumour SPECT imaging including collimator–detector response compensation and high-energy scatter correction techniques. In an elegant study by Dewaraja *et al.* [47], Monte Carlo simulations have been used to evaluate how object shape influences ‘spill-out’ and ‘spill-in’, which are major sources of quantification errors associated with the poor spatial resolution of ^{131}I SPECT and to characterize energy and spatial distributions of scatter and penetration [48].

2.4. MONTE CARLO TECHNIQUES IN NUCLEAR MEDICINE DOSIMETRY

2.4.1. Calculation of absorbed fractions

The origins of the *absorbed fraction* concept adopted by the MIRD committee for internal dose calculations trace back to the earlier work by Ellet *et al.* [49] in the 1960s. Many of the pamphlets published by the MIRD committee made extensive use of Monte Carlo calculations to derive specific absorbed fractions for photon sources uniformly distributed in organs of mathematical phantoms [50]. This has been extended later on to electrons and β particles [51, 52].

Cristy [53] demonstrated that the reciprocity theorem which states that, for any pair of regions in a uniform isotropic or uniform scatterless model, the specific absorbed fraction is independent of which region is designated source and which is designated target may also be valid for heterogeneous phantoms for certain conditions. Other approaches using the MIRD formalism have also been proposed [54]. Poston *et al.* [55] calculated photon specific absorbed fractions for both the Cristy and Eckerman gastrointestinal tract and their revised model and reported differences between electron absorbed fraction values with and without electron tracking. Previously calculated absorbed fractions for unit density spheres in an infinite unit density medium for photon and electron emitters have been recently re-evaluated

using both the EGS4 and MCNP4B Monte Carlo codes [56]. Calculation of absorbed fractions for positron emitters relevant to neurologic studies has also been reported [57].

The application of the Monte Carlo method to internal radiation dosimetry is further emphasized in two recent MIRD Pamphlets. In MIRD Pamphlet No. 15 [58], the EGS4 Monte Carlo radiation transport code has been used to revise substantially the dosimetric model of the adult head and brain originally published in MIRD Pamphlet No. 5. Pamphlet No. 17 [59] crystallizes the utility of the MIRD formalism for the calculation of the non-uniform distribution of radiation-absorbed dose in different organs through the use of radionuclide-specific S values defined at the voxel level. Skeletal S values and absorbed fractions estimates to both marrow and endosteum in trabecular and cortical bone have been further improved through the use of electron transport models [60].

Mathematical anthropomorphic phantoms are continuously being improved. Current developments are aimed at computer phantoms that are flexible while providing accurate modelling of patient populations. An important contribution came from Bouchet and Bolch [61], making available a series of five dosimetric head and brain models developed to allow more precise dosimetry in paediatric neuroimaging procedures. A new rectal model [62] and dynamic urinary bladder model [63] have also been proposed more recently. To develop more patient-specific dosimetry, new mathematical models for adults of different height have been developed using anthropometric data [64]. The use of dynamic anthropomorphic phantoms in Monte Carlo simulations is becoming possible due to the increasing availability of computing power. This includes the development of appropriate primitives that allow accurate modelling of anatomical variations and patient motion, like superquadrics [65] and non-uniform rational B-spline surfaces [66]. More recently, an image-based whole-body model, called VIP-Man, has been developed using high-resolution transversal colour photographic images obtained from the National Library of Medicine's Visible Human Project [67]. The phantom is shown in figures 2.5(b) and 2.5(c) in comparison with the conventional anthropomorphic mathematical models (figure 2.5(a)). The EGS4 code has been also used to estimate specific absorbed fractions from internal electron emitters with energies from 100 keV to 4 MeV [68].

2.4.2. Derivation of dose-point kernels

In most cases, Monte Carlo calculations are used to simulate the random distribution of sources or targets whereas the actual dosimetric calculation is performed using the so-called dose-point kernels. Such kernels, usually spherical and calculated for mono-energetic photon or electron sources, describe the pattern of energy deposited at various radial distances from photon [1, 69, 70] and electron or β [71, 72] point sources. Dose-point kernels

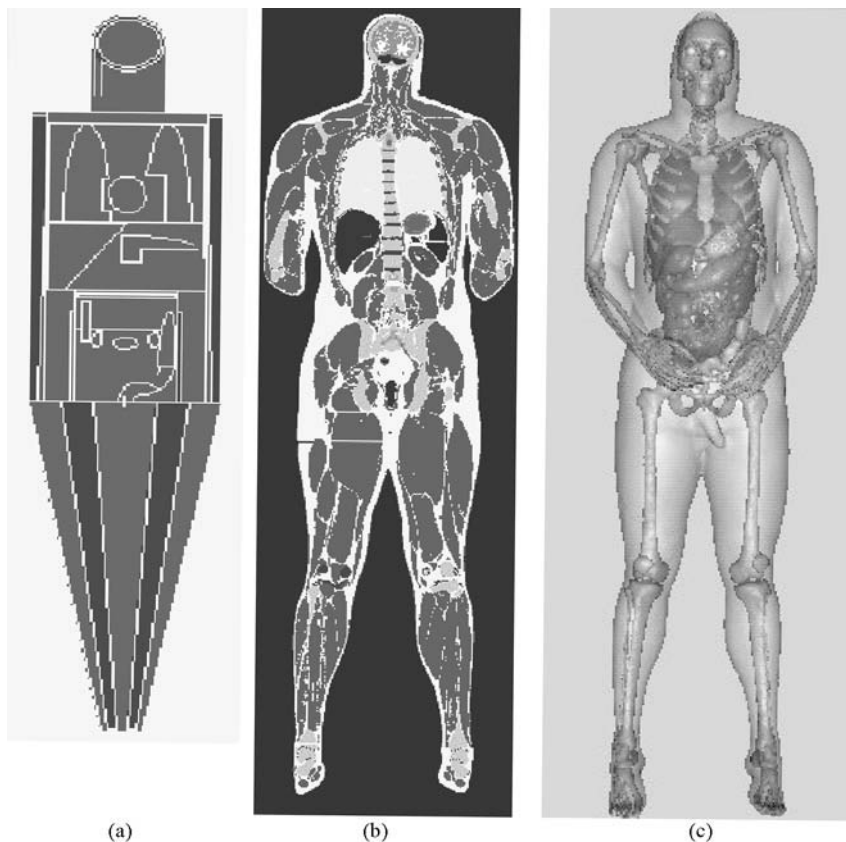


Figure 2.5. Anterior view of (a) the mathematical model and the VIP-Man model in (b) two-dimensions and (c) three-dimensions. Reprinted with permission from the Institute of Physics [68]. (See plate 1 for colour version.)

can be calculated using analytical or Monte Carlo methods. Hybrid approaches (analytical calculations using Monte Carlo data) have also been considered to decrease the computation time [73]. Three Monte Carlo systems have mainly been used for this purpose, namely, ETRAN [71], the ACCEPT code of the ITS system [74] used by Sgouros *et al.* [75], and EGS4 [72, 76]. Limitations and constraints of some of these codes have been reported in the literature whose impact on the calculated kernels is difficult to evaluate. ETRAN, for instance, had an incorrect sampling of the electron energy-loss straggling that has been corrected for in the ITS3 system (based on ETRAN); EGS4 did not include the accurate electron physics and transport algorithms which have been incorporated in the recent EGSnrc system [77]. The EGS4 system has also been used to characterize the spatial and energy distribution of bremsstrahlung radiation from β

point sources in water of relevance to RIT [78]. This study provided the initial data required for modelling and analysing the scatter, attenuation, and image formation processes in quantitative imaging of bremsstrahlung for RIT dosimetry. Furhang *et al.* [70] generated photon point dose kernels and absorbed fractions in water for the full photon emission spectrum of radionuclides of interest in nuclear medicine, by simulating the transport of particles using Monte Carlo techniques. The kernels have been then fitted to a mathematical expression.

A unified approach for photon and β particle dosimetry has been proposed by Lechner [79] by fitting Berger's tables for photons and electrons to generate an empirical function that is valid for both photons and β particles. Therefore both point-kernel and Monte Carlo techniques can be effectively employed to calculate absorbed dose to tissue from radionuclides that emit photons or electrons. The latter are computationally much more intensive; however, point-kernel methods are restricted to homogeneous tissue regions that can be mathematically described by analytical geometries whereas Monte Carlo methods have the advantage of being able to accommodate heterogeneous tissue regions with complex geometric shapes.

2.4.3. Pharmacokinetic modelling

Pharmacokinetic modelling is a useful component for estimating the cumulated activity in various source organs in the body. A few applications of Monte Carlo techniques have been reported in the field. In particular, Casciari *et al.* [80] developed a compartmental model of [F-18] fluoromisonidazole transport and metabolism to compute the volume average kappa in tissue regions from [F-18] fluoromisonidazole PET time-activity data and characterized it using Monte Carlo simulations. This model has been able to accurately determine kappa for a variety of computer generated time-activity curves including those for hypothetical heterogeneous tissue regions and poorly perfused tissue regions. Compartmental models allow also the *in vivo* analysis of radioligand binding to receptor sites in the human brain. Benzodiazepine receptor binding has been studied using a three-compartmental model [81]. The validity of the results of the coefficient of variation of each parameter has been verified with statistical results provided by Monte Carlo simulation. Burger [82] examined the possibility of using a mathematical metabolite correction, which might obviate the need for actual metabolite measurements. Mathematical metabolite correction has been implemented by estimating the input curve together with kinetic tissue parameters. The general feasibility of the approach has been evaluated in a Monte Carlo simulation using a two-tissue compartment model. A simplified approach involving linear-regression straight-line parameter fitting of dynamic scan data has been developed for both specific and non-specific models [83]. Monte Carlo simulations have been used to evaluate

parameter standard deviations, due to data noise, and much smaller noise-induced biases. The authors reported good agreement between regression and traditional methods.

Welch [84] investigated and quantified the effect of typical SPECT system resolution and photon counting statistics on the bias and precision of dynamic cardiac SPECT parameters. Simulation of dynamic SPECT projection data has been performed using a realistic human torso phantom assuming both perfect system resolution and a system resolution typical of a clinical SPECT system. The results showed that the rate constant characterizing the washing of activity into the myocardium is more sensitive to the position of the region of interest than the washout rate constant and that the main effect of increased photon noise in the projection data is to decrease the precision of the estimated parameters.

Computer simulations demonstrate that estimation of the kinetic parameters directly from the projections is more accurate than the estimation from the reconstructed images [85]. A strategy for joint estimation of physiological parameters and myocardial boundaries has been proposed and evaluated by simulated myocardial perfusion studies based on a simplified heart model [86]. A method allowing the estimation of kinetic parameters directly from SPECT cone-beam projections has also been proposed and validated with a simulated chest phantom [87]. The results showed that myocardial uptake and washout parameters estimated by conventional analysis of noiseless simulated cone-beam data had biases ranging between 3 and 26% and between 0 and 28%, respectively, while uncertainties of parameter estimates with this method ranged between 0.2 and 9% for the uptake parameters and between 0.3 and 6% for the washout parameters.

2.5. MONTE CARLO TECHNIQUES IN RADIATION PROTECTION

There is a considerable debate between scientists working in medical radiation physics and in the field of radiation safety on the term 'radiation protection' as applied to radiation medicine, and in particular to patients undergoing diagnostic medical procedures or radiation treatment. The determination of the dose delivered to different organs, for example, pertains to the standard clinical procedure or quality assurance process performed in each medical specialty, be it a diagnostic nuclear medicine or radiology technique, or a radiotherapy treatment. For a hospital physicist, dosimetry is not radiation protection but clinical practice. The radiation safety officer calls the task radiation protection. As the authors of this survey are members of the first group, it has been a natural decision not to consider dosimetry applications within this section, but as a clinical speciality in nuclear medicine (see section 2.4). Other applications of the Monte Carlo method are described below which can be considered more closely related to radiation

protection aspects. It should be emphasized, however, that considering the large uncertainties allowed in radiation protection, and the considerable man-power and time required to perform Monte Carlo simulations, many of the problems analysed by the existing applications could have been solved using rather simple analytical procedures. The use of Monte Carlo techniques in radiation protection should only be justified in cases of complex situations, either due to the presence of complicated mixed radiation sources or geometries.

2.5.1. *Shielding calculations*

Monte Carlo techniques have been used to determine detector calibration factors and to predict γ -ray spectra for well defined measurements. The techniques have sometimes been used to predict shielding requirements and critical structural specifications that must conform to radiation protection rules. Different Monte Carlo systems have been used to evaluate shielding including EGS4 [88] and MCNP for diagnostic X-ray rooms [89], and ITS to calculate door thicknesses for megavoltage radiotherapy [90]. More sophisticated applications include quantifying the effect of lead shielding on dose distributions during radiotherapy treatment planning with electron beams [91] and designing the moderator–collimator–shielding system of a neutron beam optimized for radiography that utilizes a ^{252}Cf source [92]. Monte Carlo methods have also been used to estimate the neutron and photon dose rates in a variety of locations in the vicinity of an accelerator-based neutron capture therapy facility, as well as the shielding configuration required when the device is run at maximum current [93].

2.5.2. *Characterization of detectors and radiation monitoring instruments*

Monte Carlo simulations have been shown to be useful in the evaluation of the design of collimated detectors used to measure ^{125}I or ^{131}I uptake in the thyroid gland [94]. Two detector sizes have been simulated for each radioisotope, and activity has been placed both in the gland and in the remainder of the body in varying amounts to assess the efficacy of the collimation. This study has been followed by a detailed report where the authors assessed the uncertainty introduced into an activity estimate of radioiodine in the thyroid when the size and shape of the gland differs from that of the calibration phantom [95]. The depth-dose distribution in TLD dosimeters irradiated with β rays from a ^{90}Sr – ^{90}Y source has also been investigated using the Monte Carlo method [96]. A pilot study has been conducted at the Lawrence Livermore National Laboratory to demonstrate the applicability of Monte Carlo techniques to calibrate *in vivo* measurement systems and investigate the effects of the source geometry and the detector size on the measured efficiency [97]. The development of a calibration phantom for *in vivo*

measurements of actinides using the MCNP Monte Carlo system to determine the point source distribution that closely approximates a homogeneous bone contamination has also been reported [98].

2.5.3. Radiation dose calculations to staff

A few studies have reported the use of the Monte Carlo method to calculate the dose received by medical and technical staff in a clinical environment. A recent publication estimated the dose due to radiation scattered from the roof of an adjacent radiotherapy facility where only the primary X-ray radiation had been accounted for in the shielding calculations [99]. Another group has calculated coefficients for converting dosimeter readings to equivalent dose to the foetus using the equivalent dose to the uterus and Monte Carlo modelling to simulate the equivalent dose to the foetus during the first two months of pregnancy [100]. Pattison [101] used γ -ray and β particle dose rates modelled using distributed point sources and empirically based Monte Carlo approaches, respectively, to determine the dose received by the skin of the fingers of clinical and laboratory staff during injections of ^{153}Sm . Conversion coefficients per air-kerma free-in-air for the personal dose equivalent, $H_p(10)$ have also been calculated using Monte Carlo methods for various dosimeter positions in the trunk of a voxel model of an adult male versus the direction of incidence of broad parallel photon beams with energies between 10 keV and 10 MeV [102]. Fluence-to-effective dose equivalent conversion factors as a function of radiation angles and sex for monoenergetic photon beams of 0.08, 0.3 and 1.0 MeV have also been reported elsewhere [103].

2.5.4. Revisiting release criteria for patients administered therapeutic doses

Application of the Monte Carlo method in this area has been the subject of an interesting debate between supporters [104] and detractors [105] of the utility of the technique to solve a problem that can be easily resolved otherwise. Johnson and Barnhart [105] suggested that accurate results could have been derived by using 'pen-and-paper' instead of performing an expensive Monte Carlo simulation. Siegel *et al.* [106], on the other hand, argued that it would be difficult to show that the approximations involved in the calculation by hand are accurate enough without having the Monte Carlo or other 'gold standard' results (such as a phantom study) for comparison. It should be recognized that holding a Geiger-Muller counter at 1 m from the umbilicus of a patient who has been administered a known amount of ^{131}I allows checking if the model predicts the readings or not. The results obtained by Johnson and Barnhart [105] indicated that their analytical model accurately predicted the reading without having to resort to a Monte Carlo simulation. Moreover, the limits of integration of their most

accurate model (model #3) could be changed to accommodate an individual with different torso dimensions, and obtain an answer in a fraction of the time that it would take to adapt the target geometry and run a Monte Carlo simulation.

2.6. FUTURE APPLICATIONS OF MONTE CARLO

2.6.1. Patient-specific dosimetry and treatment planning

Currently, the preferred strategy with radiolabelled antibodies is to use personalized patient dosimetry and this approach may become routinely employed clinically. The dose distribution pattern is often calculated by generalizing a point source dose distribution [75, 107], but direct calculation by Monte Carlo techniques is also frequently reported because it allows media of inhomogeneous density to be considered [108–110].

The development of a three-dimensional treatment planner based on SPECT/PET imaging is an area of considerable research interest and several dose calculation algorithms have been developed. Figure 2.6 lists the essential

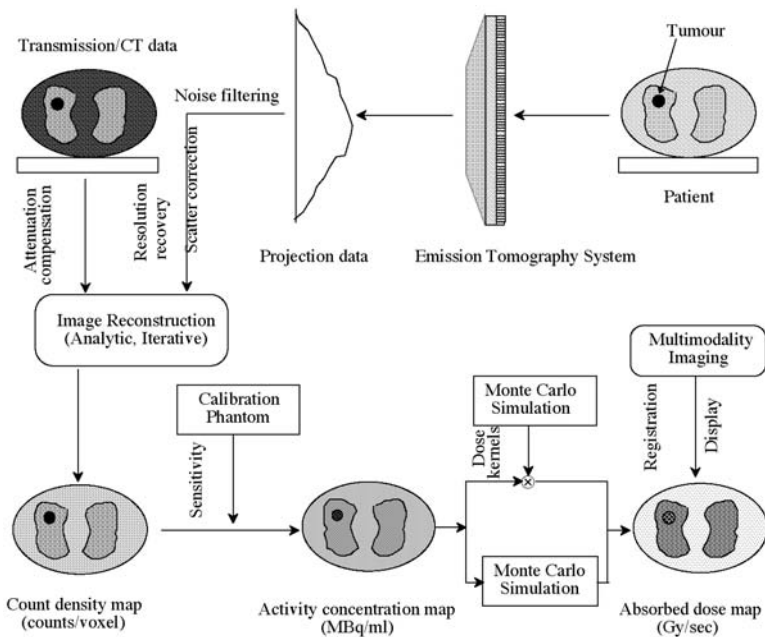


Figure 2.6. Diagram showing the essential steps required in developing a three-dimensional internal dosimetry program for treatment planning with RIT based on quantitative emission computed tomography where Monte Carlo simulations play a crucial role. Adapted and reproduced with permission from AAPM [3].

steps required in developing a three-dimensional treatment planning program for RIT. Projection data acquired from an emission tomographic imaging system are processed to reconstruct transverse section images which yields a count density map of source regions in the body. This count density is converted to an activity map using the sensitivity derived from a calibration phantom. In the final step, this activity distribution is converted to a dose rate or dose map either by convolving the activity distribution with dose point kernels or by direct Monte Carlo calculations. To elaborate a treatment plan for an individual patient, prospective dose estimates can be made by using a tracer activity of radiolabelled antibody to obtain biodistribution information prior to administration of a larger therapeutic activity. The clinical implementability of treatment planning algorithms will depend to a significant extent on the time required to generate absorbed dose estimates for a particular patient. For more details, the reader is referred to chapters 6 and 10–12, which fully cover the development steps and clinical experience gained using these tools.

2.6.2. On-line PET monitoring of radiotherapy beams

On-line monitoring of the positron-emitting activity created in patient tissues undergoing radiotherapy treatment has been a goal pursued by several investigators since the 1990s. Researchers at the Research Centre of Rossendorf in Dresden [111–113] and at the University of Michigan [114] have made important contributions to this technique in radiotherapy treatments with photons, protons and light and heavy ions. Whereas the clinical application of on-line PET monitoring in photon radiotherapy has so far been limited by the reduced activity produced in a patient using today's clinical accelerators, its use in heavy-particle radiotherapy has become a useful technique to visualize β^+ activity distributions that help to determine the effective range of heavy particles in the patient, as well as to evaluate blood flow in some organs [115].

The rationale for the preferred use of light ($Z \leq 10$) and heavy ions over conventional radiation beams is twofold. First, the dose distribution increases along the penetration depth of the beam ending with a sharp maximum at the end of the particle range (the Bragg peak), at the time that the very low scattering properties produce a very narrow penumbra in the beam. Second, there is an intense ionization pattern along the particle path, and notably at the end of its range, which results in localized bursts of energy deposition at microscopic level yielding increased cell killing and thus a radiobiological effect largely superior to that of conventional radiotherapy beams, even in conditions of hypoxia (cf. [115–117]). The resolution achieved is of 2–3 mm, which poses strict demands in target localization. Because of their lower production costs, the use of protons in radiotherapy has become well established and today the number of patients

treated with this modality is close to 30 000 [118]. From the two properties mentioned above the physical dose distribution of protons, enabling accurate dose conformation delivery, poses a clear advantage over conventional radiotherapy beams; however, their radiobiological effect is only about 8–10% higher than that of photons or electrons. The radiobiological superiority of ions heavier than protons, with an RBE augmentation of the order of three to four times higher than that of conventional beams, led to an increased interest worldwide that resulted in the construction of the Japanese HIMAC clinical facility in Chiba, near Tokyo. HIMAC started the treatment of patients mainly with carbon ions in 1994 [119], and more than 1000 patients have been treated in this facility. It had become clear that whereas heavy ions like the neon beams used in the early 1970s in Berkeley have the largest radiobiological effects, these also appear in regions close to the beam entrance and in the plateau region, where usually normal tissue is situated. In addition, due to the large penetration of the fragmentation products released by the incident ions, the tail of the dose distribution beyond the Bragg peak may be too high for sparing normal tissue beyond the primary ion range. These two aspects suggest that the ideal ions for radiotherapy are the light ions, and for this reason carbon has dominated the clinical applications at HIMAC. The GSI heavy-ion physics research facility in Darmstadt, Germany, initiated clinical treatments also with carbon ions in 1997 [115]. GSI uses advanced three-dimensional beam scanning techniques and PET imaging to monitor the delivery of dose by visualizing the positrons emitted by ^{10}C and ^{11}C ions produced in the nuclear reactions of the incident carbon ions with tissue, together with radiobiologically optimized treatment planning. Plans for building additional radiotherapy light-ion facilities have followed in Europe, and feasibility studies have been conducted for such facilities in Germany, Austria, Italy, France, Sweden and Switzerland, among others [120].

Several groups have reported the applicability of PET to *in vivo* dosimetry for proton radiotherapy using the Monte Carlo method. Different Monte Carlo codes have been used to investigate this challenging field including Berger's PTRAN [121], used by Del Guerra *et al.* [122], FLUKA [123], and specially designed software [114]. Parodi and Enghardt [123], in particular, made Monte Carlo simulations of the number and spatial distribution of the positron emitters created by therapeutic protons in PMMA. Since proton therapy requires a particle fluence up to 20 times higher than that required in carbon therapy for the same physical dose level, the authors concluded that the total activity produced within the irradiated volume should be twice as intense as that actually used at the carbon ion facility at GSI. Moreover, the considered ratio between the fluence of protons and carbon ions could increase considerably due to the higher relative biological effectiveness of carbon ions, leading to a lower physical dose than for protons at the same level of biological dose.

REFERENCES

- [1] Berger M J 1968 MIRD pamphlet 2: energy deposition in water by photons from point isotropic sources *J. Nucl. Med.* **9** 15–25
- [2] Andreo A 1991 Monte Carlo techniques in medical radiation physics *Phys. Med. Biol.* **36** 861–920
- [3] Zaidi H 1999 Relevance of accurate Monte Carlo modeling in nuclear medical imaging *Med. Phys.* **26** 574–608
- [4] Jenkins T M, Nelson W R and Rindi A 1998 *Monte Carlo Transport of Electrons and Photons* (New York: Plenum)
- [5] Ljungberg M, Strand S-E and King M A 1998 *Monte Carlo Calculations in Nuclear Medicine: Applications in Diagnostic Imaging* (London: IOP Publishing)
- [6] Boone J M, Buonocore M H and Cooper V N 2000 Monte Carlo validation in diagnostic radiological imaging *Med. Phys.* **27** 1294–304
- [7] Ma C M and Jiang S B 1999 Monte Carlo modelling of electron beams from medical accelerators *Phys. Med. Biol.* **44** R157–89
- [8] Ahnesjö A and Aspradakis M M 1999 Dose calculations for external photon beams in radiotherapy *Phys. Med. Biol.* **44** R99–155
- [9] Stabin M, Konijnenberg M, Knapp F F and Spencer R H 2000 Monte Carlo modeling of radiation dose distributions in intravascular radiation therapy *Med. Phys.* **27** 1086–92
- [10] Reynaert N, Verhaegen F, Taeymans Y, Van Eijkeren M and Thierens H 1999 Monte Carlo calculations of dose distributions around ^{32}P and ^{198}Au stents for intravascular brachytherapy *Med. Phys.* **26** 1484–91
- [11] Lee C L, Zhou X L, Kudchadker R J, Harmon F and Harker Y D 2000 A Monte Carlo dosimetry-based evaluation of the $^7\text{Li}(p,n)^7\text{Be}$ reaction near threshold for accelerator boron neutron capture therapy *Med. Phys.* **27** 192–202
- [12] Levin V, Andreo P and Dodd B eds 2001 *Current Status of Neutron Capture Therapy. IAEA Tec-Doc 1223* (Vienna: IAEA, International Atomic Energy Agency)
- [13] Gierga D P, Yanch J C and Shefer R E 2000 Development and construction of a neutron beam line for accelerator-based boron neutron capture synovectomy *Med. Phys.* **27** 203–14
- [14] Gierga D P, Yanch J C and Shefer R E 2000 An investigation of the feasibility of gadolinium for neutron capture synovectomy *Med. Phys.* **27** 1685–92
- [15] Zaidi H 1996 Quantitative SPECT: recent developments in detector response, attenuation and scatter correction techniques *Physica Medica* **12** 101–17
- [16] Webb S, Binnie D M, Flower M A and Ott R J 1992 Monte Carlo modelling of the performance of a rotating slit-collimator for improved planar gamma-camera imaging *Phys. Med. Biol.* **37** 1095–108
- [17] Ljungberg M and Strand S-E 1989 A Monte Carlo program for the simulation of scintillation camera characteristics *Comput. Meth. Programs Biomed.* **29** 257–72
- [18] de Vries D J *et al.* 1990 Development and validation of a Monte Carlo simulation of photon transport in an Auger camera *IEEE Trans. Med. Imaging* **9** 430–8
- [19] Dahlbom M, Rosenquist G, Eriksson L and Bohm C 1989 A study of the possibility of using multi-slice PET systems for 3D imaging *IEEE Trans. Nucl. Sci.* **36** 1066–71
- [20] Zaidi H, Scheurer A H and Morel C 1999 An object-oriented Monte Carlo simulator for 3D cylindrical positron tomographs *Comput. Meth. Programs Biomed.* **58** 133–45

- [21] Dahlbom M *et al.* 1998 A YSO/LSO phoswich array detector for single and coincidence photon imaging *IEEE Trans. Nucl. Sci.* **45** 1128–32
- [22] Derenzo S E 1981 Monte Carlo calculations of the detection efficiency of NaI(Tl), BGO, CsF, Ge and plastic detectors for 511 keV photons *IEEE Trans. Nucl. Sci.* **28** 131–6
- [23] Derenzo S E and Riles J K 1982 Monte Carlo calculations of the optical coupling between bismuth germanate crystals and photomultiplier tubes *IEEE Trans. Nucl. Sci.* **29** 191–5
- [24] Bottigli U *et al.* 1985 Monte Carlo simulation and experimental tests on BGO, CsF and NaI(Tl) crystals for positron emission tomography *J. Nucl. Med. Allied Sci.* **29** 221–7
- [25] Bice A N *et al.* 1990 Monte Carlo simulation of BaF₂ detectors used in time-of-flight positron emission tomography *IEEE Trans. Nucl. Sci.* **37** 696–701
- [26] Lopes M I, Chepel V, Carvalho J C, Ferreira Marques R and Policarpo A J P 1995 Performance analysis based on a Monte Carlo simulation of a liquid xenon PET detector *IEEE Trans. Nucl. Sci.* **42** 2298–302
- [27] Bradshaw J, Burnham C and Correia J 1985 Application of Monte Carlo methods to the design of SPECT detector systems *IEEE Trans. Nucl. Sci.* **32** 753–7
- [28] Kimiaei S, Ljungberg M and Larsson S A 1997 Evaluation of optimally designed planar-concave collimators in single-photon emission tomography *Eur. J. Nucl. Med.* **24** 1398–404
- [29] Pavlopoulos S and Tzanakos G 1996 Design and performance evaluation of a high-resolution small animal positron tomograph *IEEE Trans. Nucl. Sci.* **43** 3249–55
- [30] Moses W W, Virador P R G, Derenzo S E, Huesman R H and Budinger T F 1997 Design of a high-resolution, high-sensitivity PET camera for human brains and small animals *IEEE Trans. Nucl. Sci.* **41** 1487–91
- [31] Moisan C, Tupper P, Rogers J G and de Jong J K 1996 A Monte Carlo study of the acceptance to scattered events in a depth encoding PET camera *IEEE Trans. Nucl. Sci.* **43** 1974–80
- [32] Ljungberg M, Strand S-E, Rajeevan N and King M A 1994 Monte Carlo simulation of transmission studies using a planar source with a parallel collimator and a line source with a fan-beam collimator *IEEE Trans. Nucl. Sci.* **41** 1577–84
- [33] Wegmann K *et al.* 1999 Investigation of the scatter contribution in single photon transmission measurements by means of Monte Carlo simulations *IEEE Trans. Nucl. Sci.* **46** 1184–90
- [34] Gustafsson A *et al.* 1998 Evaluation of attenuation corrections using Monte Carlo simulated lung SPECT *Phys. Med. Biol.* **43** 2325–36
- [35] Zaidi H 2001 Scatter modelling and correction strategies in fully 3-D PET *Nucl. Med. Commun.* **22** 1181–4
- [36] El Fakhri G N *et al.* 1999 Respective roles of scatter, attenuation, depth-dependent collimator response and finite spatial resolution in cardiac single-photon emission tomography quantitation: a Monte Carlo study *Eur. J. Nucl. Med.* **26** 437–46
- [37] Zaidi H 2000 Comparative evaluation of scatter correction techniques in 3D positron emission tomography *Eur. J. Nucl. Med.* **27** 1813–26
- [38] Smith M F, Floyd C E, Jaszczak R J and Coleman R E 1992 Three-dimensional photon detection kernels and their application to SPECT reconstruction *Phys. Med. Biol.* **37** 605–22
- [39] Dunn W L 1981 Inverse Monte Carlo analysis *J. Comput. Phys.* **41** 154–66

- [40] Floyd C E, Jaszczak R J, Greer K L and Coleman R E 1986 Inverse Monte Carlo as a unified reconstruction algorithm for ECT *J. Nucl. Med.* **27** 1577–85
- [41] Hoffman E J, Cutler P D, Digby W M and Mazziotta J C 1990 3-D phantom to simulate cerebral blood flow and metabolic images for PET *IEEE Trans. Nucl. Sci.* **37** 616–20
- [42] Pollard K R, Bice A N, Eary J F, Durack L D and Lewellen T K 1992 A method for imaging therapeutic doses of iodine-131 with a clinical gamma camera *J. Nucl. Med.* **33** 771–6
- [43] Dewaraja Y K, Ljungberg M and Koral K F 2000 Accuracy of ^{131}I tumor quantification in radioimmunotherapy using SPECT imaging with an ultra-high-energy collimator: Monte Carlo study *J. Nucl. Med.* **41** 1760–7
- [44] Zaidi H 1996 Assessment of thyroid volume with pinhole emission computed tomography *Physica Medica* **XII** 97–100
- [45] Huili W, Jaszczak R J and Coleman R E 1996 Monte Carlo modeling of penetration effect for iodine-131 pinhole imaging *IEEE Trans. Nucl. Sci.* **43** 3272–7
- [46] Smith M F and Jaszczak R J 1997 The effect of gamma ray penetration on angle-dependent sensitivity for pinhole collimation in nuclear medicine *Med. Phys.* **24** 1701–9
- [47] Dewaraja Y K, Ljungberg M and Koral K F 2001 Monte Carlo evaluation of object shape effects in iodine-131 SPECT tumor activity quantification *Eur. J. Nucl. Med.* **28** 900–6
- [48] Dewaraja Y K, Ljungberg M and Koral K F 2000 Characterization of scatter and penetration using Monte Carlo simulation in ^{131}I imaging *J. Nucl. Med.* **41** 123–30
- [49] Ellett W H and Humes R M 1971 Absorbed fractions for small volumes containing photon-emitting radioactivity *J. Nucl. Med. Suppl.* **5** 25–32
- [50] Snyder W, Ford M R and Warner G 1978 *Estimates of Specific Absorbed Fractions for Photon Sources Uniformly Distributed in Various Organs of a Heterogeneous Phantom*, NM/MIRD (Society of Nuclear Medicine Publication, New York, Pamphlet No 5)
- [51] Akabani G, Poston J W and Bolch W E 1991 Estimates of beta absorbed fractions in small tissue volumes for selected radionuclides *J. Nucl. Med.* **32** 835–9
- [52] Siegel J A and Stabin M 1994 Absorbed fractions for electrons and beta particles in spheres of various sizes *J. Nucl. Med.* **35** 152–6
- [53] Cristy M 1983 Applying the reciprocal dose principle to heterogeneous phantoms: practical experience from Monte Carlo studies *Phys. Med. Biol.* **28** 1289–303
- [54] Cristy M and Eckerman K F 1987 *Specific Absorbed Fractions of Energy at Various Ages from Internal Photon Sources I Methods, II One Year Old, III Five Year Old, IV Ten Year Old, V Fifteen Year Old Male and Adult Female, VI New-Born and VII Adult Male ORNL/TM 8381/V1-V7* Oak Ridge National Laboratory.
- [55] Poston J W, Kodimer K A and Bolch W E 1996 A revised model for the calculation of absorbed energy in the gastrointestinal tract *Health Phys.* **71** 307–14
- [56] Stabin M and Konijnenberg M W 2000 Re-evaluation of absorbed fractions for photons and electrons in spheres of various sizes *J. Nucl. Med.* **41** 149–60
- [57] Bice A N, Links J M, Wong D F and Wagner H N 1985 Absorbed fractions for dose calculations of neuroreceptor PET studies *Eur. J. Nucl. Med.* **11** 127–31
- [58] Bouchet L G, Bolch W E, Weber D A, Atkins H L and Poston J W 1999 MIRD Pamphlet No 15: Radionuclide *S* values in a revised dosimetric model of the adult head and brain. Medical Internal Radiation Dose *J. Nucl. Med.* **40** 62S–101S

- [59] Bolch W E *et al.* 1999 MIRD pamphlet No 17: the dosimetry of nonuniform activity distributions—radionuclide S values at the voxel level. Medical Internal Radiation Dose Committee *J. Nucl. Med.* **40** 11S–36S
- [60] Bouchet L G, Bolch W E, Howell R W and Rao D V 2000 S values for radionuclides localized within the skeleton *J. Nucl. Med.* **41** 189–212
- [61] Bouchet L G and Bolch W E 1999 Five pediatric head and brain mathematical models for use in internal dosimetry *J. Nucl. Med.* **40** 1327–36
- [62] Mardirossian G *et al.* 1999 A new rectal model for dosimetry applications *J. Nucl. Med.* **40** 1524–31
- [63] Thomas S R, Stabin M, Chen C T and Samaratunga R C 1999 MIRD Pamphlet No 14 revised: A dynamic urinary bladder model for radiation dose calculations Task Group of the MIRD Committee, Society of Nuclear Medicine *J. Nucl. Med.* **40** 102S–123S
- [64] Clairand I *et al.* 2000 Improvement of internal dose calculations using mathematical models of different adult heights *Phys. Med. Biol.* **45** 2771–85
- [65] Peter J, Gilland D R, Jaszczak R J and Coleman R E 1999 Four-dimensional superquadric-based cardiac phantom for Monte Carlo simulation of radiological imaging systems *IEEE Trans. Nucl. Sci.* **46** 2211–17
- [66] Segars W P, Lalush D S and Tsui B M W 2001 Modeling respiratory mechanics in the MCAT and spline-based MCAT phantoms *IEEE Trans. Nucl. Sci.* **48** 89–97
- [67] Xu X G, Chao T C and Bozkurt A 2000 VIP-Man an image-based whole-body adult male model constructed from color photographs of the Visible Human Project for multi-particle Monte Carlo calculations *Health Phys.* **78** 476–86
- [68] Chao T C and Xu X G 2001 Specific absorbed fractions from the image-based VIP-Man body model and EGS4-VLSI Monte Carlo code internal electron emitters *Phys. Med. Biol.* **46** 901–27
- [69] Mackie T R, Bielajew A F, Rogers D W and Battista J J 1988 Generation of photon energy deposition kernels using the EGS Monte Carlo code *Phys. Med. Biol.* **33** 1–20
- [70] Furhang E E, Sgouros G and Chui C S 1996 Radionuclide photon dose kernels for internal emitter dosimetry *Med. Phys.* **23** 759–64
- [71] Berger M J 1971 MIRD Pamphlet 7: Distribution of absorbed doses around point sources of electrons and beta particles in water and other media *J. Nucl. Med.* **12** 5–23
- [72] Simpkin D J and Mackie T R 1990 EGS4 Monte Carlo determination of the beta dose kernel in water *Med. Phys.* **17** 179–186
- [73] Bardies M and Myers M J 1996 Computational methods in radionuclide dosimetry *Phys. Med. Biol.* **41** 1941–55
- [74] Halbleib J A, Kensek R P, Valdez G D, Seltzer S M and Berger M J 1992 ITS: the Integrated TIGER Series of electron/photon transport codes—version 3.0 *IEEE Trans. Nucl. Sci.* **39** 1025–30
- [75] Sgouros G *et al.* 1993 Three-dimensional dosimetry for radioimmunotherapy treatment planning *J. Nucl. Med.* **34** 1595–601
- [76] Johnson J C, Langhorst S M, Loyalka S K, Volkert W A and Ketring A R 1992 Calculation of radiation dose at a bone-to-marrow interface using Monte Carlo modeling techniques (EGS4) *J. Nucl. Med.* **33** 623–8
- [77] Kawrakow I 2000 Accurate condensed history Monte Carlo simulation of electron transport. I. EGSnrc, the new EGS4 version *Med. Phys.* **27** 485–98

- [78] Simpkin D J, Cullom S J and Mackie T R 1992 The spatial and energy dependence of bremsstrahlung production about beta point sources in H₂O *Med. Phys.* **19** 105–14
- [79] Lechner P K 1994 A unified approach to photon and beta particle dosimetry *J. Nucl. Med.* **35** 1721–9
- [80] Casciari J J, Graham M M and Rasey J S 1995 A modeling approach for quantifying tumor hypoxia with [F-18]fluoromisonidazole PET time–activity data *Med. Phys.* **22** 1127–39
- [81] Millet P, Delforge J, Pappata S, Syrota A and Cinotti L 1996 Error analysis on parameter estimates in the ligand-receptor model application to parameter imaging using PET data *Phys. Med. Biol.* **41** 2739–56
- [82] Burger C and Buck A 1996 Tracer kinetic modelling of receptor data with mathematical metabolite correction *Eur. J. Nucl. Med.* **23** 539–45
- [83] Thie J A, Smith G T and Hubner K F 1997 Linear least squares compartmental-model-independent parameter identification in PET *IEEE Trans. Med. Imaging* **16** 11–16
- [84] Welch A, Smith A M and Gullberg G T 1995 An investigation of the effect of finite system resolution and photon noise on the bias and precision of dynamic cardiac SPECT parameters *Med. Phys.* **22** 1829–36
- [85] Zeng G L, Gullberg G T and Huesman R H 1995 Using linear time-invariant system theory to estimate kinetic parameters directly from projection measurements *IEEE Trans. Nucl. Sci.* **42** 2339–46
- [86] Ping-Chun C, Rogers W L, Clinthorne N H, Fessler J A and Hero A O 1994 Model-based estimation for dynamic cardiac studies using ECT *IEEE Trans. Med. Imaging* **13** 217–26
- [87] Huesman R H, Reutter B W, Zeng G L and Gullberg G T 1998 Kinetic parameter estimation from SPECT cone-beam projection measurements *Phys. Med. Biol.* **43** 973–82
- [88] Simpkin D J 1989 Shielding requirements for constant-potential diagnostic x-ray beams determined by a Monte Carlo calculation *Health Phys.* **56** 151–64
- [89] Metzger R, Richardson R and Van Riper K A 1993 A Monte Carlo model for retrospective analysis of shield design in a diagnostic x-ray room *Health Phys.* **65** 164–71
- [90] Biggs P J 1991 Calculation of shielding door thicknesses for radiation therapy facilities using the ITS Monte Carlo program *Health Phys.* **61** 465–72
- [91] Verhaegen F, Buffa F M and Deehan C 2001 Quantifying effects of lead shielding in electron beams: a Monte Carlo study *Phys. Med. Biol.* **46** 757–69
- [92] da Silva A X and Crispim V R 2001 Moderator–collimator–shielding design for neutron radiography systems using ²⁵²Cf *Appl. Radiat. Isot.* **54** 217–25
- [93] Howard W B and Yanch J C 1995 Shielding design and dose assessment for accelerator based neutron capture therapy *Health Phys.* **68** 723–30
- [94] Kramer G H, Chamberlain M J and Yiu S 1997 A study of thyroid radioiodine monitoring by Monte Carlo simulations: implications for equipment design *Phys. Med. Biol.* **42** 2175–82
- [95] Kramer G H and Crowley P 2000 The assessment of the effect of thyroid size and shape on the activity estimate using Monte Carlo simulation *Health Phys.* **78** 727–38
- [96] Rodriguez Villafuerte M, Gamboa deBuen I and Brandan M E 1997 Monte Carlo simulation of depth-dose distributions in TLD-100 under ⁹⁰Sr–⁹⁰Y irradiation *Health Phys.* **72** 574–8

- [97] Hickman D P, Kruchten D A, Fisher S K and Anderson A L 1994 Calibration of a ^{241}Am wound-monitoring system using Monte Carlo techniques *Health Phys.* **66** 400–6
- [98] Gualdrini G *et al.* 2000 Development and characterisation of a head calibration phantom for in vivo measurements of actinides *Appl. Radiat. Isot.* **53** 387–93
- [99] Zavgorodni S F 2001 A method for calculating the dose to a multi-storey building due to radiation scattered from the roof of an adjacent radiotherapy facility *Med. Phys.* **28** 1926–30
- [100] Osei E K and Kotre C J 2001 Equivalent dose to the fetus from occupational exposure of pregnant staff in diagnostic radiology *Br. J. Radiol.* **74** 629–37
- [101] Pattison J E 1999 Finger doses received during ^{153}Sm injections *Health Phys.* **77** 530–5
- [102] Zankl M 1999 Personal dose equivalent for photons and its variation with dosimeter position *Health Phys.* **76** 162–70
- [103] Xu X G, Reece W D and Poston J W 1995 A study of the angular dependence problem in effective dose equivalent assessment *Health Phys.* **68** 214–24
- [104] Sparks R B, Siegel J A and Wahl R L 1998 The need for better methods to determine release criteria for patients administered radioactive material *Health Phys.* **75** 385–8
- [105] Johnson T K and Barnhart T 1999 An alternative to Monte Carlo in determining release criteria for patients administered radioactive material *Health Phys.* **77** 724–6
- [106] Siegel J A, Sparks R B and Wahl R L 1999 Response to Johnson and Barnhart *Health Phys.* **77** 726–7
- [107] Akabani G, Hawkins W G, Eckblade M B and Lechner P K 1997 Patient-specific dosimetry using quantitative SPECT imaging and three-dimensional discrete Fourier transform convolution *J. Nucl. Med.* **38** 308–14
- [108] Furhang E E, Chui C S, Kolbert K S, Larson S M and Sgouros G 1997 Implementation of a Monte Carlo dosimetry method for patient-specific internal emitter therapy *Med. Phys.* **24** 1163–72
- [109] Tagesson M, Ljungberg M and Strand S E 1996 A Monte-Carlo program converting activity distributions to absorbed dose distributions in a radionuclide treatment planning system *Acta Oncol.* **35** 367–72
- [110] Yoriyaz H, Stabin M and dos Santos A 2001 Monte Carlo MCNP-4B-based absorbed dose distribution estimates for patient-specific dosimetry *J. Nucl. Med.* **42** 662–9
- [111] Enghardt W, Fromm W D, Manfrass P and Scharadt D 1992 Limited-angle 3D reconstruction of PET images for dose localization in light ion tumour therapy *Phys. Med. Biol.* **37** 791–8
- [112] Enghardt W *et al.* 1992 The spatial distribution of positron-emitting nuclei generated by relativistic light ion beams in organic matter *Phys. Med. Biol.* **37** 2127–31
- [113] Enghardt W *et al.* 1999 The application of PET to quality assurance of heavy-ion tumor therapy *Strahlenther. Onkol.* **175** Suppl 2 33–6
- [114] Litzenberg D W, Becchetti F D and Roberts D A 1997 On-line PET monitoring of radiotherapy beams: image reconstruction and Monte Carlo simulations of detector geometries *IEEE Trans. Nucl. Sci.* **44** 1646–57
- [115] Kraft G 2000 Tumor therapy with heavy charged particles *Prog. Part. Nucl. Phys.* **45** S473–S544

- [116] Amaldi U 1999 Cancer therapy with particle accelerators *Nucl. Phys. A* **654** 375–99
- [117] Chu W T 1999 Hadron therapy *Biomedical Uses of Radiation—Therapeutic Applications* ed W R Hendee (Weinheim: VCH–Wiley) Part B, pp 1057–131
- [118] Sisterson J 2001 Particles *PTCOG Newsletter* 27 January
- [119] Kanai T *et al.* 1999 Biophysical characteristics of HIMAC clinical irradiation system for heavy-ion radiation therapy *Int. J. Radiat. Oncol. Biol. Phys.* **44** 201–10
- [120] Rosso D 2000 A boost for hadron therapy *Phys. World*
- [121] Berger M J 1993 Proton Monte Carlo Transport Program PTRAN *Report NISTIR 5113* (Bethesda, MD: NIST)
- [122] Del Guerra A, Di Domenico G and Mukhopadhyay D 1997 PET dosimetry in proton radiotherapy: a Monte Carlo Study *Appl. Radiat. Isot.* **18** 1617–24
- [123] Parodi K and Enghardt W 2000 Potential application of PET in quality assurance of proton therapy *Phys. Med. Biol.* **45** N151–6

Chapter 3

Medical imaging techniques for radiation dosimetry

Kenneth F Koral, Habib Zaidi and Michael Ljungberg

3.1. INTRODUCTION

Radiation dose itself cannot be imaged non-invasively. However, medical imaging can non-invasively provide information so that estimates of radiation dose can be calculated. These estimates can include those for average dose, dose spatial distribution, dose rate, etc. The status of such non-invasive imaging was reviewed comprehensively in 1993 [1] and again in 1999 [2]. At this time, the imaging has three distinct areas in which it contributes.

1. Determination of the spatial distribution of mass and of attenuation coefficient.
2. Segmentation of the patient into volumes of interest (VoIs) that represent specific organs, tumours, etc. for which the estimate of radiation dose is desired.
3. Determination of the distribution of radioactivity (MBq) in space and time. (Radioactivity will be shortened to activity below.)

We will cover each of these areas in the next three sections. Before proceeding, we note that medical imaging can be carried out for two broad dosimetric purposes:

1. To monitor radiation dose during therapy.
2. To predict radiation dose during therapy from a pre-therapy evaluation, often given the name of treatment planning.

It is clear that if monitoring is the purpose then imaging during therapy may be involved, while if treatment planning is the purpose then imaging during a pre-therapy evaluation will be necessary. However, the accuracy of predicting results during therapy from measurements carried out during evaluation can be questioned. The matter will be discussed further at the end of this

chapter. Also, monitoring radiation dose during therapy may be the purpose of interest, but you may still choose to do it from evaluative imaging rather than from intra-therapy imaging. This choice has the advantage of lower radiation exposure to imaging personnel, and of having no worries about camera deadtime.

3.2. DETERMINATION OF THE TOTAL MASS. DETERMINATION OF SPATIAL DISTRIBUTION OF ATTENUATION COEFFICIENT, AND OF MASS

If one is using traditional techniques based on Medical Internal Radiation Dose (MIRD) methods, one may employ a standard reference man for a macrodose calculation. Here macrodose is defined as the average dose for a large-size object such as a liver or a tumour. In this case, only the time integral of the total activity (MBq h) within the organ is needed. This time integral must be measured or inferred for a particular patient and so the resultant dose is patient specific. This statement is made using the phrase in its most rigorous sense. The usual use of the phrase ‘patient specific’ implies including additional input about the patient. If one wishes to carry out a patient-specific dose calculation in this more general sense, it is important to also estimate at least the total mass of the organ or tumour of interest.

The total mass of a tumour or organ is sometimes determined from VoIs that are directly calculated using the emission image. Another method is to outline specific organs and tumours on an anatomic image. For some organs, like the liver or spleen, the outlining on an anatomic image is fairly straightforward. For the kidney, where the shape is not simple, or for some tumours where the edge is not clear, the outlining is harder. Once the volume in pixels is known, it is converted to cm^3 by using the volume of a single pixel, which has been determined by a previous calibration. Except for the lungs, or bone, one usually assumes a density of 1 g/cm^3 to calculate the mass from the volume.

Once the total mass is estimated for an organ, it can be ratioed with the mass in the reference-man phantom to provide a mass-based correction to the first-order MIRD dose (that from electrons). Or the mass can be used in a more-complicated calculation of the radiation macrodose that includes the dose from γ -rays [3]. For tumours, the total mass can be used in a calculation of the radiation macrodose that usually goes back to basic considerations.

Photon (or γ -ray) attenuation is the common name for photon absorption or scattering with or without energy degradation that occurs during acquisition of projection data. Many reconstruction algorithms include compensation for photon attenuation that is based on imaging. Attenuation correction based on imaging is discussed further in sections 3.4.5 and 3.4.9.

Three-dimensional mass distributions (and perhaps material distributions) are necessary to compute three-dimensional dose distributions if one is not going to assume a water-like medium within the body skin surface. These distributions can be obtained from the X-ray computed tomography (CT) or a nuclear magnetic resonance image (MRI) if image registration has been carried out [4]. Empirical approaches are required, however.

3.3. SEGMENTATION OF PATIENT DATA INTO VoI

With conjugate-view imaging, if an anatomical image set such as one from CT or one from MRI is available, then tumours can be outlined in the anatomical space. These outlines are then available for use in the projection space with techniques such as computer assisted matrix inversion [5] discussed in section 3.4.2. Functional volume estimation from planar imaging has shown its limitations when compared with three-dimensional imaging [6].

With tomographic imaging without registration of image sets, target segmentation in the image space is needed. This statement is true for both SPECT and positron emission tomography (PET). With SPECT, many of the segmentation publications do not specifically deal with the imaging of ^{131}I or other higher-energy, single-photon emitters; they will not be reviewed here. In their early work on segmentation with ^{131}I , Fleming and colleagues [7, 8] use one of two related methods to choose a threshold percentage. This percentage multiplies the maximum pixel to give a threshold pixel value. Pixels containing a value greater than or equal to this value are included in the volume of interest. Both methods require an initial box of interest that is manually chosen to surround the object. The first method is called maximization of interclass variance [9]. For this, the threshold is calculated assuming there are two levels within the box, one for the object, and one for the surround. The weighted sum of the two squares of the difference between the mean value of the level and the mean value of the entire box is calculated. The threshold is chosen to make this weighted sum a maximum. The idea is that when the threshold is correct, both the upper level and the lower level will be far from the fixed mean of the entire box and so the above two-component sum will be large. The second method replaces the manually chosen box with the VoI chosen by the method above. It then expands this VoI in all directions by a set number of pixels. Next, it maximizes the same weighted sum referred to above to find a new threshold. This procedure is repeated, yielding an iterative approach. The stopping criterion was not specified [7]. Recently, Fleming and colleagues have proposed case-specific volume-of-interest segmentation rules [8], but they have not yet applied them to radionuclides such as ^{131}I .

With PET Erdi *et al.* use a method wherein the threshold percentage that determines the target outline is chosen so as to fit the situation [10], which is

similar to the use of case-specific rules referred to above. That is, Erdi *et al.* propose an initial segmentation, after which an approximate target to background ratio is calculated. In addition, the target volume is estimated from CT. Then, depending on the ratio and the volume, a threshold is chosen with which to carry out the final segmentation. Another approach, which is receiving considerable attention, is the use of fuzzy segmentation techniques. They demonstrate excellent performance and produce good results as automated, unsupervised tools for segmenting noisy images in a robust manner. Based on the Fuzzy C-Means (FCM) algorithm, Boudraa *et al.* segmented PET images into a given number of clusters to extract specific areas of differing activity concentration (MBq cm^{-3}) for brain lesion quantification purposes [11].

With SPECT or PET imaging, if a registration between the radiopharmaceutical tomographic image set and CT or MRI is available, the VoI outlines from CT or MRI can simply be transferred to the three-dimensional space of the reconstructed activity distribution [12]. If a multimodality imager is employed, a phantom calibration provides the transformation to place the CT outline into the activity space [13]. In that space, the outlines provide the VoI over which the total activity is found, or, if pixel-by-pixel dose, or pixel-by-pixel dose rate, is calculated, the volume over which to investigate the dose parameter. Image registration is discussed further in section 3.4.7.

3.4. DETERMINATION OF THE DISTRIBUTION OF RADIOACTIVITY IN BOTH SPACE AND TIME

In the accurate estimation of dose from imaging, it is very important to attain an accurate measurement for the amount of activity. Determining an activity value that is correct in the absolute sense is ideal and the ultimate goal. However, it should be pointed out that, within a single study, the activity value can be self-consistent but incorrect by a constant multiplier. That is, for example, such an error does not disturb the correlation of calculated radiation dose with response. When one wants to compare radiation-dose results from different groups, however, or combine them, then the importance of estimating absolute activity is clear.

Similarly, in a given patient, an accurate estimate of the distribution of activity is ideal and frequently the goal. However, if one is interested in only an estimate of the radiation dose to a tumour or organ as a whole, then one needs only the total activity and may sacrifice knowing the distribution within that tumour or organ.

Finally, to calculate radiation dose, one must know the time distribution of activity for the target. If a certain amount is present within a sealed, fixed-size object, then the amount will change at the rate of physical decay of the

radionuclide. However, even if a tumour or organ is a fixed size, or assumed to be so, usually the amount of activity within that fixed size is changing by the radiopharmaceutical entering and/or leaving. Therefore, one must measure or estimate the dependence of the activity on time. If the tumour size is changing as well, then one may define another fixed-size element, such as a voxel within the tumour, determine the time-activity curve for that voxel, and eventually calculate the dosimetry for it. Obtaining a time distribution of activity is discussed in section 3.4.6.

Unlike CT or MRI, which look at anatomy or body morphology, nuclear medicine imaging determines metabolic activity and tissue function. We therefore next look at nuclear medicine imaging. The potential for quantification of activity with whole-body imaging, spot conjugate views, SPECT or PET is examined.

3.4.1. Quantitative whole-body imaging

Whole body imaging for the determination of the amount of activity present in the body, without quantitative description of where, is of interest for the estimation of whole-body radiation dose. This radiation dose is of interest, in turn, because it has been shown to correlate with bone-marrow toxicity. Bone-marrow toxicity is of great importance in all therapies that do not employ bone-marrow support.

Whole-body imaging in this application competes with a probe survey of the patient. With both methods, the end goal is the whole-body activity as a function of time. In the dose calculation, the measured activity is assumed to be uniformly distributed at each time point. The reason is partly to simplify the calculation and partly because methods to calculate bone-marrow dose rather than whole-body dose are difficult to devise and so no use can be made of the spatial distribution.

Whole-body imaging is usually carried out with a scanning scintillation camera. A set amount of time is used for the passage of the camera from the head to the feet of the patient. The total number of counts in images acquired at different times after the initial activity administration is then plotted as a function of the start time of each image. Since the first image is taken immediately after the injection or infusion of a known amount of activity, the total measured counts correspond to that activity, yielding a conversion factor. (The rationale is that at that time all of the administered activity must be located within the patient and very little of it has yet decayed.) The conversion factor between image counts and estimated total activity is then applied to the count total in each subsequent image. The method and assumptions for the calculation of whole-body dose from total activity can be found in [14]. In ^{131}I metaiodobenzylguanidine therapy of neuroblastoma, the resulting whole-body dose has the largest coefficient for the correlation with marrow toxicity compared with other predictors [15]. In ^{131}I tositumomab

therapy of lymphoma, the correlation is best for treated patients who had not previously undergone bone-marrow transplantation when the nadir in platelet counts was used [16].

Advantages. This imaging is simple and self-calibrating.

Disadvantages. There is no resolution in space.

3.4.2. Quantitative imaging with conjugate views

For total activity within an isolated organ or tumour, one can use an imaging method that is simpler than three-dimensional imaging with SPECT or PET. That is, one can get the total activity using only two opposed views of the patient, the so-called conjugate views. Note, however, that by sacrificing the knowledge about the three-dimensional spatial distribution of the activity, one gives up accurately estimating the three-dimensional spatial distribution of the radiation dose within the organ or tumour. However, if the added information on the dose distribution does not have an application, and/or if there is no added accuracy in estimating total activity, then perhaps one should save the extra effort and estimate the total activity with spot conjugate views.

The methods for classical quantitative conjugate views [17] have been summarized in detail [2]. The well known equation for activity, A , is:

$$A = \sqrt{\frac{I_A \times I_P}{T}} \times \frac{f}{C} \quad (3.1)$$

where I_A is the count within the RoI in the anterior view, I_P is the count in the posterior view, T is the transmission through the body at the tumour location from anterior to posterior, f is a correction that is 1 for small objects, and C is a conversion factor that converts counts to activity. In this case, a transmission measurement is taken explicitly and the value for C is derived from a measurement in air, usually with a point source. Note that with this equation two objects which are located behind each other along the anterior-posterior direction, are completely unresolved. Thus, the resolution problem here is so great that one obtains a sum of two activities. This sum activity may be ascribed to one object whose volume is the sum of two objects. When radiation dose is calculated for that object, one obtains a dose which is unfortunately not even the average of the true doses to the two objects. Phantom tests of the method using ^{131}I have been carried out [18, 19].

The Siegel reference above outlines how situations more complicated than a single source in a non-radioactive attenuating medium can be handled [2]. One extension to a more complicated situation requires taking a lateral view to obtain needed information. However, it is clear that there is error involved in obtaining the needed extra information, at least from resolution problems. Perhaps for this reason the use of a third view has not been widespread.

The original method assumes narrow beam geometry for attenuation, while in the usual clinical case scattered photons are corrupting the measurement. A pseudo-extrapolation number is one of the ways introduced to counteract the corruption from inclusion of γ -rays that have been scattered by the patient and accepted by the camera. This number (2.48 for ^{67}Ga with a medium-energy collimator, for example) is determined from an experimentally measured curve of transmission versus water-phantom thickness. It multiplies the T value in equation (3.1), thus reducing the apparent activity by compensating for having counted scattered γ -rays [2]. Pixel-by-pixel scatter correction methods [20] can also be employed. For ^{131}I and usual collimators, the methods based on three or more energy windows actually compensate for patient scatter of the primary γ -ray (364 keV) and also for septal penetration of higher-energy γ -rays that deposit only part of their initial energy in the scintillation crystal. Another approach is one that employs buildup factors [2]. There are two versions of this method. Common to both versions is the need to take calibration measurements. The main problem is that the results from these measurements depend on parameters such as the shape and size of the source. Therefore, it is not clear how well they apply to a given target source in a given clinical case.

Concern over complications from the transmission measurement or from the calibration has led other investigators to related, but perhaps more robust, methods. With one ^{131}I technique, a calibrated source is included during the patient imaging [21]. This method has recently been used for neuroblastoma patients undergoing therapy with ^{131}I metaiodobenzylguanidine. The resulting tumour self-absorbed dose had a statistically significant ($p < 0.01$) correlation with degree of overall tumour response for 27 patients [22].

Another conjugate view method with ^{131}I involves a transmission measurement with a large-diameter ^{57}Co disc source [14]. It is based on earlier research using ^{111}In [23]. It requires the acquisition of two phantom calibration curves. One gives transmission versus thickness of water using an 46 cm (18 inch) square cross section water bath. The other yields efficiency as a function of thickness, where efficiency is geometric mean counts/activity. It is determined by successively imaging a syringe source of known activity that is centred in the bath filled with changing depths of water. The data for each calibration are fitted with a second-order polynomial and then thickness is eliminated between the two fitted curves to yield a final working curve.

Disadvantages stemming from lack of three-dimensional resolution are partially solved by the addition of a three-dimensional anatomical image in computer-assisted matrix inversion [5]. A required condition, however, is that you assume the activity is uniformly distributed in each of the targets and within the background region that separates the targets. The method

also requires that a CT image set, registered with the projection image, is available.

Advantages. These related methods are simple and lead directly to macrodose. The simplicity is an aid for making the repeated measurements needed for time-activity curves. Newer methods can employ information from an anatomical image.

Disadvantages. Outlining each target region in one of the projections is subject to error. Resolution in the anterior-to-posterior direction is either non-existent or not of the highest quality. In some cases, results are obtained for only one large target when there are actually two or more smaller targets.

3.4.3. Quantitative imaging with SPECT

Both SPECT and PET provide an estimate of the activity distribution in three dimensions. However, this estimate is not totally accurate due to the finite nature of the system spatial resolution. The lack of activity accuracy causes errors in dosimetric estimation. Quantitative SPECT imaging itself was well summarized in three review articles published between 1994 and 1996 [24, 25, 26]. We will describe the problem of activity quantification with SPECT for radiopharmaceuticals of most interest in therapy (we usually will use ^{131}I , since it has the highest familiarity to the authors). We will also include some of the more recent developments in the field.

First, let us note that for ^{131}I and the usual high-energy general-purpose collimator, the detector response to a point source at a distance in front of the collimator features a considerable pedestal of counts due to septal penetration from the primary (364 keV) γ -rays. Some of the events in this pedestal come from 364 keV γ -rays that both penetrate the collimator septa without energy loss and deposit their full energy in the camera crystal. Such events cannot be eliminated by scatter-compensation methods such as the triple-energy-window method [20] because their spectrum is identical to that of the correctly collimated 364 keV photons. Quantification complications from these events depend on how the counts in the reconstructed image are converted into image activity. This conversion is sometimes called camera calibration. Readers are therefore reminded that accuracy in activity quantification in this case is intimately connected with the method of camera calibration.

For ^{131}I and a collimator with thicker septa, such as a commercial collimator designed for positron imaging, or a special purpose, high-resolution, low-efficiency rotating collimator, the detector response does not have the pedestal but features a low-intensity hole pattern [27]. This hole pattern would itself be expected to cause problems, but incorporating such a pattern into a reconstruction program has recently been accomplished for ^{111}In [28] and, with their rotating collimator, Gonzales-Trotter *et al.* argue that the intensity of the hole pattern is so small that it can be neglected [29].

With standard high-energy collimator imaging of a single target volume of interest in a non-radioactive background, activity spills out into other areas of the three-dimensional image. However, this spill-out is not a problem in this case: one simply uses a volume of interest that is larger than the true target volume [8].

On the other hand, usually there are other targets or structures fairly nearby that contain activity, and a low level of activity in the regions between these targets and structures. In this more general case, two things happen:

1. One must use a restricted VoI for the target of interest in order to not include other targets or structures. Then some target activity spills out of that restricted VoI.
2. There is spill into the target VoI from the other targets and structures and from the low-activity-level background.

A solution to these problems has not yet been found. Below, we outline current attempts to minimize them.

Links *et al.* [30] studied the problems specifically for brain imaging using simulations with specified three-dimensional Gaussian spatial resolution. Their reference list includes possible solutions for particular regions of interest within the brain.

Gonzalez-Trotter *et al.* [29, 31] use a camera calibration that yields a conversion factor between planar counts and true activity, plus a reconstruction program that effectively distributes one planar count from a projection fractionally into many voxels in reconstruction space.

Their conversion factor depends on how many planar counts are obtained by the camera-collimator system from a small in-air ^{131}I source that has a known activity. They employ both attenuation and scatter-penetration compensations and take collimator characteristics into account in their Ordered-Subsets Expectation Maximization (OSEM) algorithm [32]. For a sphere inside a water bath that contains a uniform activity concentration, they compute activity as a function of the radius, r , of the volume of interest employed. The computed activity is the difference between the estimate of a large activity and that of a small underlying pedestal. For a phantom measurement with a small sphere (1.1 cm radius) in a water bath without background activity, the estimate of sphere activity approaches an almost flat plateau at the correct activity value, as the radius increases beyond that for the physical size of the sphere. At the radius of the sphere, the true activity is slightly underestimated (by about 20%) by the region of interest. These facts are shown in figure 3.1. Therefore, it appears that an accurate estimate (within 5%) can be found from the plateau value.

Fleming and colleagues have advocated quantification that uses a calibration factor proportional to that from a planar measurement of a point source of known activity but also sensitive to the details of the reconstruction algorithm [33]. To this calibration is added other procedures

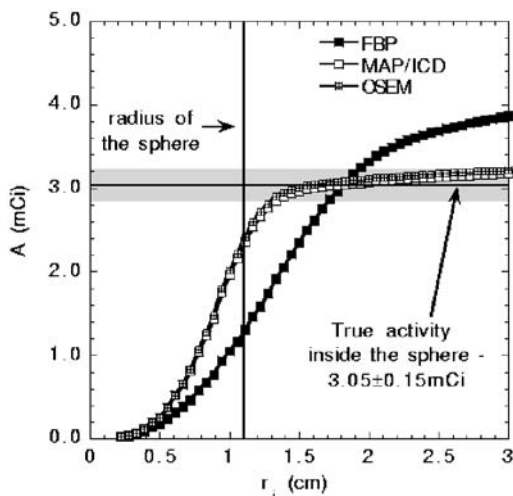


Figure 3.1. Plot of activity as a function of the radius r_i of the spherical volume of interest. OSEM is defined in the text. Two other methods of reconstruction are also presented for comparison. FBP = standard filtered backprojection. MAP/ICD = maximum a posteriori/iterative coordinate descent. Reprinted from [29] © 2001 IEEE, with permission.

that adapt the quantification to the particular case. These other procedures include the use of regression equations [8]. In cases where there is no uniform surrounding activity and no nearby objects that contain activity, a volume of interest that exactly fits the object is used but only after expansion in all directions by one pixel to account for finite SPECT resolution [33]. The regression equations relate the true activity to the measured activity with a constant greater than 1. The constant is smaller when VoI expansion has been employed, as is to be expected [33]. Also for ^{131}I , Fleming and colleagues measured the activity values for variously shaped objects in a large cylindrical water bath experimentally. Activity values ranged from 0.8 to 29.3 MBq. Using segmentation based on maximization of interclass variance (see section 3.3 above), the measured values compared with the true activities fall quite close to the line of identity [8]. With some of the procedures of Fleming and colleagues, it appears that the segmentation of the object of interest and the determination of its activity are intimately connected, rather than being two distinct steps.

Tang *et al.* have developed a set of methods for SPECT quantification using a research multimodality CT-SPECT imager. They employ attenuation correction and model the collimator but do not include scatter-penetration correction. For three neuroblastoma patients being treated with ^{131}I meta-iodobenzylguanidine, each with a large and a small tumour, they list activity concentration results from eight methods, including conjugate views [13].

Table 3.1. Ratio indicating the variation in activity concentration with the evaluation method as a function of tumour size and patient number.

Patient number	Tumour size	Ratio of maximum activity over minimum activity	
		For all 7 methods	For 5 methods
1	large	1.9	1.3
1	small	13	7.2
2	large	1.8	1.3
2	small	18	2.0
3	large	4.2	2.3
3	small	21	4.2

Herein, we exclude results from one method in a baseline mode that did not include compensation for collimator effects. Then table 3.1 shows the ratio of the largest estimate of activity concentration to the smallest by patient and tumour size.

For the large tumours, the ratio ranges from 1.9 to 4.2. For the harder-to-estimate small tumours, it ranges from 13 to 21. The authors explain that one of these methods is likely to yield a lower bound on the activity while at least one other is likely to yield an upper bound. Excluding the largest and smallest result from the seven methods, one still gets a large variation as shown in the fourth column of the table: the ratio is never less than a factor of 1.3 for the large tumours and not less than a factor of 2.0 for the small tumours. Clearly, for a given patient tumour, results can vary by a considerable factor depending on the method of quantification employed. So, the choice of method is important and, perhaps, difficult to optimize for all targets.

Koral *et al.* [14] employ a conversion factor for focal activity, C , that varies both with the radius of rotation, r , of the circular orbit of the acquisition (which affects resolution) and also with a measured parameter, b , that indicates the relative magnitude of count spill-in from a uniform background concentration compared with count spill-out from the target. Phantom measurements of the functional dependence of C on r and b are made using a 200 cm³ sphere located inside an elliptical water-bath phantom. In contrast to some of the methods of Tang [34], no explicit subtraction for the effects of spill-in of counts from the background is needed. Presumably, the noise-amplification of a subtraction is thus not present. The authors emphasize that the parameters for the SAGE reconstruction [35] of their calibration phantom are the same as for their target measurements, and that the identity of the method for phantoms and patients is also true for the attenuation compensation, the outlining of the target of interest, and the scatter-penetration compensation. The attenuation compensation is

based on a fused CT image as the target outline is transferred between SPECT and CT (such a possibility was discussed in section 3.3). In addition, the authors correct for camera dead time. However, at day 2 after the therapy administration it is usually less than 10%. Finally, the activity for a target volume that is not equal to the sphere volume is corrected by using an empirical recovery coefficient. This coefficient is dependent on volume, and, for one of two cameras, also on radius of rotation. The correction factor is 1 for a volume equal to that of the calibration sphere, greater than 1 for a smaller volume, and less than 1 for larger volumes. To date, target shapes, which are much different from spherical, have a bias [36]. However, resultant dose values tend to correspond with the degree of response in patients [37].

Advantages. One can obtain an estimate of the three-dimensional activity distribution at a given time and one can use detailed models for the imaging system to correct for problems from finite resolution.

Disadvantages. Since the data processing is usually complicated, choosing this imaging can involve a large time commitment.

3.4.4. *Effect of reconstruction algorithm on SPECT imaging*

The accuracy of a SPECT reconstruction plays an important role in a three-dimensional dosimetry calculation. Most methods for three-dimensional absorbed dose calculation assume that the input, the SPECT image set, reflects the actual activity distribution. That is, the methods simply calculate from these images the absorbed dose, either by direct Monte Carlo methods tracing individual particles or by utilizing dose-kernel convolution methods. However, if the reconstruction method has inherent limitations, they will be transferred to the absorbed dose images. Also, it is important to recognize that a SPECT image set almost always includes a degree of blurring due to the limited spatial resolution of the imaging system, as mentioned in the immediately previous section.

The simplest reconstruction method is basic backprojection. This method simply re-projects a measured projection data set into the image space. The basic backprojection method is fast but generates severe streak artefacts as well as image blurring. The streak artefacts can cause problems for quantification in two ways. First, they can create counts in parts of the image that may be outside the patient or in interior regions where there may be no activity at all. The latter result can affect the detectability of small, low-contrast lesions. Secondly, it may be that the normalization procedure in the reconstruction methods preserves the measured counts, that is, the number of counts in all projections is equal to the number of counts in the reconstruction volume. If streak artefacts are present outside the object then the count level inside the object will be lower in order to fulfil the normalization criterion. This result may then affect the activity

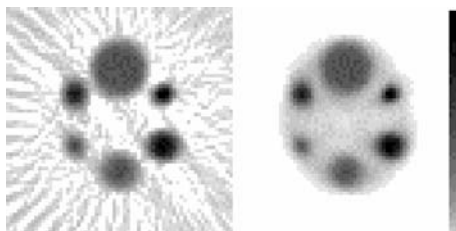


Figure 3.2. Images of a ^{99m}Tc SPECT simulation of six spheres of different activity concentration. The left image shows the result from using FBP with a ramp-filter. The right image shows the result using 12 iterations of MLEM after the initial guess of a uniform image. The projection data were simulated without scatter or attenuation. A non-linear display has been employed to better visualize the low-intensity parts of the image.

determination for an organ or tumour. Therefore, basic backprojection reconstruction has seen limited use in SPECT.

In the past and still today, projection data are often first filtered with a ramp filter (sinc filter in the spatial domain) before reconstruction. This filter theoretically only removes counts produced by the backprojection methodology and not those from measured projection data. Streak artefacts can still occur, such as shown on the left of figure 3.2. (The projection data set has been simulated with no scatter and attenuation in order to visualize the effects generated only by the reconstruction process.) Generally, the ramp filter needs to be rolled over with a smoothing low-pass filter to reduce amplification of high-frequency noise present in the projection data. The resulting procedure is called filtered backprojection (FBP). An alternative to using the rollover of the filter is to utilize post-reconstruction three-dimensional filtering. Both these low-pass filtering methods unfortunately degrade spatial resolution.

Recently, the emergence of fast computers has allowed the wide and routine use of iterative reconstruction methods. These methods are generally based on comparing measured projections with projections calculated from an initial guess of the source distribution. This guess can either be a uniform image where all pixels are set equal or can be the results from an FBP algorithm. The difference between the calculated and measured projections is then used to change the pixels in the estimated image. A common algorithm is the maximum-likelihood-expectation-maximization (MLEM) algorithm [38], which is a statistical method. A given image estimate is obtained from all the projection data. Then the image-estimation procedure is repeated (iterated) a fixed number of times, or until a specified stopping criterion is reached. Unfortunately, a quantitative stopping criterion is yet to be discovered. A sample result is shown on the right of figure 3.2.

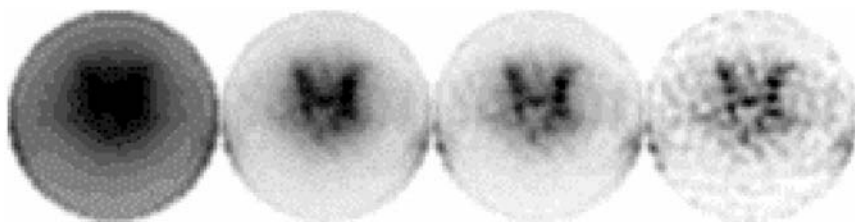


Figure 3.3. These images show a slice reconstructed by iterative MLEM after 1, 5, 10 and 50 iterations. The images show a ^{131}I -labelled monoclonal antibody in a patient at a slice location just above the bladder. Note the increase in noise as the number of iterations becomes large.

As seen in figure 3.3, the number of iterations has an effect on the result and so must be chosen carefully.

Newer algorithms use only sub-sets in a certain order before the image is updated. This procedure has been shown to decrease the number of needed iterations dramatically and is therefore one of a set of methods called accelerated methods. OSEM is such a commonly used method [32]. The iterative methods do not have the streak artefact and are generally expected to be more quantitatively accurate, especially in typical oncology ‘low-statistics’ studies.

3.4.5. *Effect of attenuation, scatter and blurring correction on SPECT imaging*

In SPECT, photon attenuation can introduce errors in the reconstructed image if the attenuation varies with the projection view. For example, in cardiac imaging, photon attenuation can cause false ischemic regions in the inferior walls. Photon attenuation also limits the accurate quantification of measured data in terms of activity and activity concentration. Correcting for this attenuation is very important. The attenuation distribution should generally be measured for each patient to get the patient outline and the internal variation in his/her density and composition. For absorbed dose calculation, the technique with an external radioactive source (transmission computed tomography or TCT) may be inaccurate because of the relatively high noise level present and the poor spatial resolution of the attenuation map. It is therefore somewhat more common to register a CT study of the patient to the SPECT study.

One method for employing a registered CT to estimate the spatial distribution (or map) of attenuation coefficients is based on a technique introduced by Nickoloff *et al.* [39]. The variation [40] yields the following piecewise linear equation:

$$\begin{aligned}
\mu &= 1.131 \times 10^{-2} \left(\frac{CT}{868.6} + 1 \right) & CT \leq -25 \\
&= 5.744 \times 10^{-6} CT + 1.113 \times 10^{-2} & -25 \leq CT \leq 485 \\
&= 8.929 \times 10^{-3} \left(\frac{CT}{868.6} + 1 \right) & CT \geq 485
\end{aligned} \quad (3.2)$$

where μ is the attenuation coefficient for 364 keV gamma rays in mm^{-1} and CT is the X-ray CT number in Hounsfield units for a scanner with an effective energy of 76 keV. Figure 3.4 shows a plot of the relationship. The Nickoloff reference specifies the means of experimentally determining the effective energy of a particular CT scanner.

Tang *et al.* [41] suggest that the above method is too simplistic if an iodine contrast agent is employed in the CT scan and the SPECT image is obtained immediately after the CT scan. In this case, they say that the iodinated regions and the bone regions in the image should be separated and treated differently. The reason is that these two regions effectively have a different slope in the relationship for linear attenuation coefficient versus CT . For their scanner at 140 kVp, they present results from a

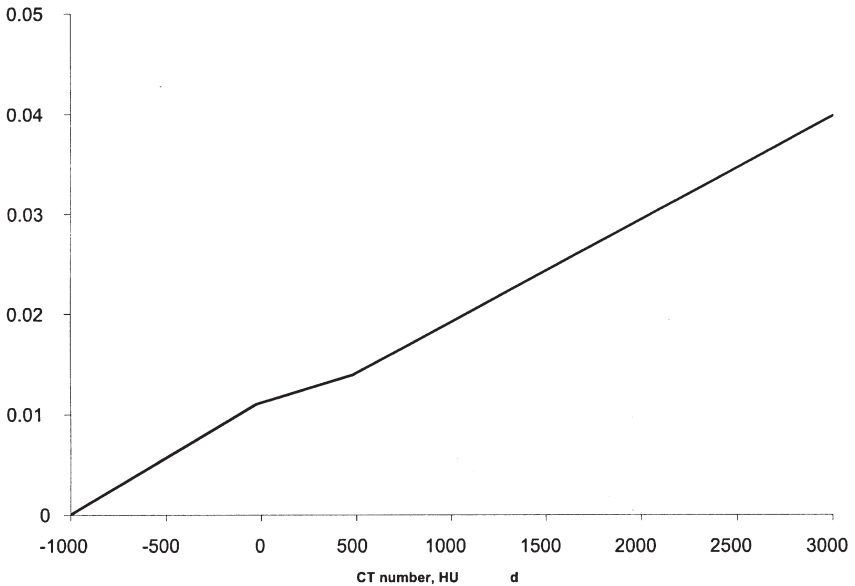


Figure 3.4. Plot of linear attenuation coefficient for gamma rays from ^{131}I versus the pixel CT number from an X-ray CT scanner with an effective energy of 76 keV. It is assumed that above $CT=485$ HU (Hounsfield units) the material is bonelike and below $CT=-25$ HU tissue-like. Between -25 HU and 485 HU, it is assumed there is a transition region.

calibration experiment that show a slope difference of a factor of 10 when converting from CT to the μ that is appropriate for the 364 keV γ -rays of ^{131}I , for example [34]. Their final relationship is also piecewise linear, but with a change in slope at $CT = 0$. Moreover, the slope for the higher CT values is larger if the region has been designated bone than if it has been designated soft tissue containing contrast material.

Attenuation correction can be applied (a) prior to reconstruction (an example is the geometric mean of opposed projections method [42]), (b) post reconstruction (an example is the Chang algorithm [43]) or (c) as part of an iterative reconstruction algorithm (see for example [26]). As part of an iterative reconstruction, the attenuation to the boundary is calculated for each pixel along the ray before summation. The comparison is then between an attenuated projection and a measured projection. This procedure will eventually make the estimated SPECT image more accurate since attenuation is also present in the measured projection. If a registered attenuation map is available, then non-homogeneous attenuation can be easily implemented [4].

Scatter corruption of images originates from the poor resolution of the NaI(Tl) crystal (about 9–10% full width half maximum at 140 keV). A relatively large energy window is needed to acquire a sufficient number of photons. This large window then includes small-angle scattered photons that pass the lower-energy-window discriminator. The crystal location of these events may not be consistent with a ray from their emission point perpendicular to the crystal face. Thus, they should be eliminated by a method such as the dual- [44] or triple-energy window scatter correction [20] methods or by some other means.

The scatter problem described above is less acute as the photon energy increases. However, for emitters that have both a high-energy primary photon and also super-high-energy emissions (such as ^{131}I), scatter in the crystal can create the addition of counts in a different way. If a super-high-energy photon partly deposits its energy into the crystal and then escapes the crystal, the event can increment the count in the main-energy photopeak window. If the photon has escaped the object without Compton scattering, the position in the image of the partly absorbed event is correct even though the energy is below the full-absorption peak of that photon. For energy-window-based scatter correction methods, such as the triple-energy window method, subtraction of these events may result in a decrease in the number of photons that are correctly positioned in space. The result will then be a higher noise level in the corrected image. Effects on the bias of the activity estimate will be negative if the calibration has included such events, but neutral if they have also been excluded there. In either case, fortunately, the number of such events is usually small.

Scatter correction methods that are included in reconstruction programs [45] have recently been developed by some research groups. Frey and Tsui [46] have been developing a method where depth-dependent scatter functions

are used to model a spatially variant scatter distribution. This so called ESSE method utilizes an attenuation map to compensate for non-homogeneous attenuation. A fast Monte Carlo-based scatter compensation method has also been developed for SPECT [47–49]. This method uses a rotation-based Monte Carlo simulation that calculates scatter using various variance reduction methods. An application is to calculate down-scatter in dual-isotope SPECT. With this method, only a fraction of all SPECT projections have to be simulated in a standard manner. The other projections can be estimated rapidly using the results of these standard calculations. For efficiency, approximations have to be made in the method with regard to the final scatter angle of the detected photons. Further speed-up is obtained by combining it with convolution-based forced detection instead of standard forced detection, which is the more common variance reduction technique. Rotation-based Monte Carlo with convolution-based forced detection was found to be about three orders of magnitude faster than standard Monte Carlo with forced detection. Even though SPECT has great potential, a major drawback is its limited spatial resolution [50], mainly caused by the inherent design of collimators. It is rare that the reconstructed spatial resolution using commercial collimators is less than 10 mm for commonly used radioisotopes in radionuclide therapy. Several groups have developed methods for compensation for distance-dependent blurring. These methods are basically attacking the previously mentioned activity spill-in and spill-out. The methods can be based on Fourier-based methods, such as the energy–distance principle [51] and Wiener filtering [52], but collimator-blur compensation is mostly incorporated in the iterative reconstruction [47, 49]. The advantage with incorporation in the iterative algorithm is that pre-calculated response functions can be placed into lookup tables and selected for use based on the corresponding pixel location.

In many cases in nuclear medicine, a low count-rate produces images with disturbing noise. The common way to reduce noise is to apply two- or three-dimensional low-pass filters. However, it is important to recognize that low-pass filtering of projections for noise reduction also will result in a degradation of image resolution. For small objects, blurring due to low-pass filtering reduces image contrast and the ability to detect lesions. The blurring also affects, for example, segmentation of volumes of interest, which may incorrectly increase the determined volume. Furthermore, the limited spatial resolution will produce ‘spill-in’ and ‘spill-out’ of activity from one region to another.

3.4.6. Time series of images

The most straightforward way to obtain the time series of information needed for dosimetry is to image the patient repeatedly over time by conjugate views or by a tomographic method (SPECT or PET). The tomographic

imaging is potentially more accurate, but is probably more complicated and possibly more time consuming. Registration of multiple tomographic images, one three-dimensional image set to another, allows the use of identical evaluation regions of interest for all time points, and/or reduces noise in the plots of bio-distribution versus time.

An alternative to a time-series of tomographic images has been employed by one research group in the imaging of lymphoma patients [37]. It consists of the use of a time-activity curve from conjugate views for a larger composite tumour to provide an estimate of time-activity curves for the smaller individual tumours of which it is composed. These time-activity curve estimates then have their ordinate axes scaled by individual corrections based upon the smaller-tumour activities determined by a SPECT image taken at a single time point.

3.4.7. *Methods used to register multimodality images*

At the very outset, let us note that achieving a high degree of accuracy for a spatial transformation between image sets can be quite complicated. Physical factors, such as noise, limited spatial resolution, scatter, and septal penetration, and biological factors such as persistent activity in the blood pool and non-specific uptake, may decrease the contrast and blur the image. Therefore, it can be difficult to locate consistent landmarks. Furthermore, diagnostic CT images are usually taken using breath-holding techniques while many radionuclide investigations involve imaging of the thorax, abdomen or pelvis, where organ motion exists. That is, the SPECT or PET data are acquired during a relatively long time period so the resultant reconstructed image set is an average of all phases of respiration. Thus, the image sets are not consistent. This inconsistency can cause complications, for example, if the body boundaries of the CT data and the SPECT or PET can be registered, but the internal structures still differ significantly. Combined CT/SPECT systems with a low-dose CT performed for a period of about 10 min are designed to avoid the breath-holding problem. The CT resolution for these systems is about 3 mm, allowing for both attenuation correction and registration of CT/SPECT data for accurate tumour localization. In spite of the difficulties, many registration methods have been published [53–68]. For a detailed survey of algorithms developed so far, the reader is referred to the comprehensive review by Hutton *et al.* [69]. Below, we will discuss newer registration methods and/or their application to dosimetry.

One type of registration method depends on mutual information, an intensity-based similarity measure [70]. A patient result that used a mutual-information-based registration for both attenuation correction and tumour localization [14, 37] is shown in figure 3.5.

Sjögreen *et al.* have developed a registration protocol that has been applied both to whole-body scintillation camera images, and to CT/SPECT

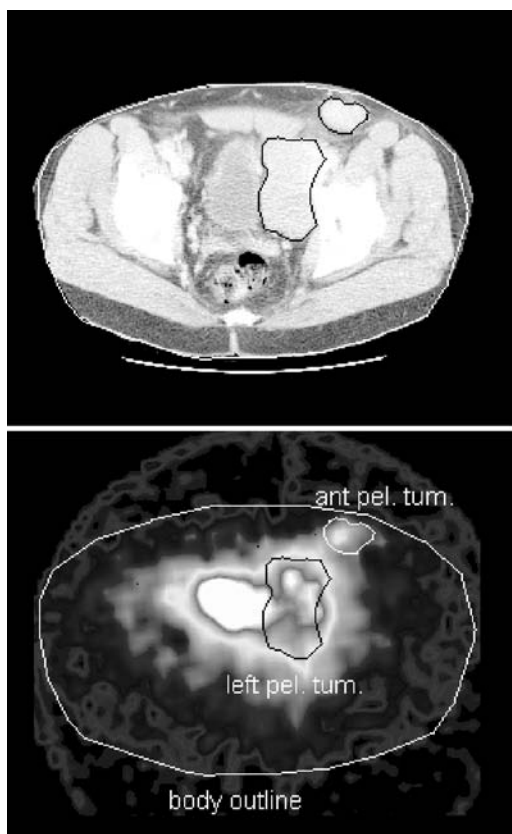


Figure 3.5. Results for one slice from a three-dimensional registration between a CT image set and a SPECT image set. The pelvic area of a non-Hodgkin's lymphoma patient (# 33) being treated with ^{131}I tositumomab is shown. The CT slice (at the top) is from a scan that was taken 13 days before the treatment infusion. The two tumours, shown by black outlines, had their edges manually chosen in this image. The SPECT slice (at the bottom) is from a scan that was taken 42 hours after the treatment infusion. The tumour outlines were placed on the bottom image by virtue of the registration. The anterior pelvic tumour (ant pel. tum.) could be evaluated even though its percent injected dose per gram was only 0.68 times that of the left pelvic tumour (left pel. tum.). ^{131}I activity in the urine of the bladder (not labelled) is a strong feature of the SPECT image. (See plate 2 for colour version.)

image registration [71]. Both mono- (emission-to-emission) and multi- (emission-to-transmission) modality image registration has been addressed. The method performs an optimization of the mutual information between the images. For the whole-body registration method, a spatial transformation based on a second-order polynomial-warping algorithm is applied,

including local transformation of regions corresponding to the legs, pelvis, upper abdomen and head. For the CT/SPECT registration, scatter images have been used as a registration feature. The photopeak and Compton scatter images are acquired simultaneously in dual-acquisition mode, and the registration can thus be performed via the scatter images, which to a larger extent reflect the body boundary. A patient positioning procedure is applied, which mainly consists of using a flat and similarly shaped couch for both CT and SPECT acquisitions, and applying co-calibrated directional lasers. Spatial transformations include rigid translations and three-dimensional rotations, and the option of applying transformations locally. The mutual information, or the normalized mutual information, is used as the similarity measure, calculated either globally or based on local regions. The contribution from the CT/SPECT image registration to the overall dosimetry error has also been evaluated by introducing deliberate misalignments between the Monte Carlo simulated SPECT images and corresponding CT images of an anthropomorphic computer phantom [72]. The activity and absorbed dose obtained when using re-registered CT images compared with the corresponding results when using perfectly matched CT images have shown that the registration method does not introduce significant errors.

Recently, a new procedure to allow three-dimensional registration of CT and SPECT has been proposed [73]. The rationale for the procedure is that it should be easier to find the correct superimposition for two transmission image sets, because they are quite similar, than for a transmission data set (CT) and an emission data set (SPECT) which can have many different features. In this particular procedure, both of the transmission sets involve planar images. Implementation is perhaps simplest for a dual-head SPECT camera system. The procedure involves two extra radionuclide transmission images, obtained before or after the SPECT acquisition. One is from anterior to posterior and the other is from left lateral to right lateral. These are compared with re-projections of the volumetric CT data along the same axes. When the CT volume image set has the correct shift, scaling and rotation, its projections should match those of the transmission images. Then the same transformation of the CT should bring it into registration with the SPECT data set acquired with the dual-head camera. The authors state that acceptable accuracy is attained in initial phantom tests [73].

3.4.8. Quantitative imaging with PET

PET is arguably the most advanced of the non-invasive nuclear medical imaging techniques. It provides both qualitative and quantitative information about the volume distribution of biologically significant radiotracers.

The sensitivity of *in vivo* tracer studies is highly developed with PET, which is based on electronic collimation and thereby offers a wide acceptance angle for detecting emitted annihilation photons. Consequently, the sensitivity

of PET per disintegration with comparable axial fields of view is two orders of magnitude greater than that of SPECT cameras. Another boost for sensitivity comes from the fact that PET usually detects molecules labelled with short-lived radioisotopes for which the decay rate is very high. Within the spectrum of medical imaging modalities, sensitivity ranges from the detection of millimolar concentrations in functional MRI to pico-molar concentrations in PET which is a difference involving a factor of 10^9 [74].

It is also generally held that PET offers better spatial resolution than SPECT. Furthermore, PET has provided the possibility of quantitative measurements of tracer concentration *in vivo* for a longer time than SPECT has. However, in practice, there are several issues that must be addressed in order to fully realize the potential of PET. That is, the measured line integrals must be corrected for a number of background and physical effects before reconstruction. The needed processes include subtraction of random coincidences, detector normalization, deadtime, attenuation and scatter corrections. Detector normalization is similar to correction for camera-collimator-system non-uniformities based on field-flood measurements in SPECT. Deadtime, attenuation and scatter correction are all also needed in SPECT. Since attenuation and scatter correction are especially important in clinical PET, they are briefly discussed in section 3.4.9 below.

Advantages. PET is based on electronic collimation and thereby offers a wide acceptance angle for detecting emitted annihilation photons. Consequently, the sensitivity of PET per disintegration with comparable axial fields of view is two orders of magnitude greater than that of SPECT cameras. A further sensitivity advantage for detecting low molecular concentration arises in PET when detecting molecules labelled with short-lived radioisotopes. With respect to imaging of molecular pathways and interactions, the specificity of PET arises due to the use of radioisotopes such as ^{18}F and, to a lesser extent, ^{11}C to label biochemical/physiological and pharmaceutical molecules within a radioactive form of one of its natural constituent elements. SPECT's ability to image some chemical processes is hindered by the fact that the isotopes are relatively large atoms and cannot be used to label some compounds due to steric reasons. Moreover, quantification techniques are well established with PET whereas they have only been more recently developed with SPECT.

Disadvantages. The high cost of PET and the need for a nearby or an on-site cyclotron and for radiochemical/radiopharmaceutical support has limited PET to only a few clinical sites, to date. The major drawback is that a short half-life puts a practical upper limit on the activity of the manufactured isotope. Moreover, for treatment planning, a radioisotope from the same element as the treatment element is required. ^{124}I , ^{86}Y and ^{64}Cu are available and have undergone some usage, however.

3.4.9. Effect of attenuation and scatter correction on PET imaging

Attenuation correction in PET is now widely accepted by the nuclear medicine community as a vital component for the production of artefact-free, quantitative data. In PET, correction for attenuation depends on the total distance travelled by both annihilation photons and is independent of the emission point along the ray defined by these photons. The most accurate attenuation correction techniques are based on measured transmission data acquired before (pre-injection), during (simultaneous) or after (post-injection) the emission scan. Alternative methods to compensate for photon attenuation in reconstructed images use assumed distribution and boundary of attenuation coefficients, segmented transmission images, or consistency condition criteria [4]. Transmission-based attenuation correction has been traditionally performed in the case of PET whereas only more recently has it been applied to SPECT imaging. There are many possible explanations for that difference, one of them being that PET started mainly as a research tool where there was greater emphasis on accurate quantitative measurements.

Techniques based on transmission image segmentation and tissue classification tools have also been proposed to minimize the acquisition time and increase the accuracy of attenuation correction, while still preserving or even reducing the noise level [75]. Representative coronal slices of a clinical study at the level of the thorax are shown in figure 3.6. The figure illustrates the improvement in image quality of the emission-data reconstructions when using fuzzy clustering-based segmented attenuation correction as compared with measured attenuation correction. The images are less noisy and show more uniform uptake of the tracer.

3.4.10. Reconstruction algorithms for fully three-dimensional PET

The development of fully three-dimensional reconstruction algorithms has been necessary in order to take advantage of the acquisition of PET data without septa. Various methods have been proposed to solve the problem of recovering the image from the resulting four-dimensional data sets. There are two major classes of image reconstruction algorithms used in PET: direct analytical methods and iterative methods. At present, the most widely used methods of image reconstruction are still direct analytical methods because they are relatively quick. However, the images tend to be streaky and display interference between regions of low and high tracer concentration. Images produced by iterative methods are computationally much more intense and, at present, the computational time of reconstruction is prohibitive. However, with the development of parallel architectures and because of the potential for using these architectures in conjunction with iterative techniques, the future for iterative reconstruction seems bright.

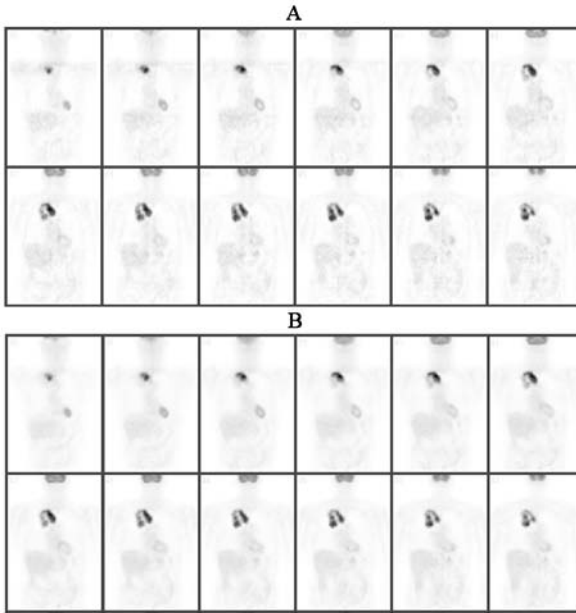


Figure 3.6. Illustration of the improvement in image quality when using segmented attenuation correction. **A.** Reconstructions using measured attenuation correction. **B.** Reconstructions using fuzzy clustering-based segmented attenuation correction. Reprinted with permission from the Institute of Physics [75].

During the past decade, much research and development has concentrated on the development of improved fully three-dimensional reconstruction algorithms and scatter compensation techniques required for quantitative PET. Increasingly sophisticated scatter correction procedures are under investigation: particularly those based on accurate scatter models and iterative reconstruction-based scatter compensation approaches [76]. In summary, PET quantification remains an open issue that requires further R&D efforts [77].

3.5. AUXILIARY CONTRIBUTION FROM PET

FDG-PET is widely used in the diagnosis, staging and assessment of tumour response to therapy, because metabolic changes generally precede the more conventionally measured parameter of change (tumour size). Although metabolic imaging is an obvious choice, the way to perform imaging is still an open issue. Combined PET/CT systems are pushing ahead for acquiring

co-registered anatomical and functional images in a single scanning session allowing more accurate and effective attenuation correction [78]. The tracers or combinations of tracers to be used [79], when the imaging should be done after therapy, what are the optimal acquisition and processing protocols, are all unanswered questions. Moreover, each tumour–therapy combination may need to be independently optimized and validated. Results, to date, for two diseases are discussed immediately below.

The use of PET with FDG, FDOPA and ^{15}O -water to assess the metabolic status of melanoma metastases after treatment with dacarbazine and α -interferon has been recently reported [79]. This approach, without pre-treatment imaging, cannot assess subtle increases or decreases in tumour metabolism. However, the approach should be able to assess whether the response has been complete or whether residual viable tumour is present. This method is appropriate if a reasonable probability exists that a single course of therapy will result in a complete response.

In imaging of BexxarTM patients with FDG-PET, response has been shown to occur as early as 6–7 days. That is: (1) FDG-PET imaging found tumour metabolism to be reduced at 33–70 days after radioimmunotherapy (RIT), compared with a baseline scan. The standardized uptake value lean (SUV_{lean}) for tumours in eight patients was reduced, and reduced proportionately to the final response (complete response patients more than partial response patients, and partial response patients more than non-response patients) [80]. (2) In five of six other patients, the same SUV_{lean} was already decreased at 6–7 days after the therapy administration.

3.6. TREATMENT PLANNING

When using imaging for dosimetry, one often assumes that the results during therapy will be the same as those during evaluation, except for scaling by the ratio of the administered activities. Since the administration for the first imaging could possibly affect the pharmacokinetics, this assumption may not hold. If it does not, the choice of administered activity might still be made in the same way but measurements would be needed during therapy to quantify the discrepancy. It is well known that in ablation of thyroid remnants, measurements seem to imply a reduction in the therapy activity compared with what one calculates by scaling. The explanation for the observed results is still under discussion, however.

In BexxarTM RIT of lymphoma, the ratio of the therapy percent-injected dose divided by the evaluation percent-injected dose has been checked for variations from 1. These checks were carried out at 2 to 3 days after the administration [81]. There is an extra biological complication here in that the RIT consists of the administration of an anti-CD20 murine monoclonal IgG2a antibody (tositumomab) pre-dose followed by

its ^{131}I -radiolabelled conjugate (iodine ^{131}I tositumomab). The evaluation was carried out with a reduced activity of iodine ^{131}I tositumomab but with the same pre-dose. For 31 chemotherapy-relapsed patients, the hypothesis that the ratio equals 1 was rejected using conjugate-view imaging [82]. However, the average of the ratio was only slightly less than one (0.93). For seven previously untreated patients, results from imaging using either conjugate views or SPECT agreed with the hypothesis of the ratio being equal to 1 [81]. So, for both types of patient, there will not be much error on average with assuming a ratio of 1.

ACKNOWLEDGMENTS

One author (KFK) acknowledges the support of Grant R01 CA87955 awarded by the National Cancer Institute, United States Department of Health and Human Services. Another author (HZ) acknowledges the support of grant SNSF 3152-062008 from the Swiss National Science Foundation. Another author (MLJ) acknowledges the support from the Swedish Cancer Foundation. The contents and views in this chapter are solely the responsibility of the authors and do not necessarily represent the official views of the institutions providing the support.

REFERENCES

- [1] Lechner P K *et al.* 1993 An overview of imaging techniques and physical aspects of treatment planning in radioimmunotherapy *Med. Phys.* **20** 569–77
- [2] Siegel J A *et al.* 1999 MIRD Pamphlet No 16: Techniques for quantitative radiopharmaceutical biodistribution data acquisition and analysis for use in human radiation dose estimates *J. Nucl. Med.* **40** 37S–61S
- [3] Snyder W S, Ford M R, Warner G G and Watson S B 1975 'S', *Absorbed Dose per Unit Cumulated Activity for Selected Radionuclides and Organs*. MIRD Pamphlet No 11 (Society of Nuclear Medicine)
- [4] Zaidi H and Hasegawa B H 2002 Determination of the attenuation map in emission tomography *J. Nucl. Med.* **43** in press
- [5] Liu A, Williams L E and Raubitschek A A 1996 A CT assisted method for absolute quantitation of internal radioactivity *Med. Phys.* **23** 1919–28
- [6] Zaidi H 1996 Comparative methods for quantifying thyroid volume using planar imaging and SPECT *J. Nucl. Med.* **37** 1421–6
- [7] Alaamer A S, Fleming J S and Perring S 1993 Evaluation of a technique for the quantification of radioactivity and volume of an object using SPECT *Nucl. Med. Commun.* **14** 1061–70
- [8] Fleming J S and Alaamer A S 1998 A rule based method for context sensitive threshold segmentation in SPECT using simulation *Phys. Med. Biol.* **43** 2309–23
- [9] Zaidi H 1996 Organ volume estimation using SPECT *IEEE Trans. Nucl. Sci.* **43** 2174–82

- [10] Erdi Y E *et al.* 1997 Segmentation of lung lesion volume by adaptive positron emission tomography image thresholding *Cancer* **80** 2505–9
- [11] Boudraa A E *et al.* 1996 Delineation and quantitation of brain lesions by fuzzy clustering in positron emission tomography *Comput. Med. Imaging Graph.* **20** 31–41
- [12] Koral K F *et al.* 1989 Calculating radiation absorbed dose for pheochromocytoma tumors in ^{131}I MIBG therapy *Int. J. Radiat. Oncol. Biol. Phys.* **17** 211–18
- [13] Tang H R *et al.* 2001 Neuroblastoma imaging using a combined CT scanner–scintillation camera and ^{131}I -MIBG *J. Nucl. Med.* **42** 237–47
- [14] Koral K F *et al.* 2000 Initial results for hybrid SPECT–conjugate-view tumor dosimetry in ^{131}I -anti-B1 antibody therapy of previously untreated patients with lymphoma *J. Nucl. Med.* **41** 1579–86
- [15] Sisson J C *et al.* 1994 Predictors of toxicity in treating patients with neuroblastoma by radiolabeled metaiodobenzylguanidine *Eur. J. Nucl. Med.* **21** 46–52
- [16] Wahl R L *et al.* 1998 Iodine-131 anti-B1 antibody for B-cell lymphoma an update on the Michigan Phase I experience *J. Nucl. Med.* **39** 21S–27S
- [17] Thomas S R, Maxon H R and Kereiakes J G 1976 *In vivo* quantitation of lesion radioactivity using external counting methods *Med. Phys.* **3** 253–5
- [18] Hammond N D, Moldofsky P J, Beardsley M R and Mulhern C B Jr 1984 External imaging techniques for quantitation of distribution of I-131 $F(ab')_2$ fragments of monoclonal antibody in humans *Med. Phys.* **11** 778–83
- [19] Eary J F, Appelbaum F L, Durack L and Brown P 1989 Preliminary validation of the opposing view method for quantitative gamma camera imaging *Med. Phys.* **16** 382–7
- [20] Ogawa K, Harata H, Ichihara T, Kubo A and Hashimoto S 1991 A practical method for position dependent Compton-scatter correction in single photon emission CT *IEEE Trans. Med. Imaging* **10** 408–12
- [21] Shulkin B L *et al.* 1988 Conjugate view gamma camera method for estimating tumor uptake of iodine-131 metaiodobenzylguanidine *J. Nucl. Med.* **29** 542–8
- [22] Matthay K K *et al.* 2001 Correlation of tumor and whole-body dosimetry with tumor response and toxicity in refractory neuroblastoma treated with ^{131}I -MIBG *J. Nucl. Med.* **42** 1713–21
- [23] Doherty P, Schwinger R, King M and Gionet M 1985 Distribution and dosimetry of indium-111 labeled $F(ab')_2$ fragments in humans. *Fourth International Radiopharmaceutical Dosimetry Symposium*, Oak Ridge, TN, CONF-851113 (DE86010102)
- [24] Zaidi H 1996 Quantitative SPECT: Recent developments in detector response attenuation and scatter correction techniques *Physica Medica* **12** 101–17
- [25] Rosenthal M S *et al.* 1995 Quantitative SPECT imaging a review and recommendations by the Focus Committee of the Society of Nuclear Medicine Computer and Instrumentation Council *J. Nucl. Med.* **36** 1489–513
- [26] Tsui B M, Zhao X, Frey E C and McCartney W H 1994 Quantitative single-photon emission computed tomography basics and clinical considerations *Semin. Nucl. Med.* **24** 38–65
- [27] Dewaraja Y K, Ljungberg M and Koral K F 2000 Accuracy of ^{131}I tumor quantification in radioimmunotherapy using SPECT imaging with an ultra-high-energy collimator: Monte Carlo study *J. Nucl. Med.* **41** 1760–67
- [28] Sayeram S *et al.* 2001 Compensation for collimator detector response in tumor SPECT imaging using In-111 with dual energy photons *J. Nucl. Med.* **42** 197P

- [29] Gonzales-Trotter D E, Bowsher J E and Jaszczak R J 2001 Absolute quantitation of a spherical I-131 activity distribution using a high-resolution rotating collimator: A phantom study *IEEE Trans. Nucl. Sci.* **48** 65–73
- [30] Links J M, Zubieta J K, Meltzer C C, Stumpf M J and Frost J J 1996 Influence of spatially heterogeneous background activity on 'hot object' quantitation in brain emission computed tomography *J. Comput. Assist. Tomogr.* **20** 680–7
- [31] Gonzalez D E, Jaszczak R J, Bowsher J E, Akabani G and Greer K L 2001 High-resolution absolute SPECT quantitation for I-131 distributions used in the treatment of lymphoma: A phantom study *IEEE Trans. Nucl. Sci.* **48** 707–14
- [32] Hudson H M and Larkin R S 1994 Accelerated image-reconstruction using ordered subsets of projection data *IEEE Trans. Med. Imaging* **13** 601–9
- [33] Alaamer A S, Fleming J S and Perring S 1994 Evaluation of the factors affecting the accuracy and precision of a technique for quantification of volume and activity in SPECT *Nucl. Med. Commun.* **15** 758–71
- [34] Tang T R 1998 *A Combined X-ray CT–Scintillation Camera Imaging System for Measuring Radionuclide Uptake in Tumors*. Thesis. University of California
- [35] Fessler J A and Hero A O 1995 Penalized maximum-likelihood image-reconstruction using space-alternating generalized EM algorithms *IEEE Trans. Imag. Proc.* **4** 1417–29
- [36] Dewaraja Y K, Ljungberg M and Koral K F 2001 Evaluation of object shape effects in I-131 SPECT tumor activity quantification *Eur. J. Nucl. Med.* **28** 900–6
- [37] Koral K F *et al.* 2000 Tumor-absorbed-dose estimates versus response in tositumomab therapy of previously untreated patients with follicular non-Hodgkin's lymphoma: preliminary report *Cancer Biother. Radiopharm.* **15** 347–55
- [38] Lange K and Carson R 1984 E-M reconstruction algorithms for emission and transmission tomography *J. Comput. Assist. Tomogr.* **8** 306–16
- [39] Nickoloff E L, Perman W H, Esser P D, Bashist B and Alderson P O 1984 Left-ventricular volume—Physical basis for attenuation corrections in radionuclide determinations *Radiology* **152** 511–15
- [40] Koral K F *et al.* 1994 CT–SPECT fusion plus conjugate views for determining dosimetry in iodine-131-monoclonal antibody therapy of lymphoma patients *J. Nucl. Med.* **35** 1714–20
- [41] Tang H R *et al.* 1999 Implementation of a combined X-ray CT–scintillation camera imaging system for localizing and measuring radionuclide uptake: Experiments in phantoms and patients *IEEE Trans. Nucl. Sci.* **46** 551–7
- [42] Sorenson J A 1974 Quantitative measurement of radioactivity *in vivo* by whole-body counting. In *Instrumentation in Nuclear Medicine* G A S ed J Hine (New York: Academic Press) vol 2 pp 311–48
- [43] Chang L T 1978 A method for attenuation correction in radionuclide computed tomography *IEEE Trans. Nucl. Sci.* **25** 638–43
- [44] Jaszczak R J, Greer K L, Floyd C E, Harris C C and Coleman R E 1984 Improved SPECT quantification using compensation for scattered photons *J. Nucl. Med.* **25** 893–900
- [45] Beckman F J, Kamphuis C and Frey E C 1997 Scatter compensation methods in 3D iterative SPECT reconstruction: a simulation study *Phys. Med. Biol.* **42** 1619–32
- [46] Frey E C and Tsui B M W 1993 A practical method for incorporating scatter in a projector–backprojector for accurate scatter compensation in SPECT *IEEE Trans. Nucl. Sci.* **40** 1107–16

- [47] Beekman F J, de Jong H W and Slijpen E T 1999 Efficient SPECT scatter calculation in non-uniform media using correlated Monte Carlo simulation *Phys. Med. Biol.* **44** N183–N192
- [48] de Jong H W and Beekman F J 2001 Rapid SPECT simulation of downscatter in non-uniform media *Phys. Med. Biol.* **46** 621–35
- [49] Beekman F J, Slijpen E T, de Jong H W and Viergever M A 1999 Estimation of the depth-dependent component of the point spread function of SPECT *Med. Phys.* **26** 2311–22
- [50] King M A, Long D T and Brill B A 1991 SPECT volume quantitation: Influence of spatial resolution source size and shape and voxel size *Med. Phys.* **18** 1016–24
- [51] Hawkins W G, Yang N-C and Lechner P K 1991 Validation of the circular harmonic transform (CHT) algorithm for quantitative SPECT *J. Nucl. Med.* **32** 141–50
- [52] King M A, Schwinger R B, Doherty P W and Penney B C 1984 Two-dimensional filtering of SPECT images using the Metz and Wiener filters *J. Nucl. Med.* **25** 1234–40
- [53] Andersson J L R, Sundin A and Valind S 1995 A method for coregistration of PET and MR brain images *J. Nucl. Med.* **36** 1307–15
- [54] Borgefors G 1988 Hierarchical chamfer matching a parametrical edge matching algorithm *IEEE Trans. Pattern Anal. Mach. Intell.* **10** 849–65
- [55] Eberl S *et al.* 1996 Automated interstudy image registration technique for SPECT and PET *J. Nucl. Med.* **37** 137–45
- [56] Flux G 1995 *Multimodality Image Registration and its Application to the Dosimetry of Intravesicular Radionuclide Therapy*. Thesis. Institute of Cancer Research & Royal Marsden Hospital, University of London
- [57] Hill D L G and Hawkes D J 2000 Across-modality registration using intensity-based cost functions. In *Handbook of Medical Imaging—Processing and Analysis* ed I N Bankman (San Diego: Academic)
- [58] Maes F, Collignon A, Vandermeulen D, Marchal G and Suetens P 1997 Multimodality image registration by maximization of mutual information *IEEE Trans. Med. Imaging* **16** 187–98
- [59] Maguire G Q, Noz M E, Lee E M and Schimpf J H 1986 Correlation methods for tomographic images using two and three dimensional techniques. In *Information Processing in Medical Imaging* ed S L Bacharach (Dordrecht: Martinus Nijhoff) pp 266–79
- [60] Maintz J B A, van den Elsen P A and Viergever M A 2001 3D multimodality medical image registration using morphological tools *Imag. Vision Comput.* **19** 53–62
- [61] Pelizzari C A, Chen G T Y, Spelbring D R, Wiechselbaum R R and Chen C 1989 Accurate three-dimensional registration of CT, PET, and/or MR images of the brain *J. Comput. Assist. Tomogr.* **13** 20–6
- [62] Rangarajan A, Chui H and Duncan J S 1999 Rigid point feature registration using mutual information *Med. Imag. Anal.* **3** 425–40
- [63] Studholme C, Hill D L G and Hawkes D J 1996 Automated 3D registration of MR and CT images of the head *Med. Imag. Anal.* **1** 163–75
- [64] Studholme C, Hill D L G and Hawkes D J 1999 An overlap invariant entropy measure of 3D medical image alignment *Pattern Recogn.* **32** 71–86
- [65] van den Elsen P A, Pol E J D and Viergever M A 1993 Medical image matching—A review with classification *IEEE Eng. Med. Biol. Mag.* **12** 26–39
- [66] Wells W M, Viola P, Atsumi H, Nakajima S and Kikinis R 1996 Multi-modal volume registration by maximization of mutual information *Med. Imag. Anal.* **1** 35–51

- [67] Woods R P, Mazziotta J C and Cherry S R 1992 Rapid automated algorithm for aligning and reslicing PET images *J. Comput. Assist. Tomogr.* **16** 620–33
- [68] Woods R P 2000 Within-modality registration using intensity-based cost functions. In *Handbook of Medical Imaging—Processing and Analysis* ed I N Bankman (San Diego: Academic)
- [69] Hutton B F, Braun M, Thurfjell L and Lau D Y H 2002 Image registration an essential tool for nuclear medicine *Eur. J. Nucl. Med.* **29** 559–77
- [70] Meyer C R *et al.* 1997 Demonstration of accuracy and clinical versatility of mutual information for automatic multimodality image fusion using affine and thin-plate spline warped geometric deformations *Med. Imag. Anal.* **1** 195–206
- [71] Sjögreen K, Ljungberg M, Wingsrdh K, Erlandsson K and Strand S-E 2001 Registration of emission and transmission whole-body scintillation camera images *J. Nucl. Med.* **42** 1563–1570
- [72] Sjögreen K 2001 *Image Processing for Quantitative Scintillation-Camera Imaging: Application to Radionuclide Therapy*. Thesis. Lund University
- [73] DeVries D J and Moore S C 2001 Registration of CT and SPECT volumes using CT reprojections and planar transmission images *Proc IEEE Nuclear Science Symposium and Medical Imaging Conference*, San Diego, CA, in press
- [74] Jones T 1996 The role of positron emission tomography within the spectrum of medical imaging *Eur. J. Nucl. Med.* **23** 207–11
- [75] Zaidi H, Diaz-Gomez M, Boudraa A E and Slosman D O 2002 Fuzzy clustering-based segmented attenuation correction in whole-body PET imaging *Phys. Med. Biol.* **47** 1143–60
- [76] Zaidi H 2000 Comparative evaluation of scatter correction techniques in 3D positron emission tomography *Eur. J. Nucl. Med.* **27** 1813–26
- [77] Zaidi H 2001 Scatter modelling and correction strategies in fully 3-D PET *Nucl. Med. Commun.* **22** 1181–4
- [78] Beyer T *et al.* 2000 A combined PET/CT scanner for clinical oncology *J. Nucl. Med.* **41** 1369–79
- [79] Dimitrakopoulou-Strauss A, Strauss L G and Burger C 2001 Quantitative PET studies in pretreated melanoma patients a comparison of 6-[¹⁸F]fluoro-L-dopa with ¹⁸F-FDG and ¹⁵O-water using compartment and noncompartment analysis *J. Nucl. Med.* **42** 248–56
- [80] Torizuka T *et al.* 2000 Metabolic response of non-Hodgkin's lymphoma to ¹³¹I-anti-B1 radioimmunotherapy evaluation with FDG PET *J. Nucl. Med.* **41** 999–1005
- [81] Koral K F *et al.* 1999 I-131 anti-B1 therapy/tracer uptake ratio using a new procedure for fusion of tracer images to computed tomography images *Clin. Cancer Res.* **5** 3004s–3009s
- [82] Zasadny K R *et al.* 1997 Do tracer dosimetry studies predict normal organ and tumor uptake of I-131-anti-B1 (anti CD-20) antibody in patients receiving radioimmunotherapy for non-Hodgkins lymphoma? *Radiology* **205** 509–509

Chapter 4

Computational methods in internal radiation dosimetry

Pat B Zanzonico and John W Poston, Sr

4.1. INTRODUCTION

Radiation dosimetry deals with the determination of the amount and the spatial and temporal distribution of energy deposited in matter by ionizing radiation. Internal radionuclide dosimetry specifically deals with radiation energy deposition in tissue for radionuclides within the body. Internal dosimetry has been applied to the determination of tissue doses and related quantities for occupational exposures in radiation protection, environmental exposures in radiation epidemiology, and diagnostic and therapeutic exposures in nuclear medicine. With the increasing therapeutic application of internal radionuclides in medicine, larger administered activities are used and higher normal-tissue doses, with associated radiation injury, may result. Treatment planning for radionuclide therapy thus requires, in addition to reliable dose–response relationships for target tissues and dose–toxicity relationships for normal tissues, increasingly more accurate and precise dose estimates for target tissue and at-risk normal tissues. Radiation dosimetry in nuclear medicine continues to evolve—from estimation of population- and organ-averaged doses for risk estimation for stochastic effects to calculation of individualized patient doses that reflect the heterogeneity of dose distributions within tumours and organs and the probability of deterministic effects [1–4]. Reviewed in this chapter, the standard computational methods developed for internal radiation dosimetry, such as the ‘MIRD schema’, have generally been based on ‘average’ kinetic and anatomic (i.e., anthropomorphic) models. These methods yield population- and organ-averaged doses for estimation of stochastic risk associated with diagnostic administered activities. In other chapters of this book, strategies for individualized patient dosimetry, more appropriate for radionuclide therapy, are developed.

4.2. RADIATION QUANTITIES AND UNITS

4.2.1. Stochastic versus deterministic quantities

Dosimetric quantities may be characterized as ‘stochastic’ or ‘deterministic’ (i.e., ‘non-stochastic’) [4–8]. A quantity subject to statistical fluctuations is termed ‘stochastic’, while the mean of a large number of determinations of the quantity is termed ‘deterministic’. Each stochastic quantity, then, has a corresponding deterministic quantity. The field of ‘microdosimetry’ deals with the number, size and spatial and temporal distributions of individual energy-deposition events, particularly in microscopic structures of the order of molecules, macromolecules and supramolecular complexes in size, characterizing such events in terms of inherently stochastic quantities [5].

4.2.2. Definitions of dosimetric quantities

A physically and biologically meaningful specification of radiation ‘dose’ is a problematic concept and has been specified in a variety of ways [9, 10]. The following definitions are extracted from [6] and [8].

‘Exposure’, X , is defined as

$$X \equiv \frac{dQ}{dm} \quad (4.1)$$

where dQ is the absolute value of the total charge of ions of one sign produced in air when all the electrons (negatrons and positrons) liberated by photons (X- and γ -rays) in air are completely stopped in air, and dm is the mass of air in which the electrons (negatrons and positrons) were liberated by photons (X- and γ -rays).

Exposure is essentially the ionization equivalent of air kerma (defined below) and, as in the case of kerma, it may often be convenient to refer to a value of exposure at a point inside a material different from air. In such a case, the exposure specified will be that which would be determined for a small quantity of air placed at the point of interest. Exposure is a deterministic quantity and thus corresponds to a sufficiently large irradiated volume and/or a sufficiently large amount of radiation to yield insignificant statistical fluctuations in its measured value.

The ‘absorbed dose’, D , is probably the most widely used quantity to characterize ‘dose’ and is defined as

$$D \equiv \frac{d\bar{E}}{dm} \quad (4.2)$$

where $d\bar{E}$ is the mean energy imparted by ionizing radiation to matter, and dm is the mass of matter to which the energy is imparted.

Absorbed dose is a deterministic quantity and is the deterministic correlate of the stochastic quantity, 'specific energy', z :

$$z \equiv \frac{\varepsilon}{m} \quad (4.3)$$

where ε is the energy imparted to matter by a single energy-deposition event and dm is the mass of the matter.

It is conceptually straightforward to relate absorbed dose to exposure [11]. The average energy required to produce an ion pair in air is nearly constant for all electron energies, corresponding to a value of the mean energy per ion pair (W) of 33.7 eV/ion pair [12]. Therefore, since the conventional unit of exposure, the roentgen (R), corresponds to 1.61×10^{12} ion pair/gm of air (i.e., $1 \text{ R} = 1.61 \times 10^{12} \text{ ion pair/gm}$), $1 \text{ eV} = 1.602 \times 10^{-12} \text{ erg}$, and $1 \text{ rad} = 100 \text{ erg/gm}$, the absorbed dose to air for an exposure of 1 R to air is

$$\begin{aligned} & 1.610 \times 10^{12} \frac{\text{ion pair/g air}}{\text{R air}} \times 33.7 \frac{\text{eV}}{\text{ion pair}} 1.602 \times 10^{-12} \frac{\text{erg}}{\text{eV}} \frac{1 \text{ rad}}{100 \text{ erg/g}} \\ & = 0.869 \frac{\text{rad}}{\text{R air}} \end{aligned} \quad (4.4)$$

Therefore,

$$D_{\text{air}} (\text{rad}) = 0.869 X_{\text{air}} (\text{R}) \quad (4.5)$$

where D_{air} is the absorbed dose (in rad) to air, and X_{air} is the exposure (in R) to air.

Under conditions of charged particle equilibrium for a point in a non-air medium (such as tissue), equation (5) may be modified to yield the absorbed dose in a non-air medium for a given exposure in air [11]:

$$D_{\text{med}} (\text{rad}) = 0.869 \frac{(\mu_{\text{en}}/\rho)_{\text{med}}}{(\mu_{\text{en}}/\rho)_{\text{air}}} X_{\text{air}} (\text{R}) \quad (4.6a)$$

$$= 0.869 \overline{(\mu_{\text{en}}/\rho)_{\text{air}}^{\text{med}}} X_{\text{air}} (\text{R}) \quad (4.6b)$$

$$= f_{\text{med}} X_{\text{air}} (\text{R}) \quad (4.6c)$$

where D_{med} is the absorbed dose (in rad) to a point in a non-air medium, $(\mu_{\text{en}}/\rho)_{\text{med}}$ is the mass energy absorption coefficient (e.g., in cm^2/gm) in a non-air medium, $(\mu_{\text{en}}/\rho)_{\text{air}}$ is the mass-energy absorption coefficient (e.g., in cm^2/gm) in air, $\overline{(\mu_{\text{en}}/\rho)_{\text{air}}^{\text{med}}} \equiv (\mu_{\text{en}}/\rho)_{\text{med}}/(\mu_{\text{en}}/\rho)_{\text{air}}$ is the mass-energy absorption coefficient ratio used to convert air kerma to dose in the medium surrounding the source, X_{air} is the exposure (in R) to air, and $f_{\text{med}} = 0.869 \overline{(\mu_{\text{en}}/\rho)_{\text{air}}^{\text{med}}}$ is the exposure-to-absorbed-dose (i.e., R-to-rad) conversion factor (in rad/R) for the non-air medium.

Fortuitously, the exposure-to-absorbed-dose (i.e., R-to-rad) conversion factor (f_{med}) is very nearly unity (0.87–0.968) for a wide range of photon energies (0.01–10 MeV) for air, water and soft tissues. Generally, therefore,

the absorbed dose (in rad) may be considered to be numerically equal to the exposure (in R).

'Kerma', K , is defined as

$$K \equiv \frac{dE_{tr}}{dm} \quad (4.7)$$

where dE_{tr} is the sum of the initial kinetic energies of all the charged ionizing particles liberated by uncharged ionizing particles (including photons) in matter, and dm is the mass of matter in which the charged ionizing particles were liberated.

In the case in which the matter is air, kerma is often referred to as 'air kerma' or 'free air kerma'.

The quality as well as the quantity of radiation are important determinants of the frequency and/or severity of radiogenic effects. The 'quality' of a radiation is related to the characteristics of the microscopic spatial distribution of energy-deposition events, determined by the mass, charge and energy (i.e., velocity) of the charged particles composing the radiation or, in the case of X-rays, γ -rays and neutrons, the charged particles produced by the radiation. Sparsely ionizing radiations such as X- and γ -rays and intermediate-to-high-energy electrons and β particles are characterized as 'low-quality' radiations, while densely ionizing radiations such as low-energy electrons (e.g., Auger electrons), protons, neutrons and α particles are typically characterized as 'high-quality' radiations. Importantly, for the same absorbed dose, the frequency and/or severity of radiogenic biological effects are generally less for sparsely ionizing, low-quality radiations than for densely ionizing, high-quality radiations.

The quality of radiation is quantitatively characterized by the 'linear energy transfer', L or LET , or the 'restricted linear energy transfer', L_{Δ} or LET_{Δ} of a material for charged particles:

$$L_{\Delta} \equiv \left(\frac{dE}{dl} \right)_{\Delta} \quad (4.8)$$

where dE is the energy lost by a charged particle in traversing a distance in matter due to those collisions in which the energy loss is less than the energy cut-off Δ , and dl is the distance traversed in matter.

The restricted linear energy transfer (L_{Δ}) requires the specification of a cut-off energy (Δ), necessitated by primary energy-deposition events resulting in relatively high-energy, relatively long-range secondary electrons (i.e., δ -rays) whose energy deposition events may be considered as separate from those along the track of the primary radiation. In radiation protection, this feature is generally disregarded by specification of the 'unrestricted linear energy transfer', L_{∞} or LET_{∞} (also known simply as the 'linear energy transfer', L or LET), where the energy cut-off (Δ) is set equal to infinity (∞).

LET is the deterministic correlate of the stochastic quantity, 'lineal energy', y :

$$y \equiv \frac{\varepsilon}{\bar{l}} \quad (4.9)$$

where ε is the energy imparted to matter by a single energy-deposition event, and \bar{l} is the mean chord length of the volume of the matter.

For the same absorbed dose, the frequency and/or severity of radiogenic biological effects are generally less for low-*LET* radiations than for high-*LET* radiations. The influence of radiation quality on the frequency and/or severity of biological effects is quantified by the 'relative biological effectiveness', or $RBE(A)$ of radiation A :

$$RBE(A) \equiv \frac{D_{\text{reference}}}{D_A} \quad (4.10)$$

where $D_{\text{reference}}$ is the absorbed dose of reference radiation (typically a widely available sparsely ionizing radiation such as ^{60}Co γ -rays) required to produce a specific, quantitatively expressed frequency and/or severity of a specific biological effect, and D_A is the absorbed dose of radiation A required to produce the same specific, quantitatively expressed frequency and/or severity of the same specific biological effect, with all pertinent parameters, except the radiation itself, maintained as identical as possible. Because the relative RBE represents a ratio of absorbed doses, it is a dimensionless quantity.

Because the actual value of RBE depends on many factors, such as the nature of the biological effect, the absorbed dose, the absorbed dose rate, etc., a simplified version of the relative biological effectiveness, the 'quality factor', Q or QF , was devised for purposes of radiation protection. However, because of variations in energy, *LET* and therefore RBE and Q along the radiation track, the so-called 'dose equivalent', H , at a point must be related to the 'mean quality factor', \bar{Q} , and the mean absorbed dose at that point:

$$H \equiv \bar{Q}D \quad (4.11)$$

where \bar{Q} is the mean quality factor,

$$\bar{Q} = (1/D) \int Q(L)D(L) dL, \quad (4.12)$$

D is the linear-energy-transfer-averaged absorbed dose at the point of calculation of the effective dose, $Q(L)$ is the quality factor for radiation of linear energy transfer L at the point of calculation of the effective dose, and $D(L)$ is the absorbed dose for radiation of linear energy transfer L at the point of calculation of the effective dose.

However, because of the difficulty of determining the energy, *LET*, and Q distributions at a point, the dose-equivalent concept is itself of limited

practical utility. A different quantity, the ‘equivalent dose’, $H_{T,R}$, in tissue or organ T due to radiation R , therefore has been devised:

$$H_{T,R} \equiv w_R D_{T,R} \quad (4.13)$$

where w_R is the radiation (R) weighting factor, a dimensionless quantity designed to account for differences in relative biological effectiveness among different radiations given by equation (4.12), and $D_{T,R}$ is the mean absorbed dose to tissue or organ T due to radiation R .

When a tissue or organ is irradiated by a combination of different radiations (i.e., radiations of different qualities), the ‘equivalent dose’, H_T , in tissue or organ T is the sum of all the mean tissue or organ doses, $D_{T,R}$, due to each component radiation R multiplied by its respective weighting factor, w_R :

$$H_T \equiv \sum_R w_R D_{T,R} \quad (4.14)$$

Like the *RBE*, the quality factors, mean quality factors and radiation weighting factors are dimensionless quantities.

For a tissue or organ, the equivalent dose is conceptually different from the dose equivalent. The dose equivalent is based on the absorbed dose at a point in tissue weighted by the *LET*-dependent distribution of quality factors ($Q(L)$) at that point. The equivalent dose, in contrast, is based on the average absorbed doses ($D_{T,R}$) in the tissue or organ weighted by the radiation weighting factor (w_R) for the radiation(s) actually impinging on the tissue or organ or, in the case of internal radionuclides, as it is actually emitted by the source.

4.3. THE MIRD SCHEMA

One of the most widely used and authoritative approaches for internal dose calculations in medicine was developed by the Medical Internal Radiation Dose (MIRD) Committee of the Society of Nuclear Medicine (SNM) and generally is referred to as the ‘MIRD schema’ or ‘MIRD formalism’ [4, 13–16]. The International Commission on Radiological Protection (ICRP) has developed a similar methodology and similar reference data [17]. The MIRD schema, including notation, terminology, mathematical methodology, and reference data, has been disseminated in the form of the collected MIRD Pamphlets and associated publications [2, 13, 18, 19]. With the publication of ORNL/TM-8381/V1-7 [20], age- and gender-specific body habitus other than the original 70 kg adult anthropomorphic model (‘Reference Man’ or ‘Standard Man’) [14, 21] are now incorporated into the MIRD schema. In addition, several computerized versions of the MIRD

schema, including *MIRDOSE* [22], *DOSCAL* (which incorporates mean tumour doses) [23] and *MABDOS* (with curve fitting and modelling features) [24–26], have been developed.

Calculation of the absorbed dose to an organ of the body from an internally distributed radionuclide is based conceptually on answering two very simple questions. First, what is the total number of nuclear transitions (decays) that occur in the organ over the time-period of interest? Second, how much energy is deposited in the organ per nuclear transition per unit mass of the organ? However, in reality, the calculation of internal absorbed dose requires knowledge of a number of factors and rests on a number of assumptions, including the anthropomorphic models of the ‘standard’ human body and its major internal organs. Fundamentally, one needs to know:

- the amount of radioactivity administered—the administered activity;
- the rate of radioactive decay of the administered radionuclide—the physical half-life (or decay constant);
- each type of radiation emitted by the decaying radionuclide and its frequency and average energy of emission—the equilibrium dose constant;
- the fraction of the administered activity which localizes in each tissue or organ (or ‘source region’)—the uptake or, more completely, the time–activity function;
- the length of time the radioactive material resides in each tissue or organ—the effective half-time (or residence time)—as derived from the time–activity function;
- the total number of decays (nuclear transitions) which occur in each tissue or organ (or source region)—the cumulated activity;
- the fraction of radiation energy which is absorbed in the tissue or organ itself as well as in other tissues and organs (or ‘target regions’)—the absorbed fractions; and
- the mass of each tissue or organ (target region).

As it is applied to *diagnostic* radiopharmaceuticals, its traditional application, the MIRD schema implicitly assumes that activity and cumulated activity are uniformly distributed within source regions and that radiation energy is uniformly deposited within target regions. Moreover, dosimetry for diagnostic radiopharmaceuticals is generally based on (a) average time–activity data in animal models and/or in a small cohort of human subjects and (b) age- and gender-specific ‘average’ models of human anatomy. The traditional MIRD schema does *not* incorporate tumours as either source or target regions.

As illustrated in figures 4.1 to 4.3 and developed below, the basic calculation in the MIRD schema, yielding the *mean* absorbed dose to target region r_k from the activity (i.e., cumulated activity) in source region

Step 1. Physical Data**A) Nuclear Decay Data**

Mean Energy Emitted
Per Nuclear Transition
(formerly known as the
Equilibrium Dose Constant)

$$\Delta = \sum_i \Delta_i$$

$$= k \sum_i n_i \bar{E}_i$$

Δ_i = mean energy of i-type radiation
emitted per nuclear transition
 n_i = number of i-type radiation
emitted per nuclear transition
 \bar{E}_i = mean energy per i-type radiation
 $k = 1$ in SI units
 $k = 2.13$ in traditional units

**S Factor**

$$S(r_k \leftarrow r_h) = \frac{\sum_i \Delta_i \phi_i(r_k \leftarrow r_h)}{M_k}$$

$$= \sum_i \Delta_i \Phi_i(r_k \leftarrow r_h)$$

M_k = mass of target region k
 $\Phi_i(r_k \leftarrow r_h)$ = specific absorbed fraction
= $\phi_i(r_k \leftarrow r_h) / M_k$

B) Radiation Absorption Data

Absorbed Fraction
for Source Region r_h and Target Region r_k

$$\phi_i(r_k \leftarrow r_h) = \frac{\text{i-type radiation emitted
in Source Region } r_h}{\text{i-type radiation emitted
in Target Region } r_k}$$

For non-penetrating (np) radiations
such as α -rays, β -rays, and electrons and
organ-size source and target regions:

$$\phi_i(r_h \leftarrow r_h) = 1 \quad k = h$$

$$\phi_i(r_k \leftarrow r_h) = 0 \quad k \neq h$$

For penetrating (p) radiations such as x- and γ -rays:

$$0 < \phi_i(r_k \leftarrow r_h) < 1$$

and evaluated by Monte Carlo analysis in mathematical anthropomorphic
phantoms representing "average" human anatomy with "simple" volumes

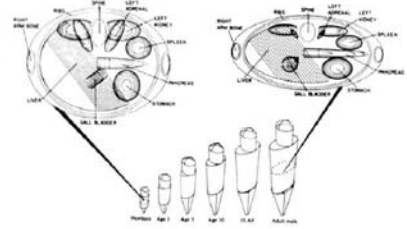


Figure 4.1. ‘Step 1’ in the MIRD schema for internal radionuclide dosimetry: compilation of the pertinent physical data (i.e., radionuclide-specific nuclear decay data) and calculation of the pertinent physical parameters (i.e., absorbed fractions and S factors for selected source region–target region pairs in a mathematically formulated ‘average’ anatomic model). Adapted, in part, from [14] and [20].

r_h , follows [4, 13–16]:

$$\bar{D}(r_k \leftarrow r_h) = \frac{\tilde{A}_h \sum_i \Delta_i \phi_i(r_k \leftarrow r_h)}{m_k} \quad (4.15a)$$

$$= \tilde{A}_h \sum_i \Delta_i \Phi_i(r_k \leftarrow r_h) \quad (4.15b)$$

$$= \tilde{A}_h S(r_k \leftarrow r_h) \quad (4.15c)$$

where \tilde{A}_h is the cumulated activity in source region r_h , that is, the total number of decays in source region r_h , m_k is the mass of target region r_k , Δ_i is the equilibrium dose constant for radiation i , that is, the average energy emitted per decay in the form of radiation i [27], $\phi_i(r_k \leftarrow r_h)$ is the absorbed fraction in target region r_k for radiation i emitted in source region r_h , that is, the fraction of energy of radiation i emitted in source region r_h absorbed in target region r_k , $\Phi_i(r_k \leftarrow r_h)$ is the *specific* absorbed fraction in target

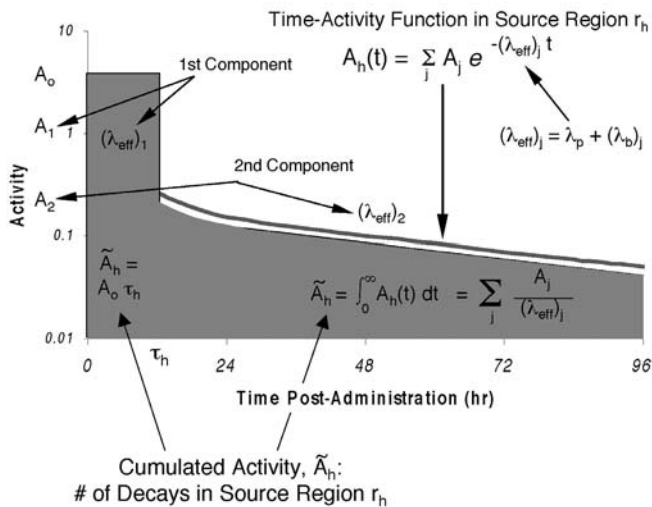
Step 2. Biological Data

Figure 4.2. ‘Step 2’ in the MIRD schema for internal radionuclide dosimetry: acquisition of the pertinent biological data (i.e., time-activity data for the radiopharmaceutical under consideration in selected organs) and calculation of the pertinent biological parameters (i.e., cumulated activities, or residence times, in the selected organs).

region r_k for radiation i emitted in source region r_h , that is, the fraction of energy of radiation i emitted in source region r_h that is absorbed per unit mass in target region r_k

$$\Phi_i(r_k \leftarrow r_h) \equiv \frac{\phi_i(r_k \leftarrow r_h)}{m_k} \quad (4.16)$$

and $S(r_k \leftarrow r_h)$ is the radionuclide-specific S factor for target region r_k and source region r_h , that is, the absorbed dose to target region r_k per unit cumulated activity in source region r_h

$$S(r_k \leftarrow r_h) \equiv \frac{\sum_i \Delta_i \phi_i(r_k \leftarrow r_h)}{m_k} \quad (4.17)$$

An important simplification of absorbed dose calculations was introduced by combining the radionuclide-specific equilibrium dose constant Δ_i , the source region-to-target region absorbed fraction $\phi_i(r_k \leftarrow r_h)$, and the target region mass m_k into a single quantity, the S factor, as defined by equation (4.17) [15]. As a result, given the cumulated activity \tilde{A}_h in a given source region r_h , one can use the tabulated S factors to yield, by a simple multiplication, the absorbed dose contribution $\bar{D}(r_k \leftarrow r_h)$ to a target region r_k . Besides computationally simplifying the determination of

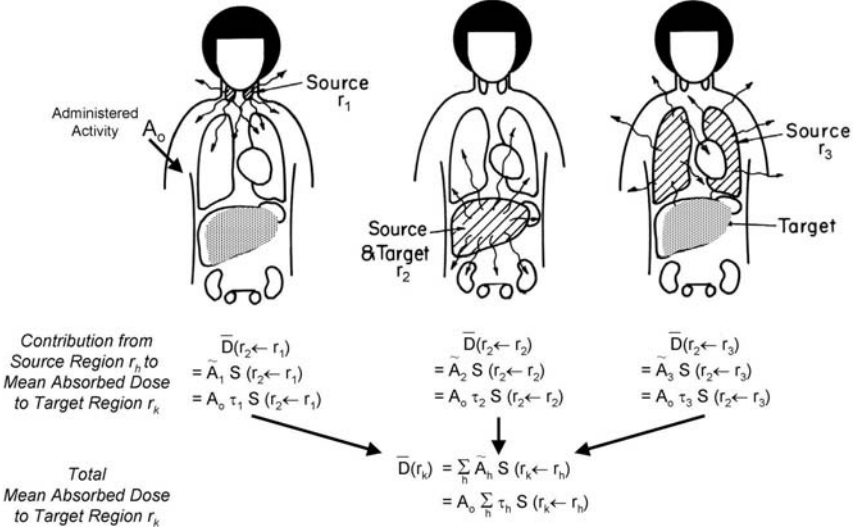
Step 3. Integration of Biological and Physical Data

Figure 4.3. ‘Step 3’ in the MIRD schema for internal radionuclide dosimetry: integration of the pertinent physical and biological parameters to calculate the mean absorbed doses to selected target regions in the mathematically formulated anatomic model. Adapted, in part, from [13].

absorbed dose, the S factor conceptually clarified this task by isolating all non-time-dependent and, largely, non-biology-dependent dosimetric factors into a single parameter.

The total mean absorbed dose $\bar{D}(r_k)$ to target region r_k is then calculated by summing of the absorbed dose contributions from all source regions r_h :

$$\bar{D}(r_k) = \sum_h \frac{\tilde{A}_h \sum_i \Delta_i \phi_i(r_k \leftarrow r_h)}{m_k} \quad (4.18a)$$

$$= \sum_h \left[\tilde{A}_h \sum_i \Delta_i \Phi_i(r_k \leftarrow r_h) \right] \quad (4.18b)$$

$$= \sum_h \tilde{A}_h S(r_k \leftarrow r_h) \quad (4.18c)$$

The cumulated activity, or time integral of activity, \tilde{A}_h , in a given target region r_h is calculated by integration from the time of administration of the radiopharmaceutical ($t = 0$) to the time of its complete elimination ($t = \infty$) of the time–activity function, $A_h(t)$:

$$\tilde{A}_h = \int_0^\infty A_h(t) dt \quad (4.19)$$

The time–activity function includes both the physical decay constant of the radionuclide and the biological disappearance constant(s) (see the detailed discussion below). It is usually determined by discrete serial measurements.

Despite the complexity of the multiple underlying biological processes, the time–activity data of virtually any radiopharmaceutical in any tissue or organ can be accurately represented by an *exponential* function:

$$A_h(t) = \sum_j (A_h)_j e^{(\lambda_h)_j t} \quad (4.20)$$

where $(A_h)_j$ is the (extrapolated) activity at time $t = 0$ for the j th exponential component of the time–activity function in source region r_h , and $(\lambda_h)_j$ is the clearance constant of the j th exponential component of the time–activity function in source region r_h , that is, the fraction per unit time of activity eliminated for the j th exponential component of the time–activity function in source region r_h .

The clearance constant, $(\lambda_h)_j$, is actually the ‘effective’ (e) clearance constant because it includes the effects of *both* biological clearance and physical (i.e., radioactive) decay:

$$(\lambda_h)_j \equiv [(\lambda_e)_h]_j \quad (4.21a)$$

$$= \lambda_p + [(\lambda_b)_h]_j \quad (4.21b)$$

where λ_p is the physical decay constant of the radionuclide, and $[(\lambda_b)_h]_j$ is the biological clearance constant of the j th exponential component of the time–activity function in source region r_h , that is, the fraction per unit time of activity biologically eliminated for the j th exponential component of the time–activity function in source region r .

For each exponential component, the half-life (or half-time) is related to its corresponding clearance constant:

$$T_{1/2} = \frac{\ln 2}{\lambda} \quad (4.22a)$$

$$= \frac{0.693}{\lambda} \quad (4.22b)$$

and the effective half-time, $T_e = (T_{1/2})_e$, includes the effects of both the biological and physical half-lives:

$$T_e = \frac{1}{T_p} + \frac{1}{T_b} \quad (4.23a)$$

$$= \frac{T_p T_b}{T_p + T_b} \quad (4.23b)$$

where T_p is the physical half-life of the radionuclide, and T_b is the biological half-time of the j th exponential component of the time–activity function.

Integration of the time–activity function, $A_h(t) = (A_0)_h e^{-(\lambda_e)_h t}$, yields the cumulated activity in source region r_h :

$$\tilde{A}_h = \sum_j \frac{(A_h)_j}{(\lambda_h)_j} = 1.44 \sum_j (A_h)_j [(T_e)_h]_j \quad (4.24a)$$

In the dosimetry literature, the quantity of cumulated activity has largely been replaced by the residence time, τ_h , in source region r_h [13], equivalent to the cumulated activity per unit administered activity:

$$\lambda_h = \frac{\tilde{A}_h}{AA} \quad (4.25a)$$

$$= 1.44 \sum_j \frac{(\tilde{A}_h)_j}{AA} [(T_e)_h]_j \quad (4.25b)$$

$$= 1.44 \sum_j (f_h)_j [(T_e)_h]_j \quad (4.25c)$$

where AA is the administered activity, and $(f_h)_j$ is the (extrapolated) fraction of the administered activity at time $t = 0$ for the j th exponential component of the time–activity function in source region r_h .

Therefore,

$$\tilde{A}_h = AA\tau_h \quad (4.26)$$

4.4. PATIENT- AND POSITION-SPECIFIC DOSIMETRY

Dr Robert Loevinger, one of the originators of the MIRD schema, has stated that ‘... there is in principle no way of attaching a numerical uncertainty to the profound mismatch between the patient and the model (the totality of all assumptions that enter into the dose calculation). The extent to which the model represents in some meaningful way a patient, or a class of patients, is always open to question, and it is the responsibility of the clinician to make that judgment’ [13]. In contrast to *diagnostic* radiopharmaceuticals, *therapeutic* radiopharmaceuticals engender much smaller risk–benefit ratios and therefore markedly reduced tolerances for such inaccuracies in dose estimation. To the extent, then, that specific patients deviate kinetically and anatomically from the respective kinetic and anatomic averages, tissue dose estimates will be inaccurate and individualized (i.e., patient-specific) dosimetry may be required.

4.4.1. Patient-specific dosimetry: case study—radioiodine therapy of metastatic thyroid cancer

The basis of radioiodine treatment of metastatic thyroid cancer is the specific uptake of administered radioiodide by and the resulting radiogenic damage

to differentiated thyroid cancer cells—assuming the cancerous thyroid has been surgically removed, any residual normal thyroid ablated, and blood levels of thyroid stimulating hormone (TSH) temporarily increased by withdrawal of replacement thyroid hormone. Historically, the most commonly employed dose prescription algorithm has been a fixed administered activity [16], typically ~ 100 mCi, possibly adjusted depending upon the extent of disease [28]. While simple and convenient, this approach ignores altogether patient-specific kinetic and anatomic factors. Alternatively, since one does not know the actual, generally low radioiodine uptakes in and resulting absorbed doses to the metastases, one should administer the maximum activity which will not induce serious side effects in order to maximize the therapeutic effect. Benua *et al.* [29] empirically determined the criteria that define the maximum ‘safe’ administered activity: the mean absorbed dose to blood (as a surrogate for the bone marrow) must not exceed 200 rad and, at 48 h post-administration, the projected lung and the total body retention must not exceed 80 and 120 mCi, respectively. In practice, the 200 rad absorbed dose limit to blood is generally *the* therapy-limiting criterion. The implementation of this patient-specific treatment planning paradigm is described below [16].

Following oral administration of a ~ 2 mCi tracer administration of ^{131}I iodide, serial measurements are performed daily (1 to 4 days post-administration) of the activity concentration in blood and the activity in the total body. The cumulated activities in the total body and the cumulated activity concentration in blood are equated with the areas (determined by numerical integration) under the total body time–activity curve and the area under the blood time–activity concentration curve, respectively [16, 29]:

area under curve

$$= \int_{i=1}^n \frac{\exp[-0.0861 t_i \{A_i - [\exp(-0.0861(t_{i+1} - t_i)A_i)]\} (t_{i+1} - t_i)]}{\ln \left[\frac{A_i}{\exp[-0.0861(t_{i+1} - t_i)A_i]} \right]} + \frac{\exp(-0.0861 t_n A_n)}{0.0861} \quad (4.27)$$

where A_i is the decay-corrected activity (%) in total body or the activity concentration (%/l) in blood) at time t_i post-administration (in days).

Thus, the time–activity data in the tumour and total body and the time–activity concentration data in blood are integrated numerically up to the last measured datum (A_n at time t_n post-administration), corresponding to the first term in the sum on the right-hand side of equation (4.27), and analytically thereafter, conservatively assuming elimination of the radionuclide by physical decay only, corresponding to the second term in the sum. An important advantage of numerical integration is its generality: it is adaptable to non-monotonic time–activity curves (e.g., the blood time–activity concentration

curve for radioiodide) and no simplifying assumptions are introduced regarding the analytic form of the time–activity curve. On the other hand, a disadvantage of the assumption of radionuclide elimination by physical decay only following the last measurement is that it results in a systematic overestimation, perhaps substantial, of the overall area under the time–activity curve. Furhang *et al.* [30] have recently modified the ‘Benuea formalism’ [29] by replacing numerical integration of the time–activity data with analytical integration of exponential fits to these data.

The absorbed doses (in rad/mCi) to blood and to tumour are equated with the sum of the mean total body absorbed dose from penetrating (γ) radiation and the mean self-irradiation absorbed dose from non-penetrating (β) radiation [30]. The mean total body absorbed dose from γ -radiation is calculated using the height- and mass-dependent mean total-body geometric factor and specific γ -ray constant for iodine-131, assuming uniform total body distribution of cumulated activity [31–34]. The mean self-irradiation absorbed dose from β -radiation is calculated using the equilibrium absorbed dose constant for β -radiation for ^{131}I [27], assuming complete local absorption [31–34]. The pertinent equations are:

mean blood absorbed dose

$$= \text{mean } \gamma \text{ absorbed dose from total body activity} \\ + \text{mean } \beta \text{ absorbed dose from ‘local’ (blood) activity,} \quad (4.28)$$

where

mean gamma absorbed dose from total body activity (rad/mCi)

$$= 0.000235 \times \bar{g}(\text{cm}) \times \Gamma(\text{R cm}^2/\text{mCi h}) \\ \times \text{area under total body time–activity curve (\% administered} \\ \text{activity day)} \quad (4.29)$$

mean gamma blood absorbed dose from local activity (rad/mCi)

$$= 0.233 \times \Delta_{np}(\text{g rad}/\mu\text{Ci h}) \times \text{area under blood time–activity} \\ \text{concentration curve (\% administered activity day)} \quad (4.30)$$

mean beta radiation tumour dose from local activity (rad/mCi)

$$= 0.233 \times \Delta_{np}(\text{g rad}/\mu\text{Ci h}) \times \text{area under tumour time–activity} \\ \text{curve (\% administered activity day/L)/[tumour mass (kg)]} \quad (4.31)$$

and \bar{g} is the height- and body-mass-dependent total body mean geometric factor [31–34], Γ is the specific γ -ray constant for ^{131}I [31–34] ($2.23 \text{ R cm}^2/\text{mCi h}$ [11]), f is the exposure-to-absorbed dose conversion factor (1 rad/R

for water/soft tissue (see above)), Δ_{np} is the equilibrium dose constant for non-penetrating radiations for ^{131}I (0.41 g rad/ $\mu\text{Ci h}$ [27]).

4.4.2. Adaptation of the MIRD schema to patient-specific dosimetry

Even though the standard anthropomorphic models used in the MIRD schema represent normal human anatomy and thus do not include tumours, the schema can be adapted to patient-specific normal-organ dosimetry for planning radionuclide therapy based on the maximum tolerated activity [16, 35]. Not surprisingly, the most important quantitative adjustment in this adaptation involves the tumour-bearing organ(s). The proposed adaptation is rather crude and, importantly, has not in any sense been validated. (In the following development, all absorbed doses are still mean values even though, to simplify the notation, the overstrike bar has been eliminated over the symbol, D).

For organ ‘non-self’ irradiation (source region $r_h \neq$ target region r_k), S factors are relatively insensitive to organ (i.e., source and target region) size and shape. Therefore, unless the source and/or target regions are *grossly* abnormal (e.g., due to the presence of tumour), Reference Man (or Reference Woman) S factors may be applied to specific patients for calculating the organ non-self absorbed dose contribution:

$$\frac{\text{patient}}{S(r_k \leftarrow r_h)} \approx \frac{\text{Reference Man}}{S(r_k \leftarrow r_h)} \quad \text{if } r_h \neq r_k \quad (4.32)$$

For organ ‘self’ irradiation (source region $r_h =$ target region r_k), S factors are approximately inversely proportion to organ mass—because most of the self-dose to any organ is contributed by non-penetrating radiations which are completely absorbed locally while absorbed dose is inversely proportional to the organ mass. Therefore, for a normal organ (i.e., an organ without tumour), S factors adjusted for the difference in masses between the patient and Reference Man organs may be applied to specific patients for calculating the self-absorbed dose contribution:

$$\frac{\text{patient}}{S(r_k \leftarrow r_h)} \approx \frac{\text{Reference Man}}{S(r_k \leftarrow r_h)} \times \frac{\text{Reference Man target region } (r_k) \text{ mass}}{\text{patient target region } (r_k) \text{ mass}} \quad (4.33)$$

if $r_h = r_k$.

In principle, patient organ masses may be estimated by computed tomography or magnetic resonance imaging. In practice, however, masses of *normal* organs may not be available. A more practical, though certainly less accurate, adaptation of equation (33) based on the patient and Reference Man total body masses may then be used:

$$S(r_k \leftarrow r_h) \approx \frac{\text{patient}}{S(r_k \leftarrow r_h)} \approx \frac{\text{Reference Man}}{S(r_k \leftarrow r_h)} \times \frac{\text{Reference Man total body mass}}{\text{patient total body mass}} \quad (4.34)$$

if $r_h = r_k$ and the patient target region (r_k) mass is not available, assuming, arbitrarily, that organ mass is directly proportional to total body mass.

For a tumour-bearing organ, adaptation of the MIRD schema is somewhat more complicated. First, the self-irradiation absorbed dose and S factor for the tumour-bearing organ can be separated into their penetrating and non-penetrating radiation components:

$$D(r_h \leftarrow r_h) \equiv D_p(r_h \leftarrow r_h) + D_{np}(r_h \leftarrow r_h) \quad (4.35)$$

$$S(r_h \leftarrow r_h) \equiv S_p(r_h \leftarrow r_h) + S_{np}(r_h \leftarrow r_h) \quad (4.36a)$$

$$= S_p(r_h \leftarrow r_h) + \frac{\sum_i (\Delta_{np})_i (\phi_{np})_i (r_h \leftarrow r_h)}{m_h} \quad (4.36b)$$

$$= S_p(r_h \leftarrow r_h) + \frac{\sum_i (\Delta_{np})_i}{m_h} \quad (4.36c)$$

$$= S_p(r_h \leftarrow r_h) + \frac{\Delta_{np}}{m_h} \quad (4.36d)$$

where $S(r_h \leftarrow r_h)$ is the total self-irradiation S factor in source and target region r_h , $S_p(r_h \leftarrow r_h)$ is the self-irradiation S factor for penetrating radiations in source and target region r_h , $S_{np}(r_h \leftarrow r_h)$ is the self-irradiation S factor for non-penetrating radiations in source and target region r_h , $(\Delta_{np})_i$ is the equilibrium dose constant for non-penetrating radiation i , $(\phi_{np})_i(r_h \leftarrow r_h)$ is the self-irradiation absorbed fraction in non-penetrating radiations for source and target region r_h ,

$$(\phi_{np})_i(r_h \leftarrow r_h) = 1 \quad (4.37)$$

m_h is the mass of the source and target region r_h , and $\Delta_{np} \equiv \sum_i (\Delta_{np})_i$ is the total equilibrium dose constant for non-penetrating radiations.

Therefore,

$$S_p(r_h \leftarrow r_h) = S(r_h \leftarrow r_h) - \frac{\Delta_{np}}{m_h}. \quad (4.38)$$

The patient-specific self-irradiation S factor for penetrating radiations can then be calculated:

$$S(r_h \leftarrow r_h) \approx \frac{\text{patient}}{S(r_h \leftarrow r_h)} \approx \frac{\text{Reference Man}}{S(r_h \leftarrow r_h)} \times \frac{\text{Reference Man target region } (r_k) \text{ mass}}{\text{patient target region } (r_k) \text{ mass}}. \quad (4.39)$$

The self-irradiation absorbed dose for non-penetrating radiations in source and target region r_h is

$$D_{np}(r_h \leftarrow r_h) = \frac{\Delta_{np}}{m_h} \times \tilde{A}_h. \quad (4.40)$$

Finally, the total absorbed dose to the patient target region r_k is the sum of the non-self-irradiation dose contributions (equation (15c)) and, primarily, the self-irradiation absorbed doses from penetrating radiations with patient S factors (equation (39)), $D_p(r_h \leftarrow r_h)$, and from penetrating radiations, $D_{np}(r_h \leftarrow r_h)$ (equation (40)). Note that the absorbed dose from penetrating radiations (X- and γ -rays) includes contributions from activity in both the normal liver and from a tumour in the liver because of the relatively long distances penetrated by such radiations. In contrast, the absorbed dose from non-penetrating radiations (β -particles) is contributed only by activity in the normal liver itself because such radiations are completely absorbed within macroscopic tumours, that is, the radiation cannot penetrate into the surrounding normal liver.

To determine masses of the tumour-bed organ plus the tumour(s), regions of interest (ROIs) may be drawn around the entire liver, including the tumour(s) as well as the normal liver, on computed tomograms (CTs) or magnetic resonance images (MRIs). ROIs can be drawn specifically around the individual tumours to determine their respective masses. The normal tumour-bed organ mass can be calculated by subtracting the combined masses of the individual tumours from the mass of the entire tumour-bed organ plus tumour(s). An analogous ROI analysis can be applied to the gamma camera images to determine the activities and cumulated activities specifically in the tumour-bed organ and tumour(s).

4.4.3. *Position-specific dosimetry: calculation of non-uniform dose distributions*

In addition to patient-specific kinetics and anatomy, the issue of spatial non-uniformity of dose has become increasingly important at the macroscopic [36–60] and microscopic [61–79] levels. There are at least three approaches to the calculation of macroscopic non-uniform dose distributions [60], dose point-kernel convolution, Monte Carlo simulation, and voxel S factors, and these will be elucidated further in other chapters. The dose point-kernel is currently the most widely used of these approaches [36–38, 41, 42, 53–56], primarily because of the demanding computational requirements of Monte Carlo simulation and the limited availability of voxel S factors. (A dose point-kernel is the radial distance-dependent absorbed dose about an isotropic point source in an infinite homogeneous medium—typically a soft tissue-equivalent medium such as water.) With the wider availability of high-speed desktop computers and of compatible simulation codes, the

use of Monte Carlo analysis has increased [39, 40, 80]. Monte Carlo-based dosimetry can more accurately account for tissue variations in mass density and atomic number as well as edge effects which may be important at the periphery of the body and at soft tissue–lung and –bone interfaces [39]. For example, if the relevant distribution data were somehow available (e.g., by autoradiography of biopsy specimens), Monte Carlo analysis might be particularly applicable to normal lung dosimetry in radioiodine treatment of metastatic thyroid cancer, particularly when in the form of dosimetrically problematic miliary disease. This method remains computationally time-consuming, however [39]. Tabulations of voxel S factors, conceptually equivalent to voxel source-kernels (the mean absorbed dose to a target voxel per radioactive decay in a source voxel, both of which are contained in an infinite homogeneous soft-tissue medium) [49, 59], are becoming available [60]. In contrast to dose point-kernel- and Monte Carlo-based techniques, the voxel S factor method does not require specialized computer facilities and is relatively fast, and thus may emerge as the practical method of choice for calculation of macroscopic non-uniform dose distributions.

Once a dose distribution has been calculated, a corresponding ‘dose–volume histogram’ can be derived [81]. Basically, a dose–volume histogram is a graph of the fraction of the tumour or organ volume receiving a specified dose versus the dose (differential form) or the fraction of the tumour or organ volume receiving less than a specified dose versus the dose (integral, or cumulative, form). It graphically presents the minimum, mean and maximum doses and the dispersion about the mean dose. The greater this dispersion, the more non-uniform is the dose distribution.

An important practical component of macroscopic non-uniform dosimetry is the ability to fuse, or register, tomographic images from multiple modalities [46, 47, 56, 82–84]. Dose distributions, calculated from three-dimensional activity distributions measured by scintigraphic imaging (i.e., SPECT or PET), may be presented as isodose contours or colour-coded images. By image fusion, such isodose contours or colour-coded images can be superimposed on or juxtaposed with the corresponding anatomy to allow correlation of doses with tumour and normal organs (as imaged by CT or MRI) [36, 56, 59, 60].

4.5. SUMMARY

Radiation dosimetry deals with the determination of the amount and the spatial and temporal distribution of energy deposited in matter by ionizing radiation. Internal radionuclide radiation dosimetry specifically deals with the deposition of radiation energy in tissue due to a radionuclide within the body. However, unlike external radiation dose (which can often be

measured), internal radiation dose must be calculated. These procedures have evolved over more than 60 years from relatively simple approaches to those with a high level of sophistication. Internal dosimetry has been applied to the determination of tissue doses and related quantities for occupational exposures in radiation protection, environmental exposures in radiation epidemiology, and diagnostic and therapeutic exposures in nuclear medicine. This chapter has reviewed the concepts associated with the computational approaches to internal radiation dosimetry.

REFERENCES

- [1] Fisher D R 1994 Radiation dosimetry for radioimmunotherapy. An overview of current capabilities and limitations *Cancer* **73** 905–11
- [2] Howell R W, Wessels B W, Loevinger R, Watson E E, Bolch W E, Brill A B, Charkes N D, Fisher D R, Hays M T, Robertson J S, Siegel J A and Thomas S R 1999 The MIRD perspective 1999. Medical Internal Radiation Dose Committee *J. Nucl. Med.* **40** 3S–10S
- [3] Stabin M, Tagesson M, Thomas S R, Ljungberg M and Strand S E 1999 Radiation dosimetry in nuclear medicine *Appl. Radiat. Isot.* **50** 73–87
- [4] Zanzonico P B 2000 Internal radionuclide radiation dosimetry: a review of basic concepts and recent developments *J. Nucl. Med.* **41** 297–308
- [5] Rossi H 1968 Microscopic energy distributions in irradiated manner. In *Radiation Dosimetry*, vol I: *Fundamentals* eds F Attix, W Roesch and E Tochlin (New York: Academic) pp 43–92
- [6] ICRU 1980 Radiation Quantities and Units. International Commission on Radiation Units and Measurements (ICRU) Report 33. International Commission on Radiation Units and Measurements (ICRU), Bethesda, MD
- [7] ICRU 1983 Microdosimetry. International Commission on Radiation Units and Measurements (ICRU) Report 36. International Commission on Radiation Units and Measurements (ICRU), Bethesda, MD
- [8] NCRP 1985 SI Units in Radiation Protection and Measurements. National Council on Radiation Protection and Measurements (NCRP) Report 82. National Council on Radiation Protection and Measurements (NCRP), Bethesda, MD
- [9] BEIR 1990 Health Effects of Exposure to Low Levels of Ionizing Radiation (BEIR V). Biological Effects of Ionizing Radiation (BEIR) Committee, National Research Council. National Academy Press, Washington, DC
- [10] ICRP 1990 1990 Recommendations of the International Commission on Radiological Protection. International Commission on Radiological Protection (ICRP) Publication 60, Annals of the ICRP 21 (Elmsford, NY: Pergamon)
- [11] Johns H and Cunningham J 1974 *The Physics of Radiology* (Springfield: Thomas)
- [12] Attix F 1986 *Introduction to Radiological Physics and Radiation Dosimetry* (New York: Wiley)
- [13] Loevinger R, Budinger T, Watson E, Atkins H, Blau M, Lathrop K, Poston J, Robertson J, Thomas S and Weber D 1991 *MIRD Primer for Absorbed Dose Calculations* (revised edition) (New York: Society of Nuclear Medicine)

- [14] Snyder W, Ford M, Warner G and Fisher H Jr 1969 Estimates of absorbed fractions for monoenergetic photon sources uniformly distributed in various organs of a heterogeneous phantom. MIRD Pamphlet No 5 *J. Nucl. Med.* **10** (Suppl. 3) 5–52
- [15] Snyder W, Ford M, Warner G and Watson S 1975 'S', Absorbed dose per unit cumulated activity for selected radionuclides and organs. Medical Internal Radiation Dose (MIRD) Pamphlet No 11 (New York: Society of Nuclear Medicine)
- [16] Zanzonico P, Brill A and Becker D 1995 Radiation dosimetry. In *Principles of Nuclear Medicine* eds H Wagner, Z Szabo and J Buchanan (Philadelphia: Saunders) 2nd edition pp 106–34
- [17] ICRP 1988 *Radiation Dose to Patients from Radiopharmaceuticals*. International Commission on Radiological Protection (ICRP) Publication 53 (New York: Pergamon)
- [18] Watson E 1999 Foreword *J. Nucl. Med.* **40** 1S–2S
- [19] Loevinger R 1989 The MIRD perspective. In *Dosimetry of Administered Radionuclides* eds S Adelstein, A Kassis and R Burt (Washington, DC: American College of Nuclear Physicians/Department of Energy) pp 29–43
- [20] Cristy M and Eckerman K 1987 *Specific Absorbed Fractions of Energy at Various Ages from Internal Photon Sources* (Parts I–VII). Oak Ridge National Laboratory Report ORNL/TM-8381/V1-7 (Springfield, VA: National Technical Information Service, Dept of Commerce)
- [21] ICRP 1975 *Report of the Task Group on Reference Man* ICRP Publication 23 (Oxford: Pergamon)
- [22] Stabin M 1996 MIRDOSE: personal computer software for internal dose assessment in nuclear medicine *J. Nucl. Med.* **37** 538–46
- [23] Sgouros G, Bigler R and Zanzonico P 1988 DOSCAL: a tumor-incorporating mean absorbed dose calculation program (Abstract) *J. Nucl. Med.* **29** 874
- [24] Johnson T 1988 MABDOS: a generalized program for internal dosimetry *Comput. Meth. Programs Biomed.* **37** 159–67
- [25] Johnson T K, McClure D and McCourt S 1999 MABDOSE. II: Validation of a general purpose dose estimation code [In Process Citation] *Med. Phys.* **26** 1396–403
- [26] Johnson T K, McClure D and McCourt S 1999 MABDOSE. I: Characterization of a general purpose dose estimation code [In Process Citation] *Med. Phys.* **26** 1389–95
- [27] Weber D, Eckerman K, Dillman L and Ryman J 1989 *MIRD: Radionuclide Data and Decay Schemes* (New York: Society of Nuclear Medicine)
- [28] Beierwaltes W H, Nishiyama R H, Thompson N W, Copp J E and Kubo A 1982 Survival time and 'cure' in papillary and follicular thyroid carcinoma with distant metastases: statistics following University of Michigan therapy *J. Nucl. Med.* **23** 561–8
- [29] Benua R, Cicale N and Sonenberg M 1962 The relation of radioiodine dosimetry to results and complications in the treatment of metastatic thyroid cancer *Am. J. Roentgenol.* **87** 171–82
- [30] Furhang E E, Larson S M, Buranapong P and Humm J L 1999 Thyroid cancer dosimetry using clearance fitting *J. Nucl. Med.* **40** 131–6
- [31] Marinelli L, Quimby E and Hine G 1948 Dosage determination with radioactive isotopes. II. Practical considerations in therapy and protection *Am. J. Roentgenol. Radium Therapy* **59** 260–80
- [32] Marinelli L, Quimby E and Hine G 1948 Dosage determination with radioactive isotopes. I. Fundamental dosage formulae *Nucleonics* **2** 56–66

- [33] Marinelli L, Quimby E and Hine G 1948 Dosage determination with radioactive isotopes. II. Biological considerations and practical applications *Nucleonics* **2** 44–9
- [34] Loevinger R, Holt J G and Hine G J 1956 Internal administered radioisotopes. In *Radiation Dosimetry* eds G J Hine and G L Brownell (New York: Academic) pp 801–73
- [35] Zanzonico P B 2001 Radiation dosimetry of rhenium-188 Lipiodol: a workshop. In *Lecture Notes: Regional Training Workshop on Radionuclide Treatment of Liver Cancer*. NMS/11/RTC-2001-01/RCA-1 (Perth) (Perth: International Atomic Energy Agency (IAEA)) pp 128–61
- [36] Erdi A K, Wessels B W, DeJager R, Erdi Y E, Atkins F B, Yorke E D, Smith L, Huang E, Smiddy M, Murray J *et al.* 1994 Tumor activity confirmation and isodose curve display for patients receiving iodine-131-labeled 16.88 human monoclonal antibody *Cancer* **73** 932–44
- [37] Erdi A K, Yorke E D, Loew M H, Erdi Y E, Sarfaraz M and Wessels B W 1998 Use of the fast Hartley transform for three-dimensional dose calculation in radionuclide therapy *Med. Phys.* **25** 2226–33
- [38] Erdi A K, Erdi Y E, Yorke E D and Wessels B W 1996 Treatment planning for radioimmunotherapy *Phys. Med. Biol.* **41** 2009–26
- [39] Furhang E E, Chui C S and Sgouros G 1996 A Monte Carlo approach to patient-specific dosimetry *Med. Phys.* **23** 1523–9
- [40] Furhang E E, Chui C S, Kolbert K S, Larson S M and Sgouros G 1997 Implementation of a Monte Carlo dosimetry method for patient-specific internal emitter therapy *Med. Phys.* **24** 1163–72
- [41] Giap H B, Macey D J, Bayouth J E and Boyer A L 1995 Validation of a dose-point kernel convolution technique for internal dosimetry *Phys. Med. Biol.* **40** 365–81
- [42] Giap H B, Macey D J and Podoloff D A 1995 Development of a SPECT-based three-dimensional treatment planning system for radioimmunotherapy *J. Nucl. Med.* **36** 1885–94
- [43] Howell R W, Rao D V and Sastry K S 1989 Macroscopic dosimetry for radioimmunotherapy: nonuniform activity distributions in solid tumors *Med. Phys.* **16** 66–74
- [44] Humm J L 1986 Dosimetric aspects of radiolabeled antibodies for tumor therapy *J. Nucl. Med.* **27** 1490–7
- [45] Humm J L and Cobb L M 1990 Nonuniformity of tumor dose in radioimmunotherapy [see comments] *J. Nucl. Med.* **31** 75–83
- [46] Koral K F, Zasadny K R, Kessler M L, Luo J Q, Buchbinder S F, Kaminski M S, Francis I and Wahl R L 1994 CT–SPECT fusion plus conjugate views for determining dosimetry in iodine-131-monoclonal antibody therapy of lymphoma patients *J. Nucl. Med.* **35** 1714–20
- [47] Koral K F, Lin S, Fessler J A, Kaminski M S and Wahl R L 1997 Preliminary results from intensity-based CT–SPECT fusion in I-131 anti-B1 monoclonal-antibody therapy of lymphoma *Cancer* **80** 2538–44
- [48] Lechner P K and Kwok C S 1993 Tumor dosimetry in radioimmunotherapy: methods of calculation for beta particles *Med. Phys.* **20** 529–34
- [49] Liu A, Williams L, Wong J and Raubitschek A 1997 A voxel source kernel (VSK) method for rapid, patient-specific dose estimates in radioimmunotherapy (RIT) (Abstract) *J. Nucl. Med.* **38**(suppl) 106P

- [50] Liu A, Williams L E, Lopatin G, Yamauchi D M, Wong J Y and Raubitschek A A 1999 A radionuclide therapy treatment planning and dose estimation system *J. Nucl. Med.* **40** 1151–3
- [51] Ljungberg M and Strand S E 1988 Dose planning with SPECT *Int. J. Cancer Suppl.* **2** 67–70
- [52] Mayer R, Dillehay L E, Shao Y, Song S, Zhang Y G, Bartholomew R M and Williams J R 1994 A new method for determining dose rate distribution from radioimmunotherapy using radiochromic media *Int. J. Radiat. Oncol. Biol. Phys.* **28** 505–13
- [53] Sgouros G, Barest G, Thekkumthala J, Chui C, Mohan R, Bigler R E and Zanzonico P B 1990 Treatment planning for internal radionuclide therapy: three-dimensional dosimetry for nonuniformly distributed radionuclides *J. Nucl. Med.* **31** 1884–91
- [54] Sgouros G, Chiu S, Pentlow K S, Brewster L J, Kalaigian H, Baldwin B, Daghighian F, Graham M C, Larson S M and Mohan R 1993 Three-dimensional dosimetry for radioimmunotherapy treatment planning *J. Nucl. Med.* **34** 1595–601
- [55] Sgouros G 1999 Treatment planning for internal emitter therapy: methods, applications and clinical implications. In *Proceedings of the Sixth International Radiopharmaceutical Dosimetry Symposium* (ORISE 99-0164) eds A Schlafke-Stelson, M Stabin and R Sparks (Oak Ridge, TN: US Dept of Energy and Oak Ridge Associated Universities) pp 13–25
- [56] Kolbert K S, Sgouros G, Scott A M, Bronstein J E, Malane R A, Zhang J, Kalaigian H, McNamara S, Schwartz L and Larson S M 1997 Implementation and evaluation of patient-specific three-dimensional internal dosimetry *J. Nucl. Med.* **38** 301–8
- [57] Uchida I, Yamada Y, Oyamada H and Nomura E 1992 Calculation algorithm of three-dimensional absorbed dose distribution due to *in vivo* administration of nuclides for radiotherapy *Kaku Igaku* **29** 1299–306
- [58] Wessels B W, Yorke E D and Bradley E W 1990 Dosimetry of heterogeneous uptake of radiolabeled antibody for radioimmunotherapy *Front. Radiat. Ther. Oncol.* **24** 104–8
- [59] Akabani G, Hawkins W, Eckblade M and Lechner P 1997 Patient-specific dosimetry using quantitative SPECT imaging and three-dimensional discrete Fourier transform convolution *J. Nucl. Med.* **38** 308–14
- [60] Bolch W E, Bouchet L G, Robertson J S, Wessels B W, Siegel J A, Howell R W, Erdi A K, Aydogan B, Costes S, Watson E E, Brill A B, Charkes N D, Fisher D R, Hays M T and Thomas SR 1999 MIRD Pamphlet No 17: The dosimetry of nonuniform activity distributions—radionuclide *S* values at the voxel level. Medical Internal Radiation Dose Committee *J. Nucl. Med.* **40** 11S–36S
- [61] Adelstein S, Kassis A and Sastry K 1986 Cellular vs organ approaches to dose estimates. In *Proceedings of the Fourth International Radiopharmaceutical Dosimetry Symposium* (Conf-85113 (DE86010102) eds A Schlafke-Stelson and E Watson (Oak Ridge, TN: US Dept of Energy and Oak Ridge Associated Universities) pp 13–25
- [62] Goddu S M, Rao D V and Howell R W 1994 Multicellular dosimetry for micrometastases: dependence of self-dose versus cross-dose to cell nuclei on type and energy of radiation and subcellular distribution of radionuclides *J. Nucl. Med.* **35** 521–30
- [63] Goddu S, Howell R, Bouchet L, Bolch W, Rao D, Budinger T, Fisher D, Hays M, Lathrop K, Robertson J, Siegel J, Thomas S, Watson E and Wessels B 1997 *MIRD Cellular S Factors: Self-Absorbed Dose per Unit Cumulated Activity for Selected Radionuclides and Monoenergetic Electrons and Alpha Particle Emitters*

- Incorporated into Different Cell Compartments* (Reston, VA: Society of Nuclear Medicine)
- [64] Griffiths G L, Govindan S V, Sgouros G, Ong G L, Goldenberg D M and Mattes M J 1999 Cytotoxicity with Auger electron-emitting radionuclides delivered by antibodies *Int. J. Cancer* **81** 985–92
 - [65] Humm J L, Howell R W and Rao D V 1994 Dosimetry of Auger-electron-emitting radionuclides: Report No 3 of AAPM Nuclear Medicine Task Group No 6 *Med. Phys.* **21** 1901–15 [published erratum appears in *Med. Phys.* 1995 **22** 1837]
 - [66] Humm J L, Macklis R M, Lu X Q, Yang Y, Bump K, Beresford B and Chin L M 1995 The spatial accuracy of cellular dose estimates obtained from 3D reconstructed serial tissue autoradiographs *Phys. Med. Biol.* **40** 163–80
 - [67] Humm J 1987 A microdosimetric model of astatine-211 labeled antibodies for radioimmunotherapy *Int. J. Radiat. Oncol. Biol. Phys.* **13** 1767–73
 - [68] Macklis R M, Lin J Y, Beresford B, Atcher R W, Hines J J and Humm J L 1992 Cellular kinetics, dosimetry, and radiobiology of alpha-particle radioimmunotherapy: induction of apoptosis *Radiat. Res.* **130** 220–6
 - [69] O'Donoghue J A and Wheldon T E 1996 Targeted radiotherapy using Auger electron emitters *Phys. Med. Biol.* **41** 1973–92
 - [70] Wrenn M E, Howells G P, Hairr L M and Paschoa A S 1973 Auger electron dosimetry *Health Phys.* **24** 645–53
 - [71] Yorke E D, Williams L E, Demidecki A J, Heidorn D B, Roberson P L and Wessels B W 1993 Multicellular dosimetry for beta-emitting radionuclides: autoradiography, thermoluminescent dosimetry and three-dimensional dose calculations *Med. Phys.* **20** 543–50
 - [72] Zalutsky M R, Stabin M, Larsen R H and Bigner D D 1997 Tissue distribution and radiation dosimetry of astatine-211-labeled chimeric $^{81}\text{C}_6$, an alpha-particle-emitting immunoconjugate *Nucl. Med. Biol.* **24** 255–61
 - [73] Kassis A I, Adelstein S J, Haydock C and Sastry K S 1980 Radiotoxicity of ^{75}Se and ^{35}S : theory and application to a cellular model *Radiat. Res.* **84** 407–25
 - [74] Kassis A I, Adelstein S J, Haydock C, Sastry K S, McElvany K D and Welch M J 1982 Lethality of Auger electrons from the decay of bromine-77 in the DNA of mammalian cells *Radiat. Res.* **90** 362–73
 - [75] Kassis A I, Adelstein S J, Haydock C and Sastry K S 1983 Thallium-201: an experimental and a theoretical radiobiological approach to dosimetry *J. Nucl. Med.* **24** 1164–75
 - [76] Kassis A I, Sastry K S and Adelstein S J 1985 Intracellular distribution and radiotoxicity of chromium-51 in mammalian cells: Auger-electron dosimetry *J. Nucl. Med.* **26** 59–67
 - [77] Kassis A I, Fayad F, Kinsey B M, Sastry K S, Taube R A and Adelstein S J 1987 Radiotoxicity of ^{125}I in mammalian cells *Radiat. Res.* **111** 305–18
 - [78] Kassis A I, Sastry K S and Adelstein S J 1987 Kinetics of uptake, retention, and radiotoxicity of $^{125}\text{IUdR}$ in mammalian cells: implications of localized energy deposition by Auger processes *Radiat. Res.* **109** 78–89
 - [79] Kassis A I 1992 The MIRD approach: remembering the limitations *J. Nucl. Med.* **33** 781–2 [editorial; comment]
 - [80] Tagesson M, Ljungberg M and Strand S E 1996 A Monte-Carlo program converting activity distributions to absorbed dose distributions in a radionuclide treatment planning system *Acta Oncol.* **35** 367–72

- [81] O'Donoghue J A 1999 Implications of nonuniform tumor doses for radioimmunotherapy [In Process Citation] *J. Nucl. Med.* **40** 1337–41
- [82] Scott A M, Macapinlac H A, Divgi C R, Zhang J J, Kalaigian H, Pentlow K, Hilton S, Graham M C, Sgouros G, Pelizzari C *et al* 1994 Clinical validation of SPECT and CT/MRI image registration in radiolabeled monoclonal antibody studies of colorectal carcinoma *J. Nucl. Med.* **35** 1976–84
- [83] Scott A M, Macapinlac H, Zhang J J, Kalaigian H, Graham M C, Divgi C R, Sgouros G, Goldsmith S J and Larson S M 1994 Clinical applications of fusion imaging in oncology *Nucl. Med. Biol.* **21** 775–84
- [84] Scott A M, Macapinlac H, Zhang J, Daghighian F, Montemayor N, Kalaigian H, Sgouros G, Graham M C, Kolbert K, Yeh S D *et al* 1995 Image registration of SPECT and CT images using an external fiduciary band and three-dimensional surface fitting in metastatic thyroid cancer *J. Nucl. Med.* **36** 100–3

Chapter 5

Mathematical models of the human anatomy

*John W Poston Sr, Wesley E Bolch
and Lionel G Bouchet*

5.1. INTRODUCTION

5.1.1. Early approaches to dose assessment

The first scientists to be involved in estimating the dose due to internally distributed radionuclides were very familiar with the techniques used for dosimetry of external radiation sources and radium implants [1]. These techniques were already relatively well developed. However, unlike external radiation exposure, the radiation-absorbed dose due to an internally deposited radionuclide usually had to be calculated rather than measured. Procedures to be followed in these dose calculations probably began with the formulations of Marinelli and his colleagues in the 1940s [2, 3]. A widely used elaboration of the Marinelli formulation was due to Loevinger and his colleagues was published in the 1950s [4, 5].

Early approaches to such calculations were very simple and took into account the activity and the ‘effective half-life’ of the radionuclide in the organ, the energy deposited in the organ, and an approximate organ mass. Typically, it was assumed that the radionuclide was uniformly distributed in the homogeneous organ of interest. Usually, the calculations were made of the absorbed dose rate from β -emitting and γ -emitting radionuclides separately. In the β -radiation calculations, it was assumed that all the β -radiation energy was absorbed in the organ containing the radionuclide. For γ -emitters, a ‘geometry factor’ was applied to account for the radiation energy escaping the organ. Dose calculations were completed for simple shapes such as right circular cylinders as well as models for specific organs such as the thyroid gland and the total body [4,5].

5.1.2. *Need for mathematical models in dose assessment*

While these relatively simple approaches to dosimetry provided reasonable estimates of the doses due to internally deposited radionuclides, researchers and practitioners longed for better representations of individual organs as well as the human body and techniques that could provide more accurate dose estimates. There was a constant desire to model the organs of the body, and the entire body itself, in a more realistic fashion. This desire led to a progression of developments that ultimately produced the very realistic and complex mathematical models (called phantoms) in use today. However, this progression took some time, starting with very simple shapes and very simple calculational approaches in the late 1950s and early 1960s.

The ICRP in its recommendations on internal exposure assumed that organs of the body could be represented by spheres of varying radii [6]. Each organ was represented by a sphere and the effective radius of the sphere was specified. In these simple calculations, the radionuclide source was assumed to be at the centre of the sphere and the ‘effective absorbed energy’ was calculated for each organ. Corrections were made for photon energy lost from the sphere. In addition, the ICRP specified a radius for the total body and assumed that it could be represented by a sphere with a radius of 30 cm. It is interesting to note that the same 30 cm radius as used for the organs designated the ‘muscle,’ the gastrointestinal tract and the small intestine.

Increases in the size and speed of digital computers allowed improvements in the models and the approaches taken to radiation transport calculations. In addition, as the number of radionuclides in use in nuclear medicine increased and more was understood about the distribution of these materials in the organs, there was a need for more detailed descriptions of the organs in which specific regions or structures within the organ were delineated.

5.1.3. *Conceptual role of mathematical phantoms*

Conceptually, the purpose of the phantom is to represent the organ or tissue of interest, to allow the radionuclide of interest to be contained in a specific volume, and to provide a medium that absorbs and scatters the radiation emitted in a manner similar to tissue. A phantom is a mathematical model designed to represent an organ or tissue of the body, an organ system or perhaps the entire body. Early designs were simple shapes such as right circular cylinders, spheres or discs. Usually, the composition of the phantom was specified and the constituents represented the major elements found in soft tissue, muscle, bone, lungs, etc. However, in early phantoms, it was often assumed that the material was simply water. As will be discussed below, the complexity of the phantoms increased as technology developed. These developments included improvements of the details of the geometrical design as well as expansions of the elemental composition of the phantom.

5.2. HISTORICAL DEVELOPMENTS

5.2.1. *Simple models of Brownell, Ellett and Reddy*

Brownell *et al.* published perhaps the most extensive early compilation of data for photon dosimetry in MIRD Pamphlet No 3 [7]. This pamphlet, which summarized much of their earlier research, provided estimates obtained via Monte Carlo calculations of the photon-absorbed fractions of energy for centrally located point sources in three phantoms with simple shapes. Phantom shapes included elliptical cylinders, right circular cylinders and spheres. All phantoms were assumed to consist of a homogeneous tissue composed of carbon, hydrogen, oxygen and nitrogen, with trace amounts of chlorine and sodium.

For phantoms shaped as elliptical cylinders, Brownell and his colleagues considered 13 monoenergetic photon sources as well as radium. Photon energies ranged from 0.02 to 2.75 MeV. There were 19 elliptical cylinders ranging in mass from 2 to 200 kg (although one wonders why such a large mass was of interest). For right circular cylinders, only six energies were considered (ranging from 0.04 to 1.46 MeV) but the same 19 masses were included in the calculations. For spherical shapes, photon energies ranged from 0.02 to 2.75 MeV and phantoms with the same 19 masses were considered.

In addition, these authors calculated absorbed fractions of energy for uniform distributions of activity in some simple phantoms. Results were presented for ellipsoids, small spheres, thick ellipsoids and flat ellipsoids. Again, monoenergetic photon sources in the range 0.02 to 2.75 MeV and phantoms of various masses were considered. For ellipsoids, the masses ranged from 2 to 200 kg, as in previous calculations. For small spheres, thick ellipsoids and flat ellipsoids only masses in the range 0.3 to 6 kg were considered.

5.2.2. *Early models developed by Snyder*

In the late 1950s and 1960s, many research groups were developing simple phantoms and Monte Carlo techniques to be used in dose assessment. One major effort was led by W S Snyder at the Oak Ridge National Laboratory (ORNL). Initially, the ORNL research group focused on the use of a right circular cylinder with dimensions suitable for simulating the trunk of an adult human (30 cm diameter with a 60 cm height). This phantom was subdivided into a large number of regions and energy deposition was scored in each of these regions. Both external and internal sources of radiation were considered and absorbed dose to a specific organ was derived from consideration of the dose to the sub-regions in which the organ was assumed to reside.

5.2.3. The Snyder–Fisher phantom

In 1966, Fisher and Snyder, at the Oak Ridge National Laboratory (ORNL), reported on the development of an adult phantom for use in radiation absorbed dose calculations [8]. The adult phantom was assumed to be standing erect with the arms at the sides of the body. Three specific regions were defined: the head and neck, the trunk including the arms, and the legs. The head and neck were represented by a $14\text{ cm} \times 20\text{ cm}$ elliptical cylinder with a height of 24 cm. The trunk and arms were modelled as a larger elliptical cylinder, $20\text{ cm} \times 40\text{ cm}$ with a height of 70 cm. The legs below the buttocks were modelled as a truncated elliptical cone with a height 80 cm. Regions of little dosimetric concern were not included, e.g., the hands, feet, ears, nose, etc. The composition of the phantom was assumed to be tissue distributed homogeneously throughout. No attempt was made to model the lungs or skeleton or to define the locations of specific organs in the phantom. Approximately 120 sub-regions were defined in the phantom that were used to assign approximate values of the absorbed doses to organs located within specific regions. In some cases, absorbed dose estimates for large organs required the evaluation of the doses deposited in several of these regions.

Also included in this research was the development of phantoms for humans of other ages. These phantoms represented humans with ages 0 (newborn), 1, 5, 10 and 15 years. These phantoms will be discussed in more detail in section 5.2.6 below.

In 1967, Fisher and Snyder reported on the development of an adult phantom with 22 internal organs and more than 100 sub-regions [9]. This phantom represented the next step in the development of anthropomorphic phantoms for use in dose calculations. However, this phantom also was homogeneous and the skeleton and lung regions were not defined—in terms of the assignment of different densities and elemental compositions for these regions. This point was very misleading in that many of the early drawings indicated such regions. However, a careful reading of the research reports from the ORNL group will confirm the homogeneous composition. Estimates of the absorbed dose to the skeleton were obtained by summing all the energy deposited in the entire skeleton and dividing by the skeletal volume. No special treatments were applied to obtain absorbed dose estimates for the lungs. Calculations using the adult phantom agreed well with those of Ellett *et al.* [10, 11] but were about 50% lower than those obtained using the ICRP spherical organ methods [6].

Even though the original phantom was designed for use with internally deposited radionuclides, Snyder saw many other applications. In addition, in 1967, he used the phantom to study the distribution of dose in the body from external point sources of γ -rays [12]. He studied four photon energies (0.07, 0.15, 0.5 and 1.0 MeV) and four different source locations at distances of 1 and 2 m from the centre of the phantom.

A heterogeneous phantom was the next logical step in the development of anthropomorphic phantoms. Snyder and his colleagues [13] published an extensive compilation of calculations of the absorbed fractions of energy for monoenergetic photon sources uniformly distributed in selected organs in this phantom. This phantom was composed of three regions: skeleton, lungs and the remainder (soft tissue). The densities of these regions were about 1.5, 0.3 and 1.0 g/cm³, respectively. The organ masses were selected to follow as closely as possible the data of Reference Man [14]. This phantom ultimately became known in the nuclear medicine community as the 'MIRD Phantom' (see section 5.2.4).

5.2.4. The MIRD-5 Phantom

The MIRD Phantom was developed by Snyder's research group at ORNL and, even though Snyder chose to call the phantom a 'standard man approximation', it was based on information being compiled for ICRP Publication 23 [14] on Reference Man. In reality, there was a parallel effort at the time to provide improved estimates of absorbed dose and dose equivalent for the International Commission on Radiological Protection (ICRP). These estimates were later published as the ICRP Publication 30 series [15].

The heterogeneous phantom contained three principal idealizations:

1. It had simple geometrical shapes that approximated the organ and body shapes and dimensions. Twenty-two internal organs were included in the design but other unimportant structures (the nose, hands, feet, etc.) were ignored. It was assumed that each organ or tissue was homogeneous in terms of composition and density. However, different compositions and densities were used for the skeletal region, the lungs and the remainder of the body (soft tissue).
2. The monoenergetic radiation source was assumed to be uniformly distributed in one of the organs (i.e., the source organ).
3. The Monte Carlo method was applied in the calculations to obtain a set of photon histories upon which estimates of the energy deposited in the organs and tissues of the phantom could be based. Only photon transport was considered and energy transferred to electrons by photon interactions was assumed to be deposited locally.

Fifteen source organs and 25 target organs or regions were included in the set of calculations. Twelve photon energies were considered ranging from 0.01 to 4.0 MeV. A limited number of histories were followed in each calculation (25 000 to 50 000 histories) and, for low energy photons, the absorbed fractions of energy for many organs were considered unreliable and were not included in the tabulations.

In 1978, Snyder *et al.* published the results of an extensive set of calculations of specific absorbed fractions of energy using an improved heterogeneous phantom [16]. As with previous calculations, these results were for monoenergetic photon sources uniformly distributed in organs of the heterogeneous phantom. However, significant improvements had been made in the phantom. These improvements included the following.

1. The head section was represented by a right elliptical cylinder topped by half an ellipsoid.
2. The leg regions consisted of the frustums of two circular cones.
3. The male genitalia were moved to a position outside the trunk and on the front of the revised model of the legs.
4. Detailed descriptions of the scapulae and the clavicles were included.
5. The stomach and upper and lower large intestine were modelled as organs with walls and contents.
6. A source and target region called the 'skin' was added to the phantom.

Twenty source organs and 20 target organs or regions were included in the set of calculations. Twelve photon energies were considered ranging from 0.01 to 4.0 MeV. The number of histories followed was increased to 60 000 in hopes of increasing the reliability of the results. However, as before, calculations for low-energy photons were very unreliable and other methods were used to provide an estimate of the specific absorbed fractions in these cases.

Over the years, a number of changes (improvements) to the heterogeneous phantom have been made (see section 5.3 below). However, the fundamental use of the phantom for internal dose calculations has been essentially unchanged since its inception.

5.2.5. *Photon and electron transport*

Initially, Monte Carlo transport codes used in internal dose assessment were capable only of transporting photons. Perhaps one of the most widely used computer codes was the ALGAM code developed at ORNL [17]. This code was used with the original Snyder–Fisher phantom and continued to be the basic code used for calculations by the ORNL group as the complexity of the phantom increased. In these calculations, it was assumed that electrons, created by photon interactions, deposited their energy at the point of creation. That is, the photon transport code was not capable of transporting electrons.

Computer codes developed more recently now have the capability of transporting both photons and electrons, including the production of bremsstrahlung, and considering other types of photon and electron interaction [18, 19]. Subsequently investigations using a coupled electron/photon transport code indicated that for most situations, this apparent deficiency was not significant [20, 21].

5.2.6. *Similitude and paediatric phantoms*

Development of the adult human phantom by Snyder and his colleagues (see section 5.2.3 above) was paralleled by the development of phantoms representing humans of other ages [8]. These phantoms represented children with ages of 0 (newborn), 1, 5, 10 and 15 years. These early designs were assumed to have outer dimensions that represented the average height, surface area and body mass of a child of the particular age. All ‘paediatric phantoms’ were obtained by applying a set of simple transformations to the axes of the Cartesian coordinate system in which the adult phantom was located. These phantoms became known as the ‘similitude phantoms’ because of their resemblance to the adult. This approach has its limitations because children generally are not just ‘little adults’. However, these phantoms were the first developed to answer a real need in the nuclear medicine community [22].

Improvements in the paediatric models were closely linked with the development of the heterogeneous adult phantom. Even though these new phantoms were heterogeneous, the paediatric phantoms were obtained through the same transformation method. That is, these phantoms also were similitude phantoms. The outside dimensions were obtained by applying a series of transformations to the coordinate system and no consideration was given to the actual organ sizes or shapes of the ‘transformed’ organs. Although the masses of these transformed organs had to be known for the calculation of absorbed dose, these masses were never published [23].

The limitations associated with transforming the major axes of the adult phantom should be clear. Children are not simply small adults and their organs are not necessarily ‘smaller adult organs’. Some organs are larger in a child than in the adult and get smaller as the individual approaches adulthood, e.g., the thymus. In addition, it was important that the actual size, shape, location and mass of each organ be known for accurate dose calculations. For these reasons, and others, a significant effort was undertaken at ORNL during the mid-1970s to develop individual paediatric phantoms based upon a careful review of the existing literature for each particular age. This effort produced the next generation of mathematical phantoms that, although they appeared to be modelled after the adult, were designed independently.

Three ‘individual phantoms’ were designed by Hwang *et al.* [24, 25]. These were the newborn, 1- and 5-year-old models. A separate effort was undertaken by Jones *et al.* [26] for the 15-year-old and Deus and Poston [27] undertook the design of a 10-year old after the other four designs were complete. The development of the 10-year-old was significantly different from those for the other four ages. In fact, this design was intended to point the way to the next generation of more realistic phantoms. Even though the design was completed and used for a limited number of dose calculations, it was not popular because of the very complex geometry, and other approaches to the development of phantoms were followed [28, 29].

5.2.7. Development of MIRDose codes

Internal dose calculations using a stylized model generally are performed by combining tabulated dose conversion factors (e.g., absorbed fractions, S values) with radionuclide activity information in source organs or regions [30]. Because this process can be tedious to perform and involves repetitive tasks, it lends itself to treatment with computer programs. The MIRDose computer program was developed to perform internal dose calculations using specific stylized models [31, 32]. The software was originally presented in 1984 by Watson and Stabin [31] and has been continuously supported and updated since then, with version 2 available in 1987, and version 3 in 1994 [32]. Using MIRDose, dose calculations are performed by searching through internal databases of radionuclide decay data and specific absorbed fractions of energy (specific for a stylized model) to generate S values of interest. These S values are combined with user-entered source organ residence times to calculate the dose in the different organs and regions of the body. Libraries used in the version 2 of the MIRDose computer program were based on 59 radionuclides derived from references [33–35] and on the paediatric phantom series of Cristy and Eckerman [28, 29]. In version 3, libraries were updated to use 224 radionuclides [33] for 10 mathematical phantoms (the six ORNL phantom series [28, 29] and the four pregnant female phantom series at different gestation times [36]) with 28 source and 28 target regions. In addition, special models for the gastrointestinal tract [15] and the bladder [37] were implemented in both MIRDose 2 and 3. To replace the ICRP Publication 30 bone model [15] used in MIRDose2 for skeletal dosimetry, the new model of the skeletal system developed by Eckerman [38] was implemented in MIRDose3, thus allowing for the calculation of doses in 15 different bone sites. To support tumour dosimetry, the ability to calculate absorbed doses to small, unit density spheres was added to MIRDose3 using absorbed fractions of energy for both photon and electron sources [7, 39–41].

5.3. THE CURRENT STYLIZED MODELS

5.3.1. The ORNL phantom series

The Oak Ridge National Laboratory (ORNL) in 1980 developed a new series of stylized models of various ages [28]. The series included an adult male, a newborn and individuals of ages 1, 5, 10 and 15 years developed from anthropological data (legs, trunk and head) and from age-specific organ masses published in ICRP Publication 23 [14]. Although some of the organ shapes and centroids were still obtained using the similitude rule from the Snyder–Fisher adult model, these phantoms represented a great improvement for paediatric dosimetry over the similitude paediatric phantoms. These phantoms

also presented new regions and improvements such as a new stylized breast tissue region for all ages, the inclusion of the new model of the heart developed by Coffey [42, 43], and a new model of the thyroid. While the ORNL paediatric model series was initially published in 1981 [28], these models were not readily utilized until 1987 with the publication of ORNL/TM-8381 [29]. In this report, the only major change in the phantom series was that the 15-year-old model was assumed also to represent the average adult female. For this purpose, the breast, uterus and ovaries were modified according to published reference average values [14]. The phantoms were used with the ETRAN Monte Carlo photon transport code [44, 45] to calculate specific absorbed fractions of energy in all five paediatric phantoms, as well as in the adult male, for 12 photon energies (0.01 to 4.0 MeV). Electron transport was not considered in these simulations and the electron energy was assumed to be locally deposited.

5.3.2. The MIRD stylized models

Since the publication of the stylized dosimetric model of Snyder *et al.* in MIRD Pamphlet 5 Revised [16], the MIRD Committee has refined several internal organs to support the development of radioimaging tracers and therapeutic nuclear medicine. Modifications to the MIRD stylized model have been published as MIRD Pamphlets, which include equations of the new geometries, tabulated absorbed fractions of energy for monoenergetic photons and electrons, and tabulated radionuclide S values.

In 1999, the MIRD Committee adopted six new age-specific models of the head and brain [46] representing average reference brain and head for a newborn, 1-, 5-, 10- and 15-year-old (also representing the average adult female) and adult male. These phantoms were intended to provide better dosimetric tools in response to the increased number of neuroimaging radiopharmaceuticals [47, 48]. Due to the regional uptake of these new agents within the brain, accurate absorbed dose calculations required the use of a detailed model of the sub-regions of the brain not available with previous models. Similar to previous stylized models, simplistic geometrical shapes (intersection of ellipsoids, elliptical cylinders, tori and planes) were used to represent the different regions of the head and brain, with volumes derived from published reference masses [14, 49] and shapes from analysis of MRI images. Twenty-one sub-regions were modelled within the head and neck, including five regions representing bony structures (simulated as a homogenized mixture of bone and red marrow with a density of 1.4 g cm^{-3}) and 16 tissue regions (density of 1.04 g cm^{-3}). Within the brain, eight sub-regions were delineated: the caudate nuclei, cerebellum, cerebral cortex, lateral ventricles, lentiform nuclei (a composite region of both the putamen and the globus pallidus), thalami, third ventricle, and white matter. Other regions considered within the head included the cranial cerebrospinal fluid (CSF),

cranium, eyes, mandible, spinal cord, spinal cerebrospinal fluid, spinal skeleton, teeth, thyroid, upper face region, and skin.

In both the ORNL phantoms of Cristy and Eckerman [28, 29] and in the MIRD adult model developed by Snyder [16] the kidneys were represented as two symmetric ellipsoids cut by a plane with no differentiation of their internal structure. However, because of their unique physiology, the kidneys are seen to concentrate radioactivity nonuniformly [50, 51]. Snyder and Ford [52] designed a dosimetric model of the human kidney to study the administration of the mercurial diuretic chlormerodrin (neohydrin) labelled with ^{197}Hg and ^{203}Hg . Besides the kidneys, other internal organs of interest included the ovaries and the bladder. The kidneys were assumed to be of equal size (with a total volume of 305.8 cm^3) and to be composed of three separate regions, the cortex, the medulla and the papillary region. Dose estimates were provided for the cortex, medulla, ovaries and bladder per millicurie hour of residence of ^{197}Hg and ^{203}Hg in the cortex, in the medulla, in the bladder and in the total body (blood).

McAfee published in 1970 a multi-region kidney model of an adult [53] representing the renal cortex and medulla as two concentric elliptical shells, and the renal pelvis as a wedge-shaped hollow structure at the centre of each kidney. In 1975, the MIRD committee used this model in MIRD Dose Estimate Report No 6 to calculate the dose to the renal cortex and renal medulla from ^{197}Hg - and ^{203}Hg -labelled chlormerodrin [54].

Patel described a multi-compartment kidney model in 1988 [55]. This model, which was similar to the model used by Snyder and Ford [52], consisted of three regions (the cortex, medulla and papillae) that served as both the source and target regions. The geometry of the kidney was the same as in the original Snyder–Fisher phantom, i.e., the kidney was assumed to be an ellipsoid cut by a plane parallel to the z -axis of the phantom. This model was incorporated into the Snyder–Fisher heterogeneous phantom in a modified version of the ALGAM transport code [17, 56] and absorbed fractions and specific absorbed fractions of energy were calculated for 12 monoenergetic photon sources in the range 0.01 to 4.0 MeV. These results were used to obtain S values for selected radionuclides for the three regions of the kidney as the sources. The radionuclides considered were ^{32}P , ^{51}Cr , ^{57}Co , ^{67}Ga , $^{99\text{m}}\text{Tc}$, ^{111}In , ^{123}I , ^{131}I , ^{127}Xe , ^{133}Xe and ^{201}Tl .

A new kidney model recently has been adopted by the MIRD Committee and will be published as MIRD Pamphlet No 19 [57]. Following the increased use of radiopharmaceuticals in therapeutic nuclear medicine and recent associated kidney toxicity [58], the MIRD Committee developed six advanced stylized models of the kidney (newborn, 1-, 5-, 10- and 15-year-old and adult male). The outer dimensions of these models conformed to those used in the ORNL single-region kidney models while 12 interior structures were defined for each kidney: five medullary pyramids, five papillae, the renal pelvis, and the renal cortex. Although the number of medullary pyramids in these

models was less than that seen in the real anatomy (6–18 pyramids), it represented a compromise between the mathematical simplicity needed for Monte Carlo transport calculations, and the need for an improved anatomic representation over the concentric ellipsoid-shell model of McAfee [53]. Each region was derived from dimensions and volumes given in ICRP Publication 23 [14] for both the newborn and the adult, and assumed constant volume ratios between the different kidney sub-regions for the other ages. In these models each medullary pyramid was modelled by half-ellipsoids (two vertical and three horizontal) with the papillae at its tip, the pelvis by a portion of an ellipsoid within the whole kidney, and the cortex was the remainder of the kidney.

In both MIRD Pamphlets No 15 and 19, the EGS4 Monte Carlo transport code [18, 59] was used for photon and electron transport. In these two pamphlets, absorbed fractions of energy were tabulated for selected source and target combinations (12 energies were simulated between 10 keV and 4 MeV). Following the MIRD method of internal dose calculation [30], mean absorbed doses to the target regions per unit cumulated activity in the source region (S values) were tabulated for specific radionuclides.

5.3.3. Stylized models of the lower abdomen

The development of nuclear medicine imaging and therapy over the past decade has resulted in the need for more accurate dosimetry in regions that either were not represented or were misrepresented in the MIRD and ORNL stylized phantoms. The lower abdomen is a particular region of the anatomy that is difficult to model properly due to the intricate geometry of its organs. Many assumptions were made in modelling these organs, leading either to the organ not being represented, or to its being over-simplified. Development of new radio-agents with specific uptake in the prostate or in the wall of the gastrointestinal tract has led to a need to modify the dosimetric model of the lower abdomen.

In 1994, Stabin developed a mathematical model of the prostate gland and included it in the ORNL stylized model [60]. This new organ was modelled as a single sphere located just below the urinary bladder, with a volume consistent with Reference Man of ICRP Publication 23 [14]. This model was used to calculate absorbed fractions of energy and S values for selected radionuclides.

In 1999, Mardirossian *et al.* recognized that the relative spatial position of the urinary bladder, rectum and prostate were incorrectly modelled in the ORNL phantom series. They developed a new model of the lower part of the colon [61], and separated the rectum from the lower large intestine. This new model included an explicitly defined rectum, an anatomically corrected sigmoid and descending colons, and a prostatic urethra and seminal duct. These modifications were implemented in the ORNL phantom series, after

changing the position of the bladder and prostate gland to properly model the relative positions of these organs. These models were developed not only for the adult male model, but also for the other phantoms in the ORNL series using physiological and anatomical descriptions published in ICRP Publication 23 [14].

Because the intestinal tract and curvatures cannot be modelled with simple geometrical shapes that can be easily coupled to a Monte Carlo transport code, all models of this region have relied on thickening the wall region to preserve anatomical wall and content mass. The critical cells for these organs have been identified as the cells within the mucosal layer. In 1994, Poston *et al.* developed a revision of the GI tract of the MIRD adult phantom to better represent these sensitive targets [20, 21]. The actual wall of the GI tract was divided in its thickness into four regions of varying radiosensitivities; these layers were very difficult to model because the thickness of each layer varied from one section to another along the different regions of the GI tract. Poston *et al.* developed two methods to model this wall. The first method divided the tissue wall into ten small, concentric layers (100 μm thick for the adult) and the dose to each layer was recorded separately. Then, the determination of the mucosal layer thickness for each section would give directly the dose to the mucosa. However, since it is not possible to determine directly the mucosal layer thickness for a specific patient, the subdivision into 10 regions has not been used for medical dose calculation. In a second method, Poston *et al.* measured the average thickness of the mucosal layer along the GI tract from anatomic slides of cross sections of a human GI tract. Different mucosal thicknesses for the stomach, the small intestine and the large intestine were obtained. This layer was included in the GI wall of the adult mathematical phantom and coupled to the EGS4 Monte Carlo transport code [18].

Stubbs *et al.* [62] presented calculations of the radiation-absorbed dose to the walls of hollow organs. These authors studied all four sections of the gastrointestinal tract but only for four radionuclides important to nuclear medicine. They presented *S* values (in units of Gy/Bq s) for ^{90}Y , $^{99\text{m}}\text{Tc}$, ^{123}I and ^{131}I . They concluded, as did Poston *et al.*, that the ICRP ‘one-half’ assumption was overly conservative for non-penetrating radiation.

More recently, an improved (but very simple) geometric model for the small intestine has been developed and used in a study of electron energy deposition in the wall of the tract [63]. Results were obtained using this model for monoenergetic electrons in the range 10 to 500 keV. Depth dose profiles were developed so that dose to the more sensitive cells could be assessed. Electron transport calculations using the computer code MCNP4A [19] and a new model of the small intestine showed that only a small fraction of the available energy reaches the critical cells in the crypts of the wall. For electron energies below 330 keV, the only contribution to absorbed dose to the stem cells came from bremsstrahlung. For higher

electron energies (i.e., >330 keV), the dose distribution curve was dominated by monoenergetic electrons.

5.3.4. Other stylized models of the human anatomy

Other modifications and additions to the ORNL and MIRD stylized models include a peritoneal cavity [64], a new model of the nasal cavity and major airway [65], and a new model of the long bones [66]. The peritoneal cavity model was developed in 1989 by Watson *et al.* [64]. They modified the MIRD phantom to include a region representing the peritoneal cavity to support the dosimetry associated with several therapeutic and diagnostic techniques involving injection of radioactive material into the peritoneal cavity. Similarly, in 1997, Deloar *et al.* developed a model of the nasal cavity and major airway to support the dosimetry associated with ^{15}O -labelled gas PET imaging agents [65]. In 2000, Clairand *et al.* modified the model of the long bones of the ORNL phantom series to properly differentiate the cortical bone, trabecular bone and medullary cavity [66]. This effort was undertaken to support bone dosimetry for photon sources and to allow more accurate marrow dose calculations for children. Because in children the active marrow is not only found in the trabecular bone but also in the medullary cavities, the stylized models of the long bones of the legs and arms (truncated circular cones) of the ORNL phantom series did not allow for accurate bone dosimetry calculations.

5.3.5. Use of stylized models in therapeutic nuclear medicine

Because stylized models are based on an average individual (Reference Man), associated dose calculations can only represent the average dose to a population. Although this average dose can sometimes be applied to specific individuals, large variations in patient weight, size and organ mass are expected, and can significantly change the dose received by an organ. Consequently, Reference Man S values have to be scaled to match a specific individual. In MIRD Pamphlet 11, Snyder *et al.* discussed methods of scaling radionuclide S values from the 70 kg Reference Man to individual patients [67]. For target organs, r_T , sufficiently distant from the source organ, r_S , values of specific absorbed fraction $\Phi(r_T \leftarrow r_S)$ for photon irradiation are reasonably independent of organ mass, and thus no scaling from Reference Man to the patient is required. In these cases, increases (or decreases) in target organ mass, m_T , are compensated (scaled) by proportional increases (or decreases) in the absorbed fraction $\phi(r_T \leftarrow r_S)$. As the target organ approaches the source organ, however, this compensation no longer exists for photons. When r_T and r_S coincide (the target organ becomes the source organ), the dose from photon emitters above 100 keV becomes proportional to $m_S^{-2/3}$. For electron sources, in which full energy absorption is typically

assumed, the dose from electrons scales as the inverse first power of the organ mass (i.e., m_S^{-1}).

To better match a stylized model to a specific patient, models of different sizes also can be used as proposed by Clairand *et al.* [68]. Using the MIRD stylized model, they developed six new models of different heights: three male models of heights 160, 170 and 180 cm and three female models of heights 150, 160 and 170 cm. Using a statistical analysis of anthropometric data gathered from 684 forensic autopsy cases for the years 1987–1991 (all subjects selected were Caucasian adults who died of external causes and showed no pathological changes), they derived organ masses as a function of height [69]. Only organs weighed during autopsy were taken into account in this study (heart, kidneys, liver, lungs, pancreas, spleen, testes and thyroid), and other organs were obtained from the ORNL models.

To support the dosimetry in therapeutic nuclear medicine, simple tumour models also have been introduced in stylized phantoms [70–74]. These approaches allow for the determination of the photon dose from a tumour to adjacent organs, but also provide the photon dose from body organs to the tumour, which for some radionuclides can be non-negligible [75]. Clairand *et al.* developed a computer program (DOSE3D) to simulate spherical tumours inside the ORNL adult phantom [70]. With this program, the user can select one or more tumours of different sizes, and the EGS4 Monte Carlo transport code is used for the particle transport. Similarly, Johnson *et al.* developed the MABDOSE software to simulate spherical tumours inside the ORNL phantom series [71–74]. In this code, the phantom series is first voxelized at a user-selectable resolution (10, 5, 2, or 1 mm), and the ETRAN Monte Carlo photon transport code used for the particle transport.

5.4. TOMOGRAPHIC MODELS

As discussed above, stylized mathematical models of human anatomy provide a relatively efficient geometry for use with Monte Carlo radiation transport codes. Nevertheless, these models are only approximations to the true anatomical features of individuals for which dose estimates are required. An alternative class of anatomic models is based upon three-dimensional imaging techniques such as magnetic resonance (MR) imaging or computed tomography (CT). These tomographic models of human anatomy represent large arrays of image voxels that are individually assigned both a tissue type (e.g., soft tissue, bone, air, etc.) and an organ identity (heart wall, femur shaft, tracheal airway, etc.). Thus, image segmentation is needed to process the original image into a format acceptable for radiation transport using codes such as EGSnrc or MNCP [19, 76].

5.4.1. Methods of construction

Two general anatomic sources exist for the construction of tomographic models of human anatomy: (1) cadavers and (2) live subjects, typically medical patients. Each data source has its distinct advantages and disadvantages. Cadaver imaging generally offers a substantially improved opportunity for full anatomic coverage including the extremities. With CT image acquisition, higher-resolution scans can be performed, as radiation dose considerations and patient motion are not of concern. For these same reasons, multiple scans on the same cadaver can be performed using different technique factors (kVp, mA, filtration, etc.). Problems associated with cadaver imaging include tissue shrinkage, body fluid pooling, air introduction to the gastrointestinal tract, collapse of the lungs, and general organ settling. Perhaps the greatest disadvantage, however, is that cadaver imaging will most likely not involve the use of CT tissue contrast agents needed for soft-tissue image segmentation.

Computed tomography is perhaps the imaging modality of choice for construction of full-body tomographic computational models. Skeletal tissues are more readily defined under CT imaging, whereas image distortions of skeletal tissues are problematic under MR imaging. With live patient imaging, CT contrast agents provide acceptable definitions of soft tissue borders needed for image segmentation, and thus MR does not offer a distinct advantage over CT for this data source. In cadaver imaging, the lack of contrast agents hinders border definitions for soft-tissue organs. To compensate, MR imaging of the cadaver might be considered. However, the frozen state of the cadaver tissues can alter both spin-lattice and spin-spin relaxation times (T_1 and T_2 , respectively), complicating and distorting MR images of the subject. Thus, CT imaging is recommended for both live and deceased subjects upon whom tomographic models are to be constructed. With continuing advances in multi-detector, multi-slice CT imaging, scan times are minimized, offering improved opportunities for live-subject imaging as potential data sources. CT-MR image fusion is another possibility for input data to image segmentation. However, patient motion artefacts within MR images, and their generally lower image resolutions, currently restrict opportunities for CT-MR co-registration to the head region where patient motion is more easily minimized.

Following image acquisition, the next step in model construction is image segmentation. In cases where the CT image provides strong tissue contrast, automated pixel-growing methods of image segmentation can be applied to rapidly delineate organ boundaries. In these methods, a central pixel is tagged and the algorithm groups all neighbouring pixels within a defined grey-level interval (e.g., skeletal regions, air lumen of nasal passages, certain soft-tissue organs under CT contrast). For those organs with poor tissue contrast, organ boundaries must be segmented manually. Final review of the tomographic model by medical personnel trained in radiographic anatomy

is highly recommended. Standardized software packages, such as IDL (Research Systems, Boulder, CO), can offer all necessary tools for construction of tomographic computational models.

5.4.2. Review of representative models

Several research groups have been involved in the development of tomographic computational models over the past decade. Most of the efforts have been directed towards adult models, but a few important studies have resulted in paediatric tomographic models for radiation dosimetry studies.

In 1994, Zubal and colleagues published their work in manually segmenting 129 CT transverse slices of a living male adult [77]. Their goal was to create a tomographic computational model for use in simulating nuclear medicine imaging data [78]. A total of 36 tissue regions were identified within the three-dimensional voxel array. The original CT images were obtained in two imaging sessions: one of 78 slices from the neck to mid-thigh with 10 mm slice thicknesses (pixel size of 1 mm), and one of 51 slices from the head to the neck region with 5 mm slices (pixel size of 0.5 mm). Image processing techniques were applied to achieve a final isotropic cubic voxel resolution of 4 mm on a side. Similar techniques also have been applied in the creation of a high-resolution, MRI-based voxel head model [79]. Stabin *et al.* have coupled the Zubal total-body model to the MCNP radiation transport code [80]. Yoriyaz *et al.* have reported estimates of cross-organ photon dose based on MCNP calculations within the Zubal model [81, 82]. Tagesson *et al.* used the segmented Zubal head model to estimate absorbed fractions and radionuclide *S* values for a variety of radiopharmaceuticals used in neuroimaging [83].

In 1997, Jones reported research performed at the NRPB on a voxel-based computational model of the adult (NORMAN) [84]. This model was used to estimate organ doses from external photon sources over a range of energies and irradiation geometries. When comparing the results with those obtained using a MIRD-type stylized model, differences in organ doses were found to range from a few per cent to over 100% at photon energies between 10 and 100 keV; differences were less than 20% at photon energies exceeding 100 keV. A subsequent study found that estimates of organ doses from internal photon sources differed widely as assessed using two different models, and differences in cross-organ doses generally increased with decreasing photon energy [85].

The National Library of Medicine's Visible Human Project also provides an excellent data source from which one may construct tomographic computational models for use in diagnostic X-ray simulations for adult patients. This data set consists of MRI, CT and anatomical images. The CT data consist of axial CT scans of the entire body taken at 1 mm intervals at a resolution of 512×512 pixels. Xu and his students have

recently reported on their efforts to merge this data set with both the MCNP and EGS4 radiation transport codes [86]. Computational results have been reported for internal electron sources [87], external photon sources [88], neutrons [89, 90] and electrons [91].

At present, three tomographic computational models have been constructed for specific use in paediatric dosimetry studies [92, 93]. Two of these are the **BABY** and **CHILD** models developed at GSF in Germany by Zankl and colleagues. **BABY** is constructed from a whole-body CT exam of an 8-week-old female 24 h after death. **CHILD** was constructed from a CT exam of a live 7-year-old female who was undergoing subsequent whole-body irradiation prior to bone marrow transplantation. Image segmentation was performed which assigned voxels to 54 regions in the baby and 64 regions in the child. The models have been used to determine paediatric organ doses in a variety of medical exposure scenarios including nuclear medicine [94], projection radiography [95–98] and computed tomography [99, 100]. The third paediatric model, **ADELAIDE**, is based upon 44 consecutive CT scans of a 14-year-old female [101]. This particular model is restricted to the torso only, and has been used with the EGS4 transport code to assess organ doses received during CT exams.

Recent efforts at GSF have resulted in a new adult reference male tomographic model, **GOLEM**. This model was segmented from whole-body medical images of a living 38-year-old male with external dimensions close to those of the ICRP Reference Man [102–105]. Recent German–Japanese collaborations also have been undertaken to establish a reference tomographic computational model for the adult Asian male [106].

5.4.3. Comparisons with stylized mathematical models

The obvious difference between tomographic and stylized mathematical models is the improved geometric descriptions of organ position, organ shape and body contour offered by the former. In estimating internal organ absorbed dose, however, only the absorbed fraction of energy and the target organ mass are of consequence. When the tomographic computational model results in estimates of the absorbed fractions and organ masses that are essentially equivalent to those in the stylized model, any improvement in anatomic description is of no consequence. When differences in dosimetry are noted, they must be considered in regard to the development of each model. As noted above, stylized models are generally constructed based upon estimates of average organ size and position as documented in ICRP Publication 23 for Reference Man or Reference Woman [14]. With a tomographic model, organ positions and locations can be very different inasmuch as the individual does not represent the average characteristics of reference subject populations. The tomographic model is highly patient specific to the individual that was imaged. When applied to other patients,

however, dosimetry data gathered from a single tomographic model could be less desirable than that obtained from a reference-stylized model, particularly when the current patient differs substantially from the tomographic model subject. Ideally, an entire series of whole-body tomographic computational models would be needed. Patient-specific estimates of internal organ doses could be made through selecting one of an array of tomographic models that best describes the current patient of interest.

Early attempts at the development of tomographic models were severely hindered by data storage and computer memory restrictions during radiation transport. At present, advances in computer hardware and software have all but eliminated these issues, except in extreme cases. Nevertheless, certain limitations of tomographic models over stylized models continue to exist that are of particular note. Voxel dimensions within tomographic models are initially restricted to those used in acquiring the image. Image slice interpolation algorithms subsequently may be applied to reduce voxel dimensions, although residual errors may persist as a result of partial-volume averaging within the original image data set. Small anatomic structures such as organ epithelial layers and GI mucosa may be missed altogether within the segmented regions of the tomographic model. For these structures, the simplicity of geometric representation within the stylized mathematical models is a distinct advantage. Peter *et al.* have recently reviewed problems related to discretization errors within tomographic computational models used in simulation studies of radiographic imaging [107].

One organ of particular importance to radionuclide therapy is the skeletal system. This anatomic region is particularly difficult to construct using stylized geometrical descriptions, and thus tomographic computational models offer a distinct advantage in providing macroscopic details of bone site contours, shapes and locations. Nevertheless, voxel dimensions are much larger than microscopic tissue sites of interest (marrow cavities, bone trabeculae, endosteal tissues, etc.). Consequently, microimaging technologies applied to *ex vivo* samples are necessary to produce usable images for charged-particle transport within trabecular regions of the skeleton [108]. Final assessment of marrow and endosteal tissue doses from photon sources external to the skeleton can be made via coupling of the photon transport within the whole-body tomographic computational model, while transport of photon-produced secondary electrons will invoke microscopic voxelized geometries of trabecular bone regions. Eckerman *et al.* have used this dual-transport technique for skeletal dosimetry utilizing (1) chord-based models of electron transport in trabecular bone, and (2) the ORNL-series of stylized models for photon transport [38]. Although no studies have been published to date, this overall dual-transport methodology can be extended to the use of macroscopic and microscopic tomographic models of the skeletal system. These concepts are discussed further in chapter 13.

5.5. SUMMARY

To some extent, mathematical formulations of organs and tissues of the body have been used in the dosimetry of internally distributed radionuclides for nearly 60 years. The concepts are not new ones. However, over this time, the sophistication of these 'phantoms' has increased significantly. This evolution began with the specification of a single organ mass, followed by the use of simple shapes to simulate organs or the entire body of an adult human. The ability to model the entire body of a 'Reference Man' and to specify the location, shape, volume and mass of organs in the body was the next logical step. These developments were followed almost immediately by the development of mathematical models for humans of other ages as well as attempts to model specific regions in important organs such as the kidneys and brain. Currently, anatomic models, based upon three-dimensional imaging techniques such as magnetic resonance imaging or computed tomography, are being widely developed and used for dosimetry. These techniques lend themselves to the design and specification of mathematical models representing the individual patient and, in addition, allow the definition of structures and/or regions in organs so that the distribution of the radionuclide can be better represented and the radiation-absorbed dose can be assessed more accurately.

REFERENCES

- [1] NCRP 1985 *The experimental basis for absorbed-dose calculations in medical uses of radionuclides* NCRP Report No 83 (Bethesda, MD: National Council on Radiation Protection and Measurements)
- [2] Marinelli L D 1942 Dosage determination with radioactive isotopes *Am. J. Roentgenol. Rad. Therapy* **47** 210–16
- [3] Marinelli L D, Quimby J H and Hine G J 1948 Dosage determination with radioactive isotopes II. Practical considerations in therapy and protection *Am. J. Roentgenol. Rad. Therapy* **59** 260–81
- [4] Loevinger R, Japha E M and Brownell G L 1965 Discrete radioisotope sources. In *Radiation Dosimetry* eds Hine G J and Brownell G L (New York: Academic) pp 693–799
- [5] Loevinger R, Hiolt J G and Hine G J 1965 Internally administered radionuclides. In *Radiation Dosimetry* eds Hine G J and Brownell G L (New York: Academic) pp 801–73
- [6] ICRP 1959 Report of committee II on permissible dose for internal radiation International Commission on Radiological Protection (Oxford: Pergamon)
- [7] Brownell G L, Ellett W H and Reddy A R 1968 MIRD Pamphlet No 3: Absorbed fractions for photon dosimetry *J. Nucl. Med. Suppl* 29–39
- [8] Fisher H L J and Snyder W S 1966 *Variation of dose delivered by ^{137}Cs as a function of body size from infancy to adulthood* ORNL-4007 (Oak Ridge, TN: Oak Ridge National Laboratory) pp 221–28

- [9] Fisher H L J and Snyder W S 1967 *Distribution of dose in the body from a source of gamma rays distributed uniformly in an organ* ORNL-4168 (Oak Ridge, TN: Oak Ridge National Laboratory) pp 245–57
- [10] Ellet W H, Callahan A B and Brownell G H 1964 Gamma-ray dosimetry of internal emitters: Monte Carlo calculations of absorbed dose from point sources *Brit. J. Radiol.* **37** 45–52
- [11] Ellet W H, Callahan A B and Brownell G H 1965 Gamma-ray dosimetry of internal emitters II: Monte Carlo calculations of absorbed dose from uniform sources *Brit. J. Radiol.* **38** 541–44
- [12] Snyder WS 1967 *The variation of dose in man from exposure to a point source of gamma rays* ORNL-4168 Oak Ridge National Laboratory Oak Ridge, TN 257–61
- [13] Snyder W S, Ford M R, Warner G G and Fisher Jr H L 1969 MIRD Pamphlet No 5: Estimates of absorbed fractions for monoenergetic photon sources uniformly distributed in various organs of a heterogeneous phantom *J. Nucl. Med.* **10** 1–52
- [14] ICRP 1975 *Report on the task group on Reference Man* ICRP Publication 23 (Oxford: International Commission on Radiological Protection)
- [15] ICRP 1979 *Limits for intakes of radionuclides by workers* Publication 30. International Commission on Radiological Protection (Oxford: Pergamon)
- [16] Snyder W S, Ford M R and Warner G G 1978 MIRD Pamphlet No 5, Revised: *Estimates of specific absorbed fractions for photon sources uniformly distributed in various organs of a heterogeneous phantom* (New York: Society of Nuclear Medicine)
- [17] Warner G G and Craig A N J 1968 *ALGAM: A computer program for estimating internal dose in a man phantom* ORNL-TM-2250 (Oak Ridge, TN: Oak Ridge National Laboratory)
- [18] Nelson W R, Hirayama R H and Rogers D W O 1985 *The EGS4 code system* SLAC Report 265 (Stanford, CA: Stanford Linear Accelerator Center)
- [19] Briesmeister J F 1993 *MCNP—a general Monte Carlo N-particle transport code, version 4A* LA-12625-M (Los Alamos, NM: Los Alamos National Laboratory)
- [20] Poston J W Jr, Kodimer K A, Bolch W E and Poston J W Sr 1996 Calculation of absorbed energy in the gastrointestinal tract *Health Phys.* **71** 300–6
- [21] Poston J W Jr, Kodimer K A, Bolch W E and Poston J W Sr 1996 A revised model for the calculation of absorbed energy in the gastrointestinal tract *Health Phys.* **71** 307–14
- [22] Kereiakes J G, Seltzer R A, Blackburn B and Saenger E L 1965 Doses to infants and children: a plea for a standard child *Health Phys.* **11** 999–1004
- [23] Poston J W 1990 The development of early pediatric models and their application to radiation absorbed dose calculations. In *Dosimetry of Administered Radionuclides* eds S J Adelstein, A I Kassis and R.W.B) (Washington, DC: American College of Nuclear Physicians) pp 105–21
- [24] Hwang J M L, Shoup R L, Warner G G and Poston J W 1976 *Mathematical description of a one- and five-year-old child for use in dosimetry calculations* ORNL/TM-5293 (Oak Ridge, TN: Oak Ridge National Laboratory)
- [25] Hwang J M L, Shoup R L and Poston J W 1976 *Mathematical description of a newborn human for use in dosimetry calculations* ORNL/TM-5453 (Oak Ridge, TN: Oak Ridge National Laboratory)
- [26] Jones R M, Poston J W, Hwang J L, Jones T D and Warner G G 1976 *The development and use of a fifteen-year-old equivalent mathematical phantom for internal dose calculations* ORNL/TM-5278 (Oak Ridge, TN: Oak Ridge National Laboratory)

- [27] Deus S F and Poston J W 1976 The development of a mathematical phantom representing a 10-year-old for use in internal dosimetry calculations. In *Proceedings of the Symposium on Radiopharmaceutical Dosimetry* HEW Publication (FDA) 76-8044 Oak Ridge, TN
- [28] Cristy M 1980 *Mathematical phantoms representing children of various ages for use in estimates of internal dose* ORNL/NUREG/TM-367 (Oak Ridge, TN: Oak Ridge National Laboratory)
- [29] Cristy M and Eckerman KF 1987 *Specific absorbed fractions of energy at various ages from internal photon sources* ORNL/TM-8381 (Oak Ridge, TN: Oak Ridge National Laboratory)
- [30] Loevinger R, Budinger T F and Watson E E 1991 *MIRD Primer for Absorbed Dose Calculations* (New York: The Society of Nuclear Medicine) p 128
- [31] Watson E E and Stabin M 1984 Basic alternative software package for internal radiation dose calculations. In *17th Midyear Topical Symposium of the Health Physics Society* eds R L Kathren, D P Higby and M A McKinney (Richland, WA)
- [32] Stabin M 1996 MIRDose: personal computer software for internal dose assessment in nuclear medicine *J. Nucl. Med.* **37** 538–46
- [33] Weber D A, Eckerman K F, Dillman L T and Ryman J C 1989 *MIRD: Radionuclide Data and Decay Schemes* (New York: Society of Nuclear Medicine)
- [34] ICRP 1983 *Radionuclide transformations* Publication 38 International Commission on Radiological Protection (Oxford: Pergamon)
- [35] Kocher D 1981 *Decay data tables* DOE TIC-11026 (Oak Ridge, TN: Oak Ridge National Laboratory)
- [36] Stabin M, Cristy M and Watson E E 1995 *Mathematical models of the adult female at various stages of pregnancy* ORNL/TM-12907 (Oak Ridge, TN: Oak Ridge National Laboratory)
- [37] Cloutier R J, Smith S A, Watson E E, Snyder W S and Warner G G 1973 Dose to the fetus from radionuclides in the bladder *Health Phys.* **25** 147–61
- [38] Eckerman K F 1985 Aspects of the dosimetry of radionuclides within the skeleton with particular emphasis on the active marrow. In *Proceedings of the Fourth International Radiopharmaceutical Dosimetry Symposium* eds A T Schlafke-Stelson and E E Watson (Oak Ridge, TN: ORAU) pp 514–34
- [39] Ellett W H and Humes R M 1971 MIRD Pamphlet No 8: Absorbed fractions for small volumes containing photon-emitting radioactivity *J. Nucl. Med.* 25–32
- [40] Siegel J A and Stabin M 1988 Absorbed fractions for electrons and beta particles in small spheres *J. Nucl. Med.* **29** 803
- [41] Siegel J A and Stabin M 1994 Absorbed fractions for electrons and beta particles in spheres of various sizes *J. Nucl. Med.* **35** 152–6
- [42] Coffey J L and Watson E E 1981 S-values for selected radionuclides and organs with the heart wall and heart contents as source organs. In *Third International Radiopharmaceutical Dosimetry Symposium* eds E E Watson, A T Schlafke-Stelson, J L Coffey and R J Cloutier (Rockville, MD: US Department of Health & Human Services) pp 563–94
- [43] Coffey J L 1978 *A revised mathematical model of the heart for use in radiation absorbed dose calculation* University of Tennessee, Knoxville, TN
- [44] Seltzer S M 1988 An overview of ETRAN Monte Carlo Methods. In *Monte Carlo Transport of Electrons and Photons* eds T M Jenkins, W R Nelson, A Rindi, A E Nahum and D W O Rogers (New York: Plenum) pp 153–81

- [45] Seltzer S M 1991 Electron-photon Monte Carlo calculations: the ETRAN code *Appl. Radiat. Isot.* **42** 917–41
- [46] Bouchet L G, Bolch W E, Weber D A, Atkins H L and Poston J W Sr 1999 MIRD Pamphlet No 15: Radionuclide *S* values in a revised dosimetric model of the adult head and brain *J. Nucl. Med.* **40** 62S–101S
- [47] London E D 1993 *Imaging Drug Action in the Brain* (Boca Raton, FL: CRC)
- [48] van Heertum R L and Tikofsky R S 1995 *Cerebral SPECT Imaging* (New York: Raven)
- [49] Blinkov S M and Glezer I I 1968 *The Human Brain in Figures and Tables* (New York: Plenum)
- [50] Petegnief Y, Petiet A, Peker M C, Bonnin F, Meulemans A and Le Guludec D 1998 Quantitative autoradiography using a radioimager based on a multiwire proportional chamber *Phys. Med. Biol.* **43** 3629–38
- [51] Willis K W, Martinez D A, Hedley-Whyte E T, Davis M A, Judy P F and Treves S 1977 Renal localization of ^{99m}Tc -stannous glucophetionate and ^{99m}Tc -stannous dimercaptosuccinate in the rat by frozen section autoradiography. The efficiency and resolution of technetium-99m *Radiat. Res.* **69** 475–88
- [52] Snyder W S and Ford M R 1967 *A dosimetric study for the administration of neohydrin labeled with ^{203}Hg and ^{197}Hg* ORNL-4168 (Oak Ridge, TN: Oak Ridge National Laboratory) pp 267–73
- [53] McAfee J G 1969 Problems in evaluating the radiation dose for radionuclides excreted by the kidneys. In *Medical Radionuclides: Radiation Dose and Effects* eds R J Cloutier, C L Edwards and W S Snyder (Oak Ridge, TN: US Atomic Energy Commission) pp 271–94
- [54] Blau M, McAfee J G, Roher R H, Snyder W S and Smith E M 1975 MIRD dose estimate No. 6: Hg-197- and Hg-203-labeled chlormerodrin *J. Nucl. Med.* **16** 1214–17
- [55] Patel J S 1988 *A revised model of the kidney for medical internal radiation dose* (College Station, TX: Texas A&M University)
- [56] Hui T Y E 1985 *A preliminary model of the circulating blood for use in radiation dose calculations* (College Station, TX: Texas A&M University)
- [57] Bouchet L G, Bolch W E, Blanco P, Rajon D A, Clairand I, Konijnnenberg M W and Wessels B W 2002 MIRD Pamphlet No 19: Absorbed fractions of energy and radionuclide *S* values for six pediatric multiregion models of the kidney (in press)
- [58] Boerman O C, Oyen W J and Corstens F H 2001 Between the Scylla and Charybdis of peptide radionuclide therapy: hitting the tumor and saving the kidney *Eur. J. Nucl. Med.* **28** 1447–9
- [59] Ford R L and Nelson W R 1978 *The EGS code system: computer programs for Monte Carlo simulation of electromagnetic cascade shower* Report 210 (Stanford: Stanford Linear Accelerator Center)
- [60] Stabin M 1994 A model of the prostate gland for use in internal dosimetry *J. Nucl. Med.* **35** 516–20
- [61] Mardirossian G, Tagesson M, Blanco P, Bouchet LG, Stabin M, Yoriyaz H, Baza S, Ljungberg M, Strand S E and Brill A B 1999 A new rectal model for dosimetry applications *J. Nucl. Med.* **40** 1524–31
- [62] Stubbs J B, Evans J F and Stabin M 1998 Radiation absorbed doses to the walls of hollow organs *J. Nucl. Med.* **39** 1989–95
- [63] Bhuiyan N U 2000 *A revised dosimetric model for calculation of electron dose in the small intestine* (College Station, TX: Texas A&M University)

- [64] Watson E E, Stabin M, Davis J L and Eckerman K F 1989 A model of the peritoneal cavity for use in internal dosimetry *J. Nucl. Med.* **30** 2002–11
- [65] Deloar H M, Watabe H, Nakamura T, Narita Y, Yamadera A, Fujiwara T and Itoh M 1997 Internal dose estimation including the nasal cavity and major airway for continuous inhalation of $C^{15}O_2$, $^{15}O_2$ and $C^{15}O$ using the thermoluminescent dosimeter method *J. Nucl. Med.* **38** 1603–13
- [66] Clairand I, Bouchet L G and Bolch W E 2000 A new macroscopic model of the long bones for skeletal dosimetry *J. Nucl. Med.* **41** 1062
- [67] Snyder W S, Ford M R, Warner G G and Watson S B 1975 MIRD Pamphlet No 11: 'S,' absorbed dose per unit cumulated activity for selected radionuclides and organs (New York: Society of Nuclear Medicine)
- [68] Clairand I, Bouchet L G, Ricard M, Durigon M, Di Paola M and Aubert B 2000 Improvement of internal dose calculations using mathematical models of different adult heights *Phys. Med. Biol.* **45** 2771–85
- [69] de la Grandmaison G L, Clairand I and Durigon M 2001 Organ weight in 684 adult autopsies: new tables for a Caucasoid population *Forensic Sci. Int.* **119** 149–54
- [70] Clairand I, Ricard M, Gouriou J, Di Paola M and Aubert B 1999 DOSE3D: EGS4 Monte Carlo code-based software for internal radionuclide dosimetry *J. Nucl. Med.* **40** 1517–23
- [71] Johnson T K, McClure D L, McCourt S L, Andl G J and Berman B D 1998 MABDOSE: A computer program for the calculation of dose. In *Proceedings of the Sixth International Radiopharmaceutical Dosimetry Symposium* ed A T Schlafke-Stelson (Oak Ridge, TN: ORAU)
- [72] Johnson T K 1988 MABDOSE: A generalized program for internal radionuclide dosimetry *Comput. Meth. Progr. Biomed.* **27** 159–67
- [73] Johnson T K, McClure D and McCourt S 1999 MABDOSE. I: Characterization of a general purpose dose estimation code *Med. Phys.* **26** 1389–95
- [74] Johnson T K, McClure D and McCourt S 1999 MABDOSE. II: Validation of a general purpose dose estimation code *Med. Phys.* **26** 1396–403
- [75] Johnson T K and Colby S B 1993 Photon contribution to tumor dose from considerations of ^{131}I radiolabeled antibody uptake in liver, spleen, and whole body *Med. Phys.* **20** 1667–74
- [76] Kawrakow I 2000 Accurate condensed history Monte Carlo simulation of electron transport. I. EGSnrc, the new EGS4 version *Med. Phys.* **27** 485–98
- [77] Zubal I G, Harrell C R, Smith E O, Rattner Z, Gindi G and Hoffer P B 1994 Computerized 3-dimensional segmented human anatomy *Med. Phys.* **21** 299–302
- [78] Zubal I G and Harrell C R 1992 Voxel based Monte Carlo calculations of nuclear medicine images and applied variance reduction techniques *Image Vision Comput.* **10** 342–48
- [79] Zubal I G, Harrell C R, Smith E O, Smith A L and Krischlunas P 1996 High resolution, MRI-based, segmented, computerized head phantom. In *Proceedings of the Sixth International Radiopharmaceutical Dosimetry Symposium* eds A T S-Stelson, M Stabin and R B Sparks (Oak Ridge, TN: ORAU) pp 319–24
- [80] Stabin M, Yoriyaz H, Brill A B and Dawant M 1999 Monte Carlo calculation of dose conversion factors for a new generation of dosimetry phantoms *J. Nucl. Med.* **40** 310P–11P
- [81] Yoriyaz H, dos Santos A, Stabin M and Cabezas R 2000 Absorbed fractions in a voxel-based phantom calculated with the MCNP-4B code *Med. Phys.* **27** 1555–62

- [82] Stabin M and Yoriyaz H 2001 Photon specific absorbed fractions calculated in the trunk of an adult male voxel-based phantom *Health Phys.* **82** 21–44
- [83] Tagesson M, Zubal I G, Ljungberg M and Strand S E 1996 S values for subregions in the brain. In *Proceedings of the Sixth International Radiopharmaceutical Dosimetry Symposium* eds A T S-Stelson, M Stabin and R B Sparks (Oak Ridge, TN: ORAU) pp 325–30
- [84] Jones D G 1997 A realistic anthropomorphic phantom for calculating organ doses arising from external photon irradiation *Radiat. Prot. Dosim.* **72** 21–29
- [85] Jones D G 1998 A realistic anthropomorphic phantom for calculating specific absorbed fractions of energy deposited from internal gamma emitters *Radiat. Prot. Dosim.* **79** 411–14
- [86] Xu X G, Chao T C and Bozkurt A 2000 VIP-Man: an image-based whole-body adult male model constructed from color photographs of the Visible Human Project for multi-particle Monte Carlo calculations *Health Phys.* **78** 476–86
- [87] Chao T C and Xu X G 2001 Specific absorbed fractions from the image-based VIP-Man body model and EGS4-VLSI Monte Carlo code: internal electron emitters *Phys. Med. Biol.* **46** 901–27
- [88] Chao T C, Bozkurt A and Xu X G 2001 Conversion coefficients based on the VIP-Man anatomical model and EGS4 *Health Phys.* **81** 163–83
- [89] Bozkurt A, Chao T C and Xu X G 2000 Fluence-to-dose conversion coefficients from monoenergetic neutrons below 20 MeV based on the VIP-man anatomical model *Phys. Med. Biol.* **45** 3059–79
- [90] Bozkurt A, Chao T C and Xu X G 2001 Fluence-to-dose conversion coefficients based on the VIP-Man anatomical model and MCNPX code for monoenergetic neutrons above 20 MeV *Health Phys.* **81** 184–202
- [91] Chao T C, Bozkurt A and Xu X G 2001 Organ dose conversion coefficients for 0.1–10 MeV electrons calculated for the VIP-Man tomographic model *Health Phys.* **81** 203–14
- [92] Zankl M, Veit R, Petoussi N, Mannweiler E, Wittmann A and Drexler G 1994 Realistic computerized human phantoms *Life Sci. Space Res.* **14** 423–31
- [93] Zankl M, Veit R, Williams G, Schneider K, Fendel H, Petoussi N and Drexler G 1988 The construction of computer tomographic phantoms and their application in radiology and radiation protection *Radiat. Environ. Biophys.* **27** 153–64
- [94] Petoussi-Henß N and Zankl M 1998 Voxel anthropomorphic models as a tool for internal dosimetry *Radiat. Prot. Dosim.* **79** 415–18
- [95] Petoussi-Henß N, Panzer W, Zankl M and Drexler G 1995 Dose–area product and body doses *Radiat. Prot. Dosim.* **57** 363–66
- [96] Veit R and Zankl M 1992 Influence of patient size on organ doses in diagnostic radiology *Radiat. Prot. Dosim.* **43** 241–43
- [97] Veit R and Zankl M 1993 Variation of organ doses in pediatric radiology due to patient diameter calculated with phantoms of varying voxel size *Radiat. Prot. Dosim.* **49** 353–56
- [98] Zankl M 1993 Computational models employed for dose assessment in diagnostic radiology *Radiat. Prot. Dosim.* **49** 339–44
- [99] Kalender W A, Schmidt B, Zankl M and Schmidt M 1999 A PC program for estimating organ dose and effective dose values in computed tomography *Eur. Radiol.* **9** 555–62
- [100] Zankl M, Panzer W, Petoussi-Henß N and Drexler G 1995 Organ doses for children from computer tomographic examinations *Radiat. Prot. Dosim.* **57** 393–96

- [101] Caon M, Bibbo G and Pattison J 1999 An EGS4-ready tomographic computational model of a 14-year-old female torso for calculating organ doses from CT examinations *Phys. Med. Biol.* **44** 2213–25
- [102] Smith T, Petoussi-Henss N and Zankl M 2000 Comparison of internal radiation doses estimated by MIRD and voxel techniques for a ‘family’ of phantoms *Eur. J. Nucl. Med.* **27** 1387–98
- [103] Smith T J, Phipps A W, Petoussi-Henss N and Zankl M 2001 Impact on internal doses of photon SAFs derived with the GSF adult male voxel phantom *Health Phys.* **80** 477–85
- [104] Zankl M, Panzer W and Herrmann C 2000 Calculation of patient doses using a human voxel phantom of variable diameter *Radiat. Prot. Dosim.* **90** 155–58
- [105] Zankl M and Wittmann A 2001 The adult male voxel model ‘Golem’ segmented from whole-body CT patient data *Radiat. Environ. Biophys.* **40** 153–62
- [106] Saito K, Wittmann A, Koga S, Ida Y, Kamei T, Funabiki J and Zankl M 2001 Construction of a computed tomographic phantom for a Japanese male adult and dose calculation system *Radiat. Environ. Biophys.* **40** 69–75
- [107] Peter J, Tornai M P and Jaszczek R J 2000 Analytical versus voxelized phantom representation for Monte Carlo simulation in radiological imaging *IEEE Trans. Med. Imaging* **19** 556–64
- [108] Jokisch D W, Bouchet L G, Patton P W, Rajon D A and Bolch W E 2001 Beta-particle dosimetry of the trabecular skeleton using Monte Carlo transport within 3D digital images *Med. Phys.* **28** 1505–18

Chapter 6

Monte Carlo codes for use in therapeutic nuclear medicine

Michael Stabin and Habib Zaidi

6.1. INTRODUCTION

The Monte Carlo method is widely used for solving problems involving statistical processes and is very useful in medical physics due to the stochastic nature of radiation emission, transport and detection processes. The method is very useful for complex problems that cannot be modelled by computer codes using deterministic methods or when experimental measurements may be impractical. However, due to computer limitations, the method has not yet fully lived up to its potential. With the advent of high-speed supercomputers, the field has received increased attention, particularly with parallel algorithms and high performance platforms, which have much higher execution rates. Recent advances in computer hardware and software have lowered, if not removed, the barriers to wider acceptance of Monte Carlo calculations by life scientists.

Many Monte Carlo programs have been in use in the field of nuclear imaging, internal dosimetry and treatment planning with many of them available in the public domain [1, 2]. Those Monte Carlo software packages are excellent research tools; however, becoming familiar with the codes can be time consuming, and most codes are not completely free of bugs. Moreover, the simulation package must be integrated in the local software environment. For that purpose, modifications may be necessary, which require a detailed working knowledge of the code structure. This chapter summarizes state-of-the-art developments of widely used Monte Carlo codes in therapeutic nuclear medicine in connection with computing facilities available for routine and research applications. Current trends and some strategies for future development in the field will also be discussed.

6.2. HISTORICAL DEVELOPMENTS

The ‘Monte Carlo method’ describes a very broad area of science, in which many processes, physical systems and phenomena are simulated by statistical methods employing random numbers (see chapter 1). In the specific application of interest here, the transport of ionizing radiation particles is simulated by creation of particles or rays from a defined source region, generally with random initial orientation in space, with tracking of the particles as they travel through the system, sampling the probability density functions (pdfs) for their interactions to evaluate their trajectories and energy deposition at different points in the system. The interactions determine the penetration and motion of particles but, more importantly, the energy deposited during each interaction gives the radiation absorbed dose, when divided by the appropriate values of mass. With sufficient numbers of interactions, the mean absorbed dose at points of interest will be given with acceptable uncertainties. The central issues include how well the real system of interest can be simulated by a geometrical model, how many histories (i.e., how much computer time) are needed to obtain acceptable uncertainties (usually around 5%, no more than 10%), and how measured data can be used to validate the theoretical calculations.

In the general sense, a problem that can be treated by a Monte Carlo method is determined by a set of parameters that in aggregate determine completely the behaviour of an element of the system in all situations modelled within that system. Specifically, in applications of Monte Carlo in therapeutic nuclear medicine, we are interested in modelling the creation and interaction of all particles (speaking somewhat imprecisely, as photons, which are of high interest in this situation, are best described as waves rather than as particles) throughout their ‘lifetime’ in the body. Particles are generally ‘created’ at random positions within a source region (which might be an entire organ or some smaller structure), with defined initial orientations, and then travel random distances before interacting with atoms within the tissues of the body and depositing energy in these interactions, and eventually being absorbed completely or escaping the body. A complete characterization of the source will include its spatial distribution, the angular distribution of its emission spectrum (most often random in 4π space, unless some unique situation exists which restricts the orientation of the emissions—this is more common in situations involving external sources, which may be collimated or shielded in certain ways), and its energy distribution. Once a particle is created and begins its journey away from the source location, the three-space location of the first interaction must be chosen. This is done by sampling the known probability distributions for its interactions with atoms in the body. The probabilities of interaction for photons are very well known—photoelectric, Compton, and pair production events occur with well defined

probabilities in materials of different atomic number. Specification of the atomic number composition of the spatial regions involved in the simulation will thus permit the characterization of the probability distributions for interaction in any location, which can be sampled using random number generators, as described elsewhere in this text. The process can be computationally intensive, as 'ray tracing', or calculation of projection paths to the geometric limits of defined spatial regions, can involve many calculations. 'Russian roulette' routines with fictitious particles [3] were developed to provide a shortcut method to an equivalent result. With the development of faster and faster computers, computational speed has become a less important issue. Groups of individual interactions are generally treated in 'steps' by the computer, and application of known interaction types and probabilities is more complicated. Good electron transport algorithms are considerably more difficult to implement than photon transport algorithms. Many individual codes have been developed with individualized Monte Carlo routines to model *photon* transport and attenuation in shields, the human body, etc. On the other hand, only a handful of Monte Carlo codes have been developed that truly model *electron* transport, and only a few of them have produced widely accepted results. In a number of applications in the human body, it is acceptable to assume that electrons do not need to be transported, i.e., that photoelectrons or emitted electrons and β particles are absorbed exactly where they are created. In many other applications, particularly in therapy, it is important to know the spatial distribution of electron dose, and so electron transport is needed.

Application of Monte Carlo processes to model any system of even moderate complexity is not possible without the use of a computer. Tables of random digits were printed in the years before the widespread availability of computing resources to the average researcher or student. Use of such tables to sample source emissions and particle interactions would be, of course, laborious and tedious to the extreme, without the possibility of generating any meaningful results in a reasonable time frame. Therefore, Monte Carlo methods did not really reach any prominence in serious scientific inquiry until computing resources became available to the general scientific community. Computing power is now quite vast; computers that in the 21st century sit on our desktops hold more power than was made available by computing systems of just a few decades ago that filled entire rooms. Large dedicated workstations and distributed computing networks continue to increase available and inexpensive computing power by orders of magnitude every few years. Currently, therefore, the ability of the investigator to model microscopic (e.g., radiation transport) or macroscopic (e.g., weather patterns) processes is limited only by his imagination, and by the availability of well defined pdfs which apply to the situation to be modelled.

6.2.1. The 'Reference Man' phantoms and the ALGAMP code

The first real treatment of internal dose assessment was done in the Manhattan project, developed by K Z Morgan, W Snyder, and others [4]. Their focus was on the protection of radiation workers and, to a degree, the general public, from the production and use of radioactive materials, in particular in relation to the war effort. They did not, however, employ Monte Carlo methods in these calculations. Their model of the human body and each of its parts was a simple homogeneous spherical construct, in which electrons were completely absorbed and for which photon absorption could be modelled by a simple analytical expression, knowing the absorption coefficient for the organ or tissue of interest. More specifically, for soft tissue, bone, lung, or any mixture thereof (such as the whole body), the photon absorbed fraction for an organ irradiating itself is given as $(1 - e^{-\mu r})$, where μ is the absorption coefficient for the tissue composition of interest and r is the assigned effective radius of the object. This information was developed for the very large number of radionuclides of interest to radiation safety at that time—products of the fission process, activation products from neutron interactions in the structural and other materials in the reactors, and others. The results were given in the context of a system of radiation protection guidelines for workers, i.e., amounts of permissible intake of each radionuclide per working year (given permissible dose limits), and permissible concentrations in air and water (given the intake limits and assumptions about standard breathing and drinking rates) [4].

The first breakthrough in the use of Monte Carlo methods was the development of the Fisher-Snyder heterogeneous, hermaphrodite, anthropomorphic model of the human body in the 1970s [5]. This model, or 'phantom', consisted of spheres, ellipsoids, cones, tori, and subsections of such objects, combined to approximate the geometry of the body and its internal structures. For the majority of cases, electron energy was assumed to be absorbed where created (exceptions included hollow organs with separate wall and contents sections, and the bone and marrow, in which 'crossfire' between adjacent regions can occur due to the small dimensions of the regions). For photons, Monte Carlo methods were developed using a computer code called ALGAM [6], which created photons at random positions within any 'source' region (organ or tissue assumed to be contaminated with radioactivity), gave these photons a random orientation in 4π space, and then followed them through various Compton and photoelectric interactions (pair productions events were quite rare, as starting energies did not exceed 4 MeV) until the photon reached a certain critical low ('cut-off') energy and was assumed to be locally absorbed, or until it escaped the surface of the body (at which point the probability of scatter from an air molecule and redirection towards the body was assumed to be negligibly low). With repeated sampling of the source, which in this time generally involved only

tens of thousands of trials (histories), a statistical average behaviour of particles originating in this source could be obtained for other regions of the body of interest to radiation dose assessment ('target' regions). This behaviour was reported as the fraction of energy emitted in the source that was absorbed in a target (absorbed fraction, AF), with an associated uncertainty (reported as the coefficient of variation). These AFs were thus a considerable improvement over the values given in ICRP Publication 2 [4], as the organ geometries were more realistic, and, more importantly, the organs could irradiate each other, whereas in the ICRP 2 model an organ could irradiate only itself. These AFs were used later by the ICRP in updated assessments for workers; of more interest in this text is that they found more immediate application in dose assessments for nuclear medicine patients, thanks to the monumental efforts of the newly formed Medical Internal Radiation Dose (MIRD) Committee of the Society of Nuclear Medicine. In a flurry of publications in its early years, this committee published decay data, methods for kinetic analyses, the AFs from the ALGAM calculations, dose conversion factors for over 100 nuclides of interest to nuclear medicine, dose calculations for various radiopharmaceuticals, methods for small scale dose calculations with electrons, and other interesting practical scientific documents.

The original phantom developed was intended mainly to represent a healthy average adult male, which well characterized the working population of its time. As noted above, the phantom did have both male and female organs (naturally with no cross-irradiation terms given!), but most structures represented the organs of 'Reference Man', as defined by the ICRP from an extensive range of medical and other literature, restricted primarily to European and North American populations. Both due to the makeup of the nuclear medicine population and the diversifying worker population, the need for other phantoms arose. In 1987, Cristy and Eckerman [7] of Oak Ridge National Laboratory (ORNL) developed a series of phantoms representing children of different ages, one of which (the 15-year-old) also served as a model for the adult female. AFs for these phantoms were developed using the ALGAMP code ('P' signifying a 'parametrized' version of the code—allowing substitution of parameters giving the radii and positions of the various organs at different ages). These values were published in an ORNL document, but never officially adopted in the MIRD or other peer-reviewed literature. Nonetheless, they were widely accepted and used for dose calculations in different age individuals. In 1995, Stabin *et al.* [8] released a set of phantoms representing the adult female at different stages of gestation, to satisfy the need to calculate radiation doses to the foetus from nuclear medicine and other applications. These calculations were also done with the ALGAMP code.

Other models were developed by independent investigators to represent certain organs or organ systems not included in these phantoms, including

subregions of the brain [9, 10], the eye [11], the peritoneal cavity [12], the prostate gland [13], bone and marrow [14, 15], rectum [16], spheres of varying size [17, 18], and others.

6.2.2. *Development of MIRDose codes*

The MIRDose computer program [19] was originally developed by Dr. Stabin to eliminate the tedium of repetitive internal dose calculations (looking up dose conversion factors from tables and adding contributions from every source to every target, even if of minor importance) to automate the calculation of organ doses in nuclear medicine. The original code was developed in 1983 on a Tektronix stand-alone workstation, which had 32k of total memory and storage limited to 8 inch soft disks. This version (MIRDose 1) was never distributed. In its second incarnation in about 1985, MIRDose 2, the code was rewritten to be usable on the IBM Personal Computer, which was rapidly growing in popularity. The code employed 59 radionuclides, and had available the AFs from the Cristy/Eckerman phantom series. Users entered cumulated activities for the source organs involved, and obtained dose estimates for chosen target organs, with contributions from all source organs included, and appropriate 'remainder of the body' corrections [20] applied.

The MIRDose3 code represented the migration of the MIRDose code from the DOS to the Windows environment. Written in the Microsoft Visual Basic[®] environment, users could select from a menu of over 200 radionuclides, whose decay data can be used with absorbed fractions from any of 10 phantoms (the six Cristy/Eckerman paediatric phantoms and the four phantoms representing the nonpregnant or pregnant adult female). The user entered residence times [21] for all source organs involved, and the program calculated and applied the appropriate *S* values to obtain organ dose estimates (for all available, not selected, target regions). The program also provided calculation of the ICRP-defined effective dose equivalent [22] and effective dose [23]. The software thus facilitated dose calculations under different conditions, in different phantoms, etc. The program has been used to calculate dose estimates for a variety of nuclear medicine compounds, and its use is widely cited in the literature.

The evolution of the MIRDose software continues today. In order to provide more computer platform independence, Dr. Stabin recently rewrote the MIRDose code entirely in the Java language and incorporated a curve-fitting algorithm for kinetic data developed by Dr. Sparks [24]. Java is compiled on each machine before execution, thus allowing the code to be used on Unix, Macintosh, Windows NT and other platforms. The code was renamed 'OLINDA' (Organ Level Internal Dose Assessment), partly to distinguish it from the activities of the MIRD Committee (which had expressed concern that the name MIRDose might imply that it was a

product of that committee), and partly to integrate the name into a new unified system of internal and external dose assessment. This unified system is deployed on an Internet website for rapid electronic access [25]. This site, called the RADiation Dose Assessment Resource (RADAR), provides decay data for over 800 radionuclides, absorbed fractions for all available stylized phantoms and some voxel phantoms, kinetic data, dose factors (for all phantoms and nuclides), risk information, and other data via electronic transfer to users worldwide.

6.3. PUBLIC DOMAIN MONTE CARLO CODES

Table 6.1 lists widely used public domain Monte Carlo codes together with a short description of their key features. Most of the packages mentioned below run virtually on different platforms and operating systems and are available free of charge from the authors or through the official channels (RSIC or NEA).

6.3.1. *The EGS code*

The electron gamma shower (EGS) computer code system is a general-purpose package for Monte Carlo simulation of the coupled transport of electrons and photons in an arbitrary geometry for particles with energies from a few keV up to several TeV [26]. The code represents the state-of-the-art of radiation transport simulation because it is very flexible, well documented and extensively tested. Some have referred to the EGS code as the *de facto* gold standard for clinical radiation dosimetry. EGS is written in MORTRAN, a FORTRAN pre-processor with powerful macro capabilities. EGS is a ‘class II’ code that treats knock-on electrons and bremsstrahlung photons individually. Such events require pre-defined energy thresholds and pre-calculated data for each threshold, determined with the cross-section generator PEGS.

6.3.2. *The MCNP code*

MCNP is a general-purpose Monte Carlo code that can be used for neutron, photon, electron, or coupled neutron/photon/electron transport [28]. The code treats an arbitrary three-dimensional configuration of materials in geometric cells bounded by first- and second-degree surfaces and fourth-degree elliptical tori. For photons, the code takes account of incoherent and coherent scattering, the possibility of fluorescent emission after photoelectric absorption, absorption in pair production with local emission of annihilation radiation, and bremsstrahlung. Electron transport in MCNP is based on the ETRAN system as in ITS where a condensed random walk

Table 6.1. Key features of public domain Monte Carlo codes used in therapeutic nuclear medicine applications.

MC code	General description
ALGAM [6]	Monte Carlo calculations using the OGRE system are employed for photon transport. The user can specify a source arbitrarily through a subroutine. Simulation for internal dosimetry calculations is specifically included.
MIRDOS [19]	Dose calculations based on Monte Carlo pre-calculated specific absorbed fractions for 10 phantom models using the ALGAMP code.
EGS4 [26]	Coupled photon/electron transport in any material through user-specified geometries. Simulation for internal dosimetry calculations is not specifically included and requires an extensive amount of user programming in Mortran.
ITS including TIGER CYLTRAN and ACCEPT [27]	Coupled photon/electron transport in any material through slabs, cylinders or combinatorial. Simulation for internal dosimetry calculations is not specifically included and requires an extensive amount of user programming in Fortran.
MCNP [28]	Coupled neutron/photon/electron transport in any material through user-generalized geometry. Simulation for internal dosimetry calculations is not specifically included and requires an extensive amount of user manipulation of input data files to model complex geometries.
GEANT [29]	Coupled photon/electron transport in any material through combinatorial geometry. Simulation for internal dosimetry calculations not specifically included and requires an extensive amount of user programming in C++ (GEANT 4).
ETRAN [30]	Coupled photon/electron transport in plane-parallel slab targets that have a finite thickness in one dimension and are unbound in the other two dimensions. Simulation for internal dosimetry calculations is not specifically included and requires an extensive amount of user manipulation of input data files to model complex geometries.

based on accepted multiple-scattering theories is implemented. Important features that make MCNP very versatile and easy to use include a powerful general source, criticality source, and surface source; both geometry and output tally plotters; a rich collection of variance reduction techniques; a flexible tally structure; and an extensive collection of cross-section data.

6.3.3. The ETRAN code

ETRAN computes the transport of electrons and photons through plane-parallel slab targets that have a finite thickness in one dimension and are unbound in the other two dimensions [30]. The incident radiation can consist of a beam of either electrons or photons with specified spectral and

directional distribution. Options are available by which all orders of the electron–photon cascade can be included in the calculation. Thus electrons are allowed to give rise to secondary knock-on electrons, continuous bremsstrahlung and characteristic X-rays; and photons are allowed to produce photo-electrons, Compton electrons, and electron–positron pairs. Annihilation quanta, fluorescence radiation, and Auger electrons are also taken into account. According to user specifications, the Monte Carlo histories of all generations of secondary radiations are followed.

6.3.4. *ITS*

The Integrated TIGER Series (ITS) of coupled electron/photon Monte Carlo transport codes is a powerful tool for determining state-of-the-art descriptions of the production and transport of the electron/photon cascade in time-independent, multi-material, multi-dimensional environments [27]. ITS is a collection of programs sharing a common source code library that can solve sophisticated radiation transport problems. A total of eight codes are in the collection which can be split into six groups: the TIGER codes (for one-dimensional slab geometries), the CYLTRAN codes (for two-dimensional cylindrical geometries), the ACCEPT codes (for arbitrary three-dimensional geometries), the standard codes (for normal applications), the P codes (for applications where enhanced ionization/relaxation procedures are needed), and the M codes (for applications which involve two- or three-dimensional macroscopic electromagnetic fields). The user selects the appropriate code from the library and supplies it with any special requirements and the physical description of the problem to be solved in an input file.

6.3.5. *The GEANT code*

The GEANT package was originally designed for high-energy physics experiments, but has found applications also outside this domain in the areas of medical and biological sciences, radiation protection and astronautics [29]. The main applications of GEANT are the transport of particles through an experimental setup for the simulation of detector response and the graphical representation of the setup and of the particle trajectories. The two functions are combined in the interactive version of GEANT. The code has been rewritten in C++ and exploits advanced software-engineering techniques and object-oriented technology to achieve transparency (GEANT 4).

6.3.6. *Other Monte Carlo codes*

Many other codes have been developed or adapted by users to match their specific needs. Interesting initiatives include the so-called ‘all-particle method’ [31] and EPIC (electron–photon three-dimensional Monte Carlo

transport) codes planned to be developed at the Lawrence Livermore National Laboratory (LLNL), which houses the world's most extensive nuclear and atomic cross section database that parametrizes the interactions of photons, electrons/positrons, neutrons, protons, and other heavy charged particles [32]. These planned codes never received any support, and as such were shelved and were never ready for public release. Among the codes that have received considerable attention during the past few years is PENELOPE, which performs Monte Carlo simulation of coupled electron–photon transport in arbitrary materials and complex quadric geometries [33]. A mixed procedure is used for the simulation of electron and positron interactions, in which ‘hard’ events (i.e., those with deflection angle and/or energy loss larger than pre-selected cut-offs) are simulated in a detailed way, while ‘soft’ interactions are calculated from multiple scattering approaches. The mixed simulation algorithm for electrons and positrons implemented in PENELOPE reproduces the actual transport process to a high degree of accuracy and is very stable even at low energies. This is partly due to the use of a sophisticated transport mechanics model based on the so-called random hinge method, with energy-loss corrections for soft events. Other differentiating features of the simulation are a consistent description of angular deflections in inelastic collisions and of energy-loss straggling in soft stopping events. Binding effects and Doppler broadening in Compton scattering are also taken into account. FLUKA is another ambitious fully integrated all-particle Monte Carlo simulation package [34]. At the beginning, electron–photon transport was the same as EGS, but the code has evolved in a very different direction during the past few years. The code looks promising and is now available from the authors upon request.

6.4. LIMITATIONS OF CURRENT NUCLEAR MEDICINE DOSE CALCULATIONS

6.4.1. *Introduction*

Currently, and for the past 20–30 years, internal dose calculations for nuclear medicine have used the standardized hermaphroditic phantoms with stylized geometries (spheres, ellipsoids, cylinders, etc.) described above to represent the major organs, skeletal system, whole body, and bone marrow of ‘Reference Man’ (70 kg), ‘Reference Woman’ (57 kg), and ‘Reference’ children and pregnant women. Doses calculated using these models do not include the detail needed for accurate assessment of risks in therapeutic administrations of radiopharmaceuticals and their results have been shown to be poor predictors of marrow radiotoxicity. These models give only average dose to whole organs (not dose distributions within organs or tissues with possibly nonuniform activity distributions) and the reported dose is applicable only to a

Table 6.2. Radiation dose estimates for the reference adult for ^{99m}Tc glucoheptonate.

Organ	Estimated radiation dose	
	mGy/MBq	rad/mCi
Kidneys	4.4×10^{-2}	1.6×10^{-1}
Liver	3.2×10^{-3}	1.2×10^{-2}
Lungs	1.7×10^{-3}	6.2×10^{-3}
Ovaries	5.5×10^{-3}	2.0×10^{-2}
Red marrow	2.5×10^{-3}	9.1×10^{-3}
Testes	3.7×10^{-3}	1.4×10^{-2}
Urinary bladder wall	7.4×10^{-2}	2.7×10^{-1}
Effective dose equivalent	1.0×10^{-2} mSv/MBq	3.8×10^{-2} rem/mCi
Effective dose	7.4×10^{-3} mSv/MBq	2.8×10^{-2} rem/mCi

person whose size and weight are close to that of the reference individual after which the model was derived. Thus the doses reported with such models really represent the dose to a *phantom*, not to a *patient*. If the biokinetic data to be applied were taken from the actual patient, then these data are patient specific. In diagnostic applications in nuclear medicine, usually a standardized kinetic model is also applied. Typically results are shown in table 6.2.

These dose estimates are based on a standard kinetic model for glucoheptonate, and AFs for the adult male phantom in the Cristy/Eckerman phantom series. If one were to use patient-specific biokinetic data for a nuclear medicine therapy agent with this same phantom, the result would be the same as in table 6.2 (except that effective dose quantities may not be used in therapy applications). One can make the dose estimates more patient specific through mass-based adjustments to the organ doses:

- Absorbed fractions for electrons and alphas scale linearly with mass.
- Absorbed fractions for photons scale with mass to a power of $1/3$.

One generally cannot:

- Account for patient-specific differences in organ geometry.
- Account for patient-specific marrow characteristics.
- Calculate dose distributions within organs.

To perform real patient-specific dose calculations, one needs a patient-specific physical model to be used with patient-specific biokinetic data. A 'one-dose-fits-all' approach to radiation therapy with these internal emitter treatments is not likely to be effective (due to the narrow range between tumour ablation and bone marrow toxicity). Individual patients not only have significantly different uptake and retention half-times of activity of

the radioactive agent, but also have significantly different physical characteristics and radiosensitivities. Many cancer patients have failed other treatments, and may enter radiotherapy with compromised marrow due to their previous treatments. Thus, their therapies should be optimized, taking into account individual parameters as much as is possible.

If one were to approach the radiation oncologist or medical physicist in an external beam therapy program and suggest that all patients with a certain type of cancer should receive exactly the same treatment schedule (beam type, energy, beam exposure time, geometry, etc.), the idea would certainly be rejected as not being in the best interests of the patient. Instead, a patient-specific treatment plan would be implemented in which treatment times are varied to deliver the same radiation dose to all patients. Patient-specific calculations of doses delivered to tumours and normal tissues have been routine in external beam radiotherapy and brachytherapy for decades. The routine use of a fixed GBq/kg, GBq/m², or simply GBq, administration of radionuclides for therapy is equivalent to treating all patients in external beam radiotherapy with the same treatment schedule. Varying the treatment time to result in equal absorbed dose for external beam radiotherapy is equivalent to accounting for the known variation in patients' physical characteristics, and radionuclide biokinetics to achieve similar tumour doses in internal-emitter radiotherapy, while watching the doses received by healthy tissues.

6.5. IMPROVEMENTS IN MODELS FOR NUCLEAR MEDICINE THERAPY

6.5.1. *Current approaches to patient-specific dose calculations*

In radionuclide therapy of cancer, the practice of managing patient therapy varies considerably, with some methods being based on patients' radiation doses and others focusing only on administered activity. In the dose-based methods, both biokinetic data and dose conversion factors may be individualized, in lieu of using published, standardized data. The subject's actual biokinetic data are usually used, at least when performing clinical trials for the purpose of establishing the dosimetry in a new agent; in routine clinical practice, such data are not often gathered. This places limitations on the efficacy of the therapy, because knowledge of individual-specific biokinetics, both for the tumour(s) and critical normal tissue(s) is essential for proper optimization of therapy. Dose conversion factors from standard phantoms, as have established the state of the art for dosimetry for the past 30 years, are generally employed, sometimes adjusting for patient-specific parameters. Recent advances in imaging technology and radiation transport methods permit the possibility of far more patient-specific dose

calculations than are possible with such standardized phantoms. A variety of approaches to patient-specific dose calculations are observed in practice, as follows.

6.5.1.1. No patient-specific parameters (an activity-based approach)

When one has a very wide therapeutic 'window' (i.e., the difference between the radiation dose delivered to the tumour and the highest dose that is delivered to a radiosensitive normal tissue, such as marrow), one may consider giving the same amount of activity to all patients without worry about optimizing the therapy. When the window is smaller, optimization becomes more critical. For over 50 years, ^{131}I treatment of thyroid cancer has been based empirically on administered activity rather than on actual radiation doses delivered [35]. The conventional approach for the post-surgical treatment of thyroid cancer when there is functioning thyroid tissue is to administer activities less than 7500 MBq, since it has been shown that the red marrow dose per MBq administered is of the order of 0.3 mGy/MBq (it is of the order of 0.15 mGy/MBq for thyroidectomized thyroid cancer patients). This approach has been shown to result in minimal haematologic toxicity, as the red marrow can receive a dose of 200 cGy without significant myelotoxicity [36]. Giving all patients the same administered activity of ^{131}I is thought by many physicians to be as good as patient-specific activity administration in functioning thyroid cancer patients. Some believe, however, that successful treatment of these patients involves radiation dose thresholds and that the success rates using a patient-specific administered activity approach are equal to or better than those reported with the empiric fixed-dose methods of ^{131}I administration [37–40].

6.5.1.2. Minimal patient-specific parameters (also an activity-based approach)

Often in trials with internal emitters, activity is administered to all patients based on a fixed amount of activity per kg of body weight or per m^2 of body surface area [41]. This is an improvement over giving every patient the same amount of activity, but does not account for patient-specific differences in biokinetics. Two patients of the same weight who had effective clearance half-times (e.g., from an organ or the total body) that were a factor of two different presumably would receive doses to those regions that were a factor of two different.

6.5.1.3. Hybrid patient-specific/standard-phantom-based dosimetry (a dose-based approach)

A more patient-specific treatment regimen involves determination of absorbed dose to tumour or to the tissue/organ expected to have toxicity

prior to administration of the therapy radioactivity. Radiation absorbed dose is defined as the energy absorbed per unit mass and is determined from the product of cumulated activity (or residence time) and a dose conversion factor (e.g., the S value, defined as the mean absorbed dose to a target organ per unit cumulated activity in the source organ, in the MIRD schema [21]). Each of these two factors can be patient dependent and can directly influence the calculated patient radiation dose to regions of the body (e.g., red marrow, tumours, etc.). Cumulated activity is directly proportional to the product of the uptake and retention half-time of activity of the radiolabelled agent in the source regions of interest. Dose conversion factors, like biokinetic data, should reflect individual patient characteristics as much as possible. For example, radiation absorbed dose estimates using 'off the shelf' S values (e.g., MIRD 11 [42], MIRDOSE3 [19], etc.) for most organs should be adjusted based on direct patient image data [43] using standard methods which correct for variations in patient organ masses. More complex, but similar, adjustments can be made to existing marrow S values, as will be discussed shortly. All dose estimates utilize models; it is the patient specificity of these models which must be adjusted. The administration of a patient-specific amount of radionuclide is based on the individual patient's biokinetics determined from a dosimetric study after administration of a tracer amount of the radiolabelled therapeutic drug product. The measured effective half-time, or residence time, of the radioactivity in the red marrow, total body, or other normal organ(s) is used to determine the necessary patient-specific therapy activity of the radiolabelled drug to deliver the desired (or maximum possible) radiation absorbed dose to the tumour while limiting the severity of toxicity to the bone marrow (for a non-myeloablative therapy) or other dose-limiting normal organ (for a myeloablative treatment). This method is potentially equivalent to the administration of activity based on MBq/kg, but only if there is no patient-to-patient variation in uptake or retention of the material. Some investigators apply patient-specific kinetics to the standard phantoms, and in addition may make some adjustments to the final results based on patient-specific physical parameters. Some examples (this is not an exhaustive review of the literature, just an overview of a few cases which demonstrate certain common techniques) are listed below.

6.5.1.3.1. Juweid *et al.* [44], employing a ^{131}I $F(ab)_2$ anti-carcinoembryonic antigen monoclonal antibody against medullary thyroid cancer, used patient image data to obtain kinetics in normal organs, blood and tumours. Dose escalation was based on prescribed radiation dose estimates to critical organs, as determined by a pretherapy dosimetric study. Blood biokinetic data were used with the Sgouros [45] method to predict marrow activity; organ, marrow and tumour doses were calculated using the MIRDOSE software [19], using the standard adult phantom.

6.5.1.3.2. Wiseman *et al.* [46] in a dosimetry study involving non-Hodgkin's lymphoma (NHL) patients treated with a ^{90}Y IgG1 monoclonal antibody, determined administered activity using a MBq/kg approach, and then retrospectively studied radiation doses. They combined patient kinetic data for whole organs (taken from nuclear medicine camera image data) with kinetic data on blood (which was extrapolated using the Sgouros method to estimate marrow residence time) to calculate organ and marrow dose estimates in over 50 patients. Marrow mass was calculated (in the Sgouros method) for individual patients, adjusting the model suggested standard mass by considering the patient's height and weight. Doses to spleen were also adjusted in cases in which the spleen mass was known (from computed tomography or other measurements) to be markedly different from that in the standard phantom. Otherwise, MIRDose estimates for the reference adult were reported for all patients (the reference adult male was used for all patients). Similarly, Divgi *et al.* [47], studying a ^{131}I antibody against renal cell carcinoma, used data from planar nuclear medicine camera images mixed with survey meter measurements to establish whole body kinetics and used MIRD Pamphlet No 11 [42] total body-to-total body S values to calculate total body dose. A liver time-activity curve was constructed, also from nuclear medicine image data, and liver dose was calculated with standard MIRD S values but modified to represent the patient's liver mass, as determined from CT images.

6.5.1.3.3. Wahl *et al.* [48], studying a ^{131}I IgG2a monoclonal antibody against NHL, used nuclear medicine camera images to obtain biokinetic data for normal organs and tumours. The administered activity was based on a prescribed radiation dose to the total body, as determined by a pre-therapy dosimetric study. They used dose to the total body to evaluate marrow response. Their total body doses were made patient specific through the use of absorbed fractions for different sized ellipsoids whose mass corresponded approximately to the total mass of the patient. Other organ and tumour doses were calculated using MIRDose.

6.5.1.3.4. Juweid *et al.* [49] treated patients with ^{131}I -labelled anti-carcino-embryonic antigen monoclonal antibodies with administered activities based either on the patient's body surface area or on a prescribed red marrow dose as determined by a pre-therapy dosimetric study.

6.5.1.4. Extension of mathematical phantom results

The MABDose [50] and DOSE3D [51] computer codes adapt the standard geometrical phantoms, allowing placement of a tumour or tumours in various locations to estimate dose contributions from these tumours to

normal organs, but do not at present use patient images. These codes work with stylized representations of average individuals, and give average dose to whole organs. The RTDS code [52] employs either the standard MIRDOSE phantom set (pre-calculated dose conversion factors for standard phantoms) or its own transport algorithms in a limited body space, based on voxel source kernels (which are useful in a single tissue type) to produce average organ doses or dose distributions within specified organs or tissues of the body.

6.5.1.5. Voxel source kernel approaches

As a step in the direction of providing pre-calculated dose conversion factors for use with three-dimensional voxel data, voxel source kernels were developed by Williams *et al.* [53] and by the MIRD Committee [54]. These dose conversion factors in principle allow calculation of three-dimensional dose information from patient-specific data, but only in limited spatial areas where there are no changes in material composition or density (these kernels were developed only for a soft tissue medium, and thus do not work in lung or bone, or where soft tissue/bone or lung interfaces occur).

6.5.1.6. Patient-specific dosimetry based on three-dimensional image data

Many specially designed computer codes have been developed for patient-specific dosimetry and treatment planning. A few groups have managed to fuse three-dimensional anatomical data, from CT or MRI images, with three-dimensional data on radionuclide distribution, from SPECT or PET images, to provide a three-dimensional representation of the radionuclide distribution in the tissues of the patient. Efforts in this area include the 3D-ID code at Memorial Sloan-Kettering Cancer Center [55, 56], the SIMDOS code from the University of Lund [57], the RMDP code from the Royal Marsden Hospital in the UK [58], the VOXELDOSE code from Rouen, France [59], and the SCMS code [60]. A detailed description of some of these tools is provided in the subsequent chapters of the book. Most of them are still research tools and have not entered the clinical area yet. The code with the most clinical experience to date is the 3D-ID code [56, 61]. This code produces three-dimensional dose distributions as well as dose-volume histograms (functions which show what fraction of an organ received what dose) for normal organs and tumours. The RMDP and VOXELDOSE codes combine the MIRD voxel source kernels for soft tissue with β point kernels to give dose distributions in unit density soft tissue regions of the body. The SCMS code of Yoriyaz *et al.* [60] uses the MCNP Monte Carlo software to transport electrons and photons in heterogeneous voxel-based phantoms, using fused CT and SPECT image data. They show an example of how different the geometries of the standardized phantom may be from that of real human subjects. Figure 6.1 shows the

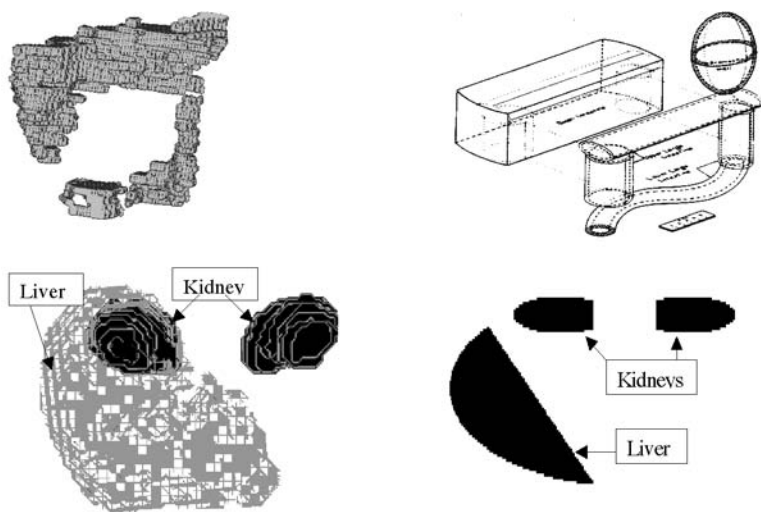


Figure 6.1. Images showing the GI tract (top) and kidney–liver region (bottom) from the Yale voxel phantom [62] (left) and the Cristy/Eckerman geometrical phantom [7] (right).

difference between the GI tract and liver–kidney regions of the Cristy/Eckerman adult male phantom and that of the voxel-based 75 kg individual image provided by the group at Yale [62]. Both the realism of the voxel-based phantoms and their representation of organ overlap are clearly superior to that of the standardized geometrical phantoms.

6.5.2. Innovation in software development tools

It is generally accepted that the biomedical research community will benefit from recent innovations in programming languages, techniques and paradigms. Several programming and software development approaches have been suggested in the literature. The choice of software development tools is further dictated by the user requirements. Unlike procedural programming languages, which separate data from operations on data defined by procedures and functions, object-oriented programming languages consist of a collection of interacting high-level units, the *objects* that combine both data and operations on data. This renders objects not much different from ordinary physical objects. This resemblance to real things gives objects much of their power and appeal. Not only can they model components of real systems, but equally well fulfil assigned roles as components in software systems. The object-oriented methodology enables an evolutionary approach to software development that still maintains a high degree of modularity [63].

When developing software systems it is possible to make use of object orientation through all the phases, in contrast to traditional methods based on structured analysis and structured design. It has been shown that object-oriented programming helps to improve design features and efficacy assessment of software development, which is not easily obtained with other programming paradigms [64]. Our experience in undertaking object-oriented software development allows us to claim that it is worthwhile to invest in the initial painful period to gain expertise in a new software development technique [65]. The potential advantages in the later stages of the software life cycle make investments in the early stages worthwhile. The powerful constructs promoted by object technology can yield an elegant, quality code. However, potential users should keep in mind that while success is possible, the object-oriented paradigm itself does not guarantee this. Several iterations may be necessary before the final goal is achieved. Since computers are continually increasing in speed and memory, it might seem at first that it is only a matter of time before Monte Carlo calculations become used routinely. However, the same advances in technology that led to faster computers also lead to bigger and more difficult problems. Thus there is a continuing need for new ideas in computer programming and algorithm development. Convincingly demonstrating that the new methods are truly more effective than the previous methods requires careful matching of the advantages of the approaches compared.

6.5.3. Parallel computing aspects

Although variance reduction techniques have been developed to reduce computation time, the main drawback of the Monte Carlo method is that it is extremely time-consuming. To obtain the good statistics required for image reconstruction or radiation dosimetry studies requires tracking hundreds of millions of particles. Consequently, a large amount of CPU time (weeks or even months) may be required to obtain useful simulated data sets. The development of advanced computers with special capabilities for vectorized or parallel calculations opened a new way for Monte Carlo researchers. Parallel computers are becoming increasingly accessible to medical physicists. This allows research into problems that may otherwise be computationally prohibitive to be performed in a fraction of the real time that would be taken by a serial machine. Historically, however, most programs and software libraries have been developed to run on serial, single-processor computers. A modification or adaptation of the code is therefore a prerequisite to run it on a parallel computer. However, it is worth pointing out that among all simulation techniques of physical processes, the Monte Carlo method is probably the most suitable one for parallel computing since the results of photon histories are completely

independent from each other. Moreover, computer aided parallelization tools designed to automate as much as possible the process of parallelizing scalar codes are becoming available. Although parallel processing seems to be the ideal solution for Monte Carlo simulation, very few investigations have been reported and only a few papers have been published on the subject [2, 66, 67].

Sequential programs make the most effective use of the available processing power: they alone guarantee maximum use of the CPU. In parallel programs, communication management introduces an unavoidable overhead, resulting in less efficient use of the overall CPU power. Scalar or serial Monte Carlo codes track the history of one particle at a time, and the total calculation time is the sum of the time consumed in each particle history. Many Monte Carlo applications have characteristics that make them easy to map onto computers having multiple processors. Some of these parallel implementations require little or no inter-processor communication and are typically easy to code on a parallel computer. Others require frequent communication and synchronization among processors and in general are more difficult to write and debug. A common way to parallelize Monte Carlo is to put identical 'clones' on the various processors; only the random numbers are different. It is therefore important for the sequences on the different processors to be uncorrelated so each processor does not end up simulating the same data [68]. That is, given an initial segment of the sequence on one process, and the random number sequences on other processes, we should not be able to predict the next element of the sequence on the first process. For example, it should not happen that if we obtain random numbers of large magnitude on one process, then we are more likely to obtain large numbers on another. In developing any parallel Monte Carlo code, it is important to be able to reproduce runs exactly in order to trace program execution.

Since a Monte Carlo particle history is a Markov chain, the next interaction or movement of a particle is always determined by the current state of the particle. The histories of two particles become identical only when the same random number sequence is used to sample the next state. To ensure that the seed tables on each processor are random and uncorrelated, Mascagni *et al.* described a canonical form for initializing separate cycles of the Fibonacci generators [69]. There are, however, many approaches to vectorized and parallel random number generation in the literature. We can distinguish three general approaches to the generation of random numbers on parallel computers: centralized, replicated and distributed. In the centralized approach, a sequential generator is encapsulated in a task from which other tasks request random numbers. This avoids the problem of generating multiple independent random sequences, but is unlikely to provide good performance. Furthermore, it makes reproducibility hard to achieve: the response to a request depends on when it arrives at the generator,

and hence the result computed by a program can vary from one run to the next. In the replicated approach, multiple instances of the same generator are created (for example, one per task). Each generator uses either the same seed or a unique seed, derived, for example, from a task identifier. Clearly, sequences generated in this fashion are not guaranteed to be independent and, indeed, can suffer from serious correlation problems. However, the approach has the advantages of efficiency and ease of implementation and should be used when appropriate. In the distributed approach, responsibility for generating a single sequence is partitioned among many generators, which can then be parcelled out to different tasks. The generators are all derived from a single generator; hence, the analysis of the statistical properties of the distributed generator is simplified.

In a review of vectorized Monte Carlo, Martin and Brown [70] described variations of event-based algorithms together with speed-up results published by different groups. During the past two decades, investigations were carried out to run different Monte Carlo codes on multiple-transputer systems [67], vector parallel supercomputers [71], parallel computers [66] and a cluster of workstations in a local area network using PVM [72]. There are large discrepancies in the performance ratio reported by different authors. In particular, Miura reported a speed-up of about 8 with the vectorized ESG4 code (EGS4V) [73]. A linear decrease in computing time with the number of processors used was also demonstrated for eight [66] and up to 32 processors [74]. This speed-up is especially significant in SPECT simulations involving higher energy photon emitters, where explicit modelling of the phantom and collimator is required.

6.5.4. Towards clinical applications of 'on-the-fly' Monte Carlo-based dosimetry calculations

It is clear that a new generation of dose modelling tools must be developed to be used with internal emitter therapy in nuclear medicine. It is unacceptable to use standardized, geometrical phantoms to do dose calculations for individual patients if we are to give meaningful information to the physician to be used in planning patient therapy. 'One dose fits all' is not a scientific approach to the problem. The evolution of methodology that was followed for external beam radiotherapy treatment planning must be followed for internal emitter therapy. The technology now exists to develop patient-specific three-dimensional dose maps, based on fusion of CT (or MRI) and SPECT (or PET) data, with individualized Monte Carlo calculations done in a reasonable amount of time using high powered computing workstations or distributed computing networks. The main difficulty to be overcome is the resistance of patients and the medical staff to the acquisition of multiple planar and SPECT images, using a tracer amount of activity, needed to adequately characterize the dosimetry.

6.6. SUMMARY

It is gratifying to see in overview the progress that internal dose modelling has made, from simple spherical geometries, through stylized models of reference individuals, and most recently towards truly patient-specific models based on patient images. Challenges remain, particularly in the areas of bone and marrow dosimetry, in image quantification, and in correlating radiation dose with effect. As these challenges are met, and experience is gained, patients can expect to receive therapy with internal emitters, based on accurate dose calculations and sound risk/benefit evaluations made by their attending physician.

ACKNOWLEDGMENTS

One of the authors (HZ) acknowledges the support of grant SNSF 3152-062008 from the Swiss National Science Foundation. The contents and views in this chapter are solely the responsibility of the author and do not necessarily represent the official views of the institution providing support.

REFERENCES

- [1] Andreo A 1991 Monte Carlo techniques in medical radiation physics *Phys. Med. Biol.* **36** 861–920
- [2] Zaidi H 1999 Relevance of accurate Monte Carlo modeling in nuclear medical imaging *Med. Phys.* **26** 574–608
- [3] Bielajew A F and Rogers D W O 1989 *Monte Carlo Transport of Electrons and Photons* eds N W Jenkins, A Rindi, A Nahum and D W O Rogers (New York: Plenum Press) pp 407–19
- [4] ICRP 1959 *Report of Committee II on Permissible Dose for Internal Radiation. ICRP Publication 2 I.C.o.R. Protection* (New York: Pergamon)
- [5] Snyder W, Ford M R and Warner G 1978 *Estimates of specific absorbed fractions for photon sources uniformly distributed in various organs of a heterogeneous phantom.* MIRD Pamphlet No 5, revised NM/MIRD (New York: Society of Nuclear Medicine)
- [6] Warner G G and Craig A M J 1968 *ALGAM, a computer program for estimating internal dose for gamma-ray sources in a man phantom* ORNL-TM-2250 (Oak Ridge National Laboratory)
- [7] Cristy M and Eckerman K F 1987 *Specific absorbed fractions of energy at various ages from internal photon sources. I Methods, II one year old, III five year old, IV ten year old, V fifteen year old male and adult female, VI new-born and VII adult male* ORNL/TM 8381/V1-V7 (Oak Ridge National Laboratory)
- [8] Stabin M *et al.* 1995 *Mathematical models and specific absorbed fractions of photon energy in the nonpregnant adult female and at the end of each trimester of pregnancy* ORNL/TM-12907 (Oak Ridge National Laboratory)
- [9] Eckerman K, Cristy M and Warner G G 1981 *Dosimetric Evaluation of Brain Scanning Agents* eds E E Watson, A T Schlafke-Stelson, J L Coffey and R J Cloutier, Third International Radiopharmaceutical Dosimetry Symposium; HHS Publication FDA

- 81-8166, US Dept of Health and Human Services, Oak Ridge, TN (Rockville, MD: Food and Drug Administration) pp 527-40
- [10] Bouchet L G, Bolch W E, Weber D A, Atkins H L and Poston J W 1999 MIRD Pamphlet No 15: Radionuclide *S* values in a revised dosimetric model of the adult head and brain. Medical Internal Radiation Dose *J. Nucl. Med.* **40** 62S-101S
- [11] Holman B L *et al.* 1983 Biodistribution and dosimetry of N-isopropyl-p-[¹²³I]iodoamphetamine in the primate *J. Nucl. Med.* **24** 922-31
- [12] Watson E E, Stabin M, Davis J L and Eckerman K F 1989 A model of the peritoneal cavity for use in internal dosimetry *J. Nucl. Med.* **30** 2002-11
- [13] Stabin M 1994 A model of the prostate gland for use in internal dosimetry *J. Nucl. Med.* **35** 516-20
- [14] Eckerman K F and Stabin M 2000 Electron absorbed fractions and dose conversion factors for marrow and bone by skeletal regions *Health Phys.* **78** 199-214
- [15] Bouchet L G, Bolch W E, Howell R W and Rao D V 2000 *S* values for radionuclides localized within the skeleton *J. Nucl. Med.* **41** 189-212
- [16] Mardirossian G *et al.* 1999 A new rectal model for dosimetry applications *J. Nucl. Med.* **40** 1524-31
- [17] Siegel J A and Stabin M 1994 Absorbed fractions for electrons and beta particles in spheres of various sizes *J. Nucl. Med.* **35** 152-56
- [18] Stabin M and Konijnenberg M W 2000 Re-evaluation of absorbed fractions for photons and electrons in spheres of various sizes *J. Nucl. Med.* **41** 149-60
- [19] Stabin M 1996 MIRDose personal computer software for internal dose assessment in nuclear medicine *J. Nucl. Med.* **37** 538-46
- [20] Cloutier R J, Watson E E, Rohrer R H and Smith E M 1973 Calculating the radiation dosage to an organ *J. Nucl. Med.* **14** 53-5
- [21] Loevinger R, Budinger T and Watson E 1988 *MIRD Primer for Absorbed Dose Calculations* S.o.N. Medicine, NM/MIRD (New York)
- [22] ICRP 1979 *Limits for Intakes of Radionuclides by Workers*. ICRP Publication 30 I.C.o.R. Protection (New York: Pergamon)
- [23] ICRP 1991 *Recommendations of the International Commission on Radiological Protection* ICRP. Publication 60 I.C.o.R. Protection (New York: Pergamon)
- [24] Stabin M and Sparks R B 1999 MIRDose4 does not exist *J. Nucl. Med. Suppl.* **40** 309P
- [25] Stabin M *et al.* 2001 RADAR—the radiation dose assessment resource. An online source of dose information for nuclear medicine and occupational radiation safety *J. Nucl. Med. Suppl.* **42** 243P
- [26] Nelson W R, Hirayama H and Rogers D W O 1985 *The EGS4 Code System* (Stanford Linear Accelerator Center)
- [27] Halbleib J A, Kensek R P, Valdez G D, Seltzer S M and Berger M J 1992 ITS: the Integrated TIGER Series of electron/photon transport codes—version 3.0 *IEEE Trans. Nucl. Sci.* **39** 1025-30
- [28] Hendricks J S and Briesmeister J F 1992 Recent MCNP developments *IEEE Trans. Nucl. Sci.* **39** 1035-40
- [29] Brun R, Bruyant F, Maire M, McPherson A C and Zanarini P 1994 GEANT detector description and simulation tool *W5013* (CERN)
- [30] Berger M J and Seltzer S M 1968 *Electron and Photon Transport Programs. I. Introduction and Notes on Program DATAPAC 4, II. Notes on Program ETRAN-15* Rep NBS 9836 and 9837 (NBS)

- [31] Cullen D E, Balingier C T and Perkins S T 1991 *The all particle method: 1991 status report* UCRL-JC-108040 (Lawrence Livermore National Laboratory)
- [32] Zaidi H 2000 Comparative evaluation of photon cross section libraries for materials of interest in PET Monte Carlo simulations *IEEE Trans. Nucl. Sci.* **47** 2722–35
- [33] Sempau J, Acosta E, Baro J, Fernandez-Varea J M and Salvat F 1997 An algorithm for Monte Carlo simulation of the coupled electron–photon transport *Nucl. Instr. Meth. B* **132** 377–90
- [34] Fasso A, Ferrari A and Sala P R 2001 *Proceedings of the MonteCarlo 2000 Conference* eds A Kling, F Barao, M Nakagawa, L Tavora and P Vaz (Berlin: Springer) pp 159–64
- [35] Zanzonico P B, Brill A B and Becker D V 1995 *Principles of Nuclear Medicine* eds H N Wagner, Z Szabo and J W Buchanan (Philadelphia, PA: Saunders) 2nd edition, pp 106–34
- [36] Benua R S, Cicale N R, Sonenberg M and Rawson R W 1962 The relation of radioiodine dosimetry to results and complications in the treatment of metastatic thyroid cancer *Am. J. Roentgenol.* **87** 171–82
- [37] Maxon H R *et al.* 1992 Radioiodine-131 therapy for well-differentiated thyroid cancer—a quantitative radiation dosimetric approach outcome and validation in 85 patients *J. Nucl. Med.* **33** 1132–36
- [38] Samuel A M and Rajashekharrao B 1994 Radioiodine therapy for well-differentiated thyroid cancer: a quantitative dosimetric evaluation for remnant thyroid ablation after surgery *J. Nucl. Med.* **35** 1944–50
- [39] Schlesinger T, Flower M A and McCready V R 1989 Radiation dose assessments in radioiodine (^{131}I) therapy. 1. The necessity for *in vivo* quantitation and dosimetry in the treatment of carcinoma of the thyroid *Radiother. Oncol.* **14** 35–41
- [40] Maxon H R 1999 Quantitative radioiodine therapy in the treatment of differentiated thyroid cancer *Q. J. Nucl. Med.* **43** 313–23
- [41] DeNardo S J 2000 Tumor-targeted radionuclide therapy trial design driven by patient dosimetry *J. Nucl. Med.* **41** 104–6
- [42] Snyder W, Ford M R, Warner G and Watson S 1975 ‘S’, *absorbed dose per unit cumulated activity for selected radionuclides and organs*. MIRD Pamphlet No 11, NM/MIRD (New York: Society of Nuclear Medicine)
- [43] J A Siegel *et al.* 1999 MIRD Pamphlet No 16: Techniques for quantitative radiopharmaceutical biodistribution data acquisition and analysis for use in human radiation dose estimates *J. Nucl. Med.* **40** 37S–61S
- [44] M E Juweid *et al.* 2000 Initial experience with high-dose radioimmunotherapy of metastatic medullary thyroid cancer using ^{131}I -MN-14 *F(ab)*2 anti-carcinoembryonic antigen MAb and AHSCR *J. Nucl. Med.* **41** 93–103
- [45] Sgouros G 1993 Bone marrow dosimetry for radioimmunotherapy theoretical considerations *J. Nucl. Med.* **34** 689–94
- [46] Wiseman G A, White C A, Witzig T A *et al.* 1999 Final dosimetry results of IDEC-Y2B8 phase I/II 90yttrium radioimmunotherapy trial in non-Hodgkin’s lymphoma *J. Nucl. Med., Suppl.* **40** 64P
- [47] Divgi C R *et al.* 1998 Phase I/II radioimmunotherapy trial with iodine-131-labeled monoclonal antibody G250 in metastatic renal cell carcinoma *Clin. Cancer Res.* **4** 2729–39
- [48] Wahl R L, Zasadny K R, MacFarlane D *et al.* 1998 Iodine-131 anti-B1 antibody for B-cell lymphoma an update on the Michigan Phase I experience *J. Nucl. Med., Suppl.* **39** 21S–27S

- [49] Juweid M E *et al.* 1999 Prediction of hematologic toxicity after radioimmunotherapy with (131)I-labeled anticarcinoembryonic antigen monoclonal antibodies *J. Nucl. Med.* **40** 1609–16
- [50] Johnson T K, McClure D and McCourt S 1999 MABDOSE. I: Characterization of a general purpose dose estimation code *Med. Phys.* **26** 1389–95
- [51] Clairand I, Ricard M, Gouriou J, Di Paola M and Aubert B 1999 DOSE3D: EGS4 Monte Carlo code-based software for internal radionuclide dosimetry *J. Nucl. Med.* **40** 1517–23
- [52] Liu A *et al.* 1999 A radionuclide therapy treatment planning and dose estimation system *J. Nucl. Med.* **40** 1151–3
- [53] Williams L E, Liu A, Raubitschek A A and Wong J Y 1999 A method for patient-specific absorbed dose estimation for internal beta emitters *Clin. Cancer Res.* **5** 3015s–3019s
- [54] Bolch W E *et al.* 1999 MIRD Pamphlet No 17: The dosimetry of nonuniform activity distributions—radionuclide *S* values at the voxel level. Medical Internal Radiation Dose Committee *J. Nucl. Med.* **40** 11S–36S
- [55] Sgouros G *et al.* 1990 Treatment planning for internal radionuclide therapy three-dimensional dosimetry for nonuniformly distributed radionuclides *J. Nucl. Med.* **31** 1884–91
- [56] Sgouros G *et al.* 1993 Three-dimensional dosimetry for radioimmunotherapy treatment planning *J. Nucl. Med.* **34** 1595–601
- [57] Tagesson M, Ljungberg M and Strand S E 1996 A Monte-Carlo program converting activity distributions to absorbed dose distributions in a radionuclide treatment planning system *Acta Oncol.* **35** 367–72
- [58] Guy M J, Flux G D, Papavasileiou P, Flower M A and Ott R J 2002 *RMDP-MC: a dedicated package for I-131 SPECT quantification, registration, patient-specific dosimetry and Monte-Carlo* ed M Stabin, 7th International Radiopharmaceutical Dosimetry Symposium, Oak Ridge, TN (Oak Ridge: Associated Universities) in press
- [59] Gardin I *et al.* 2002 *VoxelDose: a computer program for 3D dose calculation in therapeutic nuclear medicine* ed M Stabin, 7th International Radiopharmaceutical Dosimetry Symposium, Oak Ridge, TN (Oak Ridge: Associated Universities) in press
- [60] Yoriyaz H, Stabin M and dos Santos A 2001 Monte Carlo MCNP-4B-based absorbed dose distribution estimates for patient-specific dosimetry *J. Nucl. Med.* **42** 662–9
- [61] Kolbert K S *et al.* 1997 Implementation and evaluation of patient-specific three-dimensional internal dosimetry *J. Nucl. Med.* **38** 301–8
- [62] Zubal I G *et al.* 1994 Computerized 3-dimensional segmented human anatomy *Med. Phys.* **21** 299–302
- [63] Zaidi H 2000 Object-oriented programming environments: a promising tool for biomedical imaging research *Pol. J. Med. Phys. Eng.* **6** 71–89
- [64] Valdes I H 1994 Advantages of object-oriented programming *MD Comput.* **11** 282–3
- [65] Zaidi H, Herrmann Scheurer A and Morel C 1999 An object-oriented Monte Carlo simulator for 3D positron tomographs *Comput. Meth. Programs Biomed.* **58** 133–45
- [66] Zaidi H, Labbé C and Morel C 1998 Implementation of an environment for Monte Carlo simulation of fully 3D positron tomography on a high-performance parallel platform *Parallel Comput.* **24** 1523–36
- [67] Ma C 1994 Implementation of a Monte Carlo code on a parallel computer system *Parallel Comput.* **20** 991–1005

- [68] De Matteis A and Pagnutti S 1995 Controlling correlations in parallel Monte Carlo *Parallel Comput.* **21** 73–84
- [69] Mascagni M, Cuccaro S A, Pryor D V and Robinson M L 1995 A fast, high-quality, and reproducible lagged-Fibonacci pseudorandom number generator *J. Comput. Phys.* **15** 211–19
- [70] Martin W R and Brown F B 1987 Status of vectorized Monte Carlo code for particle transport analysis *Int. J. Supercomputer Appl.* **1** 11–32
- [71] Smith M F, Floyd C E and Jaszcak R J 1993 A vectorized Monte Carlo code for modeling photon transport in SPECT *Med. Phys.* **20** 1121–7
- [72] Kirkby D R and Delpy D T 1997 Parallel operation of Monte Carlo simulations on a diverse network of computers *Phys. Med. Biol.* **42** 1203–8
- [73] Miura K 1987 EGS4V: vectorization of the Monte Carlo cascade shower simulation code EGS4 *Comput. Phys. Commun.* **45** 127–36
- [74] Dewaraja Y, Ljungberg M, Majumdar A, Bose A and Koral K F 2002 A parallel Monte Carlo code for planar and SPECT imaging: implementation, verification and applications in I-131 SPECT *Comput. Meth. Prog. Biomed.* in press

Chapter 7

Dose point-kernels for radionuclide dosimetry

Manuel Bardiès, Cheuk Kwok and George Sgouros

7.1. INTRODUCTION

Dose point-kernels (DPKs) are widely used for radionuclide dosimetry. More than three decades ago Loevinger *et al.* [1] justified the use of ‘Point Source Dose Functions’ (ancestors of DPKs) for β emissions: ‘The problem of determining the absorbed dose around a localized β particle source in tissue can be separated in two steps. First, the distribution of dose around a (hypothetical) point source of β particles in tissue is determined. Second, the dose distribution in and around a localized β particle source is calculated by a suitable summation of the elementary point source distribution.’

The superposition concept, which cannot be dissociated from DPK, is implicit in this approach. Any source volume can be broken down into a set of point sources, and the determination of dose distribution around point sources allows non-point sources to be treated by ‘suitable summation’.

For Berger [2], once again in the case of β emissions, the specific absorbed fraction $\Phi(x)$ used to calculate the dose rate at some distance x from an isotopic point source can also be regarded as a ‘point kernel’ because of its use in applications of the superposition principle. Thus,

$$R(x) = Ank\bar{E}\Phi(x) \quad (7.1)$$

where $R(x)$ is the mean dose rate (in cGy/sec), x is the distance to the source (in cm), A is the activity (in Bq), n is the number of β particles emitted per decay, $k = 1.6 \times 10^{-8}$ g cGy/MeV, \bar{E} is the mean energy from β particles emitted by the source (in MeV), and $\Phi(x)$ is the point kernel (in g⁻¹).

The relation is apparent here between the DPK and the absorbed fraction, as defined by the MIRD Committee [3].

MIRD Pamphlet No 7 [4] expounded the formalism of the calculation of doses delivered at some distance from point sources of electrons or β particles

in water and other media. The definition of the variables used differentiated the specific absorbed fraction (for sources of electrons or β particles) from ‘energy-dissipation distribution’ as defined by Spencer [5] and, in particular, allowed the introduction of ‘scaled absorbed-dose distribution’.

Thus, for a point source of electrons of energy E_0 , the dose rate $R(x, E_0)$ is given by

$$R(x, E_0) = AnkE_0\Phi(x, E_0). \quad (7.2)$$

This formulation (very close to the preceding one) defines $\Phi(x, E_0)$ as the ‘point isotropic specific absorbed fraction’ expressed in g^{-1} . Thus, the quantity $4\pi\rho x^2\Phi(x, E_0)\text{d}x$ is the fraction of emitted energy absorbed in a spherical layer of radius x and thickness $\text{d}x$ in a medium of density ρ (g/cm^3). If it is assumed that all the energy emitted is finally absorbed by the medium, then

$$4\pi\rho\int_0^\infty x^2\Phi(x, E_0)\text{d}x = 1, \quad (7.3)$$

which constitutes the normalization requirement for $\Phi(x, E_0)$.

Dimensionless ‘energy-dissipation distribution’ $J(u, E_0)$, as defined according to Spencer [6], gives the energy dissipated by the primary electrons (which is not strictly equivalent to the energy absorbed in the medium) in the spherical layers of radius u around a point source:

$$J(u, E_0) = 4\pi x^2\rho\frac{E_0}{L(E_0)}\Phi(x, E_0) \quad (7.4)$$

where $L(E_0)$ is the mean energy loss of an electron per unit path length (in MeV/cm) at source energy E_0 , and $u = x/r(E_0)$ is the distance to the source expressed as a fraction of the initial electron range $r(E_0)$, in cm, according to the continuous-slowing-down-approximation (csda). The distance $r(E_0)$ is sometimes noted as r_0 in the literature. Normalization of the distance (u) and introduction of the factor $E_0/L(E_0)$ allow the dependence of $J(u, E_0)$ on E_0 to be reduced. Scaled absorbed dose distribution, $F(\xi, E_0)$, is defined by

$$F(\xi, E_0) = 4\pi\rho x^2\Phi(x, E_0)\frac{\text{d}x}{\text{d}\xi} = 4\pi\rho x^2x_{90}\Phi(x, E_0) \quad (7.5)$$

where $\xi = x/x_{90}$ is the ratio of the distance from the source x to the 90-percentile distance.

$F(\xi, E_0)$ is dimensionless and relatively independent of the medium crossed (even if x_{90} itself depends on the medium crossed). No explicit definition of the DPK is provided in the article, but the concept of scaled absorbed dose distribution was frequently applied in subsequent works and presented as the DPK. A minor modification often encountered relates to normalization, which can be performed relative to x_{90} or r_0 , depending on the author. In this chapter, $F(\xi, E_0)$ will be used for DPK, although the terminology and the normalization factor actually used in the articles cited may differ slightly.

These equations can be generalized to β particle sources, which introduces

$$R_{\beta}(x) = An_{\beta}kE_{Av}\Phi_{\beta}(x) \quad (7.6)$$

and

$$F_{\beta}(\xi) = 4\pi\rho x^2\Phi_{\beta}(x)\frac{dx}{d\xi} = 4\pi\rho x^2x_{90}\Phi_{\beta}(x). \quad (7.7)$$

The modification of the variables is self-explanatory.

In principle, the resolution of a dosimetric problem consists in considering the contribution of all emissions from a source volume to an entire target volume. This implies the integration in six dimensions of a dose deposition function at some distance from a point source. This function can be defined as the DPK. It is readily apparent that the value of this breakdown relates to the possibility of using a single function applicable to the entire area of interest. This is feasible for an isotropic homogeneous medium, in which case the determination of dose deposition at some distance from a point source allows any dosimetric problem to be solved by 'suitable summation'. Thus, a DPK approach is relevant mainly in the case of a homogeneous medium.

Another limitation relates to the calculation mode for DPK. In general, the *mean* dose (a non-stochastic value) deposited at some distance from a point source is considered, which places us implicitly in the domain of macro-dosimetry.

This chapter is divided into three parts: the first concerns how DPKs are obtained (the methods used and the limitations of these methods); the second describes the various data sets available in the literature (photons or electrons); and the third considers the domains for the use of DPKs in radionuclide dosimetry.

7.2. METHODS USED TO GENERATE DOSE POINT-KERNELS

The methods used to generate DPKs have kept pace with changes in the experimental data available and benefited from spectacular progress in the field of numerical calculation. This section describes the different methods used to generate point-kernels and their changes over time.

Until 1955, the only experimental data available concerned a dozen radionuclides in air. It has been shown that these data could be represented by the formula [1, 7]

$$\begin{aligned} \Phi(x) &= \frac{k'}{(\mu x)^2} \left\{ c \left[1 - \frac{\mu x}{c} e^{[1-(\mu x/c)]} \right] + \mu x e^{(1-\mu x)} \right\} & \mu x < c \\ \Phi(x) &= \frac{k'}{\mu x} e^{(1-\mu x)} & \mu x \geq c \end{aligned} \quad (7.8)$$

where k' is a normalization constant, μ the apparent coefficient of absorption for the medium, and c a dimensionless parameter. The coefficients μ and c were given for soft tissues and β emitters

$$\mu = 18.6(E_0 - 0.036)^{-1.37} \left(2 - \frac{\bar{E}}{\bar{E}^*}\right) \text{ cm}^2/\text{g}$$

$$c = \begin{cases} 2 & 0.17 \leq E_0 \leq 0.5 \text{ MeV} \\ 1.5 & 0.5 \leq E_0 \leq 1.5 \text{ MeV} \\ 1 & 1.5 \leq E_0 \leq 3 \text{ MeV} \end{cases} \quad (7.9)$$

where \bar{E} is the mean energy of the β spectrum, E_0 the maximal energy, and \bar{E}^* the mean energy of a spectrum representing an allowed shape of maximum energy E_0 .

At the end of the 1950s, Spencer [5] resolved electron transport equations numerically (according to the continuous slowing down approximation), while taking multiple diffusion into account according to the moments method. These calculations, as validated from experimental measurements in different media and for different energies [8], considered energy distribution as a function of the distance for isotropic point sources of monoenergetic electrons (20 keV to 10 MeV) in different homogeneous media. As a result of adoption of the csda, statistical variations in energy loss straggling were not taken into account. Consequently, there was a tendency to underestimate a dose deposited at some distance from the emission point.

Cross *et al.* [9, 10] conducted important studies for measurement and calculation of DPK (planar source or point source) based on the moments method of Spencer. Important progress was made by Berger [11], who used the Monte Carlo method to simulate electron transport. Berger was able to take both multiple scattering and energy loss straggling into account. Energy loss from δ -rays and bremsstrahlung production were also incorporated.

Although the point-kernels presented in MIRD Pamphlet No 7 [4] are derived from the work of Spencer, those discussed later [12] were calculated using the ETRAN Monte Carlo code [13]. More recently, other point-kernels have been calculated for 147 radionuclides, using a code (ACCEPT) derived from ETRAN [14].

The EGS4 Monte Carlo code has also been used to generate point-kernels for monoenergetic electrons (50 keV to 3 MeV) and for eight radionuclides (^{32}P , ^{67}Cu , ^{90}Y , ^{105}Rh , ^{131}I , ^{153}Sm , ^{186}Re and ^{188}Re) [15]. Although the results obtained with ETRAN versions prior to 1986 may differ from those obtained with EGS4 [16], due to incorrect sampling of energy loss straggling in ETRAN, there are no important differences now in the results obtained with these two codes [13].

Regardless of the method employed, current results are concordant enough to allow DPKs to be considered as reliable data usable for more complex geometries in the input of calculation programs.

7.3. REVIEW OF DOSE POINT-KERNELS AVAILABLE FOR RADIONUCLIDE DOSIMETRY

7.3.1. Photons

Monoenergetic. According to MIRD formalism [17], photon DPK in units of (cGy/decay) at a distance r from a monoenergetic γ source of energy E (MeV) in an unbounded homogeneous medium can be expressed as

$$K(r) = 1.6 \times 10^{-8} E \frac{\mu_{\text{en}}}{4\pi r^2 \rho} e^{-\mu r} B_{\text{en}}(\mu r) \quad (7.10)$$

where μ and μ_{en} are respectively the linear attenuation and energy absorption coefficients of the photon in the medium. The quantity B_{en} is the energy absorption buildup factor, defined as the ratio between the absorbed dose rate due to both primary and scattered photons and that due to primary photons alone.

Using the moments method of Spencer and Fano, Berger [17] has published B_{en} tables for photon energies from 15 keV to 3 MeV for distances μr from 0.05 to 20 mean free paths in water (1 mean free path = $1/\mu$). At individual photon energies within the energy range, Berger also expressed the buildup factor as a ten-term polynomial of distance. Coefficients of the polynomial have no obvious simple energy dependence. It has been shown by Brownell *et al.* [18] that Berger's method gives results comparable with those obtained using a Monte Carlo code for photon transport in a large soft-tissue volume.

Berger's tabulated B_{en} values were fitted to analytic functions other than polynomials by Kwok *et al.* [19] and Lechner [20]. Such fittings of data minimize computer storage space. The parameters of the fitting function have a simple relationship with photon energy for Kwok *et al.*, while a common expression applies to the absorbed fractions for photons and β particles for Lechner.

More recently, several groups of researchers have used Monte Carlo codes to derive photon DPKs in water, namely ETRAN [13], EGS4 [21–23] and MCNP [24, 25]. The agreement between the codes themselves and with Berger's calculation is within 3–5% [25–27].

Radionuclides. The DPK for any specific γ -emitting nuclide in a homogeneous medium can be obtained by summing the monoenergetic photon DPK K_i over the photon energy spectrum (n_i, E_i), where n_i is the probability of emitting γ energy E_i per decay and μ_i and $\mu_{\text{en},i}$ are, respectively, the linear attenuation and energy absorption coefficients of the photon with energy E_i in the medium:

$$K_i(r) = 1.6 \times 10^{-8} n_i E_i \frac{\mu_{\text{en},i}}{4\pi r^2 \rho} \exp(-\mu_i r) B_{\text{en}}(\mu_i r). \quad (7.11)$$

Monte Carlo codes have been used directly to derive the photon DPKs of many radionuclides including ^{123}I , ^{124}I , ^{125}I , ^{131}I , ^{111}In , ^{64}Cu , ^{67}Ga , ^{68}Ga , $^{99\text{m}}\text{Tc}$, ^{131}Cs , ^{103}Pd and ^{71}Ge [21, 25, 28, 29]. Some of the DPKs have also been parametrized to analytic functions for easy computation on personal computers [21].

7.3.2. Electrons

For dosimetry of electrons, two major types of approach are possible, depending on the problem involved. First, the problem to be resolved may consist in comparing doses (or absorbed fractions) delivered to the same target by different radionuclides. In this case, it seems preferable to calculate, once and for all, a table of absorbed fractions for monoenergetic electrons and then integrate these results into the emission spectra of the radionuclides considered. Second, when various geometric configurations need to be studied for the same radionuclide, it is often preferable to use the DPK of the radionuclide considered.

In both cases, the application of data for monoenergetic electrons to all electron emissions of a radionuclide should be performed with due care. First of all, it is essential to consider the β -emission spectra and not mean energy [30]. Some spectra can be neglected if their emission percentage is too low to contribute significantly to the delivered dose, provided that this choice is indicated and clearly documented. Monoenergetic emissions (Auger or conversion electrons) should be taken into account if they contribute significantly to the delivered dose.

For example, the electron emission values given in table 7.1 for ^{131}I have been published by the French Primary Laboratory of Ionizing Radiations [31]. A comparison of these values with those cited by the MIRD Committee [32] (in boldface in the table) indicates that the difference actually concerns less than 1% of the energy emitted by transition. This section cites various DPK sets used in the dosimetry of radionuclides.

Monoenergetic DPK. The tables in MIRD Pamphlet No 7 [4] provide $F(\xi, E_0)$ values for nine energies in water ranging from 25 keV to 4 MeV. These DPKs were generated from Spencer's energy-dissipation distributions. Insofar as the data show little variation as a function of energy, it is possible to interpolate these values, if necessary.

Berger [12] published an article initially intended as a 'preliminary report', but which became one of the most frequently cited references in the DPK field. These 'improved point-kernels' were obtained by Monte Carlo simulation using the ETRAN code [11]. Angular deflections and energy loss straggling due to multiple Coulomb scattering (by atoms and orbital electrons) were taken into account, and energy transport by secondary bremsstrahlung was included. The $F(\xi, E_0)$ tables were given for 36 energies ranging from

Table 7.1. Electron emission data for ¹³¹I.

	Energy/particle, <i>E</i> (<i>i</i>) (keV)	Particles/transition, 100 <i>n</i> (<i>i</i>) (%)	Energy/transition, Δ(<i>i</i>)	
			g cGy/μCi h	fJ/Bq s
e _{AL}	3.9 ± 1.5	5.7 ± 0.5	0.0004	0.031
e _{AK}	29.02 ± 5.51	0.7 ± 0.1	0.0004	0.027
ec _{1K}	45.622 ± 0.016	3.55 ± 0.08	0.0035	0.259
ec _{1L}	75.065 ± 0.335	0.47 ± 0.01	0.0007	0.056
ec _{1MN}	79.65 ± 0.45	0.105 ± 0.002	0.0002	0.013
ec _{3K}	129.27 ± 0.03	0.48 ± 0.09	0.0013	0.099
ec _{4K}	142.649 ± 0.016	0.050 ± 0.002	0.0002	0.011
ec _{3L}	158.48–159.15	0.23 ± 0.04	0.0008	0.058
ec _{3MN}	162.9–163.8	0.065 ± 0.010	0.0002	0.017
ec _{4L}	171.16–172.43	0.0110 ± 0.0004	0.0000	0.003
ec _{7K}	249.74 ± 0.03	0.254 ± 0.009	0.0013	0.102
ec _{7L}	278.85–279.52	0.045 ± 0.002	0.0003	0.020
ec _{7MN}	283.3–284.2	0.0112 ± 0.0005	0.0000	0.005
ec _{14K}	329.92 ± 0.02	1.55 ± 0.05	0.0109	0.819
ec _{14L}	359.03–359.70	0.25 ± 0.01	0.0019	0.144
ec _{17K}	602.417 ± 0.016	0.0285 ± 0.0003	0.0004	0.028
β _{1(max)} [−]	247.9 ± 0.6	2.11 ± 0.03	0.0031	0.235
β _{2(max)} [−]	309.9 ± 0.6	0.63 ± 0.01	0.0012	0.088
β _{3(max)} [−]	333.8 ± 0.6	7.21 ± 0.07	0.0148	1.116
β _{4(max)} [−]	606.3 ± 0.6	89.9 ± 0.6	0.368	27.59
β _{5(max)} [−]	629.7 ± 0.6	0.072 ± 0.007	0.0003	0.026
β _{6(max)} [−]	806.9 ± 0.6	~0.1	0.0006	0.045

0.5 keV to 10 MeV, which in practice allowed scanning of all of the necessary energies in the domain of β-emitting radionuclides. These data have been widely used in dosimetric models or in DPK calculations for radionuclides. Subsequently, it appeared that an incorrect sampling of energy-loss straggling in ETRAN affected the validity of these data [13, 16]. The corrected values now available extend from 20 keV to 20 MeV [33].

The tables for β-ray dose distributions in water published by Cross *et al.* [14, 34] were calculated using the ACCEPT code (derived from ETRAN). For monoenergetic emissions, comparison with values obtained with the EGS4 code [15] for six energies ranging from 50 keV to 3.0 MeV indicated that differences between the two data sets were slight (a few per cent). *F*(ξ, *E*₀) values were given for nine energies from 25 keV to 4 MeV.

Radionuclides. The tables in MIRD Pamphlet No 7 [4] give *F*_β(*x*) values for 75 radionuclides in water. The values used for β spectra were taken essentially from a compilation by Martin *et al.* [35]. These data can be extrapolated to media other than water.

The monoenergetic DPK values published by Berger [12] were used by Prestwich *et al.* [36] to calculate DPK for six radionuclides of interest in nuclear medicine (^{32}P , ^{67}Cu , ^{90}Y , ^{131}I , ^{186}Re and ^{188}Re). Only the β emissions of each radionuclide were considered. The results are presented in table form as well as in analytic form (via a fit of the data by a sum of log-normal and exponential functions).

The values published by Simpkin and Mackie [15], obtained using the EGS4 Monte Carlo code [37], concern eight radionuclides (^{32}P , ^{67}Cu , ^{90}Y , ^{105}Rh , ^{131}I , ^{153}Sm , ^{186}Re and ^{188}Re). The calculation was performed for β spectra and monoenergetic emissions.

The tables for β -ray dose distributions in water published by Cross *et al.* [14, 34] were calculated using the ACCEPT code (derived from ETRAN). The integration of monoenergetic DPKs for 147 radionuclides was performed for β emissions with a relative intensity greater than 1% and conversion or Auger electrons with energy above 30 keV and intensity greater than 1%. The results are in agreement with those obtained experimentally or by simulation using other codes (ETRAN or EGS4). As experimental values measured in water were not available, validation was performed by extrapolation of values measured in other media (air, gas, plastic or metal scintillators). The results are shown as the product of the dose rate at distance r from a point source multiplied by the squared distance, i.e., $r^2 \cdot J'(r)$, in $\text{nGy h}^{-1} \text{Bq}^{-1} \text{cm}^2$, which in fact amounts to the product obtained by multiplying r^2 by a dose per decay (similar to an S -factor in MIRD terms) [38].

Cross [39] has more recently proposed empirical expressions for calculation of doses delivered at some distance from point sources. The principle consists in adding an 'end-of-range' term to an expression similar to that proposed by Loevinger. The adjustment was made for 60 radionuclides using data derived from the ACCEPT code. The error involved is of the order of a few per cent in most cases.

The DPKs proposed for electrons rarely descend below 10–20 keV, which for most simulation codes corresponds to the limit for validity of the multiple diffusion theory. It is possible to simulate interactions on an *ad hoc* basis, and various codes have been proposed for this purpose [40]. However, their use is generally limited to energy depositions very near the emission point (e.g., for Auger emitters). These applications most often relate to microdosimetric studies, which are outside the field of DPK utilization.

7.3.3. Combined approaches

Leicher [20] proposed a unified approach to photon and β particle dosimetry based on a fit of Berger tables for photons [17] and electrons [4]. The empirical function proposed is also valid for photons and β particles.

Other point-kernels generated by the EGS4 Monte Carlo code have more recently been proposed by Furhang *et al.* [21] for 14 radionuclides in

an aqueous medium (^{123}I , ^{124}I , ^{125}I , ^{131}I , ^{111}In , ^{64}Cu , ^{67}Cu , ^{67}Ga , ^{68}Ga , ^{186}Re , ^{188}Re , ^{153}Sm , $^{117\text{m}}\text{Sn}$ and $^{99\text{m}}\text{Tc}$). The results are expressed by providing for each radionuclide the coefficients of a series of polynomials and exponentials approximating the calculated values. Once again, the equations proposed are easy to include in more complex calculation programs.

Bolch *et al.* [41] extended the DPK concept to cubic geometry by presenting S value tables at the voxel level. The objective was to use these S values in cases in which cumulated activity is determined from tomoscintigraphic images or quantitative autoradiographies, i.e., from numerical images sampled in three dimensions (voxels). For each target voxel, the mean dose is obtained by summing the doses delivered by each surrounding voxel:

$$\bar{D}(\text{voxel}_k) = \sum_{h=0}^N A_{\text{voxel}_h} \cdot S(\text{voxel}_k \leftarrow \text{voxel}_h) \quad (7.12)$$

The determination of $S(\text{voxel}_k \leftarrow \text{voxel}_h)$ is performed by Monte Carlo calculation using the EGS4 code in a homogeneous medium (soft tissue). In fact, this calculation could have been performed perfectly well directly from DPKs.

The calculation was performed for different radionuclides (^{32}P , ^{89}Sr , ^{90}Y , $^{99\text{m}}\text{Tc}$ and ^{131}I) for cubic voxels with 3 and 6 mm sides (i.e., for PET and SPECT respectively) and for ^{131}I for cubic voxels with 0.1 mm sides (for autoradiography).

It may be concluded that numerous DPK sources exist, involving either raw data directly or relations obtained by adjustment of these values. The use of approximated relations for data (experimental or calculated), which were employed in the past to reduce calculation time, seems less justified today. Insofar as any data fit introduces an element of uncertainty into the initial scheme, it seems more logical to use raw data directly.

The calculation of raw data is generally performed from Monte Carlo simulation codes. A review of current studies indicates that the various codes proposed give similar results and are sufficiently concordant with experimental values for DPKs, so that they can be considered as reliable and used as input data in more elaborate calculation models.

7.3.4. Impact of the medium

Point-kernel dose calculations implicitly assume that the absorbed dose is deposited within a uniform, isotropic medium (usually water). The effect of accounting for differences in density and atomic number variations and the potential errors associated with neglecting such variations have been studied for photon dosimetry using Monte Carlo calculations [21]. The results are abstracted in table 7.2. The first column of values (Φ)

Table 7.2. Variation of photon absorbed fractions for selected radionuclides and organs when making different assumptions regarding organs' density and atomic number.

Radionuclide	Source	Target	Φ	Φ_ρ	$\Phi_{\rho,Z}$
^{125}I	Pancreas	Spleen	1.8×10^{-4}	1.7×10^{-4}	1.7×10^{-4}
	Left kidney	Liver	5.9×10^{-7}	4.9×10^{-7}	3.3×10^{-7}
	Left kidney	Right kidney	7.0×10^{-6}	4.0×10^{-6}	4.4×10^{-7}
^{131}I	Pancreas	Spleen	7.2×10^{-5}	6.7×10^{-5}	6.7×10^{-5}
	Left kidney	Liver	5.0×10^{-6}	4.8×10^{-6}	4.8×10^{-6}
	Left kidney	Right kidney	1.4×10^{-5}	1.2×10^{-5}	1.2×10^{-5}

presents calculations performed assuming a homogeneous water phantom with air beyond the outer contour of the reference man phantom. The second column (Φ_ρ) presents calculations accounting for density (ρ) variations, and the third ($\Phi_{\rho,Z}$) for both density and atomic number (Z) variations.

Table 7.2 shows that density and atomic number variations may be neglected for geometries in which the source, target and separating medium are similar. The pancreas, spleen and separating medium, for example, have similar densities and atomic numbers. Correspondingly, the magnitude of the error in neglecting ρ and Z variations is small. Conversely, vertebral bone separates the left and right kidneys, so that failure to correct for ρ and Z could lead to dose overestimations of more than one order of magnitude (depending on the photon energy spectrum).

The effect of accounting for differences in density and atomic number variations on photon DPK was also addressed by Monroe *et al.* [29] and Janicki *et al.* [25]. Both of these groups introduced a correction factor F to allow for a change in the effective path length between a photon point source and the point where the dose is evaluated. If the path passes through different materials j of varying thickness t_j and a linear attenuation coefficient μ_j , and μ_w is the linear attenuation coefficient of water. F is multiplied by the DPK for water to become a modified DPK. This approach also assumes that an equivalent thickness of water, producing the same primary photon attenuation as the actual path through a heterogeneous geometry, predicts scatter build-up correctly:

$$F = \exp \left[- \sum_j (\mu_j - \mu_w) t_j \right]. \quad (7.13)$$

The effect of tissue inhomogeneity is much more complicated on electron/ β DPK than on photon DPK, because of rapid variation of the electron scattering cross-section with the atomic number of the scatterer and electron

energy. Kwok *et al.* [42, 43] and Nunes *et al.* [44, 45] used both Monte Carlo calculations and experiments to assess the effect of bone and air on dose distribution of point sources of low-energy electrons and β emitters near tissue boundaries. When a point source of ^{147}Pm (maximum β energy 225 keV) or ^{204}Tl (maximum β energy 763 keV) was positioned at a planar interface of cortical bone (CB) and red marrow (RM), the radiation dose in RM within 6 μm from the interface was increased by $9 \pm 1\%$ (SE) for both sources, as compared with the dose in the same region inside a homogeneous volume of RM. The dose in a spherical shell of RM 20 μm thick next to a spherical interface of CB/RM received from a monoenergetic point source of electrons at the centre of a sphere of RM with a radius of 500 μm was increased by up to $22 \pm 1\%$ (SE) compared with that for the same scoring region in the homogeneous case. The maximum dose increase occurred at 400 keV electron energy. The dependence of dose enhancement on the curvature of the interface was also demonstrated. Conversely, when a ^{32}P point source was positioned at a planar interface of air and soft tissue, the radiation dose in soft tissue 5.5 μm from the boundary was reduced by $26.44 \pm 0.02\%$ (SE) from that in the homogeneous situation. There was no simple modification of electron/ β DPK due to tissue inhomogeneity.

An ingenious way to calculate the β DPK in any homogeneous medium from that in air (or water) was suggested by Cross and co-workers [14], and is known as the ‘scaling factor’ method. Marcu and Prestwich [46] recently extended the applicability of the scaling factor method to dissimilar media with a planar interface. The investigation was done for a planar source of ^{32}P in water and the source was located at various distances from a planar interface between water and any other homogeneous medium with atomic number Z in the range $8 < Z < 50$. Dose deposition discrepancies of less than 5% were detected for the depth within which at least 95% of the emitted energy was deposited. It will be of interest to develop procedures to apply the scaling factor method to non-planar geometries and to more than one closely spaced boundary.

7.4. A GENERAL APPROACH FOR USE OF DOSE POINT-KERNELS IN CALCULATIONS

It is rather difficult to classify the different approaches for the use of DPKs in radionuclide dosimetry. The range of applications is rather broad (calculation of absorbed doses, absorbed fractions or S factors), the scales considered extend from the cell to the organ, and the methods used are numerous (numerical integration or convolution; hybrid methods associating Monte Carlo simulation and the convolution of radioactive sources by DPKs). The classification adopted here is based on the scale of the problem, from cellular to organ dimensions.

7.4.1. Absorbed fractions on a cellular scale

DPKs are frequently used for calculations on a cellular scale, for which the medium can often be considered as homogeneous (generally equivalent to water) and isotropic.

Models have been developed to evaluate the dosimetric properties of different β emitters in the context of targeted radiotherapy. For example, in the case of homogeneous uptake of electron emitters (energy E_0) throughout the cell (radius R_S), Berger [2] has shown that the self-absorbed fraction of energy can be calculated by

$$\phi(R_S \leftarrow R_S) = \frac{1}{r_0} \int_0^{2R_S} \left[1 - 1.5 \frac{x}{2R_S} + 0.5 \left(\frac{x}{2R_S} \right)^3 \right] F(\xi, E_0) dx. \quad (7.14)$$

Likewise, for uptake on the cell surface (e.g., in radioimmunotherapy), the self-absorbed fraction [47] is given by

$$\phi(R_S \leftarrow R_S) = \frac{1}{2r_0} \int_0^\infty \left(1 - \frac{x}{2R_S} \right) F(\xi, E_0) dx \quad (7.15)$$

where $F(\xi, E_0)$ is the scaled point kernel (considered above) and r_0 the maximal electron range according to the csda.

Various publications have proposed absorbed fractions on a cellular scale. All describe the geometry of the problem analytically (even though the integration or convolution used to approach the result is generally performed numerically). They often apply a geometrical reduction factor Ψ (ranging from 0 to 1) describing the efficacy of irradiation at some distance from the source point in terms of the fraction of the sphere centred on the emission point intersecting target volume. Berger [2] noted that ‘One can interpret $\Psi(x)$ very simply as the fraction of the spherical shell of radius x around the point of observation that lies within the source region’.

The frequent use of DPK on a cellular scale can be explained at least in part by the simplification introduced through spherical symmetries, both for the geometrical model and energy deposition at some distance from a point source.

7.4.2. Absorbed fractions on a millimetre scale

When a dose is delivered on a millimetre scale, e.g., in the case of tumour mass during targeted therapy trials in animals, the use of DPK can be envisaged (generally for β -emitters), provided that the medium is always homogeneous. In this case, various possibilities can be considered, depending on how activity distribution is determined.

If the activity is described analytically, the preceding case applies, i.e., appropriate integration of DPK [48]. Thus, it is possible to convolute activity distribution by DPK [19]. If the activity is described discretely, e.g., in the

case of serial autoradiographs of tumor sections, it is possible to convolute each volume element (voxel) by the DPK to obtain the dose throughout the volume [49, 50].

A mouse model for calculating cross-organ β doses for ^{90}Y -labelled immunoconjugates was proposed by Hui *et al.* [51]. This approach used the DPK convolution proposed in MIRD Pamphlet No 7 [4] to calculate self-absorbed fractions for organs with a density close to that of water, and Monte Carlo simulation [37] for organs with a different density (lungs, bone and marrow).

It is possible to simulate the geometry of the problem (size, relative position of source regions and targets) by a Monte Carlo approach and then use DPK to calculate the doses delivered at some distance from the emission points. This approach has been used to design a 'mouse bone marrow dosimetry model' [52] or in the case of dose distribution for follicular lymphomas [53].

7.4.3. Absorbed fractions on an organ scale

Doses delivered by γ emissions are generally considered on an organ scale, in which case β emissions are regarded as non-penetrating. The calculation of S factors for the best-known anthropomorphic phantoms is based in part on DPKs [54–56]. In this case, activity is considered to be uniformly distributed in organs modelled by simplified geometric forms.

DPKs have also been proposed for customized dosimetry in the case of therapeutic applications of radionuclides [28, 57, 58]. Activity is determined from quantitative tomoscintigraphy. Thus, three-dimensional discrete distribution is considered, and activity is regarded as uniform in each volume element or voxel. The calculation is performed by DPK convolution of activity distribution.

In the case of discrete convolutions, the use of fast Fourier transform (FFT) [57] or fast Hartley transform (FHT) [59] allows a significant reduction of calculation time, which could facilitate the use of these methods in a clinical context. However, it should be recalled that these methods apply to a homogeneous medium.

7.5. CONCLUSIONS

Dose point-kernels constitute one of the tools available for performing dosimetric calculations in nuclear medicine [60]. In general, doses delivered by β emitters are considered on a microscopic scale and those by γ emitters on an organ scale. Thus, DPK dosimetric methods can be applied on a microscopic or macroscopic scale, provided that the medium in which radiations propagate is considered to be homogeneous. Is it possible to go beyond this limitation of homogeneity?

DPKs constitute the most suitable approach when the medium is actually homogeneous and isotropic, but provide only a stop-gap solution when it is heterogeneous and an estimation of delivered doses is required within a reasonable time. In fact, the relevant alternative to using DPK in a heterogeneous medium consists in simulating particle transport and energy depositions integrally by Monte Carlo methods. This alternative is being used increasingly in medical physics, e.g., in nuclear medicine. However, the methods applied still require abilities in physics and computer science and involve a computing power that limits their extension. In the near future, it is likely that simulation methods will satisfy current needs for customized dosimetry on a per patient basis in targeted radiotherapy and other applications. In the meantime, uses of DPKs in a heterogeneous medium can probably be explored in dosimetry for brachytherapy and superposition methods [23].

In principle, the field of DPK applications concerns cases in which the mean absorbed dose at some distance from a point source is valid, representing a stochastic and macrodosimetric magnitude. However, this is not always true, e.g., when dose calculations are made on a cellular scale and it is necessary to verify that the situation is outside the field of application of microdosimetric methods [61].

DPKs have been used for more than 40 years in the field of radionuclide dosimetry. They represent the energy transfer function at some distance from a point source and can be used in many dosimetric approaches that apply the superposition principle. Values available in the literature both for γ and electron/ β emissions can be considered as reliable. The large number of approaches proposed, whether for simple or complex geometries described analytically or discretely, are indicative of the value and versatility of this type of data in medical physics.

REFERENCES

- [1] Loevinger R, Japha E M and Brownell G L 1956 *Discrete Radioisotope Sources in Radiation Dosimetry* ed G J Hine and G L Brownell (New York: Academic) pp 693–755
- [2] Berger M J 1970 Beta-ray dosimetry calculations with the use of point kernels. In *Medical Radionuclides: Radiation Dose and Effects* eds R J Cloutier, C L Edwards and W S Snyder (Washington, DC: US Atomic Energy Commission) pp 63–86
- [3] Loevinger R and Berman M 1968 MIRD Pamphlet No 1: A schema for absorbed-dose calculation for biologically distributed radionuclides *J. Nucl. Med.* **9** 7–14
- [4] Berger M J 1971 MIRD Pamphlet No 7: Distribution of absorbed doses around point sources of electrons and beta particles in water and other media *J. Nucl. Med.* **12** 5–23
- [5] Spencer L V 1955 Theory of electron penetration *Phys. Rev.* **98** 1597–615
- [6] Spencer L V 1959 *Energy Dissipation by Fast Electrons*. Monograph No 1 (National Bureau of Standards)
- [7] Loevinger R and Holt J G 1956 Internally administered radioisotopes. In *Radiation dosimetry* ed G J Hine and G L Brownell (New York: Academic) pp 801–73

- [8] Spencer L V 1966 *Energy Dissipation by Fast Electrons*. Monograph No 1, US Government Printing Office (National Bureau of Standards)
- [9] Cross W G and Williams G 1967 The distribution of absorbed energy from a point beta source *Canadian J. Phys.* **45** 2021–40
- [10] Cross W G, Williams G, Ing H, Freedman N O and Mainville J 1982 *Tables of beta-ray dose distributions in water, air and other media* AECL-7617 (Atomic Energy of Canada Limited)
- [11] Berger M J 1963 Monte Carlo calculation of the penetration of diffusion of fast charged particles. In *Methods in Computational Physics* F.S.a.R.M. ed B Alder (New York: Academic) pp 135–215
- [12] Berger M J 1973 *Improved point kernels for electrons and beta-ray dosimetry* NBSIR-73-107 (National Bureau of Standards)
- [13] Seltzer S M 1988 An overview of ETRAN Monte Carlo methods. In *Monte Carlo Transport of Electrons and Photons* ed T M Jenkins, W R Nelson and A Rindi (New York: Plenum) pp 153–81
- [14] Cross W G, Freedman N O and Wong P Y 1992 *Tables of beta-ray dose distributions in water* AECL-10521 (Atomic Energy of Canada Limited)
- [15] Simpkin D J and Mackie T R 1990 EGS4 Monte Carlo determination of the beta dose kernel in water *Med. Phys.* **17** 179–86
- [16] Rogers D W O and Bielajew A F 1988 A comparison of EGS4 and ETRAN. In *Monte Carlo Transport of Electrons and Photons* ed T M Jenkins, W R Nelson and A Rindi (New York: Plenum) pp 323–44
- [17] Berger M J 1968 Energy deposition in water by photons from point isotropic sources. MIRD Pamphlet No 2 *J. Nucl. Med.* **9** 15–25
- [18] Brownell G L, Ellet W H and Reddy A R 1968 MIRD Pamphlet No 3: Absorbed fractions for photon dosimetry *J. Nucl. Med.* **27** 27–39
- [19] Kwok C S, Prestwich W V and Wilson B C 1985 Calculation of radiation doses for nonuniformly distributed beta and gamma radionuclides in soft tissue *Med. Phys.* **12** 405–12
- [20] Lechner P K 1994 A unified approach to photon and beta particle dosimetry *J. Nucl. Med.* **35** 1721–9
- [21] Furhang E E, Sgouros G and Chui C S 1996 Radionuclide photon dose kernels for internal emitter dosimetry *Med. Phys.* **23** 759–64
- [22] Luxton G 1994 Comparison of radiation dosimetry in water and in solid phantom materials for I-125 and Pd-103 brachytherapy sources: EGS4 Monte Carlo study *Med. Phys.* **21** 631–41
- [23] Carlsson A K and Ahnesjo A 2000 Point kernels and superposition methods for scatter dose calculations in brachytherapy *Phys. Med. Biol.* **45** 357–82
- [24] Tsoulfanidis N and Shrestha B 1997 Photon dose equivalent rate from a cylindrical source using a point kernel technique *Health Phys.* **72** 931–5
- [25] Janicki C, Duggan D M and Rahdert D A 2001 A dose-point-kernel model for a low energy gamma-emitting stent in a heterogeneous medium *Med. Phys.* **28** 1397–405
- [26] Lubberink M *et al.* 1999 Positron emission tomography and radioimmunotargeting— aspects of quantification and dosimetry *Acta Oncol.* **38** 343–9
- [27] Luxton G and Jozsef G 1999 Radial dose distribution, dose to water and dose rate constant for monoenergetic photon point sources from 10 keV to 2 MeV: EGS4 Monte Carlo model calculation *Med. Phys.* **26** 2531–8

- [28] Giap H B, Macey D J, Bayouth J E and Boyer A L 1995 Validation of a dose-point kernel convolution technique for internal dosimetry *Phys. Med. Biol.* **40** 365–81
- [29] Monroe J I *et al.* 2001 Experimental validation of dose calculation algorithms for the GliaSite RTS, a novel ^{125}I liquid-filled balloon brachytherapy applicator *Med. Phys.* **28** 73–85
- [30] Akabani G, Poston J W Sr and Bolch W E 1991 Estimates of beta absorbed fractions in small tissue volumes for selected radionuclides *J. Nucl. Med.* **32** 835–9
- [31] Lagoutine F, Coursol N and Legrand J 1982 *Table de Radionucléides* (Gif sur Yvette, France: Laboratoire National Henri Becquerel, Commissariat à l'Energie Atomique)
- [32] Weber D A, Eckerman K F, Dillman L T and Ryman J C 1989 *MIRD: Radionuclide Data and Decay Schemes* (New York: Society of Nuclear Medicine)
- [33] Seltzer S M 1991 Electron–photon Monte Carlo calculations: the ETRAN code *Appl. Radiat. Isot.* **42** 917–41
- [34] Cross W G, Freedman N O and Wong P Y 1992 Beta-ray dose distributions from point sources in an infinite water medium *Health Phys.* **63** 160–71
- [35] Martin M J and Blichert-Toft P H 1970 Radioactive atoms—Auger electrons, alpha-, beta-, gamma-, and X-ray data *Nucl. Data Tables* **8** 1–198
- [36] Prestwich W V, Nunes J and Kwok C S 1989 Beta dose point kernels for radionuclides of potential use in radioimmunotherapy *J. Nucl. Med.* **30** 1036–46
- [37] Nelson W R, Hirayama H and Rogers D W 1985 *The EGS4 Code System* Report No 265 (Stanford Linear Accelerator Center)
- [38] Loevinger R, Budinger T F and Watson E E 1991 *MIRD Primer for Absorbed Dose Calculations, Revised* (New York: Society of Nuclear Medicine)
- [39] Cross W G 1997 Empirical expressions for beta ray point source dose distributions *Rad. Prot. Dosim.* **69** 85–96
- [40] Paretzke H G, Goodhead D T, Kaplan I G and Terrissol M 1995 *Track structure quantities in atomic and molecular data for radiotherapy and radiation research* IAEA-TECDOC-799 (International Atomic Energy Agency)
- [41] Bolch W E *et al.* 1999 MIRD Pamphlet No 17: The dosimetry of nonuniform activity distributions. Radionuclide *S* values at the voxel level *J. Nucl. Med.* **40** 11S–36S
- [42] Kwok C S, Bialobzyski P J, Yu S K and Prestwich W V 1990 Effect of tissue inhomogeneity on dose distribution of point sources of low-energy electrons *Med. Phys.* **17** 786–93
- [43] Kwok C S, Bialobzyski P J and Yu S K 1991 Effect of tissue inhomogeneity on dose distribution of continuous activity of low-energy electrons in bone marrow cavities with different topologies *Med. Phys.* **18** 533–41
- [44] Nunes J, Prestwich W V and Kwok C S 1993 Experimental determination of ^{32}P dose backscatter factors at and near soft-tissue boundaries *Med. Phys.* **20** 223–1
- [45] Nunes J, Prestwich W V and Kwok C S 1993 An evaluation of the EGS4 and CYLTRAN Monte Carlo codes with regard to boundary beta-ray dosimetry by comparison with experimental beta-ray dose backscatter factors *Med. Phys.* **20** 1243–50
- [46] Marcu S M and Prestwich W V 1998 Application of the scaling factor method to estimation of beta dose distributions for dissimilar media separated by a planar interface *Med. Phys.* **25** 1478–86
- [47] Sastry K S R, Haydock C, Basha A M and Rao D V 1985 Electron dosimetry for radioimmunotherapy: optimal electron energy *Rad. Prot. Dosim.* **13** 249–52
- [48] Langmuir V K and Sutherland R M 1988 Dosimetry models for radioimmunotherapy *Med. Phys.* **15** 867–73

- [49] Roberson P L, Buchsbaum D J, Heidorn D B and Ten Haken R K 1992 Three-dimensional tumor dosimetry for radioimmunotherapy using serial autoradiography *Int. J. Rad. Oncol., Biol., Phys.* **24** 329–34
- [50] Roberson P L, Heidorn D B, Kessler M L, Ten Haken R K and Buchsbaum D J 1994 Three-dimensional reconstruction of monoclonal antibody uptake in tumor and calculation of beta dose-rate nonuniformity *Cancer* **73** 912–8
- [51] Hui T E *et al.* 1994 A mouse model for calculating cross-organ beta doses from yttrium-90-labeled immunoconjugates *Cancer* **73** 951–7
- [52] Muthuswamy M S, Roberson P L and Buchsbaum D J 1998 A mouse bone marrow dosimetry model *J. Nucl. Med.* **39** 1243–7
- [53] Hui T E *et al.* 1992 Localised beta dosimetry of ^{131}I -labeled antibodies in follicular lymphoma *Med. Phys.* **19** 97–104
- [54] Snyder W S, Ford M R, Warner G G and Watson S B 1975 MIRD Pamphlet No 11: 'S', absorbed dose per unit cumulated activity for selected radionuclides and organs (New York: Society of Nuclear Medicine)
- [55] Ford M R, Snyder W S, Dillman L T and Watson S B 1977 Maximum permissible concentration (MPC) values for spontaneously fissioning radionuclides *Health Phys.* **33** 35–43
- [56] Cristy M and Eckerman K F 1987 *Specific absorbed fractions of energy at various ages from internal photon sources. I Methods, II One year old, III Five year old, IV Ten year old, V Fifteen year old male and adult female, VI New-born and VII Adult male* ORNL/TM-8381/V1 to ORNL/TM-8381/V7 (Oak Ridge National Laboratory)
- [57] Akabani G, Hawkins W G, Eckblade M B and Lechner P K 1997 Patient-specific dosimetry using quantitative SPECT imaging and three-dimensional discrete Fourier transform convolution *J. Nucl. Med.* **38** 308–14
- [58] Lampinen J S, Pohjonen H K and Savolainen S E 1998 Calculating internal dose by convolution from SPECT/MR fusion images *Ann. Nucl. Med.* **12** 1–5
- [59] Erdi A K *et al.* 1998 Use of the fast Hartley transform for three-dimensional dose calculation in radionuclide therapy *Med. Phys.* **25** 2226–33
- [60] Bardies M and Pihet P 2000 Dosimetry and microdosimetry of targeted radiotherapy *Curr. Pharm. Design* **6** 1469–502
- [61] ICRU 1983 *Microdosimetry* ICRU Report 36 (International Commission on Radiation Units and Measurements)

Chapter 8

Radiobiology aspects and radionuclide selection criteria in cancer therapy

Amin I Kassis

8.1. INTRODUCTION

The deposition of energy by ionizing radiation is a random process. Following energy absorption by cells, certain molecular modifications will be induced that may lead to cell death. Despite the fact that this process is stochastic in nature, the death of a few cells, in general, within a tissue or an organ will not have a significant effect on its function. As the dose increases, more cells will die and eventually organ/tissue function will be impaired.

8.2. RADIOBIOLOGICAL EFFECTS

8.2.1. *Molecular lesions*

Damage to the genome of cells is the basis for most radiation effects which display themselves generally as single- and double-strand breaks within DNA (SSB and DSB, respectively), base damage, and cross-links between DNA strands and nuclear proteins [1]. Most cells types, however, are equipped with a host of enzymes that are efficient at repairing damage to DNA. To aid in their function, such cells are also outfitted with machinery that holds up the mitotic cycle until repairs can be made. Repair of DNA damage from low-linear-energy-transfer (low-LET) radiations (photons and energetic electrons) is very efficient and sensitive to dose rate [2]. On the other hand, the repair of damage from high-LET densely ionizing radiation (α particles and Auger effects in DNA) is more complex.

Another manifestation of damage to DNA is the appearance of chromosomal and chromatidal aberrations. Chromosome-type aberrations

are induced in G_1 -phase chromosomes or in unreplicated regions of S -phase chromosomes. Chromatid-type aberrations are induced in replicated regions of S -phase chromosomes and/or in G_2 -phase chromosomes. The shape of the dose-effect relationship observed for chromosomal aberrations from low-LET radiation follows the general formula $\alpha D + \beta D^2$. With increasing LET, the relationship goes from linear-quadratic to linear. Lowering the dose rate also changes the low-LET aberration curve from the quadratic type to one increasingly more linear.

8.2.2. Cellular responses

8.2.2.1. Survival

Several *in vitro* assays have been described to measure the ability of cells to proliferate. In practice, these assays measure the capacity of cells to successfully reproduce and, thus, to form a colony. Using a colony-forming assay, it is possible to determine the decrease in survival, expressed as a surviving fraction, as a function of a graded radiation dose.

Radiation survival curves are log-linear plots of surviving fraction (log) versus dose (linear). The shape of the survival curve constructed through such a set of survival points varies and will depend on certain biological, physical, and chemical factors. In general, two types of dose-survival curve have been described (figure 8.1). For the exponential survival curve, the slope is always constant and can be expressed by

$$S/S_0 = e^{-\alpha D} \quad (8.1)$$

where S/S_0 is the surviving fraction of the irradiated cells, D is the dose delivered, and $\alpha = 1/D_0$, the dose needed to reduce survival to 0.37 (for this type of curve, D_0 is also known as D_{37}). Such exponential survival curves are observed when mammalian cells are exposed to 'densely ionizing' radiation (e.g., α particle emissions, DNA-incorporated Auger electron emitters).

In the second type of dose-response relationship, expressed by the sigmoidal survival curve (figure 8.1), the efficiency of cell kill is not constant: at low doses, a slow decrease in survival is observed and the curve has a shoulder; at higher doses, an exponential decrease in survival is seen. This type of survival curve occurs routinely when mammalian cells are exposed to sparsely ionizing radiation (e.g., X-rays, β particles, extranuclear Auger electrons). Such curves can be fitted using a second-order polynomial equation:

$$S/S_0 = aD + bD^2 \quad (8.2)$$

where a and b are the fit parameters and solving for D when $S/S_0 = 0.37$ yields the D_{37} value. Alternatively, and preferably, the curve can be fitted

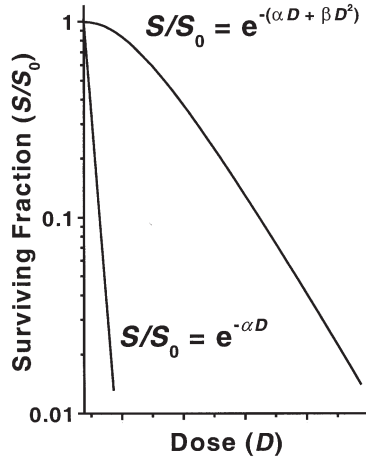


Figure 8.1. Dose-response survival curves for mammalian cells in vitro.

using a linear-quadratic equation:

$$S/S_0 = e^{-(\alpha D + \beta D^2)} \quad (8.3)$$

where α equals the rate of cell kill by a single-hit mechanism, D is the dose delivered, β equals the rate of cell kill by a double-hit mechanism, and solving for D when $S/S_0 = 0.37$ yields the D_{37} value. Rewriting equation (8.3) provides a method for calculating the rate constants α and β by graphic linearization [3]:

$$\frac{\ln(S/S_0)}{D} = -\alpha - \beta D. \quad (8.4)$$

When $\ln(S/S_0)/D$ is plotted against dose D , a linear relationship is obtained in which the y intercept with zero dose is the linear inactivation constant α and the slope of the line equals the quadratic inactivation constant β . Note that the reciprocals of α and $\sqrt{\beta}$ equal, respectively, $D_{0\alpha}$ and $D_{0\beta}$, the latter representing the D_0 value of the exponentially decreasing portion of the curve. Such plots of cell inactivation can assist in making independent components of such inactivations readily apparent, and they have significantly improved the fit of data for mammalian cell survival curves and the resolution of problems associated with the conceptual difficulty of zero slope with zero dose. Note that if radiation is protracted or the dose rate is low, as often occurs with radionuclides, the α term predominates.

8.2.2.2. Division delay

Dividing cells pass through four phases that are based on two observable events, mitosis (M) and DNA synthesis (S). Two gap phases that occur before and after the S phase are known as G_1 and G_2 , respectively.

The delay in the progression of dividing cells through their cell cycle following irradiation is a well known phenomenon. Usually it is reversible and dose dependent, occurs only at specific points in the cell cycle, and is similar for both surviving and nonsurviving cells. Cells undergoing mitosis (*M* phase) continue through division basically undisturbed; those in the G_1 phase of the cell cycle have very little delay, those in the *S* phase a moderate delay, and those in the G_2 phase maximum delay. The net result is that many cells accumulate at the G_2/M boundary, and the ratio of mitotic cells to nonmitotic cells (i.e., the mitotic index) is altered. The length of the delay and the decrease in mitotic index are both functions of dose.

8.2.2.3. *Redistribution*

The radiosensitivity of cells is a function of their position within the cell cycle. Cells in late *S* phase are most resistant (the survival curve following γ irradiation has a wide shoulder), while those in the G_2 and *M* phases are most radiosensitive (the survival curves have a steep slope and no shoulder). Consequently, following irradiation, the cells in the most sensitive phase will be killed preferentially. This redistribution of cells will lead to partial cell-cycle synchrony and a change in the overall radiosensitivity of the cell cohort. One would expect a more radioresistant cell population, but in reality the population rapidly becomes desynchronized and the net effect is sensitization of the surviving population.

8.2.2.4. *Repair*

Mammalian cells are generally capable of repairing some of the damage induced by radiation. This phenomenon is dose-rate dependent. As the dose rate decreases, the capacity of cells to repair radiation damage increases and this is manifested by a widening of the shoulder of the survival curve accompanied by an increase in D_0 (e.g., X-ray irradiation). In essence, two types of repair have been described. The first, sublethal damage (SLD) repair, occurs when a dose of radiation is split into two fractions and sufficient time is allowed (0.5–2 h) for any/all of the radiation-induced damage to be repaired. Naturally, if no repair is allowed to occur, for example, by the immediate application of a second dose of radiation, the cells will die. Sublethal damage and its repair have been shown to be important factors in the sparing of normal tissues during fractionated radiotherapy. The second, potentially lethal damage (PLD) repair, is observed only when mammalian cells are grown under suboptimal conditions following a single dose of radiation. Under such circumstances, an increase (rather than a decrease) in survival is observed. This phenomenon is believed to be a result of the delayed entry of the irradiated cells into mitosis, thereby allowing the cells to repair the PLD. Both SLD and PLD as well as their repair have been reported only for X-ray and γ irradiation (i.e., low-LET-type survival curves that have considerable

shoulders) and are practically nonexistent for neutron and α particle irradiation (i.e., high-LET radiation).

8.2.2.5. *Oxygen effect*

Oxygen radiosensitizes mammalian cells to the damaging effects of radiation. Consequently, hypoxic cells can be as much as threefold more radioresistant than well oxygenated cells. It is thought that following irradiation, oxygen enhances free radical formation and/or blocks the reversal of certain reversible chemical alterations that have occurred. Here again, it is important to note that the oxygen effect is greatest for photons and high-energy β particles (low-LET-type survival curves) and is practically absent for α particles and neutrons (high-LET-type survival curves).

8.2.3. *Tissue responses*

8.2.3.1. *Heterogeneity of response*

Following irradiation, the response of an organ/tissue/tumour will depend to a large degree on its inherent radiosensitivity. In the clinical situation, the term maximum tolerated dose (MTD) is used to indicate the highest dose that a normal organ can withstand. Once the MTD has been exceeded, the patient will exhibit the particular signs and symptoms associated with dysfunction of the organ being irradiated.

The MTD to irradiation of assorted tissues and organs is variable. The tolerance doses for the gonads and bone marrow are low (100–200 cGy); those for the intestine, kidneys and heart are moderate (2000–4500 cGy); and those for mature bone and cartilage, the bladder and the central nervous system are high (5000–7000 cGy). These doses are for external beam therapy. With radionuclides, where the dose rate is much lower, the MTD may be somewhat higher. Consequently, knowledge of the MTD for the various organs and/or tissues being irradiated is important and can help to predict with some certainty the risks associated with a radiotherapeutic dose.

8.2.3.2. *Protraction and fractionation effects*

Radiotherapists have long realized that dividing the radiation dose into daily or weekly fractions is more effective in eradicating tumours than giving a single dose, while reducing the undesirable effects in normal tissues. The size and number of the fractions, the treatment time and the total dose given depend mainly on the radiosensitivity of the tumour being eliminated and the tolerance of the surrounding normal tissues and organs. Since the response of a tumour to irradiation is determined in part by the depopulation of its dividing cells, it is expected that tumour cells react to dose fractionation

in a fashion similar to that of acutely responding rather than late responding normal tissues, i.e., have high α/β ratios (higher ratios indicate that a lower proportion of the damage will be repaired). In fact, Thames and Hendry [4] and Williams *et al.* [5] have reported significant differences between the α/β ratios for tumours and normal tissues. These authors have observed that while growing tumours exhibit a predominant α/β ratio of 10 to 20, normal tissues show a central tendency around 3 to 5. To the extent that such animal data are relevant to human tumours, it is not surprising that dose fractionation favours tumour control and minimizes normal tissue damage.

8.2.3.3. Bystander effects

Recent studies have demonstrated that a radiobiological phenomenon termed 'bystander effect' can be observed in mammalian cells grown and irradiated *in vitro*. Bystander damage describes biological effects, originating from irradiated cells, in cells not directly affected by radiation-induced ionizations. Investigators have reported that cells display lower survival and a higher rate of genetic changes than would be predicted from direct-ionization-only models [6–12] when a small fraction of a cell population growing *in vitro* has been traversed by α particles. Evidence from these reports challenges the past half-century's central tenet that radiation conveys damage to DNA either through direct ionization or indirectly via, for example, hydroxyl radicals produced in water molecules in the immediate vicinity of DNA.

To determine whether a bystander effect could be demonstrated with an *in vivo* system, we recently investigated the ability of tumour cells that are labelled with lethal doses of DNA-incorporated ^{125}I to exert a radiobiological effect on surrounding unlabelled tumour cells growing subcutaneously in nude mice (Kassis *et al.*, unpublished results). To this end, human colon adenocarcinoma LS174T cells, pre-incubated with lethal doses of the thymidine analogue 5-[^{125}I]iodo-2'-deoxyuridine ($^{125}\text{IUdR}$), were co-injected with unlabelled cells subcutaneously into nude mice, and tumour growth was measured at various times to determine the tumour's responsiveness to the co-injected 'dying' ^{125}I -labelled cells. Our data demonstrate that these ^{125}I -labelled cells have a substantial inhibitory effect on the growth of unlabelled tumour cells (figure 8.2). Since the radiation dose deposited by the radio-labelled cells into the growing tumour is less than 1/100th that needed to inhibit/delay tumour growth, we conclude that the results are a consequence of a bystander effect that is initiated by the decay of the DNA-incorporated ^{125}I atoms. These *in vivo* findings, together with those recently published by Howell and co-investigators [8, 13] in which a bystander effect was observed following the decay of DNA-incorporated tritium *in vitro*, should significantly impact the current dogma for assessing the therapeutic potential of internally administered radionuclides.

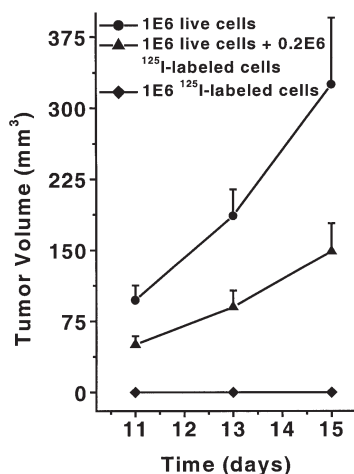


Figure 8.2. Tumour growth inhibition by the bystander effect. During the 15 day period, the presence of 0.2×10^6 ¹²⁵I-labelled cells leads to the deposition of 2 cGy only in the growing tumours (unpublished results).

8.2.4. Radiation quality

β particle, α particle and Auger electron emitters are three types of radionuclide that can be used for tumour therapy (table 8.1). Particles from these radioactive emissions produce tracks along which energy is transferred to and deposited in biological matter. The intensity of the energy transfer varies and depends on the energy, charge and mass of the traversing particle. The term linear energy transfer (LET) describes the transfer of energy (e.g., keV) along the track traversed (e.g., micrometre) by the particle. The LET of β particle emitters, such as ¹³¹I and ⁹⁰Y, is low and, depending on their energy, the particles traverse several millimetres. On the other hand, the LET of α particles emitted from ²¹¹At and ²¹³Bi and of Auger electrons emitted by ¹²⁵I is high. Actually, for Auger emitters, the electrons produce ionizations that are clustered around the point of decay (i.e., they are not along a linear track). While the tracks of α particles are several cell diameters in length, those of Auger cascade electrons are localized at the site of decay in a sphere with radius of several nanometres. The tracks at low LET are sparsely ionizing and many (thousands) are needed to produce a detectable biological effect (e.g., cell death). At high LET the distance between ionizations becomes shorter and the tracks are dense so that these particles are much more efficient at producing lethal effects. For example, several α particle traversals (fewer than five) through a cell nucleus or approximately 50 to 100 DNA-incorporated ¹²⁵I decays are sufficient to sterilize a cell.

Table 8.1. *Physical characteristics of therapeutic radionuclides.*

Decay mode	Particles	Energy	Range
β	Electrons	Medium to high (0.5–2.3 MeV)	1–12 mm
α	Helium nuclei	High (several MeV)	50–100 μm
EC/IC*	Auger electrons	Very low (eV–keV)	Several nm

* EC = electron capture; IC = internal conversion.

8.3. TARGETING PRINCIPLES IN RADIONUCLIDE THERAPY

8.3.1. Choice of radionuclide

8.3.1.1. β particles

Current radionuclide therapy in humans is based almost exclusively on β -particle-emitting isotopes. Typically, the electrons that are emitted from the nuclei of the decaying atoms (1 electron/decay) have various energies up to a maximum and thus have a distribution of ranges (table 8.2). As each particle emitted traverses matter, it follows a contorted path, loses its

Table 8.2. *Physical characteristics of β particle emitters.*

Radionuclide	Half-life	\bar{E}_β * (keV)	\bar{R}_β † (mm)	$E_{\beta(\text{max})}$ * (keV)	$R_{\beta(\text{max})}$ † (mm)
³³ P	25.4 d	77	0.09	249	0.63
¹⁶⁹ Er	9.4 d	99	0.14	350	1.1
¹⁷⁷ Lu	6.7 d	133	0.23	497	1.8
⁶⁷ Cu	61.9 h	141	0.26	575	2.1
¹³¹ I	8.0 d	182	0.39	610	2.3
¹⁵³ Sm	46.8 h	224	0.54	805	3.3
¹⁹⁸ Au	64.8 h	312	0.89	961	4.2
¹⁰⁹ Pd	13.5 h	361	1.1	1028	4.5
¹⁸⁶ Re	3.8 d	349	1.1	1077	4.8
¹⁶⁵ Dy	2.3 h	440	1.5	1285	5.9
⁸⁹ Sr	50.5 d	583	2.2	1491	7.0
³² P	14.3 d	695	2.8	1710	8.2
¹⁸⁸ Re	17.0 h	764	3.1	2120	10.4
⁹⁰ Y	64.1 h	935	4.0	2284	11.3

* Mean (\bar{E}_β) and maximum ($E_{\beta(\text{max})}$) energy of β particles emitted per disintegration [14].

† Mean (\bar{R}_β) and maximum ($R_{\beta(\text{max})}$) range of β particle in water [15].

kinetic energy and eventually comes to a stop. Since the LET of these light, charged particles is very low ($0.2 \text{ keV}/\mu\text{m}$), except for the few nanometres at the end of their range just before they stop, they are sparsely ionizing and quite inefficient at damaging DNA and killing cells. Consequently, their use as therapeutic agents predicates the presence of high radionuclide concentrations within the targeted tissue and the traversal of several thousand electrons per mammalian cell nucleus.

An important ramification of the long range (mm) of each emitted electron is the production of cross-fire, a circumstance that negates the need to target every cell within the tumour. For microscopic disease, however, long-range and some medium-range emitters may deposit a significant fraction of the energy of their particles outside the tumour [16]. This is particularly of concern in the selection of a radiopharmaceutical for the palliation of bone pain from metastatic osseous lesions [17]. Long-range emitters (e.g., ^{32}P) run the risk of significantly irradiating bone marrow as well as bony lesions, whereas short-range emitters (e.g., ^{33}P) are calculated to result in a significantly lower dose to bone marrow relative to bone/bony lesions.

The matter of inhomogeneity in the distribution of a radionuclide and its consequent dose has also been addressed. O'Donoghue [18] has derived a method for calculating an equivalent uniform biologically effective dose based on the absorbed-dose distribution represented by the biologically effective dose-volume histogram. For larger tumours he postulates that a combination of radionuclide and external beam therapy may result in optimal dose distribution.

Many of the β -particle-emitting radionuclides used for therapy also release γ photons that generally do not add significantly to the dose delivered to the target tissue. However, these photons may contribute considerably to the whole-body dose. For example, 3.7 GBq of ^{131}I distributed throughout the whole body would deposit approximately 60 cGy per day. Since the bone marrow is usually the dose-limiting organ ($200\text{--}300 \text{ cGy}$), the success or failure of therapy will depend on not exceeding its MTD.

8.3.1.2. α particles

An α particle that is emitted by any of the radionuclides suitable/available for therapy (table 8.3) is identical to a helium nucleus with energies ranging from 4 to 9 MeV . The corresponding tissue ranges are 40 to $100 \mu\text{m}$. α particles travel in straight lines, initially depositing their energy, in soft tissue, at approximately $80 \text{ keV}/\mu\text{m}$ and increasing their rate of energy deposition towards the end of their tracks. The typical energy deposition from an α particle traversing the diameter of a cell nucleus is about 600 keV ; this translates to an absorbed dose of about 0.14 Gy to the cell nucleus per hit. These numbers depend, among other parameters, on the size of the cell nucleus.

Table 8.3. *Physical characteristics of α particle emitters.*

Radionuclide	Half-life	\bar{E}_α * (MeV)	\bar{R}_α † (μm)
^{211}At	7.2 h	6.79	60
^{212}Bi	60.6 min	7.80	75
^{213}Bi	45.7 min	8.32	84

* Mean energy (\bar{E}_α) of α particles emitted per disintegration [14].

† Mean range (\bar{R}_α) of α particles calculated using second order polynomial regression fit [19]: $R = 3.87E + 0.75E^2 - 0.45$, where R is the range (μm) in unit density matter and E is the α particle energy (MeV).

Whereas the stochastics of energy distribution are unimportant for absorbed doses greater than 1 Gy for β particles because each cell experiences thousands of individual particle tracks, the *average* specific energy deposited per unit mass (i.e., the absorbed dose) is not a suitable parameter for cells traversed by a few α particles. Several authors have thus described microdosimetric approaches for calculating the specific energy deposited in *individual* cells and predicting the response of cells to α -particle irradiation [20, 21]; others (e.g., [22]) have related the specific energy distributions to the fraction of cell survivors.

The magnitude of cross-dose (from radioactive sources associated with one cell to an adjacent cell) is an important factor when evaluating α particles for therapy. This will vary considerably depending on the size of the labelled cell cluster and the fraction of cells labelled [23].

Finally, when the α particle emitter is covalently bound to the nuclear DNA of tumour cells (i.e., in the case of cell self-irradiation), the contribution of heavy ion recoil of the daughter atom must also be considered in assessing the radiobiological effects [24].

8.3.1.3. Auger electrons

During the decay of certain radioactive atoms, a vacancy is formed (most commonly in the K shell) as a consequence of electron capture (EC), with the prompt emission of a neutrino from the atomic nucleus and/or internal conversion (IC). Such vacancies are rapidly filled by electrons dropping in from higher shells. As a result of nuclear rearrangements, some Auger electron emitters also emit a γ photon that may itself be converted to a nuclear vacancy resulting in a second shower of Auger electrons (e.g., ^{125}I). Similarly, other metastable nuclei (e.g., $^{99\text{m}}\text{Tc}$, $^{80\text{m}}\text{Br}$) emit a γ photon, which may or may not be converted into an electron vacancy (only 3% of the 140 keV γ photons of $^{99\text{m}}\text{Tc}$ are converted). This process, creation of an electron vacancy within a shell and its filling up, leads to a cascade of atomic electron transitions that move the vacancy towards the outermost

Table 8.4. Physical characteristics of Auger electron emitters.

Radionuclide	Half-life	Electrons per decay*	Average energy (eV) deposited in 5 nm sphere
⁵¹ Cr	27.7 d	6	210
⁶⁷ Ga	3.3 d	5	260
⁷⁵ Se	120 d	7	270
^{99m} Tc	6 h	4	280
⁷⁷ Br	57 h	7	300
¹²³ I	13.1 h	11	420
¹¹¹ In	2.8 d	8	450
¹²⁵ I	60.1 d	20	1000
²⁰¹ Tl	73.1 h	20	1400
^{193m} Pt	4.3 d	26	1800
^{195m} Pt	4.0 d	33	2000

* Average yield of Auger and Coster–Kronig electrons.

shell. Each inner-shell electron transition results in the emission of a characteristic X-ray photon or an Auger, Coster–Kronig or super-Coster–Kronig monoenergetic electron (collectively called Auger electrons). Typically an atom undergoing EC and/or IC emits several Auger electrons with energies ranging from a few eV to approximately 80 keV. Thus, the range of Auger electrons in water is from a fraction of a nanometre to several tens of micrometres. In some cases (e.g., ¹²⁵I, ^{195m}Pt) as many as 20 to 33 Auger electrons are emitted per decay on average (table 8.4). In addition to the shower of low-energy electrons, this form of decay leaves the daughter atom with a high positive charge resulting in subsequent charge transfer processes.

The short range of Auger electrons requires their close proximity to radiosensitive targets for radiotherapeutic effectiveness. This is essentially a consequence of the precipitous drop in energy density as a function of distance in nanometres (e.g., figure 1 in Kassis *et al.* [25] and figure 4 in Kassis *et al.* [26]). These Auger electron emitters need to be located in the cell nucleus, close to or incorporated into DNA.

8.3.2. Half-life

For a radiopharmaceutical with an infinite residence time in a tumour or tissue, a radionuclide with a long physical half-life will deliver more decays than one with a short half-life if both radiopharmaceuticals have the same initial radioactivity. Moreover, there can be a striking difference in the time-dependent dose rate delivered by the two. If the number of radionuclide atoms per unit of tissue mass is n and the energy emitted (and absorbed) per

decay is E , then the absorbed-dose rate is proportional to nE/T where T is the half-life. The ratio E/T is an important indicator of the intrinsic radiotherapeutic potency of the radionuclide [27]. In general, for biological reasons (e.g., repair of SLD), higher dose rates delivered over shorter treatment times are more effective than lower dose rates delivered over longer periods. Thus, a radionuclide with a shorter half-life will tend to be more biologically effective than one with similar emission energy but a longer half-life. In addressing this complicated and multifaceted phenomenon, O'Donoghue and Wheldon [28] have noted that the relative effectiveness of ^{125}I and ^{123}I , when the same number of atoms of each is bound to a tumour, depends on the tumour doubling time and the rate at which the radiopharmaceutical dissociates from the target. When both are very long, the longer-lived ^{125}I is theoretically more effective; otherwise the shorter-lived ^{123}I is preferred.

8.3.3. Choice of vector or ligand

The selection of a suitable carrier molecule rests on many factors. These include (i) the biological specificity and *in vivo* stability, (ii) the biological mechanism(s) that bind it to target cells and the affinity of the carrier for these sites, (iii) the stability of the complex thus formed, (iv) the chemical properties of the carrier molecule which must permit the conjugation of a therapeutic radionuclide without degradation of the intrinsic characteristics of the molecule. Finally, the physical half-life of the radionuclide must be at least equal to, and preferably much longer than, the biological half-life of the carrier molecule.

One of the simplest targeting agents is radioiodine, administered as iodide for treating functional cancer of the thyroid and, potentially, breast cancers that display the iodine transporter. In the palliation of metastatic bone pain, a simple cation, radiostrontium, has been used. Its targeting relies on the accretion of alkaline-earth cation congeners of calcium on bony surfaces. The oxides of radiophosphorus as orthophosphates and the somewhat more complex phosphonates labelled with radiorhenium and radiosamarium have also been proposed.

Short peptides labelled with ^{90}Y have been used to target neuroendocrine tumours [29]. Meta- ^{131}I iodobenzylguanidine (M^{131}IBG), an iodinated neurotransmitter, is taken up by neural crest tumours [30]. Radiocolloid labelled with the α particle emitter ^{211}At has been successfully employed in treating ovarian ascites tumours in mice [31, 32].

Radioiodinated pyrimidine deoxyribose nucleosides (e.g., radioiododeoxyuridine) have been used for the experimental treatment of ovarian, brain and spinal cord tumours in animals [33–36]. Because the carrier is incorporated into the DNA of dividing cells, it is most effective when labelled with Auger-electron-emitting radionuclides.

Successful therapy of lymphomas and leukaemias has been achieved with intact antibodies and antibody fragments labelled with α - and β -particle-emitting radionuclides [37]. Specificity in this case relies on tumour-associated antigens located on the malignant cell surface.

8.3.4. *Properties of targets*

Critical tumour characteristics include (i) their accessibility, (ii) the number of carrier-molecule binding sites and (iii) the distribution of binding sites among the targeted and nontargeted cells and their relationship to the cell cycle. The microscopic environment of the target, including tumour vascularity, vascular permeability, oxygenation, microscopic organization and architecture, is also important [38, 39].

The route of administration (e.g., intravenous, intralymphatic, intraperitoneal, intrathecal) must also be considered. Some pathways may provide a mechanical means of maximizing tumour-to-nontumour ratios.

Finally, specific activity of the radiopharmaceutical should be taken into account, especially when receptors can be easily saturated and weaker non-specific binding competes with the targeting molecule. On the other hand, certain treatments, including the use of radiolabelled antibodies, may be assisted by a mass effect and optimized by the addition of unlabelled immunoglobulin.

8.4. EXPERIMENTAL THERAPEUTICS

8.4.1. *β particle emitters*

Investigators have assessed the *in vitro* toxicity of β -particle-emitting radionuclides for many years. Early work, carried out by radiobiologists, concentrated on tritium and ^{14}C , whereas later studies examined the therapeutic potential of more energetic β particle emitters (table 8.2). In these studies, the survival curves either have a distinct shoulder [40–42] or are of the high-LET type [43–45]. Invariably, the D_0 calculated is several thousand decays. The decay of such radionuclides (e.g., tritium, ^{14}C and ^{131}I) has been shown to lead to various molecular alterations (e.g., SSB, DSB, chromosomal aberrations), but only when the cells are exposed to very large numbers of decays (10 000–150 000) [40, 46–48].

Despite the rather low *in vitro* toxicity of β -particle-emitting radionuclides, they continue to be pursued for targeted therapy. This is in part due to their availability and also to the long range of the emitted electrons, which can lead to the irradiation of all the cells that are within the maximum range and path of the particle (i.e., cross-fire). As mentioned above, the main advantage of cross-fire is that it negates the necessity of the radiotherapeutic

agent's being present within each of the targeted cells, i.e., it permits a certain degree of heterogeneity. However, three factors will mainly determine whether the dose delivered to the targeted tissue will be therapeutically effective: (i) it is essential that the radiotherapeutic agent concentrate within foci throughout the targeted tissue, (ii) the distances between these hot foci must be equal to or less than twice the maximum range of the emitted energetic β particles and (iii) the concentration of the radiotherapeutic agent within each hot focus must be sufficiently high to produce a cumulative cross-fire dose to the surrounding targeted cells of approximately 10 000 cGy. Since the dose is inversely proportional to the square of the distance, it is important to note that the concentration of the therapeutic agent needed to deposit such cytotoxic doses will decrease precipitously when the distance between the hot foci decreases.

Experimentally, these predictions have been substantiated in various animal-tumour therapy studies. In many of these studies, radionuclides have been targeted after conjugation to monoclonal antibodies. For example, investigators have assessed the therapeutic efficacy of ^{131}I -labelled monoclonal antibodies in rodents bearing subcutaneous tumours. Although a substantial proportion of cells within a tumour mass show reduced/no expression of the targeted antigen and, therefore, are not targeted by the radioiodinated antibody, ^{131}I -labelled antibodies that localize in high concentrations in tumours are therapeutically efficacious and can lead to total tumour eradication in some instances [49–52]. Thus, even when ^{131}I is not-so-uniformly distributed within a tumour, the decay of this radionuclide can lead to tumour sterilization as long as it is present in sufficiently high concentrations (figure 8.3). Similar results have also been reported with other β -particle-emitting isotopes, in particular ^{90}Y [42, 53, 54] and ^{67}Cu [55, 56].

Several 'two- and three-step' approaches have also been proposed to target radioactivity to a tumour [57–61]. In general, an antibody that is not internalized by the targeted cell is injected prior to the administration of a small radiolabelled molecule that has a strong affinity to the antibody.

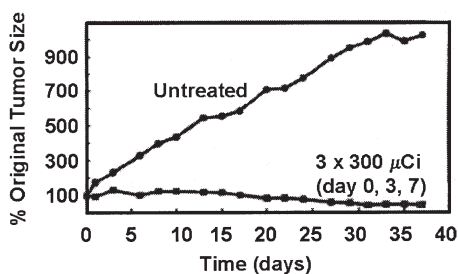


Figure 8.3. Tumour growth post-treatment with ^{131}I -labelled monoclonal antibody [51].

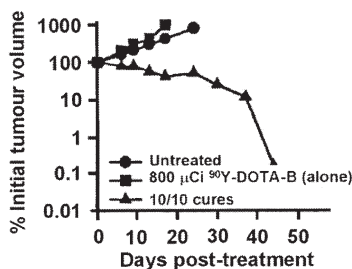


Figure 8.4. Therapeutic activity of ^{90}Y -DOTA-biotin post monoclonal anti-body-streptavidin conjugate administration in tumour-bearing mice [61]. ● and ■: controls; ▲: 800 μCi ^{90}Y -DOTA-B following pretargeting.

The most extensively studied approach utilizes the high avidity of avidin (Av) or streptavidin (SAv) for biotin, a vitamin found in low concentration in blood and tissues. Because the noncovalently bound Av/SAv-biotin complex has an extremely low dissociation constant (k_d) of about 10^{-15} M, investigators have used these two molecules as binding pairs to bridge molecules that have no affinities for each other and to target various radionuclides. A recent report [61] that examined the efficacy of this approach in tumour-bearing mice has demonstrated that 100% of the mice treated with the ^{90}Y -labelled biotin derivative have been cured of their disease (figure 8.4).

8.4.2. α particle emitters

The potential application of α -particle-emitting radionuclides as targeted therapeutic agents has been of interest for more than 25 years. If selectively accumulated in the targeted tissues (e.g., tumours), the decay of such radionuclides with their high LET and short range of a few (~ 5 – 10) cell diameters should result in highly localized energy deposition in the targeted tumour cells and minimal irradiation of surrounding normal host tissues. As a consequence of the LET of these particles (80 keV/ μm), one to four traversals of α particles through a mammalian cell nucleus will kill the cell [21, 24, 62, 63]. In comparison, the LET of negatrons emitted by the decay of β emitters is very much smaller (0.2 keV/ μm) and, thus, thousands of β particles must traverse a cell nucleus for sterilization of the cell.

The investigation of the therapeutic potential of α particle emitters has focused on three radionuclides: ^{211}At , ^{212}Bi and ^{213}Bi (table 8.3). *In vitro* studies [21, 62] have demonstrated that the decrease in survival of mammalian cells after exposure to uniformly distributed α particles from these radionuclides is monoexponential (figure 8.5) but that, as predicted theoretically [64] and shown experimentally [24], these curves develop a tail when the dose is nonuniform (figure 8.5). Such studies have shown that (i) these α

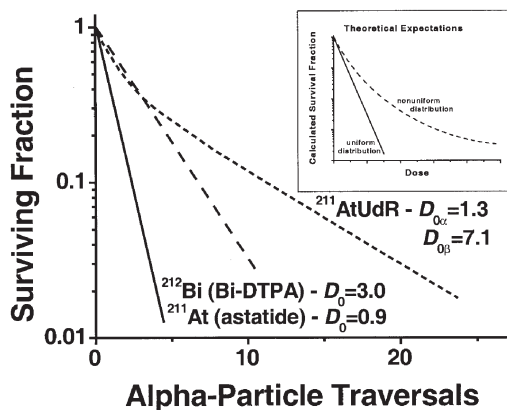


Figure 8.5. Survival of mammalian cells exposed in suspension to ^{211}At -astatide [62], ^{212}Bi -DTPA [21] or $^{211}\text{AtUdR}$ (only 50% of cells labelled) [24]. Inset: theoretical expectations [64].

particle emitters are highly toxic [21, 62, 65–70], (ii) cells in monolayers require more α particle traversals than spherical cells [21, 62], (iii) only a few (~ 1 –4) α particle traversals through a mammalian cell nucleus are necessary to sterilize a cell [21, 62, 70].

At the molecular level, the traversal of α particles through a mammalian cell nucleus leads to the efficient production of chromosomal aberrations and DSB. For example, the incubation of mammalian cells with ^{211}At -astatide causes a significant increase in chromosomal aberrations [62], but these decline with the passage of time. More recently, Walicka *et al.* [24] have established that more than ten DSBs are produced per decay of DNA-incorporated ^{211}At , a value much higher than that obtained following the decay of the DNA-incorporated Auger electron emitter ^{125}I [71, 72].

Investigators have also assessed the therapeutic potential of α particle emitters in tumour-bearing animals [31, 32, 68, 73–80]. Bloomer *et al.* [31, 32] have reported a dose-related prolongation in median survival when mice bearing an intraperitoneal murine ovarian tumour are treated with ^{211}At -tellurium colloid administered directly into the peritoneal cavity. While this α -particle-emitting radiocolloid is curative without serious morbidity, colloids of β -particle-emitting radionuclides (^{32}P , ^{165}Dy , ^{90}Y) are not (figure 8.6). In another set of *in vivo* studies examining the therapeutic efficacy of a ^{212}Bi -labelled monoclonal antibody, the radionuclide is most effective when used with a carrier having target specificity [75]. Finally, a recent report by McDevitt and co-workers [80] has demonstrated that ^{225}Ac -labelled internalizing antibodies are therapeutically effective in mice bearing solid prostate carcinoma or disseminated lymphoma. The targeting ligand is radiolabelled with ^{225}Ac ($T_{1/2} = 10$ days), a radionuclide that decays to stable ^{209}Bi via a cascade of six daughters (^{221}Fr , ^{217}At , ^{213}Bi ,

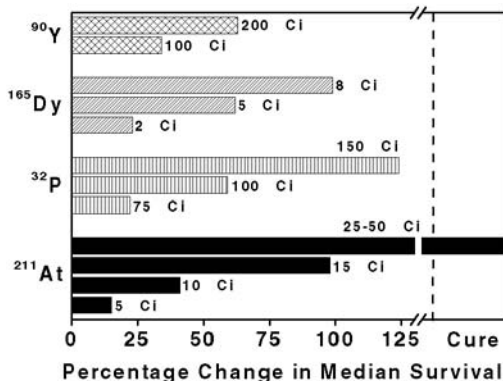


Figure 8.6. Percentage change in median survival of tumour-bearing mice treated with α - and β -emitting radiocolloids [32].

^{213}Po , ^{209}Tl , ^{209}Pb) with the emission of five α and three β particles. While the proposed approach seems promising, the use of ^{225}Ac -labelled radiopharmaceuticals in humans is very likely to generate high normal-tissue toxicity (as a consequence of the α particle recoil-energy-induced dissociation of the five chemically different radioactive atoms from the targeting carrier) post decay of the ^{225}Ac -labelled molecules that have not been internalized by the targeted tumour cells.

8.4.3. Auger electron emitters

The toxicity to mammalian cells of radionuclides that decay by EC and/or IC has, for the most part, been established with the Auger-electron-emitting radionuclide ^{125}I . Because of its predominant (93%) IC decay following EC, ^{125}I is a prolific emitter of Auger electrons (mean of ~ 20 per decaying atom [81–84]). Dosimetric calculations have predicted that the electrons most frequently produced by ^{125}I dissipate their energy in the immediate vicinity of the decaying atom and deposit 10^6 to 10^9 rad/decay within a 2 nm sphere around the decay site [26, 82, 85]. Thus, the biological effects are expected to depend critically on the proximity of the radionuclide to DNA.

The radiotoxicity of ^{125}I has been studied *in vitro* under a number of conditions including (i) when the radioelement is incorporated into the DNA duplex as iododeoxyuridine (IUDR) [26, 40, 44, 86–89], (ii) when it is intercalated between the stacked bases of DNA as 3-acetamido-5- ^{125}I iodoproflavine (A^{125}IP) [90, 91], (iii) when it is bound to the minor and major grooves of DNA as an iodinated Hoechst dye [92], (iv) as a radiolabelled triplex-forming oligonucleotide [93], (v) when it is bound to transcription elements as iodinated tamoxifen and oestrogen [94, 95] and (vi) when it is located in the cytoplasm of cultured cells as iodorhodamine (^{125}I -DR) [96].

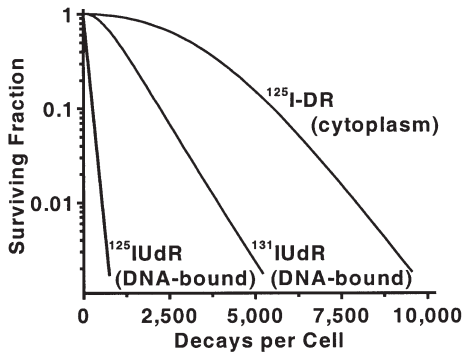


Figure 8.7. Survival of cells following exposure to ^{125}I decays: DNA-incorporated [26] or within cytoplasm [96]. The survival curve for $^{131}\text{IUdR}$ is included for comparison [41].

The decay of ^{125}I incorporated into cellular DNA as IUdR leads to an exponential decrease in clonal survival (figure 8.7). Similar responses are seen with ^{77}Br [25] and ^{123}I [97]. When plotted as a function of the total number of decays, the three curves have different slopes. If the dose to the cell nucleus is calculated, a single cell-survival curve is obtained (figure 8.8), suggesting that the radiation dose to the cell nucleus is a parameter that describes these observed biological effects adequately. When the intercalating agent A^{125}IP is incubated with cells, the survival curve is still exponential, but each decay is 1.5 times less effective than that of $^{125}\text{IUdR}$, i.e., its relative biological effectiveness (RBE) is lower (figure 8.8). On the other hand, a recent study of survival on exposure to an ^{125}I -labelled oestrogen ligand reports a D_0 similar to $^{125}\text{IUdR}$ [98].

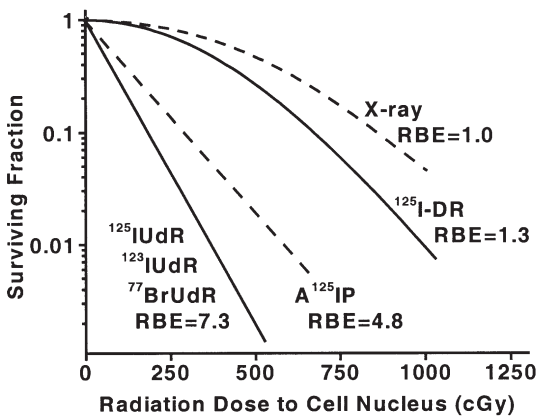


Figure 8.8. Survival fraction of V79 cells plotted as function of radiation dose to cell nucleus. RBE of each agent is calculated at the D_{37} [90].

Contrary to these survival curves, incubation of mammalian cells with an ^{125}I -labelled DNA groove binder (Hoechst 33342) results in a linear-quadratic survival curve [92]. A similar low-LET-like survival curve is also seen when ^{125}I decays within the cytoplasm (figure 8.8). Furthermore, the RBE of these agents is even lower, i.e., many more decays are required for equivalent toxicity [96].

From these experiments, it has been concluded that the position of the Auger electron emitter with regard to DNA is a major determinant of radiotoxicity and that under certain circumstances decays result in a high-LET-like response. The amount of energy deposited in the nucleus is also important, and decays taking place in the cytoplasm are much less effective.

Molecular studies have shown that the decay of ^{125}I in iodouracil leads to the creation of carbon fragments from the pyrimidine ring [99, 100]. The incorporation of the radionuclide into duplex oligonucleotides leads to shattering of the nucleic acid strands [101]. Similarly, its binding to the minor groove of plasmids results in a high yield of DSB [102, 103]. Whereas such studies have predicted correctly that the decay of DNA-incorporated ^{125}I would be highly toxic to mammalian cells, they have assumed that the radiotoxicity of $^{125}\text{IUdR}$ would be due solely to the deposition of energy directly into the DNA molecule. Experiments with radical scavenging agents have established that this is not the case and that clusters of watery radicals, formed following the decay of ^{125}I within chromatin, damage not only DNA at the site of decay but also a number of distant bases due to the packaging and compaction of DNA [71, 72]. As a result, the cytotoxicity of $^{125}\text{IUdR}$ in mammalian cells can be modified strikingly by radical scavengers [104–106]. Indeed, it now seems likely that indirect effects caused by clusters of aqueous radicals are the principal mechanism of cell damage.

The extreme degree of cytotoxicity observed with DNA-incorporated ^{125}I has been exploited in experimental radionuclide therapy using $^{125}\text{IUdR}$. Since this radiopharmaceutical breaks down rapidly after systemic administration, studies have been carried out in animal models and in patients where locoregional administration is feasible. For example, the injection of $^{125}\text{IUdR}$ into mice bearing an intraperitoneal ascites ovarian cancer has led to a 5-log reduction in tumour cell survival [33]. Similar results are obtained with $^{125}\text{IUdR}$ [34]. When $^{125}\text{IUdR}$ is administered *intracerebrally* to rats bearing an intraparenchymal gliosarcoma, the survival of treated animals is significantly prolonged [35]. Therapeutic doses of $^{125}\text{IUdR}$ injected *intrathecally* into rats with intrathecal 9L-rat-gliosarcoma tumours significantly delay the onset of paralysis in these animals [107]. Most recently, Kassis *et al.* [36, 108] have shown that the therapeutic efficacy of $^{125}\text{IUdR}$ in rats bearing intrathecal human TE-671 rhabdomyosarcoma is substantially enhanced by the co-administration of methotrexate, an antimetabolite that enhances IUdR uptake by DNA-synthesizing cells

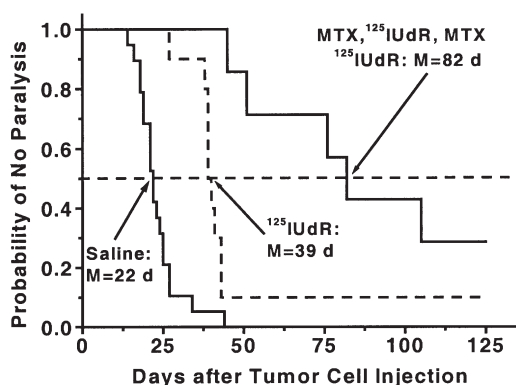


Figure 8.9. Therapy of rats bearing human intrathecal rhabdomyosarcoma. $^{125}\text{IUdR} \pm \text{methotrexate}$ was injected intrathecally [108].

(figure 8.9). This chemo–radio combination in fact leads to 5–6-log kill and cures approximately 30% of the animals.

REFERENCES

- [1] Ward J F 1986 Mechanisms of DNA repair and their potential modification for radiotherapy *Int. J. Radiat. Oncol. Biol. Phys.* **12** 1027–32
- [2] Goodhead D T 1985 Saturable repair models of radiation action in mammalian cells *Radiat. Res.* **104** S-58–67
- [3] Chapman J D 1980 Biophysical models of mammalian cell inactivation by radiation. In *Radiation Biology in Cancer Research* eds R E Meyn and H R Withers (New York: Raven) pp 21–32
- [4] Thames H D and Hendry J H 1987 *Fractionation in Radiotherapy* (London: Taylor and Francis)
- [5] Williams M V, Denekamp J and Fowler J F 1985 A review of α/β ratios for experimental tumors: implications for clinical studies of altered fractionation *Int. J. Radiat. Oncol. Biol. Phys.* **11** 87–96
- [6] Nagasawa H and Little J B 1992 Induction of sister chromatid exchanges by extremely low doses of α -particles *Cancer Res.* **52** 6394–6
- [7] Azzam E I, de Toledo S M, Gooding T and Little J B 1998 Intercellular communication is involved in the bystander regulation of gene expression in human cells exposed to very low fluences of alpha particles *Radiat. Res.* **150** 497–504
- [8] Bishayee A, Rao D V and Howell R W 1999 Evidence for pronounced bystander effects caused by nonuniform distributions of radioactivity using a novel three-dimensional tissue culture model *Radiat. Res.* **152** 88–97
- [9] Nagasawa H and Little J B 1999 Unexpected sensitivity to the induction of mutations by very low doses of alpha-particle radiation: evidence for a bystander effect *Radiat. Res.* **152** 552–7

- [10] Zhou H, Randers-Pehrson G, Waldren C A, Vannais D, Hall E J and Hei T K 2000 Induction of a bystander mutagenic effect of alpha particles in mammalian cells *Proc. Natl Acad. Sci. USA* **97** 2099–104
- [11] Azzam E I, de Toledo S M and Little J B 2001 Direct evidence for the participation of gap junction-mediated intercellular communication in the transmission of damage signals from α -particle irradiated to nonirradiated cells *Proc. Natl Acad. Sci. USA* **98** 473–8
- [12] Brenner D J, Little J B and Sachs R K 2001 The bystander effect in radiation oncogenesis: II. A quantitative model *Radiat. Res.* **155** 402–8
- [13] Bishayee A, Hall H Z, Stein D, Rao D V and Howell R W 2001 Free radical-initiated and gap junction-mediated bystander effect due to nonuniform distribution of incorporated radioactivity in a three-dimensional tissue culture model *Radiat. Res.* **155** 335–44
- [14] Kocher D C 1981 *Radioactive Decay Data Tables: A Handbook of Decay Data for Application to Radiation Dosimetry and Radiological Assessments* DOE/TIC-11026 (Springfield, VA: National Technical Information Center, US Department of Energy)
- [15] ICRU 1984 *Stopping Powers for Electrons and Positrons* Report 37 (Bethesda, MD: International Commission on Radiation Units and Measurements) p 206
- [16] Wheldon T E 1994 Targeting radiation to tumours *Int. J. Radiat. Biol.* **65** 109–16
- [17] Bouchet L G, Bolch W E, Goddu S M, Howell R W and Rao D V 2000 Considerations in the selection of radiopharmaceuticals for palliation of bone pain from metastatic osseous lesions *J. Nucl. Med.* **41** 682–7
- [18] O'Donoghue J A 1999 Implications of nonuniform tumor doses for radioimmunotherapy *J. Nucl. Med.* **40** 1337–41
- [19] ICRU 1993 *Stopping Powers and Ranges for Protons and Alpha Particles* Report 49 (Bethesda, MD: International Commission on Radiation Units and Measurements) p 256
- [20] Charlton D E and Sephton R 1991 A relationship between microdosimetric spectra and cell survival for high-LET irradiation *Int. J. Radiat. Biol.* **59** 447–57
- [21] Charlton D E, Kassiss A I and Adelstein S J 1994 A comparison of experimental and calculated survival curves for V79 cells grown as monolayers or in suspension exposed to alpha irradiation from ^{212}Bi distributed in the growth medium *Radiat. Prot. Dosim.* **52** 311–15
- [22] Roeske J C and Stinchcomb T G 1999 The use of microdosimetric moments in evaluating cell survival for therapeutic alpha-particle emitters *Radiat. Res.* **151** 31–8
- [23] Goddu S M, Howell R W and Rao D V 1994 Cellular dosimetry: absorbed fractions for monoenergetic electron and alpha particle sources and S-values for radionuclides uniformly distributed in different cell compartments *J. Nucl. Med.* **35** 303–16
- [24] Walicka M A, Vaidyanathan G, Zalutsky M R, Adelstein S J and Kassiss A I 1998 Survival and DNA damage in Chinese hamster V79 cells exposed to alpha particles emitted by DNA-incorporated astatine-211 *Radiat. Res.* **150** 263–8
- [25] Kassiss A I, Adelstein S J, Haydock C, Sastry K S R, McElvany K D and Welch M J 1982 Lethality of Auger electrons from the decay of bromine-77 in the DNA of mammalian cells *Radiat. Res.* **90** 362–73
- [26] Kassiss A I, Sastry K S R and Adelstein S J 1987 Kinetics of uptake, retention, and radiotoxicity of ^{125}I UDR in mammalian cells: implications of localized energy deposition by Auger processes *Radiat. Res.* **109** 78–89

- [27] O'Donoghue J A 1994 The impact of tumor cell proliferation in radioimmunotherapy *Cancer* **73** 974–80
- [28] O'Donoghue J A and Wheldon T E 1996 Targeted radiotherapy using Auger electron emitters *Phys. Med. Biol.* **41** 1973–92
- [29] Smith M C, Liu J, Chen T, Schran H, Yeh C-M, Jamar F, Valkema R, Bakker W, Kvols L, Krenning E and Pauwels S 2000 OctreoTher: ongoing early clinical development of a somatostatin-receptor-targeted radionuclide antineoplastic therapy *Digestion* **62** (suppl 1) 69–72
- [30] Loh K-C, Fitzgerald P A, Matthay K K, Yeo P P B and Price D C 1997 The treatment of malignant pheochromocytoma with iodine-131 metaiodobenzylguanidine (^{131}I -MIBG): a comprehensive review of 116 reported patients *J. Endocrinol. Invest.* **20** 648–58
- [31] Bloomer W D, McLaughlin W H, Neirinckx R D, Adelstein S J, Gordon P R, Ruth T J and Wolf A P 1981 Astatine-211–tellurium radiocolloid cures experimental malignant ascites *Science* **212** 340–1
- [32] Bloomer W D, McLaughlin W H, Lambrecht R M, Atcher R W, Mirzadeh S, Madara J L, Milius R A, Zalutsky M R, Adelstein S J and Wolf A P 1984 ^{211}At radiocolloid therapy: further observations and comparison with radiocolloids of ^{32}P , ^{165}Dy , and ^{90}Y *Int. J. Radiat. Oncol. Biol. Phys.* **10** 341–8
- [33] Bloomer W D and Adelstein S J 1977 5- ^{125}I -iododeoxyuridine as prototype for radionuclide therapy with Auger emitters *Nature* **265** 620–1
- [34] Baranowska-Kortylewicz J, Makrigiorgos G M, Van den Abbeele A D, Berman R M, Adelstein S J and Kassis A I 1991 5- ^{123}I iodo-2'-deoxyuridine in the radiotherapy of an early ascites tumor model *Int. J. Radiat. Oncol. Biol. Phys.* **21** 1541–51
- [35] Kassis A I, Wen P Y, Van den Abbeele A D, Baranowska-Kortylewicz J, Makrigiorgos G M, Metz K R, Matalka K Z, Cook C U, Sahu S K, Black P M and Adelstein S J 1998 5- ^{125}I iodo-2'-deoxyuridine in the radiotherapy of brain tumors in rats *J. Nucl. Med.* **39** 1148–54
- [36] Kassis A I, Dahman B A and Adelstein S J 2000 In vivo therapy of neoplastic meningitis with methotrexate and 5- ^{125}I iodo-2'-deoxyuridine *Acta Oncol.* **39** 731–7
- [37] Foon K A 2000 Monoclonal antibody therapies for lymphomas *Cancer J.* **6** 273–8
- [38] Jain R K 1990 Tumor physiology and antibody delivery *Front. Radiat. Ther. Oncol.* **24** 32–46
- [39] Netti P A, Hamberg L M, Babich J W, Kierstead D, Graham W, Hunter G J, Wolf G L, Fischman A, Boucher Y and Jain R K 1999 Enhancement of fluid filtration across tumor vessels: implication for delivery of macromolecules *Proc. Natl Acad. Sci. USA* **96** 3137–42
- [40] Chan P C, Lisco E, Lisco H and Adelstein S J 1976 The radiotoxicity of iodine-125 in mammalian cells. II. A comparative study on cell survival and cytogenetic responses to ^{125}I UdR, ^{131}I UdR, and $^3\text{HTdR}$ *Radiat. Res.* **67** 332–43
- [41] Burki H J, Koch C and Wolff S 1977 Molecular suicide studies of ^{125}I and ^3H disintegration in the DNA of Chinese hamster cells *Curr. Top. Radiat. Res. Q.* **12** 408–25
- [42] Govindan S V, Goldenberg D M, Elsamra S E, Griffiths G L, Ong G L, Brechbiel M W, Burton J, Sgouros G and Mattes M J 2000 Radionuclides linked to a CD74 antibody as therapeutic agents for B-cell lymphoma: comparison of Auger electron emitters with β -particle emitters *J. Nucl. Med.* **41** 2089–97

- [43] Ragni G and Szybalski W 1962 Molecular radiobiology of human cell lines II. Effects of thymidine replacement by halogenated analogues on cell inactivation by decay of incorporated radiophosphorus *J. Mol. Biol.* **4** 338–46
- [44] Burki H J, Roots R, Feinendegen L E and Bond V P 1973 Inactivation of mammalian cells after disintegrations of ^3H or ^{125}I in cell DNA at -196°C *Int. J. Radiat. Biol.* **24** 363–75
- [45] Liber H L, LeMotte P K and Little J B 1983 Toxicity and mutagenicity of X-rays and [^{125}I]dUrd or [^3H]TdR incorporated in the DNA of human lymphoblast cells *Mutat. Res.* **111** 387–404
- [46] Cleaver J E and Burki H J 1974 Biological damage from intranuclear carbon-14 decays: DNA single-strand breaks and repair in mammalian cells *Int. J. Radiat. Biol.* **26** 399–403
- [47] Gutiérrez S, Carbonell E, Galofré P, Creus A and Marcos R 1998 The alkaline single-cell gel electrophoresis (SCGE) assay applied to the analysis of radiation-induced DNA damage in thyroid cancer patients treated with ^{131}I *Mutat. Res.* **413** 111–19
- [48] Hengstler J G, Bockisch A, Fuchs J, Grimm W, Görges R, Oesch-Bartlomowicz B, Zapf A-O, Lade K, Tanner B, Teichmann E, Thelen M, Gebhard S and Oesch F 2000 Induction of DNA single-strand breaks by ^{131}I and $^{99\text{m}}\text{Tc}$ in human mononuclear blood cells *in vitro* and extrapolation to the *in vivo* situation *Radiat. Res.* **153** 512–20
- [49] Esteban J M, Schlom J, Mornex F and Colcher D 1987 Radioimmunotherapy of athymic mice bearing human colon carcinomas with monoclonal antibody B72.3: histological and autoradiographic study of effects on tumors and normal organs *Eur. J. Cancer Clin. Oncol.* **23** 643–55
- [50] Riklund K E, Makiya R A, Sundström B E, Thornell L-E and Stigbrand T I 1990 Experimental radioimmunotherapy of HeLa tumours in nude mice with ^{131}I -labeled monoclonal antibodies *Anticancer Res.* **10** 379–84
- [51] Buchsbaum D, Khazaeli M B, Liu T, Bright S, Richardson K, Jones M and Meredith R 1995 Fractionated radioimmunotherapy of human colon carcinoma xenografts with ^{131}I -labeled monoclonal antibody CC49 *Cancer Res.* **55** (suppl) 5881s–7s
- [52] Sato N, Saga T, Sakahara H, Yao Z, Nakamoto Y, Zhang M, Kuroki M, Matsuoka Y, Iida Y and Konishi J 1999 Intratumoral distribution of radiolabeled antibody and radioimmunotherapy in experimental liver metastases model of nude mouse *J. Nucl. Med.* **40** 685–92
- [53] Otte A, Mueller-Brand J, Dellas S, Nitzsche E U, Herrmann R and Maecke H R 1998 Yttrium-90-labelled somatostatin-analogue for cancer treatment *Lancet* **351** 417–18
- [54] Chinn P C, Leonard J E, Rosenberg J, Hanna N and Anderson D R 1999 Preclinical evaluation of ^{90}Y -labeled anti-CD20 monoclonal antibody for treatment of non-Hodgkin's lymphoma *Int. J. Oncol.* **15** 1017–25
- [55] DeNardo G L, Kukis D L, DeNardo S J, Shen S, Mausner L F, O'Donnell R T, Lamborn K R, Meyers F J, Srivastava S C and Miers L A 1997 Enhancement of ^{67}Cu -2IT-BAT-Lym-1 therapy in mice with human Burkitt's lymphoma (Raji) using interleukin-2 *Cancer* **80** 2576–82
- [56] DeNardo G L, Kukis D L, Shen S, Mausner L F, Meares C F, Srivastava S C, Miers L A and DeNardo S J 1997 Efficacy and toxicity of ^{67}Cu -2IT-BAT-Lym-1 radioimmunoconjugate in mice implanted with human Burkitt's lymphoma (Raji) *Clin. Cancer Res.* **3** 71–9

- [57] Hnatowich D J, Virzi F and Rusckowski M 1987 Investigations of avidin and biotin for imaging applications *J. Nucl. Med.* **28** 1294–302
- [58] Goodwin D A, Meares C F, McCall M J, McTigue M and Chaovapong W 1988 Pre-targeted immunoscintigraphy of murine tumors with indium-111-labeled bifunctional haptens *J. Nucl. Med.* **29** 226–34
- [59] Le Doussal J-M, Gruaz-Guyon A, Martin M, Gautherot E, Delaage M and Barbet J 1990 Targeting of indium 111-labeled bivalent hapten to human melanoma mediated by bispecific monoclonal antibody conjugates: imaging of tumors hosted in nude mice *Cancer Res.* **50** 3445–52
- [60] Kassis A I, Jones P L, Matalka K Z and Adelstein S J 1996 Antibody-dependent signal amplification in tumor xenografts following pretreatment with biotinylated monoclonal antibody and avidin or streptavidin *J. Nucl. Med.* **37** 343–52
- [61] Axworthy D B, Reno J M, Hylarides M D, Mallett R W, Theodore L J, Gustavson L M, Su F-M, Hobson L J, Beaumier P L and Fritzberg A R 2000 Cure of human carcinoma xenografts by a single dose of pretargeted yttrium-90 with negligible toxicity *Proc. Natl Acad. Sci. USA* **97** 1802–7
- [62] Kassis A I, Harris C R, Adelstein S J, Ruth T J, Lambrecht R and Wolf A P 1986 The *in vitro* radiobiology of astatine-211 decay *Radiat. Res.* **105** 27–36
- [63] Raju M R, Eisen Y, Carpenter S and Inkret W C 1991 Radiobiology of α particles III. Cell inactivation by α -particle traversals of the cell nucleus *Radiat. Res.* **128** 204–9
- [64] Humm J L, Chin L M, Cobb L and Begent R 1990 Microdosimetry in radioimmunotherapy *Radiat. Prot. Dosim.* **31** 433–6
- [65] Kurtzman S H, Russo A, Mitchell J B, DeGraff W, Sindelar W F, Brechbiel M W, Gansow O A, Friedman A M, Hines J J, Gamson J and Atcher R W 1988 ^{212}Bi linked to an antipancreatic carcinoma antibody: model for alpha-particle-emitter radioimmunotherapy *J. Natl Cancer Inst.* **80** 449–52
- [66] Larsen R H, Bruland Ø S, Hoff P, Alstad J, Lindmo T and Rofstad E K 1994 Inactivation of human osteosarcoma cells *in vitro* by ^{211}At -TP-3 monoclonal antibody: comparison with astatine-211-labeled bovine serum albumin, free astatine-211 and external-beam X rays *Radiat. Res.* **139** 178–84
- [67] Strickland D K, Vaidyanathan G and Zalutsky M R 1994 Cytotoxicity of α -particle-emitting m - ^{211}At astatobenzylguanidine on human neuroblastoma cells *Cancer Res.* **54** 5414–9
- [68] Larsen R H and Bruland Ø S 1998 Intratumour injection of immunoglobulins labelled with the α -particle emitter ^{211}At : analyses of tumour retention, microdistribution and growth delay *Br. J. Cancer* **77** 1115–22
- [69] Palm S, Bäck T, Claesson I, Delle U, Hultborn R, Jacobsson L, Köpf I and Lindegren S 1998 Effects of the alpha-particle emitter At-211 and low-dose-rate gamma-radiation on the human cell line Colo-205 as studied with a growth assay *Anticancer Res.* **18** 1671–6
- [70] Nikula T K, McDevitt M R, Finn R D, Wu C, Kozak R W, Garmestani K, Brechbiel M W, Curcio M J, Pippin C G, Tiffany-Jones L, Geerlings M W Sr, Apostolidis C, Molinet R, Geerlings M W Jr, Gansow O A and Scheinberg D A 1999 Alpha-emitting bismuth cyclohexylbenzyl DTPA constructs of recombinant humanized anti-CD33 antibodies: pharmacokinetics, bioactivity, toxicity and chemistry *J. Nucl. Med.* **40** 166–76
- [71] Walicka M A, Adelstein S J and Kassis A I 1998 Indirect mechanisms contribute to biological effects produced by decay of DNA-incorporated iodine-125 in mammalian cells *in vitro*: double-strand breaks *Radiat. Res.* **149** 134–41

- [72] Kassis A I, Walicka M A and Adelstein S J 2000 Double-strand break yield following ^{125}I decay: *effects of DNA conformation Acta Oncol.* **39** 721–6
- [73] Kozak R W, Atcher R W, Gansow O A, Friedman A M, Hines J J and Waldmann T A 1986 Bismuth-212-labeled anti-Tac monoclonal antibody: α -particle-emitting radionuclides as modalities for radioimmunotherapy *Proc. Natl Acad. Sci. USA* **83** 474–8
- [74] Harrison A and Royle L 1987 Efficacy of astatine-211-labeled monoclonal antibody in treatment of murine T-cell lymphoma *Natl Cancer Inst. Monogr.* **3** 157–8
- [75] Macklis R M, Kinsey B M, Kassis A I, Ferrara J L M, Atcher R W, Hines J J, Coleman C N, Adelstein S J and Burakoff S J 1988 Radioimmunotherapy with alpha-particle-emitting immunoconjugates *Science* **240** 1024–6
- [76] Link E M and Carpenter R N 1990 ^{211}At -methylene blue for targeted radiotherapy of human melanoma xenografts: treatment of micrometastases *Cancer Res.* **50** 2963–7
- [77] Zalutsky M R, McLendon R E, Garg P K, Archer G E, Schuster J M and Bigner D D 1994 Radioimmunotherapy of neoplastic meningitis in rats using an α -particle-emitting immunoconjugate *Cancer Res.* **54** 4719–25
- [78] Kennel S J and Mirzadeh S 1998 Vascular targeted radioimmunotherapy with ^{213}Bi —an α -particle emitter *Nucl. Med. Biol.* **25** 241–6
- [79] Adams G P, Shaller C C, Chappell L L, Wu C, Horak E M, Simmons H H, Litwin S, Marks J D, Weiner L M and Brechbiel M W 2000 Delivery of the α -emitting radioisotope bismuth-213 to solid tumors via a single-chain Fv and diabody molecules *Nucl. Med. Biol.* **27** 339–46
- [80] McDevitt M R, Ma D, Lai L T, Simon J, Borchardt P, Frank R K, Wu K, Pellegrini V, Curcio M J, Miederer M, Bander N H and Scheinberg D A 2001 Tumor therapy with targeted atomic nanogenerators *Science* **294** 1537–40
- [81] Charlton D E and Booz J 1981 A Monte Carlo treatment of the decay of ^{125}I *Radiat. Res.* **87** 10–23
- [82] Sastry K S R and Rao D V 1984 Dosimetry of low energy electrons. In *Physics of Nuclear Medicine: Recent Advances* eds D V Rao, R Chandra and M C Graham (Woodbury, NY: American Institute of Physics) pp 169–208
- [83] Pomplun E, Booz J and Charlton D E 1987 A Monte Carlo simulation of Auger cascades *Radiat. Res.* **111** 533–52
- [84] Charlton D E, Pomplun E and Booz J 1987 Some consequences of the Auger effect: fluorescence yield, charge potential, and energy imparted *Radiat. Res.* **111** 553–64
- [85] Kassis A I, Sastry K S R and Adelstein S J 1985 Intracellular localisation of Auger electron emitters: biophysical dosimetry *Radiat. Prot. Dosim.* **13** 233–6
- [86] Hofer K G and Hughes W L 1971 Radiotoxicity of intranuclear tritium, ^{125}I and ^{131}I *Radiat. Res.* **47** 94–109
- [87] Porteous D D 1971 The toxicity of ^{125}I UDR in cultured mouse BP8 tumour cells *Br. J. Cancer* **25** 594–7
- [88] Bradley E W, Chan P C and Adelstein S J 1975 The radiotoxicity of iodine-125 in mammalian cells. I. Effects on the survival curve of radioiodine incorporated into DNA *Radiat. Res.* **64** 555–63
- [89] Hofer K G, Harris C R and Smith J M 1975 Radiotoxicity of intracellular ^{67}Ga , ^{125}I and ^3H : nuclear versus cytoplasmic radiation effects in murine L1210 leukaemia *Int. J. Radiat. Biol.* **28** 225–41

- [90] Kassiss A I, Howell R W, Sastry K S R and Adelstein S J 1988 Positional effects of Auger decays in mammalian cells in culture. In *DNA Damage by Auger Emitters* eds K F Baverstock and D E Charlton (London: Taylor and Francis) pp 1–13
- [91] Kassiss A I, Fayad F, Kinsey B M, Sastry K S R and Adelstein S J 1989 Radiotoxicity of an ^{125}I -labeled DNA intercalator in mammalian cells *Radiat. Res.* **118** 283–94
- [92] Walicka M A, Ding Y, Roy A M, Harapanhalli R S, Adelstein S J and Kassiss A I 1999 Cytotoxicity of [^{125}I]iodoHoechst 33342: contribution of scavengeable effects *Int. J. Radiat. Biol.* **75** 1579–87
- [93] Sedelnikova O A, Panyutin I G, Thierry A R and Neumann R D 1998 Radiotoxicity of iodine-125-labeled oligodeoxyribonucleotides in mammalian cells *J. Nucl. Med.* **39** 1412–18
- [94] Bloomer W D, McLaughlin W H, Milius R A, Weichselbaum R R and Adelstein S J 1983 Estrogen receptor-mediated cytotoxicity using iodine-125 *J. Cell. Biochem.* **21** 39–45
- [95] Yasui L S, Hughes A and DeSombre E R 2001 Cytotoxicity of ^{125}I -oestrogen decay in non-oestrogen receptor-expressing human breast cancer cells, MDA-231 and oestrogen receptor-expressing MCF-7 cells *Int. J. Radiat. Biol.* **77** 955–62
- [96] Kassiss A I, Fayad F, Kinsey B M, Sastry K S R, Taube R A and Adelstein S J 1987 Radiotoxicity of ^{125}I in mammalian cells *Radiat. Res.* **111** 305–18
- [97] Makrigiorgos G M, Kassiss A I, Baranowska-Kortylewicz J, McElvany K D, Welch M J, Sastry K S R and Adelstein S J 1989 Radiotoxicity of 5-[^{123}I]iodo-2'-deoxyuridine in V79 cells: a comparison with 5-[^{125}I]iodo-2'-deoxyuridine *Radiat. Res.* **118** 532–44
- [98] Yasui L S, Hughes A and DeSombre E R 2001 Relative biological effectiveness of accumulated ^{125}I dU and ^{125}I -estrogen decays in estrogen receptor-expressing MCF-7 human breast cancer cells *Radiat. Res.* **155** 328–34
- [99] Halpern A and Stöcklin G 1977 Chemical and biological consequences of β -decay. Part 1 *Radiat. Environ. Biophys.* **14** 167–83
- [100] Halpern A and Stöcklin G 1977 Chemical and biological consequences of β -decay. Part 2 *Radiat. Environ. Biophys.* **14** 257–74
- [101] Martin R F and Haseltine W A 1981 Range of radiochemical damage to DNA with decay of iodine-125 *Science* **213** 896–8
- [102] Kassiss A I, Harapanhalli R S and Adelstein S J 1999 Comparison of strand breaks in plasmid DNA after positional changes of Auger electron-emitting iodine-125 *Radiat. Res.* **151** 167–76
- [103] Kassiss A I, Harapanhalli R S and Adelstein S J 1999 Strand breaks in plasmid DNA after positional changes of Auger electron-emitting iodine-125: direct compared to indirect effects *Radiat. Res.* **152** 530–8
- [104] Walicka M A, Adelstein S J and Kassiss A I 1998 Indirect mechanisms contribute to biological effects produced by decay of DNA-incorporated iodine-125 in mammalian cells *in vitro*: clonogenic survival *Radiat. Res.* **149** 142–6
- [105] Bishayee A, Rao D V, Bouchet L G, Bolch W E and Howell R W 2000 Protection by DMSO against cell death caused by intracellularly localized iodine-125, iodine-131 and polonium-210 *Radiat. Res.* **153** 416–27
- [106] Walicka M A, Ding Y, Adelstein S J and Kassiss A I 2000 Toxicity of DNA-incorporated iodine-125: quantifying the direct and indirect effects *Radiat. Res.* **154** 326–30

- [107] Sahu S K, Wen P Y C, Foulon C F, Nagel J S, Black P M, Adelstein S J and Kassis A I 1997 Intrathecal 5- ^{125}I iodo-2'-deoxyuridine in a rat model of leptomeningeal metastases *J. Nucl. Med.* **38** 386–90
- [108] Kassis A I, Dahman B A and Adelstein S J 2000 In vivo therapy of neoplastic meningitis with methotrexate and 5- ^{125}I iodo-2'-deoxyuridine *Acta Oncol.* **39** 731–7

Chapter 9

Microdosimetry of targeted radionuclides

John C Roeske and John L Humm

9.1. INTRODUCTION

Microdosimetry is the study of the stochastic process of energy deposition from radiation within small volumes. Small in the context of microdosimetry typically refers to tissue equivalent volumes commensurate with the size of the biological targets of relevance. This has commonly meant spherical volumes of between 0.3 and 20 μm —the realm in which energy deposition can be experimentally measured using a proportional counter. Such chambers are constructed of tissue equivalent plastic and operated with a tissue equivalent gas. Since these devices, used for the purpose of measuring microdosimetric spectra, were developed by Rossi [1] they are frequently referred to as ‘Rossi chambers’. One of the greatest applications of the Rossi chambers is to characterize unknown mixed radiation beams found at reactor facilities. Since Rossi counters measure radiation deposits within the chamber event by event, accumulation of the magnitude of events using a multi-channel analyser results in a spectrum of the energy deposition. Because the magnitude and spectrum of energy deposition differs for radiations of different LET (linear energy transfer), microdosimetry has developed methods of curve stripping to separate the contribution to the absorbed dose from photons, electrons, neutrons (recoil protons) and heavy ions. This has been an important contribution to radiation protection, where the radiobiological effectiveness (RBE) of different radiations depends upon the LET of the radiation. In fact, microdosimetry goes further than measuring the LET of the radiation field. By measuring the stochastics of individual radiation interactions within small, cell-equivalent volumes, it serves as a methodology of determining the entire spectrum of radiation deposits and LETs experienced by a cell or population of cells.

The energy deposition spectra measured by Rossi counters are presented in two formats: specific energy z and lineal energy y . Specific energy is defined as $z = \varepsilon/m$, where ε is the magnitude of the energy deposit within a mass m . It is the stochastic analogue of absorbed dose D . Lineal energy is defined as $y = \varepsilon/l$, where l is the mean chord length of the simulated cavity. Lineal energy is the stochastic analogue of LET.

To study energy deposition within volumes $<0.3\ \mu\text{m}$ in diameter, track structure simulation codes are required. These codes use Monte Carlo methods to model individual particle histories as they traverse matter. Coupled with models of the biological target, these track structure codes have been used to make predictions of DNA strand break and base damage [2–6]. With the development of increasingly sophisticated radionuclide targeting techniques, an understanding of the microdosimetry for these systems will assist in the interpretation of biological effects.

Radiolabelled antibodies and other nuclear medicine radionuclide targeting compounds are used either at diagnostic or therapeutic activities. Diagnostic activities administered to patients result typically in whole body doses on the order of 1 cGy. While at first glance one would expect that microdosimetric methods are required to characterize the stochastic nature of energy deposition, a closer evaluation reveals that this may not be necessary. For low LET radiations such as β -, X- and γ -rays emitted by radionuclides, an absorbed dose of 1 cGy corresponds to an average of approximately 50 individual track traversals of a cell (depending upon the assumed cell diameter). The relative deviation in the number of hits (assuming Poisson statistics) is 14% ($1/\sqrt{50}$). Applying the criteria of Kellerer and Chmelevsky [7], who state that microdosimetry should be applied when the relative deviation of the specific energy spectrum is greater than 20%, the need for microdosimetry at these absorbed doses is borderline for diagnostic tracers. However, the application of Poisson statistics is warranted only when the radionuclide distribution is uniform. This is rarely the case for any radionuclide administered to man. As a consequence, an extended application of microdosimetry, which deals not only with the stochastics of the energy deposition process (classical microdosimetry) but also with the unique biodistribution of the radionuclide, may be warranted in the analysis of energy deposition at all administered tracer activities. This concept is exemplified by the study of Makrigiorgos *et al.* [8] who performed measurements of the microdistribution of a routine diagnostic tracer $^{99\text{m}}\text{Tc}$ -Microlite from liver tissue samples and showed that, relative to other cells, the colloidal agent was concentrated 200- to 1000-fold higher in liver macrophages relative to the average activity per gram of liver.

There are two types of radionuclide for which classical microdosimetry has the greatest relevance, even at therapeutically administered activities: α and Auger electron emitters. Since α and Auger electron therapies using antibody and other carrier molecules have become a clinical reality over

the past few years, the remainder of this chapter will focus on a discussion of each.

9.2. ALPHA EMITTERS

Over the past several years, researchers have taken an interest in the use of α particle emitters as a potential form of therapy for micrometastatic disease [9–19]. The radiobiological advantages of α particles are their high linear energy transfer (LET) and independence from dose rate and oxygen effects [20]. When combined with a suitable carrier (e.g., antibody), the short range of α particles in tissue (40–90 μm) results in a highly localized deposition of energy near the point of emission (presumably in the tumour) and limits the volume of normal tissues irradiated.

The dosimetry of α particle emitters is challenging due to the stochastic nature of energy deposited in small, subcellular targets as shown schematically in figure 9.1. In this diagram, some cell nuclei receive multiple α particle hits, while others receive no hits whatsoever. (In this context, we define a hit as any α particle that intersects a cell nucleus, regardless of the energy deposited.) Additionally, an α particle may traverse a variety of path lengths in passing through a cell nucleus. For example, an α particle that intersects a spherical nucleus through the exact centre will have a path length equal to twice the radius, whereas an α particle that intersects nearly tangent to the cell nucleus

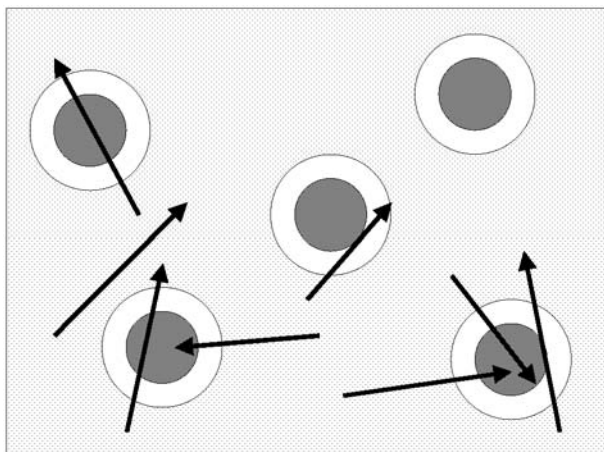


Figure 9.1. Schematic diagram illustrating the stochastic nature of energy deposited in individual cell nuclei (shaded circles) by α particles (lines with arrows). Some cells will receive no hits, while others will receive a number of hits based on the Poisson distribution.

will have little or no path length. Since the energy deposited by an α particle is proportional to its path length, each α particle in the above scenario produces one hit; however, the amount of energy deposited is significantly different. Since the distribution of hits to the cell nucleus is often characterized by using Poisson statistics, this problem is often referred to as a compound Poisson process—a Poisson distribution in the number of events where the magnitude of each event varies. Other effects that influence the dosimetry of α particles include the variation in energy loss (LET) along an individual particle's path, the size and shape of the target, and the source configuration (within the cell versus outside the cell, etc.). Thus, it is generally accepted that the analysis of the cellular response to α particle irradiation requires microdosimetric methods. The importance of microdosimetry in therapeutic applications (e.g., radioimmunotherapy) is that while two different microdosimetric distributions may have the same average specific energy (absorbed dose), they can result in significantly different levels of cell kill [21, 22].

9.2.1 Monte Carlo simulation of energy deposition by α particle emitters

Microdosimetric spectra may be calculated using either analytical or Monte Carlo methods [23]. Analytical methods use convolutions (via Fourier transforms) of the single-event spectrum to calculate multi-event distributions. The single-event spectrum represents the pattern of specific energy depositions for exactly one α particle hit. While analytical codes are computationally efficient, they are often limited to simple source–target geometries as the single-event spectrum must be known for each source–target configuration. Monte Carlo codes offer greater flexibility than analytical methods, and can simulate a wide variety of geometries and source configurations. While Monte Carlo codes may be computationally intensive, the recent availability of fast desktop computers has made the calculation time less of a concern.

α -Particle Monte Carlo codes require the developer to specify both the source and target geometry, as well as providing a characterization of the α particle energy loss. Idealizations are often made to simplify the coding and reduce calculation time. A typical algorithm initially selects an α particle emitter and determines whether the source decays based on its effective half-life. Next, the energy of the α particle emission is determined by random sampling of the branching ratios. Based on isotropic emission, the directional cosines of the α particle track are randomly assigned. In nearly all Monte Carlo codes, α particles are assumed to travel in straight lines. This approximation is valid for α particles having energies less than 10 MeV [24]. In addition, the range of δ -rays and the width of the α particle track (~ 100 nm) are often ignored since the targets that are often studied (i.e., cell nucleus) are much larger than these dimensions [25]. Using this straight-line approximation, the parametric equations [26] can be solved to determine

whether the α particle intersects the cell nucleus:

$$x = x' + t \cos(\theta_1) \quad (9.1)$$

$$y = y' + t \cos(\theta_2) \quad (9.2)$$

$$z = z' + t \cos(\theta_3). \quad (9.3)$$

In equations (9.1)–(9.3), x' , y' and z' are the coordinates of the α particle emission, and x , y and z are the intercepts of the α particle with the nucleus. The angles θ_1 , θ_2 and θ_3 are the angles of the α particle path relative to the x , y and z axes, respectively. If the nucleus is spherical (or some other simple geometry), equations (9.1)–(9.3) can be substituted into the target's analytical form to determine the distance traversed by the particle upon entering the leaving the nucleus. For example, a spherical nucleus is given by

$$(x - x_0)^2 + (y - y_0)^2 + (z - z_0)^2 = r_n^2, \quad (9.4)$$

where x_0 , y_0 and z_0 are the centre coordinates of a nucleus with radius r_n . Substituting equations (9.1)–(9.3) into equation (9.4) and solving for t yields two solutions— t_1 corresponding to the distance from the source to where the α particle enters the nucleus, and t_2 corresponding to the distance between the source and where the α particle exits the nucleus. Note that when the α particle emission occurs within the nucleus (starter), t_1 is chosen to be zero, while t_2 is the intercept with the nuclear surface. If the α particle terminates its track within the nucleus (stopper) the value of t_2 is set to the range of the particle. A hit occurs when the solutions for t_1 and t_2 are both real, positive numbers.

Next, the energy deposited within the cell nucleus is calculated. This energy is given by

$$\varepsilon_1 = \int_{R-t_2}^{R-t_1} \frac{dE}{dx} dx. \quad (9.5)$$

The energy deposited by a single α particle transit is transformed into specific energy using the relation

$$z_1 = \varepsilon_1/m. \quad (9.6)$$

In equation (9.5), (dE/dx) is the stopping power, and the limits of integration are over the residual range of the particle upon entering $(R - t_1)$ and leaving the target $(R - t_2)$, respectively. The stopping power, which characterizes the rate of energy loss per unit path length, folds in the individual processes involved in α particle energy loss [27]. Stopping power data for a variety of media can be obtained from the literature [28–32]. Inherent in the stopping power formulation is the continuous slowing down approximation (CSDA). As the name implies, this approximation assumes that α particles lose energy continuously as they traverse matter.

Thus, the determination of the specific energy deposited relies heavily on the choice of stopping powers used. In a comparison of the impact of stopping power formulation, Stinchcomb and Roeske [23] calculated specific energy spectra for the same source–target geometry as Humm [22]. The former case used Janni’s stopping power [33] for protons (appropriately scaled for α particles), while in the latter case Walsh’s stopping power [34] was utilized. In general, a disparity of 1–7% was observed in the average specific energies using these two different characterizations of the stopping power. However, in practical situations, it is expected that the uncertainty in the activity distribution will be much larger than that of the stopping powers used in the Monte Carlo calculation.

The process of determining the specific energy deposited for an individual interaction can be repeated to determine the multi-event specific energy spectrum. In this case, all sources within the maximum range of the α particle emission are evaluated to determine whether they intersect the nucleus and the subsequent specific energy deposited is calculated and summed. This scenario represents one possible outcome. Next, the process is repeated and, most likely, a different total specific energy will be calculated. By repeating this process, the entire outcome of specific energies deposited can be determined. A histogram of these individual results is the multi-event distribution. An alternative is to determine the single-event specific energy spectrum. This distribution is calculated by examining only those α particle emissions that result in exactly one hit to the cell nucleus. Each time an individual α particle intersects the nucleus, the specific energy is determined and recorded. All of these single-event specific energies are then histogrammed to determine the single-event spectrum. Single-event spectra are often used in conjunction with analytical codes whereby the multi-event spectra are calculated by multiple convolutions of the single-event spectrum. Stinchcomb and Roeske [23] demonstrated that both methods produce the same multi-event spectra within the uncertainty of the calculation itself. An example of a single-event spectrum for ^{212}Bi distributed on the cell surface is shown in figure 9.2. A multi-event spectrum for 15 ^{212}Bi sources on the cell surface is shown in figure 9.3.

Microdosimetric spectra are often combined with a model of cell survival to estimate the survival following a particular type of irradiation. The surviving fraction following α particle irradiation is given by [22, 23, 35]

$$S(\bar{z}) = \int_0^\infty f(z) e^{-z/z_0} dz \quad (9.7)$$

where $f(z)$ is the multi-event specific energy spectrum representing the fraction of cells receiving specific energies between z and $z + dz$, z_0 is the specific energy deposited within an individual cell that reduces the average cell survival to $1/e$, and $\exp(-z/z_0)$ is the fraction of cells that survive. The use of the exponential function assumes that there are no bystander

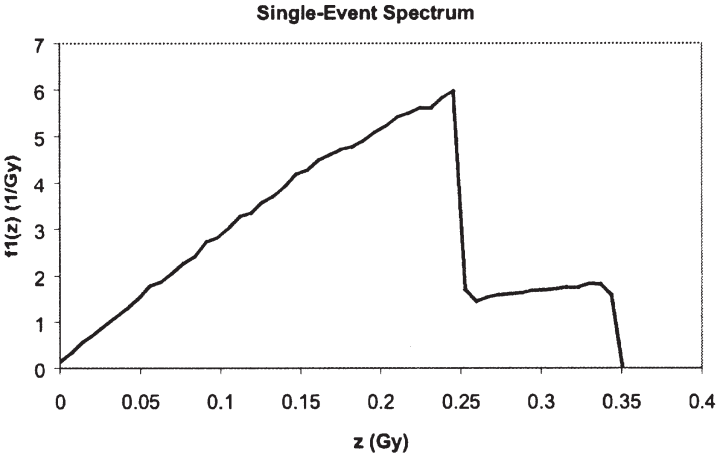


Figure 9.2. Single-event specific energy distribution for ^{212}Bi sources distributed on a cell surface. The cell radius is $10\text{ }\mu\text{m}$ and the nuclear radius is $5\text{ }\mu\text{m}$. The two peaks correspond to the two emissions from ^{212}Bi : 6.05 MeV (36%) and 8.78 MeV (64%).

effects and that intratrack interactions are dominant relative to intertrack interactions. When using the single-event spectrum, the relationship is given by [23]

$$S(\bar{z}) = \exp[-\langle n \rangle \{1 - T_1(z_0)\}] \tag{9.8}$$

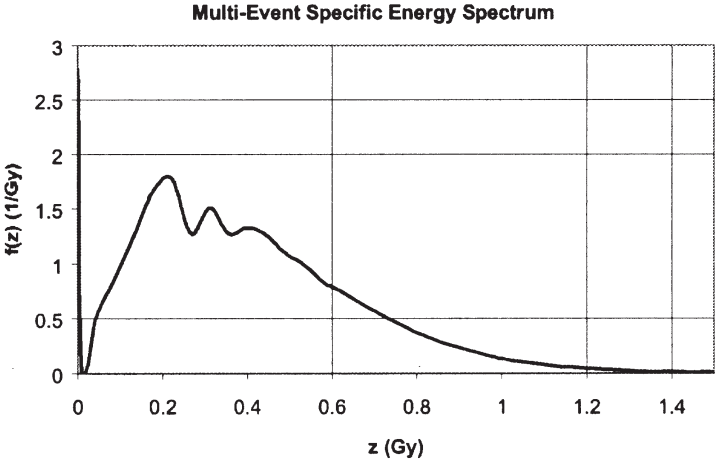


Figure 9.3. Multi-event specific energy spectrum for 15 α particle sources (^{212}Bi) distributed randomly on a cell surface with radius $10\text{ }\mu\text{m}$. The nuclear radius is $5\text{ }\mu\text{m}$. Note that a significant fraction of the cells receive zero hits to the cell nucleus.

where $\langle n \rangle$ is the average number of hits to the cell nucleus, and $T_1(z_0)$ is the Laplace transform of the single-event spectrum. Note that the same value of z_0 satisfies both equations (9.7) and (9.8).

It is important to point out that z_0 is not equal to D_0 , which is determined from the slope of the cell survival curve. Rather it is a more fundamental quantity as D_0 has folded into it not only the effects of the radiation, but also the effects of the source-target geometry. In the applications to be discussed a recurrent theme is to use the observed surviving fraction to determine the inherent cell sensitivity, z_0 .

9.2.2. Applications of microdosimetry to α particle emitters

Microdosimetry has been used in a number of α particle applications, particularly RIT. These applications can be broadly characterized as theoretical studies of simple cellular geometries, experimental analysis of cell survival following α particle irradiation, and the microdosimetry of realistic geometries such as multicellular spheroids and bone marrow. The work in each of these categories will be discussed separately.

Fisher [36] was among the first to demonstrate the utility of microdosimetry for therapeutic applications. This particular report used an analytical code based on the previous work of Roesch [37], and suggested a number of geometries for RIT including sources distributed on and within individual cells, sources distributed within spherical clusters of cells, and sources located in cylinders (i.e., blood vessels) that deposited energy within spherical cell nuclei a short distance away. These geometries have served as the basis of those used in subsequent theoretical studies. In one such study, Humm [21] combined the physical calculation of specific energy (using Monte Carlo methods) with a model for cell survival to analyse the impact of stochastic energy deposition on the expected surviving fraction of a group of cells. In particular, two geometries were considered—cells located outside a capillary and cells located within a tumour consisting of a uniform distribution of ^{211}At . The results of this analysis demonstrated that although the mean dose was similar for these two types of geometry, there was a significant variation in the expected cell survival due to the differences in the specific energy spectra. In particular, the fraction of cells without α particle hits increased with distance from the capillary (due to the short range of the α particles) resulting in a bi-exponential cell survival curve. Initially, the slope of this curve was similar to that of a uniformly irradiated tumour. However, with increasing doses, the curve was less steep and asymptotically approached a value corresponding to the fraction of non-hit cells. Building upon the previous analysis, Humm and Chin [22] analysed the effects of cell nucleus size, binding fraction, cell volume fraction and nonuniform binding on calculated specific energy spectra. Their results demonstrated that the expected cell survival curves, produced by nonuniform

distributions of α -particle-emitting radiolabelled antibodies can depart significantly from the classical mono-exponential curves that were produced by an uniform, external source of α particles. In particular, although the inherent cell sensitivity (z_0) was held constant, the slope of the cell survival curve as a function of absorbed dose to the medium was highly dependent upon the source configuration. Those cases in which cells were more uniformly irradiated had steeper cell survival curves than simulations in which the distribution of α emitters was highly heterogeneous. Stinchcomb and Roeske [38] further studied the effects of cell size and shape on expected cell survival. In this study, the cell and nucleus were allowed to take on shapes ranging from spheres to ellipsoids where the ratio of the major-to-minor axis was varied from 1 to 5, while the volume of the nucleus was held constant. Separately, the size of the nucleus was varied while the nuclear shape was held constant. Using calculated specific energy spectra and a model of cell survival, they determined that the expected cell survival was not a strong function of the target shape, provided the volume was fixed. However, they noted significant variations in cell survival as the volume of the sensitive target was varied. In a recent study by Kvinnsland *et al.* [39], microdosimetric spectra were calculated for a heterogeneous expression of cell surface antigens, as well as various diameters of cells and cell nuclei. Their results indicated that cell survival may be underestimated by two orders of magnitude if the mean values of any of these parameters are used. The largest contributor to this effect was use of the average antigen concentration. All of these studies point out a number of features related to α particle microdosimetry. In particular, they demonstrate the importance of accurately simulating the source/target geometry. Inaccuracies (such as using mean values) may impact the specific energy spectrum and subsequent estimation of cell survival.

Stinchcomb and Roeske [40] applied the previously developed methods of predicting cell survival to the analysis of experimentally produced cell survival curves. Two types of source configuration were considered. The first case consisted of cells irradiated in suspension by an ionic solution of ^{212}Bi . In this case, a small fraction of the ^{212}Bi accumulates on or within the cell. The second case consisted of ^{212}Bi chelated to DTPA—a geometry where the source remains in solution outside the cell. By calculating the specific energy distribution and knowing the resultant cell survival for the irradiation condition, the inherent cell survival (z_0) was determined using iterative methods. In this particular case, the authors observed a small difference in z_0 for the two source geometries. These differences were attributed to using the average cell size (as opposed to the cell size distribution), and thus demonstrated the importance of including the cell size distribution in future microdosimetric calculations. A microdosimetric approach was used by Larsen *et al.* [17] to determine the inherent cell sensitivity of human glioma and melanoma cell lines. Both cells lines were grown in microcolonies and

irradiated by ^{211}At -labelled antibodies. A Monte Carlo method was used to calculate the single-event spectra of microcolonies modelled as an infinite plane. This analysis indicated that one or two hits to the cell nucleus reduced the surviving fraction to 37%. Furthermore, the microdosimetric analysis revealed that the sensitivity of individual cells was much greater than would be expected using a nonstochastic dose analysis. Charlton [41] made refinements to the Larsen [17] model by incorporating the effects of finite cluster sizes. The results of this work indicated that the dose was a maximum in the centre of the individual clusters and decreased by nearly a factor of 2 near the edges, dependent upon the size of the clusters. In particular, it was observed that for smaller clusters of cells (i.e., <25) the average number of passages for 37% survival was 1.26, which was smaller than the 1.62 estimated using the infinite plane assumption. This analysis indicates the importance in accurately modelling cell geometry and its effect in interpreting cell survival studies. Aurlien *et al.* [42] compared the biological effects of ^{211}At radioimmunoconjugates to external γ -rays for osteosarcoma cells. Experiments were performed with cells in suspension containing a uniform solution of the α -particle-emitting radioactivity. The distribution of cell sizes was measured and a Monte Carlo code was used to calculate the specific energy spectra. Their results indicated that when survival was plotted as a function of the average dose there was a significantly higher level of cell kill in osteosarcoma cells relative to bone marrow cells. Thus, this form of therapy may prove efficacious. In a departure from the previous studies, Charlton *et al.* [43] applied a model of cell survival to *predict* cell survival following α particle irradiation. Initially, the microdosimetric spectra were calculated for cells grown both as a monolayer and in suspension. Using these spectra, and a model of cell survival that took into account the specific energy deposited and the incident particle's LET, a theoretical cell survival curve was generated. A comparison of theoretical with experimental survival data indicated agreement within experimental uncertainties. This approach demonstrated that if knowledge of the cell response as a function of LET is available, it is possible to use microdosimetric spectra with a model of individual cell survival to accurately predict cell survival following α particle irradiation.

The previous studies focused on combining microdosimetric spectra with biological models to analyse or predict survival of cells irradiated in suspension or as a monolayer. A logical extension of this work is the modelling of more complex geometries. One such geometry, multicellular spheroids, mimics small micrometastatic clusters and is therefore therapeutically relevant. However, because of the additional complexity, the computation is significantly more difficult and therefore few studies have been performed in this area. Kennel *et al.* [44] considered cell survival following the irradiation of multicellular spheroids with an α -particle-emitting radiolabelled antibody. Following irradiation, the spheroids were

divided into three regions corresponding to an outer, middle and inner layer of cells. Cell survival was assessed individually for each layer. Additionally, a Monte Carlo code was developed to calculate specific energy spectra as a function of depth within the spheroid assuming the activity was concentrated on the outer 10 μm . Their results demonstrated a wide variation in the specific energy distribution in the three different levels of the spheroid. The average dose was a maximum near the outer spheroid surface and decreased rapidly with depth. Conversely, the fraction of cells receiving zero hits was a minimum near the surface and increased rapidly with depth. Additionally, they noted a qualitative correlation that cells near the outer edges of the spheroids had a lower surviving fraction compared with those inside. Charlton [45] produced a calculational model for multicellular spheroids and simulated their subsequent survival. The distribution of α particle tracks throughout cells within the spheroid was calculated and combined with a cell survival model that takes into account the survival as a function of LET [46]. The results of this analysis indicated that cell survival decreased from 57 to 37% as the spheroid diameter increased from 75 to 225 μm for a uniform source with one decay per cell, and 50% packing. Longer ranged α particle emitters increased the number of hits per cell for the larger spheroids. Increasing the packing fraction from 40 to 70% decreased the survival from 46 to 26% in 200 μm diameter spheroids, again with one decay per cell. This significant decrease in survival was due to the increased crossfire dose component as cells were brought closer together. In a different simulation, a small fraction of cells (20%) was assumed not to take up any activity due to lack of expression of a surface antigen. In this simulation, the unlabelled fraction did not significantly change the expected cell survival. In both of these studies, there is evidence of a highly nonuniform specific energy distribution that varies with distance from the spheroid surface. Thus, a single specific energy distribution is not representative of that through the entire tumour. Combining specific energy distributions with a model of cell survival may provide an overall measure of the therapeutic effectiveness. However, these cell survival models do not take into account second-order processes such as bystander effects. These processes are more difficult to simulate and may play a significant role for these types of geometry. The ongoing refinement of these cell survival models is currently an area of active research [47].

Bone marrow is often the dose-limiting organ in RIT. The dosimetry of bone marrow is difficult due to the complex geometry as well as the presence of tissue inhomogeneities. Thus, idealized models, as have been utilized in previous studies, must be replaced by more realistic geometries. The work to date on estimating specific energy spectra for bone marrow has focused largely on using histological samples obtained from humans or animal models. While there has been considerable interest in bone marrow microdosimetry for protection purposes [48–51] this review will focus only on

studies related to RIT. Akabani and Zaltusky [52] obtained histological samples of beagle bone marrow, and manually measured chord length distributions. Using a Monte Carlo program, they calculated the single-event spectra for both sources in the extracellular fluid and sources located on the surface of red marrow cells. These single-event distributions were combined with a model of cell survival. This analysis demonstrated that activity concentrated on the cell surface resulted in significantly higher levels of cell kill than activity in the extracellular fluid. The effect of LET on the survival of human haemopoietic stem cells in various geometries was studied by Charlton *et al.* [53]. These geometries were determined from human marrow samples obtained from cadavers. The authors measured the distribution of distances between stem cells and fat cells. Microdosimetric spectra and cell survival were calculated for three different source/target geometries: (i) isolated cells labelled on the surface, (ii) non-targeted distribution of decays in an extended volume and (iii) non-targeted decays in marrow with 36% of the marrow volume occupied by fat. Two different radionuclides were considered, ^{149}Tb and ^{211}At . These simulations indicated that for targeted decays, ^{149}Tb was five times more effective than ^{211}At when compared on a hit-by-hit basis. This enhancement was due to the lower energy of ^{149}Tb resulting in a higher LET of the incident α particles. They also concluded that cell survival was a function of the position of decay relative to the cell nucleus. Using a similar model to Charlton [53], Utteridge *et al.* [54] considered the risk of developing secondary malignancies (i.e., leukaemia) from α particles. This risk may be important in evaluating the future therapeutic application of α particles in patients who have an excellent prognosis. Three α -emitting radionuclides were considered based on the particle's relative range (short, medium and long). In this analysis, the authors calculated the fraction of cells that are hit and would survive (as these would potentially cause secondary malignancies). They determined that lowest fraction occurred for low energies and the highest fraction occurred for the highest energy α particle emitter.

While α particle Monte Carlo codes have been used in a variety of theoretical and *in vitro* analyses, direct clinical application of microdosimetry has been limited due to a lack of knowledge of the source distribution as a function of time and location on the microscopic level. However, the previously described studies have provided valuable insight into the stochastics of α particle dosimetry that may be useful in interpreting the clinical results of patients treated with α particle emitters.

9.3. AUGER ELECTRON EMITTERS

Auger electrons are emitted by any radionuclide that decays by either electron capture or internal conversion. Both these decay processes result in an inner

atomic electron vacancy, usually in the innermost *K*-shell. This vacancy initiates a cascade of inner atomic shell transitions in which a number of low energy Auger, Coster–Kronig and super-Coster–Kronig electrons are liberated with emission energies corresponding to the differences in the binding shell energies involved in the transition. The total energy emitted following electron capture corresponds to the binding energy of a *K*-shell (or *L*-shell) electron for the appropriate atom. This energy is shared between all of the electrons and any fluorescent X-ray photons emitted. For this reason, the total energy emitted is small, and has often been disregarded in organ and total body dosimetry estimates. After internal conversion, the same Auger cascade ensues, with the difference that a potentially much higher ‘conversion electron’ from the *K*-shell (or *L*-shell) can be ejected with an energy corresponding to the difference between the nuclear excitation energy and the appropriate inner shell electron binding energy.

Radionuclides which undergo electron capture and/or internal conversion are extremely common. They constitute about half of the isotopes in the table of radionuclides, including many of the isotopes employed in routine diagnostic nuclear medicine studies, e.g., ^{99m}Tc , ^{67}Ga , ^{123}I , ^{201}Tl , etc. The relevance of the soft electrons emitted as a consequence of electron capture or internal conversion went unnoticed until the studies by Ertl *et al.* [55] and Hofer and Hughes [56]. These independent investigators discovered that when ^{125}I , which decays by electron capture followed by internal conversion, is directly incorporated into the cellular genome, via the thymidine analogue ^{125}I -iodiodeoxyuridine, that the cell survival curves resemble the appearance of α particles. Estimates of the radiation absorbed dose revealed that intranuclear decays of ^{131}I deposited more dose to the cell nucleus than ^{125}I , yet investigators found ^{125}I was >12 times more lethal than ^{131}I on a per decay basis [57, 58]. This led radiobiologists to wonder how low energy and low LET electrons could exhibit high LET properties. The history of ^{125}I radiobiology has been reviewed by Sastry [59]. In brief, Charlton and Booz [60] simulated the atomic relaxation of ^{125}I following electron capture and internal conversion and revealed that on average 21 electrons are emitted per decay. The large number of electrons emitted, and the positive charge build-up in their wake, results in a massive local energy deposit within a few Ångströms of the decay site. It was microscopic track structure simulations that revealed the physical explanation for the high radiotoxicity of ^{125}I , when Charlton [61] showed that the density of ionizations around the decay site of ^{125}I is greater than in the core of an α -particle track. Since this time, improved calculations of Auger spectra for a number of electron capture and internal conversion decaying radionuclides have been generated [62], more elaborate models of the DNA have been created [4, 63], and better experimental data on strand break damage versus distance from the decay site has been measured on high resolution denaturing polyacrylamide gels [64, 65].

Out of this work and that of many other contributors have emerged the following inferences:

1. The radiobiological effectiveness of Auger electron sources is no different from any other low LET source, provided the decay does not occur adjacent to a critical cellular target [58].
2. The range of effectiveness of Auger-electron-emitting isotopes is extremely short and decay at or within 1 nm of a sensitive structure, such as the DNA, is subject to high LET effects [66].
3. Since it is the pharmaceutical carrier which determines the sub-cellular location, the radiobiological effectiveness for any Auger emitting radionuclide depends not only on the isotope but also on the carrier molecule [67].

9.3.1. Monte Carlo simulation of Auger decays and their energy deposition

There is considerable stochastic variability in the way that energy is released from electron capture or internal conversion of decaying radionuclides. This variability was first modelled by Monte Carlo simulation of the decay process of ^{125}I [60]. Since then, Auger electron spectra have been calculated for several other radionuclides [62]. The number and distribution of energy between the electrons (and photons) emitted in an Auger cascade varies between individual disintegrations as governed by the inner shell transition probabilities. The number of permutations of possible de-excitation pathways through the atom can be hundreds, depending on the atomic number of the isotope. The way in which electron capture (or internal conversion) and the ensuing Auger cascade are computer simulated is described in detail by Charlton and Booz [60], Humm [68] and Howell [62]. In brief, a random number generator is used to select an initial inner shell vacancy according to the probabilities of capture within each of the respective orbitals K , $L1$, $L2$, $L3$ etc. The probabilities for all transitions to this vacancy are normalized to one, where each allowed transition is weighted by its respective probability according to published values for radiative [69] and non-radiative [70] transitions, determined from quantum mechanical calculations of oscillator strengths. A second random number is then used to select one of these transitions, according to their respective weights. The new electron occupancy of the orbitals is recorded and the next innermost shell vacancy is selected. This process then repeats until all of the vacancies have moved to the outermost shells (the lowest energy state), when further transitions are no longer possible.

For high Z elements (e.g., tellurium) following K -capture in iodine, the fluorescent yield is high (0.877). This means that 87.7% of the transitions to fill a K -shell vacancy emit characteristic X-rays and only 12.3% result in a K -shell Auger electron. This results in a variable total amount of electron

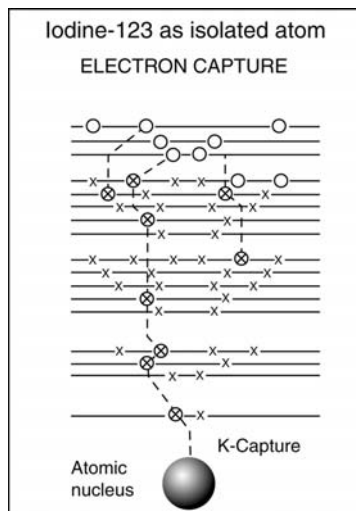


Figure 9.4. Schematic diagram of an ^{123}I atom undergoing electron capture. The crosses denote electron occupancy of each shell. A vacancy is represented by a empty circle, and a filled vacancy (as a consequence of a transition) by a circle containing a cross. Each transition moves a vacancy to a higher orbital until all vacancies occupy the outermost shells.

energy released, contingent upon the photon transitions which occur. One example of a possible atomic de-excitation pathway following electron capture for ^{123}I spectra is schematically depicted in figure 9.4.

Simulation of 10 000 individual atomic de-excitations results in an output of individual Auger electron and X-ray spectra, containing the stochastics of the de-excitation process. These data can be averaged to yield an average Auger electron emission spectrum, an example of which is shown in figure 9.5. Note that this does not denote an emission spectrum from an individual decay, but rather a frequency weighted average of 10 000 simulated decays. Dosimetric estimates to different compartments of the cell have been performed using the average Auger electron spectrum, and the results are the same as when multiple individual Auger electron spectra are used. The stochastics of individual spectra is only pertinent when calculating the energy deposition along the DNA.

Charlton and Humm [71] performed Monte Carlo electron track simulations for 10 000 individual Auger electron spectra resulting from ^{125}I and other radionuclides [66]. They scored the coordinates of each energy deposition generated by the electron track structure code of Paretzke [72], relative to the origin of the site of decay placed at the position of a base in a computer-simulated geometric model of the DNA double helix. This model consisted of a central cylinder representing the bases surrounded by

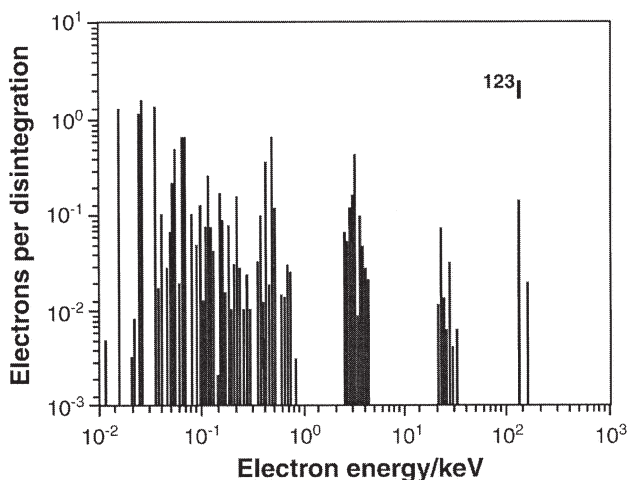


Figure 9.5. An example of an average electron energy spectrum from ^{123}I following 10 000 simulated decays.

a concentric helical cylinder of pitch 0.36 nm, representing the sugar phosphate strands. The resulting energy depositions within opposing strand segments of this DNA model were then compared with experimental data on the radius of the strand break damage measured with DNA sequencing gels relative to the ^{125}I decay site by Martin and Haseltine [73]. Matching the theoretical profile of stochastic energy deposition versus distance from the site of ^{125}I decay with the measured single-strand break frequency profile allowed a threshold energy for strand break damage to be estimated. It was a threshold energy of 17.5 eV for single-strand break production which provided the best agreement with the experimental data. To improve statistics, the energy deposition was calculated for the same individual Auger spectrum 10 times, and it was found that the variability in local energy deposition was substantial and added yet another layer of stochastic variability in the data. In summary, variation in energy deposition results from the inherent variability on atomic de-excitation and from the track structure of these emissions relative to the modelled target sites. Whereas these stochastics are not important for cellular level dosimetry estimates, except at very low numbers of decays per cell, they are important for predicting strand break damage. This is because any threshold model of strand break damage does not bear a linear relationship to the mean energy deposition.

The stochastic effects of Auger electron emitters and the high LET effects are relevant within a few nanometres of the decay site, since most Auger and Coster–Kronig electrons have ranges of this order. Therefore, for Auger sources that decay at the extracellular locations (as is the case for most diagnostic tracers used in nuclear medicine), concerns of high

LET and the consequent radiotoxicity effects are unwarranted. However, the extreme short range effects of Auger electron emitters do pose a new problem in assessing the dosimetry of novel radiopharmaceuticals. Humm *et al.* [74] and Goddu *et al.* [75] have recommended some guidelines for their evaluation, which requires the initial determination of the partition of the agent into extracellular, cell surface bound, intracellular, intranuclear and appended to the DNA. Cellular *S*-factors for the former four compartments have been calculated by Goddu *et al.* [76, 77] for a number of electron capture and internal conversion decaying radionuclides. The average radiation dose to the nucleus (or other compartment) can be determined by the piecewise addition of each contribution, upon experimental determination of the relative compartmental partitions.

9.3.2. Targeted therapy with Auger electron emitters

Auger electron emitters have been used in pre-clinical and clinical studies in a number of radiopharmaceutical forms designed to selectively deliver radiation to tumour cells. These include thymidine precursors [78–82], thymidine precursor prodrugs [83], minor DNA groove binding bisbenzimidazole ligands [84], triplet-forming oligonucleotides [85], hormones [86] and antibodies [87–90]. A review of the emerging role of Auger targeting therapies can be found in Mariani *et al.* [91]. The most effective therapies target the Auger source directly to the DNA, such as iododeoxyuridine, Hoechst 33258 or triplex-forming oligonucleotides. One drawback of these agents is the lack of tumour specificity, although attempts to attach these agents to tumour-specific carriers, such as antibodies, as a means of selective tumour targeting and intracellular access are currently under investigation. The potential therapeutic advantages of using Auger emitters for therapy with internalizing antibodies are described by Daghighian *et al.* [92] and Behr *et al.* [93]. In brief, the short range of Auger electrons renders them ineffectual in sterilizing the usual dose limiting tissues such as bone marrow, since they neither bind nor are internalized by these cells. This was clinically demonstrated by Welt *et al.* [89], who administered to patients activities in excess of 29 GBq (800 mCi) of ^{125}I -labelled A33 antibody and still did not reach dose-limiting toxicity. The cell cytoplasm acts to shield the nucleus and cellular genome from the low energy electron emissions. Antibody binding to cell surface antigen and eventual internalization increases the spatial proximity of the Auger source to the targets of cell inactivation, thus giving rise to a significant geometric and hence dosimetric differential between tumour and normal cells. However, the deposition of energy from Auger electron emitters with antibody (or hormone) approaches to the tumour targeting do not result in the high LET effects observed with ^{125}I -iododeoxyuridine. With these approaches the Auger source is treated like a very soft β source, such as tritium. As a consequence, for targeted Auger

therapy to be successful, the radiolabel carrier must reach every clonogenically potent tumour cell. This is a severe limitation. However, the theoretical rewards are enticing and it is this reason which drives researchers to further pursue the enormous potential of high radiotoxicity associated with Auger emitters with limited toxicity to normal tissues.

9.4. FUTURE DIRECTIONS

While Monte Carlo codes have produced an increased understanding of stochastic patterns of energy deposition by α particle and Auger electron emitters in both simple and complex geometries, and for different sub-cellular distributions, application to clinical practice has been limited. The principal reason is that these codes are not readily available and that often, the activity distribution as a function of time at the sub-cellular level is not well known (especially *in vivo*). One potential solution to the first problem is to combine the detailed information provided by microdosimetry with the ease of use and availability of MIRDO. Roeske and Stinchcomb [94] have provided a formalism for determining three parameters that are considered important in α particle dosimetry: average dose, standard deviation in specific energy, and the fraction of cells receiving zero hits. These parameters are determined using tables of the S value, and the first and second moments of the single-event spectra. For example, the average dose is given by the product of the S value and the cumulated activity. Dividing the average dose by the first moment of the single-event spectrum yields the average number of hits, which can be used to determine the fraction receiving zero hits (assuming Poisson statistics). The standard deviation is given by the product of the average number of hits and the second moment of the single-event spectrum. These individual moments may be determined using either analytical methods or Monte Carlo calculations. Stinchcomb and Roeske [95] have produced tables of the S value, and the individual moments for a number of geometries and source configurations appropriate for RIT. Roeske and Stinchcomb [96] applied these tables to the analysis of cell survival following α particle irradiation. Similar to previous work, they used microdosimetry to determine the inherent cell survival parameter, z_0 . However, the approach they took was to approximate the single-event spectrum by its series expansion. Terms containing moments greater than the second were dropped. In general, this approximation (using only the first and second moments) resulted in values of z_0 that agreed to within 1–2% of the value calculated by direct determination using the full spectrum. Thus, the moments approach is validated for the analysis of cell survival studies.

Monte Carlo codes for the calculation of Auger electron spectra are also not readily available. However, spectra for several electron capture and

internal conversion decaying radionuclides have been published for radionuclides relevant for diagnostic and therapeutic applications [62], allowing users to perform their own energy deposition calculations. Most of the published spectra, whereas adequate for microdosimetric calculations, have assumed static energy levels, using the $Z + 1$ or $Z + N$ approximation in the determination of the individual Auger electron emission energies. Such simplified approaches result in ever-increasing inaccuracies in the energy estimates as the number of inner shell electron vacancies increases, especially for high Z atoms. More advanced methods, based on relativistic Dirac-Fock calculations, provide a perfect energy balance of the considered atomic system when applied to Monte Carlo simulations of Auger cascades [97]. These and other developments, such as the consideration of shake-up and shake-off, will improve the accuracy of the Auger energy spectra [98, 99]. Of more immediate practical utility, a dedicated MIRD publication on cellular S factors has been published, which contains data on several Auger electron as well as α sources [100]. A method of implementation of cellular S values for Auger sources has been proposed by Humm *et al.* [74].

Another problem of α particle and Auger electron microdosimetry involves how to undergo the transition from modelled uniform or non-uniform radionuclide distributions to actual tissue (and sub-cellular) distributions. There has been significant work over the past few years that has focused on multicellular spheroids and bone marrow geometries. It is expected that researchers will obtain tissue samples and perform microautoradiography for other critical organs (e.g., liver, kidneys, etc.) to perform analyses similar to Akabani *et al.* [52] and Humm *et al.* [101]. However, as we move towards more complex geometries, radiobiological models of cell survival and normal tissue damage will require modification. This will include the modelling of the effects of nonuniform distributions of activity, the dynamics of biokinetic processes, variation of cell radiosensitivity during the different phases of the cell cycle, and bystander effects.

A final direction involves using microdosimetry to predict cell survival. Charlton *et al.* [43] showed the utility of this method by accurately predicting cell survival using the cell sensitivity as a function of LET. This approach may be useful in the design of new drugs. For example, computer simulations can be performed to predict cell survival for a new type of antibody. Various possible radionuclides can be tested with this antibody to demonstrate which combination would yield the most effective therapy. The best combination can then be experimentally verified. Such an approach would potentially speed the design and testing of new radiolabelled drugs. Another potential, along the same line, involves using microdosimetry to predict the therapeutic effectiveness within individual patients. For example, tumour cells may be obtained from a patient. By analysis of etch pits on a plastic sensitive to heavy ion tracks, as proposed by Soyland *et al.* [102–104], the cell response as a function of LET may be determined. Next, using Monte Carlo codes,

the activity distribution, cell geometry and LET response may be combined to predict cell survival. Since cell response *in vitro* may not correlate with tumour response *in vivo*, such an approach will require feedback to refine such models. It is the hope that such an approach would help avoid useless therapies in patients who may not benefit (such as those with highly resistant cells), or aid in determining the optimal dosing within an individual patient. Such applications are potentially years away from implementation, but may provide a method of optimizing radionuclide therapy to improve the therapeutic gain.

REFERENCES

- [1] Rossi H H 1968 Microdosimetric energy distribution in irradiated matter. In *Radiation Dosimetry* vol I *Fundamentals* eds F H Attix and W C Roesch (New York: Academic)
- [2] Charlton D E, Nikjoo H and Humm J L 1989 Calculation of initial yields of single- and double-strand breaks in cell nuclei from electrons, protons and alpha particles *Int. J. Radiat. Biol.* **56**(1) 1–19
- [3] Brenner D J 1990 Track structure, lesion development and cell survival *Radiat. Res.* **124**(1) (suppl) S29–37
- [4] Pomplun E 1991 A new DNA target model for track structure calculations and its first application to I-125 Auger electrons *Int. J. Radiat. Biol.* **59**(3) 625–42
- [5] Friedland W, Jacob P, Paretzke H G, Merzagora M and Ottolenghi A 1999 Simulation of DNA fragment distributions after irradiation with photons *Radiat. Environ. Biophys.* **38**(1) 39–47
- [6] Nikjoo H, O'Neill P, Terrissol M and Goodhead D T 1999 Quantitative modelling of DNA damage using Monte Carlo track structure method *Radiat. Environ. Biophys.* **38**(1) 31–8
- [7] Kellerer A M and Chmelevsky D 1975 Criteria for the applicability of LET *Radiat. Res.* **63**(2) 226–34
- [8] Makrigiorgos G M, Ito S, Baranowska-Kortylewicz J, Vinter D W, Iqbal A, Van den Abbeele A D, Adelstein S J and Kassis A I 1990 Inhomogeneous deposition of radiopharmaceuticals at the cellular level: experimental evidence and dosimetric implications *J. Nucl. Med.* **31**(8) 1358–63
- [9] Kozak R W, Atcher R W, Gansow O A, Friedman A M, Hines J J and Waldmann T 1986 Bismuth-212 labeled anti-Tac monoclonal antibody: alpha-particle-emitting radionuclides as modalities for radioimmunotherapy *Proc. Natl Acad. Sci.* **83** 474–8
- [10] Kurtzman S H, Russo A, Mitchell J B, DeGraff W, Sindelar W F, Brechbiel M W, Gansow O A, Friedman A M, Hines J J, Gamson J and Atcher R W 1988 ²¹²Bismuth linked to an antipancreatic carcinoma antibody: Model for alpha-particle-emitter radioimmunotherapy *J. Natl Cancer Inst.* **80** 449–52
- [11] Macklis R M, Kinsey B I, Kassis A I, Ferrara J L M, Atcher R W, Hines J J, Coleman C N, Adelstein S J and Burakoff S J 1989 Radioimmunotherapy with alpha-particle-emitting immunoconjugates *Science* **240** 1024–6
- [12] Zalustky M R, McLendon R E, Garg P K, Archer G E, Schuster J M and Bigner D D 1994 Radioimmunotherapy of neoplastic meningitis in rats using an alpha-particle-emitting immunoconjugate *Cancer Res.* **54** 4719–25

- [13] Zalutsky M R, Stabin M, Larsen R H and Bigner D D 1997 Tissue distribution and radiation dosimetry of astatine-211-labeled chimeric 81C6, an alpha-particle-emitting immunoconjugate *Nucl. Med. Biol.* **24** 255–1
- [14] Rotmensch J, Whitlock J L, Schwartz J L, Hines J J, Reba R C and Harper P V 1997 *In vitro* and *in vivo* studies on the development of the alpha-emitting radionuclide bismuth 212 for intraperitoneal use against microscopic ovarian carcinoma *Am. J. Obstet. Gyne.* **176** 833–41
- [15] Kennel S J and Mirzadeh S 1997 Vascular targeting for radioimmunotherapy with ^{213}Bi *Radiochimica Acta* **79** 87–91
- [16] Larsen R H, Vaidyanathan G and Zalutsky M R 1997 Cytotoxicity of alpha-particle-emitting 5- ^{211}At astato-2'-deoxyuridine in human cancer cell *Int. J. Radiat. Biol.* **72**(1) 79–90
- [17] Larsen R H, Akabani G, Welsh P and Zalutsky M R 1998 The cytotoxicity and microdosimetry of astatine-211-labeled chimeric monoclonal antibodies in human glioma and melanoma cells in vitro *Rad. Res.* **149** 155–62
- [18] Couturier O, Faivre-Chauvet A, Filippovich I V, Thedrez P, Sai-Maurel C, Barides M, Mishra A K, Gauvrit M, Blain G, Apostolodis C, Molinet R, Abbe J-C, Bataille R, Wijdenes J, Chatal J-F and Cherel M 1999 Validation of ^{213}Bi -alpha radioimmunotherapy for multiple myeloma *Clin. Cancer Res.* **5** 3165s–70s
- [19] Sgouros G, Ballangrud A M, Jurcic J G, McDevitt M R, Humm J L, Erdi Y E, Mehta B M, Finn R D, Larson S M and Scheinberg D A 1999 Pharmacokinetics and dosimetry of an alpha-particle emitter labeled antibody: ^{213}Bi -HuM195 (Anti-CD33) in patients with leukemia *J. Nucl. Med.* **40**(11) 1935–46
- [20] Hall E J 2000 *Radiobiology for the Radiologist* (Philadelphia: Lippincott, Williams and Wilkins)
- [21] Humm J L 1987 A microdosimetric model of astatine-211 labeled antibodies for radioimmunotherapy *Int. J. Radiat. Oncol. Biol. Phys.* **13** 1767–73
- [22] Humm J L and Chin L M 1993 A model of cell inactivation by alpha-particle internal emitters *Rad. Res.* **134** 143–50
- [23] Stinchcomb T G and Roeske J C 1992 Analytic microdosimetry for radioimmunotherapeutic alpha emitters *Med. Phys.* **19**(6) 1385–93
- [24] Polig E 1978 The localized dosimetry of internally deposited alpha-emitters *Curr. Top. Rad. Res.* **13** 189–327
- [25] Olko P and Booz J 1990 Energy deposition by protons and alpha particles in spherical sites of nanometer to micrometer diameter *Radiat. Environ. Biophys.* **28** 1–17
- [26] Eckerman K F, Ryman J C, Taner A C and Kerr G D Traversal of cells by radiation and absorbed dose fraction estimates for electrons and alpha particles. In *Proceedings of the Fourth International Radiopharmaceutical Dosimetry Symposium* eds A T Sch Lafke-Stelson and E E Watson (CONF-851113) (Oak Ridge, TN: Oak Ridge Associated Universities) pp 67–86
- [27] Attix F H 1986 *Introduction to Radiological Physics and Radiation Dosimetry* (New York: Wiley)
- [28] Ziegler J F, Biersack J P and Littmark U 1985 *The Stopping and Range of Ions in Matter* (New York: Pergamon)
- [29] Ziegler J F 1988 The stopping and range of ions in solids. *Ion Implantation: Science and Technology* (San Diego: Academic) pp 3–61
- [30] Ziegler J F 1999 The stopping of energetic light ions in matter *Appl. Phys. Rev., J. Appl. Phys.* **85** 1249–72

- [31] Bichsel H 1992 *Stopping powers of fast charged particles in heavy elements* NIST Report IR-4550 (Springfield, VA: US National Technical Information Service)
- [32] ICRU 1993 *Stopping powers and ranges for protons and alpha particles* Report No 49 (Bethesda, MD: International Commission of Radiation Units)
- [33] Janni J F 1966 *Calculation of energy loss, range, path length, straggling, multiple scattering and the probability of inelastic nuclear collisions for 0.1 to 1000 MeV protons* Technical Report No AFWL-TR-65-150
- [34] Walsh P J 1970 Stopping power and range of alpha particles *Health Phys.* **19** 312–16
- [35] Charlton D E and Sephton R 1991 A relationship between microdosimetric spectra and cell survival for high-LET irradiation *Int. J. Radiat. Biol.* **59**(2) 447–57
- [36] Fisher D R 1985 The microdosimetry of monoclonal antibodies labeled with alpha emitters. In *Proceedings of the Fourth International Radiopharmaceutical Dosimetry Symposium* eds A T Schlafke-Stelson and E E Watson (CONF-851113) (Oak Ridge, TN: Oak Ridge Associated Universities) pp 26–36
- [37] Roesch W C 1977 Microdosimetry of internal sources *Radiat. Res.* **70** 494–510
- [38] Stinchcomb T G and Roeske J C 1995 Survival of alpha particle irradiated cells as a function of the shape and size of the sensitive target (nucleus) *Radiat. Prot. Dosim.* **62**(3) 157–64
- [39] Kvinnsland Y, Stokke T and Aurilien E 2001 Radioimmunotherapy with alpha-particle emitters: Microdosimetry of cells with heterogeneous antigen expression and with various diameters of cells and nuclei *Radiat. Res.* **155** 288–96
- [40] Stinchcomb T G and Roeske J C 1994 Analysis of survival of C-18 cells after irradiation in suspension with chelated and ionic bismuth-212 using microdosimetry *Radiat. Res.* **140** 48–54
- [41] Charlton D E 1999 The survival of monolayers of cells growing in clusters irradiated by ^{211}At appended to the cell surfaces *Radiat. Res.* **151** 750–3
- [42] Aurilien E, Larsen R H, Akabani G, Olsen D R, Zalutsky M R and Bruland O S 2000 Exposure of human osteosarcoma and bone marrow cells to tumor-targeted alpha-particles and gamma-irradiation: Analysis of cell survival and microdosimetry *Int. J. Radiat. Biol.* **76**(8) 1129–41
- [43] Charlton D E, Kassia A I and Adelstein S J 1994 A comparison of experimental and calculated survival curves for V79 cells grown as monolayers or in suspension exposed to alpha irradiation from ^{212}Bi distributed in growth medium *Radiat. Prot. Dosim.* **52** 311–15
- [44] Kennel S J, Stabin M, Roeske J C, Foote L J, Lankford P K, Terzaghi-Howe M, Patterson H, Barkenbus J, Popp D M, Boll R and Mirzadeh S 1999 Radiotoxicity of bismuth-231 bound to membranes of monolayer and spheroid cultures of tumor cells *Radiat. Res.* **151** 244–56
- [45] Charlton D E 2000 Radiation effects in spheroids of cells exposed to alpha emitters *Int. J. Radiat. Biol.* **76**(11) 1555–64
- [46] Charlton D E and Turner M S 1996 Use of chord lengths through the nucleus to simulate the survival of mammalian cells exposed to high-LET alpha-radiation *Int. J. Radiat. Biol.* **69**(2) 213–17
- [47] Iyer M and Lehnert B E 2002 Alpha-particle-induced increases in the radioresistance of normal human bystander cells *Radiat. Res.* **157** 3–7
- [48] Humphreys E R and Humm J L 1988 A Monte-Carlo approach to the microdosimetry of ^{224}Ra in murine compact and cancellous bone *Health Phys.* **54**(6) 607–15

- [49] Charlton D E, Utteridge T D and Beddoe A H 1996 Microdosimetry of haemopoietic stem cells irradiated by alpha particles from short-lived products of ^{222}Rn decays in fat cells and haemopoietic tissue *Int. J. Radiat. Biol.* **69**(5) 585–92
- [50] Charlton D E, Salmon P L and Utteridge T D 1998 Monte Carlo/numerical treatment of alpha-particle spectra from sources buried in bone and resultant doses to surface cells *Int. J. Radiat. Biol.* **73**(1) 89–92
- [51] Austin A L, Ellender M, Haines J W, Harrison J D and Lord B I 2000 Microdistribution and localized dosimetry of the alpha-emitting radionuclides ^{239}Pu , ^{241}Am and ^{233}U in mouse femoral shaft *Int. J. Radiat. Biol.* **76**(1) 101–11
- [52] Akabani G and Zalutsky M R 1997 Microdosimetry of astatine-211 using histological images: Application to bone marrow *Radiat. Res.* **148** 599–607
- [53] Charlton D E, Utteridge T D and Allen B J 1998 Theoretical treatment of human haemopoietic stem cell survival following irradiation by alpha particles *Int. J. Radiat. Biol. Phys.* **74**(1) 111–18
- [54] Utteridge T D, Charlton D E and Allen B J 2001 Monte Carlo modeling of the effects of injected short-, medium- and longer-range alpha-particle emitters on human marrow at various ages *Radiat. Res.* **156** 413–18
- [55] Ertl H H, Feinendegen L E and Heiniger H J 1970 Iodine-125, a tracer in cell biology: physical properties and biological aspects *Phys. Med. Biol.* **15**(3) 447–56
- [56] Hofer K G and Hughes W L 1971 Radiotoxicity of intranuclear tritium, 125 iodine and 131 iodine *Radiat. Res.* **47**(1) 94–101
- [57] Chan P C, Lisco E, Lisco S and Adelstein S J 1978 Cell survival and cytogenetic responses to ^{125}I -UdR in cultured mammalian cells *Curr. Top. Radiat. Res.* **12**(1–4) 426–35
- [58] Hofer K G 1980 Radiation biology and potential therapeutic applications of radionuclides *Bull. Cancer* **67**(3) 343–53
- [59] Sastry K S 1992 Biological effects of the Auger emitter iodine-125: A review. Report No 1 of AAPM Nuclear Medicine Task Group No 6 *Med. Phys.* **19**(6) 1361–70
- [60] Charlton D E and Booz J 1981 A Monte Carlo treatment of the decay of ^{125}I *Radiat. Res.* **87**(1) 10–23
- [61] Charlton D E 1986 The range of high LET effects from ^{125}I decays *Radiat. Res.* **107**(2) 163–71
- [62] Howell R W 1992 Radiation spectra for Auger-electron emitting radionuclides: Report No 2 of AAPM Nuclear Medicine Task Group No 6 *Med. Phys.* **19**(6) 1371–83
- [63] Nikjoo H, Martin R F, Charlton D E, Terrissol M, Kandaiy S and Lobachevsky P 1996 Modelling of Auger-induced DNA damage by incorporated ^{125}I *Acta Oncol.* **35**(7) 849–56
- [64] Lobachevsky P N and Martin R F 1996 DNA strand breakage by ^{125}I -decay in a synthetic oligodeoxynucleotide. 2. Quantitative analysis of fragment distribution *Acta Oncol.* **35**(7) 809–15
- [65] Lobachevsky P N and Martin R F 2000 Iodine-125 decay in a synthetic oligodeoxynucleotide. I. Fragment size distribution and evaluation of breakage probability *Radiat. Res.* **153**(3) 263–70
- [66] Humm J L and Charlton D E 1989 A new calculational method to assess the therapeutic potential of Auger electron emission *Int. J. Radiat. Oncol. Biol. Phys.* **17**(2) 351–60

- [67] Narra V R, Howell R W, Harrapanhalli R S, Sastry K S and Rao D V 1992 Radio-toxicity of some iodine-123, iodine-125 and iodine-131-labeled compounds in mouse testes: implications for radiopharmaceutical design *J. Nucl. Med.* **33**(12) 2196–201
- [68] Humm J L 1984 *The analysis of Auger electrons released following the decay of radio-isotopes and photoelectric interactions and their contribution to energy deposition* (KFA Report Jülich No 1932, PhD thesis, Germany, June)
- [69] Salem S I, Panossian S L and Krause R A 1974 Experimental K and L relative X-ray emission rates *At. Data Nucl. Data Tables* **14** 91–109
- [70] Chen M H, Crasemann B and Mark H 1979 Relativistic radiationless transition probabilities for atomic K and L shells *At. Nucl. Data Tables* **24** 13–37
- [71] Charlton D E and Humm J L 1988 A method of calculating initial strand breakage following the decay of 125-I *J. Radiat. Biol.* **53** 353–65
- [72] Paretke H 1987 Radiation track structure. In *Kinetics of Non-Homogeneous Processes* ed C R Freeman (New York: Wiley)
- [73] Martin R F and Haseltine W A 1981 Range of radiochemical damage to DNA with decay of iodine-125 *Science* **21** 213(4510) 896–8
- [74] Humm J L, Howell R W and Rao D V 1994 Dosimetry for Auger electron emitters: Report No 3 of AAPM Nuclear Medicine Task Group No 6 *Med. Phys.* **21** 1901–15
- [75] Goddu S M, Howell R W and Rao D V 1996 Calculation of equivalent dose for Auger electron emitting radionuclides distributed in human organs *Acta Oncol.* **35**(7) 909–16
- [76] Goddu S M, Rao D V and Howell R W 1994 Cellular dosimetry: absorbed fractions for monoenergetic electron and alpha particle sources and *S*-values for radionuclides uniformly distributed in different cell compartments *J. Nucl. Med.* **35**(2) 303–16
- [77] Goddu S M, Rao D V and Howell R W 1994 Multicellular dosimetry for micrometastases: dependence of self-dose versus cross-dose to cell nuclei on type and energy of radiation and subcellular distribution of radionuclides *J. Nucl. Med.* **35**(3) 521–30
- [78] Bagshaw K D, Sharma S K, Southall P J, Boden J A, Boxer G M, Partridge T A, Antoniow P and Pedley R B 1991 Selective uptake of toxic nucleoside (¹²⁵IuDR) by resistant cancer *Br. J. Radiol.* **64**(757) 37–44
- [79] Mariani G, Di Sacco S, Volterrani D, Di Luca L, Buralli S, Di Stefano R, Baranowska-Kortylewicz J, Bonora D, Matteucci F, Ricci S, Bellina C R, Falcone A, Salvadori P A, Mosca F, Adelstein S J and Kassis A I 1996 Tumor targeting by intra-arterial infusion of 5-[¹²³I]iodo-2'-deoxyuridine in patients with liver metastases from colorectal cancer *J. Nucl. Med.* **37**(4) (Suppl) 22s–25s
- [80] Chiou R K, Dalrymple G V, Baranowska-Kortylewicz J, Holdeman K P, Schneiderman M H, Harrison K A and Taylor R J 1999 Tumor localization and systemic absorption of intravesical instillation of radio-iodinated iododeoxyuridine in patients with bladder cancer *J. Urol.* **162**(1) 58–62
- [81] Macapinlac H A, Larson S M, Daghighian F, Finn R, Zhang J, Humm J L, Squire O and Kemeny N 1996 I-125-5'-Iododeoxyuridine (IUdR) in the treatment of colorectal cancer metastatic to the liver: 1. Pilot clinical trial *J. Nucl. Med.* **37** 25s–29s
- [82] Kassis A I, Adelstein S J and Mariani G 1996 Radiolabeled nucleoside analogs in cancer diagnosis and therapy *J. Nucl. Med.* **40**(3) 301–19
- [83] Baranowska-Kortylewicz J, Kortylewicz Z P, Hoffman D, Winoto A, Lai J and Dalrymple G V 1996 Colon-specific prodrugs of 5-radioiodo-2'-deoxyuridine *Acta Oncol.* **35**(7) 959–64

- [84] Karagiannis T C, Lobachevsky P N and Martin R F 2000 Cytotoxicity of an ^{125}I -labelled DNA ligand *Acta Oncol.* **39**(6) 681–5
- [85] Panyutin I G, Winters T A, Feinendegen L E and Neumann R D 2000 Development of DNA-based radiopharmaceuticals carrying Auger-electron emitters for anti-gene radiotherapy *Q. J. Nucl. Med.* **44**(3) 256–67
- [86] DeSombre E R, Hughes A, Hanson R N and Kearney T 2000 Therapy of estrogen receptor-positive micrometastases in the peritoneal cavity with Auger electron-emitting estrogens—theoretical and practical considerations *Acta Oncol.* **39**(6) 659–66
- [87] Brady L W, Miyamoto C, Woo D V, Rackover M, Emrich J, Bender H, Dadparvar S, Steplewski Z, Koprowski H and Black P 1992 Malignant astrocytomas treated with iodine-125 labeled monoclonal antibody 425 against epidermal growth factor receptor: a phase II trial *Int. J. Radiat. Oncol. Biol. Phys.* **22**(1) 225–30
- [88] Derui L, Woo D V, Emrich J, Steplewski Z, Rodeck U, Herlyn D, Koprowski H, Miyamoto C and Brady L W 1992 Radiotoxicity of ^{125}I -labeled monoclonal antibody 425 against cancer cells containing epidermal growth factor receptor *Am. J. Clin. Oncol.* **15**(4) 288–94
- [89] Welt S, Scott A M, Divgi C R, Kemeny N E, Finn R D, Daghighian F, St Germain J, Richards E C, Larson S M and Old L J 1996 Phase I/II study of iodine 125-labeled monoclonal antibody A33 in patients with advanced colon cancer *J. Clin. Oncol.* **14**(6) 1787–97
- [90] Adelstein S J, Kassis A I, Baranowska-Kortylewicz J, van den Abbeele A D, Mariani G and Ito S 1991 Potential for tumor therapy with I-125 labelled immunoglobulin *Int. J. Radiat. Appl. Inst. B* **18** 43–4
- [91] Mariani G, Bodei L, Adelstein S J and Kassis A I 2000 Emerging roles for radiometabolic therapy of tumors based on auger electron emission *J. Nucl. Med.* **41**(9) 1519–21
- [92] Daghighian F, Barendswaard E, Welt S, Humm J L, Scott A, Willingham M C, McGuffie E, Old L J and Larson S M 1996 Enhancement of radiation dose to the nucleus by vesicular internalization of iodine-125-labeled A33 monoclonal antibody *J. Nucl. Med.* **37** 1052–7
- [93] Behr T M, Behe M, Lohr M, Sgouros G, Angerstein C, Wehrmann E, Nebendahl K and Becker W 2000 Therapeutic advantages of Auger electron- over beta-emitting radiometals or radioiodine when conjugated to internalizing antibodies *Eur. J. Nucl. Med.* **27**(7) 753–65
- [94] Roeske J C and Stinchcomb T G 1997 Dosimetric framework for therapeutic alpha-particle emitters *J. Nucl. Med.* **38** 1923–9
- [95] Stinchcomb T G and Roeske J C 1999 Values of 'S', $\langle z1 \rangle$ and $\langle z12 \rangle$ for dosimetry using alpha-particle emitters *Med. Phys.* **26**(9) 1960–71
- [96] Roeske J C and Stinchcomb T G 1999 The use of microdosimetric moments in evaluating cell survival for therapeutic alpha-particle emitters *Radiat. Res.* **151** 31–8
- [97] Pomplun E, Booz J and Charlton D E 1987 A Monte Carlo simulation of Auger cascades *Radiat. Res.* **111**(3) 533–52
- [98] Pomplun E 2000 Auger electron spectra—the basic data for understanding the Auger effect *Acta Oncol.* **39**(6) 673–9
- [99] Stepanek J 2000 Methods to determine the fluorescence and Auger spectra due to decay of radionuclides or due to a single atomic-subshell ionization and comparisons with experiments *Med. Phys.* **27**(7) 1544–54

- [100] Goddu S M, Howell R W, Bouchet L G, Bolch W E and Rao D V 1997 *MIRD Cellular S Values* (Reston, VA: Society of Nuclear Medicine)
- [101] Humm J L, Macklis R M, Bump K, Cobb L M and Chin L M 1993 Internal dosimetry using data derived from tissue autoradiographs *J. Nucl. Med.* **34** 1811–17
- [102] Soyland C, Hassfjell S P and Steen H B 2000 A new alpha-particle irradiator with absolute dosimetric determination *Radiat. Res.* **153** 9–15
- [103] Soyland C and Hassfjell S P 2000 A novel ^{210}Po -based alpha-particle irradiator for radiobiological experiments with retrospective alpha-particle hit per cell determination *Radiat. Environ. Biophys.* **39** 125–30
- [104] Soyland C and Hassfjell S P 2000 Survival of human lung epithelial cells following in vitro alpha-particle irradiation with absolute determination of the number of alpha-particle traversals of individual cells *Int. J. Radiat. Biol.* **76** 1315–22

Chapter 10

The MABDOSE program for internal radionuclide dosimetry

Timothy K Johnson

10.1. INTRODUCTION—THE NEED FOR BETTER DOSIMETRY

Internal radionuclide dosimetry from unsealed sources of radioactivity has always been a challenge. A formalism for estimating organ doses from internally deposited radionuclides was published in 1968 by the Medical Internal Radiation Dose (MIRD) Committee of the Society of Nuclear Medicine [1, 2]. In its most general form, the MIRD formalism reduced the dosimetry problem to one of adding all of the emitted radiation from a radionuclide located within a given region, and depositing fractions of that emitted radiation in individual organs. The practical implementations of this formalism—the MIRD Pamphlet 11 [3] and the comparable MIRDose program [4]—were based around the construction of a geometric phantom that approximated the average dimensions and locations of human organs. The decay of a variety of radionuclides was simulated, with the radionuclides sequentially located within regions of the geometric phantom corresponding to regular organ and anatomic spaces. The results of this simulation were tabulated for each radionuclide.

Unfortunately, the manner in which these tables were published—as static objects, existing on either hardcopy paper or as software lookup tables—made them unable to adapt to the changing requirements imposed by rapid advances in biotechnology. Specifically, the series of tables were not designed to account for the effects of an arbitrarily shaped source of activity at an arbitrary location. Additionally, deviation of a person's anatomy from that of the geometric phantom could give rise to substantial errors in dose calculations, since the assigned dose is inversely proportional to the organ's actual mass. In general, these tables were used in the evaluation of diagnostic amounts of radioactivity. The errors associated with this use were not significant in terms of determining whether a diagnostic amount of activity was safe or

not. Dose estimates that differed from the ‘true’ value by factors of 2 to 10 still resulted in numbers that fell within the diagnostic range. This allowed for the creation of simple dose-per-unit administered activity tables such as are found on all package inserts for modern day commercial radiopharmaceuticals.

The advent of hybridoma technology raised the possibility of attempting to treat cancer with antibodies targeted to specific tumour antigens. Antibodies offer a carrier medium that is potentially selective at the molecular level. Hybridoma technology created a vehicle whereby the antibodies could be manufactured in abundance. The possibility of tagging these ‘magic bullets’ with radioactivity to treat cancers became suddenly a reality. The desire to use radiolabelled antibodies in a therapeutic modality, however, placed an entirely new demand on the dosimetry community. Factors of 2 and 10 were no longer acceptable. Delivering an estimated dose of 200 mCi to the bone marrow would allow a patient to survive. If this estimate were off by a factor of 2, the difference could result in death.

The initial clinical trials that infused radiolabelled antibodies into patients demonstrated that the concept of a ‘magic bullet’ was a mistaken one. Radioactivity did not localize in the tumour exclusively: it concentrated in other organs that were clearly visible on whole body scans. If the carrier antibody was classified as a ‘good’ antibody, it localized preferentially in the tumour, but NOT exclusively. Consequently, investigators were forced to consider the following question: *Given that radioactivity localizes in tissues other than tumour, how much radioactivity can the patient tolerate?* This question had to be weighed in conjunction with its corollary: *How much radioactivity must be administered to sterilize the tumour?* Having to consider both questions simultaneously, investigators wondered if it was possible to obtain the latter before the former. Answers required accurate knowledge of the kinetics of a particular antibody, the physical decay parameters associated with the radiolabel, and a thorough knowledge of the geometric composition and anatomic makeup of an individual patient. This knowledge did not exist in a form that was usable on a practical scale.

10.2. DOSIMETRY SOFTWARE DESIGN CONSIDERATIONS

To begin addressing the problem of tumour dose versus normal organ dose in the context of radiolabelled antibodies, the sources of error during the process of forming an internal radionuclide dose estimate were analysed. Additionally, the pace of computer technology development was evaluated. These areas of inquiry resulted in a list of design features that an optimal dosimetry solution should consider. The solution that was arrived at—a practical software tool for estimating monoclonal antibody doses—was developed in direct response to the design considerations. These design considerations are summarized below.

10.2.1. Dosimetry considerations

First, it is impossible to quantify activity accurately at the voxel level using NaI as a detector. The goal of most imaging studies in nuclear medicine is to maximize contrast between areas of low and high uptake. Nuclear medicine images are quantum limited, in the sense that photon statistics drive the overall impression of image quality. In order to obtain adequate count statistics in a reasonable period of time, cameras routinely acquire images using a $\pm 10\%$ energy window. The consequence of using a window this wide is that scattered radiation is accepted into the image acquisition matrix, distorting the impression of underlying activity. Typical resolution within a patient scatter medium is 1.0–1.5 cm. Although camera manufacturers will specify 3–4 mm resolution at ^{99m}Tc energies, this is for a line source at the face of the collimator, and is not realizable in a patient under normal acquisition constraints of limited time and limited activity.

Second, other measurements having higher accuracy than NaI(Tl) imaging are available for quantifying some organ spaces. On a regular basis, the spaces that can be directly sampled include the urine and blood. Less frequently, faecal samples can be collected and counted, as can serial biopsies of superficial tumours and some normal organs. The latter may include bone marrow, lung and liver. Obviously, it makes no sense to implement a dosimetry approach that relies solely on imaging data at the expense of throwing away higher-accuracy data. Unless a methodology can be adapted to a variety of input data forms, it risks incorporating unreliable and inaccurate data at the expense of higher-accuracy data.

Third, activity at a given physical location changes as a function of time, the product of both physical decay and biological accumulation and excretion mechanisms. It is not enough to calculate the activity at a single point in time. One must align the location for each activity measurement, fit those data points to some sort of mathematical function, and integrate the function to achieve the total amount of radiation released from that location. This time integral is referred to as the cumulated (or cumulative) activity. In the limit, this implies that each voxel must be precisely aligned with its temporally displaced counterparts derived from images obtained at different times. Alignment of this precision is currently only practised in radiation oncology teletherapy treatment plans. Because of the poor resolution in nuclear medicine (1–1.5 cm in patients), sets of marker sources would have to be placed on each and every patient at each and every time point for alignment. Attention to marker source placement, collimator angulation, gantry rotation, bed position, and collimator-to-patient distance would have to be rigorously observed. This level of rigour is currently not practised in most nuclear medicine departments. The reality of internal organs shifting from day to day as a patient moves implies that this is a practical impossibility.

Fourth, the total body remains as the single most important space in which intravenously administered activity concentrates. This implies that quantification of the total body should be performed. If one chooses to use a SPECT acquisition, this becomes time prohibitive. Typically, when SPECT has been used, investigators have decided to select for quantification only organs that fall within the field of view of a single acquisition rotation. If one is serious about quantifying activity at the voxel level, one should quantify each and every voxel where activity occurs. Investigators, however, evidently find this too great an expenditure of time since no one has ever performed it in a clinical trial. The primary reason for not quantifying total body activity from a series of total body SPECT acquisitions (aside from the time commitment) is the gross errors introduced into the quantification process, upwards of 400%!

Fifth, the most radiosensitive organ in the body is the bone marrow. The current experience with radiolabelled antibodies suggests that binding affinities are not so great that one gets wholesale uptake in the tumour and none anywhere else. With intravenous infusions of radiolabelled antibody and the assumption that higher amounts of activity will result in improved response rates, the bone marrow continues to be the critical organ. This organ (more properly an organ *space*) is beneath the resolution limits of modern scintillation cameras. For the foreseeable future, it must be dealt with by means of a mathematical model that is predictive of biological outcome. This model should be capable of incorporating measures of bone marrow size (reserve) as well as measures of bone marrow viability (patency) given the reality that radioimmunotherapy patients have usually undergone several rounds of chemotherapy. This treatment is only amenable to a mathematical modelling analysis. This statement derives from the fact that the anatomy of interest is not visualizable on a practical basis.

Sixth, the fact that cancers are the target for infused radiation means that one does not have the luxury of being able to use an 'average' organ located at an average position within the mathematical representation of an average person. Each patient that presents will have a unique number of cancer foci. Each focus will have a unique position and shape within the patient's body. A completely general dosimetry program should have the ability to allow for the creation and construction of these arbitrary volumes on a patient-by-patient basis, and incorporate them into the dose calculation scheme.

Seventh, in 1985 the speed of microprocessors was increasing regularly, while the surface area occupied by integrated circuits was shrinking. The likelihood for CRAY supercomputer speeds on a desktop computer system in the near future was considered high. Calculation algorithms that previously had been considered time prohibitive might be judged feasible if given a second look.

10.2.2. Dosimetry approaches

The dosimetry solutions divided into three general approaches: convolution, adaptation of the existing MIRD paradigm, and reinventing the wheel under a more general guise. The preceding observations immediately ruled out the convolution approach: inability to quantify activity at the voxel level, inability to align each and every voxel with its temporally separated counterparts, and the use of convolution kernels derived from transport in a homogeneous media when the human body has a minimum of three distinct media, weighed heavily against adopting this solution. Although it was possible to fabricate situations and target geometries where this solution would yield accurate results, it was equally possible to fabricate situations where the solution was totally wrong. The quest for generality left this solution unacceptable.

The second approach—that of trying to adapt the current MIRD tables—was equally unacceptable. The primary problem was that there was no simple way of scaling dose estimates to account for differences in patient geometry from the Reference Man phantoms. Similarly, there was no accurate method for including a tumour dose that was completely general. With regard to patient geometry, depending on how large and how close a real target organ was to a source of activity would determine how good an estimate the MIRD11 absorbed fraction was. As with the convolution solutions, although it was possible to invent situations and source/target organ pairs where this approximation was a good one, it was equally possible to invent situations where this approximation was poor. With respect to absorbed fractions for a tumour, the photon contribution would suffer similar shortcomings. It would deteriorate into an infinite number of perturbations, with each perturbation appropriate to an individual set of conditions.

The implemented solution involved a return to the fundamentals upon which the MIRD formalism was based. This solution was envisioned as an integrated program, and was christened MABDOSE [5–14]. MABDOSE incorporates solutions that address each of the first six points enumerated above, and takes advantage of the increases in computer CPU speeds to address point seven. The foundation of the program is the assumption that homogeneous activity concentrations exist at a statistical level that is determined by the user. As a fairly intuitive first approximation, the qualities of cells that define an organ's function are also the qualities that should result in homogeneity of radioactivity concentration. Even in an organ system having more than one distinct cell type (e.g., the liver, composed of Kupffer cells and hepatocytes), the relative distribution of cell types throughout the organ is approximately the same in each unit mass of organ tissue, resulting in uniform uptake. This makes the idea of activity quantification on an organ basis a reasonable starting point for a statistical criterion of homogeneous activity concentration.

If a single organ concentrates activity inhomogeneously, that organ can be subdivided into distinct subregions until the criterion of activity homogeneity *is* met. Each subregion is then treated as an independent activity source. At an acceptance level determined by the user's segmentation resolution requirements, any remaining activity variation among a single organ's voxels is assumed due to measurement error. The fact that one typically has available a large ensemble of voxels with which to average out statistical variations implies that this approach should be favoured over inaccurate unit voxel approaches. Calculating a total organ activity at a single time point, then apportioning that activity *equally* among all voxels that compose that organ, is the approach adopted by MABDOSE.

10.3. HISTORIC DEVELOPMENT OF MABDOSE

10.3.1. Version 1

The development of the MABDOSE program has evolved in a series of stages. The first version of the program was presented at the Annual Meeting of the American Association of Physicists in Medicine in 1986 [5]. To set the historic record straight, the original version was called MABDOS because file names were restricted to being six letters under the DOS operating system (The MIRDOS program that Oak Ridge produced one year later was subjected to similar constraints). With the relaxation in subsequent years of filename size limits to allow longer and more descriptive filenames, the current appellation is MABDOSE. The name is an acronym that stands for **M**onoclonal Antibody **D**osimetry. The acronym is a bit misleading, because it is indicative of the program's origins rather than its functionality. MABDOSE is a completely general internal radionuclide dosimetry program. It was initially conceived to address the shortcomings inherent in the standard approach when dealing with dosimetry problems posed by monoclonal antibodies as carrier molecules for radionuclides. It is not restricted, however, to only performing dose estimates for monoclonal antibodies.

The first version of the MABDOSE program had defining characteristics that included (i) selection of an arbitrary radionuclide from the spectral library assembled by Kocher [16], (ii) creation of a graphical interface for defining mathematical models that predates the appearance of Apple's Macintosh GUI, (iii) curve fitting routines as alternatives to mathematical modelling, (iv) incorporation of numerical integration routines to obtain cumulated activities, (v) implementation of the ALGAM67 Monte Carlo code for photon transport, (vi) incorporation of local deposition of non-penetrating radiation for modelling electron and particulate radiation transport and (vii) display of mean organ dose in a list format [7]. The program used the

equations for the Adult Reference Man phantom [17] to create a 'logical' target geometry, as opposed to a 'virtual' target geometry. The difference is important: the former merely exists as a set of equations that are checked for determining whether an $x/y/z$ coordinate triplet falls within the volume's boundary. Thus, if the left kidney were declared a source organ, and a starting coordinate desired, the equations for the left kidney would be consulted. A random number generator would be used to obtain an arbitrary $x/y/z$ coordinate triplet from within the rectangular volume that just superscribed the organ's surface boundary. The triplet would then be checked against the equations governing the left kidney to determine if the triplet satisfied the defining equations.

The Monte Carlo simulation engine of the MABDOSE code was derived from ALGAM67, a software code originally obtained from the Oak Ridge Radiation Shielding Information Center in 1984. Historically, ALGAM67 was the code that was used to create the MIRD11 tables. It was deemed prudent at the time to use the same simulation code, because ultimately the MABDOSE results would be compared back to the MIRD11 tables as the nominal standard for internal radionuclide dosimetry calculations.¹ The simulation was structured so that each photon greater than 10 keV was simulated for the same, user-determined, number of histories. A random starting coordinate was selected from within a declared source organ, and the photon tracked until it had either deposited all of its energy or had escaped from the target phantom. Average dose to organs identified in the Reference Man phantom were reported in a list.

The MABDOSE program was written in Fortran. The initial phase of a dose estimate (source organ declaration, time-activity data entry, curve fitting, curve integration, radionuclide selection) and the final phase (combination of absorbed fractions with cumulated activities, display of dose by organ) were completed on a Texas Instruments Professional microcomputer. The intermediate portion of the program (Monte Carlo simulation of radioactive decay using the declared source organs and declared radionuclide spectrum) was performed on a Cray supercomputer. This intermediate step necessitated the uploading of the solution's intermediate 'state', then downloading the results for final dose output.

10.3.2. Version 2

The second version of the program implemented a number of refinements to Version 1. The speed of microcomputers was increasing exponentially. It was

¹ In the interim, three other codes have gained prominence in simulation circles: EGS4, BCMP and ETRAN. Their popularity does not detract from the applicability of the ALGAM67 algorithm, nor the practical extensions to it that includes non-penetrating radiation from a nuclide's spectrum.

readily seen that it was only a matter of time before microcomputers would have calculation speeds approaching those of a CRAY. The simulation portion of the program was ported to a microcomputer platform, resulting in a tightly coupled program intended to execute completely from within a single desktop hardware platform. At the same time, the entire MABDOSE program was rewritten in the C++ language. This rewrite was occasioned by the large size the original program had grown to. Changes to the code for refinements, enhancements, and added functionality were impeded by the use of a non-object-oriented language.

10.3.3. Version 3

The third version of the program opted for the creation of a full-fledged virtual target geometry dataset. A three-dimensional lattice was physically created in computer memory, with each voxel in the lattice representing a single tissue type of the target. Each voxel in the lattice contained a single index representative of its tissue type. The collection of lattice voxels created a target geometry that served as the space in which the Monte Carlo simulation was carried out. The same space served as the means for declaring sources of activity. The source data structure encapsulated a column vector whose elements corresponded to all voxels containing the index representing that source. Selecting a starting coordinate was reduced to calling a pseudo-random number generator to provide a value distributed between 0 and 1, then multiplying by the length of the source's column vector.

Once created, a three-dimensional target lattice could be stored in a database library for future recall. The rules governing the six different Reference Man phantoms specified by Cristy and Eckerman [17] were implemented in a hidden layer. If a target of the selected age and resolution existed in the library, it was 'checked out' for use in the current simulation. If the target did not exist, it was created by first allocating the lattice in memory. The equations governing the appropriate age phantom were then consulted to determine which organ index should be assigned each voxel.

10.3.4. Version 4

The fourth version of the program decoupled the target lattice from the Reference Man phantom. This was accomplished by prefacing the lattice data set with a header. The header contains a simple list of each voxel *type* that will be encountered when reading in the lattice. Each voxel type is represented by three fields: the first field is the integer index assigned to represent that tissue type; the second is an ASCII descriptor of the tissue type the index represents; and the third is an integer index that represents the medium type, governing the voxel's interaction characteristics with

radiation, and currently restricted to selection from among bone, soft tissue and lung tissue. In a manner analogous to that of decoupling the target lattice from the Reference Man, it is possible to generalize the assignment of media types so that they can be incorporated after dynamic declaration (see section 10.5).

10.4. MABDOSE: FROM START TO FINISH

10.4.1. Overview

The majority of an internal radionuclide dose estimate deals with manipulating data into a form that is usable by other program components. Too much emphasis has been placed on the fact that MABDOSE uses a Monte Carlo algorithm for photon transport based on the ALGAM67 code, and that it does not use one of the more modern codes such as EGS4 or ECMP. The reality is that MABDOSE accounts for all radiation: the algorithm used for transporting penetrating (i.e., photon) radiation is based on ALGAM67; the algorithm used for transporting non-penetrating radiation (i.e., electrons, β particles, photons <10 keV, and α particles) is local absorption. It is logically inconsistent to simulate electron transport when the resolution from nuclear medicine scans routinely supersedes the range of β particles. Instead, R&D effort on MABDOSE has been devoted to generalizing the user interface for ease of use, and to expanding the range of problems for which the interface is applicable. This means that doses at boundaries between source and target will necessarily have an error associated with them, since β particles will in reality ‘spill over’ the boundary edge and lose some of their energy in the adjacent tissue, rather than stopping abruptly at the interface boundary. This error is mitigated somewhat by adjacent whole body activity.

MABDOSE requires four objects be declared during a dosimetry session. These are (i) a target lattice, (ii) a set of source volumes, (iii) cumulated activities for each source volume in the set and (iv) a radionuclide from which the dose is desired. Each of these four objects is discussed below in detail. The order for making these objects known to the program is general, with two exceptions. First, a source cannot be declared until a target lattice has been created. Second, cumulated activities for a source cannot be generated until the source has been defined. A declared source is not considered defined until it has at least one time–activity point assigned to it.

10.4.2. The target lattice

The foundation of the MABDOSE program is the concept of the target lattice. This exists as a three-dimensional array that is dynamically allocated at run time. Dynamic memory allocation generalizes the memory requirements

necessary for program execution: computers having smaller amounts of RAM can still execute MABDOSE at the expense of being limited to a coarser resolution lattice.

As mentioned previously, Version 3 of the program was the first to implement the target lattice as a virtual three-dimensional array. This lattice was restricted to the family of Reference Man phantoms, with resolution of 10, 5, 2 and 1 mm³ voxels. The coordinates of each voxel were tested against a chain of if-then loops to determine which organ system the voxel belonged to. The voxel was then assigned an integer index representing the organ system. The defined lattice was stored to disk in a library of target lattices. If the lattice representing the selected Reference Man phantom at the selected resolution did not exist in memory, it was created and stored to disk. Subsequent selection of that particular resolution phantom resulted in the lattice being read in from disk.

In the original version of MABDOSE, the Reference Man geometry could be redefined to include spaces that functioned as tumour foci. A graphical interface for tumour definition allowed the operator to place spherical perturbations within the Reference Man geometry. These perturbations functioned as additional source/target organs. Although they could in theory represent any separate and distinct source of—or target for—radiation, they were typically associated with tumours.

The current version of MABDOSE retains this capability with respect to lattices composed of the Reference Man phantoms. However, the generalization of a source data structure to be potentially whatever is segmented (see section 10.3.4) leaves the decision of what needs to be segmented up to the individual. If there are tumour spaces that are deemed significant, and worthy of segmentation, they can be contoured and assigned an organelle index. They will then be made available to the MABDOSE system as a distinct target and potential source for radioactivity within the three-dimensional target lattice. This obviates the need for all of the graphics routines that redefine the target lattice. As an example, the Zubal segmented three-dimensional computed tomography data set ‘YaleMan’ is bundled with the current version of MABDOSE as a target lattice. A user can employ this actual human anatomic data set as a target lattice instead of a Reference Man phantom. Alternatively, any three-dimensional data set can be read in provided the structures of interest have all been segmented.

10.4.3. Declaring source volumes

The MABDOSE program creates three rectangular panes on the lower half of the home screen. Once a target lattice is defined (see above), the list of organelles that compose that target lattice is displayed on the leftmost pane (figure 10.1). Each organelle is represented by a unique index. A unique index is assigned to each voxel of the target lattice.

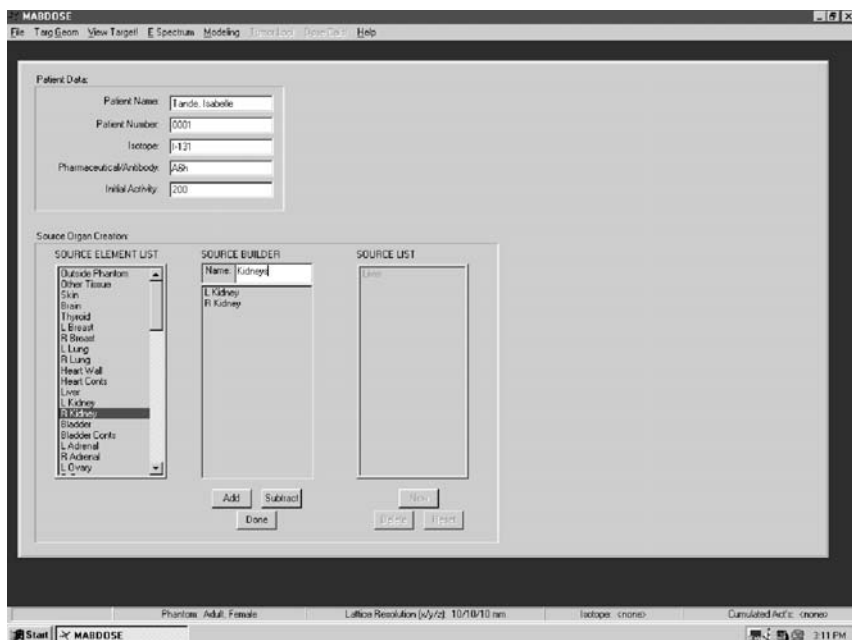


Figure 10.1. The MABDOSE main window, showing descriptors for the possible voxel ‘types’ in the bottom left most list. The source ‘Kidneys’ has been constructed in the bottom middle list from the voxel types, ‘L Kidney’ and ‘R Kidney’. When this list is closed, the source ‘Kidneys’ will be added to the patient source list displayed in the bottom right. Each source must have a separate time–activity data set associated with it. Cumulated activity is apportioned equally among voxels that comprise the source.

The target list in the left-most pane corresponds to the *possibilities* for declaring and defining a source. A source is a logical construct that has a physical space in the target lattice associated with it. The underlying theme of a source is homogeneity of activity concentration: no matter what sub-volume of a given source is sampled, when compared with another sub-volume from the same source, the activity concentration will be the same. This is realizable in a statistical sense. Thus, one could expect both the left and right kidneys to handle a given radiopharmaceutical in exactly the same way. One could then construct a single source, called ‘Kidneys’ from the two volumes that comprise the left and right kidney spaces.

The centre pane is essentially a temporary workspace that allows one to construct a source from the left-most list of organelle possibilities. When a list of all organselles that are to be treated as a single source has been constructed, the list in the centre pane is closed, and the source added to the patient’s current source list. The right-most pane on the lower half of the program’s main window represents the current source list.

10.4.4. Time-activity data and the generation of cumulated activities

For each declared source, an estimate must be made of the amount of activity in that source as a function of time. This is frequently, but not exclusively, derived from nuclear medicine scintigrams. The ability to incorporate higher accuracy measurements from blood samples, urine collections and tissue biopsies motivated the development of the current MABDOSE interface. Each source has associated with it a list of time-activity data point pairs. The interface object for identifying time-activity point pairs to the MABDOSE system is a two-column spreadsheet. Right clicking on a declared source displays the spreadsheet associated with that source. Individual time-activity data are input according to the abundance obtained for each source.

The time-activity data are fitted to a mathematical function, and integrated. The integral of the time-activity curve gives the total number of nuclear disintegrations, a quantity known as the cumulated activity. Combined with knowledge of the radionuclide's decay spectrum, the type and total number of each energy in the spectrum is known. The cumulated activity is divided by the number of voxels that compose the source being simulated. Again, the rationale for doing this is the concept of source homogeneity: what defines a source is uniformity of function over the set of discrete voxels that compose the source.

The mathematical functions that are integrated to achieve the cumulated activity are arrived at using two main approaches. The first is curve fitting. Curve fitting presupposes that the operator knows how the functional form of the data should look, although not the function's magnitude. Therefore, the operator must have an appropriate function beforehand. The functions that MABDOSE currently implements are a mono-exponential function, a bi-exponential function, and a linear function. Additionally, MABDOSE can perform a piecewise integration using discrete trapezoidal or Riemann steps between data points.

The second technique for obtaining cumulated activities is mathematical modelling. MABDOSE implements a graphical interface for composing a mathematical model (figure 10.2). Each source has associated with it a colour-coded rectangle. These are positioned on the screen in a format that is convenient to the user. Directed pathways are then established by starting a line segment within an activity source, and terminating the line segment in an activity sink. The interrelationships specified by the created model define a series of differential equations whose solutions are sums of exponentials.

An initial estimate of the exchange rate between linked compartments is made. Starting from these estimates, a derivative-free version of the Levenberg-Marquardt algorithm minimizes the sum of squares difference between the raw data points and the differential equations by altering the rate constants in a stepwise fashion [18]. The amplitude of each exponential term corresponds to an initial value problem, and can be calculated given the

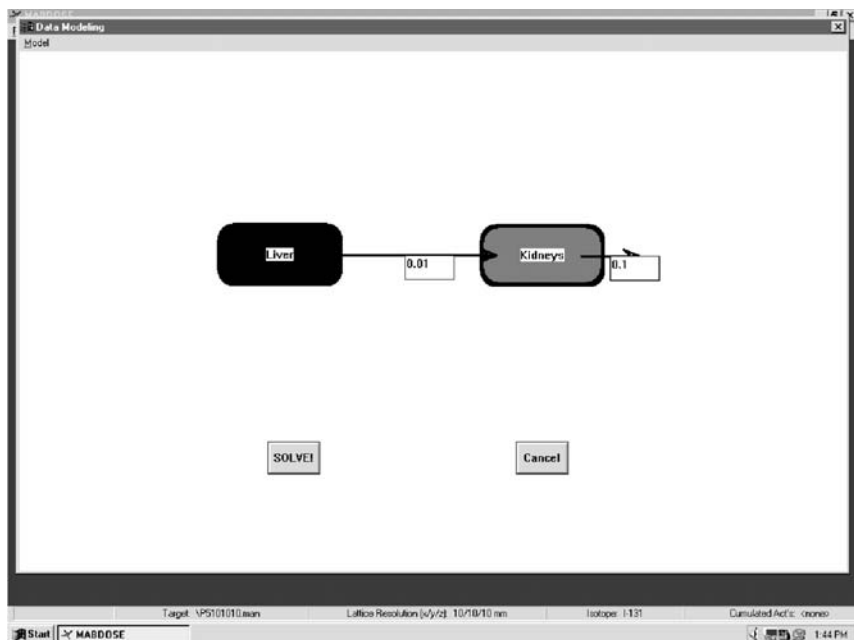


Figure 10.2. Sample model definition describing a simple two-compartment model.

boundary condition of the activity distribution at time $t = 0$. For antibody problems, this boundary condition is typically taken to be 100% of the activity distributed homogeneously in the total body at time $t = 0$.

This analysis results in a least squares estimate of the individual decay constants, and a functional representation of the time–activity curve for each organ system that localizes activity. These differential equations are integrated using a fourth-order Runge–Kutta method to arrive at cumulated activities.

10.4.5. Selection of a radionuclide

The list of radionuclides available in MABDOSE is derived from the DLC-80 database of Kocher [16]. The radionuclide list is displayed in a scrollable window. The display is enhanced by an adjacent window exhibiting an individual radionuclide's decay data. Highlighting a radionuclide in the scrollable list results in the adjacent window showing the nuclide's spectrum, with all radiations divided by type (α , positrons, electrons, photons), their percentage abundance, maximum energy and mean energy (if the energy has an associated distribution).

10.4.6. Simulation of radioactive decay

Prior to simulating radioactive decay, the radiation spectrum is divided into penetrating and non-penetrating radiation types. For the penetrating radiation, the percentage abundance of each radiation above 10 keV is summed to form a cumulative probability distribution. This probability distribution is sampled to determine the energy of the photon to be simulated. This probability distribution preferentially samples those photons that are most abundant.

10.4.7. Simulation—cross section lookup tables

Cross section data for the Monte Carlo transport of photons is obtained from a lookup table maintained in system RAM. The lookup table brackets an energy range from 2 keV to 16 MeV. This energy range is divided into 13 intervals, with 64 energy bins allocated per interval. Instead of linearly dividing the energy range into 13 equal intervals, each interval represents a doubling of the interval preceding it. Thus the first interval ranges from 2 to 4 keV; the second interval from 4 to 8 keV; the third interval from 8 to 16 keV; and so on. This scheme allows for increased resolution at lower energies where dramatic changes in the photoelectric interaction coefficient are realized.

The lookup table is constructed for composite media using the DLC-7c photon cross section library assembled by Roussin *et al.* [19]. This library is an elemental cross section database; cross sections for composite materials (i.e., soft tissue, lung and bone) are constructed using a mass weighted average of the interaction coefficients for the media's constituent atoms [20, 21]. The compositions for soft tissue, lung and bone used by MABDOSE are those specified by Cristy and Eckerman [17].

In accord with the ALGAM transport code used to generate the data for MIRD Pamphlet No 5 [22] (and subsequently used to generate MIRD Pamphlet No 11), the lookup table is constructed to reflect incoherent (Compton) scatter, pair production, and total attenuation coefficients for a composite medium. With respect to incoherent scatter, the interaction coefficient is calculated according to the Klein–Nishina equation for a free electron, and scaled up by each element's electron density. After weighting each elemental coefficient by the element's mass abundance in the composite media, the coefficients are summed. The interaction coefficient is stored as a probability after dividing it by the total attenuation coefficient.

With respect to pair production, probabilities are constructed using a log–log interpolation of elemental pair production cross sections read in directly from the DLC-7c library. Each elemental coefficient is weighted by the element's mass abundance in the composite media and summed. Analogous to the incoherent scatter coefficient, the composite pair production interaction

coefficient is divided by the total attenuation coefficient and stored as a pure probability.

With respect to total attenuation, interaction coefficients are constructed by summing the incoherent scatter and pair production cross sections created as above, and augmenting the sum with a log-log interpolation of elemental photoelectric cross sections read in from DLC-7c. Appropriate conversion factors are applied in order to store the total attenuation coefficient in units of cm^{-1} . Coherent scatter interactions are deemed negligible, and are ignored.

It should be noted that photoelectric probabilities are not stored in the lookup table. Instead, they are calculated at run time by differencing the incoherent scatter and pair production probabilities from unity. This implementation characteristic is a holdover from an era when computer memory was limited and expensive.

10.4.8. Simulation—radiation transport

The Monte Carlo simulation uses the same transport algorithm used by Snyder *et al.* [2] in the ALGAM67 code to generate the MIRD11 tables. The algorithm uses the maximum attenuation coefficient from among all materials that make up the target geometry as the basis for decreasing a photon's 'probability of existence'. For the family of Reference Man phantoms, this number is equal to three, representing bone, soft tissue and lungs. Use of this data reduction technique obviates the need to sample the photoelectric probability distribution directly.

A starting coordinate is selected from within a source volume, and an initial direction chosen from the isotropic distribution. Interaction coefficients are read in for the energy photon being transported. The well known expression for the distance to collision site— $\log(\text{rand_}\#()) * (1/\mu)$ —is used to transport the photon. At this juncture, a game of chance is played with probability of acceptance equal to $\mu_{\text{media}}/\mu_{\text{max}}$. If a random number is greater than this value, the photon is allowed to continue along its current trajectory. If the random number is less than or equal to this value, an interaction is deemed to have taken place, and energy weighted by the respective interaction coefficients deposited within the voxel containing the interaction point. The photon's new direction is determined from sampling the Klein–Nishina distribution. The photon continues until either it escapes from the phantom, or its 'probability of existence' becomes less than 0.00005.

If a photon's energy is determined to be greater than 1.02 MeV after an interaction has taken place, pair-production is simulated. The state of the current photon is stored temporarily while a daughter photon is started. The daughter is assigned an initial energy of 0.511 keV, and a direction selected from the isotropic distribution. The daughter is assigned a weight

twice that of the parent, so as to represent a pair of photons. The daughter is followed until it escapes from the target lattice or its weight falls to less than 0.00005. Radiation transport simulation of the parent photon is then resumed from where it left off [23].

At the end of the simulation, each voxel's contents reflect the amount of penetrating energy absorbed for the photon histories simulated. Since photon energies have been simulated based on their percentage abundance, the voxel contents are a statistical measure of the voxel's absorbed fraction for penetrating radiation. Each voxel in the lattice is divided by the total energy simulated, multiplied by the penetrating radiation-per-decay, and multiplied by the source's cumulated activity. This yields a dose lattice for penetrating radiation originating from the given source volume.

Simulation of non-penetrating radiation is then carried out for the same source volume in a second three-dimensional lattice. The current algorithm for simulating the transport of non-penetrating radiation—local absorption—follows the same number of histories as for the simulation of penetrating radiation. If N non-penetrating radiation histories are followed, and the source volume is composed of n voxels, on average N/n histories will originate in each voxel. If the value N/n is multiplied by the radionuclide's total non-penetrating energy, an estimate of the dose contribution from non-penetrating radiation is obtained. This value is assigned to each voxel of the source only.

At the end of the non-penetrating radiation simulation, each voxel's contents reflect the amount of non-penetrating energy absorbed for the non-penetrating histories simulated. As with the penetrating radiation simulation, each voxel in the lattice is divided by the total energy simulated and multiplied by the source's cumulated activity. This yields a dose lattice for non-penetrating radiation originating from the given source volume. The non-penetrating radiation dose lattice is added to the penetrating radiation dose lattice, with the sum stored in an accumulator dose lattice. The process is repeated for additional sources if present in the source list. Although the simulation of non-penetrating radiation in this manner may seem like a great deal of effort that could be bypassed with a few algebraic simplifications, it prepares MABDOSE for the incorporation of other transport algorithms that follow individual particles.

10.4.9. Dose display

Average dose is displayed on a per-organelle basis (figure 10.3). Regular composite organs (e.g., skeleton, total body) are also displayed. The beauty of having a lattice-based target geometry is that the mapping of total dose deposited on a per-voxel basis is maintained. It is the raw result of the simulation. MABDOSE has implemented the display of dose-volume histograms (DVHs) for highlighted targets. Alternatively, a series

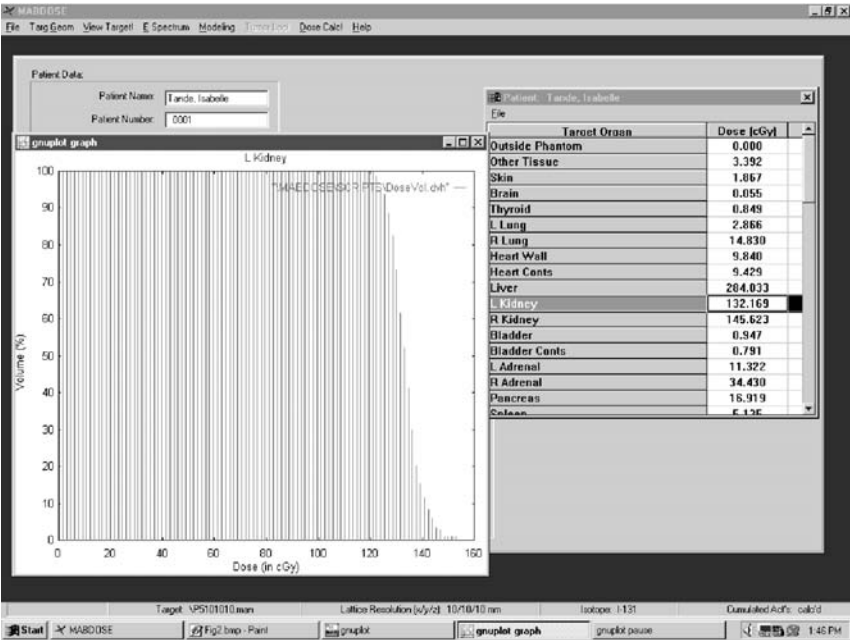


Figure 10.3. Dose display, accompanied by a DVH for the selected liver volume.

of organs can be highlighted and the DVH for this composite organ list displayed.

10.5. FUTURE DEVELOPMENTS

There are a number of enhancements that are envisioned for further development. Each of these enhancements provides flexibility to the overall program that increases the generality of the problem specification.

10.5.1. Automated or semi-automated image segmentation

This remains as one of the truly difficult problems left in the field of medical physics dosimetry. Use of the blood pool as the means for delivery of radiolabelled compounds has the consequence of exposing all organs in the body to the administered radiation. Only rarely can this be ignored (e.g., instances where extraction from the blood pool is virtually instantaneous). It follows that all organs would need to be contoured in a general purpose dosimetry program, since the user could not know beforehand which organs would prove to be dose-limiting critical structures. However,

manual contouring is the only method that is currently error free, and this is time prohibitive for implementation on a routine patient basis. Robust segmentation algorithms that require minimal operator interaction are necessary to surmount this hurdle. The algorithm currently being investigated is a thin-plate spline routine [24–26]. The routine would operate on a spiral CT data set that brackets a patient volume from head to foot. Output from the routine would be a three-dimensional data set with all organs surfaces segmented according to the RTOG format [27].

10.5.2. Generalization of the atomic composition of target voxels

Currently, a voxel is classified as bone, soft tissue or lung. [Note: a voxel can be marked as ‘Outside the target-of-interest’, so there are actually four indices for characterizing a voxel.] This precludes other atomic ‘types’, such as polystyrene, lucite, nylon, acrylic, aluminium, copper and water, from which test phantoms are frequently made. The proposed addition would allow the dynamic creation of an atomic type. It would decouple the meaning of an index from one of only three types, allowing the user to associate meaning to a voxel in a completely general way. The user would define the atomic abundance of individual atoms that compose a substance. This information would construct effective cross section tables from atomic cross section tables using mass weighted abundance. These tables would be read in from information provided in the file header regarding atomic make-up. As with the target lattice geometries, these cross section tables could be stored for future reference, or generated dynamically each time a dosimetry simulation was affected.

10.5.3. Incorporation of electron simulation

Although currently not warranted by image resolution in nuclear medicine, the ability to simulate electron transport is desirable based on arguments of physics completeness. It is also possible that higher resolution imaging modalities may become the devices of choice for measuring and gauging dose effects. PET imaging has the potential to provide the order of magnitude increase in resolution that is necessary for assigning activity on a per-voxel basis. It makes logical sense to expand the transport code to include a Monte Carlo implementation of electron transport. The incorporation of the ETRAN code of Berger and Seltzer is especially attractive.

10.5.4. Incorporation of nonlinear models

MABDOSE divides the dosimetry calculation into two parts that correspond to the terms \bar{A} and S in the MIRD formalism. To calculate \bar{A} , mathematical modelling software was written to implement linear models as previously

mentioned. However, the rationale for using radiolabelled antibodies is that the carrier medium targets unique binding sites at the cellular level. This paradigm is somewhat limited if the user is restricted to defining and using linear models, since targeting cell surface-binding sites implies that the number of sites can be saturated. If this occurs, a twofold increase in antibody will not result in a twofold increase in activity, and the mathematics necessary to describe the time-course of activity concentration requires nonlinear mathematics.

The application of nonlinear mathematics is closely aligned with the idea of a completely segmented anatomic data set. From the physiology literature can be obtained estimates of the number of binding sites per unit mass for a given organ. This specification will have built into it an inherent link with the size or mass of an individual patient's organ. Thus, a nonlinear model whose rates of incorporation/extraction/excretion are dependent on the ensemble of mass-dependent terms would allow the specification of homoeomorphic models that would be true over a much larger range of antibody amounts and radioactivity doses. Models that are more predictive over a wider range of conditions result in higher accuracy dose estimates.

10.6. SUMMARY

Prior to MABDOSE, there was no general method to perform dosimetry resulting from the introduction of an arbitrary source of activity (as exemplified by a tumour focus). MABDOSE was developed as both an extension of the MIRD philosophy and as a software program to implement that philosophy. MABDOSE accounts for all radiations in all organ systems that localize activity including tumour. It represents a synthesis of interactive modelling and dosimetry software. MABDOSE, when finally implemented as envisioned, will be a completely general, all-inclusive internal radionuclide dosimetry program.

REFERENCES

- [1] Loevinger R and Berman M 1968 A schema for absorbed-dose calculations for biologically distributed radionuclides *J. Nucl. Med.* **1** (suppl) 7
- [2] Loevinger R and Berman M 1976 *A revised schema for calculating the absorbed dose from biologically distributed radionuclides*, MIRD Pamphlet No 1, Revised. With a foreword by R J Cloutier and E M Smith (New York: Society of Nuclear Medicine)
- [3] Snyder W S, Ford M R, Warner G G and Watson S B 1975 'S': *absorbed dose per unit cumulated activity for selected radionuclides and organs*, MIRD Pamphlet No 11 (New York: Society of Nuclear Medicine)
- [4] Stabin M 1996 MIRDose: personal computer software for internal dose assessment in nuclear medicine *J. Nucl. Med.* **37** 538-46

- [5] Johnson T K 1986 A tumor preferential dosimetry schema for generalized use in radionuclide monoclonal antibody therapy *Med. Phys.* **13** 586 (abst)
- [6] Johnson T K and Vessella R L 1987 A generalized dosimetry schema for tumor preferential uptake of monoclonal antibodies in radionuclide immunotherapy *J. Nucl. Med.* **28**(4) (suppl) 680 (abst)
- [7] Johnson T K 1988 MABDOS: a generalized program for internal radionuclide dosimetry *Comput. Meth. Programs Biomed.* **27** 159–67
- [8] Johnson T K and Vessella R L 1989 On the possibility of ‘real-time’ Monte Carlo calculations for the estimation of absorbed dose in radioimmunotherapy *Comput. Meth. Programs Biomed.* **29** 205–10
- [9] Johnson T K and Vessella R L 1989 On the application of parallel processing to the computation of dose arising from the internal deposition of radionuclides *Comput. Phys.* **3** 69–72
- [10] Johnson T K, McClure D L, McCourt S L, Andl G J, Berman B D and Newman F D MABDOSE: a computer program for the calculation of dose. In *Proceedings of the 6th International Radiopharmaceutical Dosimetry Symposium*, Gatlinburg, TN, 7–10 May 1996 (ORISE 99-0164, January 1999) pp 425–39
- [11] Johnson T K, McClure D, McCourt S and Newman F 1997 MABDOSE: Characterization and validation of a general purpose dosimetry code *Med. Phys.* **24** 1025 (abst).
- [12] Johnson T K 1997 Implementation of a 3-D internal dosimetry system on a PC *Med. Phys.* **24** 990–1 (abst)
- [13] Johnson T K, McClure D L and McCourt S L 1999 MABDOSE. I. Characterization of a general purpose dosimetry code *Med. Phys.* **26**(7) 1389–95
- [14] Johnson T K, McClure D L and McCourt S L 1999 MABDOSE II: Validation of a general purpose dosimetry code *Med. Phys.* **26**(7) 1396–403
- [15] Zubal I G, Harrell C R, Smith E O, Rattner Z, Gindi G and Hoffer P B 1994 Computerized 3-dimensional segmented human anatomy *Med. Phys.* **21** 299–302
- [16] Kocher D C *DLC-80/DRALIST data package* (RSIC Data Library DLC-80, Oak Ridge National Laboratory)
- [17] Cristy M and Eckerman K F 1987 *Specific absorbed fractions of energy at various ages from internal photon sources. I. Methods* (ORNL/TM-8381/V1 April)
- [18] Press W H, Teukolsky S A, Vetterling W T and Flannery B P 1992 *Numerical Recipes in C: the Art of Scientific Computing* 2nd edition (Cambridge: Cambridge University Press) pp 656–706
- [19] Roussin R W, Knight J R, Hubbell J H and Howerton R J 1983 *Description of the DLC-99/HUGO package of photon interaction data in ENDF/B-V format* ORNL/RSIC-46 (Oak Ridge National Laboratory)
- [20] Hubbell J H 1969 *Photon cross sections, attenuation coefficients and energy absorption coefficients from 10 keV to 100 GeV* NSRDS-NBS 29
- [21] Seltzer S M 1993 Calculation of photon mass energy-transfer and mass energy-absorption coefficients *Radiat. Res.* **136** 147–70
- [22] Snyder W S, Ford M R and Warner G G 1975 MIRD Pamphlet No 5, Revised: *Estimates of specific absorbed fractions for photon sources uniformly distributed in various organs of a heterogeneous phantom* (New York: Society of Nuclear Medicine)
- [23] Warner G G and Craig A M Jr 1986 *ALGAM: a computer program for estimating internal dose from gamma-ray sources in a man phantom* ORNL/RSIC CCC-152 (Oak Ridge National Laboratory) reviewed November 1986

- [24] Wust P, Gellermann J, Beier J, Wegner S, Tilly W, Troger J, Stalling D, Oswald H, Hege H C, Deuflhard P and Felix R 1998 Evaluation of segmentation algorithms for generation of patient models in radiofrequency hyperthermia *Phys. Med. Biol.* **43** 3295–307
- [25] Boes J L, Weymouth T E, Meyer C R, Quint L E, Bland P H and Bookstein F L 1990 Generating a normalized geometric liver model with warping *Radiology* **177**(P) 134 (abst)
- [26] Baldock R A and Hill B 2000 Image warping and spatial data mapping. In *Image Processing and Analysis: a Practical Approach* eds R Baldock and J Graham (New York: Oxford University Press)
- [27] RTOG Data Exchange Specification v3.30, available from http://rtog3dqa.wustl.edu/exchange_files/tapeexch330full.htm

Chapter 11

The three-dimensional internal dosimetry software package, 3D-ID

George Sgouros and Katherine S Kolbert

11.1. INTRODUCTION

The standard formalism for patient dosimetry was developed by the Medical Internal Radiation Dose (MIRD) Committee and is described in reference [1], and also reviewed in chapter 4 of this book. As indicated above, to simplify absorbed dose calculations, the MIRD Committee developed ‘*S* factor’ tables and an associated procedure for their use [2]. This procedure has been implemented in a software package, MIRDOSE3 [3]. To generate tables of *S* factors for different radionuclides and source–target organ combinations, a standard model of human anatomy was adopted in which organ position, dimensions, and composition were mathematically defined. The radioactivity was assumed to be uniformly distributed throughout each source organ and the *S* factors were defined as the mean absorbed dose to a target organ per unit cumulated activity in a source organ. Since the position and size of tumours may vary within the body and since a standard model of human anatomy was adopted for generating the *S* factor tables, tumours are not included in the published tables. A number of approaches have been developed for estimating the absorbed dose to tumours and the dose contribution from tumours to normal organs. The simplest approximation is made by assuming that all electrons are deposited locally and that the relative contribution to the tumour-absorbed dose from photons is negligible. Alternatively, the fraction of electron energy absorbed may be considered assuming the tumour can be modelled as a sphere [4, 5]. Using tables of photon-absorbed fraction to spheres or ellipsoids, the photon self-dose may be added by assuming that the tumour is a sphere or ellipsoid [6]. If this assumption is made, the photon dose to and from normal organs may also be calculated by placing the idealized tumour geometry in a defined position relative to the standard geometry used for the *S* factor calculations [7, 8].

If a point-kernel convolution technique is used in estimating absorbed dose, the true tumour and normal tissue geometry as well as the activity distribution may be taken into account to yield a spatial absorbed dose or dose-rate distribution [9–20]. Tissue composition and density variations are not easily accounted for using point-kernel techniques. To account for these, Monte Carlo techniques are needed to estimate absorbed dose [21–32].

The 3D-ID software package takes the distribution of radiolabelled antibody for a given patient (e.g., from SPECT or PET) and combines it with anatomical information (e.g., CT or MRI) to yield absorbed dose estimates that are specific to a particular patient's biodistribution and anatomy [9, 11, 21, 32, 33]. This work introduced the concept of dose-volume histograms for internally administered radionuclides [9, 21, 34]. The software package, 3D-ID, may be used to carry out both Monte Carlo and point-kernel-based calculations. It has been used to examine the impact of different radionuclides on the dose distribution, given a fixed cumulated activity distribution [21]. More recently, it has been used in a detailed analysis of tumour dose versus response in the treatment of non-Hodgkin's lymphoma using ^{131}I -anti-B1 antibody [35] and also in thyroid cancer patients using ^{124}I PET imaging data with CT [36].

11.2. BACKGROUND TO 3D-ID DEVELOPMENT

3D-ID was developed in response to the increasing use of targeted radionuclide therapy. Although point-kernel convolution as well as patient-specific Monte Carlo calculations had been implemented in external radiotherapy [37], no package was available to provide the platform and support structure required to carry out such calculations for patients treated with targeted radiopharmaceuticals. Likewise, although the fundamental schema of the MIRD methodology does not preclude patient-specific dosimetry calculations, translation of this schema, however, had focused primarily on diagnostic uses of radionuclides in which standardized anatomy, uniform activity distribution and estimation of mean absorbed dose were deemed adequate in assessing the hazards involved in the use of radionuclides [2]. In targeted therapy, administered activities greatly exceeding those used for diagnosis are combined with therapeutic radionuclides and tumour to non-tumour ratios that could easily lead to normal organ toxicity.

11.3. PROGRAMMING ASPECTS/DEVELOPMENT PHILOSOPHY

Most of the effort in patient-specific three-dimensional dosimetry has been in the development of algorithms and computational techniques. Application of such techniques, however, requires a software system that: translates

studies from multiple imaging modalities (CT or MR and PET or SPECT) into a single data format, provides the tools needed to draw contours around regions of interest for identifying source and target regions and outputs the absorbed dose calculations as images, isodose contours or dose-volume histograms [9]. Each of these steps requires considerable user interaction and is input/output intensive. 3D-ID was developed in order to provide a comprehensive and user-friendly framework in which to carry out the various and necessary steps to calculate absorbed dose rate or total dose to any user-defined target region.

In order to relate patient anatomy to radionuclide distribution, it is necessary to register the appropriate functional and anatomic image. The non-trivial issue of image registration has been kept separate from the 3D-ID software system in order to keep the focus on the logistics of image handling, region-of-interest definition and dose calculation.

11.4. MONTE CARLO-BASED IMPLEMENTATION

Monte Carlo-based dosimetry techniques can account for density (ρ) and atomic number (Z) variations that are not easily accounted for using a point-kernel approach. A Monte Carlo dosimetry algorithm was developed for 3D-ID implementation that accounts for individual patient details by using a SPECT or PET radionuclide activity distribution to initialize a simulation of photons across a CT geometry. For a given radionuclide, initial photons are generated according to the voxelized activity distribution provided by SPECT or PET. Photon energies for the given radionuclide are sampled from a published decay scheme and transport is performed using the EGS4 transport code [38]. Efficient particle transport within the discrete geometry was achieved by treating contiguous voxels having similar Z as a single medium, and correcting for density variations by adjusting the path length of the particle in proportion to the density, as determined from CT. Discrimination between bone and water (which was used to represent tissue) was carried out using a water-bone density threshold (WBT) with $\text{WBT} < 1.4 \text{ g cm}^{-3}$ considered water or air and $\text{WBT} \geq 1.4 \text{ g cm}^{-3}$ to be bone. An additional gain in efficiency was obtained by scoring the absorbed dose along photon, rather than electron, tracks. The method was verified by creating discrete density and activity arrays for the Standard Phantom geometry and comparing specific absorbed fraction for various organ and energy combinations.

It is important to note that Monte Carlo-based dosimetry in which activity, density and medium distribution are obtained directly from imaging can lead to artefacts due to problems with the input information. For example, images of Monte Carlo-derived dose distributions will depict higher absorbed doses in the lungs than in tumour lesions in the lungs, even

if the tumour uptake is substantially greater than in normal lung parenchyma. This is because partial volume effects and imperfect scatter correction cause a ‘smearing’ of radioactivity outside the activity-containing tissue. The lower density of lung relative to the tumour tissue leads to a much greater dose to lung than to the tumour (i.e., greater energy deposition per unit mass) [21].

11.5. POINT-KERNEL-BASED IMPLEMENTATION

Point-kernels and point-kernel-based implementations of patient-specific three-dimensional dosimetry are described in detail in chapter 7 of this book. In this section the implementation of the point-kernel methodology as used in 3D-ID will be reviewed.

Although 3D-ID requires a specific format for point-kernel input, the origin of the point-kernels is left to the software user. The point-kernels that have been previously used for 3D-ID were generated by Monte Carlo simulation of photon spectrum transport through water [10]. The point-kernel calculation provides the user with the option of invoking the assumption, *a priori*, that all electron energy will be deposited within each activity-containing voxel. Since the voxel dimensions used for SPECT or PET imaging (of humans) are greater than the path length of the electron or β emissions currently used for radionuclide therapy, this assumption is usually invoked for human dosimetry studies. When 3D-ID is used for animal or autoradiography studies, the point-kernel scale must be matched accordingly, and the kernel values at smaller dimensions are generally dominated by electron emissions.

11.6. INDIVIDUAL MODULES

The 3D-ID software package consists of a set of three modules sharing a common interface style [9] (figure 11.1). The first step provides an entry point into the software package for the diverse modality- and vendor-dependent image formats. Images in standard DICOM or Interfile3.3 can be read in directly while those in non-standard format can also be read providing the user is aware of details regarding file size, two-dimensional image matrix size and voxel bit size, image offset, etc. It is important that voxel dimensions are correct so that accurate calculations based on the image elements can be made. All three-dimensional images sets that are to be subsequently used by 3D-ID are saved in a platform- and system-independent format with minimal header information defining modality, imaging isotope, voxel dimensions and patient name and id.

The second step provides tools to define regions of interest and to calculate source to target dose. Aligned multi-modality image sets are

3D-ID System

INPUT: Registered anatomic and functional images

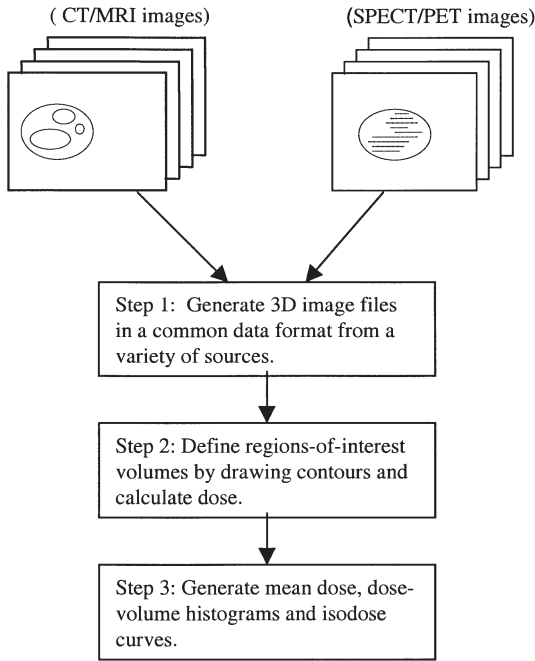


Figure 11.1. 3D-ID system flowchart.

arranged in two rows corresponding to an anatomical modality (CT/MRI) and to a radionuclide modality (SPECT/PET) (figure 11.2). Images are displayed separately rather than fused or overlaid so that all available data from both modalities are preserved.

Contour drawing for region-of-interest (ROI) definition is carried out on a side-by-side, dual modality display of individual two-dimensional image slices, thus providing access to information from both imaging modalities (figure 11.3). Prior to drawing, the cursor appears over both images so that the user can easily identify corresponding points within the two images. Contours are drawn using either image and it is possible to switch back and forth between images during drawing. A number of drawing tools are provided: region growing which automatically generates a contour plot by using a percentage of the ratio between a user selected image value interior to the region and a selected background value outside the region [39]; edge following which is effective in images of high contrast; and standard copy and paste of individual ROI contours. ROIs can be quantified

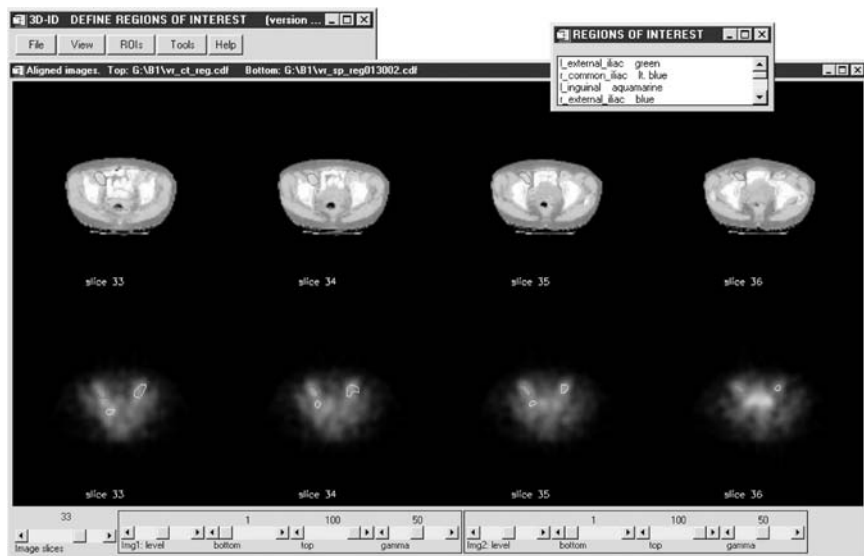


Figure 11.2. Multi-image display from 3D-ID showing four transverse slices from a set of CT-SPECT aligned images. The top row shows the CT with ROIs drawn over three lesions identified as: right external iliac in blue, left external iliac in green, and right common iliac in light blue. The bottom row shows the corresponding ^{131}I SPECT slices with the lesions indicated. (See plate 3 for colour version.)

in terms of total volume, pixel count, and magnitude and location of maximum value within the ROI.

Once ROI volumes have been defined, they may be identified as source or target for a particular dose calculation. A point-kernel file must also be specified to complete input for the dose calculation.

The dose distribution for selected source and target combinations is calculated by convolving the point-kernel with the activity image. Convolution is implemented either by fast Fourier transform or by a table lookup procedure. In either case, the electron dose is deposited within the activity containing voxel for most human dosimetry calculations. If the electron range is significant relative to patient organ dimensions, an electron point-kernel may be added to the early portion of the photon point-kernel to account for the spatial distribution of the electron dose deposition.

Depending upon the size of the image files, the dose calculation can be a computationally intensive and time-consuming calculation. In such circumstances, batch mode execution of the dose calculation is possible. If multiple processors or multiple workstations are available, the dose calculation can be divided into a number of individual parallel batch jobs; the user may select



Figure 11.3. Regions of interest are defined by drawing individual contours using aligned image sets. As contours are drawn, they appear in the multi-slice, two-row, main display window (seen here behind the drawing window).

the operating system for the dose calculation (currently UNIX or PC) and the resulting batch file will be appropriately defined. An estimated number of calculations as well as sample timings are provided as a guideline for the user.

The dose calculation yields a three-dimensional array of dose values, which are essentially images of dose distribution and can be viewed as ‘maps’ of the spatially varying dose in a target volume from a particular source volume or volumes. The modular characteristic of 3D-ID provides the flexibility to replace the current dose calculation technique with other techniques that may be either point-kernel or Monte Carlo based.

Once the calculation has been performed, the final step in 3D-ID is the display and analysis of the three-dimensional dose data set. This includes: calculation of the mean absorbed dose to a target per unit cumulated activity from a source (or sources); generation of dose–volume histograms of source to target regions in order to summarize the dose information in a clinically interpretable manner; and presentation of all image data in a summary display of anatomic, functional and dose distribution images.

If absorbed dose instead of dose-rate is desired and time-sequential SPECT or PET studies are unavailable, the absorbed dose in each target

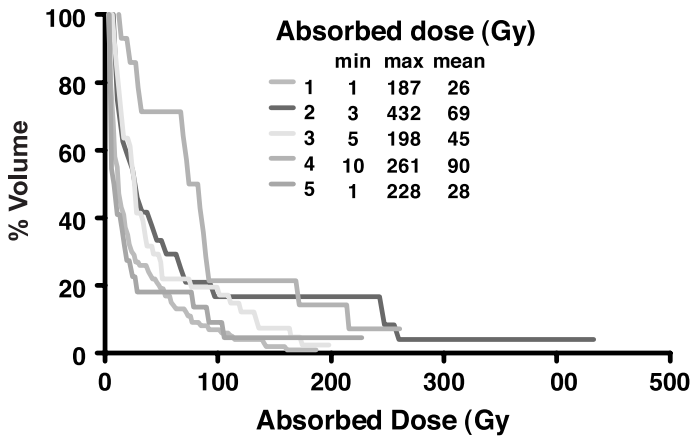


Figure 11.4. Sample integral dose–volume histogram showing distribution of dose over four lesions. Histograms were derived from ^{124}I PET studies in patients with thyroid carcinoma [36]. Each curve represents an individual lesion seen in a single patient.

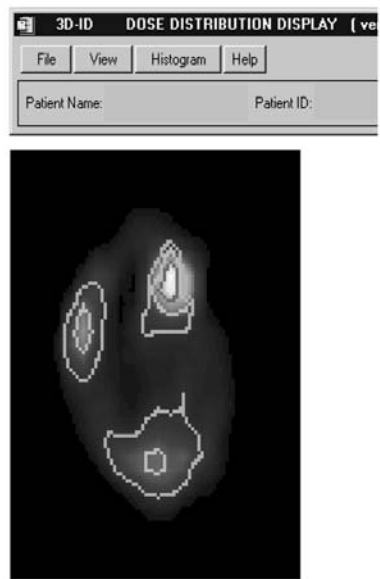


Figure 11.5. The spatial absorbed dose distribution is depicted so that image intensity corresponds to absorbed dose values. Isodose contour levels for 10% (green), 25% (blue), 50% (red) and 75% (yellow) of the maximum dose to the tumour mass are shown. The image was obtained from 3D-ID analysis of ^{124}I PET studies in patients with thyroid carcinoma [36]. (See plate 4 for colour version.)

voxel may be scaled by a total source organ cumulated activity that is typically obtained from planar imaging kinetics. In this way, the spatial distribution of activity is assumed to be preserved throughout the study period. This is a first-order approximation, which may be improved upon if additional (three-dimensional) pharmacokinetic data are obtained. Cumulated activity estimation is external to the system, as this will depend upon the details of patient imaging and pharmacokinetic data acquisition.

The mean dose over a target volume is determined by taking the mean of all values in the dose array. Either integral or differential dose-volume histograms can be generated. In the former, the percentage of volume receiving less than or equal to a particular dose value is plotted as a function of the dose value (figure 11.4). In the latter, the percentage of volume receiving a particular absorbed dose range is plotted versus the dose range.

Multiple iso-dose levels can be displayed in the multi-modality image display by selecting either a specific percentage of the maximum dose or the actual dose value (figure 11.5).

11.7. CONSIDERATIONS IN CLINICAL IMPLEMENTATIONS

The logistics associated with performing fully patient-specific three-dimensional dosimetry are considerable. To define the anatomy and also to provide tissue density information a CT scan over the region of interest is required. To provide the activity distribution a PET or SPECT scan is required. If absorbed dose rather than absorbed dose-rate is desired, then kinetic information is required. In conventional dosimetry, kinetic information that is averaged over the whole source organ volume suffices; in three-dimensional dosimetry variations in pharmacokinetics within an organ must be taken into account. Ideally kinetic information on a voxel-by-voxel basis should be used. This would require multiple SPECT or PET studies taken over time, each registered to each other, and also registered to the CT study. Assuming such data are available, a voxel-by-voxel-based integration of the activity would have to be performed to yield a three-dimensional representation of residence time or cumulated activity. To achieve this type of comprehensive three-dimensional dosimetry calculation a number of logistical, technical and fundamental hurdles must be overcome. The logistical difficulties arise because it may not be feasible to perform PET or SPECT imaging of a particular patient multiple times. The time required for such imaging is considerably greater than planar imaging. This may lead to difficulties with patient compliance and camera availability. The technical difficulties include registration of PET or SPECT images to each other and to a CT study. Although this step is independent of the dosimetry algorithm itself, the fidelity of the registration impacts on the quality of the input which, in turn, will determine the reliability of the dose estimates.

Registration accuracy will depend upon the anatomical ROI, the agent being imaged and the technique that is used for registration. Since it is likely that the total number of counts associated with any given voxel will be low, yielding a high standard deviation, the voxel-by-voxel-based integration outlined above may be fundamentally limited by the error associated with each voxel value. Integration on a voxel-by-voxel basis may yield unreliable values for residence time or cumulated activity due to these errors. A number of techniques and approximations may be adopted to overcome some of these difficulties. It is possible to derive a residence time or cumulated activity image, for example, by using planar imaging to obtain kinetics and SPECT or PET imaging to obtain the spatial distribution. A residence time or cumulated activity image may be obtained by assuming that all points making up the spatial distribution of activity follow the same kinetics [33].

11.8. FUTURE POTENTIAL USES

3D-ID has proved to be a particularly versatile software package with features that extend beyond patient-specific dosimetry. Given appropriate information regarding anatomy and spatial distribution, it is possible to carry out absorbed dose calculations for a number of different circumstances. For example, by using radionuclide kernels with a greater spatial resolution such that dose contributions are dominated by electron deposition, it is possible to carry out dosimetry calculations for experimental animals. The advent and increasing interest in small animal imaging makes this application particularly compelling. Using 3D-ID with high-resolution MR images and assuming a uniform cumulated activity distribution in individual organs of a mouse, we have recently generated murine *S* factors [40]. A similar effort could be undertaken using autoradiography and histology slides. In short, because 3D-ID allows input of images and point-kernels from a wide variety of sources, almost any spatial distribution of radionuclide can be used to generate the corresponding absorbed dose distribution.

ACKNOWLEDGMENTS

This work was supported by NIH grants R01 CA62444, U01 CA58260 and P01 CA33049 and DOE grant DE-FG02-86ER-60407.

REFERENCES

- [1] Loevinger R, Budinger T F and Watson E E 1991 *MIRD Primer for Absorbed Dose Calculations* revised edition (New York: Society of Nuclear Medicine)

- [2] Snyder W S, Ford M R, Warner G G and Watson S B 1975 MIRD Pamphlet No 11: 'S' absorbed dose per unit cumulated activity for selected radionuclides and organs (New York: Society of Nuclear Medicine)
- [3] Stabin M 1996 MIRDOSE: personal computer software for internal dose assessment in nuclear medicine *J. Nucl. Med.* **37** 538–46
- [4] Stabin M and Konijnenberg M W 2000 Re-evaluation of absorbed fractions for photons and electrons in spheres of various sizes *J. Nucl. Med.* **41** 149–60
- [5] Siegel J A and Stabin M 1994 Absorbed fractions for electrons and beta particles in spheres of various sizes *J. Nucl. Med.* **35** 152–6
- [6] Ellett W H and Humes R M 1971 MIRD Pamphlet No 8: Absorbed fractions for small volumes containing photon-emitting radioactivity *J. Nucl. Med.* **12**(5) (suppl) 25–32
- [7] Johnson T K, McClure D and McCourt S 1999 MABDOSE I: Characterization of a general purpose dose estimation code *Med. Phys.* **26** 1389–95
- [8] Johnson T K and Colby S B 1993 Photon contribution to tumor dose from considerations of ^{131}I radiolabeled antibody uptake in liver, spleen and whole body *Med. Phys.* **20** 1667–74
- [9] Kolbert K S, Sgouros G, Scott A M *et al.* 1997 Implementation and evaluation of patient-specific three-dimensional internal dosimetry *J. Nucl. Med.* **38** 301–8
- [10] Furhang E E, Sgouros G and Chui C S 1996 Radionuclide photon dose kernels for internal emitter dosimetry *Med. Phys.* **23** 759–64
- [11] Sgouros G, Barest G, Thekkumthala J *et al.* 1990 Treatment planning for internal radionuclide therapy: three-dimensional dosimetry for nonuniformly distributed radionuclides *J. Nucl. Med.* **31** 1884–91
- [12] Liu A, Williams L E, Wong J Y and Raubitschek A A 1998 Monte Carlo-assisted voxel source kernel method (MAVSK) for internal beta dosimetry *Nucl. Med. Biol.* **25** 423–33
- [13] Flux G D, Webb S, Ott R J, Chittenden S J and Thomas R 1997 Three-dimensional dosimetry for intralesional radionuclide therapy using mathematical modeling and multimodality imaging *J. Nucl. Med.* **38** 1059–66
- [14] Giap H B, Macey D J and Podoloff D A 1995 Development of a SPECT-based three-dimensional treatment planning system for radioimmunotherapy *J. Nucl. Med.* **36** 1885–94
- [15] Giap H B, Macey D J, Bayouth J E and Boyer A L 1995 Validation of a dose-point kernel convolution technique for internal dosimetry *Phys. Med. Biol.* **40** 365–81
- [16] Akabani G, Hawkins W G, Eckblade M B and Lechner P K 1997 Patient-specific dosimetry using quantitative SPECT imaging and three-dimensional discrete Fourier transform convolution *J. Nucl. Med.* **38** 308–14
- [17] van Dieren E B, Plaizier M A, van Lingem A, Roos J C, Barendsen G W and Teule G J 1996 Absorbed dose distribution of the Auger emitters ^{67}Ga and ^{125}I and the beta-emitters ^{67}Cu , ^{90}Y , ^{131}I and ^{186}Re as a function of tumor size, uptake and intracellular distribution *Int. J. Radiat. Oncol. Biol. Phys.* **36** 197–204
- [18] van Dieren E B, van Lingem A, Roos J C, Huijgens P C, Barendsen G W and Teule G J 1994 A dosimetric model for intrathecal treatment with ^{131}I and ^{67}Ga *Int. J. Radiat. Oncol. Biol. Phys.* **30** 447–54
- [19] Erdi A K, Yorke E D, Loew M H, Erdi Y E, Sarfaraz M and Wessels B W 1998 Use of the fast Hartley transform for three-dimensional dose calculation in radionuclide therapy *Med. Phys.* **25** 2226–33

- [20] Liu A, Williams L E, Lopatin G, Yamauchi D M, Wong J Y and Raubitschek A A 1999 A radionuclide therapy treatment planning and dose estimation system *J. Nucl. Med.* **40** 1151–3
- [21] Furhang E E, Chui C S, Kolbert K S, Larson S M and Sgouros G 1997 Implementation of a Monte Carlo dosimetry method for patient-specific internal emitter therapy *Med. Phys.* **24** 1163–72
- [22] Bouchet L G, Jokisch D W and Bolch W E 1999 A three-dimensional transport model for determining absorbed fractions of energy for electrons within trabecular bone *J. Nucl. Med.* **40** 1947–66
- [23] Clairand I, Ricard M, Gouriou J, Di Paola M and Aubert B 1999 DOSE3D: EGS4 Monte Carlo code-based software for internal radionuclide dosimetry *J. Nucl. Med.* **40** 1517–23
- [24] Bolch W E, Bouchet L G, Robertson J S *et al.* 1999 MIRD Pamphlet No 17: The dosimetry of nonuniform activity distributions—radionuclide *S* values at the voxel level. Medical Internal Radiation Dose Committee *J. Nucl. Med.* **40** 11S–36S
- [25] Bardies M and Myers M J 1996 Computational methods in radionuclide dosimetry *Phys. Med. Biol.* **41** 1941–55
- [26] Tagesson M, Ljungberg M and Strand S E 1996 A Monte-Carlo program converting activity distributions to absorbed dose distributions in a radionuclide treatment planning system *Acta Oncol.* **35** 367–72
- [27] Leichner P K 1994 A unified approach to photon and beta particle dosimetry *J. Nucl. Med.* **35** 1721–9
- [28] Kwok C S, Bialobzyski P J, Yu S K and Prestwich W V 1990 Effect of tissue inhomogeneity on dose distribution of point sources of low-energy electrons *Med. Phys.* **17** 786–93
- [29] Johnson T K and Vessella R L 1989 On the possibility of ‘real-time’ Monte Carlo calculations for the estimation of absorbed dose in radioimmunotherapy *Comput. Meth. Programs Biomed.* **29** 205–10
- [30] Johnson T K 1988 MABDOS: a generalized program for internal radionuclide dosimetry *Comput. Meth. Programs Biomed.* **27** 159–67
- [31] Bardies M and Myers M J 1990 A simplified approach to alpha dosimetry for small spheres labelled on the surface *Phys. Med. Biol.* **35** 1551–61
- [32] Furhang E E, Chui C S and Sgouros G 1996 A Monte Carlo approach to patient-specific dosimetry *Med. Phys.* **23** 1523–9
- [33] Sgouros G, Chiu S, Pentlow K S *et al.* 1993 Three-dimensional dosimetry for radioimmunotherapy treatment planning *J. Nucl. Med.* **34** 1595–601
- [34] Kolbert K S, Sgouros G, Scott A M *et al.* 1994 Dose–volume histogram representation of patient dose distribution in 3-dimensional internal dosimetry *J. Nucl. Med.* **35** P123–P124
- [35] Sgouros G, Squeri S, Kolbert K S *et al.* 1998 Tumor response following ^{131}I -anti-B1 antibody therapy of non-Hodgkin’s lymphoma: patient-specific tumor dosimetry and the time-course of tumor volume changes *Cancer Biotherm. Radiopharm.* **13** 303
- [36] Mun E F, Kolbert K S, Sheikh A *et al.* 2002 Patient-specific I-124 PET-based 3-D dosimetry for I-131 thyroid cancer therapy *J. Nucl. Med.* **43** 86P
- [37] Mohan R, Barest G, Brewster L J *et al.* 1988 A comprehensive three-dimensional radiation treatment planning system *Int. J. Radiat. Oncol. Biol. Phys.* **15** 481–95

- [38] Nelson W R, Hirayama H and Rogers D W O 1985 *The EGS4 code-system* SLAC Report No 265 (Stanford, CA: SLAC)
- [39] Erdi Y E, Mawlawi O, Larson S M *et al.* 1997 Segmentation of lung lesion volume by adaptive positron emission tomography image thresholding *Cancer* **80** 2505–9
- [40] Kolbert K S, Watson T, Matei C, Xu S, Koutcher J A and Sgouros G 2002 Murine-specific *S*-factors *J. Nucl. Med.* **43** 88P

Chapter 12

Evaluation and validation of dose calculation procedures in patient-specific radionuclide therapy

*Michael Ljungberg, Yuni Dewaraja, George Sgouros
and Sven-Erik Strand*

12.1. INTRODUCTION

The traditional method of absorbed dose calculation has been based on a simplified MIRD formalism with S values, which have been calculated from a generalized geometry. Until recently, the most common approach was to calculate the absorbed dose averaged over a tumour or organ volume. Estimates of the radioactivity in these volumes could be obtained from two-dimensional whole-body scintillation camera imaging or from SPECT or PET imaging. The two latter technologies allow for three-dimensional information if proper corrections for various physical and camera-specific effects, such as photon attenuation, contribution from scatter in the object and crystal, septum penetration and its degradation in spatial resolution, are applied. Three-dimensional techniques also have the potential to account for heterogeneous uptakes and thus enable absorbed dose determination down to the voxel level. If a three-dimensional attenuation distribution of the patient that is aligned to the SPECT data is available, these two information sets (physiology and morphology) can be combined in a calculation scheme to produce three-dimensional absorbed dose distributions. This is an advantage compared with mean-average dose calculation and should therefore be the main future direction for dosimetry development in radionuclide therapy.

12.2. DOSE-VOLUME INFORMATION VERSUS MEAN-AVERAGE ORGAN/TUMOUR DOSE

The ability of three-dimensional dosimetry to provide absorbed dose

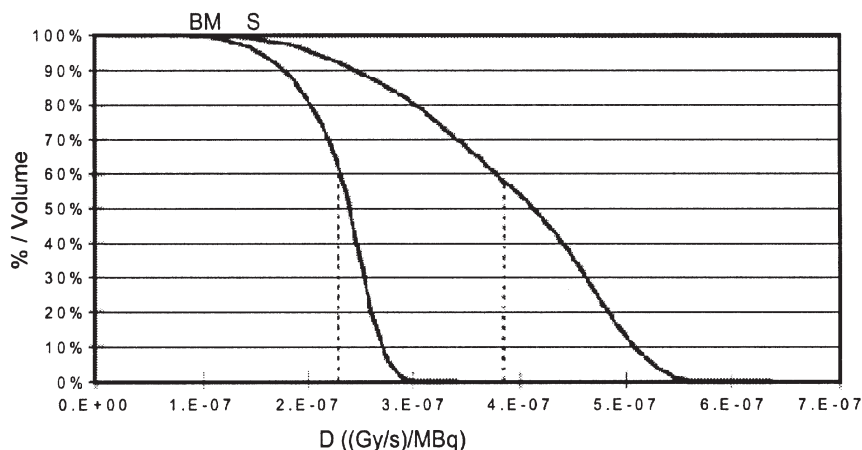


Figure 12.1. An example of an integral dose-volume histogram. The curves depict the percentage of the bone marrow (BM) and the spleen (S) target volumes that receives an absorbed dose rate less than or equal to the dose on the x axis. The dotted lines denote the mean absorbed dose rates to each organ. Redrawn with permission from [1].

information on a voxel-by-voxel basis means that the absorbed dose is averaged over a much smaller volume compared with the earlier standard geometry S factor absorbed-based dose calculations. Regional variation in absorbed doses can, therefore, be monitored. Three-dimensional information, combined with accurate morphological information, provides better estimates of the absorbed doses since patient-specific geometry and attenuation can be included in the calculation. This puts, however, more demands on the registration procedure between anatomical and physiological images. The absorbed dose distribution within a region can also be presented as dose-volume histograms, i.e., the probability of voxels having a particular absorbed dose. These histograms provide useful information of how the absorbed dose is locally distributed. Further processing of this information will be linked to histograms of proper dose-response functions for regional treatment but also be able to combine with, for example, external beam therapy. Figure 12.1 shows an example of an integral dose-volume histogram.

12.3. MONTE CARLO SIMULATION OF IMAGING SYSTEMS

Since SPECT and planar imaging provide the underlying information for activity quantification and biokinetics, evaluation and validation of the dosimetry should also consider reconstruction methods, registration methods of CT and SPECT/PET data, scatter and attenuation compensation methods

and distance-dependent collimator response corrections. In addition, partial volume effects and camera limitations, such as count rate and pile-up effects, need to be evaluated. The latter is important for intra-therapy imaging of patients undergoing treatments with high activities. The validation can be performed by physical measurements using phantoms, from computer-generated data or a combination of both.

12.3.1. Monte Carlo programs for radionuclide imaging

Several Monte Carlo programs, designed to simulate scintillation camera imaging for both SPECT and PET, have been described in the literature [2]. The main use of these programs has been to provide a comparison between ideal images and images improved by correction for, e.g., photon attenuation and scatter, on a pixel-by-pixel basis. The design of the programs varies by its complexity and aimed application area.

The SIMIND program, developed at the Lund University, is a Fortran-90 code that runs on the major platforms. Included in the program is simulation of SPECT and planar imaging using arbitrary voxel-based phantoms. In its native form, the program can also simulate transmission SPECT imaging. The user can modify the program by linking user-written scoring; source or isotope routines where the two latter routines provide spatial coordinates for the decay and photon energies. These routines access a global common block and the user-written code that can be linked to the main code without interference. The code can be coupled with the collimator routine of deVries *et al.* [3] where photon transport is modelled realistically including scatter and penetration events. Recently, the code has also been parallelized using the MPI system for use on large-scale parallel computers.

The SimSET program is a package, developed at the University of Washington, which simulates both SPECT and PET imaging. The software is written in a modular format in C. The main module is the PHG module, which models photon transport through heterogeneous media for both SPECT and PET. A collimator module tracks the photons further through a collimator. Finally, a detector module receives the photons, tracks the photons through the detector and scores the interactions within the detector.

For accurate modelling of scintillation camera imaging with higher energy photon emitters it is essential to include complete photon transport in the collimator. These photons have a high probability of penetrating the collimator septa or undergoing scatter in the collimator. Only a few Monte Carlo algorithms have been used in nuclear medicine to model the collimator in its physical entirety because of the demanding computational requirements [3–6]. The MCNP program [6] has been shown to be useful for investigation of collimator characteristics due to its combinatorial geometry package that makes it easy to build regular patterns such as hex-hole shaped collimators.

12.3.2. Software phantoms

Anthropomorphic software phantoms with internally segmented structures make clinically realistic Monte Carlo simulations possible. Both voxel-based and analytic phantoms are used. The voxel-based phantoms are mostly derived from segmented tomographic images of the human anatomy obtained by either X-ray CT or MRI. The analytic phantoms consist of regularly shaped continuous objects defined by combinations of simple mathematical geometries. An advantage of analytical phantoms over voxelized phantoms is that changes of the geometry can more easily be carried out to allow for anatomical variability. Below are examples of three software torso phantoms useful for nuclear medicine imaging simulations and RNT dosimetry evaluation.

12.3.2.1. The Zubal phantom

This is a computerized anatomically correct three-dimensional volume array, which represents an adult male. The phantom was created using manual segmentation of X-ray CT slices of a living male human [7]. All major internal structures have been segmented and pixels inside each structure have been given a unique code. These codes are then used to assign activity or density values to each structure. The phantom data are available as a $128 \times 128 \times 246$ matrix with a cubic resolution of 4 mm. A further development of the phantom has been made by Dr Stuchly, University of Victoria, who copied the arms and legs from the Visible Human (VH) and attached them to the original torso phantom [8]. Because the arms of the VH cadaver were positioned over the abdominal part, Dr Sjögreen at Lund University mathematically straightened the arms out along the phantom's side to make the phantom useful for whole-body imaging simulations [9]. Figure 12.2 shows rendered images of all three versions. Zubal and colleagues have also developed a high-resolution brain phantom, based on an MRI scan, which can be used for detailed investigations in the head.

12.3.2.2. The MCAT phantom

The MCAT phantom has been developed mainly for cardiac studies [10]. The program creates voxel images of the heart and some of the major organs (liver, kidney, lungs, ribs, stomach and spleen) from mathematical descriptions. The main advantage is the ability to modify the shape, size and location of the phantom and organs including motion of the heart.

12.3.2.3. The NCAT phantom

This phantom is an extension on the MCAT but utilizes a technology called non-uniform rational B-splines (NURBS) when creating the shapes. NURBS define continuous surfaces and allow the phantom to be defined at any

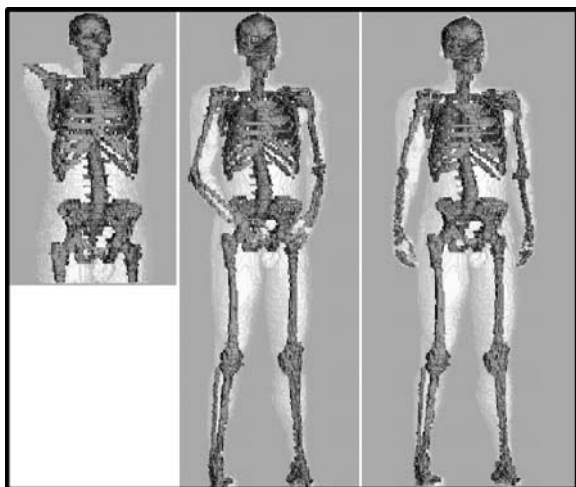


Figure 12.2. The left image shows the rendered image of the original Zubal phantom. The middle image shows the extensions of arms and legs that Stuchly et al made using the VH data set. The right image shows the straightening of the arms that makes the phantom useful for patient-like whole-body simulations in RNT.

spatial resolution [11, 12]. By fitting NURBS to patient data, the phantom generated is more realistic than methods based on solid geometry definitions. The NCAT phantom also includes temporal functions, such as modelling of the heart motion and the respiratory movements. All organ and skeletal models (except for the heart model) are based on CT information of the VH male data set. The heart originates from a gated MRI scan of a human.

12.4. EVALUATION OF IMAGE QUALITY DEGRADATION BY MONTE CARLO METHODS

The accuracy of the activity quantification is an essential part of the absorbed dose calculation. SPECT image quality and quantification accuracy are degraded by scatter, penetration, attenuation and finite spatial resolution. Methods that compensate for these effects have been described in the literature, but most have been developed for ^{99m}Tc (photon energy = 140 keV) since this radionuclide is the most widely used in diagnostic nuclear methods. Radionuclides that have been widely used in therapy and diagnosis prior to therapy are, for example, ^{131}I and ^{111}In . Some of these radionuclides emit several photons in the decay. These additional photons may degrade the accuracy in the quantification of the principal energy depending on their energy and abundance. Consider ^{131}I as an example of a useful radionuclide

that has multiple photon emission. The four highest-intensity emissions of ^{131}I are: 284 keV (6.1%), 364 keV (82%), 637 keV (7.2%) and 723 keV (1.8%) [11]. Although the 637 and 723 keV photons are low in intensity, they contribute significantly to the image since higher-energy photons have a relatively low attenuation in the patient and a higher probability of penetrating the collimator (which is optimized for 364 keV). The 637 and 723 keV photons that have lost part of their energy due to Compton scatter can be included in the 364 keV photopeak window events. A comparison between energy pulse-height distributions from a 'simple' decay, such as $^{99\text{m}}\text{Tc}$, and the more complicated ^{131}I that involves multiple photon emission is shown in Figure 12.3. Here the un-scattered primary component has been separated.

Figure 12.4 shows image quality degradation by comparing an ideal ^{131}I WB study without any physical or camera-based limitation (A) and a realistic WB study with all degradation effects (B). The differences in image quality between A and B mainly consist of degraded spatial resolution and contrast resolution, due to limited system resolution, scatter and septum penetration. The difference is striking and shows how complicated it will be to properly obtain a correct activity measurement from scintillation camera imaging.

12.4.1. Evaluation of planar ^{131}I imaging

A fundamental imaging parameter to study is the spatial resolution where the point-spread function (PSF) describes the imaging system's response to an infinitely small point-source (a δ function). Figure 12.5 shows a comparison between measured and simulated energy spectra and PSFs for a ^{131}I point source in air for a high-energy collimator (HEGAP) and a ultra-high-energy collimator (UHEGAP). The reason for using two collimators was to investigate how well the UHEGAP collimator, with its thicker lead septa, reduces septum penetration. The good agreement between measured and simulated energy spectra was achieved only after inclusion of backscatter photons in the simulation model [13, 14]. Validation of the energy spectrum was also carried out for a case where there was significant object scatter using a phantom consisting of a hot sphere centred in a cylindrical water tank [14]. The wide tails of the ^{131}I PSF (see figure 12.5) are due to septum penetration, which degrades focal quantification accuracy because of the spread of regional counts to surrounding areas. Correcting for this is especially important in ^{131}I RNT where antibody uptake by surrounding organs is significant compared with tumour uptake.

Monte Carlo is ideal for assessing penetration and scatter since, unlike in experimental measurement, these events can be tracked separately in a simulation. For ^{131}I , a quantitative comparison of scatter and penetration has been performed for the HEGAP and the UHEGAP collimators [13]. The geometric, scatter and penetration components of 364 keV photo-peak

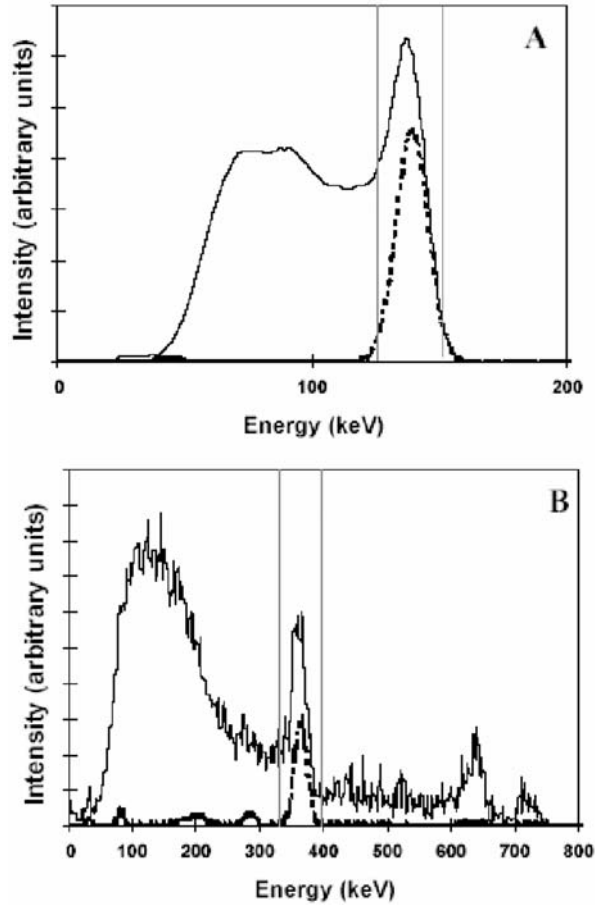


Figure 12.3. Energy spectral distributions detected in the scintillation camera, for (A) ^{99m}Tc and (B) ^{131}I . Solid lines show the total detected spectra and dashed lines show the primary spectra due to photons that have not been scattered in the object, the camera head, or penetrated through the collimator septa. The spectra were obtained by Monte Carlo simulation of a point source, located centrally in an elliptical water-phantom, at a depth of 10 cm.

events were separated for a planar acquisition of a point source in air. ‘Geometric’ implies traversing the collimator hole without interaction; ‘scatter’ implies Compton scattering in the collimator lead while ‘penetration’ implies penetration of one or more septa without scatter. The results are shown in table 12.1. The UHEGAP collimator significantly reduces the scatter and penetration components compared with the HEGAP collimator. This was achieved at the expense of some loss in resolution and sensitivity.

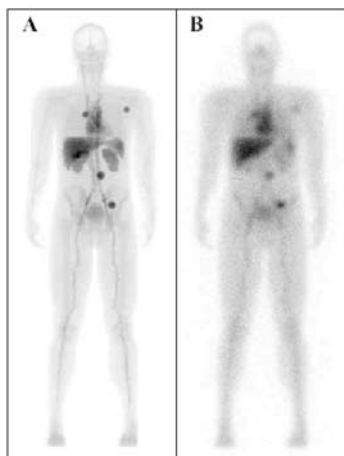


Figure 12.4. *Simulated whole-body images of ^{131}I with the activity distribution corresponding to a ^{131}I labelled monoclonal antibody distribution and four simulated tumours. Image A represents the true distribution, obtained by analytical integration. Image B represents a measured image, obtained by Monte Carlo simulation and detector parameters representing a typical scintillation camera system. The intensity distribution is altered, i.e., the contrast resolution is heterogeneous, due to the variable attenuation and scattering properties of the body.*

The suppression of collimator scatter and penetration with the use of the UHEGAP collimator is also evident in the comparison of ^{131}I energy spectra and PSFs for the two collimators (figure 12.5).

12.4.2. Evaluation of SPECT ^{131}I imaging

Validation of ^{131}I SPECT simulations has been carried out for a clinically realistic situation using a computerized version of the experimental Radiological Support Devices (RSD) thorax phantom. The physical phantom was altered by inserting a water-filled plastic sphere, representing a tumour, close to the liver. The organ and tumour relative activity concentration ratios were realistic values based on ^{131}I RIT patient images. Because of the demanding computational requirements, the simulation was carried out using the parallel implementation of SIMIND on an IBM-SP2 distributed memory architecture [15]. There was good agreement between the measured and simulated images, as demonstrated in figure 12.6.

Tumour activity quantification, such as the one simulated in figure 12.6, is affected by the spread or blurring of regional counts to surrounding areas due to the finite spatial resolution of the system. The 'spill-out' of counts

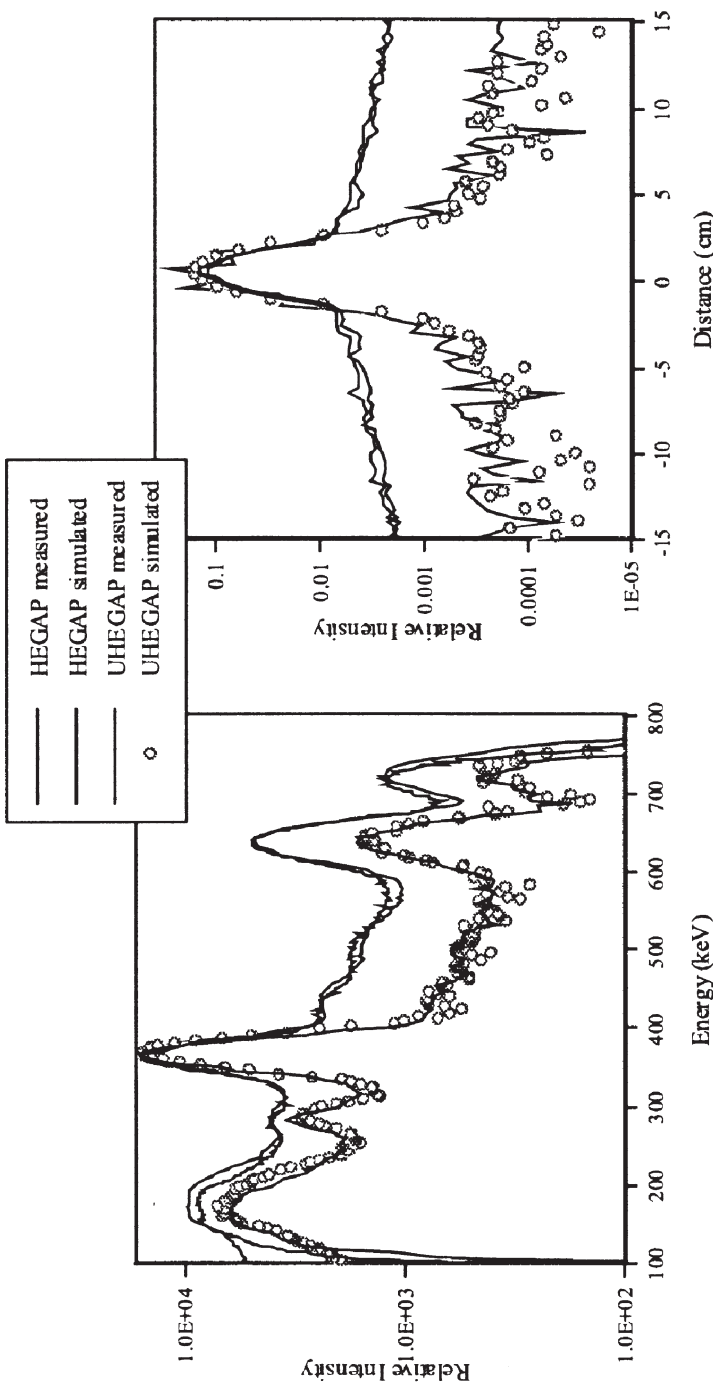


Figure 12.5. Comparison of the measured and simulated ^{131}I energy spectra and PSFs for Picker's collimators HEGAP and UHEGAP.
(Reprinted by permission of the Society of Nuclear Medicine from [13].)

Table 12.1. Monte Carlo comparison of geometric, penetration and scatter component of events within the photo-peak window for the point source in air.

Collimator	Geometric (%)	Penetration (%)	Scatter (%)
HEGAP	27.3	43.3	29.4
UHEGAP	72.4	17.3	10.3

from the target to the background decreases the tumour activity quantification, as the source structure gets smaller while the ‘spill-in’ contribution from the background to the target increases the tumour activity quantification. The spill-out depends on the shape and size of the source structure and the system resolution while spill-in depends on these parameters as well as the activity level and distribution in the background. An experimental evaluation of the effect of different tumour sizes and shapes on activity quantification can be technically difficult to achieve, while Monte Carlo simulation is a powerful tool to carry out such a study. The effects of object shape, size and background on SPECT ¹³¹I activity quantification without detector response compensation has been reported in a recent Monte Carlo study [16]. The results of the study are summarized in table 12.2. Here *b* is the background to tumour activity concentration ratio. Note that the activity error is 0% for one of the simulations because the calibration factor was also determined from this simulation. The activity quantification was carried out using a constant calibration factor and no partial volume correction. The physical object boundary was used to define the volume of interest (VOI), which is consistent with patient quantification procedures where CT-defined tumour boundaries are superimposed on to the registered SPECT image. Results of table 12.2 show that the activity error increases significantly with decreasing tumour size because of the increased spill-out of counts. The activity error for cylindrical tumours is consistently higher than the error for the spherical tumours because spill-out is more significant for non-spherical objects. Also, activity error depends significantly on *b* because of the effect of spill-in.

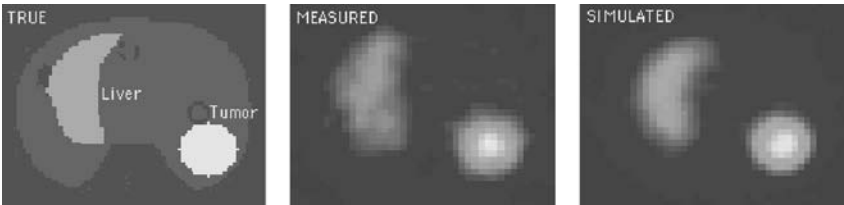


Figure 12.6. Images and profiles corresponding to a slice of the heart/thorax phantom are shown. The true activity distribution as well as the measured and simulated reconstructed images are shown. (Reprinted by permission of Elsevier from [15].)

Table 12.2. *The activity error presented as the percentage difference between the true ^{131}I activity and the SPECT estimated activity for different sizes, shapes and b values.*

Tumour volume (cm^3)	Tumour shape	b	Activity error (%)
50	Sphere	1/5	-12.7
50	Sphere	1/3	-6.7
50	Sphere	0	-23.0
100	Sphere	1/5	-9.8
100	Sphere	1/3	-6.6
100	Sphere	0	-15.2
200	Sphere	1/5	0
200	Sphere	1/3	+0.5
200	Sphere	0	-1.3
50	Cylinder	1/5	-44.0
50	Cylinder	1/3	-28.0
50	Cylinder	0	-79.0
100	Cylinder	1/5	-32.0
100	Cylinder	1/3	-22.0
100	Cylinder	0	-50.0
200	Cylinder	1/5	-9.0
200	Cylinder	1/3	-4.0
200	Cylinder	0	-18.0

12.4.3. Other radionuclides

In RNT with ^{90}Y -labelled monoclonal antibodies, ^{111}In is often used as an analogue tracer because of the absence of γ -ray emissions associated with ^{90}Y . Some of the same problems associated with ^{131}I imaging apply to ^{111}In , which has γ -ray emissions at 172 keV (91%) and 245 keV (94%). In a Monte Carlo study, the fraction of ^{111}In photons, which penetrate or scatter in the collimator, was determined for different values of collimator lead content [17]. For the 172 keV window the penetration component was up to 15% while the scatter component was up to 7%. For the 245 keV window the penetration component was up to 58% while the scatter component was up to 23%.

Monte Carlo simulation using a modified MCNP code has been used to characterize scatter and penetration of ^{123}I , which has several high-energy emissions above the main photo-peak at 159 keV [4]. This work showed that for sources in air and for the 159 keV window, the fraction of counts due to high-energy photons was 10–20% for a medium-energy collimator and 30–50% for a low-energy collimator. For the medium-energy collimator the reported scatter:primary and penetration:primary ratios were 8–12% and 12–18%, respectively while these ratios for the low-energy collimator were 20–50% and 65–120%, respectively.

The multiple γ -rays associated with ^{67}Ga range in energy from 91 to 1856 keV. The challenging problems of scatter, penetration and lead X-rays in ^{67}Ga SPECT has been investigated in a Monte Carlo study [18]. The study shows that as photo-peak energy increases the fraction of detected photons classified as geometric decreases rapidly while the collimator scatter and penetration fractions increase. The reported spill-down of higher energies to lower-energy windows ranged from 7% to 20%.

12.5. EVALUATION OF ABSORBED DOSE CALCULATION PROCEDURES BY MONTE CARLO METHODS

The Monte Carlo method has been shown to be very efficient in both calculating the absorbed dose and also as a tool for evaluating various parts of the calculation schemes [19]. The key point is that if a simulation of SPECT images (including all inherent limitations such as photon attenuation, scatter contribution, collimator and septum penetration effects) can accurately be made, then the output from a proposed calculation procedure can be compared directly with the corresponding dose calculation using the known activity and attenuation distribution on which the imaging simulations were based.

Figure 12.7 shows the basic steps in such an evaluation. An advantage of Monte Carlo methodology is that simulations can be made of realistic distributions of, in principle, any radiopharmaceutical distribution and that complex density distributions can be included.

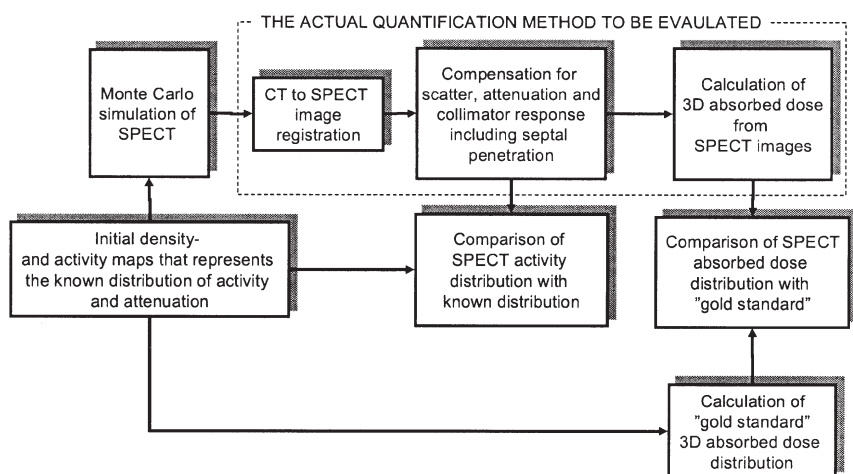


Figure 12.7. A flow-chart describing different steps for which a quantitative SPECT dose planning software could be validated.

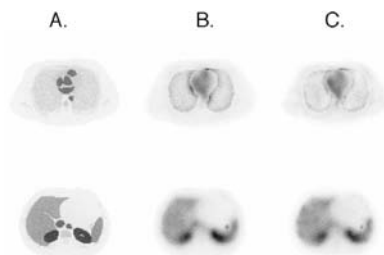


Figure 12.8. Example of how the Monte Carlo method can help evaluate the accuracy in a three-dimensional absorbed dose calculation program. The figure shows a transversal section through the lungs (top row) and a section through the kidneys (bottom row). From the definition of the true activity distribution (A) ideal images without scatter and attenuation effects can be simulated (B) and used as reference with which the particular scatter and attenuation method should be compared (C). Note (a) the higher absorbed dose shown as a border around the lungs which originated from in-spill counts from the nearby located tissue and (b) the hot-spot that is a result of an air-cavity that result in a very local high absorbed dose due to the low density of the air.

The Monte Carlo method offers a key advantage in SPECT quantification of, e.g., ^{131}I compared with experimental measurements since results of correction methods can be compared with the ideal. These different results can then be input to a three-dimensional absorbed dose calculation program (point-dose kernel program on full photon/electron program based on MC methodology). The final absorbed dose images as a function of different correction methods can then be compared with ‘gold standards’ (figure 12.7). Figure 12.8 shows such a comparison of simulated ^{131}I distributions in the Zubal phantom [19].

Verification of the dosimetry program has been described extensively elsewhere in this book. We here only draw attention to a few references that have been based on Monte Carlo simulations. Furhang *et al.* [20] have described a streamlined approach for carrying out Monte Carlo calculations in a voxelized geometry. A detailed validation and comparison of the Monte Carlo method versus MIRD standard geometry *S* factors was provided. The study also examined the impact of non-homogeneous density distribution and variation in the atomic number. The group has also described a full implementation of patient-specific MC dosimetry, showing spillover artefacts [1]. The algorithm was validated by comparing with dosimetric quantities using the MIRD Standard Man phantom for representative case studies. Validation by comparing with other published data has also been made by Tagesson *et al.* [21]. An implementation of a patient-specific point-dose kernel dosimetry program for SPECT/PET images with information from anatomical modalities has been described by Kolbert *et al.* [22].

These are further described in chapter 11. An MCNP4B-based program for patient-specific dosimetry has been described by Yoriyaz *et al.* [23] where the Zubal phantom was used as a patient and absorbed photon fractions verified against reference values from a standard geometry phantom [24].

12.6. EVALUATIONS BASED ON DIRECT MEASUREMENTS

Due to logistical constraints, absorbed dose distributions within patients are necessarily calculated using limited data sets. Quantitative imaging information, as discussed above, is obtained to provide the absorbed dose-program with relevant information on the activity kinetics and anatomy of the patient. Dosimetry calculations are performed either using predefined standard anatomy with associated conversion factors or in three dimensions taking into account the individual anatomy and attenuation properties of each patient. Although sophisticated computational techniques have been applied to these problems, there is a great need for direct absorbed dose measurements to verify the complete calculation/treatment chain.

Measurements of absorbed dose for verification of calculations can be divided into verification in phantoms or *in vivo*. The latter part could be either in experimental animals or in humans. A previous overview of absorbed dose estimation methods in radionuclide therapy has been summarized by Strand *et al.* [25]. Radionuclide dosimetry measurements, especially when applying the dosimeter *in vivo* or in contact with the skin, means that besides energy imparted by photons also the β particle contribution has to be considered.

12.6.1. Thermoluminescence dosimeters

The most-used dosimeter for verifications of absorbed dose calculations has been the thermoluminescence dosimeter (TLD). The properties of TLDs have extensively been investigated, because of their wide usage in external beam therapy [26]. Wessels and Griffith [27] in the mid-1980s suggested applying mini-TLDs *in vivo*. Using sufficiently small TLDs, absorbed dose non-uniformities can be measured within tissues and tumours. The $\text{CaSO}_4(\text{Dy})$ dosimeter has been used as a mini-TLD due to its high light output at low absorbed doses. The method has been extensively explored by several groups for its dosimetric characteristics [28–30] and parameters such as the sensitivity, signal loss, pH-sensitivity and supra-linearity have been studied. Signal loss in tissue was found to be as high as 70% after 9 days, and varied with the temperature in the tissue. Strong pH dependence was also found. The increase in sensitivity, i.e., the supra-linearity factor, was 2–3 at 20 Gy. The mini-TLDs can be used *in vivo* if care is taken for their signal loss due to environmental impact on the dosimetry material.

There is a recent development of encapsulated mini-TLDs that should be able to resist the mentioned environmental factors and should be more rigorous for *in vivo* use. These show no pH dependence and are not affected by the aquatic environment [31].

Volumetric dosimetry using TLDs has been suggested by Aissi and Poston [32] using a mixture of paraffin, tetrachlorobenzene and LiF TLD-100. The dosimeter is tissue equivalent and can be shaped arbitrarily.

12.6.2. Biological dosimeters

Ionizing radiation induces a number of specific and stable alterations in biological materials. Such changes have been examined as a possible approach for estimating radiation exposure and absorbed dose. Historically, this approach has been driven by the need to provide a retrospective evaluation of absorbed dose following accidental or uncontrolled exposures to radiation. In the search for a reliable biological dosimeter, investigators have considered procedures based on biochemical indicators, peripheral blood cell count (lymphocytes, reticulocytes and other peripheral blood mononuclear cells), chromosomal aberrations, and formation of micronuclei [33–37]. Chromosomal aberrations include transient changes such as acentrics (lacking a centromere), dicentrics (having two centromeres) and ring chromosomes as well as stable changes such as chromosomal translocations (transposition of chromosomal segments between two different chromosomes). The former are typically observed by Giemsa staining; the latter require fluorescence *in situ* hybridization (FISH) with chromosome-specific DNA libraries. Micronuclei are small secondary nuclei that arise from acentric chromosomal fragments or whole chromosomes that fail to incorporate into the daughter nuclei during mitosis [38]. A detailed review of biological dosimetry is outside the scope of this section; rather, this section will focus on biological dosimetry as used to validate or evaluate computational methods for radionuclide dosimetry.

One of the earliest applications of biological dosimetry in radionuclide therapy was in the treatment of thyroid cancer with radioiodine [39]. Recent studies have compared the calculated with biologically derived absorbed dose to bone marrow after single and repeated treatment with ^{131}I [40, 41]. Chromosomal aberrations in peripheral lymphocytes were assessed by conventional means (Giemsa staining) and also by FISH. Calibration of the biological dosimeters was obtained, *in vitro*, using ^{60}Co (high-dose-rate) and ^{131}I (low-dose-rate) irradiation. The lowest dose detected, *in vitro*, was 0.2 Gy. Consistent with previous studies, frequency of aberrations was not significantly dependent on dose-rate. Induced translocations were about three- to eightfold more frequent than dicentrics for each dose of irradiation, again consistent with earlier studies [42, 43]. Based upon the frequency of chromosomal aberrations in peripheral

lymphocytes 4 days after administration of 3.7 GBq ^{131}I , an absorbed dose of 0.5 Gy was estimated for a patient population in which thyroid uptake ranged from 0 to 9.1% of administered activity. This is close to the 0.3 to 0.4 Gy range expected for a 3.7 GBq ^{131}I administration for patients with similar thyroid uptake values [44, 45]. Interestingly, the biologically determined absorbed dose correlated with total body retention but not with thyroid uptake.

Patients that were retreated over a 5 year time-period showed an increase in chromosomal aberrations before and after each administration of 3.7 GBq ^{131}I consistent with the 0.5 Gy estimate obtained for patients treated only once. The cumulated increase in chromosomal aberrations, however, did not reflect the expected cumulative absorbed dose. Based on the product of 0.5 Gy and the number of re-treatments, a cumulative dose of 1 to 3.5 Gy should have been obtained; instead the cumulated chromosomal aberrations (including translocations) yielded a dose of only 0.5 to 1.23 Gy. This finding was attributed to the possible loss of cells with chromosomal abnormalities via apoptosis.

The micronucleus assay has also been used in examining radiotoxicity after ^{131}I treatment of thyroid cancer or hyperthyroidism [46–53]. These studies all observed an increase in micronucleus frequency after ^{131}I treatment. In patients with thyroid cancer receiving 3.7 GBq ^{131}I , the biologically determined absorbed dose was typically 0.3 Gy. In one report, the same technique was used to investigate biological dose for thyroid cancer and hyperthyroid patients, the latter receiving three- to tenfold less radioactivity than the former. Surprisingly, the results showed the same increase in micronuclei, corresponding to a dose of ~ 0.3 Gy [49], although this is not supported by conventional dosimetry calculations which yield approximately a twofold increase in the marrow absorbed dose per unit administered activity [54].

Biological dosimetry has also recently been applied to investigate marrow absorbed dose in radioimmunotherapy and in radionuclide therapy for bone pain palliation [55–59]. In a series of patients participating in a Phase I radioimmunotherapy trial of ^{90}Y -cT84.66, a ^{90}Y -labelled human/mouse chimeric antibody against the carcinoembryonic (CEA) antigen [59]. The frequency of stable chromosomal translocations (SCTs) in 18 patients receiving one or more cycles of the radiolabelled antibody was measured after each cycle. Red marrow doses were estimated assuming a marrow activity concentration equal to 0.3 times that of blood [58]. A linear correlation was observed ($r = 0.79$ and 0.89) between increases in SCT for chromosomes 3 ($r = 0.79$) and 4 ($r = 0.89$) and calculated marrow absorbed dose. Despite this observation, a weak correlation was observed between haematological toxicity (fractional decrease in platelet and white blood cell count) and red marrow dose ($r = 0.61$ and 0.53 , respectively) or translocation frequency ($r < 0.4$).

In a detailed series of murine studies examining marrow dosimetry for bone-targeting radionuclides, survival of granulocyte-macrophage colony-forming cells (GM-CFCs) was calibrated and used as a biological dosimeter [55, 56, 58]. Calibration for dose-rate was obtained using an external ^{137}Cs source that could be differentially attenuated to achieve a given exponentially decreasing dose-rate profile. An initial dose rate of 0.37 cGy/h per kBq of femur activity was measured for ^{90}Y -citrate with the dose-rate decreasing exponentially with a 62 h half-time. The same approach was used to demonstrate that shorter-ranged Auger electron emitters such as $^{117\text{m}}\text{Sn}$ and ^{33}P are promising candidates for bone pain palliation because of lower marrow absorbed dose and lower expected toxicity. Since GM-CFC cells are progenitor cells that reside in the marrow, these studies required highly invasive procedures to collect adequate marrow for colony formation assays. To overcome the highly invasive nature of these studies, the induction of micronuclei in peripheral reticulocytes was also examined [57]. These studies gave initial dose-rates of 0.0020 ± 0.0004 and 0.0026 ± 0.0002 cGy/h per kBq administered for ^{32}P -orthophosphate and ^{90}Y -citrate, respectively. Corresponding values obtained using the GM-CFC survival assay were 0.0031 ± 0.0004 and 0.0030 ± 0.0003 cGy/h per kBq administered.

To summarize, biological dosimeters have been used extensively in the treatment of thyroid disease with ^{131}I . These studies have shown that biologically estimated blood or marrow absorbed doses are in generally good agreement with calculated values. Use of biological dosimeters in radioimmunotherapy and bone palliation therapy has only recently been examined and although a correlation between biologically estimated and calculated absorbed dose has been established in patients, absolute comparison of the two approaches has not yet been carried out.

12.6.3. Other dosimetry methods

MOSFET dosimeters [60] can be used as *in vivo* probes since the absorbed dose and absorbed dose rate can be measured simultaneously. One drawback is the electrical coupling; another is its non-tissue equivalence.

A novel idea is to use laser induced fluorescence (LIF) in crystal materials [61]. Here the crystal is mounted on an optical fibre. The dosimeter can be very small and no electrical circuitry is connected to the patient. The dosimeter signal is linear with absorbed dose over several decades and simultaneously the absorbed dose and dose rate can be measured [62, 63].

Electron paramagnetic resonance (EPR) signal of irradiated mineralized tissues has been suggested as a dosimetry system to be used in the dosimetry of bone-seeking radiopharmaceuticals [64, 65]. Chemical dosimeters could be an alternative with the benefit of the possibility of having any shape. Methods suggested for *in vivo* dosimetry are electron spin resonance (ESR) using L- α -alanine, almost tissue equivalent regarding mass stopping power

(S_{col}/ρ) and mass energy absorption coefficient (μ_{en}/ρ) [66, 67]. The system, however, has low sensitivity and can only be used for higher absorbed doses, as expected in therapeutic nuclear medicine. Another system that could be suggested is the gel dosimetry system read with ordinary MR cameras. Here one uses gels containing ferrous ions. These dosimeters are soft tissue equivalent, however, also requiring relative high absorbed doses [68]. They can be made in arbitrary shapes.

12.6.4. Phantoms for experimental measurements

In an early attempt to verify the MIRD formalism Grönberg *et al.* [69] built a phantom of the MIRD mathematical model and filled it with water. The urinary bladder, liver or kidney was filled with $^{99\text{m}}\text{Tc}$, ^{123}I or ^{131}I and sealed LiF dosimeters were placed at the liver, kidneys, lungs and ovaries. Measurements showed that the calculated absorbed dose compared with the measured only differed within $\pm 20\%$. Aissi *et al.* [32, 81] compared the MIRD calculations with experimental absorbed doses in the MIRD mathematical phantom obtained with a volumetric dosimeter. Results showed an agreement between the calculated and measured data with a slight overestimation of calculated values.

Kwok *et al.* [70] calculated the absorbed dose for ^{32}P in interfaces and compared those with LiF measurements. They simulated a soft-tissue–bone planar interface by a polystyrene (PST)–aluminium junction and measured the change in β dose from the dose value in homogeneous PST due to a point source of ^{32}P using LiF thermoluminescent dosimeters. With the point source at the interface, the dose rates increased by up to 12%. With the point source at a PST–air planar interface to simulate a soft-tissue–air junction, the dose rates decreased as much as 25%. Giap *et al.* [71] compared the absorbed dose calculations based on a three-dimensional activity map from SPECT and point dose kernels with measurements by TLDs in a large water phantom. Comparisons were also made with MIRD S values in an Alderson abdominal anthropomorphic phantom. The results showed that their three-dimensional method was in good agreement with both the TLD measurements and the MIRD formalism. Their measurements were within 8% of calculated values and in good agreement (14%) with MIRD formalism. TLDs have also been used in a water phantom for verification of calculated absorbed doses for ^{131}I by Aschan *et al.* [72].

12.6.5. In vivo verifications—experimental animals

Mini-TLDs have been used in animals in several experiments [73]. In another study correction for signal loss, spectral shift of photon energy spectra and calibration in equivalent media was done for rats injected with ^{131}I -labelled

antibodies. Absorbed dose calculations were based on animal-specific S values [74]. The corrected mini-TLD measurements overestimated the absorbed dose, which might be explained due to no correction for void volume [75].

Desrosiers *et al.* [76] have used EPR for determination of absorbed doses to bone tissue from different radiopharmaceuticals aimed at therapy and palliation. Results for beagle bone exposed to radiopharmaceuticals under clinical conditions indicated that the EPR gave approximately the calculated absorbed dose based on MIRD formalism, but suggest that the absorbed dose distribution may be non-uniform. In another study, Ignatiev *et al.* [65] used EPR dosimetry in dogs injected with ^{90}Y .

12.6.6. *In vivo verifications—humans*

Using TLDs on the skin of patients the absorbed dose in radionuclide therapy has been measured. In clinical settings, also, mini-TLDs have been used [77, 78]. TLDs were used by Aschan *et al.* [72] in patients with pseudomyxoma undergoing radioimmunotherapy with ^{131}I B72.3 monoclonal antibody. They determined the absorbed dose to the kidneys from TLD measurements on the skin and compared with MIRD formalism and point-dose kernel technique. The overall accuracy in phantom measurements was 15% and in patients around 50%.

12.6.7. *Stack phantom for realistic RNT dosimetry verifications*

Verification of arbitrary absorbed dose distributions requires access to phantoms that easily can configure arbitrary activity distributions. A novel idea is to use the stack phantom for such purposes [79]. The idea is based on the stack phantom for diagnostic imaging [80]. For clinical nuclear medicine with this technique, it is possible to obtain ‘ideal’ experimental images without disturbance from photon interaction with the phantom material.

In principle, the method is based on discrete sampling of a radioactivity distribution in three-dimensional objects by means of equidistant two-dimensional planes. These two-dimensional planes or templates can be obtained by processing X-ray CT images. The automation of the CT images is obtained by image processing programs to make it possible to introduce different pathological patterns, simply by simulating some regions inside the image with different sphere sizes and greyscale levels. These digital activity distribution maps, visualized on the computer screen, can then be printed out on paper sheets by using an ordinary ink-jet printer, where the ink has been mixed with an appropriate radionuclide. The radioactive sheets can then be stacked or mounted in an equidistantly spaced pattern to form a three-dimensional structure with some arbitrary dense material

stacked in between. This stacking material is optional. If attenuation and scatter free projections are the goal some low-density material may be used. When the demand is to obtain patient-like projections, some tissue-equivalent material should be used.

Utilizing the stack phantom any software phantom geometry and activity distribution can easily be transferred into a real phantom to perform direct absorbed dose measurements for verification of the dosimetry/treatment calculations.

ACKNOWLEDGMENTS

This work was partially funded by US Public Health Service grant RO1 CA80927, the Swedish Cancer Foundation, The Gunnar Nilsson Foundations and the Bertha Kamprads Foundations.

REFERENCES

- [1] Furhang E E, Chui C S, Kolbert K S, Larson S M and Sgouros G 1997 Implementation of a Monte Carlo dosimetry method for patient-specific internal emitter therapy *Med. Phys.* **24**(7) 1163–72
- [2] Ljungberg M, Strand S-E and King M A 1998 *Monte Carlo Calculation in Nuclear Medicine: Applications in Diagnostic Imaging* (Bristol: IOP Publishing)
- [3] DeVries D J, Moore S C, Zimmerman R E, Friedland B and Lanza R C 1990 Development and validation of a Monte Carlo simulation of photon transport in an Auger camera *IEEE Trans. Med. Imag.* **4** 430–8
- [4] Baird W H, Frey E C, Wang W T and Tsui B M W 2000 Characterization of collimator scatter and penetration response for I-123 imaging *J. Nucl. Med.* **41**(5) 133P
- [5] Pollard K P, Bice A N, Eary J F, Durack L D and Lewellen T K 1992 A method for imaging therapeutic doses of iodine-131 with a clinical gamma camera *J. Nucl. Med.* **33** 771–6
- [6] Yanch J C and Dobrzeniecki A B 1993 Monte Carlo simulation in SPECT: complete 3D modeling of source, collimator and tomographic data acquisition *IEEE Trans. Nucl. Sci.* **40** 198–203
- [7] Zubal I G and Harrell C R 1994 Computerized three-dimensional segmented human anatomy *Med. Phys.* **21** 299–302
- [8] Dawson T W, Caputa K and Stuchly M A 1997 A comparison of 60 Hz uniform magnetic and electric induction in the human body *Phys. Med. Biol.* **42**(12) 2319–29
- [9] Sjögreen K, Ljungberg M, Wingårdh K, Erlandsson K and Strand S-E 2001 Registration of emission and transmission whole-body scintillation camera images *J. Nucl. Med.* **42**(10) 1563–70
- [10] Pretorius P H, Xia W, King M A, Tsui B M, Pan T S and Villegas B J 1997 Evaluation of right and left ventricular volume and ejection fraction using a mathematical cardiac torso phantom *J. Nucl. Med.* **38**(10) 1528–35
- [11] Segars W P, Lalush D S and Tsui B M W 2002 Modeling respiratory mechanics in the MCAT and spline-based MCAT phantoms *IEEE Trans. Nucl. Sci.* **48** 89–97

- [12] Segars W P 2001 *Development of a new dynamic NURBS-based cardiac-torso (NCAT) phantom* (University of North Carolina)
- [13] Dewaraja Y K, Ljungberg M and Koral K F 2000 Accuracy of ^{131}I tumor quantification in radioimmunotherapy using SPECT imaging with an ultra-high-energy collimator: Monte Carlo study *J. Nucl. Med.* **41**(10) 1760–7
- [14] Dewaraja Y K, Ljungberg M and Koral K F 2000 Characterization of scatter and penetration using Monte Carlo simulation in ^{131}I imaging *J. Nucl. Med.* **41**(1) 123–30
- [15] Dewaraja Y K, Ljungberg M, Bose A, Majumdar A and Koral K 2002 A parallel Monte Carlo code for planar and SPECT imaging: implementation verification and applications in I-131 SPECT *Comp. Meth. Progr. Biomed.* **67** 115–24
- [16] Dewaraja Y K, Ljungberg M and Koral K 2001 Monte Carlo evaluation of object shape effects in I-131 SPECT tumor activity quantification *Eur. J. Nucl. Med.* **28** 900–6
- [17] Moore S C 1998 Design of a collimator for imaging ^{111}In . In *Monte Carlo Calculation in Nuclear Medicine: Applications in Diagnostic Imaging* ed M Ljungberg, S-E Strand and M A King (Bristol: IOP Publishing) pp 183–93
- [18] DeVries D J, King M A and Moore S C 1999 Characterization of spectral and spatial distributions of penetration, scatter and lead X-rays in Ga-67 SPECT. *Conference Records of the IEEE Medical Imaging Conference* (M9-6) pp 1701–10
- [19] Ljungberg M, Sjögreen K, Liu X, Frey E C, Dewaraja Y K and Strand S-E 2002 A three-dimensional absorbed dose calculation method based on quantitative SPECT for radionuclide therapy evaluation for ^{131}I using Monte Carlo simulation *J. Nucl. Med.* **43** 1101–9
- [20] Furhang E E, Chui C S and Sgouros G A 1996 Monte Carlo approach to patient-specific dosimetry *Med. Phys.* **23**(9) 1523–9
- [21] Tagesson M, Ljungberg M and Strand S E 1996 A Monte-Carlo program converting activity distributions to absorbed dose distributions in a radionuclide treatment planning system *Acta Oncol.* **35**(3) 367–72
- [22] Kolbert K S, Sgouros G, Scott A M, Bronstein J E, Malane R A, Zhang J *et al.* 1997 Implementation and evaluation of patient-specific three-dimensional internal dosimetry *J. Nucl. Med.* **38**(2) 301–8
- [23] Yoriyaz H, Stabin M and dos Santos A 2001 Monte Carlo MCNP4B-based absorbed dose distribution estimates for patient-specific dosimetry *J. Nucl. Med.* **42**(4) 662–9
- [24] Yoriyaz H, dos Santos A, Stabin M and Cabezas R 2000 Absorbed fractions in a voxel-based phantom calculated with the MCNP-4B code *Med. Phys.* **27**(7) 1555–62
- [25] Strand S-E, Jönsson B-A, Ljungberg M and Tennvall J 1993 Radioimmunotherapy dosimetry—a review *Acta Oncol.* **33** 807–17
- [26] Horowitz Y S 1984 Thermoluminescence dosimetry. In *Thermoluminescence and Thermoluminescent Dosimetry* ed Y S Horowitz (Boca Raton, FL: Chemical Rubber Company) pp 43–130
- [27] Wessels B W and Griffith M H 1986 Miniature thermoluminescent dosimeter absorbed dose measurements in tumor phantom models *J. Nucl. Med.* **27** 1308–14
- [28] Demidecki A J, Williams L E, Wong Y C, Wessels B W, Yorke E D, Strandh M *et al.* 1993 Considerations on the calibration of small thermoluminescent dosimeters used for measurement of beta particle absorbed doses in liquid environments *Med. Phys.* **20**(4) 1079–87

- [29] Strand S-E and Strandh M 1994 Parameters to consider for measurements of absorbed doses *in vivo* with mini-thermoluminescent dosimeters *Cancer* **73**(3) 985–8
- [30] Strandh M and Strand S-E 1996 *In vivo* absorbed dose measurements with mini-TLDs. Parameters affecting the reliability *Acta Oncol.* **35**(6)
- [31] Martin S, Lisbona A, Richard J, Morteau S, Denizot B and Bardies M 2000 Production of new thermoluminescent mini-dosimeters *Phys. Med. Biol.* **45**(2) 479–94
- [32] Aissi A and Poston J W 1984 An improved volumetric dosimeter for internal dose verification *Health Phys.* **46**(2) 371–6
- [33] Skalka M 1971 *Biochemical Indicators of Radiation Injury in Man* (Vienna: International Atomic Energy Agency)
- [34] Bender M A and Gooch PC 1962 Types and rates of X-ray-induced chromosome aberrations in human blood irradiated, *in vitro* *Proc. Natl Acad. Sci. USA* **48** 522–32
- [35] Chambers K A, Harrington N P, Ross W M and Filion L G 1998 Relative alterations in blood mononuclear cell populations reflect radiation injury in mice *Cytometry* **31**(1) 45–52
- [36] Pantelias G E and Maillie H D 1984 The use of peripheral blood mononuclear cell prematurely condensed chromosomes for biological dosimetry *Radiat. Res.* **99**(1) 140–50
- [37] Lenarczyk M and Slowikowska M G 1995 The micronucleus assay using peripheral blood reticulocytes from X-ray-exposed mice *Mutat. Res.* **335**(3) 229–34
- [38] Fenech M and Morley A A 1985 Measurement of micronuclei in lymphocytes *Mutat. Res.* **147**(1/2) 29–36
- [39] Boyd E, Buchanan W W and Lennox B 1961 Damage to chromosomes by therapeutic doses of radioiodine *Lancet* **i** 977–8
- [40] M'Kacher R, Schlumberger M, Legal J D, Violot D, Beron-Gaillard N, Gaussen A *et al.* 1998 Biologic dosimetry in thyroid cancer patients after repeated treatments with iodine-131 *J. Nucl. Med.* **39**(5) 825–9
- [41] M'Kacher R, Legal J D, Schlumberger M, Voisin P, Aubert B, Gaillard N *et al.* 1996 Biological dosimetry in patients treated with iodine-131 for differentiated thyroid carcinoma *J. Nucl. Med.* **37**(11) 1860–4
- [42] Tucker J D, Ramsey M J, Lee D A and Minkler J L 1993 Validation of chromosome painting as a biodosimeter in human peripheral lymphocytes following acute exposure to ionizing radiation *in vitro* *Int. J. Radiat. Biol.* **64**(1) 27–37
- [43] Schmid E, Zitzelsberger H, Braselmann H, Gray J W and Bauchinger M 1992 Radiation-induced chromosome aberrations analysed by fluorescence *in situ* hybridization with a triple combination of composite whole chromosome-specific DNA probes *Int. J. Radiat. Biol.* **62**(6) 673–8
- [44] Zanzonico P B 1997 Radiation dose to patients and relatives incident to ¹³¹I therapy *Thyroid* **7**(2) 199–204
- [45] Smith T and Edmonds C J 1984 Radiation dosimetry in the treatment of thyroid carcinoma by ¹³¹I *Radiat. Prot. Dosim.* **5** 141–9
- [46] Wuttke K, Streffer C, Muller W U, Reiners C, Biko J and Demidchik E 1996 Micronuclei in lymphocytes of children from the vicinity of Chernobyl before and after ¹³¹I therapy for thyroid cancer *Int. J. Radiat. Biol.* **69**(2) 259–68
- [47] Watanabe N, Yokoyama K, Kinuya S, Shuke N, Shimizu M, Futatsuya R *et al.* 1998 Radiotoxicity after iodine-131 therapy for thyroid cancer using the micronucleus assay *J. Nucl. Med.* **39**(3) 436–40

- [48] Ramirez M J, Surrallés J, Galofre P, Creus A and Marcos R 1997 Radioactive iodine induces clastogenic and age-dependent aneugenic effects in lymphocytes of thyroid cancer patients as revealed by interphase FISH *Mutagenesis* **12**(6) 449–55
- [49] Monsieurs M A, Thierens H M, van de Wiele C V, Vral A M, Meirlaen I A, de Winter H A *et al.* 1999 Estimation of risk based on biological dosimetry for patients treated with radioiodine *Nucl. Med. Commun.* **20**(10) 911–17
- [50] Livingston G K, Foster A E and Elson H R 1993 Effect of *in vivo* exposure to iodine-131 on the frequency and persistence of micronuclei in human lymphocytes *J. Toxicol. Environ. Health* **40**(2/3) 367–75
- [51] Lambert V, Thierens H, Monsieurs M, Roncancio C and Laurent C 2001 Translocation frequencies measured in patients one year after radioactive iodine therapy for thyrotoxicosis *Int. J. Radiat. Biol.* **77**(6) 679–85
- [52] Gutierrez S, Carbonell E, Galofre P, Creus A and Marcos R 1997 Micronuclei induction by ^{131}I exposure: study in hyperthyroidism patients *Mutat. Res.* **373**(1) 39–45
- [53] Catena C, Villani P, Nastasi R, Conti D, Righi E, Salerno G *et al.* 1994 Micronuclei and 3AB-index in patients receiving iodine-131 therapy *J. Nucl. Biol. Med.* **38**(4) 586–93
- [54] McEwan A C 1977 Absorbed doses in the marrow during ^{131}I therapy *Br. J. Radiol.* **50** 329–31
- [55] Goddu S M, Howell RW, Giuliani D C and Rao D V 1998 Biological dosimetry of bone marrow for incorporated yttrium-90 *J. Nucl. Med.* **39**(3) 547–52
- [56] Goddu S M, Bishayee A, Bouchet L G, Bolch W E, Rao D V and Howell R W 2000 Marrow toxicity of ^{33}P - versus ^{32}P -orthophosphate: implications for therapy of bone pain and bone metastases *J. Nucl. Med.* **41**(5) 941–51
- [57] Lenarczyk M, Goddu S M, Rao D V and Howell R W 2001 Biologic dosimetry of bone marrow: induction of micronuclei in reticulocytes after exposure to ^{32}P and ^{90}Y *J. Nucl. Med.* **42**(1) 162–9
- [58] Siegel J A, Wessels B, Watson E E, Stabin M, Vriesendorp H M, Bradley E W *et al.* 1990 Bone marrow dosimetry and toxicity for radioimmunotherapy *Antibody Immunoc. Radiopharm.* **3** 213–33
- [59] Wong J Y, Wang J, Liu A, Odom-Maryon T, Shively J E, Raubitschek A A *et al.* 2000 Evaluating changes in stable chromosomal translocation frequency in patients receiving radioimmunotherapy *Int. J. Radiat. Oncol. Biol. Phys.* **46**(3) 599–607
- [60] Gladstone D J, Lu X Q, Humm J L, Bowman H F and Chin L M 1994 A miniature MOSFET radiation dosimeter probe *Med. Phys.* **21** 1721–8
- [61] Miller S D and Endres G W 1990 Laser-induced optically stimulated M centre luminescence in LiF *Radiat. Prot. Dosim.* **33**(1) 59–62
- [62] Strandh M, Johansson J and Strand S E A 2001 BaF(Br,I)Eu dosimeter based on laser induced fluorescence for *in vivo* measurements (<http://www.doseinfo-radar.com/1-pos.htm>)
- [63] Strandh M, Strand S-E, Johansson J and Malmgren L 2002 Dosimetry based on laser induced fluorescence in LiF for *in vivo* measurements (<http://www.doseinfo-radar.com/1-pos.htm>)
- [64] Schauer D A, Desrosiers M F, Le F G, Seltzer S M and Links J M 1994 EPR dosimetry of cortical bone and tooth enamel irradiated with X and gamma rays: Study of energy dependence *Radiat. Res.* **138** 1–8
- [65] Ignatiev E A, Lyubashevskii N M, Shishikina E A and Romanyukha A A 1999 EPR dose reconstruction for bone-seeking ^{90}Sr *Appl. Radiat. Isot.* **51**(2) 151–9

- [66] Wielopolski L, Maryanski M, Ciesielski B, Forman A, Reinstein L E and Meck A G 1987 Continuous three dimensional radiation dosimetry in tissue equivalent phantoms using electron paramagnetic resonance in L- α -alanine *Med. Phys.* **14** 646–52
- [67] Olsson S, Lund E and Erickson R 1996 Dose response and fading characteristics of an alanine-agarose gel *Appl. Radiat. Isot.* **47**(11) 1211–17
- [68] Olsson L E, Bäck S Å J, Magnusson P and Haraldsson P 1998 *3D Dosimetry Using Gels and MRI* eds J D Hazle and A L Boyer (College Park, American Association of Physicists in Medicine. Imaging in Radiation Therapy) pp 475–504
- [69] Grönberg T, Persson B and Strand S-E 1977 Experimental evaluation of organ doses from exposure to Tc-99m, I-123 and I-131 *Proc. IVth Int. Cong. Int. Radiat. Prot. Assoc. (Paris 1977)* pp 493–6
- [70] Kwok C S, Irfan M, Woo M K and Prestwich W V 1987 Effect of tissue inhomogeneity on beta dose distribution of ^{32}P *Med. Phys.* **14** 98–104
- [71] Giap H B, Macey D J, Bayouth J E and Boyer A L 1995 Validation of a dose-point kernel convolution technique for internal dosimetry *Phys. Med. Biol.* **40**(3) 365–81
- [72] Aschan A C, Toivonen M J, Lampinen J S, Tenhunen M, Kairemo K J A, Korppi-Tommola E T *et al.* 1999 The use of TL detectors in dosimetry of systemic radiation therapy *Acta Oncol.* **38**(2) 189–96
- [73] Klein J L, Nguyen T H, Laroque P, Kopher K A, Williams J R, Wessels B W *et al.* 1989 ^{90}Y trium and ^{131}I odine radioimmunoglobulin therapy of an experimental hepatoma *Cancer Res.* **49** 6383–9
- [74] Hui T E, Fisher D R, Kuhn J A, Williams L E, Nourigat C, Badger C C *et al.* 1994 A mouse model for calculating cross-organ beta doses from yttrium-90-labeled immunoconjugates *Cancer* **73**(3) 951–7
- [75] Strand S E, Strandh M, Ljungberg M and Tagesson M 1994 Mini-TL-dosimeters for *in vivo* measurements *J. Nucl. Med.* **35** 78P
- [76] Desrosiers M F, Avila M J, Schauer D A, Coursey B M and Parks N J 1993 Experimental validation of radiopharmaceutical absorbed dose to mineralized bone tissue *Appl. Radiat. Isot.* **44** 459–63
- [77] Chiou R K, Wessels B W, Woodson M and Limas C 1991 Study of clinical thermoluminescent dosimeters (Cl.TLD) in direct measurement of absorbed dose for radioimmunotherapy *Int. J. Radiat. Appl. Instrum. A* **42** 181–6
- [78] Lechner P K, Yang N-C, Wessels B W, Hawkins W G, Order S E and Klein J L 1990 Dosimetry and treatment planning in radioimmunotherapy *Front. Radiat. Ther. Oncol.* **24** 109–20
- [79] El-Ali H H, Strand S-E, Larsson S A, Johnsson C, Palmer J, Ljungberg M *et al.* 2002 A new phantom based on ink jet technique for imaging and dosimetry. In *Proceedings of the Seventh International Radiopharmaceutical Dosimetry Symposium*, Nashville, TN
- [80] Larsson S A, Jonsson C, Pagani M, Johansson L and Jacobsson H 2000 A novel phantom design for emission tomography enabling scatter- and attenuation-‘free’ single-photon emission tomography imaging *Eur. J. Nucl. Med.* **27** 131–9
- [81] Aissi A and Poston J W 1987 Comparison of measured and calculated internal absorbed doses in a heterogenous phantom *Phys. Med. Biol.* **32** 1245–56

Chapter 13

Monte Carlo methods and mathematical models for the dosimetry of skeleton and bone marrow

*Lionel G Bouchet, Wesley E Bolch, Michael Stabin,
Keith F Eckerman, John W Poston, Sr
and A Bertrand Brill*

13.1. INTRODUCTION

13.1.1. Anatomy of the skeletal system

The entire skeleton in an adult consists of 200 distinct bones divisible into four classes: long, short, flat and irregular bones [1]. These 200 bones form a rigid framework to which the softer tissues and organs of the body are attached. Microscopically, the human skeletal system is a complex structure that can be classified into two distinct types: trabecular bone and cortical bone (figure 13.1). The trabecular bone (also called cancellous bone) is a porous, spongy structure found in the interior of the flat bones and at the ends of the long bones. It is formed of a complex network of bone trabeculae and tissue cavities. Each cavity is lined by a layer of osteogenic cells called the endosteum and is filled with marrow that is either haematopoietically active (red marrow) or inactive (yellow marrow). The cortical bone is a hard, dense structure also called compact bone. It is found in the shafts of the long bones and in the outer cortex of all bones. The dominant microstructure of the cortical bone is the osteon, which is formed by a central Haversian canal lined with a layer of endosteum and surrounded by bone lamellae. Typical dimensions of the microstructures of an adult trabecular and cortical bone are given in table 13.1.

Radiosensitive cells in the human skeletal system have been identified as (a) haematopoietic cells present in bone marrow, (b) endosteal cells lying close to bone surfaces and (c) epithelial cells close to bone surfaces in the

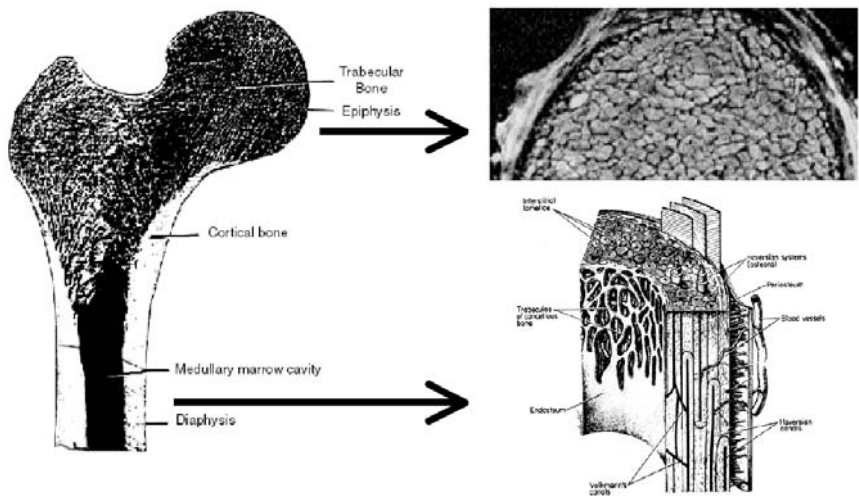


Figure 13.1. Diagram of the upper half of a femur showing the trabecular bone regions in the femur head (NMR image) and neck, and the cortical bone regions in the diaphysis.

air sinuses of the skull [2]. Dosimetrically important regions in therapeutic nuclear medicine are considered to be the haematopoietic stem and precursor cells in the marrow cavities and the osteogenic cells on the surface of the bone trabeculae. Doses to epithelial cells lining ethmoid, sphenoid, mandibular and maxillary sinuses from α emitters in bone or in gaseous form [3–5] are generally not applicable for nuclear medicine dosimetry.

Table 13.1. Typical geometrical dimensions of trabecular and cortical microstructures of an adult [6].

Feature	Typical dimensions (μm)
Trabecular bone	
Bone trabeculae in parietal bone	511
Bone trabeculae in cervical vertebra	279
Bone trabeculae in femur head	232
Marrow cavity in parietal bone	389
Marrow cavity in cervical vertebra	910
Marrow cavity in femur head	1157
Cortical bone	
Osteon length (between Volkmann canals)	2500
Concentric lamellae thickness	7
Osteon diameter	200–400
Haversian canal diameter	20–200

13.1.2. Dosimetry of the skeletal system

In radioimmunotherapy (RIT) and radionuclide bone pain palliation, the skeletal system, and more precisely the bone marrow, has been one of the main dose-limiting organs [7–11]. Dose calculations in nuclear medicine are principally based on the MIRD methodology [12]. In a practical approach, the MIRD methodology simply decomposes the average dose to a target region from a specific source region into a ‘biological’ term, $\tilde{A}_{\text{source}}$, and a ‘physical’ term, $S(\text{target} \leftarrow \text{source})$:

$$\bar{D}(\text{target} \leftarrow \text{source}) = \tilde{A}_{\text{source}} S(\text{target} \leftarrow \text{source}), \quad (13.1)$$

where $\tilde{A}_{\text{source}}$ is the cumulated activity or the total number of nuclear transitions of the radionuclide in the source region, and $S(\text{target} \leftarrow \text{source})$ is the S value or the average absorbed dose in the target per unit cumulated activity in the source region. The cumulated activity is generally determined on a per-patient basis from SPECT, planar imaging (scintigraphy) [13] or blood activity count [9–11]. S values are tabulated for specific radionuclide, source and target combinations. The calculation of an S value requires knowledge of the radiations emitted by the radionuclide and information on the distribution of absorbed energy within target regions of interest in the anatomical model for monoenergetic sources distributed within source regions of the model; such data are referred to as absorbed fractions of energy. The calculation of absorbed fractions of energy requires the use of a model of the anatomy of interest (source, target and surrounding media) and a particle transport code. For most source–target regions in the body, both models are well differentiated and anatomical models are based on the combination of simple mathematical shapes approximating the anatomy [14], and the particle transport is based on Monte Carlo techniques [15] and/or point kernel algorithms [16].

Macroscopically, the skeletal system is well defined throughout the body, and its geometry can be modelled using simple mathematical shapes [15–17]. However, it is an inhomogeneous region with radiosensitive tissues embedded within a dense bone matrix defined at the microscopic level. Therefore, a different approach must be employed to incorporate both the macroscopic and microscopic anatomy and, because directly ionizing and indirectly ionizing radiations have widely different interaction ranges, they are separately considered in the dosimetry modelling.

There are three approaches that have been developed and used to calculate the energy deposited by indirectly-ionizing radiations in the sensitive regions of the skeletal system. These three methods are all based on the use of a homogeneous macroscopic model of the skeletal system (uniform mixture of bone and soft tissue with density 1.4 g cm^{-3}) within mathematical anthropomorphic phantoms [15, 16] that is coupled to a photon transport Monte Carlo code. The first method was developed

by Snyder *et al.* for the tabulation of dose conversion factors for various radionuclides [18], and was subsequently used in MIRD Pamphlets Nos. 5 and 11 [14, 15]. Snyder *et al.* calculated the energy deposited by photon interactions in the macroscopic skeletal model, and partitioned it by target mass to generate the energy deposited in the sensitive tissues of the skeletal system. This approach assumed that the range of secondary electrons was smaller than the marrow cavity sizes and equivalence in the mass absorption coefficients for marrow and bone. In an effort to improve upon these assumptions, Eckerman presented a new approach in which photon fluence calculated in a homogenous skeletal region of the anthropomorphic phantom is coupled with dose per unit fluence response factors derived considering the creation and transport of the secondary electrons in a microscopic model of the skeletal region [16, 19, 20]. This second approach was used in the tabulation of specific absorbed fractions of energy (absorbed fraction of energy per unit mass of target region) published in ORNL TM 8381 [16], which were subsequently used in MIRDose 3 [21]. A similar approach proposed by Bouchet *et al.* consisted of calculating the energy of the secondary electrons created by photon interactions in the macroscopic model of the skeletal system and coupling them to electron absorbed fractions of energy calculated using a microscopic model of the skeletal system [22]. The last two methods differed principally in the use of two different microscopic models of the skeletal system that will be presented and compared in subsequent sections.

For directly ionizing radiations, there are essentially two approaches to calculate the energy deposited in the sensitive regions of the skeletal system. The first is to focus the modelling on closely representing the anatomical microstructures of the skeletal system and to couple the model to a Monte Carlo particle transport code. However, because of its intricate anatomy and its complex microstructure, it is difficult to exactly model the skeletal system without using three-dimensional imaging, and only a few investigators have used three-dimensional data. The second approach is to model the particle transport in such a way that the traversed distance across a given microscopic region (bone trabeculae or marrow cavity for example) by a particle matches exactly the real path of the particle in the skeletal microstructure. This approach initially was proposed by the research group of Spiers [6, 23–29] and subsequently was used in several skeletal dosimetry models [19, 20, 30].

In the next sections of this chapter, the different microscopic models of the cortical and trabecular bone regions that have been used with Monte Carlo techniques to generate dosimetric data for nuclear medicine are presented. Because a model is based upon specific assumptions, and is derived for a reference individual, correction methods for patient-specific applications are given as well.

13.2. TRABECULAR BONE MODELS

13.2.1. Research at the University of Leeds

The foundation of all bone dosimetry modelling was established through the research of Spiers and his students at the University of Leeds between 1949 and 1981 [6, 23–29]. From this research group, three major dissertations on bone dosimetry are of particular note: one by Darley in 1972 [25], one by Whitwell in 1973 [26], and one by Beddoe in 1976 [6]. Spiers determined through this research that the microstructure of trabecular bone could not be well described using simple geometrical shapes. Instead, he used frequency distributions of linear path lengths through trabeculae and marrow cavities as a quantitative description of the three-dimensional structure of this region of the skeleton. For this purpose, Darley and Beddoe designed an optical bone scanner capable of automatically measuring bone and cavity space chord length distributions of thin sections of human trabecular bone [26, 27]. Assuming a direction of alignment of the cavities, they derived corresponding omnidirectional chord length distributions. A total of seven bone sites were measured including the cervical vertebra, lumbar vertebra, femur head, femur neck, iliac crest, parietal bone, and rib. Whitwell used the experimentally measured omnidirectional chord length distributions to calculate dose conversion factors (ratio of absorbed dose in target to the absorbed dose in hypothetical trabecular bone assuming complete absorption of the β emissions) for seven radionuclides (^{14}C , ^{18}F , ^{22}Na , ^{32}P , ^{45}Ca , ^{90}Sr , ^{90}Y) distributed within the volume of trabeculae. A Monte Carlo process was used to sample the chord length distributions and select electron paths through marrow cavities and bone trabeculae. The energy deposited in those different regions was determined using range–energy relationships in both the bone trabeculae and marrow cavities (continuous slowing down approximation) assuming a straight electron path through these regions. Although these calculations were performed assuming the electron deposits all its energy in the trabecular bone, Whitwell applied correction factors to simulate the escape of electrons from the trabecular bone for high-energy electron sources. In this study, only bone- and surface-seeking radionuclides were considered, and only the marrow cavity and endosteum were chosen as target regions.

13.2.2. Model of trabecular bone in MIRD Pamphlet 11

The research of Whitwell focused on radionuclides of interest for radiation protection and, therefore, nuclear medicine dosimetry was not of primary importance. To apply Whitwell's data to additional radionuclides, Snyder *et al.* approximated the specific absorbed fractions for monoenergetic sources by expressing the skeletal-averaged dose conversion factors for the seven

radionuclides as a function of their average β energy [26, 27]. Using these specific absorbed fractions, trabecular bone S values were tabulated as part of MIRD Pamphlet No. 11 [14]. In these reports, four source regions were considered (trabecular bone, cortical bone, red marrow, and yellow marrow) and four target regions (skeletal bone, red marrow, yellow marrow, and skeletal endosteum). For the skeletal source–target combinations not considered by Whitwell, Snyder *et al.* applied one of the following five assumptions to estimate values of absorbed fraction: (a) no energy deposition in the target region, (b) full energy deposition in the target region, (c) conservation of energy within neighbouring regions, (d) uniform energy deposited per unit mass in both the source and target regions, and/or (e) the reciprocity theorem [12, 31].

13.2.3. Skeletal dosimetry in ICRP Publication 30

In 1979, the ICRP issued its Publication 30 [32], which recommended absorbed fractions of energy for β particles for use in radiation protection. For β particles originating in the bone volume, a single value of absorbed fraction was recommended. For β particles originating on the bone surface, one absorbed fraction for low-energy β particles (average β energy less than 0.2 MeV), and one for high-energy β particles (average β energy greater than or equal to 0.2 MeV) were recommended. These absorbed fraction values were based on the dose conversion factors from Whitwell [26, 27], and were intended to be conservative, as their objective was to provide a system of radiation protection for workers and not for clinical RIT. Subsequently, these relatively energy-independent absorbed fractions of energy were implemented in the MIRDose2 program [21] for use in nuclear medicine dosimetry. In this same computer program, the self-absorbed fraction to the marrow was assumed to be unity as suggested in Part 3 of the ICRP Publication 30.

13.2.4. Spherical model of trabecular bone

Chen and Poston [33] proposed a model in 1982 that assumed the marrow spaces in trabecular bone were spherical in shape. The marrow space dimensions and the trabecular thicknesses were chosen randomly from the chord-length distributions and other data of Spiers and his colleagues [6, 23–29]. A computer code, DAB-BE, was written which could be used to calculate the absorbed energies deposited by β particles or electrons inside human trabecular bone. The radiation source geometry could be either uniformly distributed in the whole bone or located at a fixed point inside the bone. Bremsstrahlung production was not considered in these calculations. Results were presented for six monoenergetic electron sources (0.1, 0.5, 0.8, 1.0, 1.5 and 2.0 MeV) distributed uniformly in a mathematical

representation of the arm [18]. In addition, a fixed point source of 1.0 MeV monoenergetic electrons was studied.

This spherical model was improved by Zuzarte de Mendoca by consideration of the endosteal layer as well as the marrow space and trabecular dimensions [34]. She used the Monte Carlo code EGS4 [35] and considered both surface and volume sources. These calculations produced absorbed fractions and specific absorbed fractions of energy for six monoenergetic electron sources (0.1, 0.2, 0.5, 1.0, 2.0 and 4.0 MeV) for source–target combinations in the spine, the cranium and the pelvis. She found that the absorbed fractions in bone marrow were strongly dependent on the ratio of trabecular bone to bone marrow volume. The higher the ratio, the lower the absorbed fraction in bone marrow.

Parry [36] continued this research and devised a modified model of the trabecular bone for use in the EGS4 code [35]. He calculated electron absorbed fractions for red marrow and the endosteal tissue on trabecular bone. The model was based on measured omnidirectional chord length distributions through trabeculae and marrow cavities in nine skeletal locations. Absorbed fractions were calculated for only two target regions and all other skeletal regions were estimated based on these results. In addition, the absorbed fractions were used to calculate S values for a variety of β -emitting radionuclides at each of 15 skeletal regions containing red bone marrow. Absorbed fractions and S values were calculated for sources in the marrow, on the bone surface and in the bone volume. Comparisons were made between these results and those published in ICRP Publication 30 [32] as well as those determined using MIRDose2 software [21].

13.2.5. The Eckerman trabecular bone model

Eckerman [19, 20] presented new electron absorbed fractions of energy in the trabecular bone region based on the chord length distributions measured by Darley [6, 23, 25]. Using Whitwell's approach [26, 27] of combining Monte Carlo sampling of chord length distributions in bone cavities and trabeculae with electron range–energy relationships, Eckerman derived absorbed fractions of energy for monoenergetic electrons for the seven trabecular bone sites measured by Darley. Source regions explicitly considered in this model were marrow cavity, bone trabeculae and bone surface, with target regions being the marrow cavity, endosteum and bone trabeculae. To simulate a bone surface source, the Eckerman model assumed that electrons were emitted at the surface between the trabeculae and marrow cavities. For the endosteal target, a 10 μm layer of soft tissue was assumed on the bone surface as recommended in ICRP-30 [32]. Because the radiosensitive active marrow target was part of the simulated marrow cavity, Eckerman derived the absorbed fraction to this sensitive structure by partitioning the energy deposited in the full marrow cavity by the cellularity factor (percentage of

total marrow mass that is active). This model simulated no escape of the electron from the trabecular bone, and assumed that all energy emitted was deposited in the trabecular bone. In 1994, results from this model were implemented in the MIRDose3 program [21]. Reference masses for the endosteum and active marrow in trabecular bone of the 15 skeletal regions defined in the anthropomorphic phantoms [16] were derived as described in [20] and used to convert Eckerman's absorbed fractions of energy to radionuclide S values. This implementation allowed for explicit calculation of regional absorbed dose in the 15 different bone sites as well as for the whole skeleton, for two trabecular bone target regions (red marrow and the endosteum) and three trabecular bone sources (trabecular bone volume, red marrow and trabecular bone surface).

13.2.6. *The Bouchet et al. trabecular bone model*

In 1999, Bouchet *et al.* extended the one-dimensional transport model for electrons in trabecular bone to a three-dimensional model [30]. This model was based on the chord length distributions of the group of Spiers. A series of three-dimensional spherical half-spaces of bone or marrow, with radii consistent with the measured chord distributions, were presented to the particle during Monte Carlo radiation transport. In this manner, allowances were made for potential differences between the particle path-length and its linear displacement through the media, for backscattering electrons, as well as for the production of both δ -rays and bremsstrahlung. Electron transport in the endosteum was performed by creating a three-dimensional spherical half-space with radii selected randomly from a random entry angle in a 10 μm thick layer. The EGS4-PRESTA Monte Carlo transport code [35, 37] was used to simulate the electron interaction within this three-dimensional model, assuming no escape of energy from the trabecular bone. Similar to Eckerman's simulations, Bouchet *et al.* calculated absorbed fractions of energy for monoenergetic electrons for the seven trabecular bone sites for which the Spiers group tabulated the chord length distributions. Source and target regions considered were the trabecular marrow space, the trabecular bone volume and the trabecular bone endosteum. Results from these simulations were combined with reference masses derived from ICRP Publication 70 for 22 skeletal sites and nine source–target tissue combinations within the trabecular bone [38].

13.2.7. *Differences between the three-dimensional model of Bouchet et al. and the one-dimensional model of Eckerman*

The benefits of a three-dimensional transport model over a one-dimensional model were investigated by Bouchet *et al.* [30]. They constructed a one-dimensional model for electron transport in trabecular bone following the

chord length sampling methodology employed in their three-dimensional model. The energy deposited in a given region was scored assuming a straight electron trajectory through each tissue region and using the range-energy relationships adopted by Whitwell and Eckerman. They reported improvements over one-dimensional transport at low electron energies (less than ~ 200 keV). Large differences were observed when the source and the target were not adjacent regions (30–50% and upward for energies less than 100 keV) due to the possible variations in the range of the electrons modelled by the EGS4 Monte Carlo transport code (i.e., range straggling).

Three additional differences in the methodologies used by Eckerman and by Bouchet *et al.* are associated with the selection of source and target for the active marrow and the bone surfaces. The first difference is associated with the derivation of absorbed fractions for self-irradiation of red marrow. In the Eckerman model, absorbed fractions of energy in the red marrow were calculated by multiplying the absorbed fractions in the marrow cavity by reference cellularity values for each bone region. In the Bouchet *et al.* model, it was assumed that the absorbed fractions of energy to the red marrow and marrow cavity were numerically equal. As a result of this difference in methodology, skeletal average S values for an active marrow source and target calculated by Eckerman were determined to be $\sim 50\%$ lower than those calculated by Bouchet *et al.*. Recent research at the University of Florida has explored these differences using three-dimensional radiation transport techniques in trabecular bone based upon images acquired through NMR microscopy [39], and based upon calculations for the femur and humerus, has concluded that (i) the Eckerman model provides acceptable estimates of AF(red marrow red marrow) at energies above 200 keV, (ii) the Bouchet *et al.* model provides acceptable estimates of these same values at energies less than 20 keV and (iii) neither model accurately predicts the absorbed fraction for self-irradiation of the active marrow in the energy range 20–200 keV. Results from these two models were recently combined using the University of Florida findings to generate more accurate absorbed fractions of energy for the active marrow [40].

The second difference between these involves bone surface sources. For a bone surface source, the Eckerman model uses a two-dimensional planar surface source, selected at the interface between the trabeculae and marrow cavities as recommended in ICRP 30 [32]. The Bouchet *et al.* model assumes that the source is distributed throughout the $10\text{ }\mu\text{m}$ layer of soft tissue (endosteum) on the bone interface. Consequently, the Eckerman skeletal average S values for a 'bone surface' source and a marrow target are $\sim 15\%$ lower than those of Bouchet *et al.* for low-energy sources.

The third difference is associated with an endosteal target. Both models assume the same $10\text{ }\mu\text{m}$ layer of soft tissue on the bone surface. However, because the Eckerman model is a one-dimensional model, electrons are assumed to enter this target with a uniform distribution of angles as

compared with the three-dimensional transport of Bouchet *et al.* that assumes a uniform distribution of the cosine of the angle. The one-dimensional assumption leads to a decrease in the pathlength through the endosteum. As a result of the differences associated with the modelling of the surface source and endosteal target, calculated S values for a surface source and an endosteal target are 60% lower in the MIRDOSE3/Eckerman model than in the Bouchet *et al.* model for low-energy sources. Resolution of these last two issues awaits acquisition and analysis of further data.

13.2.8. Model of a trabecular bone lesion

A different type of trabecular bone model was developed in 1995 by Samaratunga *et al.* [41]. This group developed an anatomical model of trabecular bone designed specifically to calculate the dose to skeletal metastases from the surface seeker ^{186}Re . This model was based on anatomical measurements of chord length distributions of cavities and bone trabeculae on 25 samples from skeletal metastases. Bone trabeculae were represented by ellipsoids located in an infinite marrow-tissue medium. Finally, the transport of electrons was simulated in a three-dimensional geometry using the Monte Carlo electron transport code EGS4. Even though the procedure was very sophisticated, the model developed by Samaratunga was intended for transport of electrons in trabecular bone metastases, and therefore was not applicable for Reference Man tabulations.

13.2.9. High-resolution imaging for trabecular bone dosimetry

An alternative to chord-based transport models for trabecular bone dosimetry is the use of three-dimensional digital images of these skeletal sites coupled directly to Monte Carlo radiation transport codes. This technique offers several distinct advantages over chord-based models. First, absorbed fractions of energy are acquired within a skeletal site for which mass estimates also are known. In chord-based models, only the absorbed fraction is obtained from the transport calculations; independent assignments of target tissue mass are required to report absorbed dose. Second, the full three-dimensional structure of the anatomical site is available for particle tracking, enabling one to include energy loss to the cortical bone cortex of the skeletal site for high-energy sources. Most current chord-based transport models continue to utilize an infinite trabecular-region transport geometry. Third, explicit partitioning of the marrow source and target tissues into active (red marrow) and inactive (yellow marrow) is accommodated within three-dimensional models of trabecular bone, avoiding scaling approaches necessary within chord-based models to account for marrow cellularity.

Three imaging techniques have been applied to the general study of trabecular bone microarchitecture: nuclear magnetic resonance (NMR)

microscopy (resolution: $\sim 50\text{--}100\text{ }\mu\text{m}$), micro-computed tomography (resolution: $\sim 20\text{--}50\text{ }\mu\text{m}$) and synchrotron microtomography (resolution: $<20\text{ }\mu\text{m}$). Jokisch *et al.* investigated the use of NMR microscopy to establish three-dimensional electron transport models of trabecular bone [42, 43]. In these studies, cadaveric sources of thoracic vertebral bodies were subjected to marrow digestion, immersion in Gd-doped water, and imaging at 14.1 T using a three-dimensional spin-echo pulse sequence. Electron transport with the EGS4 code was conducted under a dual transport geometry: one utilizing a segmented, voxel model of the bone trabeculae and marrow cavities, and one utilizing a stylized representation of the trabecular spongiosa and cortex of cortical bone. These studies were extended by Bolch *et al.* to include explicit consideration of active marrow as both a source and target region [44]. This study showed that, for nonspecific uptake of radioactivity in the active marrow, marrow cellularity is an important parameter to consider in patient-specific assessments of active marrow self-irradiation for high-energy therapy radiopharmaceuticals. For low-energy emitters, reference values of cellularity are sufficient for dose estimation.

In studies by Patton *et al.*, energy loss to cortical bone was explored and compared with results from infinite trabecular region transport [45]. This study indicated that *S* value corrections on the order of 5–8% for ^{32}P and 8–11% for ^{90}Y were required to properly account for the finite size of skeletal site. In a subsequent study, Patton *et al.* established that the overall methodology employed in NMR microscopy and radiation transport was reproducible to $\sim 1\text{--}2\%$ at energies below 1 MeV, and no more than 4% at 4 MeV [46]. Furthermore, the study established that nearly identical absorbed fraction energy profiles could be obtained via either marrow-intact or marrow-free NMR imaging, thus suggesting the potential for *in vivo* patient-specific dosimetric models of the skeleton. This conclusion was supported by the theoretical study by Rajon *et al.* [47] noting that image resolutions no finer than $\sim 300\text{ }\mu\text{m}$ were sufficient for the development of three-dimensional dosimetry models of trabecular bone for high-energy electron emitters employed in radionuclide therapies.

13.3. CORTICAL BONE MODELS

13.3.1. Research at the University of Leeds

Similar to trabecular bone dosimetry, the foundation of cortical bone dosimetry was established by F W Spiers at the University of Leeds. In 1976, Beddoe used the bone scanning microscope to measure transverse chord lengths through Haversian cavities and the intervening cortical bone matrix [6]. Initially developed for path-length measurements in trabecular bone, this bone-scanning microscope was refined to measure the small cavities in cortical bone. Stained sections of transverse slices of cortical

bone (20–30 μm thick) were scanned to obtain transverse chord length distributions of the Haversian cavity sizes and cortical bone matrix, the latter defined as the distances between Haversian cavities in the plane perpendicular to the bone axis. With this optical scanning system, an effective resolution of about 8 μm was achieved. Beddoe made measurements of the cortex in three cortical bones: the humerus, tibia and femur. In his measurements, Beddoe assumed that the Haversian cavities ran parallel to the long axis of the bone, which is generally the case for the long bones. He also assumed that the number of transverse canals (Volkmann canals) appearing in the transverse planes was negligibly small. This last assumption was verified visually on his stained sections of cortical bones. Beddoe included measurements of the iliac crest, but his results showed irregular fluctuations due to scanning only one small section.

For dosimetry calculations, Beddoe followed the technique employed by Whitwell [26, 27] in the dosimetry of trabecular bone. Assuming a straight electron path through Haversian cavities and cortical bone matrix, a Monte Carlo sampling technique was used to randomly select electron paths through the Haversian canal and cortical bone matrix. The energy deposited in these regions was determined using range–energy relationships in bone and soft tissues, and was used to calculate dose conversion factors for several radionuclides. These dose conversion factors were only published in the dissertation of Beddoe, and only for a limited number of radionuclides (^{14}C , ^{18}F , ^{22}Na , ^{32}P , ^{45}Ca , ^{90}Sr , ^{90}Y). Moreover, the only source considered in his study was the bone volume, where both the endosteum and Haversian canals are of interest for nuclear medicine and health physics dosimetric applications.

13.3.2. *The ICRP-30 cortical bone model*

In ICRP Publication 30, recommended absorbed fractions for cortical bone are only given for the endosteum as target region and for the cortical surface and bone volume as source regions [32]. For β emitters originating on the cortical surface, the Commission recommended an absorbed fraction to the endosteum of 0.25 for mean β energies below 200 keV, and an absorbed fraction of 0.015 for mean β energies greater than or equal to 200 keV. For β emitters originating in the cortical bone volume, an energy-independent absorbed fraction of energy to the endosteum of 0.015 was recommended. These absorbed fractions values were based on the dose conversion factors of Beddoe, and were intended to be conservative, as their objective was to provide a system of radiation protection for workers.

13.3.3. *The Eckerman cortical bone model*

Eckerman and Stabin [20] presented absorbed fraction for monoenergetic electron sources distributed in the volume and on the surface of cortical

bone matrix. Details regarding these calculations were, however, not provided in reference [20]. The absorbed fractions were based on a cylindrical model of the Haversian canal located within an infinite cortical bone matrix. The diameter of the Haversian canal was taken to be 40 μm and the energy deposition within the 10 μm layer lining the canal was evaluated based on the range–energy relationship (CSDA approximation).

13.3.4. *The Bouchet et al. cortical bone model*

In 1999, Bouchet *et al.* developed a three-dimensional transport model for electrons in cortical bone [48] using the same methodology they used for trabecular bone dosimetry [30]. They modelled the transport geometry experienced by an electron travelling in the cortical bone using the transverse chord length distributions through Haversian cavities and cortical bone matrix measured by Beddoe. Because the chord length distributions were measured within the plane perpendicular to the bone axis, each region was represented by parallel portions of cylinders with radii sampled from the chord length distributions. By sampling many different chords, for many electrons, the average transport of an electron in cortical bone was simulated. However, the escape of the particle from the cortical bone was not simulated and, therefore, these cylinders were not limited by any planes along the direction of their axes. Electron transport in the endosteum was performed by creating a three-dimensional cylindrical half-space with radii selected randomly from an entry angle in a 10 μm thick layer. The EGS4-PRESTA Monte Carlo transport code was used to simulate the electron interaction within this three-dimensional model, thus allowing for modelling of (a) the non-linear electron trajectories, (b) full transport of the electrons with δ -rays and bremsstrahlung, (c) the distribution of sizes of Haversian canals and (d) cross-osteon irradiation. Absorbed fraction results for source and target regions—the cortical endosteum, the Haversian canal or the cortical bone matrix—were tabulated for the three cortical bone sites for which Beddoe tabulated the chord length distributions. Results from these simulations were combined with reference masses derived from ICRP Publication 70 for 22 skeletal sites and nine source–target tissue combinations within the trabecular bone [38].

13.3.5. *The research of Akabani*

In 1993, Akabani developed an anatomical model [49] for the dosimetry of a single Haversian canal, and derived dose factors for several β -emitting radionuclides (^{32}P , ^{45}Ca , ^{89}Sr , ^{90}Sr , ^{90}Y , ^{131}I , ^{153}Sm). This single Haversian canal was modelled as a cylinder surrounded by an infinite cortical bone matrix. Six Haversian canal sizes were individually considered with radii of 5, 10, 20, 30, 40 and 50 μm . The Monte Carlo transport code EGS4-PRESTA

was used to derive electron absorbed fractions of energy for two sources (Haversian canal and bone surface) and three targets (Haversian canal, endosteum and the bone matrix). From these calculations, dose conversion factors were tabulated for these seven radionuclides as a function of the Haversian canal radius. Although elegant in its design, this anatomical model only considered a single size for the Haversian canal, and it did not consider the cross-osteon irradiation.

13.4. IMPROVING THE MODELS: PATIENT-SPECIFIC DOSIMETRY

13.4.1. *The clinical experience—ability to predict toxicity with current dosimetric models*

Nuclear medicine therapy is used increasingly in the treatment of cancer (thyroid, leukemia/lymphoma with RIT, primary and secondary bone malignancies, and neuroblastomas) and marrow toxicity generally limits the amount of treatment that can be administered safely. The most difficult problem in calculating bone marrow dose arises from the complex distribution of bone marrow in bone. The microanatomy of the marrow and its diffuse intra-skeletal distribution make it difficult to calculate red marrow dose accurately using only classical physical approaches, as discussed above. Although stem cells and their primordial derivatives are presumed to be the primary targets, the stroma that supports the red and yellow marrow also plays an important role in facilitating marrow function, and is an important secondary target [50, 51]. Dose to the bone marrow comes mainly from activity within the marrow itself (specific binding to a cellular component of either the marrow or blood), with the next highest contribution coming from tracer accumulation, when it occurs, in the surrounding bone, with lesser contributions from more remote sources. Due to limited spatial resolution, nuclear medicine imaging devices are unable to resolve the source distribution in bone, and other methods are needed to calculate the contributions from these sources.

Bone marrow toxicity is the major dose-limiting factor in RIT, but there is no consensus on how to calculate that dose accurately, or of individual patients' ability to tolerate the planned therapy [8, 13, 52–59]. Experience with external beam therapy has shown that there is a narrow margin between the delivered dose that kills a tumour and that which causes serious injury to the patient. Given that with modern imaging methods the dose from external beam treatments can be accurately calculated, the remaining major issues are tumour sensitivity and patient tolerance. In nuclear medicine, in contrast to external beam radiotherapy, marrow absorbed dose may not be accurately calculated, even when a treatment-planning dosimetry study is performed

[60]. Nonetheless, both external beam and internal emitter therapy share the same uncertainty regarding predicted patient tolerance. Nuclear medicine physicians in general have less experience in the therapy regime than those who deal with external treatment approaches, and typically undertreat patients in order to minimize the risk of even low-grade toxicity. If treatment of cancer with radionuclides and RIT are to become a primary means of treating cancer patients, the activity to be administered to individual patients should be based on accurate evaluations of the dose to be delivered to the tumour and of patient tolerance [61].

Radionuclide therapy has been most effective in the treatment of thyroid cancer because of the high specific uptake of radioactive iodine by thyroid tissue, but there is still no agreement on the means for choosing an optimal therapeutic radiation dose to be delivered. The hope for RIT derives from the notion that it can achieve selective high tumour uptake based on improved targeting of tumour specific/associated antigens. Intravascular tumours, including leukaemia and lymphoma, have the highest likelihood of successful treatment with RIT, partly because tumour targeting efficiency is high, and partly because of the high radiation sensitivity of lymphocytes, and to a lesser extent of granulocytes. A major problem with RIT treatment of most solid tumours has been low uptake per unit tumour mass, so that the delivered dose is often too low for successful therapy. If one gives very large doses intending to ablate marrow and tumour followed by marrow transplantation, then lungs, liver or kidneys will become the dose limiting organs. Bone marrow transplantation (BMT) is being employed routinely in the treatment of breast cancer with high doses of chemotherapy and/or of some solid tumours with RIT. A reasonable goal would be to develop an improved means of defining an appropriate intermediate dose that provides high 'cure'/complete remission rates, without the need for BMT.

Progress is being made in the development of improved calculation methods and tools for patient-specific treatment-planning focusing primarily on tumour dose optimization [62–64]. Still, problems remain in the accurate assessment of bone marrow dose and in the estimation of marrow reserve. Better patient-specific knowledge of both dose and marrow reserve is needed if one is to develop a good predictor of tolerance dose. Two analytical approaches have been taken. The first is the physical method, in which one measures the biokinetics and computes dose based on knowledge of the amount injected, the radionuclide emission characteristics, and the measured residence times in the different organs using accepted dose calculation methods [12]. A complementary approach attempts to use patient-specific characteristics to estimate residual damage from prior therapeutic treatments to estimate the amount of added dose that would be tolerated by normal organs, including bone marrow.

The importance of including pre-therapy patient status in toxicity predictions has been studied by several groups [59, 65], and it is clear that

prior patient therapy and disease status must be factored into treatment decisions. Nonetheless, to date poor correlations have been observed between administered dose and marrow toxicity, which are somewhat improved by more carefully calculated marrow doses [54]. This suggests the need for more patient-specific information, including better dose estimates and better information on other patient characteristics, including perhaps patient-specific indicators of response (i.e., biomarkers).

Marrow toxicity from RIT is manifest by haematological changes in circulating platelets, lymphocytes, granulocytes and reticulocytes, and later changes are seen in red blood cells. Due to the high sensitivity of the marrow, second organ toxicity is not a problem unless doses which are known to be lethal to the marrow are intentionally given. Attempts to correlate haematological toxicity with marrow dose, when marrow cells are specifically targeted, have not been particularly successful in the past, in part due to uncertainties in the actual absorbed dose, but also due to the difficulty in assessing marrow functional status prior to therapy [8, 13, 53–58]. The best correlations obtained to date have had a value of r around 0.8 [53, 57, 66, 67]. Whole-body absorbed dose and red marrow absorbed dose are usually the best indicators of haematological toxicity, as measured by platelet toxicity grade, with red marrow dose being slightly better. However, the poor correlation coefficients obtained from these analyses emphasize the need to better account for prior patient therapy and bone marrow reserve. That red marrow absorbed dose is the best (albeit not appropriate on a patient-by-patient basis) predictor of haematological toxicity has been confirmed using data from other antibody trials [68]. Most recently, a survey of the literature using data from different antibodies, different patient populations and different disease sites has confirmed this observation over a much larger scale [69]. Blumenthal *et al.* showed that plasma FLT3-L (a stromal-cell produced positive stimulatory cytokine) levels predicted excess platelet toxicity in patients receiving RIT after chemotherapy [70].

Many other studies have found little or no correlation between calculated marrow dose for large numbers of patients and observed toxicity, as determined by various haematological parameters (platelet nadir, percentage platelet drop, percentage lymphocyte drop, percentage granulocyte drop, etc.). The primary reason for this is probably that all available marrow dose models are patterned after a normal healthy young adult with good marrow reserve, while the treated population is generally older (with inherently different trabecular bone structures and less marrow reserve), often with compromised marrow due to disease, prior chemotherapy or radiotherapy.

13.4.2. Correcting the models using patient-specific data

It is unreasonable to expect that doses calculated from a single model representing an average healthy adult will yield good correlations of

radiation dose with observed effects in a heterogeneous patient population. Many patients are older, with presumably less active marrow mass than younger people, have more osteoporotic trabecular bones, and many have disease or have had prior therapies which may affect marrow status and trabecular bone micro-anatomy. Simple adjustments to standard model S values may be made, assuming that patient marrow mass changes in some predictable way with lean body mass, body surface area, or other easily measured anatomic features. Such approximations will of course be imperfect, but better than simply applying the standard model to all patients equally. Some improvements in correlations between marrow dose and observed marrow toxicity can be realized by calculating patient-specific contributions to marrow dose and by making patient-specific adjustments to relevant parameters such as marrow mass and cellularity (as implied by patient age, disease, and prior therapeutic treatment) [54, 67].

More patient-specific evaluations can be envisioned, which could be realized with some additional investigational effort. Functioning marrow could be evaluated through the use of marrow scanning agents, such as ^{99m}Tc -sulfur colloid, ^{18}F -fluorothymidine [71], or other marrow avid agents. If some quantitative measure of uptake in different regions can be obtained, model-specific trabecular bone dose conversion factors [19, 20, 38] may be modified to be more specific to the patient. For example, skeletal averaged S values in MIRDose3 [19, 20] were calculated from skeletal averaged absorbed fractions:

$$\overline{\text{AF}(\text{RM} \leftarrow \text{RM})} = \sum_{\text{bone}} \text{CF}_{\text{bone}} f_{\text{RM,bone}} \text{AF}(\text{MS} \leftarrow \text{RM})_{\text{bone}} \quad (13.2)$$

where CF_{bone} is the cellularity factor for a given bone, $f_{\text{RM,bone}}$ is the fraction of the red marrow (RM) associated with a given bone, and $\text{AF}(\text{MS} \leftarrow \text{RM})_{\text{bone}}$ is the absorbed fraction for the energy originating in the marrow of a given bone and irradiating the marrow space of that bone. The values of $f_{\text{RM,bone}}$ and CF_{bone} may be assigned based on information gained in individual radionuclide marrow scans; that is, the fraction of marrow calculated to be in each of the model regions and the cellularities may be calculated on a patient-specific basis. In the absence of patient-specific values of cellularity derived from marrow biopsies, values from age-dependent models (e.g., [72, 73]) may be applied or, as will be discussed in the next section, magnetic resonance imaging methods could also be used to determine patient-specific active marrow mass and location [74–77]. Bone marrow uptake of RIT agents in expected marrow sites which have diminished or absent marrow function on radionuclide scans may be assumed to be tumour, and the computed dose calculated using a more specific model (e.g., [41]). Time–activity integrals may be calculated and doses estimated for the different bone marrow regions in which marrow localization has been scored, assigning the total marrow residence time to

each region using the values of $f_{\text{RM,bone}}$. Whole marrow weighted average dose and differential and integral dose–volume histograms then may be calculated.

Determining marrow time–activity integrals for internal emitters is an area of difficulty, as marrow activity is heterogeneous even in normal subjects, and more so in patients with cancer, with or without a history of previous treatment. Different imaging methods rely on either (i) the quantification of activity in a certain segment of the marrow (e.g., the lumbar spine or sacrum) and extrapolation of total marrow activity assuming the total amount of red marrow in the body and the fraction of the total that resides in individual segments [13], or (ii) the assumption that the dose is derived only from blood contributions, with the assumption of normal marrow size [9] and/or (iii) combined blood and marrow-fixed activity methods. The correlation between dose calculated in the different manners, biomarker results, and clinical predictors with observed toxicity and patient cure rates should be used to assess the potential utility of the different dose calculation and marrow indices for improving treatment outcome. This is not currently in standard practice, but should be considered if we are to seek more meaningful dose and risk assessment in individual patients, as is routine in external beam therapy.

13.4.3. *In vivo high-resolution imaging*

Accurate dose calculations in external beam radiotherapy treatments have been made possible with routine use of three-dimensional anatomical images (CT/MR). For skeletal dosimetry, patient-specific high-resolution three-dimensional images need to provide information on the microstructure of the trabecular bone, on the distribution of the red marrow target and associated sensitive tissues, and on the distribution of the radionuclide.

The use of three-dimensional anatomical images in the determination of trabecular bone microstructure is limited by the image resolution. In order to limit partial volume effect, the voxel size has to be smaller than the structure to be imaged. In 2000, Rajon *et al.* presented a theoretical study of the variations of the absorbed dose (S values) as a function of image resolution, and determined that voxel sizes of 300–400 μm were sufficient for accurate marrow dose calculations (calculated relative error less than 5% for voxel size $< 400 \mu\text{m}$) [47]. As previously described, resolution of 20–50 μm has been achieved with NMR microscopy to determine the microstructures of trabecular bone from cadaveric bone samples. Modern high-field clinical MR scanners (1.5–3 T) also have been used to provide *in vivo* high-resolution images of the distal radius and calcaneus of osteoporotic patients with in-plane resolution of $\sim 150 \mu\text{m}$ and slice thickness $\sim 300 \mu\text{m}$ [78]. Although sufficient for dosimetry of trabecular bone, this high resolution is achieved using special coils with a very small field of view, therefore limiting their

applications to body extremities (hands and feet) which are of no direct interest for dosimetry. With the development of fast helical CT scanning using multislices, CT imaging may become ideal for *in vivo* determination of trabecular bone microstructures due to its high spatial integrity and its higher contrast between bone and soft tissue. Current state-of-the-art clinical CT scanners allow in-plane image resolution of $\sim 200\mu\text{m}$ with $\sim 500\mu\text{m}$ slice thickness to be acquired over a 20 cm length in less than 2 minutes (Rajon *et al.* [47] estimated that a $500\mu\text{m}$ voxel size would lead to a dose calculation error $< 7\%$ for a marrow source and target). Although the number of detectors, their size and their efficiency currently limit the acquisition time and the image resolution, Saito and Artawara recently reported the development of a real-time three-dimensional CT scanner using 256 detectors [79].

As previously discussed, patient-specific determination of marrow cellularity and marrow reserve is important to improve bone dosimetry calculations. In most dosimetric models, a reference marrow cellularity has been used to convert absorbed fractions of energy calculated from a Monte Carlo transport code to S values [19, 20, 38]. Several investigators have developed techniques to measure *in vivo* distribution of marrow cellularity in trabecular bone using clinical MR scanners and have correlated *in vivo* measurements to bone biopsies [74–77, 80, 81]. Although these techniques have been used to assess the composition of bone marrow prior to and after bone marrow transplant [82], they have not yet been applied in dosimetry. It is expected that patient-specific knowledge of bone marrow cellularity throughout trabecular bone would increase prediction of bone marrow toxicity, and allow optimal selection of the amount of therapeutic radiation dose to be delivered.

13.5. SUMMARY

Skeletal dosimetry is complicated by the intricate nature of its microstructure and by the irregular distribution of the radiosensitive red marrow tissue, both of which can vary greatly between patients and throughout various bone regions. Accurate patient-specific skeletal dose calculations are a primary concern in radioimmunotherapy and radionuclide bone pain palliation as the red marrow is usually the dose-limiting tissue. Significant improvements have been made in the use of skeletal dosimetric models for bone marrow dose calculations, mainly from the development of better models (more appropriate for therapeutic nuclear medicine dosimetry) and a better understanding of the models and how to use them. Correlations of radiation toxicity to marrow dose, however, remain weak, and will only improve as more patient-specific dosimetric models are developed and used. The increase in the speed of digital computers has recently permitted the coupling of

high-resolution three-dimensional digital images of the skeletal microstructures acquired *in vitro* to a Monte Carlo transport code. New imaging techniques also allow the *in vivo* distribution of marrow cellularity in trabecular bone to be determined. Application of these and other techniques *in vivo* will allow improvement in the quality of patient-specific marrow dose calculations for a better prediction of bone marrow toxicity and an optimal selection of the amount of therapeutic radiation dose to be delivered.

REFERENCES

- [1] Gray H 1974 *Gray's Anatomy* (Philadelphia, PA: Running)
- [2] ICRP 1995 *Basic anatomical and physiological data for use in radiological protection: the skeleton* ICRP Publication 70, International Commission on Radiological Protection (Oxford: Pergamon)
- [3] Rowland R E, Stehney A F and Lucas H F 1978 Dose-response relationships for female radium dial workers *Radiat. Res.* **76** 368–83
- [4] Littman M S, Kirsh I E and Keane A T 1978 Radium-induced malignant-tumors of mastoid and para-nasal sinuses *Am. J. Roentgenol.* **131** 773–85
- [5] Rowland R E, Stehney A F and Lucas H F 1983 Dose-response relationships for radium-induced bone sarcomas *Health Phys.* **44** 15–31
- [6] Beddoe A H 1976 *The Microstructure of Mammalian Bone in Relation to the Dosimetry of Bone-Seeking Radionuclides* (Leeds: University of Leeds)
- [7] Lewington V J 1996 Cancer therapy using bone-seeking isotopes *Phys. Med. Biol.* **41** 2027–42
- [8] Siegel J A, Wessels B W, Watson E E, Stabin M, Vriesendorp H M, Bradley E W, Badger C C, Brill A B, Kwok C, Stickney D R, Eckerman K F, Fisher D R, Buchsbaum D J and Order S E 1990 Bone marrow dosimetry and toxicity for radioimmunotherapy *Ab. Immunconj. Radiopharm.* **3** 213–33
- [9] Sgouros G 1993 Bone marrow dosimetry for radioimmunotherapy: theoretical considerations *J. Nucl. Med.* **34** 689–94
- [10] Sgouros G, Stabin M, Erdi Y, Akabani G, Kwok C, Brill A B and Wessels B 2000 Red marrow dosimetry for radiolabeled antibodies that bind to marrow, bone, or blood components *Med. Phys.* **27** 2150–64
- [11] Shen S, DeNardo G L, Sgouros G, O'Donnell R T and DeNardo S J 1999 Practical determination of patient-specific marrow dose using radioactivity concentration in blood and body *J. Nucl. Med.* **40** 2102–6
- [12] Loevinger R, Budinger T F and Watson E E 1991 *MIRD Primer for Absorbed Dose Calculations* (New York: Society of Nuclear Medicine)
- [13] Siegel J A, Lee R E, Pawlyk D A, Horowitz J A, Sharkey R M and Goldenberg D M 1989 Sacral scintigraphy for bone marrow dosimetry in radioimmunotherapy *Int. J. Radiat. Appl. Instrum. B* **16** 553–9
- [14] Snyder W S, Ford M R, Warner G G and Watson S B 1975 MIRD Pamphlet No 11: 'S', *absorbed dose per unit cumulated activity for selected radionuclides and organs* (New York: Society of Nuclear Medicine)
- [15] Snyder W S, Ford M R and Warner G G 1978 MIRD Pamphlet No 5, Revised: *Estimates of specific absorbed fractions for photon sources uniformly distributed*

- in various organs of a heterogeneous phantom (New York: Society of Nuclear Medicine)
- [16] Cristy M and Eckerman K F 1987 *Specific absorbed fractions of energy at various ages from internal photon sources* ORNL/TM-8381 (Oak Ridge, TN: Oak Ridge National Laboratory)
- [17] Clairand I, Bouchet L G and Bolch W E 2000 A new macroscopic model of the long bones for skeletal dosimetry *J. Nucl. Med.* **41** 1062
- [18] Snyder W S, Ford M R, Warner G G and Watson S B 1974 *A tabulation of dose equivalent per microcurie-day for source and target organs of an adult for various radionuclides* ORNL-5000 (Oak Ridge, TN: Oak Ridge National Laboratory)
- [19] Eckerman K F 1985 Aspects of the dosimetry of radionuclides within the skeleton with particular emphasis on the active marrow. In *Proceedings of the Fourth International Radiopharmaceutical Dosimetry Symposium* eds A T Schlafke-Stelson and E E Watson (Oak Ridge, TN: ORAU) pp 514–34
- [20] Eckerman K F and Stabin M 2000 Electron absorbed fractions and dose conversion factors for marrow and bone by skeletal regions *Health Phys.* **78** 199–214
- [21] Stabin M 1996 MIRDOSE: personal computer software for internal dose assessment in nuclear medicine *J. Nucl. Med.* **37** 538–46
- [22] Bouchet L G, Clairand I and Bolch W E 2000 Improvement of skeletal dosimetry associated with photon sources *J. Nucl. Med.* **41** 1049
- [23] Beddoe A H, Darley P J and Spiers F W 1976 Measurements of trabecular bone structure in man *Phys. Med. Biol.* **21** 589–607
- [24] Darley P J 1968 Measurement of linear path length distributions in bone and bone marrow using a scanning technique. In *Symposium on Microdosimetry* EAEC Report EUR 3747 Ispra, Italy pp 509–26
- [25] Darley P J 1972 *An Investigation of the Structure of Trabecular Bone in Relation to the Radiation Dosimetry of Bone-Seeking Radionuclides* (Leeds: University of Leeds)
- [26] Whitwell J R 1973 *Theoretical Investigations of Energy Loss by Ionizing Particles in Bone* (Leeds: University of Leeds)
- [27] Whitwell J R and Spiers F W 1976 Calculated beta-ray dose factors for trabecular bone *Phys. Med. Biol.* **21** 16–38
- [28] Spiers F W 1949 The influence of energy absorption and electron range on dosage in irradiated bone *Br. J. Radiol.* **22** 521–33
- [29] Spiers F W 1966 A review of the theoretical and experimental methods of determining radiation dose in bone *Br. J. Radiol.* **39** 216–21
- [30] Bouchet L G, Jokisch D W and Bolch W E 1999 A three-dimensional transport model for determining absorbed fractions of energy for electrons within trabecular bone *J. Nucl. Med.* **40** 1947–66
- [31] Howell R W, Wessels B W, Loevinger R, Watson E E, Bolch W E, Brill A B, Charles N D, Fisher D R, Hays M T, Robertson J S, Siegel J A and Thomas S R 1999 The MIRD perspective 1999 *J. Nucl. Med.* **40** 3S–10S
- [32] ICRP 1979 *Limits for intakes of radionuclides by workers* Publication 30, Part 1. International Commission on Radiological Protection (Oxford: Pergamon)
- [33] Chen H T and Poston J W 1982 Estimates of absorbed energy in trabecular bone due to beta-particles or electrons *Health Phys.* **43** 647–53
- [34] Zuzarte de Mendonca A 1993 *Trabecular Bone Dosimetry Using a Monte Carlo Code* (College Station, TX: Texas A&M University)

- [35] Nelson W R, Hirayama R H and Rogers D W O 1985 *The EGS4 code system* SLAC Report 265 (Stanford, CA: Stanford Linear Accelerator Center)
- [36] Parry R A 1995 *Revised Estimates of Electron Absorbed Fractions and Radionuclide S-Values in Trabecular Bone* (College Station, TX: Texas A&M University)
- [37] Bielajew A F and Rogers D W O 1987 PRESTA, the 'parameter reduced electron step transport algorithm' for electron Monte Carlo transport *Nucl. Instrum. Meth. B* **18** 165–81
- [38] Bouchet L G, Bolch W E, Howell R W and Rao D V 2000 *S values for radionuclides localized within the skeleton* *J. Nucl. Med.* **41** 189–212
- [39] Patton P 2000 *NMR Microscopy for Skeletal Dosimetry: an Investigation of Marrow Cellularity on Dose Estimates* (Gainesville, FL: University of Florida)
- [40] Stabin M, Eckerman K F, Bolch W E, Bouchet L G and Patton P W 2002 Evolution and status of bone and marrow dose models *Cancer Biother. Radiopharmaceut.* In press
- [41] Samaratunga R C, Thomas S R, Hinnefeld J D, Von Kuster L C, Hyams D M, Moulton J S, Sperling M I and Maxon H R 1995 A Monte Carlo simulation model for radiation dose to metastatic skeletal tumor from rhenium-186(Sn)-HEDP *J. Nucl. Med.* **36** 336–50
- [42] Jokisch D W, Patton P W, Inglis B A, Bouchet L G, Rajon D A, Rifkin J and Bolch W E 1998 NMR microscopy of trabecular bone and its role in skeletal dosimetry *Health Phys.* **75** 584–96
- [43] Jokisch D W, Bouchet L G, Patton P W, Rajon D A and Bolch W E 2001 Beta-particle dosimetry of the trabecular skeleton using Monte Carlo transport within 3D digital images *Med. Phys.* **28** 1505–18
- [44] Bolch W E, Patton P W, Rajon D A, Shah A P, Jokisch D W and Inglis B A 2002 Considerations of marrow cellularity in 3-dimensional dosimetric models of the trabecular skeleton *J. Nucl. Med.* **43** 97–108
- [45] Patton P W, Rajon D A, Shah A P, Jokisch D W, Inglis B A and Bolch W E 2002 Site-specific variability in trabecular bone dosimetry: considerations of energy loss to cortical bone *Med. Phys.* **29** 6–14
- [46] Patton P W, Jokisch D W, Rajon D A, Shah A P, Myers S L, Inglis B A and Bolch W E 2002 Skeletal dosimetry via NMR microscopy: investigations of sample reproducibility and signal source *Health Phys.* **82** 316–26
- [47] Rajon D A, Jokisch D W, Patton P W, Shah A P and Bolch W E 2000 Voxel size effects in three-dimensional nuclear magnetic resonance microscopy performed for trabecular bone dosimetry *Med. Phys.* **27** 2624–35
- [48] Bouchet L G and Bolch W E 1999 A three-dimensional transport model for determining absorbed fractions of energy for electrons within cortical bone *J. Nucl. Med.* **40** 2115–24
- [49] Akabani G 1993 Absorbed dose calculations in Haversian canals for several beta-emitting radionuclides *J. Nucl. Med.* **34** 1361–6
- [50] Breems D A, Blokland E A, Neben S and Ploemacher R E 1994 Frequency analysis of human primitive haematopoietic stem cell subsets using a cobblestone area forming cell assay *Leukemia* **8** 1095–104
- [51] Neben S, Anklesaria P, Greenberger J and Mauch P 1993 Quantitation of murine hematopoietic stem cells *in vitro* by limiting dilution analysis of cobblestone area formation on a clonal stromal cell line *Exp. Hematol.* **21** 438–43
- [52] Bolch W E, Bouchet L G, Robertson J S, Wessels B W, Siegel J A, Howell R W, Erdi A K, Aydogan B, Costes S, Watson E E, Brill A B, Charkes N D, Fisher D R,

- Hays M T and Thomas S R 1999 MIRD pamphlet No 17: the dosimetry of nonuniform activity distributions—radionuclide S values at the voxel level. Medical Internal Radiation Dose Committee *J. Nucl. Med.* **40** 11S–36S
- [53] DeNardo D A, DeNardo G L, O'Donnell R T, Lim S M, Shen S, Yuan A and DeNardo S J 1997 Imaging for improved prediction of myelotoxicity after radioimmunotherapy *Cancer* **80** 2558–66
- [54] Lim S M, DeNardo G L, DeNardo D A, Shen S, Yuan A, O'Donnell R T and DeNardo S J 1997 Prediction of myelotoxicity using radiation doses to marrow from body, blood and marrow sources *J. Nucl. Med.* **38** 1374–8
- [55] Eary J F, Krohn K A, Press O W, Durack L and Bernstein I D 1997 Importance of pre-treatment radiation absorbed dose estimation for radioimmunotherapy of non-Hodgkin's lymphoma *Nucl. Med. Biol.* **24** 635–8
- [56] Breitz H B, Fisher D R and Wessels B W 1998 Marrow toxicity and radiation absorbed dose estimates from rhenium-186-labeled monoclonal antibody *J. Nucl. Med.* **39** 1746–51
- [57] Behr T M, Sharkey R M, Juweid M E, Dunn R M, Vgg R C, Siegel J A and Goldenberg D M 1996 Hematological toxicity in the radioimmunotherapy of solid cancers with ^{131}I -labeled anti-CEA NP-4 IgG1: dependence on red marrow dosimetry and pretreatment. In *Proceedings of the Sixth International Radiopharmaceutical Dosimetry Symposium* Gatlinburg, TN, pp 113–25
- [58] Juweid M E, Zhang C H, Blumenthal R D, Hajjar G, Sharkey R M and Goldenberg D M 1999 Prediction of hematologic toxicity after radioimmunotherapy with (^{131}I) -labeled anticarcinoembryonic antigen monoclonal antibodies *J. Nucl. Med.* **40** 1609–16
- [59] Emami B, Lyman J, Brown A, Coia L, Goitein M, Munzenrider J E, Shank B, Solin L J and Wesson M 1991 Tolerance of normal tissue to therapeutic irradiation *Int. J. Radiat. Oncol. Biol. Phys.* **21** 109–22
- [60] Erdi A K, Erdi Y E, Yorke E D and Wessels B W 1996 Treatment planning for radioimmunotherapy *Phys. Med. Biol.* **41** 2009–26
- [61] DeNardo G L, DeNardo S J, Macey D J, Shen S and Kroger L A 1994 Overview of radiation myelotoxicity secondary to radioimmunotherapy using ^{131}I -Lym-1 as a model *Cancer* **73** 1038–48
- [62] Sgouros G, Barest G, Thekkumthala J, Chui C, Mohan R, Bigler R E and Zanzonico P B 1990 Treatment planning for internal radionuclide therapy: three-dimensional dosimetry for nonuniformly distributed radionuclides *J. Nucl. Med.* **31** 1884–91
- [63] Akabani G, Hawkins W G, Eckblade M B and Lechner P K 1997 Patient-specific dosimetry using quantitative SPECT imaging and three-dimensional discrete Fourier transform convolution *J. Nucl. Med.* **38** 308–14
- [64] Furhang E E, Chui C S and Sgouros G 1996 A Monte Carlo approach to patient-specific dosimetry *Med. Phys.* **23** 1523–9
- [65] DeNardo G L, Lamborn K R, DeNardo S J, Goldstein D S, Dolber-Smith E G, Kroger L A, Larkin E C and Shen S 1995 Prognostic factors for radioimmunotherapy in patients with B-lymphocytic malignancies *Cancer Res.* **55** 5893s–98s
- [66] Sgouros G, Jureidini I M, Scott A M, Graham M C, Larson S M and Scheinberg D A 1996 Bone marrow dosimetry: regional variability of marrow-localizing antibody *J. Nucl. Med.* **37** 695–8
- [67] Wessels B, Breitz H B, Meredith R, Juweid M E, Pastor M, Colburn M and DeNardo G L 2000 Bone marrow dosimetry model adjustments based on age, gender and prior therapy *J. Nucl. Med.* **41** 83P

- [68] Sgouros G, Deland D, Loh A C, Divgi C R and Larson S M 1997 Marrow and whole-body absorbed dose vs marrow toxicity following ^{131}I -G250 antibody therapy in patients with renal-cell carcinoma *J. Nucl. Med.* **38** 252P
- [69] O'Donoghue J A, Baidoo N and Sgouros G 1998 Calculated red marrow absorbed dose predicts hematological toxicity in radioimmunotherapy *J. Nucl. Med.* **39** 186P
- [70] Blumenthal R D, Lew W, Juweid M, Alisauskas R, Ying Z and Goldenberg D M 2000 Plasma FLT3-L levels predict bone marrow recovery from myelosuppressive therapy *Cancer* **88** 333–43
- [71] Shields A F, Grierson J R, Dohmen B M, Machulla H J, Stayanoff J C, Lawhorn-Crews J M, Obradovich J E, Muzik O and Mangner T J 1998 Imaging proliferation *in vivo* with [F-18]FLT and positron emission tomography *Nat. Med.* **4** 1334–6
- [72] Mauch P, Constine L, Greenberger J, Knospe W, Sullivan J, Liesveld J L and Deeg H J 1995 Hematopoietic stem cell compartment: acute and late effects of radiation therapy and chemotherapy *Int. J. Radiat. Oncol. Biol. Phys.* **31** 1319–39
- [73] Koo K H, Dussault R, Kaplan P, Kim R, Ahn I O, Christopher J, Song H R and Wang G J 1998 Age-related marrow conversion in the proximal metaphysis of the femur: evaluation with T1-weighted MR imaging *Radiology* **206** 745–8
- [74] Ballon D, Dyke J, Schwartz L H, Lis E, Schneider E, Lauto A and Jakubowski A 2000 Bone marrow segmentation in leukemia using diffusion and T2 weighted echo planar magnetic resonance imaging *NMR Biomed.* **13** 321–28
- [75] Ballon D, Jakubowski A A, Tulipano P K, Graham M C, Schneider E, Aghazadeh B, Chen Q S and Koutcher J A 1998 Quantitative assessment of bone marrow hematopoiesis using parametric magnetic resonance imaging *Magn. Reson. Med.* **39** 789–800
- [76] Ballon D, Jakubowski A A, Graham M C, Schneider E and Koutcher J A 1996 Spatial mapping of the percentage cellularity in human bone marrow using magnetic resonance imaging *Med. Phys.* **23** 243–50
- [77] Ballon D, Jakubowski A, Gabrilove J, Graham M C, Zakowski M, Sheridan C and Koutcher J A 1991 *In vivo* measurements of bone marrow cellularity using volume-localized proton NMR spectroscopy *Magn. Reson. Med.* **19** 85–95
- [78] Link T M, Majumdar S, Grampp S, Guglielmi G, van Kuijk C, Imhof H, Glueer C and Adams J E 1999 Imaging of trabecular bone structure in osteoporosis *Eur. Radiol.* **9** 1781–8
- [79] Saito Y and Ortawara B S 2001 Development and evaluation of a real-time 3-dimensional CT (4D-CT) scanner. In *87th Annual Meeting of the Radiological Society of North America* Chicago, IL
- [80] Nonomura Y, Yasumoto M, Yoshimura R, Haraguchi K, Ito S, Akashi T and Ohashi I 2001 Relationship between bone marrow cellularity and apparent diffusion coefficient *J. Magn. Reson. Imaging* **13** 757–60
- [81] Schick F, Einsele H, Kost R, Duda S, Jung W I, Lutz O and Claussen C D 1994 Hematopoietic reconstitution after bone marrow transplantation: assessment with MR imaging and H-1 localized spectroscopy *J. Magn. Reson. Imaging* **4** 71–8
- [82] Schick F, Einsele H, Weiss B, Forster J, Lutz O, Kanz L and Claussen C D 1996 Assessment of the composition of bone marrow prior to and following autologous BMT and PBSCT by magnetic resonance *Ann. Hematol.* **72** 361–70

Chapter 14

Monte Carlo modelling of dose distributions in intravascular radiation therapy

Michael Stabin and Dennis M Duggan

14.1. INTRODUCTION

The treatment of coronary artery disease, specifically to prevent restenosis after percutaneous transluminal coronary angioplasty (PTCA) with high doses of ionizing radiation, is a relatively new field of investigation. Monte Carlo approaches are particularly well suited to the calculation of dose distributions in this area. In this section, we will briefly review the technical basis for this area of dose calculation and summarize current efforts to calculate dose, including Monte Carlo applications.

Coronary arteries have diameters generally between 3 and 5 mm at their origin, and then taper to smaller sizes [1]. Atherosclerotic plaque is formed as fatty debris from blood accumulates in an artery, followed by the proliferation of smooth muscle cells from the vessel's internal elastic membrane and media. Accumulation of collagen, elastin, and lipids ensues, with the formation of the plaque, which consists of lipids, necrotic cells and collagen. Over time, the core of the plaque necroses, calcifies and haemorrhages. This causes a reduction in the blood flow (stenosis) within the artery, with the threat of myocardial ischaemia or infarction. PTCA can be performed with a number of techniques, to re-establish a stable lumen with an acceptable inner diameter for appropriate blood flow to the coronary muscle. Techniques include the use of balloons (to mechanically expand the lumen), cutting and ablating devices (to remove the plaque) and stent implantation (to stabilize the artery and provide structure).

Unfortunately, in about 35–40% of patients undergoing PTCA, the coronary arteries restenose within a few months or years, and the benefits of the original therapy are lost. The reasons for this are complex, but the process seems to involve the following steps: fracture of the plaque from balloon expansion occurs, followed by lining of the injury by platelets, and

formation of a fibrous mesh of platelets and red blood cells. Monocytes then phagocytize the mesh, and smooth muscle cells migrate into the intimal subendothelial space, leading to neointimal formation. Over weeks, the neointima becomes less cellular and the healing site resembles a plaque. In about 40% of patients, the neointimal hyperplasia is excessive and results in more narrowing of the lumen than was resolved by angioplasty [1].

Various preclinical and clinical studies have shown that the delivery of between perhaps 15 and 50 Gy of ionizing radiation to the coronary artery wall after balloon angioplasty can markedly reduce the rate of restenosis, with few or no complications [1]. Due to the geometry, internal sources are thought to be more efficacious than external beams of radiation, thus a science of 'intravascular brachytherapy' (IVB) or 'intravascular radionuclide therapy' is under development. This form of therapy principally takes two approaches:

1. *The use of temporary implants*—seeds, wires and balloons with radioactive walls or filled with radioactive solutions to deliver between 15 and 20 Gy to a 2–3 cm length of vessels between 2 and 5 cm in diameter. The desired dose rate is about 5 Gy/min, to deliver the dose in a short time and reduce complications from reduced blood flow. The technique of afterloading with high dose rate sources is common.
2. *The use of permanent implants*—i.e., radioactive stents, that deliver a similar dose, but with a lower dose rate.

The effectiveness of using high dose-rate intravascular radioisotope sources for the inhibition of arterial restenosis has been demonstrated in a variety of animal models and clinical trials [2]. This technology has been applied primarily to the coronary arteries for the inhibition of intimal hyperplasia following balloon angioplasty and/or stent placement. This neointimal hyperplasia is considered to be pathologic, as the narrowing or restenosis of a coronary artery can be life threatening [3, 4]. The current concept of the mechanism of action is based on the inhibition of myofibroblast stimulation in the adventitia by radiation [3]. Vessel wall irradiation with β particles has been demonstrated to prevent the onset of restenosis after stent implantation or angioplasty in a porcine model [5–8].

Calculation of the radiation dose delivered to the coronary artery wall, as well as to other organs and tissues in the body, is important to fully evaluate the possible risks and benefits of this procedure. Computational methods for these calculations are well developed and simply need to be implemented appropriately. Both analytical and Monte Carlo methods are available and have been used to calculate dose distributions around these sources. Monte Carlo methods have the advantage of explicit treatment of the radiation transport of electrons and photons at interfaces of materials of different density and composition (e.g., at the interface of an atherosclerotic plaque and soft tissue). The different approaches to the delivery of this radiation

dose include the use of radioactive wires, balloons with radioactive walls or filled with radioactive solutions, and stents. There are also numerous candidate radionuclides, including β and γ emitters, of low and high energy, which are currently under investigation.

14.2. CANDIDATE RADIONUCLIDES AND TECHNOLOGIES

Treated lesions are generally 1–5 cm in length [1]. In conventional brachytherapy, in interstitial applications, photons of 20–30 keV are known to be efficacious in some sites such as the prostate, while in other sites and in intracavitary applications, photons of >50 keV are needed. Electron sources of high energy (e.g., $^{90}\text{Sr}/^{90}\text{Y}$) are sometimes used to treat superficial tumours (e.g., of the eye). For intravascular applications, it is thought that photon energies need to exceed 20 keV and electron energies need to be at least 1 MeV [1]. Much experience has been gained with the use of ^{192}Ir in conventional brachytherapy, and its use is prevalent in studies for IVB. ^{192}Ir has a mixture of photons between 300 and 500 keV and two β s of maximum energy 500–650 keV. Much of the photon energy will be deposited away from the source, in the heart and other tissues of the patient, as well as outside the patient (thus delivering a dose to the attending physician and other staff). β sources, such as ^{32}P and ^{90}Y (maximum β energies around 1.7 and 2.2 MeV, respectively) offer the advantage of delivering all of their energy locally, to the vascular wall and immediately surrounding tissue. Other β sources, notably ^{188}Re (two important β s with maximum energies between 1.9 and 2.2 MeV, with a photon of 155 keV at 15%) have been suggested as well.

For temporary implants, calculations have shown that, for γ emitters, between 10 and 30 GBq of activity (250–500 mCi) will be needed to attain a dose rate of 4–5 Gy/min and thus maintain an acceptable dwell time. Beta emitters can probably achieve the same goal with activities more like 0.5–1.5 GBq (14–38 mCi). With the higher activities of the γ emitters, there are more radiation safety problems created for source handling, shielding and storage, management of staff procedures, etc., while with the β sources the principal radiation safety concerns involve doses to the extremities during source manipulation. If one is using a wire or seed type source, it has been shown that problems of source centring are more important for the β emitters than for γ emitters [8] (see analysis below). The issue of source centring is an important one; if the source is not well centred, one side of the artery will receive a substantially higher dose than the other, resulting in underdosing to one side (and perhaps suboptimal therapy) and overdosing to the other (raising the risk of radiation-related complications, e.g., direct tissue damage, induction of aneurisms). Centring of these sources can be aided with specifically designed devices. Alternatively,

the use of liquid-filled balloons has been proposed, as this inherently solves the problem of source uniformity. In this application, however, there is the risk of balloon rupture and release of the radioactive liquid into the bloodstream. This would presumably act like an intravenous injection of the material, with its subsequent distribution, retention and radiation dosimetry being determined by the radionuclide and chemical compound (if any) to which it is attached. The use of a balloon with radioactive walls can give the same uniformity with a much lower risk of releasing the radioactive materials.

The use of radioactive stents has been proposed, to provide structure and stability to the affected artery as well as delivering the radiation dose to the vessel wall. In these applications, to date, only β emitters (principally ^{32}P) have been proposed. The activity may be coated on the surface of the stent (which raises the possibility of activity leaching over time into the bloodstream) or impregnated into the metal of the stent (by a manufacturing process or neutron activation of extant metal components). These stents have the advantages that low activities (kBq to MBq range) can be employed (as the dose is delivered over many hours or days as the radionuclide decays in situ), and that the stent conforms in shape to the lesion site. Non-radioactive stents, however, do not inhibit the process of restenosis; in fact, there is evidence that they may even stimulate it [1].

These are not the only candidate technologies and nuclides available or suggested. Many strategies and nuclides have been proposed, including low energy X- or γ -ray emitters, the use of inserted X-ray generation devices, and others. As many ideas are being generated and tested, one cannot generalize about the future. Many factors, scientific, economic and logistic, will influence the final suitability of different technologies and will determine those that find the greatest acceptance.

14.3. RADIATION DOSIMETRY STUDIES

14.3.1. *Vessel wall dose—calculations*

For both electron and photon sources, calculation of radiation dose distributions may be performed by either analytical (point-kernel) techniques or Monte Carlo transport simulations. Point-kernel techniques employ lookup tables of dose-response values, usually based originally on some Monte Carlo studies carried out for point or other simple sources in a uniform infinite medium, and extend the results to more complex geometries through numerical methods. In Monte Carlo studies, the problem geometry is described, and the history of many elementary particles is simulated using random sampling of known probability distributions (for emissions from an isotropic source, cross sections for interactions, production of secondary

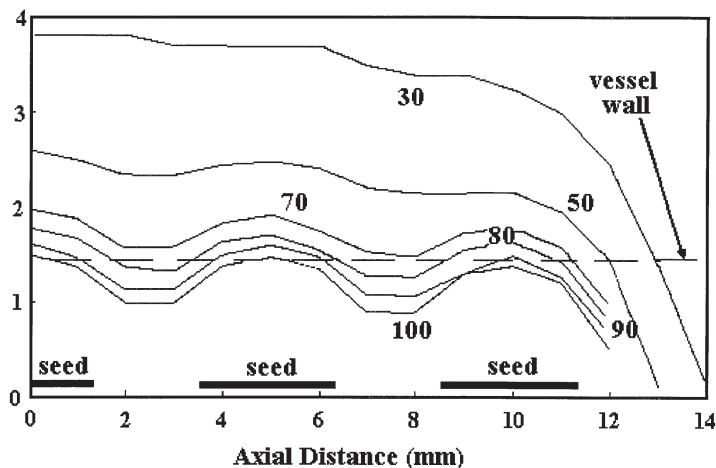
Radial Distance (mm)

Figure 14.1. Isodose distributions, based on point-kernel calculations, for a linear array of ^{192}Ir seeds (adapted from a study by Wiedermann *et al* [8], as given in AAPM Report No 66 [1]. Reprinted with permission from AAPM.

particles, etc.). Point kernel methods generally apply to only a single medium (generally water), but can be adapted to approximate particle behaviour in other media [9,10]. Monte Carlo methods have the advantage of explicitly treating particle behaviour in various media. For example, in this application, a fluid in a filled balloon, the wall of the balloon, and the vessel wall will all have similar compositions (water or soft tissue equivalent), but a central guide wire or source wire will be different (metallic) and the plaque will also be different (calcified tissue, with a composition and density significantly different from that of soft tissue). Monte Carlo methods can have the disadvantage of only being able to treat certain predefined geometries in combinations (e.g., cylinders, spheres).

Most early attempts to characterize the dosimetry of various intra-vascular sources employed point-kernel approaches, while later ones employ more Monte Carlo applications. Figure 14.1 shows isodose distributions, based on point-kernel calculations, for a linear array of ^{192}Ir seeds (adapted from a study by Wiedermann *et al.* [8], as given in AAPM Report No 66 [1]). Prestwich *et al.* [11] used analytical kernels, which were based ultimately on measurements, to calculate dose from a ^{32}P coated stent. They showed one-dimensional radial dose distributions; two-dimensional isodose contours and three-dimensional dose distributions for a 3 mm \times 20 mm cylindrical source. Li *et al.* [12] used MCNP to calculate doses from a single strut of a stent with radioisotope (^{48}V , ^{32}P) distributed throughout, then used superposition to calculate dose distributions for an

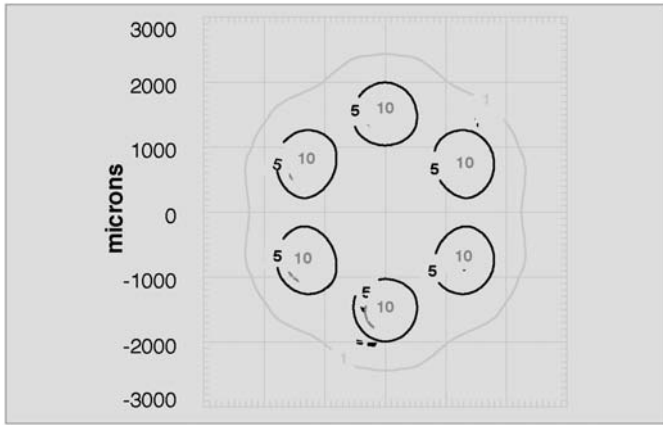


Figure 14.2. Dose rate distribution in a plane transverse to the axis of a ^{48}V impregnated stent obtained by Li *et al.* Reprinted from [15] with permission from AAPM.

entire stent containing ^{48}V and ^{32}P (figure 14.2). Janicki *et al.* [13] used a more realistic geometry but still used an analytic kernel, and calculated three-dimensional dose distributions in tissue around a $3.5\text{ mm} \times 20\text{ mm}$ wire mesh stent. Later, Janicki *et al.* [9] extended this model to cases in which the stent was surrounded by layers of materials with different compositions and densities (figure 14.3). Duggan *et al.* [14] performed a calculation similar to that of Prestwich *et al.* but with a Monte-Carlo generated kernel from Simpkin *et al.* [15]. McLemore [16] also used MCNP to calculate dose from a single strut with a ^{103}Pd coating on the outside and then used superposition to calculate the dose from the entire stent.

Many complete sources, with realistic geometries and materials, have now been simulated. These include entire radioactive stents [17]. Seed or wire sources are usually encapsulated, often in high atomic number materials. This can have a dramatic effect on the dose distribution, especially for β or low-energy photon sources. Monte Carlo simulation is the most accurate technique for predicting the dose distribution for such sources. Examples of simulations of encapsulated sources that are now in clinical use include that of the Novoste BetaCath ^{90}Sr seed by Soares *et al.* [18] and the Guidant encapsulated ^{32}P wire source by Mourtada *et al.* [19] (figure 14.4). In addition, many other proposed sources have been simulated, including a coil-shaped wire β source [20] and a soft X-ray device [21].

As mentioned above, an important issue in the use of radioactive wires or seeds is the centring of the source within the vessel. A study done by Amols *et al.* [22] showed that centring is substantially more important for β sources than for photon sources (although it is clearly important for both). Figure 14.5 shows that a centring error of 0.5 mm in a 5 mm diameter

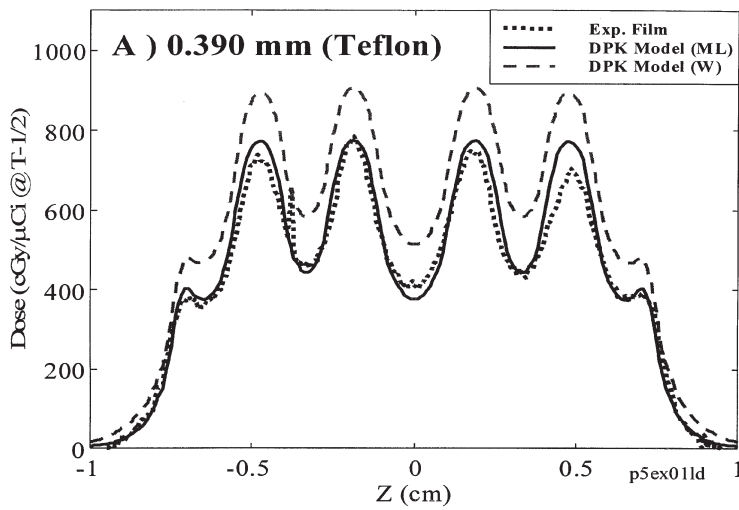


Figure 14.3. Comparison of calculations with all water DPK model (W) and multilayer DPK model (ML) with radiochromic film measurements (blue) for a ^{32}P stent in a block of solid water with a layer of Teflon in between the stent and the radiochromic film. Reprinted with permission from AAPM (Janicki et al [9]).

vessel will result in an error of 1.6 for ^{192}Ir (i.e., the actual dose received on the overdosed side will be 1.6 times that calculated for a centred source) and 2.1 for ^{90}Y (figure 14.5).

Extensive calculations, using both the MCNP 4B [23] and EGS4 [24] Monte Carlo codes, were made for a number of fixed artery sizes and for

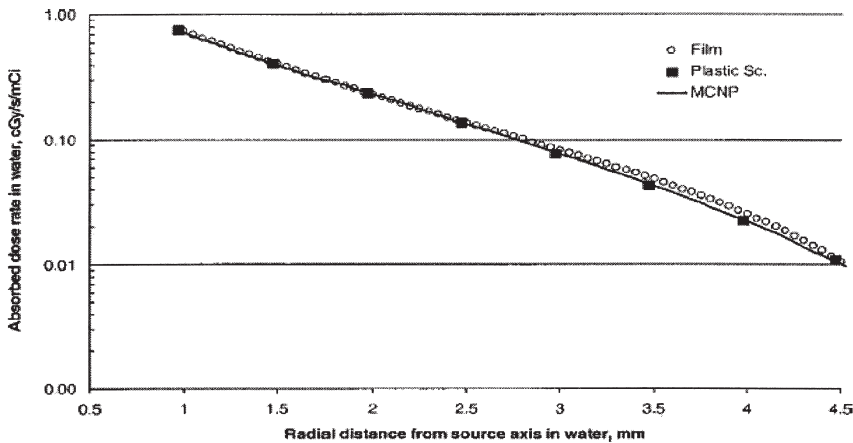


Figure 14.4. Comparison of Monte Carlo and measured values for the Guidant encapsulated ^{32}P wire source [19]. Reprinted with permission from AAPM.

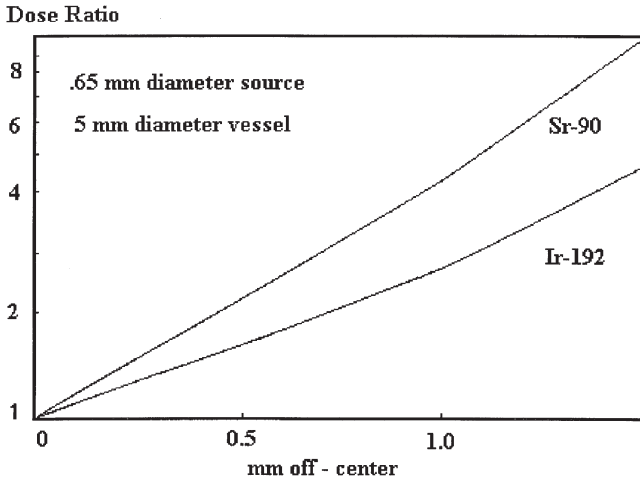


Figure 14.5. Dose asymmetry (ratio of maximum to minimum dose in vessel wall) resulting from inaccurate centring of 5 mm long ^{192}Ir and ^{90}Sr sources within 5 mm diameter artery obtained by Amols *et al.* Adapted from [22] and reprinted with permission from ASTRO.

wire and liquid-filled balloon sources by Stabin *et al.* [25]. They performed calculations for monoenergetic photons and electrons over a broad range of energies, then applied decay spectra for over 800 radionuclides to the monoenergetic results, and incorporated the data into an interactive PC computer program that provided rapid comparisons of candidate radionuclides and geometries. Their blood vessel models were simple cylinders 3 cm in length, half of whose inner circumference had an atherosclerotic plaque and half which did not. Results were given for radial dose as a function from the vessel wall (diameters of 1.5, 3 and 4.5 mm), and comparisons for some candidate nuclides were given (figure 14.6).

14.3.2. Vessel wall dose—measurements

Measurements are made using thin strips of film (GAF Chromic) or thin TLD chips, to evaluate the doses over the short distances (from perhaps 0.02 to 10 mm) of interest in this application. Janicki *et al.* [9] made measurements and performed point-kernel calculations for a Palmaz–Schatz stent containing ^{32}P (figures 14.7–14.10).

14.3.3. Dose to body organs in the case of a balloon rupture

In the case of a balloon rupture, the radioactive material in the balloon will enter the bloodstream, and may distribute to other organs, delivering an

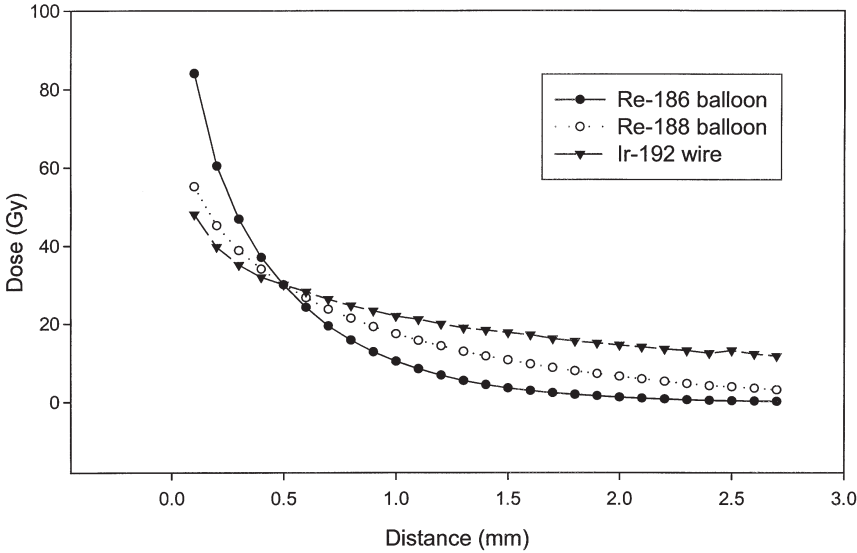


Figure 14.6. Dose comparison for ^{186}Re and ^{188}Re balloons and an ^{192}Ir wire in a 3 mm diameter vessel. In all cases, the activities were calculated so that the vessel would receive a dose of 30 Gy in 5 min at 0.5 mm from the vessel surface (comparisons performed on the non-plaque side of the vessel). The calculated activities were 2.48 GBq of ^{186}Re , 1.02 GBq of ^{188}Re and 64.1 GBq of ^{192}Ir .

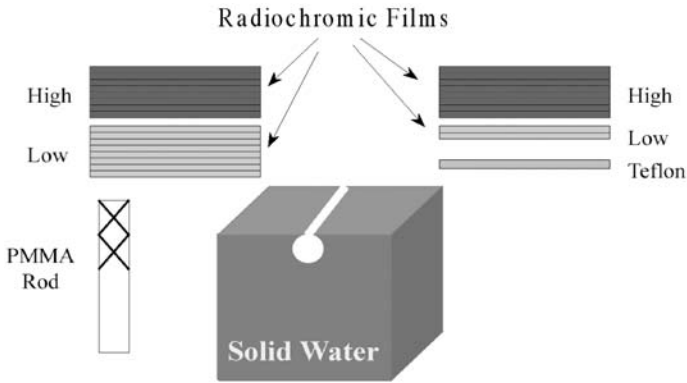


Figure 14.7. Diagram of solid water phantom used to expose radiochromic film to the β -emitting stent. Four stents were exposed. For two stents, a layer of Teflon was placed on the stent before the radiochromic film was stacked on top. Low and high refer to low- and high-sensitivity radiochromic film, respectively. The measured thicknesses of the different layers were Teflon, 386 μm ; low-sensitivity radiochromic film, 108 μm ; and high-sensitivity radiochromic film, 257 μm . Reprinted with permission from Janicki et al [9].

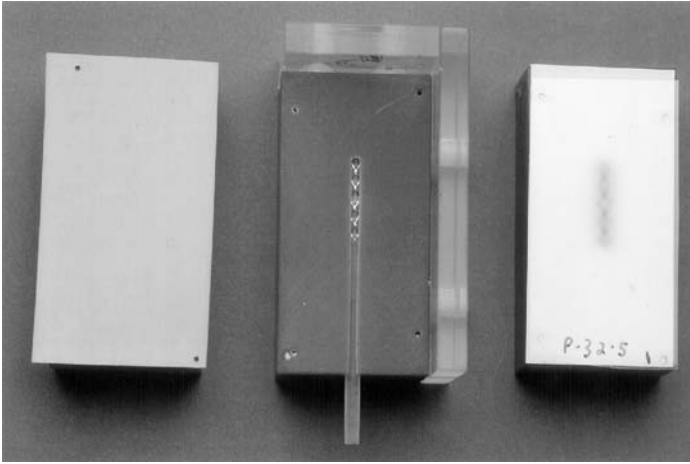


Figure 14.8. Photograph of a stent mounted on a polymethyl-methacrylate (PPMA) rod and inserted into a solid water block like the one shown in figure 14.7. On the right is the radiochromic film exposed while placed directly, emulsion side toward the stent, on top of the block. Reprinted with permission from Janicki et al. [9].

unwanted radiation dose to these organs. A comparison was made of the possible radiation dose distributions for four candidate radionuclides, ^{32}P , ^{90}Y , ^{186}Re and ^{188}Re (table 14.1). The pharmaceutical or carrier to which the nuclide is attached will determine its behaviour *in vivo*; here the forms assumed were ^{32}P phosphate, ^{90}Y in ionic form and the rhenium isotopes as perrhenate. The kinetic model chosen for ^{32}P and ^{90}Y came from ICRP

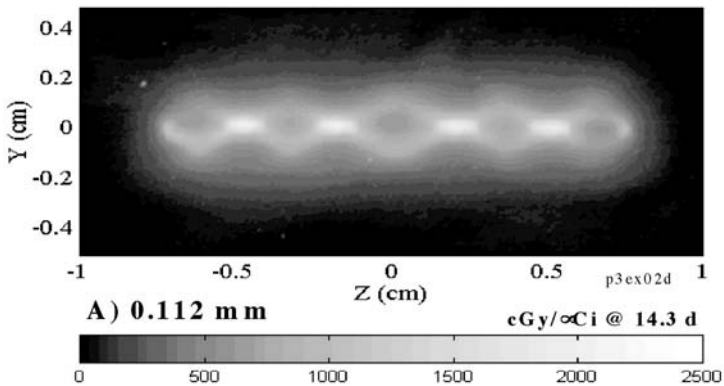


Figure 14.9. Radiochromic film results. Reprinted with permission from Janicki et al. [9].

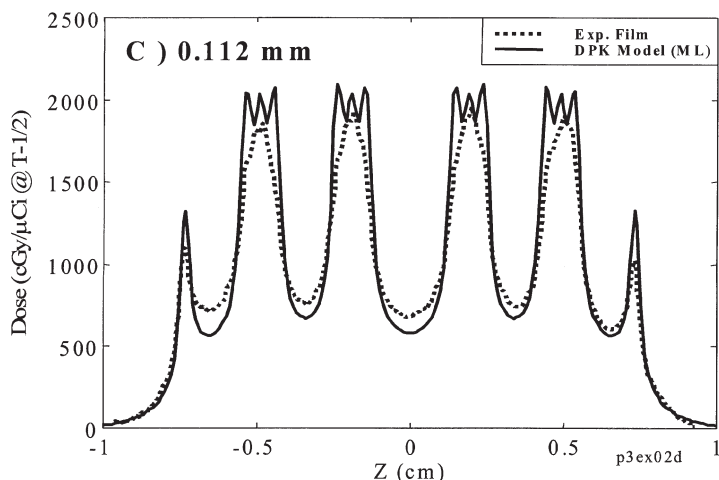


Figure 14.10. Comparison of the radiochromic film results and the DPK multi-layer (ML) model. Reprinted with permission from Janicki *et al.* [9].

Publication 30 [26]; the model for perhenate was the MIRD Dose Estimate Report No 8 model (Lathrop *et al.* [27]) for sodium pertechnetate in nonresting subjects, which was simply adapted for use with the rhenium isotopes, as suggested by the data of Kotzerke *et al.* [28]. Organ doses for the four radiopharmaceuticals assuming release of unit quantities into the bloodstream are shown in table 14.1. For ^{32}P and ^{90}Y , the organ receiving the highest dose is red marrow with a dose of 8.12 and 3.26 Gy per GBq respectively. With ^{186}Re and ^{188}Re , the organs receiving the highest dose are the large intestine, thyroid and urinary bladder.

Calculations show that one would require 1.04 GBq of ^{32}P or 0.92 GBq of ^{90}Y in a balloon source to give 30 Gy in 5 min at 0.5 mm in a 3 mm diameter artery. It is clear from these data and the dose estimates in the above table that use of ^{32}P or ^{90}Y in the forms assumed here (liquid sources of ^{32}P as phosphate or ionic ^{90}Y) will represent a significant risk to the patient, as the predicted absorbed doses to red marrow from the quantities of activity assumed are near or above median lethal doses. For the rhenium isotopes, there are significant doses predicted to the intestines, but not at levels that would be considered life threatening. Other strategies may improve the radiation dose picture, such as the use of perchlorate to block thyroid uptake, or attaching the rhenium isotopes to other chemical compounds, such as MAG3, and to obtain different biological behaviour. In these cases, obviously different biokinetic behaviour will result in different dose estimates, which need to be calculated in each case to evaluate the possible radiation doses.

Table 14.1. Organ doses from injection of radionuclides into the bloodstream due to balloon rupture (Gy per GBq injected).*

	^{32}P	^{90}Y	^{186}Re	^{188}Re
Adrenals	7.60×10^{-1}	9.07×10^{-2}	3.17×10^{-2}	4.45×10^{-2}
Brain	7.60×10^{-1}	9.07×10^{-2}	3.10×10^{-2}	4.35×10^{-2}
Breasts	7.60×10^{-1}	9.07×10^{-2}	3.09×10^{-2}	4.34×10^{-2}
Gallbladder wall	7.60×10^{-1}	9.07×10^{-2}	3.38×10^{-2}	4.66×10^{-2}
LLI wall	7.60×10^{-1}	9.07×10^{-2}	1.95×10^0	1.97×10^0
Small intestine	7.60×10^{-1}	9.07×10^{-2}	3.66×10^{-2}	4.97×10^{-2}
Stomach	7.60×10^{-1}	9.07×10^{-2}	2.64×10^{-1}	4.33×10^{-1}
ULI wall	7.60×10^{-1}	9.07×10^{-2}	1.95×10^0	1.98×10^0
Heart wall	7.60×10^{-1}	9.07×10^{-2}	3.14×10^{-2}	4.42×10^{-2}
Kidneys	7.60×10^{-1}	9.07×10^{-2}	3.20×10^{-2}	4.48×10^{-2}
Liver	7.60×10^{-1}	3.89×10^0	3.18×10^{-2}	4.46×10^{-2}
Lungs	7.60×10^{-1}	9.07×10^{-2}	3.13×10^{-2}	4.38×10^{-2}
Muscle	7.60×10^{-1}	9.07×10^{-2}	3.18×10^{-2}	4.45×10^{-2}
Ovaries	7.60×10^{-1}	9.07×10^{-2}	3.67×10^{-2}	4.99×10^{-2}
Pancreas	7.60×10^{-1}	9.07×10^{-2}	3.24×10^{-2}	4.55×10^{-2}
Red marrow	8.12×10^0	3.26×10^0	3.19×10^{-2}	4.48×10^{-2}
Bone surfaces	1.04×10^1	3.91×10^0	3.32×10^{-2}	4.52×10^{-2}
Skin	7.60×10^{-1}	9.07×10^{-2}	3.10×10^{-2}	4.35×10^{-2}
Spleen	7.60×10^{-1}	9.07×10^{-2}	3.19×10^{-2}	4.48×10^{-2}
Testes	7.60×10^{-1}	9.07×10^{-2}	3.18×10^{-2}	4.47×10^{-2}
Thymus	7.60×10^{-1}	9.07×10^{-2}	3.12×10^{-2}	4.38×10^{-2}
Thyroid	7.60×10^{-1}	9.07×10^{-2}	6.06×10^{-1}	1.10×10^0
Urinary bladder wall	1.91×10^0	8.02×10^{-1}	1.04×10^0	1.51×10^0
Uterus	7.60×10^{-1}	9.07×10^{-2}	3.52×10^{-2}	4.87×10^{-2}
Total body	1.52×10^0	5.21×10^{-1}	4.37×10^{-2}	5.74×10^{-2}

* Chemical forms assumed: ^{32}P as sodium phosphate, ^{90}Y in ionic form, ^{186}Re and ^{188}Re as perrhenate.

14.4. RADIATION EFFECTS—ARTERY WALLS

As this is a new technology and some of the effects we might expect are expressed over longer times, there will be a delay before we know what complications to expect. However, there is some clinical experience with arterial damage and complications from external beam radiation. Acute and chronic morphological changes have been seen in femoral arteries in dogs given 40 Gy in 10 days [29]. In one radiation therapy centre, 20 patients had blood vessel-associated injuries associated with radiation therapy over a 20 year period, including arterial rupture and occlusion, over a 7–24 year period after therapy [30]. To effectively employ this promising technology, we must make use of the best information that we can obtain from

radiation dose calculations and measurements, and proceed with care in patient studies.

REFERENCES

- [1] Task Group 60 of the American Association of Physicists in Medicine 1999 AAPM Report No 66, Intravascular brachytherapy physics *Med. Phys.* **26** 119–52
- [2] Waksman R 1999 *Vascular Brachytherapy* 2nd edition (Armonk, NY: Futura)
- [3] Wilcox J, Waksman R, King S and Scott N 1996 The role of the adventitia in the arterial response to angioplasty: the effect of intravascular radiation *Int. J. Radiat. Oncol. Biol. Phys.* **36** 789–96
- [4] Shi Y, Pieniek M, Fard A, O'Brien J, Mannion J D and Zalewski A 1996 Adventitial remodeling after coronary arterial injury *Circulation* **93** 340–8
- [5] Waksman R, Robinson K, Croker I, Gravanis M B, Palmer S J, Wang C, Cipolla G D and King S B III 1995 Intracoronary radiation before stent implantation inhibits neointima formation in stented porcine coronary arteries *Circulation* **92** 1383–6
- [6] Waksman R, Robinson K, Croker I, Wang C, Gravanis M B, Cipolla G D, Hillstead R A and King S B III 1995 Intracoronary low-dose beta-irradiation inhibits neointima formation after coronary artery balloon injury in the swine restenosis model *Circulation* **92** 3025–31
- [7] Waksman R, Robinson K, Croker I, Gravanis M B, Cipolla G D and King S B III 1995 Endovascular low-dose irradiation inhibits neointima formation after coronary artery balloon injury in swine *Circulation* **91** 1533–9
- [8] Wiedermann J, Marboe C, Amols H, Schwartz A and Weinberger J 1994 Intracoronary irradiation markedly reduces restenosis after balloon angioplasty in a porcine model *J. Am. Coll. Cardiol.* **23** 1491–8
- [9] Janicki C, Duggan D M, Gonzalez A, Coffey C W II and Rahdert D A 1999 Dose model for a beta-emitting stent in a realistic artery consisting of soft tissue and plaque *Med. Phys.* **26** 2451–60
- [10] Janicki C, Duggan D M and Rahdert D A 2001 A dose-point-kernel (DPK) model for a low energy gamma-emitting stent in an heterogeneous medium *Med. Phys.* **28** 1397–405
- [11] Prestwich W V, Kennett T J and Kus F W 1995 The dose distribution produced by a ³²P-coated stent *Med. Phys.* **22** 313–20
- [12] Li A N, Eigler N L, Litvack F and Whiting J S 1998 Characterization of a positron emitting V48 nitinol stent for intracoronary brachytherapy *Med. Phys.* **25** 20–8
- [13] Janicki C, Duggan D M, Coffey C W, Fischell D R and Fishchell T A 1997 Radiation dose from a phosphorus-32 impregnated wire mesh vascular stent *Med. Phys.* **24** 437–45
- [14] Duggan D M, Coffey C W and Levit S 1998 Dose distribution for a ³²P-impregnated coronary stent: comparison of theoretical calculations and measurements with radiochromic film *Int. J. Radiat. Oncol. Biol. Phys.* **40** 713–20
- [15] Simpkin D J and Mackie T R 1990 EGS4 Monte Carlo determination of the betadose kernel in water *Med. Phys.* **17** 179–86
- [16] McLemore L 2000 Dosimetry characterization of a palladium 103 implanted stent for intravascular brachytherapy, Master's Thesis, University of Texas

- [17] Reynaert N F, Verhaegen F, Taeymans Y, Van Eijkeren M and Thierens H 1999 Monte Carlo calculations of dose distributions around ^{32}P and ^{198}Au stents for intravascular brachytherapy *Med. Phys.* **26** 1484–91
- [18] Soares C G, Halpern D G and Wang C 1998 Calibration and characterization of betaparticle sources for intravascular brachytherapy *Med. Phys.* **25** 339–46
- [19] Mourtada F A, Soares C G, Seltzer S M and Lott S H 2000 Dosimetry characterization of ^{32}P catheter based vascular brachytherapy source wire *Med. Phys.* **27** 1770–6
- [20] Hafeli U O, Roberts W K, Meier D S, Ciezki J P, Pauer G J, Lee E J and Weinhaus M S 2000 Dosimetry of a W-188/Re-188 beta line source for endovascular brachytherapy *Med. Phys.* **27** 668–75
- [21] Gierga D P and Shefer R E 2001 Characterization of a soft X-ray source for intravascular radiation therapy *Int. J. Radiat. Oncol. Biol. Phys.* **49** 847–56
- [22] Amols H, Zaider M, Weinberger J, Ennis R, Schiff P and Reinstein L 1996 Dosimetric considerations for catheter-based beta and gamma emitters in the therapy of neointimal hyperplasia in human coronary arteries *Int. J. Radiat. Oncol. Biol. Phys.* **36** 913–21
- [23] Briesmeister J 1993 MCNP—A general Monte Carlo n-particle transport code. *MCNP User's Manual* Los Alamos National Laboratory
- [24] Bielajew A and Rogers D 1987 PRESTA: the parameter reduced electron-step transport algorithm for electron Monte Carlo transport *Nucl. Instrum. Meth.* **B18** 165–81
- [25] Stabin M, Konijnenberg M, Knapp Jr F F and Spencer R H 2000 Monte Carlo modeling of radiation dose distributions in intravascular radiation therapy *Med. Phys.* **27** 1086–92
- [26] *International Commission on Radiological Protection. Limits for Intakes of Radionuclides by Workers* 1979 ICRP Publication 30 (New York: Pergamon)
- [27] Lathrop K, Atkins H, Berman M, Hays M and Smith E 1976 MIRD Report No 8: Summary of current radiation dose estimates to normal humans from $^{99\text{m}}\text{Tc}$ as sodium pertechnetate *J. Nucl. Med.* **17** 74–77
- [28] Kotzerke J, Fenchel S, Guhlmann A, Stabin M, Rentschler M, Knapp F Jr and Roeske S 1998 Pharmacokinetics of $^{99\text{m}}\text{Tc}$ -pertechnetate and ^{188}Re -perrhenate after oral administration of perchlorate: Option for subsequent care after the use of liquid ^{188}Re in a balloon catheter *Nucl. Med. Comm.* **19** 795–801
- [29] Fonkalsrud E W, Sanchez M, Zerubavel R and Mahoney A 1977 Serial changes in arterial structure following radiation therapy *Surg. Gynecol. Obstet.* **145** 395–400
- [30] McCready R A, Hyde G L, Bivins B A, Mattingly S S and Griffen W O Jr 1983 Radiation-induced arterial injuries *Surgery* **93** 306–12

Chapter 15

The Monte Carlo method as a design tool in boron neutron capture synovectomy

David Gierga, Jacquelyn Yanch and Ruth Shefer

15.1. INTRODUCTION

Boron neutron capture synovectomy (BNCS) is a potential application of the $^{10}\text{B}(\text{n},\alpha)^7\text{Li}$ reaction for the treatment of rheumatoid arthritis. Rheumatoid arthritis is a chronic disease characterized by painful inflammation of the membrane (the synovium) lining the inner joint capsule of articulating joints. If left unchecked, synovial inflammation can lead to cartilage destruction, bone erosion and joint disability [1]. BNCS is envisioned as a two-part procedure involving, first, the injection of a ^{10}B -labelled compound directly into the joint, and second, irradiation of the joint with a beam of epithermal neutrons. The resulting $^{10}\text{B}(\text{n},\alpha)^7\text{Li}$ reaction imparts highly localized energy to regions selectively loaded with ^{10}B . The goal of BNCS is thus to deliver enough energy to ablate the synovium, thereby relieving the symptoms of rheumatoid arthritis.

The boron neutron capture reaction is also under investigation as a means of treating intracranial tumours and metastatic melanoma of the periphery by many different groups worldwide [2–5]. A number of Phase I and Phase I/Phase II clinical trials of boron neutron capture therapy (BNCT) are currently underway or have recently been completed. However, while both BNCT and BNCS rely on the same nuclear reaction to impart local dose to diseased cells, there are significant differences in the two clinical approaches that necessitate the design of neutron beams specific to each application. To date, published investigations of the development of BNCS have been limited to our group; hence this chapter will focus on the Monte Carlo-based neutron beam design that we have performed. Specifically, we will present both our strategy for the design of clinically relevant neutron beams for BNCS and the results of this design process. The optimized neutron delivery system has been constructed; this assembly will

be described and results of experimentally verifying the simulation predictions will be presented. The chapter will conclude with a discussion of Monte Carlo and experimental determination of patient dose and optimal patient shielding configurations.

15.1.1. Rheumatoid arthritis and current methods of treatment

Rheumatoid arthritis (RA) is a chronic, systemic disease of unknown origin characterized by painful inflammation of articular joints. The incidence in women is about 2–3 times higher than in men. RA occurs in all racial and ethnic groups, and affects approximately 1% of the worldwide adult population. RA can occur at all ages, but 80% of RA patients experience the onset of the disease between the ages of 35 and 50 [1]. Patients with RA can experience considerable distress as a result of joint pain and significantly restricted mobility. In addition to these debilitating conditions, those afflicted with RA have a shorter median life expectancy compared with the general population [6].

The first clinical signs of the disease are usually fatigue, fever and morning joint stiffness. Affected joints eventually become enlarged, tender and painful to move. RA initially involves small joints such as hands, wrists, knees and feet. As the disease progresses, elbows, shoulders, hips and ankles may be affected. The first manifestation of RA is a proliferation of synovial cells (synovitis), although the cause of the initial inflammatory response is unknown. During the onset of RA, synovial cells start to proliferate, increasing in number and in size. The amount of synovial fluid generated by the synovial cells also increases. As a result of synovial proliferation, a vascularized tissue (the pannus) forms and attacks the articular cartilage and bone, which if left unchecked can lead to cartilage destruction, bone erosion and joint disability.

The primary treatment for RA consists of using various drugs administered to reduce synovial inflammation. In approximately 10% of patients, however, one or more joints remain unresponsive to drug treatment and surgical management may be necessary. For patients who have suffered severe cartilage and bone damage and suffer from significant joint dysfunction, the only alternative is total joint replacement. The long-term durability of the total knee replacement is a concern. Subsequent to surgery, a 6 to 8 week period of physical therapy is required to allow the joint to become weight-bearing. Recovery from the surgery could also be complicated if the patient has multiple joints with RA. The cost of the procedure is also significant, ranging from \$25 000 to \$30 000 as of 1990 [7]. For these reasons, despite the high success rate of total knee replacement surgery, the procedure is only advised when there is severe joint pain from cartilage destruction and when the joint has not responded to drug therapy [7].

For patients who experience continued pain and inflammation from synovitis, an alternative to total knee replacement is available to preclude or slow the progression of cartilage or bone damage. This option is termed synovectomy, which is the physical removal of the inflamed synovium from the joint. The removal of this inflamed tissue leads to a reduction in joint swelling and pain, with the aim of providing better joint function. Synovectomy was initially performed as an open surgical procedure, although this has been replaced by arthroscopic synovectomy in recent years. Open surgical synovectomy has a number of disadvantages, including the potential for haemorrhage, the risks of anaesthesia, a long recovery period (3–6 weeks), unpredictable efficacy, and the ability to only remove about 80% of the synovium. Arthroscopic synovectomy is a much simpler procedure than open synovectomy, with post-operative hospital stays averaging only 3 days.

In many countries, radiation synovectomy has been used as an alternative to surgical synovectomy. Radiation synovectomy involves the intra-articular injection of a radionuclide (usually a β emitter), and relies on the energy deposition of the β particles to ablate the inflamed synovium. Radiation synovectomy is a much simpler procedure than both open and arthroscopic surgery, with only a local anaesthesia necessary, and the elimination of any rehabilitation time that would follow surgery. The most frequently used isotope is ^{90}Y , which has a 2.7 day half life, and a maximum β energy of 2.2 MeV. Radiation synovectomy using ^{90}Y (in the form of a silicate colloid) has been compared with open surgical synovectomy in knee joints, with both procedures showing similar recurrence rates [8]. Although radiation synovectomy using ^{90}Y or other β emitters has been shown to be effective, the US Food and Drug Administration has not approved its use because of the substantial risk of leakage of the radionuclide from the treated joint. Healthy tissue doses can be quite large, with doses between 250 and 500 cGy for the liver and between 5000 and 10 000 cGy for the lymph nodes [9].

15.2. BORON NEUTRON CAPTURE SYNOVECTOMY

Boron neutron capture synovectomy (BNCS) has been proposed as a method of performing radiation synovectomy that does not involve the use of any radioactive material [10]. BNCS is a two-part procedure (illustrated schematically in figure 15.1) in which a non-radioactive compound containing ^{10}B is injected into the joint fluid; next, after allowing time for synovial uptake of the compound, a beam of neutrons causes the ^{10}B to fission releasing two high-LET, high-RBE particles that travel distances less than the diameter of a cell. The $^{10}\text{B}(\text{n},\alpha)^7\text{Li}$ reaction delivers intense radiation damage to those cells that have previously been loaded with ^{10}B or their nearest

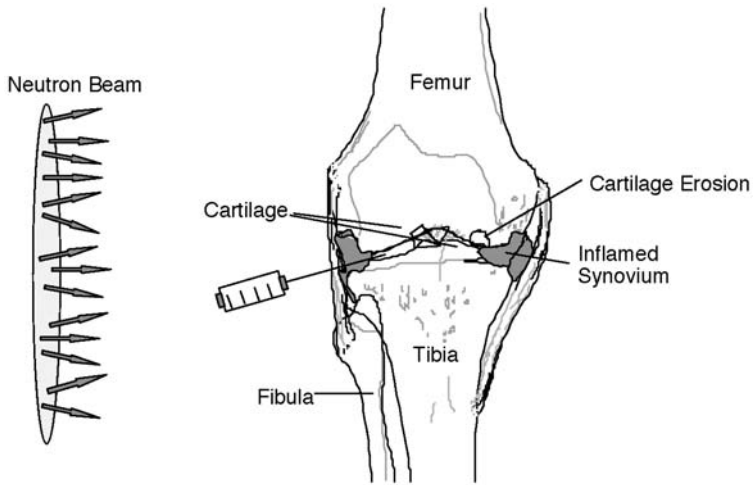


Figure 15.1. Schematic illustration of boron neutron capture synovectomy showing a coronal view of a rheumatoid human knee joint, the largest articulating joint in the body. In a rheumatoid knee the joint space is enlarged resulting from increased synovial fluid and thickened inflamed synovial tissue which, in this example, has begun to erode adjoining articular cartilage. For BNCS a boron-labelled compound will be injected directly into the joint space using a standard lateral approach. The joint will then be irradiated by a low-energy neutron beam.

neighbours. Like radiation synovectomy, BNCS results in synovial ablation by the delivery of radiation energy to the diseased membrane. The procedure could be performed on an outpatient basis and would require no rehabilitation. Unlike radiation synovectomy, there is no radiation hazard associated with leakage of the injected compound out of the joint. The ^{10}B remains stable both before and after the neutron bombardment. The radiation dose is only delivered while the tissue is undergoing neutron irradiation.

The use of the $^{10}\text{B}(\text{n},\alpha)^7\text{Li}$ nuclear reaction to treat diseases is not a novel concept. Boron neutron capture therapy (BNCT) was proposed in 1936 by Locher [11] as a potential treatment for cancer. Early clinical assessment of BNCT for malignant gliomas using thermal neutrons was initiated in the 1950s at Brookhaven National Laboratory (BNL) and at MIT [12, 13]. These clinical trials were not successful because of the insufficient penetration of thermal neutrons and the lack of tumour specificity of the boron compounds used. These factors contributed to excessive doses to normal brain tissue, and the trials were ended in 1961. BNCT trials were resumed, however, in Japan in 1968, and continue there to this day [2]. Recent advances in epithermal neutron beams and in boron-delivery agents led to a resumption of BNCT clinical trials: at MIT for intracerebral or sub-cutaneous melanoma and glioblastoma multiforme

[3], and at BNL [4] and the High Flux Reactor, Petten, The Netherlands [5] for glioblastoma. These clinical trials all use a nuclear reactor as an epithermal neutron source. Accelerator-based BNCT for glioblastoma is also under development [14–17].

There are several important differences between BNCS and BNCT. First, the target tissue in BNCS is the synovium, which is only 0.4 to 1.3 cm below the skin surface (depending on the affected joint), while brain tumours treated by BNCT can occur at depths up to 7 cm. Second, *in vivo* ^{10}B uptake studies have indicated that boron levels in the synovium on the order of thousands or tens of thousands of ppm are readily achievable [7]. In BNCS, the boron-labelled compound is injected directly into the fluid adjacent to the target tissue. In BNCT, conversely, the boronated compound is delivered systemically, so ^{10}B levels in the target tissue are significantly lower, usually on the order of 30–50 ppm. Finally, the joints to which BNCS would be most frequently applied (knee and finger joints) are not located near any radiosensitive organs of the body, whereas this is not the case in BNCT clinical trials in the brain. All of these factors result in significantly different neutron beam requirements for BNCS compared with BNCT.

15.3. NEUTRON BEAM DESIGN CALCULATIONS FOR BNCS

BNCS could, in principle, be performed using any prolific neutron source, including nuclear reactors, isotopic sources or charged-particle accelerators. Isotope sources, however, may have limited practical application as a result of their relatively low neutron output; storage of neutron-emitting sources can also be problematic. Accelerators are compact and inexpensive compared with nuclear reactors, and could be more easily installed in a hospital environment. Research in BNCS at the Laboratory for Accelerator Beam Applications (LABA) at MIT has therefore focused on accelerator sources for BNCS. A tandem electrostatic accelerator [18] capable of generating the proton and deuteron currents needed for the production of high-intensity neutron beams is in operation at MIT LABA; this accelerator was used extensively in the experimental evaluation of neutron beams for BNCS and in the investigation of the efficacy of BNCS in an animal model (see section 15.5 below).

The accelerator-based charged-particle reactions considered for BNCS included $^7\text{Li}(p,n)$, $^9\text{Be}(p,n)$, $^9\text{Be}(d,n)$, $^{13}\text{C}(d,n)$, $^2\text{H}(d,n)$ and $^3\text{H}(d,n)$ [19, 20]. However, these and all other charged particle reactions generate energetic neutrons. Since the cross-section for the boron neutron capture reaction increases as the neutron energy decreases (i.e., very low energy neutrons are desired for BNCS) then regardless of the neutron-producing reaction used, the emitted neutrons must be moderated or filtered down to an

energy suitable for clinical application. How to generate a clinically useful spectrum was then investigated using Monte Carlo simulation of neutron transport, as described below.

The Monte Carlo simulation code MCNP4B [21] was used for all beam design calculations. MCNP is public-domain simulation code developed at the Los Alamos National Laboratory and capable of handling coupled neutron–photon–electron transport problems. The code includes very robust geometry specifications, physics and cross section packages, and variance reduction capabilities. The code has been widely benchmarked [22–24] and examples of MCNP used to model neutron capture therapy problems abound in the literature [14, 15, 25–29].

15.3.1. *Optimal beam energy*

The first step in beam development was to determine the range of neutron energies that would be most useful for joint irradiation. Given the shallow depth of the synovium the optimal beam energy was expected to be lower than the energies determined to be optimal for BNCT. Using Monte Carlo simulation, an extensive ‘ideal beam’ study was performed in which the dosimetric effects of 20 monoenergetic neutron beams, ranging from 0.025 eV to 10 keV, were evaluated in a tissue-equivalent model of the human knee [7]. Both planar and isotropic beams were investigated. Each beam was evaluated in terms of its effect on two therapeutic ratios, namely the synovium dose to skin dose ratio and the synovium dose to bone surface dose ratio. A ^{10}B concentration of 1000 ppm was assumed in the synovium. This concentration is quite conservative relative to values measured in both *ex vivo* and *in vivo* experiments [7, 30].

Plotting therapeutic ratios as a function of incident beam energy showed similar trends for both therapeutic ratios and for both planar and isotropic beams. Dose ratios are high (approximately 80–120) for all energies below roughly 500 eV or 1 keV after which energy they begin to fall rapidly [7]. These results indicated that neutron beams with energies from thermal to approximately 0.5 keV to 1 keV are optimal for BNCS. This energy range is significantly lower than the range considered useful for BNCT and was used as a goal in subsequent studies to design a practical and therapeutically useful neutron beam.

15.3.2. *Optimal beam design*

Monte Carlo calculations using MCNP were performed to examine the ability of various moderator/reflector configurations to generate high-intensity neutron beams with low fast-neutron contamination. Early in the investigation the $^2\text{H}(\text{d},\text{n})$ and $^3\text{H}(\text{d},\text{n})$ reactions were dropped from consideration due to insufficient intensity in the moderated beam. However,

Table 15.1. Summary of charged-particle nuclear reactions considered for BNCS.

Reaction	Ion energy (MeV)	Average neutron energy at 0° (MeV)	Maximum neutron energy (MeV)	Neutron yield (n/min/mA)
$^7\text{Li(p,n)}$	2.5	0.6	0.79	5.34×10^{13}
$^9\text{Be(p,n)}$	4.0	1.06	2.12	6.0×10^{13}
$^9\text{Be(d,n)}$	2.6	2.02	6.95	8.4×10^{13}
	1.5	1.66	5.81	$1.67 \times 10^{13} *$
$^{13}\text{C(d,n)}$	1.5	1.08	6.77	1.09×10^{13}

* This yield was determined by matching simulated and measured phantom dose rates at MIT LABA. Yields in the literature range from 1.98×10^{13} to 9.64×10^{13} n/min/mA [32, 33].

encouraging results were obtained with the $^9\text{Be(p,n)}$ reaction at proton energies of 4.0, 3.7 and 3.4 MeV [31], the $^9\text{Be(d,n)}$ reaction at deuteron energies of 2.6 and 1.5 MeV [32, 33], the $^{13}\text{C(d,n)}$ reaction at a deuteron energy of 1.5 MeV [34], and the $^7\text{Li(p,n)}$ reaction at a proton energy of 2.5 MeV [35]. Table 15.1 provides initial yield and spectral information for these reactions at various particle bombarding energies.

A number of moderator/reflector configurations were evaluated by examining the dosimetric effect of each moderated beam in tissue-equivalent phantoms of the human knee and finger [20]. Each joint phantom (see figure 15.2) consisted of cylindrically concentric layers of tissue: bone, articular cartilage, joint fluid space, synovial lining, subsynovium, and fat and skin. The outer diameters of the knee and finger joint are 8.7 and 2.23 cm, respectively. Modelling of the human finger served a dual purpose since the dimensions of the arthritic finger are similar to the dimensions of the arthritic knee joint in rabbits. The arthritic rabbit model has been extensively used by various investigators in the development and evaluation of treatments for RA; we have also used this model to evaluate synovial

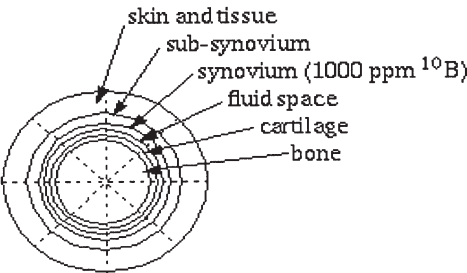


Figure 15.2. A cross-section through the cylindrically symmetric phantom representing the knee or the finger joint. Realistic tissue compositions were used and dimensions of each phantom were obtained from MR images.

uptake of boronated compounds *in vivo* [10] as well as to investigate the efficacy of BNCS (see below). Initial beam design simulations were carried out assuming a synovial concentration of 1000 ppm. Because of the magnitude of this concentration the boron in the synovium was explicitly modelled in all calculations [20]. All healthy tissues were assumed to contain 1 ppm ^{10}B . No data exist regarding RBE values of neutrons and $^{10}\text{B}(\text{n},\alpha)$ reactions in joint tissues. Therefore the RBE values commonly used for BNCT of brain tumors were adopted for this work: 4.0, 3.8 and 1.0 for the ^{10}B reaction products, neutrons and photons, respectively.

For all moderator/reflector configurations evaluated the moderator material was assumed to be D_2O and the length was varied to examine the effect on therapeutic ratios and dose rate. Extremely large therapeutic dose ratios were obtained with relatively small thicknesses of D_2O (i.e., high fast/thermal neutron ratios) due to the high ^{10}B concentration assumed in the target tissue. That is, neutron beams with significant fast neutron contamination may still be therapeutically useful since the joint will be exposed to the neutron beam for only a short period of time. High boron levels thus lead to considerable flexibility in beam design for BNCS as compared with the requirements for BNCT.

A number of reflector materials were examined including lead, graphite, $^7\text{Li}_2\text{CO}_3$ and D_2O . Highest dose rates at the phantom position were obtained with a graphite reflector. Use of D_2O as a reflector material (i.e., simply extending the moderator diameter) led to the highest therapeutic ratios as a result of its low atomic number, with the ratios using graphite only slightly lower. Since graphite is significantly less expensive than D_2O and provided the highest dose rate, it became the reflector of choice. Thus, a moderator/reflector assembly composed of D_2O and graphite was selected for subsequent optimization [20].

Results of these studies indicated that a superior beam would be produced by the $^7\text{Li}(\text{p},\text{n})$ reaction due to its high yield of low energy neutrons. However, given the practical difficulties in constructing and cooling a lithium target [36], our initial efforts to design and construct a useful BNCS beam have focused on the beryllium reactions listed above. Beryllium is well suited as an accelerator target material because of its mechanical strength, its high melting point and its high heat conductivity.

Two methods of improving both therapy time and therapeutic ratio were investigated [20]. The first involved parallel beam irradiation. That is, the joint (or the beam) would be moved such that the beam would be incident on the back of the joint for the second half of the irradiation. It was found that significant improvements in both therapy time and therapeutic ratios were possible using two parallel-opposed beams. However, little further improvement was seen as the number of irradiation directions increased beyond two since the beam is larger than the diameter of the phantom [19].

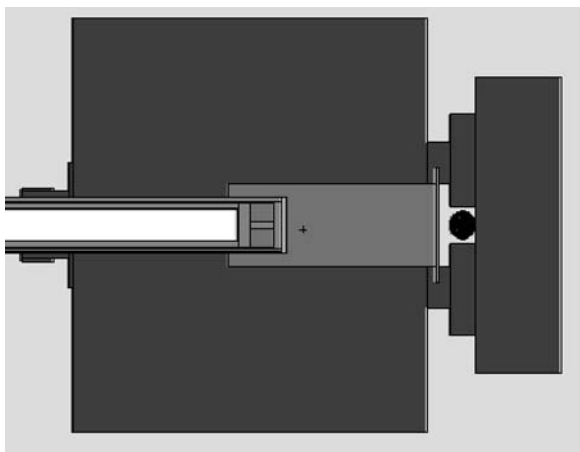


Figure 15.3. Two-dimensional plot through the MCNP model of the BNCS moderator/reflector assembly including target, cooling apparatus, phantom and graphite side and back reflectors around the phantom.

The second method of improvement involved the use of reflecting material placed immediately behind and to the sides of the joint during irradiation. This material provides the opportunity for neutrons to scatter back into the joint, increasing the synovium dose per incident neutron. Each scattering also serves to reduce the neutron energy. Thus, the effect of the back and side reflectors is to significantly reduce therapy time as well as to increase therapeutic ratios. While a number of possible low- Z materials could be used for this purpose, graphite was again chosen due to its low cost, availability and solid form.

Figure 15.3 shows an MCNP-generated plot of the optimized beamline configuration including graphite reflector, D_2O moderator, knee phantom surrounded by graphite side and back reflectors, and target with complete target cooling apparatus. Using the MCNP model, therapy parameters for joint treatments using various neutron-producing reactions were calculated as a function of ^{10}B uptake over a range of 1 to 20 000 ppm. This range of ^{10}B concentration was based on *in vivo* uptake studies using arthritic rabbits which showed that *average* boron levels of 19 000 for 30 min post-injection are readily achievable in the synovium. Boron tissue concentrations were explicitly included in the Monte Carlo simulations. Results are shown in table 15.2 for parallel irradiations of human knee and finger joints, using optimized graphite side and back reflector geometry. The therapy times listed in table 15.2 are based on an accelerator beam current of 1 mA, synovial boron concentrations of 1000 ppm ^{10}B , and the delivery of 10 000 RBE-cGy to the synovium, a value based on empirical estimates of the dose required to produce a clinical effect in β particle synovectomy [37].

Table 15.2. BNCS therapy parameters for human knee and human finger joints. These results are for the optimized configuration shown in figure 15.3, including side and back reflectors, assuming 1000 ppm ^{10}B uptake in the synovium, and parallel-opposed irradiations.

Neutron source	Moderator length (cm)	Therapy time (min mA)	Skin dose (RBE-cGy)	Bone ratio
Human knee				
2.6 MeV $^9\text{Be}(\text{d},\text{n})$	23	13	335	38
1.5 MeV $^9\text{Be}(\text{d},\text{n})$	20	48	586	22
4.0 MeV $^9\text{Be}(\text{p},\text{n})$	15	7.3	203	73
3.7 MeV $^9\text{Be}(\text{p},\text{n})$	15	10	190	79
2.5 MeV $^7\text{Li}(\text{p},\text{n})$	15	7	129	108
Human finger				
2.6 MeV $^9\text{Be}(\text{d},\text{n})$	23	6.1	227	42
1.5 MeV $^9\text{Be}(\text{d},\text{n})$	20	24	406	24
4.0 MeV $^9\text{Be}(\text{p},\text{n})$	15	3.6	161	62
3.7 MeV $^9\text{Be}(\text{p},\text{n})$	15	4.8	136	69
2.5 MeV $^7\text{Li}(\text{p},\text{n})$	15	3.3	91	108

Simulating a low boron concentration of 1000 ppm leads to therapy times of generally less than 15 min for a knee joint and less than 7 min for a finger joint. These times decrease significantly when higher synovial boron concentrations are assumed.

Based on the design predictions and results of the simulation studies, a fully operational BNCS beam line, including accelerator target, cooling system, and neutron moderator and reflector assembly has been constructed and installed on the high-current tandem accelerator at MIT LABA. A photograph of the installed assembly is shown in figure 15.4. The beamline consists of a 9 cm diameter, 23 cm long D_2O moderator surrounded by an 18 cm thick graphite reflector. The graphite reflector has been resin coated on its inner surface to make it impervious to the D_2O . The diameter of the D_2O moderator was chosen to be approximately the size of a human knee joint. The accelerator target assembly can be placed at any position along the central axis of the reflector/moderator assembly, which allows flexibility in the amount of D_2O between the target and the moderator exit window [20]. The neutron target itself consists of a beryllium tube 4 cm long and 3.2 cm in diameter which seals to an aluminium tube. The target length was chosen to minimize the number of secondary electrons escaping from the target during irradiation, thereby enabling the accelerator beam current to be measured more accurately. Beryllium was chosen as the target material because it is chemically stable and has good heat transfer characteristics including high melting point and thermal conductivity of 1283°C and $1.84\text{ W/cm}^\circ\text{C}$, respectively. The beryllium target is electrically insulated

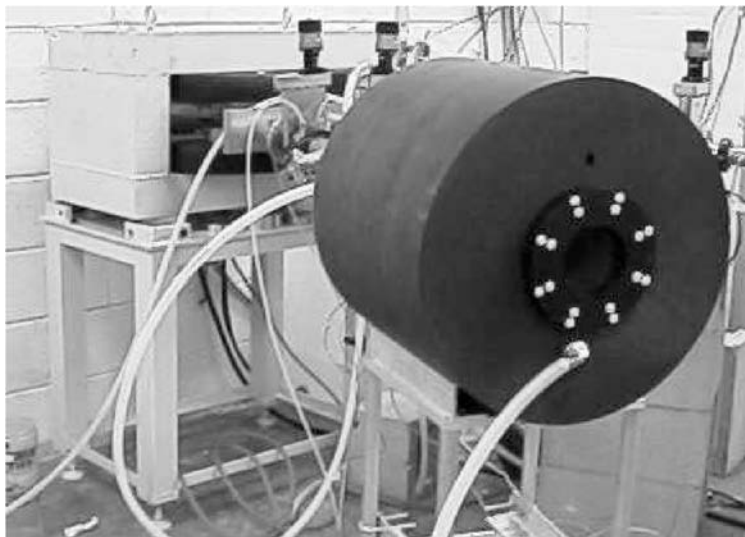


Figure 15.4. Photograph of the reflector (graphite) and moderator (D_2O) assembly installed on a dedicated beamline at MIT LABA.

from the aluminium tube, and target temperature is measured by a thermocouple attached to the centre of the target, on the coolant side of the beryllium. The target is cooled using the submerged jet-impingement technique, described by Blackburn *et al.* [36]. This technique can remove peak heat densities of over 5 kW/cm^2 and average heat densities of $1\text{--}2 \text{ kW/cm}^2$ over an 8 cm^2 target area. The target cooling system is schematically illustrated as part of the MCNP model shown in figure 15.3. The aluminium target tube is surrounded by two concentric coolant tubes. The water coolant enters the outer tube and is forced through a Teflon plug, which leads to a jet of water impinging on the beryllium target. Water then flows between the inner coolant tube and the aluminium target tube before exiting the assembly.

15.4. EXPERIMENTAL CHARACTERIZATION OF THE BNCS BEAM

The neutron beamline assembly shown in figure 15.4 was used in a dose escalation study to characterize the effects of BNCS in an animal model (see section 15.5). Prior to the initiation of these animal experiments, however, the MCNP predictions of the neutron and photon output of the BNCS moderator/reflector assembly were experimentally verified. Accurate knowledge of the thermal neutron flux in the phantom is important to quantify the boron dose and thus treatment time. Photon and fast neutron doses are also important in terms of dose to healthy structures such as the

skin and bone. Experimental validation of the MCNP-predicted in-phantom dose rates was performed using the dual ionization chamber technique in conjunction with foil activation analysis. This method of mixed field dosimetry is discussed in detail by Rogus *et al.* [38], and has been used extensively to characterize accelerator and reactor-produced epithermal beams for BNCT [38–40]. Given the difficulty of measuring the various dose components in a realistic (i.e., heterogeneous and small) model of the rabbit knee, beam characterization was performed in a water-filled phantom; experimental results were compared with MCNP predictions using a model of the same phantom.

Measurements were performed using the 1.5 MeV $^9\text{Be(d,n)}$ neutron source for moderator lengths of 8 and 23 cm, which result in very different neutron spectra at the output of the moderator/reflector assembly [20]. Figure 15.5 compares the thermal neutron and fast neutron dose rates determined by both experiment and simulation for the moderator length of 23 cm. The simulation results have been scaled to experiment at a depth of 4 cm. The experimental thermal neutron dose rates agree very well with simulation over the range of depths in the phantom. The data agree within one standard deviation from 2 to 10 cm, and agree within two standard deviations at the 1 cm dose point. The experimental fast neutron dose rates do not show such good agreement with simulation, but the data are still within two standard deviations.

Figure 15.6 compares the measured neutron dose rates with simulation for the 8 cm moderator length. In figure 15.6(a), simulation results are compared with the results of several experiments. Initial experiments only measured the thermal neutron dose at depths of 1 and 3 cm, while later experiments measured the full range of depths. It is difficult to compare with simulation at only one or two positions, especially if the neutron yield is uncertain, since the full shape of the dose profile is not available. The results from experiment 3 agree best with simulation when scaled at the 4 cm depth, and the effective neutron yield determined as a result of this scaling agrees well with the neutron yield determined from the 8 cm data, as well as the neutron yield determined from the fast neutron data at 23 cm. The results of all experiments are consistent in that they do agree within one to two standard deviations (depending on the depth in phantom) with each other and with simulation. Figure 15.6(b) compares simulation and experiment for the fast neutron dose rates in the phantom, with very good agreement between the measured and simulated values [20].

The neutron yield for the 1.5 MeV $^9\text{Be(d,n)}$ reaction varies widely in the literature. An effective neutron yield was determined by scaling simulation to experiment. Thermal and fast neutron dose rates were scaled at a depth of 4 cm in the phantom, as shown in figures 15.5 and 15.6. This allows the shape of the measured and simulated dose profiles to be compared even though there is uncertainty in the neutron yield. The consistency of the

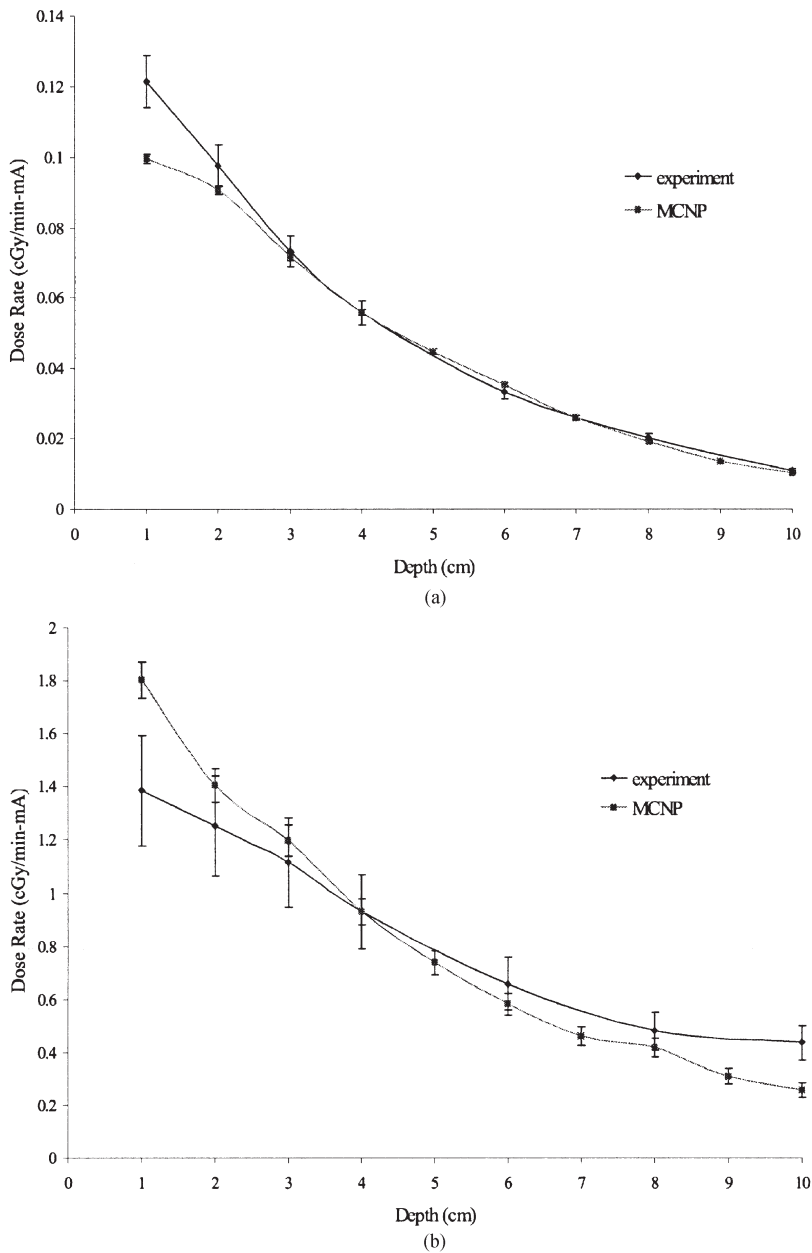


Figure 15.5. Comparison of experimental and simulation results for (a) the thermal neutron dose rate and (b) the fast neutron dose rate for a BNCS target position of 23 cm. Simulation and experiment have been normalized at a depth of 4 cm.

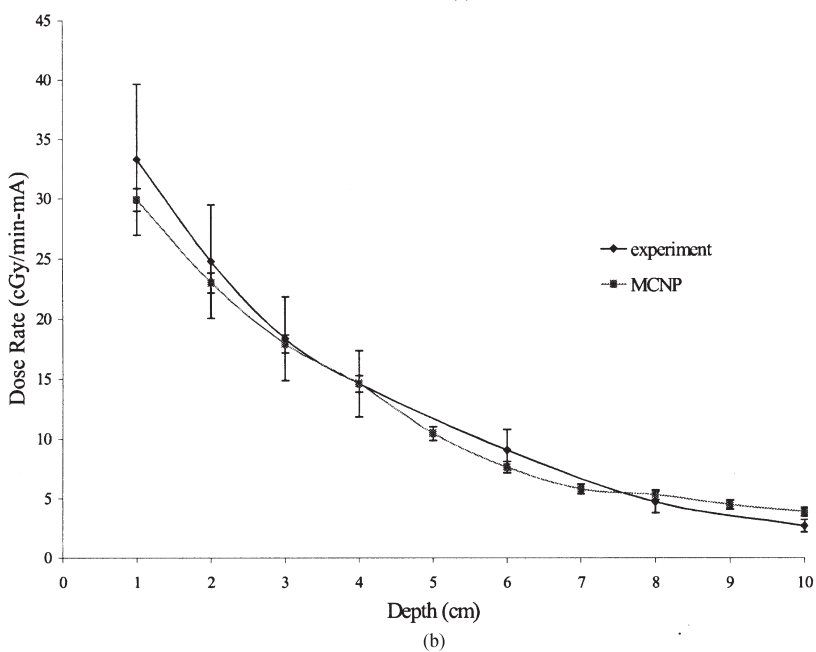
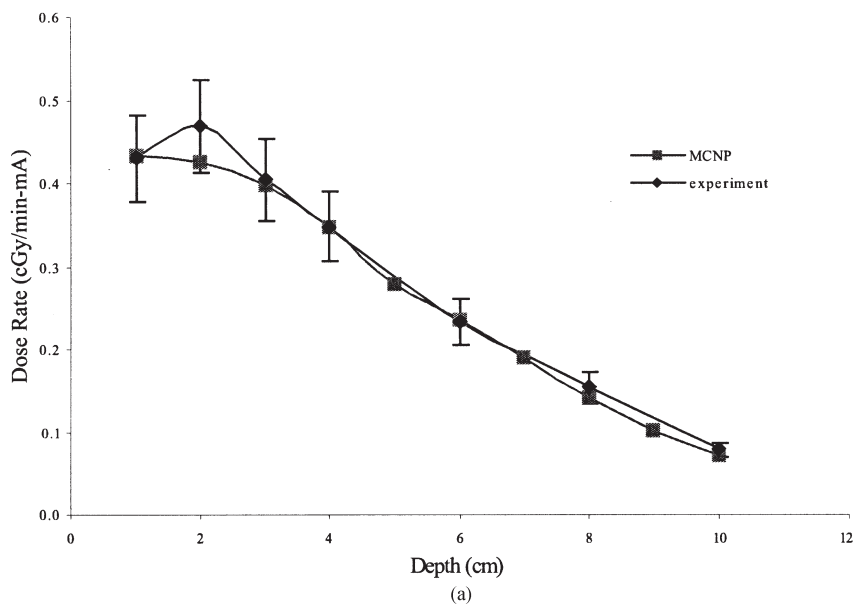


Figure 15.6. Comparison of experimental and simulation results for (a) the thermal neutron dose rate and (b) the fast neutron dose rate for a BNCS target position of 8 cm. Simulation and experiment have been normalized at a depth of 4 cm.

Table 15.3. Experimentally determined neutron yields for the 1.5 MeV $^9\text{Be}(d,n)$ reaction, determined by scaling thermal and fast neutron doses at two target positions.

Dose component	Scaling factor (n/min mA)	
	8 cm moderator length	23 cm moderator length
Thermal neutron	1.82×10^{13}	1.62×10^{13}
Fast neutron	1.64×10^{13}	1.58×10^{13}
Averaged	$1.67 \times 10^{13} \pm 1.1 \times 10^{12}$	

measured and calculated results was also assessed in terms of the effective neutron yield, as determined by scaling either the fast or thermal neutron dose rates at both target positions. Since the neutron yield of the 1.5 MeV $^9\text{Be}(d,n)$ reaction is a constant, the effective neutron yield determined by scaling either the thermal or fast neutron dose, under any initial conditions (i.e., for any target position), should also be constant.

Table 15.3 shows the effective neutron yield, determined by scaling thermal and fast neutron doses at two target positions. The neutron yields, for both dose components and target position, are very consistent and differ by no more than 13%, with an average value of 1.67×10^{13} n/min mA. The uncertainty in the effective neutron yield is estimated as 1.1×10^{12} n/min mA, based on the standard deviation of the four values given in table 15.3. Determining the neutron yield in this manner should be reasonable (assuming the neutron energy and angular distributions used in the simulation are fairly accurate), since the level of agreement in both the thermal and fast neutron doses is good for two target positions that lead to very different neutron spectra in the phantom.

15.5. EXPERIMENTAL INVESTIGATION OF BNCS IN AN ANIMAL MODEL

The efficacy of BNCS in an animal model was investigated through a series of rabbit irradiations using the BNCS neutron moderator/reflector assembly shown in figure 15.4. The purpose of these irradiations was to determine, in an animal model, if the combination of boron and neutrons could kill arthritic tissue without adversely affecting healthy tissues. In addition, the $^{10}\text{B}(n,\alpha)^7\text{Li}$ dose necessary to achieve synovial necrosis was investigated by examining histological sections taken from rabbits irradiated over a wide range of doses. The empirical estimate of the required dose, based on β particle radiation synovectomy studies, is 10 000 cGy [37]. However, a detailed dose study for β particle radiation synovectomy has not been

reported in the literature. The dose-delivering particles in BNCS are very different from those encountered in β particle radiation synovectomy and, in addition, the RBE values that should be used for BNCS are not known. The dose escalation study was therefore performed to characterize the therapeutic dose necessary in BNCS, and to study the effects of BNCS as a function of dose. This section will present a description of the rabbit irradiations and a determination of the BNCS dose response in rabbits.

The animals used in this dose escalation study were New Zealand white rabbits, using the antigen-induced arthritis (AIA) model. The complete protocol for the arthritis induction is described in Binello [7]. The rabbits were irradiated three days after the arthritis induction. After the rabbit was anaesthetized, the knee was injected intra-articularly with a $K_2^{10}B_{12}H_{12}$ solution containing 150 000 ppm ^{10}B . An injection of this concentration has been shown to lead to an average ^{10}B uptake of 19 000 ppm in the synovium [7, 30] for 30 min post-injection. Rabbits were irradiated with synovial doses ranging from 800 to 81 000 RBE-cGy. The 1.5 MeV $^9Be(d,n)$ charged particle reaction produced using the MIT LABA accelerator was used for these experiments. The beryllium target was placed 8 cm from the exit of the moderator/reflector system. MCNP was used to model the rabbit irradiation geometry and to calculate accelerator currents and irradiation times for various synovial dose levels.

Three types of control rabbit were also used. One set of controls consisted of arthritic rabbits not subjected to either the neutron irradiation or the injection of the boron compound (arthritic only). The second set received the boron compound, but were not irradiated (compound only). The third set consisted of rabbits that were irradiated for the same amount of time as the 81 000 RBE-cGy rabbits, but without boron in the synovium (neutron only). The synovium will receive some dose from the incident neutron beam and induced photons, but not from boron neutron capture events.

Twenty-eight rabbits were irradiated as part of the BNCS dose escalation study. Rabbits were sacrificed three days post-irradiation. At each dose point two animal knees were kept whole and decalcified for whole-knee histological examination, and the third knee was dissected, synovium removed, sectioned and stained with hematoxylin and eosin and examined for signs of tissue necrosis, cellular debris and inflammatory cell infiltrates [7]. A brief summary of the results is presented here.

The arthritic only control rabbits showed the expected features of the rabbit AIA model. The compound only and neutron only controls did not exhibit any effects different from the arthritic only controls. This implies that any effects seen in the other rabbits were a result of the combination of boron injection and subsequent neutron irradiations. At the 800 RBE-cGy dose, a decrease in the density of inflammatory cells and a decrease in the thickness of the synovial lining was observed. These effects were also

observed, to a greater extent, at the 2030 RBE-cGy dose, suggesting a dose-dependent response. At 3660 RBE-cGy, a further reduction in the number of inflammatory cells was observed, but still without examples of severe radiation-induced necrosis.

Clear evidence of synovial necrosis was observed at the 6900 and 7300 RBE-cGy doses. There was a decrease in the number and size of the synovial cells. There was evidence of cartilage damage, but it was unclear if this resulted from the arthritic condition or from the irradiation. At the very high doses (38 900 and 81 000 RBE-cGy), synovial necrosis was accompanied by what appeared to be radiation-induced damage to the femoral cartilage. The empirical estimate of the therapeutic dose from radiation synovectomy is 10 000 RBE-cGy, and there is a significant uncertainty associated with this estimate. Necrosis in this study was observed at 6900 and 7300 RBE-cGy (with an estimated uncertainty of 23%), about 30% lower than expected. Given the uncertainties in the dose calculation, this agreement is entirely within reason. Also, no synovial doses between 7300 and 38 900 RBE-cGy were examined; this dose range should be examined in further study. Since control rabbits showed no adverse effects, it can be concluded that the combination of boron and neutrons is effective in killing arthritic tissue in a rabbit model.

15.6. WHOLE-BODY DOSIMETRY FOR BNCS

The previous sections have focused on simulation and experiment to characterize the dose delivery to the targeted joint. The dose to the rest of the patient is also important, and should be minimized. Monte Carlo calculations were performed to characterize the effective dose for a number of neutron sources and shielding configurations that could be utilized in BNCS. To validate that Monte Carlo methods can be used to predict effective doses, experiments were performed using a whole-body phantom and the BNCS moderator/reflector assembly installed at LABA [20]. Experiments were done for both shielded and unshielded configurations. These results were compared with Monte Carlo simulations of the same configurations to assess the accuracy of MCNP predictions of whole-body dose.

The MCNP model of the BNCS moderator/reflector assembly was combined with an anthropomorphic phantom [41] of the human body in order to study the whole-body effective dose received during a knee treatment. The anthropomorphic phantom, shown in figure 15.7(a), is based on data from a number of sources, including MIRD [42], Cristy and Eckerman [43], Tsui *et al.* [44] and the Visible Man project [45]. Dosimetry calculations were performed for several of the candidate charged-particle reactions for BNCS. Several shielding configurations and materials were tested in an effort to reduce the effective dose. Shielding options included

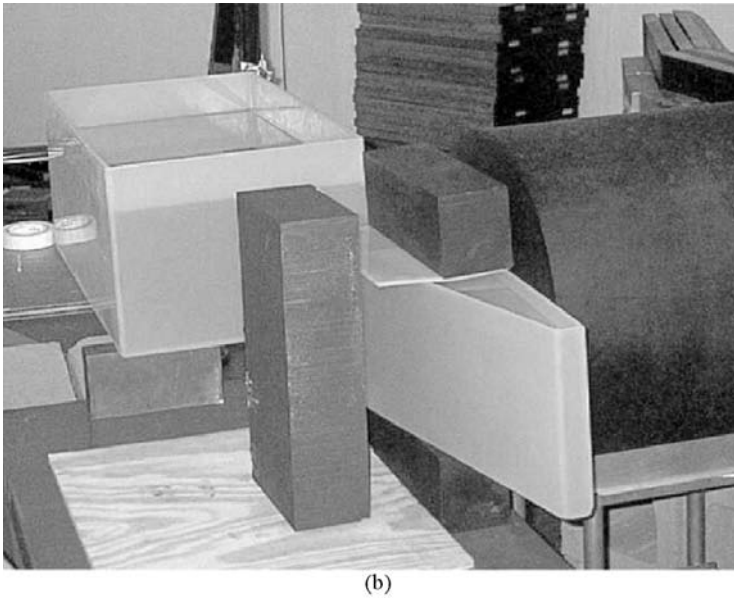
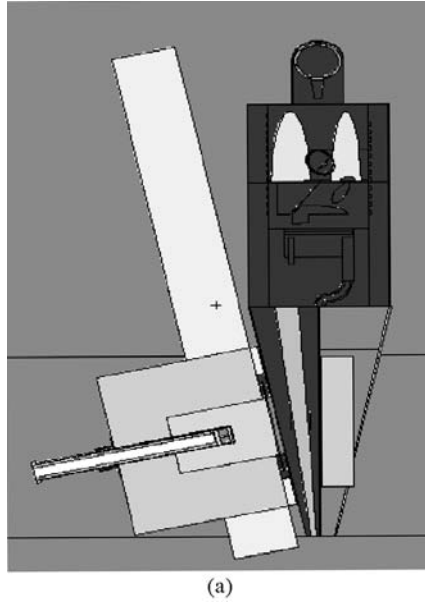


Figure 15.7. (a) MCNP simulation model including the anthropomorphic phantom and the BNCS moderator/reflector assembly. (b) Photograph of the phantom positioned for experiments without whole-body shielding. (See plate 5 for colour version.)

embedding the moderator/reflector assembly in a wall of boronated polyethylene, adding a neutron beam delimiter to the cylindrical graphite reflector assembly, and inserting additional shielding around the patient's legs. Results were generated for 19 000 ppm of ^{10}B uptake in the synovium.

The most effective shielding configuration was a combination of wall, delimiter and leg shields. This shielding configuration reduced the unshielded doses by a factor of roughly 2. For synovial boron uptake levels of 19 000 ppm, the effective doses for a shielded patient ranged from 0.13 rem to 0.72 rem for the 4 MeV $^9\text{Be}(\text{p},\text{n})$ and 2.6 MeV $^9\text{Be}(\text{d},\text{n})$ reactions, the softest and hardest spectra examined, respectively. Simulations indicated that a major component of whole-body dose resulted from neutrons entering the knee joint, and then scattering through the rest of the body; it is difficult to reduce this dose component without degrading neutron delivery to the targeted area.

Since the main clearance pathway of many boron compounds from the joint is through the urine, the dose to the bladder was specifically examined as a function of boron uptake. Depending on the source reaction, the bladder dose increases significantly when the boron uptake is in the range of 10–1000 ppm, and the whole-body effective dose increases significantly when the bladder boron uptake reaches several hundred to a thousand ppm. The estimated boron uptake in the bladder corresponding to an uptake of 19 000 ppm $\text{K}_2\text{B}_{12}\text{H}_{12}$ in the synovium was 2630 ppm. For the 4 MeV $^9\text{Be}(\text{p},\text{n})$ neutron source, this would increase the bladder dose from 0.12 rem to 0.45 rem.

Experiments were performed to verify that Monte Carlo methods could be used to predict effective doses, using a whole-body phantom and the BNCS moderator/reflector assembly installed at LABA. The whole-body phantom, composed of two water-filled tanks to represent the torso and one leg, is shown in figure 15.7(b). Experiments were done for both shielded and unshielded configurations. These results were compared with Monte Carlo simulations of the experimental configurations.

A combination of two dosimeters was chosen to characterize the mixed-field radiation dose for the whole-body dosimetry experiments: thermoluminescent dosimeters (TLDs) and bubble detectors. TLDs were chosen to characterize the photon dose, while the bubble detectors were chosen to measure the thermal and fast neutron dose. TLDs are attractive because they are sensitive to low doses, the dosimeters are small and thus will not significantly perturb the radiation field, and tissue equivalence is possible. Bubble detectors are also sensitive to low doses, are tissue equivalent, and insensitive to photons. Bubble detectors are available with and without thermal neutron sensitivity, so the neutron dose over a wide range of energies can be characterized.

In general, the total equivalent doses for both the shielded and unshielded experiments agreed well with simulation. The measured values

were less than the simulated values, which suggests that from the perspective of radiation protection, the MCNP calculations are conservative. In most cases, the measured individual dose components agreed within a factor of 2 with the simulated values. This level of agreement is considered reasonable for shielding problems and, in particular, for shielding measurements in a mixed radiation field. The exception to this was the thermal neutron doses for the shielded phantom, which agreed, on average, within a factor of 4 with simulation.

There are several reasons why the simulated and measured dose values were only expected to agree within a factor of a few. For the simulation, the results are only as accurate as the initial source specification. As described earlier, the neutron and photon sources may not be robust enough to accurately predict doses far from the target. In addition, the simulation results have been shown to be sensitive to the surrounding materials in the radiation vault. While an attempt has been made to accurately describe the vault in the Monte Carlo model, it is possible that further refinements in any approximations in the model of the vault may lead to better agreement between simulation and measurement. Furthermore, the simulation model neglects all radiation streaming effects, i.e., it assumes that the boronated polyethylene wall contains no cracks. Streaming effects could have a large effect on the shielded simulations, since the dose rates have been greatly reduced by the presence of the shield.

The determination of the photon dose rate is dependent on a correction for the induced TLD response from thermal neutrons, which can be quite significant. The thermal neutron response for the TLDs has been experimentally characterized in a thermal neutron beam at the MIT Research Reactor. The correction is also dependent, however, on the measured thermal neutron dose determined by the bubble detectors. The measured thermal neutron doses have been shown to be about a factor of 4 higher than calculated for the shielded results, and the experimentally determined photon response is about a factor of 3 lower than calculated. This may result from an over-correction of the induced thermal neutron response in the TLDs.

15.7. SUMMARY AND CONCLUSIONS

Boron neutron capture synovectomy is a promising modality for the treatment of rheumatoid arthritis and has been shown to be effective in causing synovial ablation in an animal model. Based on a single injection of a boron-labelled compound into the affected joint followed by neutron beam irradiation, BNCS is expected to be a simple procedure performed on an outpatient basis. The goal is to destroy the inflamed synovial tissue, thereby alleviating the symptoms of pain and disability. Similar to all existing methods of treating RA, BNCS addresses the symptoms of this disease

and not the cause, which remains unknown. Hence, recurrence is expected 2–5 years later. However, a repeat BNCS procedure, unlike a repeat surgical synovectomy, is expected to be a simple and straightforward procedure.

Monte Carlo methods have been used extensively in the design and evaluation of several aspects of BNCS. Monte Carlo calculations indicate, for a variety of neutron-producing charged particle reactions, that BNCS treatment times are very reasonable. Times based on a low ^{10}B concentration of only 1000 ppm are generally less than 15 min for a knee joint and less than 7 min for a finger joint, assuming an accelerator current of 1 mA. These times decrease even further when higher synovial boron concentrations are assumed. Associated whole-body effective doses can be kept low with appropriate shielding. Whenever possible, Monte Carlo predictions have been verified experimentally using a combination of detector types. Given the wide range of neutron energies encountered and the simultaneous presence of photons, detection and dosimetry is challenging. Combinations of ion chambers, foil activation, bubble detectors and thermoluminescent dosimeters have been used in the experimental evaluation of Monte Carlo predictions for BNCS. Agreement between simulation and experimental measurement of in-phantom therapy dose-rates was within two standard deviations.

REFERENCES

- [1] Lipsky P E 1991 *Rheumatoid Arthritis. Harrison's Principles of Internal Medicine* ed J D Wilson *et al.* (New York: McGraw-Hill) 12th edition pp 1437–43
- [2] Hatanaka H and Nakagawa Y 1994 Clinical results of long surviving brain tumor patients who underwent boron neutron capture therapy *Int. J. Radiat. Oncol. Biol. Phys.* **28** 1061–6
- [3] Busse P M, Zamanhof R, Harling O K, Kaplan J, Kaplan C, Chuang Goorley J, Kiger W S, Riley K, Tang L, Solares G and Palmer M 2001 The Harvard–MIT BNCT Program: overview of the clinical trials and translational research. In *Frontiers in Neutron Capture Therapy* eds M F Hawthorne, K Shelley and R J Wiersema (New York: Kluwer–Plenum) vol 1 pp 37–60
- [4] Diaz A Z, Chanana A D, Capala J, Chadha M, Coderre J A, Elowitz E H, Iwai J, Joel D D, Liu H B, Ma R, Shady M D, Slatkin N, Tyson G W and Wielopolski L 2001 Boron neutron capture therapy for glioblastoma multiforme: results from the initial phase I/II dose escalation studies. In *Frontiers in Neutron Capture Therapy* eds M F Hawthorne, K Shelley and R J Wiersema (New York: Kluwer–Plenum) vol 1 pp 61–72
- [5] Sauerwein W, Moss R, Hideghety K, Stecher-Rasmussen F, deVries M, Reulen H-J, Gytz C, Paquis P, Wiestler F and Gabel D 2001 Status report on the European clinical trial of BNCT at Petten. In *Frontiers in Neutron Capture Therapy* eds M F Hawthorne, K Shelley and R J Wiersema (New York: Kluwer–Plenum) vol 1 pp 81–86

- [6] Schiff M 1997 Emerging treatments for rheumatoid arthritis *Am. J. Med.* **102** (suppl 1A) 11S–15S
- [7] Binello E 1999 Efficacy of boron neutron capture synovectomy in an animal model. PhD Thesis. Massachusetts Institute of Technology
- [8] Gumpel J M and Roles N C 1975 A controlled trial of intra-articular radiocolloids versus surgical synovectomy in persistent synovitis *Lancet* **1** 488–9
- [9] Davis M A and Chinol M 1989 Radiopharmaceuticals for radiation synovectomy: evaluation of two yttrium-90 particulate agents *J. Nucl. Med.* **30** 1047–55
- [10] Yanch J C, Shortkroff S, Shefer R E, Johnson S, Binello E, Gierga D, Jones A G, Young G, Vivieros C, Davison A and Sledge C 1999 Boron neutron capture synovectomy: treatment of rheumatoid arthritis based on the $^{10}\text{B}(\text{n},\alpha)^7\text{Li}$ nuclear reaction *Med. Phys.* **26** 364–75
- [11] Locher G L 1936 Biological effects and therapeutic possibilities of neutrons *Am. J. Roentgenol.* **36** 1–13
- [12] Slatkin D N 1991 A history of boron neutron capture therapy of brain tumors: postulation of a brain radiation dose tolerance limit *Brain* **114** 1609–29
- [13] Farr L, Sweet W H, Robertson J S, Foste C G, Locksley H B, Sutherland D L, Mendelsohn M L and Stickley E E 1954 Neutron capture therapy with boron in the treatment of glioblastoma multiforme *Am. J. Roentgenol.* **71** 279–91
- [14] Yanch J C, Zhou X-L, Shefer R E and Klinkowstein R E 1992 Accelerator-based epithermal neutron beam design for neutron capture therapy *Med. Phys.* **19** 709–21
- [15] Allen D A, Beynon T D, Green S and James N D 1999 Toward a final design for the Birmingham boron neutron capture therapy neutron beam *Med. Phys.* **26** 77–86
- [16] Chris Wang C-K, Blue T E and Gahbauer R 1988 A neutronic study of an accelerator-based neutron irradiation facility for boron neutron capture therapy *Nucl. Technol.* **84** 93–107
- [17] Bleuel D L, Donahue R J, Ludewigt B A and Vujic J 1998 Designing accelerator-based epithermal neutron beams for boron neutron capture therapy *Med. Phys.* **25** 1725–34
- [18] Klinkowstein R E, Shefer R E, Yanch J C, Howard W B, Song H, Binello E, Blackburn B W, Daigle J L, Sears S M, Goldie C H and Ledoux R J 1997 Operation of a high current tandem electrostatic accelerator for boron neutron capture therapy. In *Advances in Neutron Capture Therapy* eds B Larson, J Crawford and R Weinreich (Amsterdam: Elsevier) vol I pp 522–7
- [19] Binello E, Shefer R E and Yanch J C 1997 Neutron beam design for boron neutron capture synovectomy. In *Advances in Neutron Capture Therapy* (Amsterdam: Elsevier) vol II pp 459–63
- [20] Gierga D P, Yanch J C and Shefer R E 2000 Development and construction of a neutron beamline for accelerator-based neutron capture synovectomy *Med. Phys.* **27** 203–14
- [21] Briesmeister J F 1997 *MCNP—A General Monte Carlo N-Particle Transport Code* Version 4B 1997. Los Alamos National Laboratory Report LA-12625-M
- [22] Whalen D J, Cardon D A, Uhle J L and Hendricks J S 1991 *MCNP: Neutron Benchmark Problems* Los Alamos National Laboratory Report LA-12212
- [23] Whalen D J, Hollowell D E and Hendricks J S 1991 *MCNP: Photon Benchmark Problems* Los Alamos National Laboratory Report LA-12196
- [24] Gierga D P and Adams K J 1999 *Electron/Photon Verification Calculations using MCNP4B* Los Alamos National Laboratory Report LA-13440

- [25] Zamenhof R, Redmond E, Solares G, Katz D, Riley K, Kiger S and Harling O K 1996 Monte-Carlo based treatment planning for boron neutron capture therapy using custom design models automatically generated from CT data *Int. J. Radiat. Oncol. Biol. Phys.* **35** 383–97
- [26] Allen D A, Beynon T D and Green S 1999 Design for an accelerator-based orthogonal epithermal neutron beam for boron neutron capture therapy *Med. Phys.* **26** 71–6
- [27] Lee C L, Zhou X L, Kudchadker R J, Harmon F and Harker Y D 2000 A Monte Carlo dosimetry-based evaluation of the ${}^7\text{Li}(\text{p},\text{n}){}^7\text{Be}$ reaction near threshold for accelerator-based boron neutron capture therapy *Med. Phys.* **27** 192–202
- [28] Kiger W S, Sakamoto S and Harling O K 1999 Neutronic design of a fission converter-based epithermal neutron beam for neutron capture therapy *Nucl. Sci. Eng.* **131** 1–22
- [29] Reed M K, Dobelbower M C, Woollard J E and Blue T E 1998 Mixed-field dosimetry measurement of a target assembly for an accelerator-based neutron source for boron neutron capture therapy *Nucl. Instrum. Meth. A* **419** 160–6
- [30] Yanch J C, Shortkroff S, Shefer R E, Binello E, Gierga D, Jones A G, Young G, Vivieros C and Blackburn B W 2001 Progress in the development of boron neutron capture synovectomy for the treatment of rheumatoid arthritis. In *Frontiers in Neutron Capture Therapy* eds M F Hawthorne, K Shelley and R J Wiersema (New York: Kluwer–Plenum) vol 2 pp 1389–98
- [31] Howard W B, Yanch J C, Grimes S M, Massey T N, Al-Quaraishi S I, Jacobs D K and Briant C E 2001 Measurement of the ${}^9\text{Be}(\text{p},\text{n})$ thick target spectrum for use in accelerator-based boron neutron capture therapy *Nucl. Sci. Eng.* **138** 145–60
- [32] Meadows J W 1991 *The thick-target ${}^9\text{Be}(\text{d},\text{n})$ neutron spectra for neutron energies between 2.6 and 7.0 MeV* Argonne National Laboratory Nuclear Data and Measurements Series ANL/NDM-124
- [33] Guzek J 1998 PhD Thesis, University of Witwatersrand, South Africa
- [34] Colonna N, Beaulieu L, Phair L, Wozniak G J, Moretto L G, Chu W T and Ludewigt B A 1999 Measurements of low-energy (d,n) reactions for BNCT *Med. Phys.* **26** 793–79
- [35] Liskien H and Paulsen A 1975 Neutron production cross sections and energies for the reaction ${}^7\text{Li}(\text{p},\text{n}){}^7\text{Be}$ and ${}^7\text{Li}(\text{p},\text{n}){}^7\text{Be}^*$ *At. Data Nucl. Data Tables* **15** 57–84
- [36] Blackburn B W, Yanch J C and Klinkowstein R E 1998 Development of a high-power water cooled beryllium target for use in accelerator-based boron neutron capture therapy *Med. Phys.* **25** 1967–74
- [37] Deutsch V, Brodack J W and Deutsch K R 1993 Radiation synovectomy revisited *Eur. J. Nucl. Med.* **20** 1113–27
- [38] Rogus R D, Harling O K and Yanch J C 1994 Mixed field dosimetry of epithermal neutron beams for boron neutron capture therapy at the MITR-II research reactor *Med. Phys.* **21** 1611–25
- [39] Raaijmakers C P J, Konijnenberg M W, Verhagen H W and Minkheer B J 1995 Determination of dose components in phantoms irradiated with an epithermal neutron beam for boron neutron capture therapy *Med. Phys.* **22** 321–9
- [40] White S M 1998 Beam characterization for accelerator-based boron neutron capture therapy using the ${}^9\text{Be}(\text{d},\text{n})$ nuclear reaction. MS Thesis. Massachusetts Institute of Technology
- [41] Lambeth M 1997 Development of a computerized anthropomorphic phantom for determination of organ doses for diagnostic radiology. BS Thesis. Massachusetts Institute of Technology

- [42] Snyder W S, Ford M R, Warner G G and Fisher H L Jr 1969 MIRD Pamphlet No 5 Supplement 3: Estimates of absorbed fractions for monoenergetic phantom sources uniformly distributed in various organs of a heterogeneous phantom *J. Nucl. Med.* **10** 46–52
- [43] Cristy M and Eckerman K F 1987 *Specific absorbed fractions of various ages from internal photon sources. I. Methods* ORNL/TM-8381/VI
- [44] Tsui B M W, Zhao X D, Gregoriou G K, Lalushl D S, Frey E C, Johnston R E and McCartney W H 1994 Quantitative cardiac SPECT reconstruction with reduced image degradation due to patient anatomy *IEEE Trans. Nucl. Sci.* **41** 2838–44
- [45] Lorensen W 1995 *Marching Through the Visible Man Proceedings of Visualization '95* (IEEE Press)

Chapter 16

Summary

Habib Zaidi and George Sgouros

Monte Carlo analysis in nuclear medicine has been used for several decades. Over this time, its use has evolved from a tool available to only a few expert physicists to one that may reside on a desktop computer and that is now potentially available for routine use. This evolution has been driven by four fundamental and critical developments:

1. The ever-increasing sophistication of imaging instrumentation and associated image analysis and processing methodologies, an area in which simulation studies have become essential.
2. The emergence of targeted radionuclides as a therapeutic modality, requiring improved and patient-specific dosimetry at the macro and micro level.
3. The availability of three- and four-dimensional computer phantoms providing flexibility and accurate modelling of populations of patient anatomies, and attenuation and scatter properties as well as biodistributions of radiopharmaceuticals in the patients.
4. The near exponential increase in the speed and proportional reduction in size and cost of computing power.

These four interrelated developments have fostered the work reviewed in this book.

The recent development of combined modality systems (e.g., SPECT/PET/CT/MRI) has created new opportunities for Monte Carlo simulation in imaging. These new imaging modalities in turn make it possible to meet the new requirements on dosimetry that have been driven by therapeutic nuclear medicine. The increasing availability of end-user image formation/analysis and dosimetry software packages that incorporate Monte Carlo calculations reflects all four of the developments listed above.

It is important to note that although Monte Carlo techniques have existed for decades, their use in therapeutic nuclear medicine and, in particular, in imaging-based patient-specific dosimetry is still in its infancy. This book may, therefore, be viewed as an early album containing several of the many and varied snapshots of this rapidly growing area.

Biosketches

The authors in this book are drawn from the leading research groups around the world. Habib Zaidi is senior physicist and head of the PET Instrumentation and Neuroscience Laboratory at Geneva University Hospital and his research activities centre on modelling nuclear medical imaging systems using the Monte Carlo method, dosimetry, image correction, reconstruction and quantification techniques in emission tomography. Dr George Sgouros is Associate Member, Department of Medical Physics at Memorial Sloan-Kettering Cancer Center and his research activities are in the field of dosimetry and systemic radiation therapy physics.

Habib Zaidi, PhD

Dr Habib Zaidi is senior physicist and head of the PET Instrumentation and Neuroscience Laboratory at Geneva University Hospital. He received a PhD in medical physics from Geneva University for a dissertation on Monte Carlo modelling and scatter correction in positron emission tomography. His research activities centre on modelling nuclear medical imaging systems using the Monte Carlo method, dosimetry, image correction, reconstruction and quantification techniques in emission tomography as well as functional brain imaging, and more recently on novel design of dedicated high-resolution PET scanners in collaboration with CERN. He is an associate editor for *Medical Physics* journal, member of the editorial board of the *International Journal of Nuclear Medicine*, regional editor for *Electronic Medical Physics News*, a publication of the International Organization for Medical Physics (IOMP), and scientific reviewer for several medical physics, nuclear medicine and computing journals. He is also affiliated to several international medical physics and nuclear medicine organizations and a member of the professional relations committee of the IOMP. He is involved in the evaluation of research

proposals for European and International granting organizations and participates in the organization of international symposia and conferences.

email: habib.zaidi@hcuge.ch

Web: <http://dmnu-pet5.hcuge.ch/>

George Sgouros, PhD

Dr George Sgouros is Associate Member, Department of Medical Physics at Memorial Sloan-Kettering Cancer Center. His research activities are in the field of dosimetry and systemic radiation therapy physics. He received his bachelor's degree from Columbia University School of Engineering and Applied Science and his PhD from Cornell University, Graduate School of Medical Sciences. He is the author of numerous chapters, peer-reviewed publications and conference proceedings in targeted radionuclide therapy and radionuclide dosimetry. He is a member of the Steering Committee of the American Association of Physicists in Medicine (AAPM), Task Group on internal emitter dosimetry and also a member of the Society of Nuclear Medicine's Medical Internal Radiation Dose (MIRD) Committee.

email: sgouros@mskcc.org

Pedro Andreo, PhD, DSc

Professor Pedro Andreo graduated (MSc) in Theoretical Physics in 1974, and got his PhD degree in 1982 at the University of Zaragoza (Spain). He moved to the Department of Medical Radiation Physics, Karolinska Institute–University of Stockholm (Sweden) as a Research Fellow in 1987, becoming Associate Professor and Doctor in Sciences (DSc) in Radiation Physics at the University of Stockholm in 1989. He was appointed Full Professor in Radiotherapy Physics at the University of Lund (Sweden) in 1993, and head of the Radiotherapy Physics group of this University Hospital. Between 1995 and 2000 he was the Head of the Dosimetry and Medical Radiation Physics Section of the International Atomic Energy Agency (IAEA), during which period he was the Secretary of the IAEA/WHO network of Secondary Standards Dosimetry Laboratories. Since 2000 he has been Full Professor of Medical Radiation Physics of the University of Stockholm. His scientific activities have emphasized the use of the Monte Carlo method in radiotherapy physics, mainly for absolute dosimetry and for treatment planning with electron and photon beams, where he was one of the pioneers in the field. His most recent activities have been focused on fundamental radiotherapy dosimetry of therapeutic proton and heavy ion beams using Monte Carlo methods.

e-mail: pedro.andreo@ks.se

Web: <http://www.ki.se/onkpat/radfys/>

Manuel Bardies, PhD

Dr Manuel Bardies was born in 1963. He obtained his MSc in Biomedical Engineering in 1988, then a PhD in Radiological Physics in 1991. During his PhD, he stayed at the Hammersmith Hospital in London for a year, with Dr M J Myers. He then joined INSERM (National Institute of Health and Medical Research) in 1992, and is working there as a research scientist in Professor J F Chatal's team. His fields of interest are all related to dosimetry for targeted radiotherapy, including quantitative imaging, dose calculations and small scale dosimetry.

email: manu@nantes.inserm.fr

Wesley Bolch, PhD

Wesley Bolch, PhD, PE, CHP, is Professor of Radiological and Biomedical Engineering at the University of Florida in the Department of Nuclear and Radiological Engineering. His current research interests include: (1) NMR microscopy of trabecular bone for improved dosimetric models of the skeleton, (2) development of tomographic computational models of newborn anatomy in support of paediatric radiology dosimetry, (3) incorporation of uncertainty analysis in internal dosimetry models, and (4) molecular models of radiation damage to DNA. Dr Bolch is a member of the Society of Nuclear Medicine's Medical Internal Radiation Dose (MIRD) Committee. He presently serves on the Board of Directors for the Health Physics Society.

email: wbolch@ufl.edu

Web: <http://www.nuceng.ufl.edu/>

Lionel Bouchet, PhD

Lionel G Bouchet was born in Grenoble, France, in 1971. He attended Lycée Pierre du Terrail high school in the French Alps, graduating in 1989. From 1989 until 1991, he prepared the entry exam to the French Engineering School at the Lycée Champollion in Grenoble, France. He entered the Engineering Physics School of Grenoble (ENSPG), France where he graduated in 1994. The same year, he entered graduate school at Texas A&M University in the Department of Nuclear Engineering, where he developed the new MIRD mathematical head and brain dosimetric model, which earned him an MSc degree in December 1994. In 1995 he commenced his doctoral research in Medical Health Physics in the Department of Nuclear and Radiological Engineering at the University of Florida, where he developed in collaboration with the MIRD Committee several dosimetric models for use in nuclear medicine. In 1999, he joined the Department of Neurological Surgery at the University of Florida as a Postdoctoral Research

Assistant working on image-guided radiotherapy and radiosurgery. In July 2000, he began an appointment as an Assistant Professor in the Department of Neurological Surgery at the University of Florida. His current research interests include three-dimensional image guidance in surgical procedures and in radiosurgery/radiotherapy, patient-specific virtual reality as applied to neurosurgical procedures, radiation transport and detection, and patient-specific internal dosimetry for nuclear medicine.

email: bouchet@neurosurgery.ufl.edu

A Bertrand Brill, MD, PhD

Randy Brill received his MD at the University of Utah in 1956, and his PhD at the University of California, Berkeley (Biophysics) in 1961. His dissertation advisor was Hardin Jones, and the topic was radiation leukemogenesis, a study based on the Hiroshima/Nagasaki A-bomb survivors. Randy started his career as a Public Health Service Officer assigned to the Atomic Bomb Casualty Committee following which he returned to the University of California to complete his PhD. He was assigned to Johns Hopkins (Assistant Professor, Radiology), where he set up a radiation epidemiology study to investigate the possible relation between ^{131}I administered to people and leukaemia, as a counterpart to the then known effects in the A-bomb survivors. Randy returned to academic medicine (Vanderbilt University) after 7 years in the PHS. He was an Associate Professor, then Professor, in Medicine/Physics/Radiology, co-Director, then Director of the Division of Nuclear Medicine and Biophysics. After 15 years, he left for Brookhaven National Laboratory where he served as Nuclear Medicine Program Coordinator for 7 years. Thereafter, he served as Professor and Research Director of the Nuclear Medicine Department at the University of Massachusetts Medical School for 10 years, following which he returned to Vanderbilt as Research Professor of Radiology and Physics. His current work involves the development of new nuclear medicine imaging receptors, and radiation dosimetry, particularly oriented to radioimmunotherapy and bone marrow effects.

email: Aaron.brill@vanderbilt.edu

Yuni Dewaraja, PhD

Yuni Dewaraja received her BS in Electrical Engineering from the University of Western Australia in 1986 after which she worked for 2 years as an engineer for the Atomic Energy Authority in Colombo, Sri Lanka. She received her MS in Nuclear Engineering from Kansas State University in 1990. She received her PhD in Nuclear Engineering from the University of Michigan in 1994 with a dissertation entitled 'Imaging neutron activation analysis and multiplexed gamma-ray spectrometry'. In 1996, she joined the Division of Nuclear

Medicine at the University of Michigan Medical Center where she is now an Assistant Research Scientist. Dr Dewaraja's current research activities include quantitative SPECT imaging, Monte Carlo methods in nuclear medicine imaging and three-dimensional absorbed dose calculation. Dr Dewaraja is a member of the Society of Nuclear Medicine and the IEEE.

e-mail: yuni@umich.edu

Dennis M Duggan, PhD

Dennis M Duggan received a PhD in Physics from the University of Southern California in 1986. Over 18 years, he worked as a computer programmer, microwave and electro-optical engineer, and solid-state physicist before beginning a fellowship in medical physics under Charles W Coffey II, PhD at the University of Kentucky in 1992. He followed Charles Coffey to Vanderbilt University and finished his fellowship there in 1994, and has been there ever since. His present research interests include radiation dosimetry, both theoretical and experimental, and quality assurance for all types of conformal radiotherapy including brachytherapy, both interstitial and intravascular, stereotactic radiosurgery, and intensity modulated radiotherapy, and the application of functional imaging, such as positron emission tomography and magnetic resonance spectroscopy imaging, to radiation therapy planning.

email: dennis.duggan@mcmail.vanderbilt.edu

John Humm, PhD

John Humm was awarded a PhD in 1983 for a dissertation entitled 'The analysis of Auger electrons released following the decay of radioisotopes and photoelectric interactions and their contribution to energy deposition', performed at the Institute for Nuclear Medicine, Nuclear Research Center in Jülich, Germany. He then worked at the MRC Radiobiology Unit in Harwell, Oxfordshire from 1983 to 1987, Charing Cross Hospital, London, in 1988 and Harvard Medical School, Boston, from 1989 to 1993. John Humm is currently the chief of the Nuclear Medicine Physics section at Memorial Sloan-Kettering Cancer Center, New York, where he has been since 1993. His interests are wide, spanning radiation biology to imaging and radiotherapy physics, with a special focus on targeted therapy, microdosimetry, and more recently positron emission tomography and molecular imaging.

email: hummj@mskcc.org

Web: <http://www.ski.edu/>

Timothy K Johnson, PhD

Dr Timothy K Johnson is currently Associate Professor in the Department of Radiation Oncology at the University of Colorado Health Sciences Center, Denver, Colorado. Dr Johnson received his MS degree in Medical Physics from the University of Colorado in 1981 and his PhD from the University of Minnesota in Biophysical Sciences, Medical Physics in 1990. From 1991 to 2001, he was the director of the Graduate Program in Medical Physics at the University of Colorado. He is a diplomate of the American Board of Radiology in Diagnostic Radiological Physics and Nuclear Medical Physics. Dr Johnson has served on AAPM Task Group No 7, Radionuclide Therapy and Data Acquisition Methods, since its inception. His research interests include activity quantification, mathematical modelling, image registration, image fusion, image segmentation, and Monte Carlo radiation transport.

email: Tim.Johnson@uchsc.edu

Amin I Kassis, PhD

Dr Amin I Kassis, Associate Professor of Radiology at the Harvard Medical School and Director of Radiation Biology, is a leader in the field of radiation biology. A major objective of his research has been an understanding of the implications of densely ionizing radiations (Auger electrons and α particles) emitted by diagnostic and therapeutic radionuclides. He has defined and established the biophysical relationship between the intracellular localization of low-energy electron-emitting radionuclides and the biological consequences of the resulting microdistribution of energy and has demonstrated the limitations of conventional MIRD dosimetry in estimating radiation risks to the patient. Another focus of his research has been the development of radionuclide carrier systems suitable for the precise delivery of diagnostic and therapeutic radioactive moieties to cancerous cells.

email: amin_kassis@hms.harvard.edu

Web: <http://www.jpnm.org/>

Katherine S Kolbert, MS

Katherine Kolbert has a master's degree in computer science from the Courant Institute at New York University, New York, and is currently with the Department of Medical Physics at Memorial Sloan-Kettering Cancer Center in New York City. She has developed a three-dimensional patient-specific dosimetry software package as well as other image analysis tools useful to the nuclear medicine-physics community. Copies of her software packages have been distributed to researchers around the world. She is also an author and contributor to numerous peer-reviewed papers and abstracts.

email: kolbertk@mskcc.org

Web: <http://www.ski.edu/>

Kenneth F Koral, PhD

Ken Koral received his BS degree in physics from Case Institute of Technology and his PhD in nuclear physics from its successor, Case Western Reserve University, Cleveland, Ohio. His dissertation advisor was Philip R Bevington, author of *Data Reduction and Error Analysis for the Physical Sciences*. Ken started his research career in medical physics during a year's postdoc in the United Kingdom. William H Beierwaltes recruited him to the University of Michigan Medical Center where his current title is Senior Research Scientist. Long-time collaborators and friends are Les Rogers and Neal Clinthorne. Ken's main research goal has been activity quantification in nuclear-medicine single-photon emission computed tomography. Assisted by Jeff Fessler and Yuni Dewaraja, he is the principal investigator of a US National Cancer Institute grant entitled 'Techniques for calculating tumor dosimetry from imaging'. Ken belongs to a family consisting of himself, his wife Mary and their three adopted children, one each from Viet Nam, India and South Korea. Those children have children: Maekong, Dante and Meagen Ann. They all enjoy movies, reading and hiking. Ken is a member of the Society of Nuclear Medicine and of the American Association of Physicists in Medicine.

email: kenkoral@umich.edu

Web: <http://www.rad.med.umich.edu/>

Cheuk S Kwok, PhD

Cheuk S Kwok received his PhD in Radiation Biophysics, Council for National Academic Awards, England, in 1979. He worked initially as a Medical Physicist with the Department of Clinical Physics and Bioengineering, West of Scotland Health Boards, Scotland, for about 2 years and then worked until the late 1990s as a Medical Physicist with the Ontario Cancer Treatment and Research Foundation, Ontario, Canada. Academic affiliation was with the Departments of Radiology and Physics, McMaster University, Ontario, Canada. He currently works as an Associate Professor with the Department of Optometry and Radiography, Hong Kong Polytechnic University and will work as a Senior Research Physicist, Department of Radiation Oncology, City of Hope National Medical Center, California, from September 2002. His current research is related to antibody-based targeted therapy of cancer and combination of specific traditional Chinese medicine with biological agents in cancer prevention and treatment. Dr Kwok has been awarded 26 peer-reviewed research grants at local and international levels and has published more than 50 papers in international refereed journals, conference proceedings and monographs.

email: orcskwok@inet.polyu.edu.hk

Web: <http://www.cityofhope.org/>

Michael Ljungberg, PhD

Michael Ljungberg began his studies in physics, mathematics and radiation physics in 1979 at the Lund University, Sweden, and received a BSc degree in physics in 1983. He started his research project in the Monte Carlo field with a project aimed at developing a Monte Carlo code for calibration of whole-body counters. This track developed into a more general Monte Carlo program, SIMIND, for simulation of nuclear medicine imaging and SPECT. This is a program that today is internationally recognized and used by several groups. Parallel with his continuing development of SIMIND, he started working in 1985 with quantitative SPECT and the problem of attenuation and scatter. He graduated for a PhD degree in 1990 and received a research assistant position at the Department of Radiation Physics, Lund University, where he continued work on the SIMIND code and on quantitative SPECT and in particular on ^{131}I imaging. In 1994, he became an associate professor at Lund University. His current research includes an extensive ongoing project in oncological nuclear medicine, developing methods based on quantitative SPECT and Monte Carlo absorbed dose calculations for patient-specific dosimetry and the development of co-registration methods for an accurate three-dimensional dose planning scheme for internal radionuclide therapy. In Lund, he is also involved in undergraduate education of medical physicists, course developments and supervising of PhD students. For several years, Dr Ljungberg has also worked as a certified medical physicist in diagnostic nuclear medicine at Helsingborg Hospital.

email: michael.ljungberg@radfys.lu.se

Web: <http://www.radfys.lu.se/>

John W Poston Sr, PhD, Professor

Since 1985, Dr John W Poston Sr has been a Professor in the Department of Nuclear Engineering at Texas A&M University in College Station, Texas. He received his PhD in Nuclear Engineering from the Georgia Institute of Technology in 1971. Professor Poston has served as President of the Health Physics Society (HPS) and was elected as a Fellow of this Society in 1987. He was elected Fellow of the American Nuclear Society (ANS) in 1996. In the autumn of 2001, he was elected Fellow of the American Association for the Advancement of Science (AAAS), the oldest scientific organization in the United States having been formed in the mid-1800s. He served as an elected member of the National Council on Radiation Protection and Measurements for 12 years and in 2002 was elected to Honorary Membership (lifetime) on the Council. His areas of expertise include internal dose assessment as well as external dosimetry of mixed radiation fields.

email: poston@ne.tamu.edu

John Roeske, PhD

John C Roeske obtained his undergraduate degree in Physics and Mathematics from DePaul University in Chicago. He subsequently attended the University of Chicago and received his doctorate in Medical Physics in 1992. His dissertation research focused on the dosimetry of radiolabelled antibodies for the treatment of ovarian cancer. Following graduation, Dr Roeske joined the faculty of the Department of Radiation and Cellular Oncology at the University of Chicago, and is currently an Associate Professor. His research has concentrated on the microdosimetry of α particles as well as the dosimetry of targeted therapy. His current interests include intensity-modulated radiotherapy and functional imaging.

email: roeske@rover.uchicago.edu

Web: <http://www.radonc.uchicago.edu/>

Ruth Shefer, PhD

Dr Ruth Shefer is president and co-founder of Newton Scientific, Inc. in Cambridge, Massachusetts, a company specializing in the development of particle accelerators and radiation sources for medicine and industry. Her research interests include the development of specialized neutron and X-ray sources for radiation therapy and diagnostic applications, and the development of accelerators and targets for radioisotope production. She received a BA in Physics from the University of Pennsylvania and a PhD in Physics from the Massachusetts Institute of Technology.

email: res@theworld.com

Web: <http://www.newtonscientificinc.com/>

Michael Stabin, PhD

Dr Stabin's areas of specialty are the dosimetry of internal emitters and radiation protection. He worked for 15 years at the Radiation Internal Dose Information Center in Oak Ridge, Tennessee, and currently works at Vanderbilt University in Nashville, Tennessee. The emphasis of his current research is on radiation dosimetry for nuclear medicine patients. He works as an associate editor for several journals and is active in the Health Physics Society and the Society of Nuclear Medicine.

email: michael.g.stabin@Vanderbilt.Edu

Web: <http://www.doseinfo-radar.com/>

Sven-Erik Strand, PhD

Professor Sven-Erik Strand was born 1946, received his MSc in 1972, his PhD in 1979 and his Medical Bachelor in 1981. He became Associate

Professor in 1981 and full Professor in 1995. Since 1981 he has been a lecturer at the University of Lund and teaching director at the Department of Radiation Physics. Since 1997 he has been director of the Jubileum Institute. From September 1991 until December 1992 he spent a sabbatical year at the Nuclear Medicine Department, Brookhaven National Laboratory. He has published about 160 regular articles, four book chapters and holds two patents. He has served as member of various international committees, such as the ICRU task group on internal dosimetry, the AAPM Nuclear Medicine Task Groups on dosimetry, and the EANM task group on radionuclide therapy dosimetry. He has served as reviewer for peer-written manuscripts in several journals and organized international symposia and conferences. Sven-Erik Strand's research activities are in the field of systemic radiation therapy physics including: registration of time-sequence three-dimensional pre-therapy radionuclide images from SPECT/PET with CT/MRI anatomical information for improved image quantification and to provide the basis for a three-dimensional radiotherapy planning method, the application of radioactivity quantification methods to determine tumour and non-target tissue radionuclide uptake; the use of regional radionuclide pharmacokinetics from time course quantitative SPECT/PET images, Monte Carlo methods to produce three-dimensional radiation dose distributions. He also participated in the EMERALD project and received the Bergman-Loevinger award in 2002 for his research in the field of internal dosimetry.

email: Sven-Erik.Strand@radfys.lu.se

Web: <http://www.radfys.lu.se/>

Jacquelyn C Yanch, PhD

Jacquelyn Ciel Yanch earned her PhD in Physics from the University of London in 1988. In 1989 she joined the faculty of the Nuclear Engineering Department at the Massachusetts Institute of Technology with a secondary appointment in MIT's Whitaker College of Health Sciences and Technology. Research in her laboratory, the MIT Laboratory for Accelerator Beam Applications, centres around medical and biological applications of low-energy accelerators including the development of novel therapies for treatment of disease and the development of a charged particle microbeam for single cell, single particle irradiations.

email: jcyanch@mit.edu

Web: <http://web.mit.edu/laba/www/>

Pat Zanzonico, PhD

Dr Pat Zanzonico received his PhD from the Cornell University Graduate School of Medical Sciences in 1972. He is currently Associate Attending

Physicist and Associate Laboratory Member at Memorial Sloan-Kettering Cancer Center and Manager of the Center's Nuclear Medicine Research Laboratory. Dr Zanzonico is also Associate Professor of Physics in Radiology at Weill-Cornell Medical College. He is a member of the Editorial Board and past Associate Editor of the *Journal of Nuclear Medicine*, a Member of the National Council on Radiation Protection and Measurement (NCRP), and Secretary of the Nuclear Medicine Section of the New York Academy of Medicine. He is actively involved in biomedical research on immune effector-cell trafficking, patient-specific dosimetry for radionuclide therapies, radionuclide-based methods for detecting and localizing tumour hypoxia, and small-animal imaging.

email: zanzonip@mskcc.org

Index

Numbers in **bold** refer to **figures** and those in *italics* refer to *tables*.

- 3D-ID, 148, 249, 250
- Absorbed dose, 28, 39, 41, 46, 61, 66, 68, 69, 74, 85, 86, 87, 88, 89, 90, 92, 96, 97, 98, 99, 100, 108, 111, 112, 114, 115, 116, 120, 126
- Absorbed fractions, 38, 110
- Activity distribution, 58, 63, 66, 101
- α particles, 15, 30, 175, 176, 179, 181, *184*, 189, 190, 204, 205, 206, 209, 219
- Analytic reconstruction, 71
- Annihilation photons, 74, 75, 76
- Attenuation, 31
 - Chang, 70
 - coefficients, 9, 68, 76, 241
 - non-uniform, 31
- Auger electrons, 87, 141, 164, 176, 181, 184, 185, 191, 213
- Backscattering, 393
- Bias, 18, 20, 42, 66, 70
- Bone, 44, 56, **69**, 110, 118
 - cortical, 39, 120
 - trabecular, 120, 125
- Bone-marrow, 59
- Boron neutron capture therapy, 29, 324, 327
- Boron neutron capture synovectomy (BNCS), 324, 326
- Brachytherapy, 144, 171
- Brain, 30, 186
- Blood flow, 12, 46
- Centroids, 12, 115
- Charged particles, 15, 87, 142, 182
 - bremssstrahlung, 13, 14, 40, 41, 113
 - class I, 14, 139
 - class II, 14
- Collimators, 34, 61, 71
 - cone beam, 42
 - design, 31, 37, 62
 - efficiency, 18, 63
 - hole, 37, 268
 - lead, 267, 26
 - high-energy, 37, 62, 267
 - medium energy, 272
 - parallel-hole, 36, 37
 - penetration, 37, 61, 62, 72, 262
 - pinhole, 37
 - scatter, 269, 273
 - septa, 62, 264, **268**
- Computational methods, 84, 276, 311
- Coster-Kronig, 185, 213
- Correction factors, 290
- Count rate, 72, 264
- Cumulated activities, 91, **92**, 96, 100, 234
- Cross section library, 12, 242
 - XCOM, **10**, **11**
 - PHOTX, 9, **10**
 - PETSIM, 9, **10**, **11**
 - GEANT, 9, **10**, *140*, 141
- ¹³⁷Cs, 35, 278
- CT images, 72, 73, 123, 147
 - Hounsfield units, 69
- Dead time, 56, 66, 75
- Detection, 13, 19, 31, 75, 133
 - forced, 71
- Detectors, 304, 342, 343, 344
 - BaF₂, 34

Detectors (*contd*)

- BGO, 7, **8**, 33, 34
- block detectors, 34
- CsF, 34
- energy resolution, 13, 34
- NaI, 230
- NaI(Tl), 34, 70, 230
- Diagnostic imaging, 22, 280
- DICOM, 252
- Directional cosines, 205
- DOSE3D, 121, 147
- Dosimetry, 14, 28
 - external dosimetry, 139
 - internal dosimetry, 33, 39, **45**, 84
- Dual-isotope, 71
- Dynamic allocation, 236
- EGS4, 9, 12, 14, 21, 30, 40
 - PEGS, 139
 - PRESTA, 293, 298
- EGSnrc, 21, 40
- Eidolon, 36
- Electron, 12
 - energy, 14, 116, 119, 136, 167, 216, **217**
 - interaction, 14, 293, 298
 - transport, 1, 7, 13, 14, 18, 22, 39, 115
- Emission, 10, 18, 30, 31
- Energy distribution, 34, 40, 135, 161
 - pulse-height distribution, 267
- Energy resolution, 13, 34
- ETRAN, 14, 40
- ¹⁸F-Fluorodeoxyglucose (FDG), 37
- FORTRAN, 5, 139, 234
 - Fortran-90, 264
- FWHM, 34, 36
- Gamma rays, 56, 61, 62, **69**, 111
- Gaussian, 13, 63
- GEANT, 9, **10**, 141
- Geometrical efficiency, 18
- Heart, 42, 116, 121, 179
- Human anatomy, 90, 98, 121, 249
- ¹³¹I, 36, 38, 43, 45, **68**, 96, 97, 98, 117, 119, 161, 163, *164*, 165, 166, 186
- ¹¹¹In, 117, 161, 163, 166
- Interfile, 252
- Intravascular radiation therapy, 29
- Iterative reconstruction, 67, 70, 76, 77
- ITS, 9, 40, 43, 139, 141

Klein–Nishina, 12, 241, 242
 Kernels, 36, 39, 46, 101, 148, 158

Light output, 275

Luminescence, 275

MABDOS, 90, 121, 147, 232, 233

MCNP, 3, 9, 43, 123, 139

MCNP-4B, 30, 39

MIRD, 28, 38, 39, 56, 84, 89, **91**, **92**, **93**, 95, 110, 112, 123

MIRDOSE, 90, 115, 116, 148

Mechanical, 187, 215, 310, 331

Microdosimetry, 85, 202, 203, 205

Monoclonal antibodies, 28, 147, 188

Monte Carlo codes, 1, 7, 15, 36, 38, 133, 135, 139, *140*

event-based, 152

photon history, 13

Monte Carlo methods, 3, 4, 22, 34, 40, 43, 44, 66, 135, 203

analogue, 16, 19

modelling, 9, 22, 31, 34, 38, 44

simulations, 7, 29, 34, 36, 38, 41

Monte Carlo techniques, 1, 2, 22, 28, 29, 31, 41, 110, 249, 288

MORTRAN, 139

Magnetic resonance imaging, 126, 302

Maximum-Likelihood-Expectation-

Maximization (MLEM), 67, **68**

MRI images, 57, 116, 148

Neutrons, 2, 30, 87, 124

beam, 30, 43, 324, 327, 328, 329

Noise, 42, 65, 67, **68**, 70, 72, 74

Poisson, 18, 203, **204**, 205, 219

Non-homogeneous, 70, 71, 274

Nonlinear, **67**, 246, 298

Nonuniform, 142, 189, 209, 212, 220

¹⁵O-water, 78

Optical coupling, 34

Ordered Subsets Expectation Maximization (OSEM), 63, **64**, 68

ORNL phantoms, 117, 118, 120, 121

Parallel computers, 6, 150, 151, 152, 264

Parallel processing, 31, 150

Path length, 21, 159, 167, 205, 206, 251, 252, 290

PET scanners, 13, **35**, 36

design, 34

- detector module, 264
- scintillation crystal, 61
- sensitivity, 34, 74, 75
- time-of-flight, 34
- PETSIM, 9, **10**, **11**
- Phantoms, 39, 65, 109, 110, 111, 114, 115, 265
 - 3D Hoffman, 12, 36, **37**
 - MCAT, 265
 - NCAT, 265
 - anthropomorphic, 39, 111
 - female organs, 137
 - mathematical, 28, 114, 115
 - shape-based, 110
 - voxel-based, 123, 149, 264, 265
 - VIP-Man, 39, **40**
 - Zubal phantom, 265
- Photomultipliers, 13
- Photomultiplier tubes (PMTs), 34
- Photon fluence, 289
- Photon histories, 112, 150, 243
 - history weight, 18
- Photon history generator (PHG), 264
- Photon interactions, 7, 14, 112, 113, 289
 - bound electrons, 9
 - coherent scattering, 7, 13, 139
 - Compton scattering, 14, 70, 142, 268
 - cross section tables, 245
 - incoherent scattering, 7, 12, 17
 - lookup tables, 241, 242, 254, 313
 - pair production, 9, 134, 136, 139, 242
 - photoelectric absorption, 12, 13, 139
 - photoelectric effect, 12
- Photon transport, 7, 12, 18, 112, 113, 116, 121, 125, 135, 142, 162, 233, 236
 - heterogeneous media, 264
- Photopeak, 34, 74, 265
- Pile-up, 264
- Planar imaging, 31, 57, 257, 258, 263, 288
- Point-spread function (PSFs), 267
 - exponential, 38
 - Gaussian, 63
 - geometric component, 267
 - penetration component, 267, 272
 - scatter component, 267, 272
 - radially symmetric, 38
 - simulated, 38
- Position blurring, 13
- Positrons, 47, 85, 141, 142, 241
 - emitters, 39, 46, 47
 - range, 13
- Positron emission tomography (PET), 7, 31, 57
- Probability density functions, 2, 3, 33, 134
- Probability distributions, 13, 134, 241, 242, 313
- Pulse sequence, 296
- Quality factor, 88, 89
- Radiation protection, 29, 42, 43, 84, 87, 88, 102, 136, 141, 202, 290, 291, 297, 343
- Radiation therapy, 22, 29, 143, 321
- Radiation transport, 2, 6, 7, 12, 22, 28, 31, 39, 109, 121, 123, 124, 139, 141, 144, 233, 243, 293, 294, 295, 296, 311
- Radioactive decay, 90, 101, 234, 241
- Radiobiology, 214
- Radioimmunotherapy, 28, 78, 277, 278, 280, 288, 304
- Radionuclide dosimetry, 84, **91**, **92**, **93**, 158, 160, 168, 171, 228, 233, 234, 246, 275, 276
- Radionuclide therapy, 29, 71, 84, 98, 125, 144, 182, 193, 221, 250, 252, 262, 275, 276, 277, 280, 300, 311
- Random coincidences, 75
- Random numbers, 1, 3, 4, 5, 6, 16, 29, 33, 134, 151
- Reference man, 56, 89, 98, 112, 118, 120, 124, 126, 136, 142, 167, 232, 234, 236, 237, 242, 295
- Reflector, 30, 329, 330, 331, **332**, **333**, **334**, 338, 339
- Sampling, 1, 3, 13, 16, 17, 18, 20, 21, 28, 33, 40, 137, 162, 164, 205, 280, 292, 293, 297, 298, 313
 - direction, 242
 - selection of the type of photon interaction, 134
- Sampling techniques, 33
 - collimator, 268, 69, 273
 - Compton, 2, 13, 34, 70, 142, 267
 - Compton window, 74
 - cumulative distribution function, 16, 17
 - direct method, 17
 - effective scatter (ESSE), 71
 - energy threshold, 34, 139
 - mixed methods, 17
 - multiple scattering, 14, 20, 21, 142, 161
 - object, 267
 - patient, 61, 230
 - rejection method, 17
 - scatter, 34, **35**, 36
 - scattered photons, 12, 16, 34, 61, 70, 162

- Sampling techniques (*contd*)
 - single scattering, 14
 - subtraction, 70
 - transmission images, 34, 60, 61, 68, 75, 76, 77, 264
 - transport equation, 31, 161
- Scatter correction methods, 36, 61, 70
 - convolution, 70
 - dual-energy window, 70
 - energy-based, 36, 70
 - inverse Monte Carlo, 36
 - iterative reconstruction, 77
 - model, 77
 - Monte Carlo method, 71
 - response functions, 71
 - triple-energy window, 70
 - Wiener filtering, 71
- Scatter fractions, **35**, 36
- Scatter response functions, 70
- Scintillation camera, 34, 36, 59, 72, 231, 262, 264, 267, **268**
- sensitivity, 37, 46, 74, 268
- Segmentation, 55, 57, 58, 64, 71, 76, 121, 122, 124, 233, 237, 245, 265
- Shielding, 13, 20, 43, 44, 234, 312, 325, 340, **341**, 342, 344
- SIMIND, 264, 269
- SimSET, 264
- Single-photon emission computed tomography (*see* SPECT), 31
- Software, 36, 47, 115, 121, 123, 125, 133, 138, 141, 146, 148, 149, 150, 228, 229, 234, 245, 246, 249, 250, 251, 252, 258, 264, 265, **273**, 281, 292, 348
 - phantoms, 265, 281
- Source geometry, 43, 211, 291
- Spatial resolution, 13, 34, 37, 62, 66, 68, 71, 74, 258, 259, 266, 271
 - collimator, 36, 38, 62, 65, 264
 - FWHM, 36
 - system resolution, 42, 267, 271
- Specific absorbed fraction, 28, 38, 39, 91, 113, 115, 116, 117, 120, 158, 159, 251, 289, 290, 292
- SPECT, 31, 32, 34, 36, 38, 42, 45, 57, 58, 59, 60, 62, 66, 67, 68, 69, 70, 71, 72, **73**, 74, 75, 76, 77, 79, 148, 152, 231, 251, **254**, 255, 257, 262
 - contrast, 66, 71, 72, 89, 267, **269**
 - myocardial perfusion studies, 42
 - projection data, 42, 45, 56, 66, **67**
 - quantification, 64, 274
 - reconstruction, 66
 - resolution, 64, 71, 75
 - simulation, **67**, 152, 269
 - transmission, 34, 68, 76, 264
- Statistical uncertainty, 3
- Statistical variations, 161, 233
- Stratification, 19
- ^{99m}Tc, 34, **67**, 117, 119, 163, 166, 203, 214, 266, 267, 269, 302
- Therapy, 30, 36, 47, 55, 56, 59, 61, 62, 66, 77, 96, 118, 135, 143, 144, 145, 146, 152, 153, 181, 182, 184, 187, 204, 218, 220, 273, 278, 279, 296, 299, 300, 301, 310, 311, 313, 322, 325, 331, 332, 333, 344
- Treatment planning, 29, 43, **45**, 46, 47, 59, 75, 84, 96, 133, 148, 153, 299
- ²⁰¹Tl, 117, 214
- Tomographic imaging, 46, 57, 58, 71, 72, 101, 265
- Transmission scanning, 34
 - single-photon sources, 34
- Transmission simulation, 34
- Tumour, 30, 36, 38, 55, 56, 57, 59, 60, 61, 64, 65, 67, 72, **73**, 77, 78, 84, 90, 96, 97, 98, 100, 101, 144, 145, 147, 148, 179, 186, 186, 187, 189, 208, 218, 220, 228, 229, 231, 232, 237, 246, 249, 251, 262, 267, **269**, 271, 299, 300, 312
- User interface, 236
- Validation, 29, 34, 165, 263, 264, 267, 269, 274, 335
- Variance, 3, 16, 20, 22, 57, 64
- Variance reduction, 1, 3, 18, 20, 29, 36, 71, 140, 150, 329
 - forced detection, 71
 - Russian roulette, 20, 135
 - splitting, 20
 - stratification, 19
- Vector processors, 151
 - vectorizable, 4
 - vectorization, 3
- Vessel wall, 311, 313, 314, **317**
- Weight factor, 20, 89
- Whole-body imaging, 59, 265
- ¹³³Xe, 117
- X-rays, 87, 141, 273
- XCOM, 10, 11